Jet evolution in a dense QCD medium

Paul Caucal

université
PARIS-SACLAY

Jet evolution in a dense QCD medium

Thèse de doctorat de l'Université Paris-Saclay

École doctorale n° 564 : physique en l'Île-de-France (PIF)
Spécialité de doctorat: physique
Unité de recherche: Université Paris-Saclay, CNRS, CEA, Institut de physique théorique, 91191, Gif-sur-Yvette, France.
Référent: Faculté des sciences d'Orsay

Thèse présentée et soutenue à Gif-sur-Yvette, le 4 septembre 2020, par

Paul Caucal

Composition du jury:

Samuel Wallon Professeur des universités, Université Paris-Saclay, IJCLab	Président
Carlos Salgado Professeur des universités, Galician Institute of High Energy Physics	Rapporteur & Examinateur
Konrad Tywoniuk Directeur de recherche, Université de Bergen	Rapporteur & Examinateur
Matteo Cacciari Professeur des universités, Université Paris Diderot, LPTHE	Examinateur
Leticia Cunqueiro Chargée de recherche, Oak Ridge National Laboratory, CERN	Examinatrice
Edmond Iancu Directeur de recherche, Institut de Physique Théorique	Directeur
Gregory Soyez Directeur de recherche, Institut de Physique Théorique	Codirecteur

Thèse de doctorat

NNT: 2020UPASP002

Abstract

Besides the emblematic studies of the Higgs boson and the search of new physics beyond the Standard Model, another goal of the LHC experimental program is the study of the quark-gluon plasma (QGP), a phase of nuclear matter that exists at high temperature or density, and in which the quarks and gluons are deconfined. This state of matter is now re-created in the laboratory in high-energy nucleus-nucleus collisions. To probe the properties of the QGP, a very useful class of observables refers to the propagation of energetic jets. A jet is a collimated spray of hadrons generated via successive parton branchings, starting with a highly energetic and highly virtual parton (quark or gluon) produced by the collision. When such a jet is produced in the dense environment of a nucleus-nucleus collision, its interactions with the surrounding medium lead to a modification of its physical properties, phenomenon known as jet quenching.

In this thesis, we develop a new theory to describe jet quenching phenomena. Using a leading, double logarithmic approximation in perturbative QCD, we compute for the first time the effects of the medium on multiple vacuum-like emissions, that is emissions triggered by the virtuality of the initial parton. We show that, due to the scatterings off the plasma, the in-medium parton showers differ from the vacuum ones in two crucial aspects: their phase-space is reduced and the first emission outside the medium can violate angular ordering. A new physical picture emerges from these observations, with notably a factorisation in time between vacuum-like emissions and medium-induced parton branchings, the former constrained by the presence of the medium. This picture is Markovian, hence well suited for a Monte Carlo implementation. We develop then a Monte Carlo parton shower called `JetMed` which combines consistently both the vacuum-like shower and the medium-induced emissions.

With this numerical tool at our disposal, we investigate the phenomenological consequences of our new picture on jet observables and especially the jet nuclear modification factor R_{AA}, the Soft Drop z_g distribution and the jet fragmentation function. Our Monte Carlo results are in good agreement with the LHC measurements. We find that the energy loss by the jet is increasing with the jet transverse momentum, due to a rise in the number of partonic sources via vacuum-like emissions. This is a key element in our description of both R_{AA} and the z_g distribution. For the latter, we identify two main nuclear effects: incoherent jet energy loss and hard medium-induced emissions. Regarding the fragmentation function, the qualitative behaviour that we find is in agreement with the experimental observations at the LHC: a pronounced nuclear enhancement at both ends of the spectrum. While the enhancement of hard-fragmenting jets happens to be strongly correlated with R_{AA}, hence controlled by jet energy loss, the enhancement of soft fragments is driven by the violation of angular ordering mechanism and the hard medium-induced emissions. We finally propose a new observable, which describes the jet fragmentation into subjets and is infrared-and-collinear safe by construction (therefore less sensitive to hadronisation effects) and we present Monte Carlo predictions for the associated nuclear modification factor.

Résumé

Outre les tests du Modèle Standard des particules, un autre objectif du programme expérimental du grand collisionneur de hadrons (LHC) est l'étude du plasma de quarks et de gluons, une phase de la matière qui existe à haute température ou densité, et dans laquelle les quarks et les gluons sont déconfinés. Ce plasma est aujourd'hui recréé en laboratoire dans des collisions d'ions lourds de haute énergie. Pour sonder les propriétés du plasma, on mesure des observables associées à la propagation de "jets" en son sein. Un jet est une gerbe collimatée de hadrons très énergétiques générée par des émissions successives de partons à partir d'un quark ou d'un gluon virtuel produit par la collision. Quand de telles gerbes se propagent dans le milieu dense créé par la collision de noyaux lourds, leurs interactions avec ce milieu entraînent une modification de leurs propriétés physiques, phénomène que l'on appelle "réduction des jets".

Dans cette thèse, nous développons une nouvelle théorie permettant de décrire la réduction des jets. En utilisant l'approximation double logarithmique en chromodynamique quantique perturbative, nous calculons pour la première fois les effets du milieu dense sur les émissions de type vide dans les jets. Ces émissions sont précisément celles déclenchées par la virtualité initiale du parton source. Nous montrons que les cascades de partons dans le milieu diffèrent de celles qui se développent dans le vide à cause des diffusions multiples par les constituants du milieu: l'espace de phase pour les émissions de type vide est réduit et la première émission à l'extérieur du milieu peut violer l'ordonnancement angulaire. Une nouvelle image physique émerge alors de ces observations, dans laquelle les émissions de type vide sont factorisées en temps par rapport à celles induites par le milieu. Cette image a l'avantage d'être markovienne, et donc adaptée pour une implémentation Monte-Carlo des cascades de partons, que nous développons dans le programme `JetMed`. Ce programme combine donc de façon cohérente les cascades de type vide et les cascades induites par le milieu.

Grâce à cet outil numérique, nous nous intéressons ensuite aux prédictions de notre théorie sur des observables de jets, et en particulier le facteur de modification nucléaire des jets R_{AA}, la distribution Soft Drop z_g et la fonction de fragmentation. Ces prédictions se révèlent être en bon accord avec les mesures du LHC. Nous trouvons que la perte d'énergie des jets augmente avec leur impulsion transverse à cause d'une augmentation du nombre de sources partoniques produites par les émissions de type vide dans le milieu. C'est un élément essentiel dans notre description de R_{AA} et de z_g. Pour cette dernière observable, nous identifions deux principaux effets nucléaires: la perte d'énergie incohérente des jets et les émissions induites par le milieu relativement dures. Le comportement de la fonction de fragmentation que nous obtenons est en accord avec les mesures du LHC ; en particulier nous observons une augmentation prononcée du nombre de fragments durs et mous. Dans la partie dure, cette augmentation est corrélée avec R_{AA} et donc controllée par la perte d'énergie des jets. Au contraire, l'augmentation de fragments mous est due à la violation de l'ordonnancement angulaire et aux émissions dures à petit angle induites par le milieu. Nous proposons finalement une nouvelle observable qui décrit la fragmentation des jets en termes de sous-jets, donc moins sensible aux effets d'hadronisation, et nous la calculons en collisions d'ions lourds.

Remerciements - Acknowledgements

Cette thèse est le fruit de trois ans de travail, dont trois mois et demi d'écriture entre avril et juillet 2020. Je tiens à remercier ici les personnes qui ont rendu possible l'émergence de ce manuscrit. En premier lieu, il y a évidemment mes directeurs, Edmond et Gregory. Ils m'ont fait découvrir leur domaine de recherche et leur passion avec une générosité rare. Je mesure de plus en plus la chance que j'ai eu de travailler avec eux pendant ces trois années, et je pense qu'une thèse ne suffirait pas pour écrire tout ce qu'ils m'ont apporté.

Je souhaite ensuite remercier Al Mueller qui est aussi à l'origine des travaux présentés dans la suite de ce document. Les discussions que nous avons pu avoir ont été riches d'enseignement. Ces moments dans ma vie de physicien balbutiant me sont précieux.

Merci aux membres de l'équipe QCD de l'Institut de Physique Théorique, permanents ou seulement de passage, en particulier Jean-Paul Blaizot, François Gelis, Giuliano Giacalone, Davide Napoletano, Jean-Yves Ollitrault et Vincent Theeuwes dont la présence au laboratoire a donné à mes journées de travail cette dimension humaine essentielle. Les échanges scientifiques sur des sujets connexes au mien m'ont beaucoup aidé à me faire une idée d'ensemble du domaine dans lequel s'inscrit cette thèse.

I thank the referees Carlos Salgado and Konrad Tywoniuk for accepting to read and comment this way too long manuscript. I thank also Matteo Cacciari, Leticia Cunqueiro and Samuel Wallon for accepting the invitation to be part of my jury, and for having physically been at my PhD defence in spite of the complications caused by the Covid19.

I would like to thank all the researchers of the nuclear theory group at the Brookhaven National Laboratory for their hospitality during my stay in July 2019. Je voudrais en particulier remercier Yacine Mehtar-Tani pour cette invitation. Ce séjour a été très enrichissant et stimulant pour la suite.

Merci aux membres de la SFDJAP pour ces réunions fort instructives qui m'ont permis de prendre du recul sur mon propre travail. Mes charges d'enseignement en physique et les étudiants de première année de licence en physique et biologie de l'université d'Orsay ont aussi beaucoup contribué à cette prise de recul indispensable. Je remercie mes élèves et les responsables des unités d'enseignement, en particulier Brigitte Pansu et Cyprien Morize.

Pour conclure, et non sans émotions, merci à mes amis, à ma famille, et à Manon.

Contents

Chapter 1

General introduction

1.1 Quantum chromodynamics

1.1.1 Quarks and gluons

Quantum chromodynamics (QCD) is the quantum theory of the strong interaction. The strong interaction binds together the protons and neutrons in atomic nuclei. However, protons and neutrons and the other bound states of the strong force called *hadrons*, such as the pions, kaons, etc, which are detected in high-energy experiments are not the elementary degrees of freedom of the theory. These elementary degrees of freedom from which quantum chromodynamics is formulated are called *quarks* and *gluons*: they are the fundamental constituents of the hadronic matter, the matter sensitive to the strong interaction.

The existence of "point-like" constituents inside hadrons is revealed in high energy scattering experiments, such as the deeply inelastic electron-proton scattering: at asymptotically high momentum transferred (squared) Q^2 during the collision process, the scattering cross-section behaves as if the proton was made of free elementary particles. This phenomenon was one of the first experimental evidence for quarks and gluons within hadrons [1, 2, 3].

In high energy experiments like deep inelastic electron-proton scattering or those described in Section 1.2 of this introduction, special relativity effects cannot be neglected. The theoretical framework to deal with quarks and gluons is thus quantum field theory. Quarks and gluons are the elementary degrees of freedom in the sense that they appear as *elementary fields* in the Lagrangian $\mathcal{L}_{\mathrm{QCD}}(\psi_f, A_\mu)$ of quantum chromodynamics. $\psi_f(x)$ are the quark Dirac fields labelled by their flavour indices $f = u, d, s, c, b, t$ for the six quark flavours of the Standard Model and $A_\mu(x)$ is the gluon vector field.

1.1.2 Non abelian local gauge symmetry and asymptotic freedom

Local $SU(3)$ gauge symmetry. This Lagrangian is strongly constrained by the *local* gauge invariance principle. More precisely, on imposes that $\mathcal{L}_{\mathrm{QCD}}$ is invariant under $SU(N_c = 3)$ local transformations of the quark fields:

$$\psi'_f(x) = U(x)\psi_f(x)\,, \qquad U(x) = \exp(i\epsilon_a(x)t^a) \tag{1.1}$$

with $\{t^a\}_{1\leq a\leq N_c^2-1}$ a set of generators in the fundamental representation of the $\mathfrak{su}(N_c)$ Lie algebra and $\epsilon_a(x)$ arbitrary functions of the space-time coordinates. The index a is called a colour index. Since the group $SU(N_c)$ is non commutative for $N_c > 1$, the $SU(N_c)$ gauge symmetry is said non-abelian [4]. As part of the fundamental representation of $SU(N_c)$, quarks

carry a colour charge, pretty much like electrons and positrons carry an electric charge in quantum electrodynamics (QED). The number N_c of possible "colours" is 3 in the physical world.

A system of *free* quarks with (bare) masses m_f is simply described by the free Lagrangian[1]:

$$\mathcal{L}(\psi_f) = \sum_{f=1}^{n_f} \bar{\psi}_f \big(i\gamma^\mu \partial_\mu - m_f\big)\psi_f \tag{1.2}$$

but is not invariant under (1.1). In order for this Lagrangian to be invariant under the transformation (1.1), a gluon field A_μ belonging to the adjoint representation of $SU(N_c)$ must be included, with the following transformation rule:

$$A'_\mu(x) = U(x)A_\mu U^{-1}(x) - \frac{i}{g_s}\partial_\mu U(x)U^{-1}(x)\,, \qquad A_\mu(x) = A^a_\mu(x)t^a, \tag{1.3}$$

and the quark fields must couple with A_μ via a covariant derivative $\partial_\mu \to D_\mu = \partial_\mu - ig_s A_\mu$ in (1.2). g_s is the (bare) strong coupling constant that quantifies the strength of the strong interaction. The fact that gluons carry also a colour charge, as member of a non-trivial representation of the gauge group, leads to a rich set of phenomena specific to the strong interaction.

One can then check that the following Lagrangian is invariant under the transformations (1.1)-(1.3) and is unique if renormalizability and parity invariance are also enforced:

$$\mathcal{L}_{\rm QCD}(\psi_f, A) = -\frac{1}{4}{\rm Tr}F_{\mu\nu}F^{\mu\nu} + \sum_{f=1}^{n_f} \bar{\psi}_f \big(i\gamma^\mu D_\mu - m_f\big)\psi_f \tag{1.4}$$

The gauge field tensor $F_{\mu\nu}$ depends on the gluon gauge field A_μ as:

$$F_{\mu\nu} = \partial_\mu A_\nu - \partial_\nu A_\mu + g_s[A_\mu, A_\nu] \tag{1.5}$$

This gluon field is the analogous of the photon field in quantum electrodynamics: gluons are said to mediate the strong interaction. This mediation is realized by means of the covariant derivative D_μ in the second term of the Lagrangian. The QCD Lagrangian is remarkable in several respects.

Gluon self-interaction. The gauge field A_μ is self interacting at tree level because of the non-abelian term $g_s[A_\mu, A_\nu]$. In comparison, the gauge field of quantum electrodynamics is the photon field, and photons do not interact between themselves at the lowest non trivial order in the electromagnetic coupling e. This has important phenomenological consequences, especially for QCD jets, as we shall see.

Asymptotic freedom. As it is, the Lagrangian (1.4) has no predictive power beyond tree-level in perturbation theory because of the UV divergences appearing from the one-loop order. These divergences are cured thanks to the renormalization procedure: the bare coupling g_s is discarded for the benefit of the *renormalized* strong coupling constant g. A by-product of this procedure is that g acquires a scale dependence, $g(\mu)$, with μ a sliding energy scale one chooses to define the renormalized coupling. Measurable quantities are invariant with respect to the choice of μ. To satisfy this requirement, the variations of the function $g(\mu)$ are constrained

[1] We adopt standard particle physics units with $\hbar = c = 1$.

by the β-function of QCD which is calculable order by order in perturbation theory (hence assuming that $g(\mu)$ is small)[2]:

$$\frac{\partial g(\mu)}{\partial \log(\mu)} = \beta(g(\mu)) = -\beta_0 \frac{g^3}{4\pi} + \mathcal{O}(g^5)\,, \qquad \beta_0 = \frac{11C_A - 2n_f}{12\pi} > 0 \tag{1.6}$$

$C_A = (N_c^2 - 1)/(2N_c)$ is the Casimir factor of the adjoint representation of $\mathfrak{su}(N_c)$. At one loop order in perturbation theory, that is using only the first term in the Taylor expansion of $\beta(g)$, one gets:

$$\alpha_s(\mu) = \frac{1}{\beta_0 \log\left(\frac{\mu^2}{\Lambda_{\text{QCD}}^2}\right)}\,, \qquad \alpha_s = \frac{g^2}{4\pi} \tag{1.7}$$

where $\Lambda_{\text{QCD}} \sim 0.2$ GeV[3] is the confinement or QCD scale discussed in the next point. A striking feature of the strong running coupling is that $\alpha_s(\mu) \to 0$ as $\mu \to \infty$. This property is known as *asymptotic freedom* [5, 6, 7, 8]. For a physical process governed by the strong interaction and involving a typical momentum transfer of order Q, the more Q is large: $Q \gg \Lambda_{\text{QCD}}$, the more $\alpha_s(Q)$ is small and hence the more the process becomes similar to what one would expect of a non interacting theory of quarks and gluons. In this regime, perturbative techniques, generically gathered under the term "perturbative QCD" (pQCD) are the standard tools to predict the behaviour of such physical processes. This is the realm of high energy collision experiments such as those performed at the Large Hadron Collider (LHC).

Confinement. On the other hand, when $\mu \to \Lambda_{\text{QCD}} \sim 0.2$ GeV, the strong coupling becomes very large suggesting that perturbative techniques and perturbative degrees of freedom (quarks and gluons) become irrelevant. This is closely related to another property of QCD, *confinement*, even if it is still not clear how confinement emerges from the QCD Lagrangian. This property states that in normal conditions of temperature and pressure, free quarks and gluons cannot exist and are always confined within colour neutral bound states called hadrons. At least, this is an experimental fact up to now: there are no free quarks and gluons, nor coloured particles, measured in low temperature/pressure experiments. At low energy scales, below or around Λ_{QCD}, the QCD Lagrangian is "solved" using lattice field theory. The quark and gluon fields are anchored on a finite lattice and the equations are studied numerically on a computer. Lattice QCD is very powerful to compute the mass spectrum of hadrons for instance.

1.1.3 Phases of hadronic matter

In our discussion of confinement, we have avoided to precise what we meant by "normal conditions of temperature and pressure". This paragraph intends to specify these conditions. Let us enclose some hadronic matter in a finite box of volume V, in thermodynamical equilibrium with a heat bath of temperature T and a particle reservoir with baryon chemical potential μ_B. The baryon chemical potential is the chemical potential associated with the baryon number B:

$$B = \frac{1}{3}(N_q - N_{\bar{q}}) \tag{1.8}$$

for a system with N_q quark and $N_{\bar{q}}$ antiquark. How does this matter behave as the temperature of the heat bath, the volume of the box or the chemical potential μ_B are varied? This section is a short review of what is known on this subject.

[2] In this thesis, the natural logarithm of x is noted $\log(x)$.

[3] 1 GeV $\simeq 1.6 \times 10^{-19}$ J and 1 fm $= 1 \times 10^{-15}$ m.

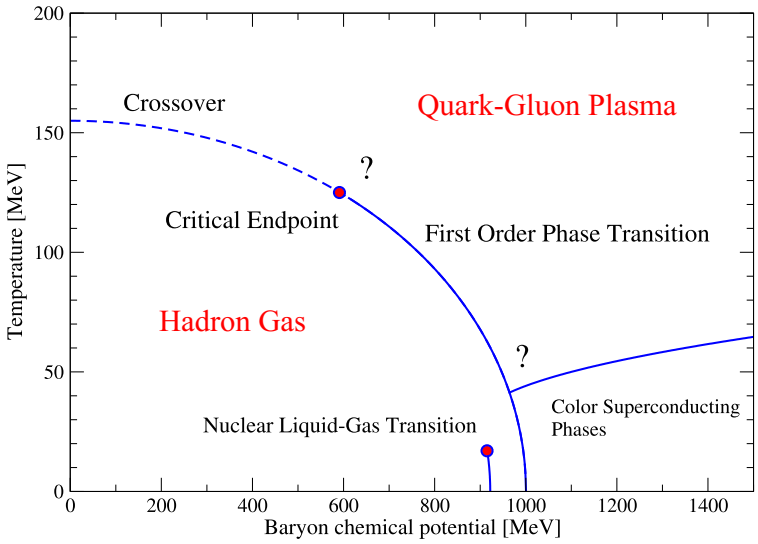

Figure 1.1: The conjectured phase diagram of QCD matter (extracted from [9]) projected on the plane (μ_B, T). The Boltzmann constant is set to one $k_B = 1$ for the units of the horizontal and vertical axis. The nuclear liquid-gas phase transition is the small line at the bottom of the diagram. The low temperature but high μ_B part of the diagram with the "colour superconducting" phase is not discussed here, but is relevant for neutron star physics.

Basic features. Some features can be guessed with very few physical inputs. For instance, as the radius of hadrons is of order $R_h \sim 1$ fm, there should exist a critical volume for our box, of order $V_c = 4\pi R_h^3/3$. Indeed, for a volume smaller than V_c, hadrons cannot fit in the box any more. Another interesting regime is the very high temperature regime. We have seen that pQCD has a self-emergent scale characteristic of the strong interaction, $\Lambda_{\rm QCD}$: one expects that quarks and gluons are the relevant degrees of freedom for $T \gg \Lambda_{\rm QCD}/k_B$, because the strong coupling constant $\alpha_s(k_B T)$ — naturally evaluated at a scale of the order of the thermal energy of the system — becomes very small from the asymptotic freedom property of QCD. Thus, in the high temperature phase $T \gg \Lambda_{\rm QCD}/k_B$, the system behaves like an ideal gas of (free) quarks and gluons. This phase is known as quark-gluon plasma. In the present thesis, there is almost no need to give further details on this phase as all the knowledge required to understand these lines is encoded in this definition. For completeness, we provide now some additional materials from hadronic physics and lattice QCD on the conjectured phase diagram of QCD shown Fig. 1.1.

Liquid-gas phase transition of nuclear matter. We start from the ordinary temperature $T \sim 270$-290 K and baryon chemical potential $0.9 \lesssim \mu_b \lesssim 1$ GeV$/k_B$. Under these conditions, the hadronic matter in our box is a mixed phase between vacuum and droplets of Fermi liquid formed by the nucleons — protons and neutrons — inside nuclei. The interaction between the nucleons looks very much like the Van der Waals interaction between electrostatic dipoles: this is confirmed by lattice QCD results on the nucleon-nucleon force and by calculation in the chiral field theory which is an effective field theory of QCD at low energy (see [10] for a review). Thus, in the same way as water undergoes a liquid-gas transition, we expect a first order phase transition towards a Fermi gas of free nucleons when the temperature increases. The critical point of the transition is located around $T_c' \sim 10$-20 MeV$/k_B$ and $\mu_{Bc}' \sim 900$-920 MeV$/k_B$.

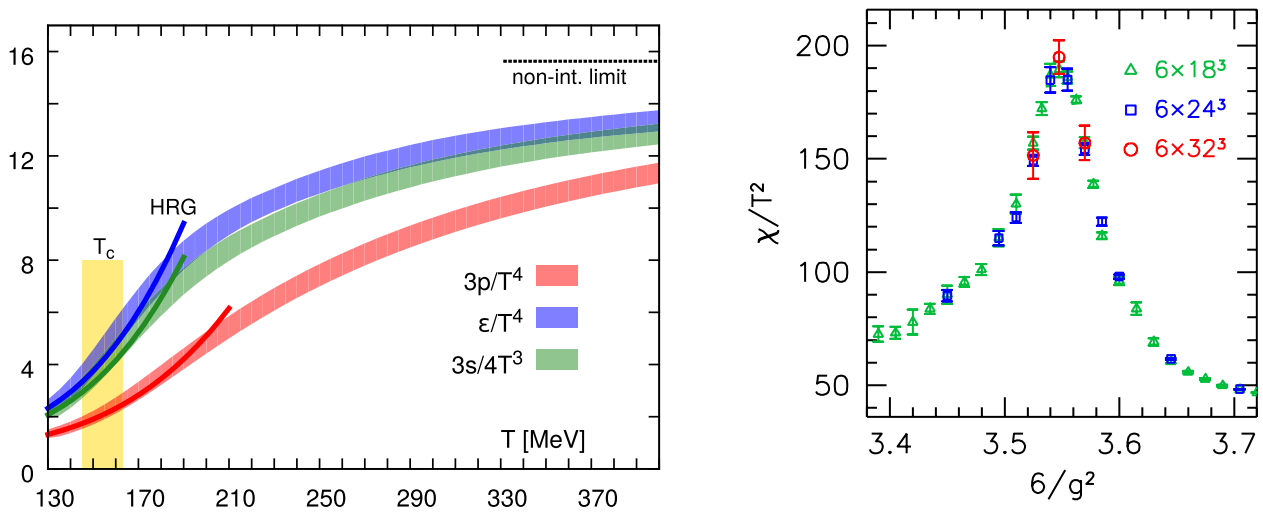

Figure 1.2: (Left) QCD equation of state at zero chemical potential $\mu_B = 0$ obtained from lattice calculations by the HotQCD collaboration [13]. The curve labelled "HRG" corresponds to the prediction from the hadron resonance gas model, whereas the dotted line at the top is the non-interacting (free) gas limit. (Right) Variation of the chiral susceptibility defined by (1.10) with $6/g^2$ (g is the gauge coupling, and T grows with $1/g^2$) for several lattice volumes $N_t \times N_s^3 \times a^4$ with a the lattice spacing. The figure is taken from [14].

Hadron resonance gas. Now, let us heat even more this system of free nucleons (or pions at lower chemical potential). This corresponds to the phase diagram of hadronic matter for $\mu_B \lesssim 1$ GeV and $T \gtrsim 10$ MeV. If we heat this system, we know from experiments that more and more hadronic resonances are produced: the number density $\rho(m)$ of hadronic states with mass between m and $m+\mathrm{d}m$ grows exponentially $\rho \sim \exp(cm)$. This hadronic phase is called "hadron resonance gas" (the degrees of freedom are still hadrons). The exponential growth cannot go forever, otherwise, the partition function of the system diverges at a temperature known as the Hagedorn temperature $T_h = 1/c$ [11]. From experimental data, $T_h \approx 150$ MeV$/k_B$, value close to Λ_{QCD}. This suggests that T_h should be interpreted as an upper limit for the hadronic phase and should be close to the transition temperature between this phase and a deconfined phase where quarks and gluons are liberated [12]. The exact nature of this phase transition is still unknown.

Lattice QCD results for $\mu_B = 0$. As explained in the first part of this introduction, lattice QCD is extremely useful to understand QCD in the strong coupling regime. In thermal QCD at finite temperature, the partition function is evaluated numerically on a finite lattice. Unfortunately, because of the so-called *sign problem*, lattice simulations cannot access non-zero baryon chemical potential (at least until now) [15]. Hence, lattice QCD provides reliable informations on the QCD phase space restricted to the line $\mu_B = 0$. Results from the HotQCD collaboration [13] are shown in Fig. 1.2-left for the energy density ϵ, the pressure p and the entropy density $s = (\epsilon + p)/T$ as a function of the temperature T of the bath. At low temperature, the predictions from the hadron resonance gas description are in good agreement with the lattice QCD results. At high temperature, the curves converge towards the non-interacting limit of a free gas of massless quarks and gluons following the Stefan-Boltzmann equation of state:

$$\frac{3p}{T^4} = \frac{\epsilon}{T^4} = n\frac{\pi^2}{30} \tag{1.9}$$

with $n = 2(N_c^2 - 1) + 7N_c n_f/2$ the total number of internal degrees of freedom. However, even at $T \sim 400$ MeV$/k_B$, the free limit is not reached suggesting that residual interactions have still an important role, in agreement with perturbative results in QCD at finite temperature. To sum up, at zero chemical potential, lattice QCD predicts a gradual transition between the hadron resonance gas and the deconfined phase.

There is another transition related to the deconfinement transition known as the chiral phase transition: at high temperature $T \gg \Lambda_{\rm QCD}/k_B$, the light quarks (up and down) can be considered as massless and the QCD Lagrangian (1.4) is symmetric under global chiral transformations of the light quark fields. At low temperature $T \ll \Lambda_{\rm QCD}/k_B$, chiral symmetry is spontaneously broken, with the pions being the Nambu-Goldstone bosons associated with this symmetry breaking. Lattice QCD enables to have a more quantitative insight on the location of the transition. The order parameter is the chiral susceptibility defined by:

$$\chi = \frac{T}{V}\frac{\partial \log(Z_{\rm QCD})}{\partial m_l} \tag{1.10}$$

where $Z_{\rm QCD}$ is the QCD partition function in the grand canonical ensemble at $\mu_B = 0$ and m_l is the mass of the light quarks. A plot of the chiral susceptibility for several values of the volume lattice is shown in Fig. 1.2-right from [14]. A clear peak is visible as a function of $6/g^2$ ($6/g^2$ scales like the temperature T of the heat bath). However, this peak is independent of the volume of the lattice, showing that the chiral transition at $\mu_B = 0$ is not first nor second order but rather an analytic cross-over. The location of the peak defines the pseudo-critical temperature T_c of the transition, whose value is around 150 MeV$/k_B$.

For non vanishing chemical potential the nature of the chiral transition is still unknown, even if there is a hint for a first order phase transition as shown Fig. 1.1. The determination of the critical point is an active field of research both on the theoretical and experimental sides. Regarding the link between the chiral and the deconfinement transition, they should occur at about the same temperature. Therefore, understanding the chiral transition is crucial to precise the shape of the phase diagram of hadronic matter.

1.2 Heavy-ion collisions

How do physicists probe the QCD phase diagram experimentally? The very early Universe was probably a hot soup of free quarks and gluons, so physicists could look for relics of this epoch to infer some properties of the quark-gluon plasma. Also, the heart of neutron stars might be an interesting natural laboratory for studying QCD at high density. Besides these two occurrences of QCD matter at extreme temperature or density in Nature, this matter is studied on Earth in high energy experiments by colliding together heavy nuclei with a large number of nucleons. The two main accelerators used for this purpose are the Relativistic Heavy Ion Collider (RHIC) based at the Brookhaven National Laboratory on Long Island (US) and the Large Hadron Collider (LHC) based at the border between France and Switzerland, near Geneva.

1.2.1 Experimental aspects

We start by describing briefly some experimental aspects relating to nucleus-nucleus collisions relevant for this thesis, and especially the second Part. At RHIC, the heavy nuclei are mainly atoms of copper (Cu), gold (Au) or uranium (U). At the LHC, most of the data discussed in

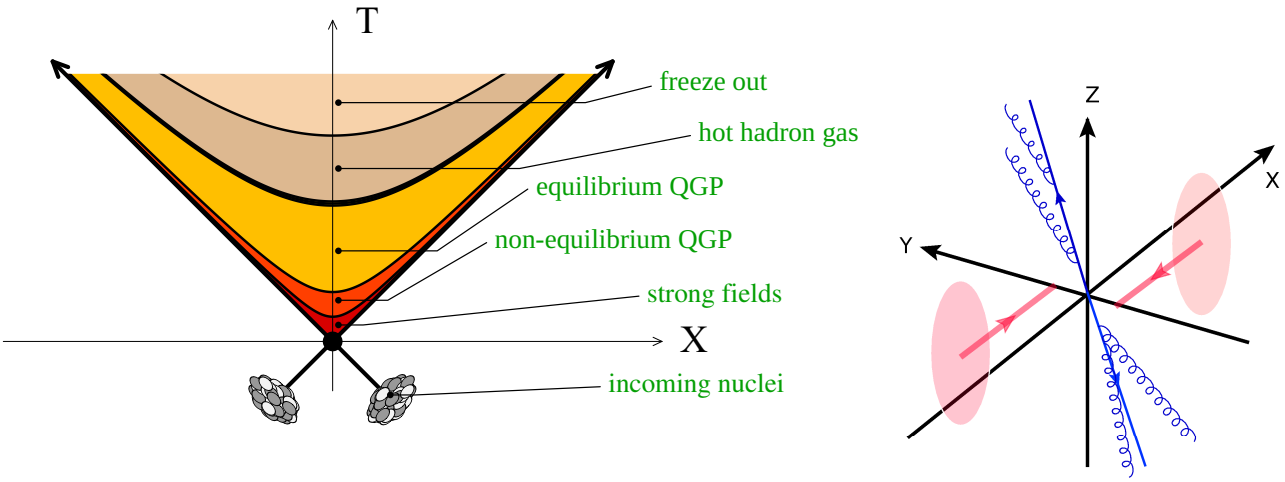

Figure 1.3: (Left) Space-time diagram of a nucleus-nucleus collision (figure from [16]). The horizontal axis is the beam axis, and the vertical axis is the proper time of an observer in the laboratory frame. As the nuclei are ultra-relativistic, their worldlines lie on the light cone with apex at the collision event. By Lorentz contraction, the nuclei appear as thin sheets of matter. The hyperboles are lines with constant fluid proper time $\tau = \sqrt{T^2 - X^2}$: it is the proper time of an observer comoving with a fluid element in the Bjorken expansion model. The several stages of the collision between two values of τ are described. The first stage, during which the partons (mostly gluons) are freed by the collision, lasts ~ 0.2 fm. In the second stage, with $0.2 \lesssim \tau \lesssim 1$ fm, the partonic matter rapidly approaches thermal equilibrium. The longest stage in the yellow region corresponds to a QGP in thermal equilibrium, up to $\tau \sim 10$ fm at the LHC. The cooling of the QGP leads to a hot system of hadron resonances which finally becomes a system of free hadrons at the freeze-out proper time $\tau \sim 10 - 20$ fm. (Right) The coordinate system in the laboratory frame adopted in this thesis. The two incoming nuclei are shown *before* the collision, together with their trajectories. A dijet event is illustrated as well: two cascades of energetic partons develop back to back in the transverse plane with respect to the beam axis.

Part II come from lead-lead (Pb) collisions analysis. A run of xenon-xenon collisions (Xe) also took place at the LHC during fall 2017.

In such high-energy collisions, two beams of heavy and entirely ionised nuclei accelerated at nearly the speed of the light circulate in opposite directions in a large synchrotron. The Lorentz factor of the nuclei in larger than 2500 at the LHC! These two beams meet in specific locations of the ring where particle detectors are built. When the two beams meet, two nuclei belonging to their respective beam collide and create a myriad of particles (~ 35000 on average in frontal collisions at the LHC) which are measured in the detectors. Understanding what happens between the collision and the particle detection is the main goal of these experiments. The current "standard model" of a high energy nucleus-nucleus collision is pictured in Fig. 1.3-left. Shortly after the collision, a plasma of free quarks and gluons is created that lives during approximatively 10 fm ($\sim 10^{-23}$ seconds). After being formed, it expands essentially along the beam direction, cools down and hadronises into final-state hadrons.

To understand the experimental data shown in Chapter 7, a bit of vocabulary and kinematic notations are useful.

Laboratory frame. The laboratory frame is an inertial frame such that the center of mass frame of the two nuclei is fixed at the origin O of the coordinate system. In this frame, the total 3-momenta of the colliding nuclei vanishes and O is the location of the collision event. To each event in Minkowksi space, one associates a four vector $X^\mu \mathbf{e}_\mu$, with $\{\mathbf{e}_\mu\}$ the basis vectors

of the laboratory coordinate system and X^μ the coordinates of the event. This basis is chosen so that $\mathbf{e}_1 = \mathbf{e}_{\text{X}}$ is parallel to the beam axis. The vector $\mathbf{e}_2 = \mathbf{e}_{\text{Y}}$ is parallel to the impact vector. The impact vector is a vector in the plane transverse to the collision axis connecting the centers of the two incoming nuclei. The vector $\mathbf{e}_3 = \mathbf{e}_{\text{Z}}$ lies in the transverse plane and is orthogonal to $\mathbf{e}_2$. Finally, $\mathbf{e}_0 = \mathbf{e}_{\text{T}} = u$ where u is the 4-velocity of an observer fixed in the laboratory frame. This coordinate system is pictured Fig. 1.3-right. For collisions with exactly zero impact parameter, the choice of the vectors $\mathbf{e}_2$ and $\mathbf{e}_3$ is arbitrary as long as the basis $\{\mathbf{e}_\mu\}$ is orthonormal and direct (in the sense of the metric tensor $g_{\mu\nu}$).

In this frame and coordinate system, one defines the following quantities related to a generic 4-momentum $p = p^\mu \mathbf{e}_\mu$ of a particle:

$$\text{Energy:} \qquad E = p^0 \tag{1.11}$$

$$\text{Transverse momentum:} \qquad p_T = \sqrt{p_2^2 + p_3^2} \tag{1.12}$$

$$\text{Rapidity:} \qquad y = \frac{1}{2}\log\left(\frac{p^0 + p^1}{p^0 - p^1}\right) \tag{1.13}$$

$$\text{Pseudo-rapidity:} \qquad \eta = \frac{1}{2}\log\left(\frac{\sqrt{p_1^2 + p_2^2 + p_3^2} + p^1}{\sqrt{p_1^2 + p_2^2 + p_3^2} - p^1}\right) \tag{1.14}$$

For massless particles ($p^2 = p^\mu p_\mu = 0$), one has $y = \eta$, and in the mid-rapidity region ($y = 0$), one has $E \simeq p_T$. In this thesis, the geometrical aspects of high-energy massless particle production are simplified: they are considered as produced in the transverse plane with $p^1 = 0$. Energy and transverse momentum are therefore synonyms. The pseudo-rapidity is related to the angle θ in the spherical coordinate with axis $\mathbf{e}_1$ by $\eta = -\log(\tan(\theta/2))$. Finally the azimuthal angle in these spherical coordinates is defined as $p_T \cos(\phi) = p^{\text{Y}}$.

Collision energy. An important quantity is the center of mass energy of the collision, noted $\sqrt{s}$ defined by the first Mandelstam variable:

$$s = (p_1 + p_2)^2 \tag{1.15}$$

where p_1 and p_2 are the 4-momenta of the two colliding particles. Experimentalists control this quantity by tuning the beam energy E_{beam} in the laboratory frame, since $\sqrt{s} = 2E_{\text{beam}}$. In nucleus-nucleus collision, this quantity is averaged per nucleons, so that the common quantity is the $\sqrt{s}$ per nucleon pair:

$$\sqrt{s_{\text{NN}}} = \frac{Z}{A}\sqrt{s} \tag{1.16}$$

for a generic nucleus ${}^A_Z X$. At the LHC, most of the data related to jets in heavy-ion collisions discussed in this thesis have $\sqrt{s_{\text{NN}}} = 2.76$ TeV or $\sqrt{s_{\text{NN}}} = 5.02$ TeV.

Centrality. The impact vector is difficult to measure experimentally and especially its length, the impact parameter. Instead, experimentalists use the concept of centrality. Centrality can be obtained directly from data. There are several ways of defining a centrality. Starting from a set of events called minimum-biased (meaning there is no further requirement on how these data should be, besides the registration trigger), these events are sorted according to the value of an observable N which is a monotonic function of the impact parameter. For instance, one can bin the events according to the total particle multiplicity or the total energy deposited in the detectors. One easily understands that the more the impact parameter is small, the more

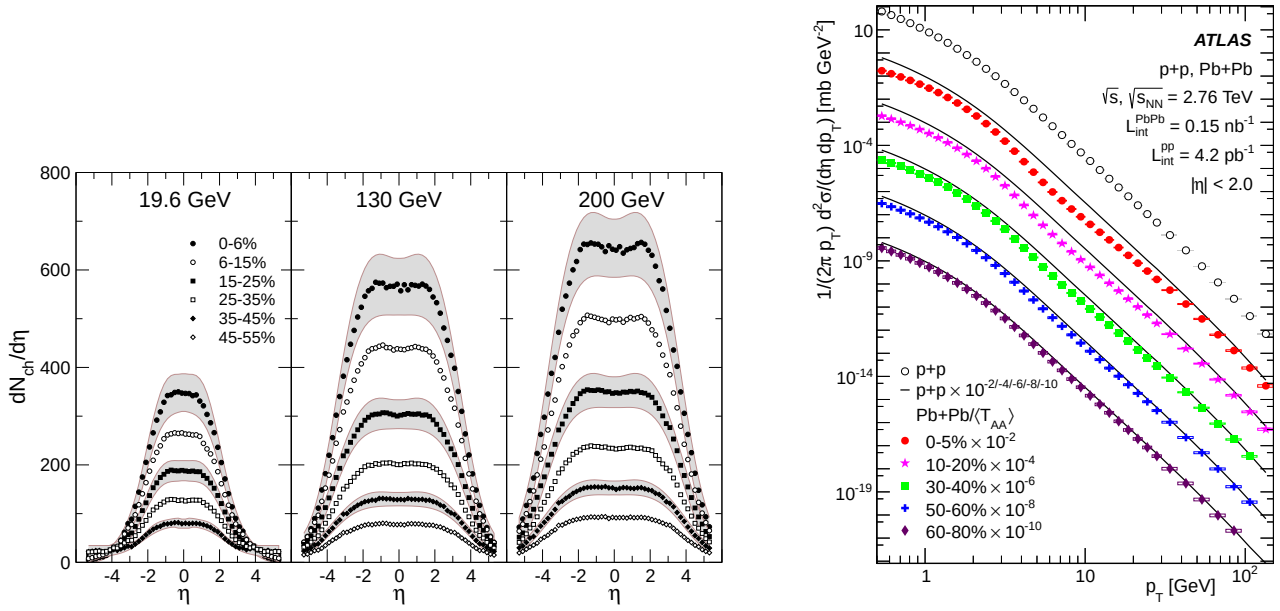

Figure 1.4: (Left) Pseudo-rapidity distribution of charged particles measured by the PHOBOS detector at RHIC in gold-gold collisions for several centrality classes [18]. The bands correspond to systematic uncertainties. From the left to the right panels, $\sqrt{s_{NN}}$ increases from 19.6 GeV up to 200 GeV. The more the centrality is small, the more the rapidity plateau is high. (Right) p_T spectra of charged particles measured by the ATLAS Collaboration [19] in proton-proton and lead-lead collisions for several centrality classes. Note that the Pb-Pb spectra are rescaled by the thickness function $\langle T_{AA} \rangle$ to account for the higher hard scattering rate in Pb-Pb collisions (w.r.t pp) as a single nucleus contains several nucleons.

the total multiplicity or energy is large. Another possible observable is the energy deposited in the "zero-degree" calorimeter, located close to the beam direction. This energy is related to the number of spectator nucleons, and therefore increases as the impact parameter increases.

A centrality class $0 - c(n)$ is then a subset of the data such that a fraction $c(n)$ satisfies $N \geq n$. For instance, in Fig. 7.1a, $0 - 10\%$ centrality means that the events selected for the measurement belong to the 10% events with highest particle multiplicity.

To relate quantitatively the centrality to the impact parameter b, one uses the following geometric relation (see e.g. [17]):

$$c \simeq \frac{\pi b^2}{\sigma_{\text{in}}^{AA}} \tag{1.17}$$

This formula neglects the fluctuations in the probability distribution of measuring a value n of N given the impact parameter b, and assumes that the nucleus A behaves like a "black disk" for $b \lesssim R$, with R the nucleus radius.

Single particle spectra. As emphasized, nucleus-nucleus collisions at high energy produce a myriad of particles. To organise the data and get an intuition about the event shape, one first looks at particle spectra. Once a centrality class is selected, experimentalists measure in this class the multiplicity of particles more differentially with respect to their kinematics or their species. There are two basics but important features regarding the particle spectra as a function of the rapidity (or pseudo-rapidity) and transverse momentum:

- At mid-rapidity, for $|y| \simeq |\eta| \lesssim 2$, the particle multiplicity (averaged over all events in a centrality class) exhibits a flat plateau (see Fig. 1.4-left), meaning that the distribution

is approximatively boost-invariant along the beam direction. This boost invariance is a natural consequence of the initial symmetry of the collision: at very high center of mass energy, all inertial observers sightly boosted with respect to the beam axis in the laboratory frame see the same collision of two ultra-relativistic nuclei, and thus the same final particle distribution. As a boost along the beam is equivalent to a shift in the rapidity y, this explains the central rapidity plateau. The boost invariance with respect to the beam axis is often called "Bjorken hypothesis" or "Bjorken model" [20].

- The transverse momentum spectra of detected particles is steeply falling with p_T, as shown Fig. 1.4-right. The majority of particles produced in heavy-ion collisions are "soft", with $p_T \lesssim \mathcal{O}(1)$ GeV at the LHC. It has recently been observed that the mean p_T of charged hadrons is proportional to the temperature of the plasma [21]. The shape of the spectrum shown in Fig. 1.4-right naturally divides the possible measurements into two categories: those related to the "bulk" where soft particles dominate, and those related to the hard tail of the p_T spectrum, called "hard probes". As we shall see, the physical mechanisms at play are very different, although each kind provides valuable informations on the nature of the matter produced in heavy-ion collisions.

1.2.2 Flow in heavy-ion collisions

To understand more precisely the pattern of the bulk particles, one can perform a more refined measurement than the simple rapidity or p_T distribution we have just discussed: measuring pair correlations. More precisely, one can measure the distribution of particle pairs separated by an azimuthal angle $\Delta\phi$ and (pseudo)-rapidity $\Delta\eta$ in a given centrality class. This distribution $C(\Delta\phi, \Delta\eta)$ is shown Fig. 1.5-right, as measured by the ATLAS detector at the LHC in PbPb collisions. On the left figure, the same distribution is shown in *pp* collisions for comparisons. They are dramatically different, enlightening that new physics is involved in heavy-ion collisions with respect to *pp*. Indeed, if a heavy-ion collision was only an incoherent "sum" of elementary *pp* collisions, the distributions should look the same.

For central and no too peripheral collisions, the pair correlation is almost independent of η, the large peak at $\Delta\phi = \Delta\eta = 0$ excepted. As a function of $\Delta\phi$, one observes by eye a cosine modulation of the correlation, maximal at $\Delta\phi = 0$ and π. The picture in *pp* is very different even if the peak at $\Delta\phi = \Delta\eta = 0$ is present. The correlation depends strongly on η and there is no cosine-like modulation. We leave the discussion of the peak at $\Delta\phi = \Delta\eta = 0$ for the next section: we will see that QCD predicts strong correlations between almost collinear particles (thus with $\Delta\phi = \Delta\eta = 0$) due to the existence of high p_T QCD *jets*.

On the contrary, what explains the specific pattern of the two-particle correlations in heavy-ion collisions is generically called "flow". The flow picture for multi-particle correlations relies on the following hypothesis (see e.g. [24]): particles are emitted independently in a single event so that all multi-particle correlations in an event can be obtained from the single particle probability distribution. This probability distribution $P_1(\phi, y, p_T)$ determines the probability of having one particle with a given rapidity, azimuth and transverse momentum. This probability density is itself a random variable, as it fluctuates from one event to another. Non trivial correlations among pairs (as well as higher numbers of particles) are generated by these fluctuations.

In the Bjorken model, $P_1(\phi, y, p_T)$ does not depend upon rapidity, but has a non trivial dependence with the azimuthal angle. It is usually expanded as a Fourier series:

$$P_1(\phi, y, p_T) = \frac{1}{2\pi} \sum_{n=-\infty}^{+\infty} V_n(p_T) \exp(-in\phi) \tag{1.18}$$

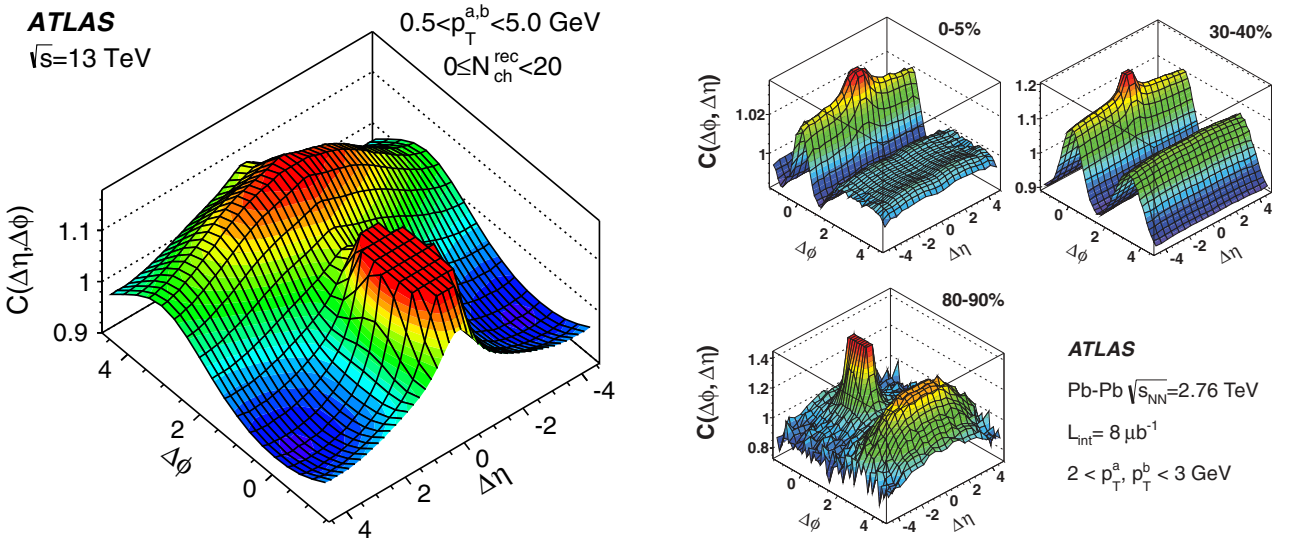

Figure 1.5: (Left) Two-particle correlation measured by the ATLAS Collaboration in pp collisions with $\sqrt{s} = 13$ TeV and small total multiplicity (less than 20 reconstructed charged particles in the final state) [22]. The peak at $\Delta\phi = \Delta\eta = 0$ due to QCD jets has been truncated. The other local maximum at $\Delta\eta = 0$ and $\Delta\phi = \pi$ is caused primarily by back-to-back dijet events (i.e. momentum conservation). (Right) Same quantity measured by the ATLAS Collaboration in lead-lead collisions with $\sqrt{s_{NN}} = 2.76$ TeV [23]. The panels display three different centrality classes. For peripheral collisions (80-90% centrality), the 2-particle correlation distribution looks like the one in proton-proton collisions on the left. In most central collisions (0-10%) or a mid-centrality (30-40%), the boost invariance is manifest, one observes a $\Delta\phi$ wave, and strong correlations at $\Delta\phi = 0$ even for large values of $\Delta\eta$.

and $v_n = V_n/V_0$ is called n^{th} anisotropic flow.

What motivates the flow hypothesis? If the medium created after the collision thermalizes, the flow hypothesis is naturally justified, since thermalization destroys initial correlations so that particles are finally emitted independently. If thermalization is a sufficient condition for flow, one should keep in mind that it is not a necessary condition [25]. The great success of the flow hypothesis combined with hydrodynamical predictions for P_1 in explaining the experimental data is in itself the best argument in its favour.

From a given model (usually an hydrodynamic picture for the medium evolution), theorists can predict the single particle distribution P_1 and its fluctuations. How is this compared to data? One cannot measure directly this probability distribution because it is defined event-by-event: the particle spectrum in one event has intrinsic large statistical fluctuations (essentially because the number of particles is not that large once kinematic cuts are applied). Instead, by measuring the pair correlation as in Fig. 1.5, which is averaged of many events, one can infer the value of the underlying theoretical single particle probability density. Indeed, the flow hypothesis leads to the following probability distribution for the event-by-event pair correlation (neglecting for simplicity the p_T dependence of V_n):

$$C(\Delta\phi, \Delta\eta) = \frac{1}{2\pi} \sum_{n=-\infty}^{+\infty} |V_n|^2 \exp(n\Delta\phi) \tag{1.19}$$

$$= \frac{V_0^2}{2\pi} \Big(1 + 2 \sum_{n=1}^{+\infty} |v_n|^2 \cos(n\Delta\phi)\Big) \tag{1.20}$$

so that the n^{th} Fourier harmonics of $C(\Delta\phi)$, traditionally called $v_n\{2\}$ [26] reads

$$v_n\{2\} \equiv \langle\langle \exp(n\Delta\phi)\rangle\rangle = \frac{\langle |V_n|^2\rangle}{\langle V_0^2\rangle} \tag{1.21}$$

where the double bracket on the left is an average over pairs in a single event followed by an average over all events in a centrality class. The average on the right is an event average since P_1 and therefore V_n are also random variables.

In the hydrodynamical picture of the plasma evolution, P_1 is dictated by the anisotropy of the initial energy density profile. This holds for the values of V_n in a single event, but also for their fluctuations (meaning that the fluctuations of the initial geometry translate into fluctuations of P_1). In non-central collisions, the medium created after the collision is strongly deformed in the transverse plane (it has an "almond shape"): pressure gradients push more particles in the direction parallel to the impact parameter than in its perpendicular direction. This means that one expects higher pair correlations for $\Delta\phi = 0$ and $\Delta\phi = \pi$. This explains the strong cosine modulation, or mathematically the large v_2 (elliptic flow [27]), observed in Fig. 1.5-right at mid-centrality where the initial collision anisotropy is larger. Higher harmonics in the modulation are driven by v_3, v_4 etc, [28, 29] themselves related to the anisotropy of the initial energy density profile and its fluctuations.

Measurements of $v_n\{2\}$ are confronted to theoretical predictions of v_n. This constrains the parameters entering into the hydrodynamical calculation of the single particle distribution P_1 such as the viscosity of the plasma [30] (see [31] for a review).

1.2.3 Other probes of the quark-gluon plasma

It is not our intention to give an exhaustive discussion of the experimental probes of the quark-gluon plasma. Beside flow measurements, other informations about the QCD matter produced in nucleus-nucleus collisions are inferred from electromagnetic probes: for instance if the medium thermalizes, thermal photons are emitted and their distribution can provide interesting informations about the thermodynamics of the plasma (see [32] for a review). There are also a lot of theoretical and experimental efforts to measure the production of bound states of heavy quark-antiquark, called quarkonia, in heavy-ion collisions (see [33] for a recent review). The hot surrounding medium can destroy the binding between the quark and the antiquark. The suppression of quarkonia was therefore proposed as a signature of quark-gluon plasma formation [34].

1.3 QCD jets and jet quenching

Jets are collimated spray of energetic hadrons. The formation of such structure at high energy is predicted by perturbative QCD: the enhancement of soft and collinear radiative processes is a common feature of (unbroken) gauge theories with a massless gauge boson such as QED or QCD. In QCD, as gluons can easily radiate soft and collinear gluons because of the self interaction highlighted in the first section, the development of soft/collinear cascades is accentuated with respect to QED. Thus, the formation of jets is a direct consequence of the non-abelian nature of the gauge symmetry. Nowadays, jets are used on a daily basis in collider experiments and precise tests of the Standard Model often rely on precise predictions regarding QCD jet production. For a theoretical introduction to jets in pp collisions, we refer the reader to the first part of Chapter 4.

In heavy-ion collisions, jets are also produced. This shows that even if new physical phenomena such as flow are at stake in nucleus-nucleus collisions, the standard features of the strong interaction like jet production have not disappeared. In Fig. 1.5-left, the peak at $\Delta\phi = \Delta\eta = 0$ is caused by QCD jets, since a jet is essentially a collection of collinear particles. In flow physics, QCD jets are considered as "non-flow" correlations which are removed by implementing a rapidity gap $\Delta\eta > \Delta\eta_{\rm cut}$ when measuring $v_n\{2\}$. On the contrary, for jet physics in heavy-ion collisions, the main topic of this thesis, bulk particles and flow are treated as part of the background which must be removed.

To reduce the effect of this background, it is advantageous to focus on high p_T jets, as those produced at the LHC. Jet observables belong then to the set of "hard probes" of the quark-gluon plasma. By the Heisenberg uncertainty principle, high-p_T jets are formed over a very short time, of order $1/p_T$, after the collision and thus before the medium formation. For such short time scales, it is allowed to deal with the perturbative degrees of freedom of QCD: the quarks and gluons. The general physical picture for the jet evolution in proton-proton collision is the following: a hard scattering between two partons inside the incoming protons typically produces a pair of high p_T partons that propagate back-to-back in the transverse plane. By hard scattering, we mean that the momentum transfer is large, of order p_T. What happens next to one of these partons? As the parton is not yet on its mass-shell (strictly speaking, on-shell quarks or gluons do not exist), it can further radiate, predominantly soft and collinear gluons, which further radiate and so on (as illustrated Fig 1.3-left). This partonic cascade develops over a large time scale, of order $1/\Lambda_{\rm QCD} \gg 1/p_T$ since for times larger than $1/\Lambda_{\rm QCD}$ the partonic picture breaks down.

In heavy-ion collisions, this cascade interacts with the surrounding medium created after the collision. We shall discuss extensively these interactions in this thesis (e.g. the Introduction 2 of Part I for a brief overview of the plasma-parton interactions). These latter have a significant effect on jet measurements in heavy-ion collisions with respect to pp collisions. The modification of jet properties in heavy-ion collisions is commonly named jet quenching. We refer the reader to Chapter 7 for an introduction about jet quenching measurements at the LHC. The most salient one is the strong suppression of high p_T jets in lead-lead collisions at the LHC.

This thesis deals with jet quenching physics. Starting from pQCD and the parton language, we develop a new picture for the parton shower in the presence of a quark-gluon plasma (Part I). This picture includes so far only the expected dominant effects of the plasma-jet interaction in the so-called leading logarithmic approximation of pQCD. We tried to circumscribe the validity of our approximations and acknowledge the limitations of this picture as best as possible. The good qualitative agreements between our calculations and the measurements done at the LHC for several observables (Part II) are encouraging, and we hope for a better understanding of jet quenching phenomena from this new foundation in the future.

1.4 Reading guide

To conclude this introduction, we would like to provide a short "reading guide" to precise the internal logic of this thesis and highlight the new contributions to the field. This thesis is divided into two parts. The first part is theoretical, while the second part is dedicated to the phenomenology of jet quenching at the LHC.

The main purpose of Part I is to explain in details the new factorised picture of jet evolution in a dense QCD medium which is the heart of this work: this is done in Chapter 5 and the description of the Monte Carlo parton shower based on these ideas is the subject of Chapter 6.

In that respect, the interest of the two opening chapters, Chapter 3 and Chapter 4 is

twofold. On one hand, it enables to provide the material necessary to understand the arguments presented in Chapter 5 and the concepts used in Part II. On the other hand, even though no significant breakthrough is presented in these two introductory chapters, there are some new developments:

1. We give new (as far as we know) simple analytic formulas for the on-shell and off-shell gluon emission spectra in a dense medium (Section 3.3.3.3, Eq. (3.140)-(3.141)) with full dependence on transverse momenta and energy, valid in an expanding medium. We use these formulas to justify the factorisation between virtuality driven processes and medium-induced processes detailed in Chapter 5.

2. Still in an expanding medium, the medium-induced spectrum integrated over transverse momenta from a colour singlet dipole is derived in Section 3.4.2, Eq. (3.198).

3. In the same spirit, the effect of decoherence on in-medium vacuum-like emissions with *short formation times* studied in Section 3.4.3 is very important for the resummation scheme presented in Chapter 5, Section 5.2. This calculation is an important step to prove that angular ordering holds inside the medium.

4. In Chapter 4, Section 4.2.3.3 (and Appendix E), we present and calculate a new jet substructure observable relevant in heavy-ion collisions and studied in this context in Chapter 10: the fragmentation function from subjets [35, 36].

5. In Chapter 4, Section 4.3.4 we give a criterion for the medium dilution so that medium-induced jet fragmentation satisfies scaling properties.

Then, Chapter 5 is essentially based on the work published in [37]. We give further arguments to justify the physics exposed in this short Letter, and we clearly delineate the approximations behind the resummation scheme. The extension of [37] to Bjorken expanding media is also extensively discussed.

In Chapter 6, the Monte Carlo parton shower `JetMed` [38] is presented in details, and compared to other existing in-medium Monte Carlo parton showers.

The phenomenological study of Part II is entirely based on the theoretical picture for jet fragmentation and its implementation as a Monte Carlo parton shower described in details in the first part. All the phenomenological results on the jet nuclear modification factor and jet substructure observables in PbPb collisions presented in Part II are new. We point out that, Section 8.3.2 excepted, Chapter 8, Chapter 9 and Chapter 10 are essentially extracted from the following papers [35, 39, 40].

Part I

Theory: jets in a dense QCD medium

Chapter 2

Introduction: jet quenching theory

The next chapter develops in detail the formalism for calculating emission processes in a dense medium. We will make of course several assumptions, both in the modelling of the medium and in the dominant effects at play. On the contrary, with the present chapter, we would like to provide a broad overview of the field in order for the reader to get an intuition about the context of this thesis.

We have divided this introduction into two sections. The first section focuses on the energy loss of a test particle while propagating in a quark-gluon plasma. This problem is very well documented in the literature since the first measurement of the suppression of highly energetic hadrons in gold-gold collisions at RHIC.

The second section deals with the interplay between the medium effects (and in particular the energy loss covered in the first section) and the virtuality of the leading parton produced in the hard partonic scattering. This virtuality is the driven mechanism of jet fragmentation in the vacuum. There are many models for describing this interplay, but a first principle derivation in QCD is often missing.

2.1 Parton energy loss in media

There are two approaches for the problem of parton energy loss in a quark-gluon plasma depending on the modelling of the medium. For a weakly coupled medium, the medium can be described as a collection of scattering centers, and one can calculate the interaction between the test parton and the scattering centers using weak coupling techniques. In this section, we review the two main mechanisms for energy loss at weak coupling: the collisional and the radiative energy loss.

I will not discuss AdS/CFT calculations in the strong coupling regime, as this thesis relies on perturbative methods. We refer to [41] for a review on this topic. Nevertheless, we point out that weak coupling methods in QCD at finite temperature work very well even when the strong coupling constant evaluated at the plasma thermal energy $\alpha_s(k_B T_{\rm p})$ is not that small (~ 0.4) [42].

2.1.1 Collisional or elastic energy loss

The collisional energy loss is due to the *elastic* scattering of an incoming energetic on-shell parton with a plasma constituent. A typical Feynman diagram for the elastic process is shown Fig. 2.1-left. Bjorken has given a first estimation of the collisional energy loss for a massless

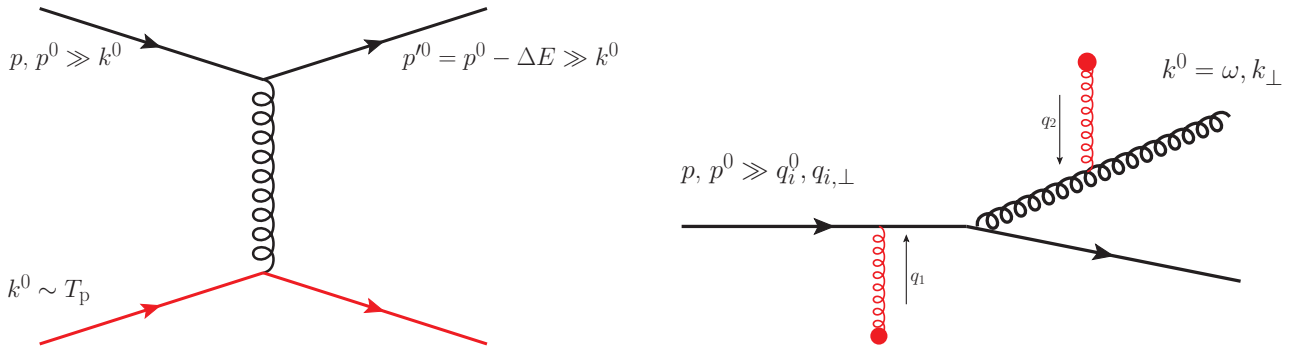

Figure 2.1: (Left) Typical Feynman diagram for the leading order calculation of the elastic energy loss. The red parton is a medium constituent. (Right) Typical Feynman diagram involved in the calculation of the inelastic energy loss. In the opacity expansion scheme, this diagram appears at the $N = 2$ order since there are two scattering centers. The BDMPS-Z result resums all orders in opacity, in the regime where all momenta transferred are soft.

quark, per unit length x in the plasma [43]:

$$\frac{\mathrm{d}E}{\mathrm{d}x} = -\frac{8}{3}\pi\alpha_s^2 T_{\rm p}^2\left(1+\frac{n_f}{6}\right)\log\left(\frac{q_{\rm max}}{q_{\rm min}}\right) \tag{2.1}$$

where $T_{\rm p}$ is the plasma temperature, n_f the number of active quark flavours in the plasma and $q_{\rm min/max}$ the minimal (maximal) momentum transferred by the collision. The minimal momentum transferred is of order of the Debye mass $\mu_D \sim gT_{\rm p}$ which characterizes the plasma (see Chapter 3, section 3.2.3), whereas the maximal momentum transferred is of order p^0.

This calculation has then been improved, taking into account quark masses [44], plasma screening effects [45, 46], finite length effects [47] or running coupling corrections [48] and corrections beyond t-channel scattering [49]. Multiple elastic collisions are often included via the linear Boltzmann transport equation with a collision kernel incorporating the elastic $2 \to 2$ process, as in the LBT jet quenching model [50].

Collisional energy loss is the dominant process at low particle momentum and can bring non-negligible corrections to radiative processes when quark masses are taken into account [51, 52]. The goal of this thesis is to develop an unified picture for *high-p_T* jet fragmentation. For this reason, direct elastic contributions to the energy loss are neglected (i.e. processes like in Fig. 2.1-left), but the effects of elastic collisions on radiative emissions and transverse distributions are taken into account.

2.1.2 Radiative or inelastic energy loss

In the radiative process, the scattering centers trigger a gluon emission by putting the incoming parton off its mass shell. The process is *inelastic* as an additional parton populates the final state. We first present the theoretical calculations where only one additional (soft) gluon is emitted. Then, we present the current strategies to go beyond the single gluon emission process.

2.1.2.1 Single gluon emission

A typical Feynman diagram is shown in Fig. 2.1-right. Radiative energy loss is the dominant process at high momentum. That is why the second chapter of this thesis is partly dedicated to the computation of the medium-induced gluon spectrum. From the single gluon emission

spectrum per unit energy ω, noted $\mathrm{d}N/\mathrm{d}\omega$, it is straightforward to calculate the energy loss:

$$\Delta E = \int \mathrm{d}\omega\, \omega \frac{\mathrm{d}N}{\mathrm{d}\omega} \tag{2.2}$$

where the integration boundaries depend on the validity regime of the calculation of $\mathrm{d}N$. To get the energy loss per unit length, one can differentiate the result with respect to the path length of the parton through the medium, noted L.

There are several formalisms in the literature related to the calculation of the radiative gluon emission and energy loss. For a detailed comparison between all these formalisms, see [53].

- The Baier-Dokshitzer-Mueller-Peigne-Schiff and Zakharov (BDMPS-Z) formalism resums multiple scatterings on static colour charges via a path integral that can be computed explicitly in the multiple *soft* scattering regime [54, 55, 56, 57, 58, 59, 60, 61]. For a static medium with quenching parameter $\hat{q}$ defined as the mean transverse momentum $k_\perp$ squared acquired via collisions per unit (light cone) time along the eikonal test parton trajectory, $\hat{q}\Delta t \sim \langle k_\perp^2 \rangle$, the gluon emission spectrum per unit energy ω reads:

$$\omega \frac{\mathrm{d}N_{\mathrm{BDPMS-Z}}}{\mathrm{d}\omega} \approx \frac{2\alpha_s C_R}{\pi} \begin{cases} \sqrt{\frac{\omega_c}{2\omega}} & \text{for } \omega \ll \omega_c \\ \frac{1}{12}\left(\frac{\omega_c}{\omega}\right)^2 & \text{for } \omega \gg \omega_c \end{cases} \tag{2.3}$$

  with $\omega_c \equiv \hat{q}L^2/2$. The $\sqrt{\omega_c/(2\omega)}$ tail is characteristic of the Landau-Pomeranchuk-Migdal effect in QCD (see Chapter 3, Section 3.3.3.4). The angular dependence of the gluon spectrum has been obtained in [62, 63], the generalization to massive quarks in [64] and expanding media in [62, 65, 66].

- The opacity expansion scheme organizes the calculation in terms of the number of static scattering centers. This approach has been pioneered by Gyulassy, Levai, and Vitev (GLV) in [67, 67, 68] for the first leading terms and Wiedemann in [69] for the all order resummation. This all order resummation reproduces the BDMPS-Z result when the scatterings are soft. However, the gluon spectrum with $N = 1$ scattering center gives somehow a significantly different result:

$$\omega \frac{\mathrm{d}N_{\mathrm{GLV}}}{\mathrm{d}\omega} \approx \frac{\alpha_s C_R}{\pi} \frac{\hat{q}L}{\mu_D^2} \begin{cases} \log\left(\frac{\mu_D^2 L}{2\omega}\right) & \text{for } \omega \ll \frac{1}{2}\mu_D^2 L \\ \frac{\pi}{4}\left(\frac{\mu_D^2 L}{2\omega}\right) & \text{for } \omega \gg \frac{1}{2}\mu_D^2 L \end{cases} \tag{2.4}$$

  for a medium with quenching parameter $\hat{q}$.

- Whereas the two previous formalisms consider static scattering centers, Arnold, Moore and Yaffe (AMY) calculate gluon production directly in a thermal QCD background [70, 71].

As emphasized in [72, 73], the modern view to unify the GLV and BDMPS-Z results is the following: the GLV formula gives an accurate description of the hard tail $\omega \gg \omega_c \sim \hat{q}L^2/2$ of the medium-induced spectrum coming from hard single scattering and the Bethe-Heitler regime $\omega \ll \omega_{\mathrm{BH}} \sim \hat{q}\ell^2/2$, with ℓ the medium mean free path, whereas the BDMPS-Z result encompasses the multiple soft scattering regime $\omega_{\mathrm{BH}} \leq \omega \leq \omega_c$.

On the other hand, the AMY formalism gives a more rigorous description of the interaction between the test parton and the scattering centers using results from QCD at finite temperature:

instead of relying on the Gyulassy-Wang model [74] for the elementary scattering cross-section off plasma constituents as in the BDMPS-Z or GLV calculations, the AMY formalism uses an hard-thermal-looped resummed version of this cross-section. In the multiple soft scattering regime, this amounts to a redefinition of the quenching parameter $\hat{q}$.

In Chapter 3, we present a detailed calculation of the gluon radiative spectrum within a "CGC-like" formalism inspired by the close relation between gluon production in proton-nucleus collisions and parton energy loss in heavy-ion collisions [75].

Even if the first QCD calculations of radiative energy loss in plasma date back to the mid nineties, this is still an active topic. The systemic analytic expansion around the harmonic oscillator solution started in [72] has been carried out up to the next-to-next-to-leading order in [76] for the energy spectrum and next-to-leading order for the broadening distribution [77]. A novel method for resumming multiple scatterings beyond the standard harmonic approximation can be found in [78].

2.1.2.2 Multiple emissions

Going beyond the single gluon emission in inelastic processes is a complicated task in perturbative QCD, even in the vacuum. Formally, this requires to compute Feynman diagrams with multiple gluons in the final state. For two gluons, such calculations have been performed in the series of papers [79, 80, 81, 82] with several approximations (static medium and multiple soft scatterings approximations for instance).

That said, there is a physical regime where multiple medium-induced emissions can be seen as a classical branching process, in an approach pioneered by Baier, Mueller, Schiff and Son to describe thermalization in heavy-ion collisions [83]. In this regime, the resummation of multiple branchings is done via a Boltzmann kinetic equation with a branching rate given by the BDPMS-Z one and a collision kernel taking into account elastic $2 \to 2$ processes. This will be studied at length in Chapter 4, section 4.3 (see also references therein). Former attempts to resum multiple medium-induced gluons consider that these emissions follow a Poisson process [62, 84]. In a certain sense, the effective theory for medium-induced jets described in Chapter 4 Section 4.3 is a generalization of these ideas beyond the Poisson ansatz.

2.2 Interplay between virtuality and medium effects

So far in this introduction, we have implicitly ignored the virtuality of the parton losing part of its energy in the plasma: the incoming test parton was on its mass shell. However, the driven mechanism for jet fragmentation in the vacuum[1] is the initial virtuality of the parton escaping the hard scattering. For a jet fragmenting in a dense environment, this should be also true, at least for high p_T jets. Consequently, a picture combining together virtuality-driven radiations and medium-induced emissions is essential to have a more precise understanding of how jets evolve in the plasma.

Models. The current treatment of this question is rather incomplete and unsatisfactory. Some models postulate that the fragmentation occurs as in the vacuum up to some arbitrary virtuality scale before quenching effects or that the vacuum-like fragmentation occurs completely outside the medium after the quenching of the virtual leading parton. A more detailed comparison between Monte Carlo event generators is given in Chapter 4, Section 6.5. There are some notable

[1] In this thesis, by "vacuum", we always mean in e^+e^- or pp collisions.

counter-examples. For instance, the higher-twist approach [85, 86] in which the vacuum-like fragmentation in the plasma involves modified DGLAP splitting functions including higher-twist contributions due to the medium. The parton shower `Q-Pythia` [87] uses also medium modified DGLAP splitting functions taking into account medium induced emissions in the multiple soft scattering regime. Finally, the Monte Carlo event generator `Jewel` [88] which uses a selection rule based on formation time arguments in the generation of a vacuum-like branching or a medium scattering.

Colour coherence. On the theory side, this question has driven recently a lot of activity. The most important results obtained in this direction are related to the concept of coherence. A jet is a quantum object, and as such, it has a typical coherence size, or more precisely a coherence angle in this context. For a jet fragmenting in the vacuum, an emission with a transverse wavelength larger that the opening angle of the leading dipole at the formation time of the emission is emitted coherently by the dipole, irrespectively of its internal structure. For a leading colour singlet dipole, large angle gluon emissions are therefore suppressed. The medium modifies this coherence property: the multiple interactions with the scattering centers break the quantum coherence of the jet after a time called the decoherence time. This phenomenon has been highlighted in [89, 90, 91] from pQCD first principles and some phenomenological applications are considered in [92, 93, 94]. Note that a similar idea appears also in the reference [95]. Medium-induced decoherence and the coherence property of jets with respect to the plasma show that the (quantum) interplay between virtuality and medium effects is not trivial.

Towards an unified picture of jet fragmentation. The presence of a finite volume medium addresses the problem of jet fragmentation (or more generally the decay of virtual particles) in an inhomogeneous space-time. In that respect, jet quenching in heavy-ion collisions is a unique background for understanding QCD jet properties in an open quantum system. There are still open questions but we believe that the theoretical first part of this thesis answers part of them :

- the concept of "off-shellness" and "on-shellness" when a parton is embedded in a dense weakly coupled medium is clarified in Chapter 5, Section 5.1.
- In contrast to prior expectations, decoherence has no significant role for the in-medium vacuum-like fragmentation at leading logarithmic accuracy. However, decoherence plays a crucial role for the subsequent fragmentation in the vacuum once the medium is diluted. This is explain in Chapter 5, Section 5.2.
- At this accuracy and in the multiple soft scattering regime, the vacuum-like fragmentation factorises from the "higher-twist" medium effects. The factorisation scale is not an ad-hoc arbitrary choice: it is given by the virtuality scale that marks the transition between off-shellness and on-shellness. This virtuality scale is set by the medium itself.

Chapter 3

Emissions and decays in a dense QCD medium

In this chapter, we calculate cross-sections for the decays of off-shell or on-shell partons in the presence of a dense QCD medium. These calculations are performed at leading order in the strong coupling constant α_s when this coupling is not enhanced by the large density of medium scattering centers, and to all orders in α_s in the opposite situation. We provide new analytic formulas for the full dependence of these cross-sections with the emission kinematics.

Such formulas will be the building blocks for the jet calculations made in the next chapters since these chapters deal with the all order resummation of the simple processes calculated here. The formalism used to derive them is inspired from the Colour Glass Condensate (CGC) formalism [96].

The first section provides benchmark results for the decay of off-shell particles in the vacuum. The second section deals with our modelling of the dense QCD medium. In the third section, we discuss medium-induced emissions. In the last section, we examine the medium effects on quantum interferences in emission processes.

3.1 Some benchmark results in the vacuum

In this section, we recall the main results regarding the decay of a time-like slightly off-shell parton in perturbative QCD. Roughly speaking, a slightly off-shell time-like parton is an internal leg of a Feynman diagram such that the kinematics of the final state particles enforce the 4-momentum squared q^2 of the leg to be positive and almost 0 (the propagator "blows up"). A more precise definition will be given in the context of collinear and soft factorisation.

For simplicity, we consider the e^+e^- annihilation process so that we do not have to deal with incoming space-like partons[1]. As we will only perform leading order calculations in this chapter, we focus on the corresponding leading order calculation in the vacuum. However, many results exist beyond leading order [98, 99, 100].

3.1.1 Collinear factorisation at leading order

In this e^+e^- annihilation process, we assume that the final state is made of n QCD partons, with 4-momenta labelled by p_i, $i \in \{1, ..n\}$ — there is no additional difficulty if the final states particles are non-QCD partons. We are interested in the limit of the $e^+e^- \to \{n \text{ partons}\}$

[1] Considering together initial and final state almost on-shell partons rises additional difficulties, see [97]

amplitude squared when two outgoing partons (say 1 and 2) become collinear. In this configuration, one defines p^μ as this collinear direction, with $p^2 = 0$. The splitting fraction z and the transverse momentum $k_\perp^\mu$ of the splitting are defined thanks to the standard Sudakov decomposition of p_1 and p_2:

$$p_1^\mu = zp^\mu + k_\perp^\mu - \frac{k_\perp^2}{z}\frac{n^\mu}{2p^\mu n_\mu}\,, \qquad p_2^\mu = (1-z)p^\mu - k_\perp^\mu - \frac{k_\perp^2}{1-z}\frac{n^\mu}{2p^\mu n_\mu} \tag{3.1}$$

with n^μ a light-light vector such that $k^\mu n_\mu = 0$. The collinear limit is defined by $k_\perp \to 0$.

The leading order factorisation theorem for the *tree-level* amplitude squared of the process states that [101]:

$$|\mathcal{M}_n(p_1, p_2, .., p_n)|^2 \underset{k_\perp \to 0}{\longrightarrow} |\mathcal{M}_{n-1}(p, p_3, ..p_n)|^2 4\pi\alpha_s \frac{z(1-z)}{-k_\perp^2}\Phi_i^{ab}(z) \tag{3.2}$$

in the limit where the partons 1 and 2 become collinear. In this result, the colour sums have been performed as well as the *average* over the polarizations of the decaying parton i. a and b are the flavour index of partons 1 and 2 whereas i is the flavour index of the parent parton. In the collinear limit $-k_\perp^2 = z(1-z)(p_1+p_2)^2 \simeq p^0(z(1-z)\theta)^2$, with θ the polar angle between the 3-vectors $\vec{p}_1$ and $\vec{p}_2$.

This formula says that in the collinear limit, the amplitude squared of the process factorizes into two subprocesses: the $e^+e^- \to \{n-1 \text{ partons}\}$ process and the decay of the almost on-shell parton i into a and b. Therefore, a classical picture for multiple collinear decays emerges from this factorisation theorem. In the additional soft limit $z \to 0$, this factorisation formula becomes, written now at the level of the full differential cross-section:

$$\mathrm{d}\sigma_n(p_1, p_2, .., p_n) \underset{k_\perp \to 0}{\longrightarrow} \mathrm{d}\sigma_{n-1}(p, p_3, ..p_n)\frac{\alpha_s C_i}{\pi}\frac{\mathrm{d}k_\perp^2}{k_\perp^2}\frac{\mathrm{d}z}{z} \tag{3.3}$$

In this thesis, the factor appearing in front of $\mathrm{d}\sigma_{n-1}$ will often be denoted as the Bremsstrahlung spectrum or vacuum-like emission spectrum. In this chapter and especially in Section 3.3, we aim at calculating this soft-collinear factor in the presence of a dense QCD medium. To calculate this factor, we use the fact that it can be derived considering the $i \to \{a, b\}$ process alone, where i is the decaying parton created at a fixed vertex x_i^μ.

3.1.2 Eikonal factor: soft factorisation at leading order

There is another regime where the same kind of factorisation holds: when one of the final state gluon is soft. The soft limit of, say p_1, is defined as $p_1^\mu \to 0$, meaning that all components of the four-vector of the gluon go to zero. In this case, the n-parton tree-level amplitude squared discussed above factorizes as [100]:

$$|\mathcal{M}_n(k, p_2, .., p_n)|^2 \underset{k^\mu \to 0}{\longrightarrow} 4\pi\alpha_s \sum_{i,j=2}^{n} \mathcal{S}_{ij}(k)|\mathcal{M}_{n-1}^{(i,j)}(p_2, ..p_n)|^2\,, \qquad \mathcal{S}_{ij}(k) = \frac{p_i^\mu p_{j\mu}}{(p_i^\mu k_\mu)(p_j^\mu k_\mu)} \tag{3.4}$$

The sum, which formally breaks the exact factorisation (contrary to Eq. (3.2)), is a consequence of gluons carrying colour and thus producing colour correlations between the outgoing partons.

The amplitude squared $|\mathcal{M}_{n-1}^{(i,j)}|^2$ depends on the prong (i,j) which emits the soft gluon:

$$|\mathcal{M}_{n-1}^{(i,j)}(p_2,..p_n)|^2 = [\mathcal{M}_{n-1}^{a_1,..,b_i,..,b_j,..,a_n}(p_2,..p_n)]^\star T^c_{b_i c_i} T^c_{b_j c_j} [\mathcal{M}_{n-1}^{a_1,..,c_i,..,c_j,..,a_n}(p_2,..p_n)] \tag{3.5}$$

with all the colour indices left explicit. The factor $\mathcal{S}_{ij}(q)$ is called the eikonal or soft factor. It encompasses the soft gluon radiation pattern of an off-shell antenna. We calculate it in details in the vacuum and estimate it in the presence of a dense medium in Section 3.4.3.

This eikonal factor $\mathcal{S}$ has a very interesting property, known as angular ordering. To see this, let us rewrite it in terms of the opening angle θ_{ij} of the prong and the angles $\theta_{gi(j)}$ between the gluon and the parton $i(j)$:

$$\mathcal{S}_{ij}(k) = \frac{1}{k^{0\,2}} \frac{1-\cos(\theta_{ij})}{(1-\cos(\theta_{gi}))(1-\cos(\theta_{gj}))} \tag{3.6}$$

$$= \frac{1}{k^{0\,2}} \left(\tilde{\mathcal{S}}^i_{ij} + \tilde{\mathcal{S}}^j_{ij} \right) \tag{3.7}$$

In the second line, we split the eikonal factor into two symmetric pieces:

$$\tilde{\mathcal{S}}^i_{ij} = \frac{1}{2} \left(\frac{1-\cos(\theta_{ij})}{(1-\cos(\theta_{gi}))(1-\cos(\theta_{gj}))} + \frac{1}{1-\cos(\theta_{gi})} - \frac{1}{1-\cos(\theta_{gj})} \right) \tag{3.8}$$

For $\tilde{\mathcal{S}}^j_{ij}$, one switches $i \leftrightarrow j$. When the kernel $\tilde{\mathcal{S}}^i_{ij}$ is averaged over the azimuthal angle in the plane transverse to the direction of the 3-momentum of i, this vanishes if $\theta_{gi} \geq \theta_{ij}$ (and similarly if one averages over the azimuthal angle in the plane transverse to j). This means that the soft gluon radiation is confined inside a cone of opening angle θ_{ij} around either the i or the j direction. This is the angular ordering property. For a general presentation of colour coherence, we refer the reader to Ref. [102], Chapter 4. A detailed calculation of the azimuthal integral is done in [101], and we will perform a similar calculation in Section 3.4.3.

3.2 Modelling of the dense QCD medium

In this section, we develop the formalism necessary to set up the calculation of radiative gluon emissions in the presence of a dense QCD medium. To summarize, the medium is a classical background gauge field generated by static colour charges in the rest frame of the plasma. These static colour charges have Gaussian fluctuations to account for the thermal fluctuations of the plasma. A test particle propagating through the plasma undergoes a Coulomb-like interaction with the scattering centers.

3.2.1 Infinite momentum frame and conventions

Boosted frame. In order to use the technology and computational tools developed in the context of eA and pA collisions [75], we always consider the scattering of a projectile moving with the velocity of light in the positive $x^3 \equiv z$ direction on a dense medium, the target, boosted very close to the light cone and moving in the negative z direction. The projectiles considered throughout this chapter will be an on-shell or off-shell parton, or a colour dipole. In the off-shell case, we have of course in mind the decay of highly virtual parton coming from the hard scattering process.

The frame where the dense medium is boosted near the light-cone branch $x^+ = 0$, named "boosted frame" therein, is not the same as the laboratory frame defined in the Introduction 1.

They are related by a boost transformation with parameter $\beta \to -1$ which leaves the plane $(x, y) = (x^1, x^2) = (X^1, X^2)$ invariant:

$$\begin{pmatrix} x^0 \\ x^3 \end{pmatrix} = \begin{pmatrix} \cosh(\psi) & \sinh(\psi) \\ \sinh(\psi) & \cosh(\psi) \end{pmatrix} \begin{pmatrix} X^0 \\ X^3 \end{pmatrix}, \qquad \beta = \tanh(\psi) \tag{3.9}$$

In the end, the differential cross-sections obtained in this chapter are boosted back to the laboratory frame for phenomenological applications. As these cross-sections are boost invariant along the z direction, this transformation is equivalent to use the laboratory frame values of all the physical parameters in the formulas derived in the boosted frame. To say it differently, when plugging numbers into the final cross-section formulas, one can directly use quantities measured in the laboratory frame, such as the quenching parameter (related to the density of scattering centers) or the jet path length, to get the cross-section in the laboratory frame.

Light-cone coordinates. It is convenient to introduce the light-cone coordinates defined by the following transformation:

$$x^+ = \frac{x^0 + x^3}{\sqrt{2}}, \qquad x^- = \frac{x^0 - x^3}{\sqrt{2}} \tag{3.10}$$

where $x^\mu \equiv (x^0, x_\perp, x^3)$ is the coordinate system in the boosted frame. The transverse coordinate $x_\perp = (x^1, x^2) \equiv x^i$ orthogonal to the z direction is unchanged by the light-cone transformation. We adopt the following convention for the metric signature $\eta_{\mu\nu}$: $(+,-,-,-)$. The product of two four vectors $u \cdot v$ is $\eta_{\mu\nu} u^\mu v^\nu = u^+ v^- + u^- v^+ - u_\perp v_\perp$ and the Lorentz invariant phase space is:

$$\mathrm{d}^4 p \, \delta(p^2 - m^2) = \frac{\mathrm{d}p^+ \mathrm{d}^2 p_\perp}{2p^+} \tag{3.11}$$

We note $\partial_\mu \equiv \frac{\partial}{\partial x^\mu}$ the derivative operator. In the light cone coordinate system, $\partial_{+/-} = \frac{\partial}{\partial x^{+/-}}$. Due to the particular form of the metric in light cone coordinates, $\partial^+ = \partial_-$ and $\partial^- = \partial_+$ so that $\partial_\mu \partial^\mu = 2\partial^+\partial^- - \partial_\perp^2$. We point out that the subscript $\perp$ refers to the transverse coordinate with respect to the direction of motion of the projectile which is also the z axis. This notation is adopted in order to make a clear distinction with the transverse coordinate with respect to the *beam* axis, noted with a "T" subscript. Also, we use contravariant indices for the transverse vectors, meaning that $\partial^i_{x_\perp} \equiv \frac{\partial}{\partial x_i} = -\frac{\partial}{\partial x^i}$. The minus factor is crucial to get the right result for the interference spectrum in Section 3.4.2.

When dealing with an off-shell incoming projectile, we will always call x_i^μ the coordinate vector of the vertex where the off-shell particle is emitted. The particle enters the plasma at light-cone time $x^+ = x_0^+$. We consider massless QCD partons only.

Cross-sections. In this chapter, we basically compute cross-sections. In order to obtain the right prefactors in front of our formulas, one should be careful with both the normalization of single particle states and the cross-section definition.

Let us consider that the scattering occurs in a finite 4-dimensional box of volume $V_{\mathfrak{B}} = S_{\mathfrak{B}} \times T_{\mathfrak{B}}^2$ where $S_{\mathfrak{B}}$ is the transverse area of the box and $T_{\mathfrak{B}}$ is the size of the box in the time and longitudinal direction. In our final formulas, the volume of the box will be sent to infinity. The cross-section is then defined as:

$$\mathrm{d}\sigma = \frac{1}{T_{\mathfrak{B}} \Phi_0} \mathrm{d}P \tag{3.12}$$

where Φ_0 is the flux of incoming particles. In the case at hand, the incoming state is a single particle state moving with the speed of light in the $+z$ direction. The flux is then given by $|\vec{v}|/(S_{\mathfrak{B}}T_{\mathfrak{B}}) = 1/(S_{\mathfrak{B}}T_{\mathfrak{B}})$ (in high energy physics units, with $c = 1$).

The emission probability $\mathrm{d}P$ reads

$$\mathrm{d}P = \frac{|\langle \mathrm{out}|\mathrm{in}\rangle|^2}{\langle \mathrm{out}|\mathrm{out}\rangle \langle \mathrm{in}|\mathrm{in}\rangle} \prod_j \frac{T_{\mathfrak{B}}S_{\mathfrak{B}}}{(2\pi)^3} \mathrm{d}p_j^3 \mathrm{d}^2 p_{j\perp} \tag{3.13}$$

with all the produced particles in the out state labelled by j. The factor $T_{\mathfrak{B}}S_{\mathfrak{B}}$ is required to enforce

$$\int \frac{T_{\mathfrak{B}}S_{\mathfrak{B}}}{(2\pi)^3} \mathrm{d}p^3 \mathrm{d}^2 p_\perp = 1 \tag{3.14}$$

The single particle states are normalized as follows:

$$\langle p|p\rangle = 2p^0(2\pi)^3\delta(p^3 = 0)\delta(p_\perp = 0) \tag{3.15}$$

$$= 2p^0 \int \mathrm{d}x^3 \int \mathrm{d}^2 x_\perp \tag{3.16}$$

$$= 2p^0 S_{\mathfrak{B}}T_{\mathfrak{B}} \tag{3.17}$$

Combining all these expressions together when the incoming state is a single particle state one finds:

$$\mathrm{d}\sigma = \frac{1}{T_{\mathfrak{B}}} \frac{|\langle \mathrm{out}|\mathrm{in}\rangle|^2}{2p^0} \prod_j \frac{\mathrm{d}p_j^3 \mathrm{d}^2 p_{j\perp}}{(2\pi)^3 2p_j^0} \tag{3.18}$$

$$= \frac{1}{T_{\mathfrak{B}}} \frac{|\langle \mathrm{out}|\mathrm{in}\rangle|^2}{2p^0} \prod_j \frac{\mathrm{d}p_j^+ \mathrm{d}^2 p_{j\perp}}{(2\pi)^3 2p_j^+} \tag{3.19}$$

To get the second line, we have recognized the Lorentz invariant phase space for the emitted particles. Note the unusual remaining size factor $T_{\mathfrak{B}}$. Of course, it will cancel in all our final results.

3.2.2 The background gauge field $\mathcal{A}_m^\mu$

The dense medium generates a *classical* background gauge field $\mathcal{A}_m^\mu$. The classical approximation is natural in the weak coupling limit where the QCD coupling constant $g(k_B T_\mathrm{p})$, evaluated at the typical thermal energy of the in-medium partons, is small. At weak coupling, the tree-level order dominates the projectile-target interactions. As tree-level and classical approximation are equivalent, the weak coupling limit supports the classical nature of the background gauge field. This gauge field is produced by a classical current of colour charges. In a non-abelian gauge theory, such a clear separation between sources and gauge field is rather unusual because the colour current is only *covariantly* conserved. The choice of the light-cone gauge leads nevertheless to this simple picture.

We first consider the case of a static medium with a time-independent colour charges density in the laboratory frame. The extension to the case of a longitudinally expanding medium is discussed in Section 3.2.4. In the laboratory frame, the 4-current density $\mathcal{J}_{m,\mathrm{lab}}^\mu$ — in the adjoint representation of $\mathrm{SU}(N_c)$ — reads:

$$\mathcal{J}_{m,\mathrm{lab}}^\mu = \bar{\rho}_a(x_\perp, X^3) t^a U^\mu \,, \qquad U^\mu = (1,0,0,0) \tag{3.20}$$

$$= \bar{\rho}_a\big(x_\perp, (X^+ - X^-)/\sqrt{2}\big) t^a U^\mu \,, \qquad U^\mu = (\underbrace{1/\sqrt{2}}_{+}, \underbrace{1/\sqrt{2}}_{-}, 0, 0) \tag{3.21}$$

with $\bar{\rho}_a$ the charge density and U^μ the four velocity of the fluid in the laboratory frame (which is also the rest frame of the plasma since the fluid is static).

In the boosted frame defined in 3.2.1, with boost parameter $\beta = \tanh(\psi) \to -1$, the 4-current $\mathcal{J}^\mu_m$ becomes:

$$\mathcal{J}^\mu_m = \bar{\rho}_a\big(x_\perp, (e^{-\psi}x^+ - e^{\psi}x^-)/\sqrt{2}\big)t^a u^\mu\,, \quad u^\mu = (\overbrace{e^{\psi}/\sqrt{2}}^{+}, \overbrace{e^{-\psi}/\sqrt{2}}^{-}, 0, 0) \tag{3.22}$$

$$\simeq \rho_a(x^+, x^-, x_\perp)t^a\delta^{\mu-} \tag{3.23}$$

In the second line, we neglect the + component of the 4-velocity of the fluid, since for $\beta \simeq -1$, $\psi \to -\infty$ and only the minus component remains in this limit. The density ρ_a is now the density in the boosted frame $\rho_a \simeq e^{-\psi}\bar{\rho}_a/\sqrt{2}$ which is larger than $\bar{\rho}_a$ because of the Lorentz contraction in the z direction. Now, we argue that the x^- dependence of the current is irrelevant. We are interested in high energy scatterings where the partons propagating through the medium conserves the + component of their momenta. This boost invariant statement is formalized within the eikonal regime presented Section 3.3.1.1. We will see that neglecting the x^- dependence of the medium gauge field leads to an exact conservation of the + component of the projectiles. Consequently, one can take $\rho_a(x^+, x^-, x_\perp)$ as independent of x^- and evaluated at $x^- = 0$ since the right-mover partons propagate near this light cone branch

$$\rho_a(x^+, x_\perp) \approx \frac{e^{-\psi}}{\sqrt{2}}\bar{\rho}_a\left(x_\perp, \frac{e^{-\psi}}{\sqrt{2}}x^+\right) \tag{3.24}$$

To sum up, the current (3.23) has only one non-trivial minus component, meaning that all the colour charges of the medium are left movers with the speed of light, and is taken as independent of $x^- \approx 0$, simplification valid for eikonal scattering of right-movers. Note however that the standard approximation in pA collision within the CGC formalism $\rho_a \propto \delta(x^+)$ is not allowed here for reasons that will become obvious at the end of our calculation: this would neglect emissions with formation time smaller than the projectile in-medium path length and those are precisely the interesting ones in jet quenching physics.

Now, let us choose the light cone gauge $\mathcal{A}^+_m = 0$ and the 4-current form given by (3.23)-(3.24). In this gauge, the colour current associated with the colour charges of the medium does not couple with the gauge field $\mathcal{A}_m$, leading to a lot of simplifications. Indeed, the 4-current (3.23)-(3.24) is, in principle, a leading order result which could receive higher order corrections from the feedback of the gauge field on the current. However, it is not the case in this gauge (and in the Lorentz gauge $\partial_\mu\mathcal{A}^\mu_m = 0$ as well, see [103] or [104]). To see this, let us write the covariant conservation of the colour current $[D_\mu, \mathcal{J}^\mu_m] = 0$, which reads in the light cone gauge:

$$\partial^+\mathcal{J}^-_m - ig[\mathcal{A}^+_m, \mathcal{J}^-_m] = 0 \tag{3.25}$$

and is automatically satisfied by the form (3.23) with our gauge choice provided that $\partial^+\mathcal{J}^-_m = 0$. This means that the colour charge distribution ρ_a in the current (3.23) is independent of x^- to all orders in g. In an other gauge, the current $\mathcal{J}^-_m$ would acquire a higher order x^- dependence via Wilson line conjugation associated with the colour precession of the medium colour charges in the self-generated gluon field. Thus, the light cone gauge $\mathcal{A}^+_m = 0$ enables to have a simple picture of the medium in the infinite momentum frame with a clear separation between colour sources and gauge field.

In the light-cone gauge $\mathcal{A}^+_m = 0$, it is furthermore possible to solve the classical Yang-Mills

equations $[D_\mu, \mathcal{F}^{\mu\nu}_m] = \mathcal{J}^\nu$ for the gauge field [105]:

$$\partial^+(\partial_\mu \mathcal{A}^\mu_m) + ig[\mathcal{A}^i_m, \partial^+ \mathcal{A}^i_m] = 0 \tag{3.26}$$

$$[D^-, \partial^+ \mathcal{A}^-_m] - [D^i, \mathcal{F}^{i-}_m] = \mathcal{J}^- \tag{3.27}$$

$$\partial^+ \mathcal{F}^{-i}_m + [D^-, \partial^+ \mathcal{A}_{m\perp}] - [D^j, \mathcal{F}^{ji}_m] = 0 \tag{3.28}$$

One easily sees that $\mathcal{A}^\mu_m(x^+, x_\perp)$ is a solution of (3.26), (3.27) and (3.28) if

$$\mathcal{A}^i_{m,a} = 0\,, \qquad \partial^2_\perp \mathcal{A}^-_{m,a} = -g\rho_a(x^+, x_\perp) \tag{3.29}$$

The equation (3.29) is very similar to the Poisson equation in electrostatic. It can be solved in Fourier space:

$$\boxed{\mathcal{A}^-_{m,a}(x^+, x_\perp) = g \int \frac{\mathrm{d}^2 k_\perp}{(2\pi)^2} \frac{e^{-ik_\perp x_\perp}}{k^2_\perp} \rho_a(x^+, k_\perp)} \tag{3.30}$$

This equation is our starting point to calculate the statistical correlations of the gauge field in the next subsection.

3.2.3 Statistical properties of $\mathcal{A}^\mu_m$

The collection of colour charges $\rho_a(x^+, x_\perp)$ is a statistical field, as in the McLerran-Venugopalan model [106, 107, 108]. In our modelling of the quark-gluon plasma, this accounts for the thermal fluctuations of the distribution. For gauge symmetry reasons, the 1-point correlation function vanishes $\langle \rho_a \rangle = 0$. For an ideal (non-interacting) quark-gluon plasma in thermal equilibrium, the colour charges are uncorrelated so that the 2-points correlation functions read:

$$\langle \rho_a(x^+, x_\perp) \rho_b(y^+, y_\perp) \rangle \approx n \delta_{ab} \delta(x^+ - y^+) \delta(x_\perp - y_\perp) \tag{3.31}$$

As ρ_a, the average squared charge density n is the one measured in the boosted frame, $n = e^{-\psi} \bar{n}/\sqrt{2}$, with $\bar{n}$ the average squared charge density in the plasma rest frame, which scales like the plasma temperature T^3_{p} for an ideal quark-antiquark gas with vanishing baryon chemical potential. For a static, infinite, homogeneous plasma, $\bar{n}$ does not depend on x^+ nor $x_\perp$. The form of the correlator (3.31) in a longitudinally expanding medium is discussed in the next section.

We assume Gaussian statistics meaning that the probability distribution is entirely known from these one-point and two-points correlations. This amounts to neglect the interactions between the scattering centers and the non-linear self interactions. As we shall see, the latter approximation is not valid for very long range correlations, larger than the Debye screening length.

From the linear property of (3.30), the background gauge field $\mathcal{A}^-_m$ is also Gaussian distributed. Combining equations (3.31) and (3.30) together, one easily finds its 2-point correlator in coordinate space:

$$\boxed{\langle \mathcal{A}^-_{m,a}(x^+, x_\perp) \mathcal{A}^-_{m,b}(y^+, y_\perp) \rangle = n \delta_{ab} \delta(x^+ - y^+) \Upsilon(x_\perp - y_\perp)} \tag{3.32}$$

with

$$\Upsilon(u_\perp) = g^2 \int \frac{\mathrm{d}^2 k_\perp}{(2\pi)^2} \frac{e^{-ik_\perp u_\perp}}{k^4_\perp} \tag{3.33}$$

Note that we ignore the potential transverse dependence of the squared charge density n in this calculation. The function Υ is the inverse Fourier transform of the Coulomb elastic scattering

cross-section $\tilde{\Upsilon}(k_\perp) = g^2/k_\perp^4$. Written like this, the Fourier transform is not well defined due to the infrared singularity as $k_\perp \to 0$. It has to be regulated in some way. Actually, even for an ideal quark-gluon plasma, one cannot ignore screening effects: in the rest frame of the plasma, long range interactions are screened above the characteristic Debye length $\lambda_D = 1/\mu_D$ where μ_D is the Debye mass. This provides a natural infrared cut-off $|k_\perp| \geq \mu_D$ for the integral (3.33).

To be more precise and for the sake of completeness, we briefly review the two mains regularizations of(3.33) encountered in the literature:

1. for a thermal plasma in equilibrium, the two-point correlation function of the gauge field (3.32) is naturally regularized by the retarded propagator with hard thermal loops resummed. This accounts for Debye screening and Landau damping of the colour fields. The elastic cross-section reads then [109]:

$$\frac{1}{2}\bar{n}\tilde{\Upsilon}_{\mathrm{HTL}}(k_\perp) = \frac{\mu_D^2 T_{\mathrm{p}}}{k_\perp^2(k_\perp^2+\mu_D^2)} \tag{3.34}$$

2. Another way to regulate the Coulomb divergence is to consider a Yukawa type cross-section by analogy between mass screening and Debye screening [110]:

$$\tilde{\Upsilon}_{\mathrm{Yuk}}(k_\perp) = \frac{g^2}{(k_\perp^2+\mu_D^2)^2} \tag{3.35}$$

The emergence of the scale μ_D in this problem enables to clarify the validity regime of the assumption of instantaneous and independent interactions during the longitudinal motion of a test parton through the medium, namely the $\delta(x^+ - y^+)$ in (3.31). First of all, from QCD at finite temperature (see [42] for a review), one knows that:

$$\mu_D \sim g T_{\mathrm{p}} \tag{3.36}$$

in the plasma rest frame. Then, the elastic mean free path $\ell \sim 1/(\bar{n}\sigma_\ell)$ in this frame is parametrically of order $\mu_D^2/(g^4\bar{n}) \sim (g^2 T_{\mathrm{p}})^{-1}$ with g^4/μ_D^2 the order of magnitude of the elastic cross-section σ_ℓ. Thus, for a weakly coupled quark-gluon plasma:

$$\ell \gg \lambda_D \tag{3.37}$$

The elastic mean free path being much larger than the typical duration of plasma interaction, it is allowed to treat collisions as independent and instantaneous, at least in the weak coupling regime.

3.2.4 Bjorken expansion

In order to include the longitudinal expansion of the quark-gluon plasma in our medium modelling, we use a pragmatic approach relying on the results derived in the static case following [65, 111] for example. By longitudinal expansion, we mean here the expansion of the plasma in the beam direction $X \equiv X^1 = x^1$, which is *not* the $X^3 = Z$ axis of the coordinate system in the laboratory frame (see Introduction 1). In the Bjorken model, the plasma is homogeneous in the transverse direction with respect to beam axis and boost invariant along the beam direction. This implies that the fluid state variables depend on the proper time $\tau = \sqrt{X^{0\,2} - X^{1\,2}} = \sqrt{T^2 - X^2}$ of fluid elements only. Fluid state variables such as temperature or density are well defined if the fluid reaches local thermal equilibrium.

The temperature field is a function of τ: $T_{\rm p}(X^\mu) = \hat{T}_{\rm p}(\tau)$. For an ideal hydrodynamical expansion, $\hat{T}_{\rm p}(\tau)$ satisfies [20]:

$$\frac{1}{\hat{T}_{\rm p}}\frac{{\rm d}\hat{T}_{\rm p}}{{\rm d}\tau} + \frac{c_s^2}{\tau} = 0 \tag{3.38}$$

where $c_s \leq 1/3$ is the sound velocity in the plasma, assumed to be constant. The resolution of (3.38) gives:

$$\left(\frac{\hat{T}_{\rm p}}{\hat{T}_0}\right)^3 = \left(\frac{\tau_0}{\tau}\right)^{3c_s^2} \tag{3.39}$$

meaning that the average squared charge density $\bar{n}$ (defined in the rest frame of a fluid element) follows also a power law since $\bar{n}$ is proportional to $T_{\rm p}^3$ for an ideal quark-gluon plasma,

$$\bar{n}(\tau) = \bar{n}_0\left(\frac{\tau_0}{\tau}\right)^{3c_s^2}. \tag{3.40}$$

Now we argue that the dominant effect of the longitudinal cooling on the results obtained in the static case is to introduce a x^+ dependence of the squared charge density $n(x^+)$ in (3.31) and (3.32). Indeed, if we focus on a space-time region close to the plane $x^1 = X = 0$ and close to the light-cone branch $x^- = 0$, one has the following identities:

$$\tau = T = X^3 = \frac{e^{-\psi}}{\sqrt{2}}x^+ \tag{3.41}$$

This means that in this space-time domain, the longitudinal cooling can be mimicked by a X^3 modulation of a static current. We have already justified why the region $x^- = 0$ is relevant in high energy scatterings. By focusing on the region $x^1 = 0$, we also assume that the highly energetic partons propagate through the medium in the plane transverse to the beam axis. To generalize the present results for dijet production at non-zero rapidity, one can use a boost along the *beam* direction [111].

Therefore, we can refer to the calculations done in the static case to obtain the current and the gauge field in the boosted frame (see Eqs. (3.23)-(3.24) and (3.30)). In the end, the only difference relies in the x^+ dependence of $n(x^+)$ in the 2-point correlators (3.31) and (3.32). Using (3.40) and (3.41), one finds $n(x^+) \simeq e^{-\psi}\bar{n}_0(x_0^+/x^+)^{3c_s^2}$ with $x_0^+ = e^{-\psi}\tau_0$ the light cone time at which the projectile enters the plasma in the boosted frame. With $n_0 = e^{-\psi}\bar{n}_0$ the initial density in the boosted frame, this is rewritten:

$$n(x^+) = n_0\left(\frac{x_0^+}{x^+}\right)^\gamma, \qquad 0 \leq \gamma \equiv 3c_s^2 \leq 1 \tag{3.42}$$

We will use explicitly this formula inside the quenching parameter defined in the next section. The resulting x^+ dependence of the quenching parameter is important for the discussions in Chapter 5, sections 5.1.3 and 5.2.4.

3.3 Medium-induced emissions

3.3.1 Transverse momentum distribution in the eikonal approximation

Before exploring the medium-induced emission spectrum, let us start with the following more simple exercise as a warm-up. The projectile is a highly energetic on-shell quark with four-momentum $p^\mu = (p^+, p^-, p_\perp)$ and we want to compute the cross-section for producing one quark

with four momentum $p'^{\mu} = (p'^{+}, p'^{-}, p'_{\perp})$ out of the medium, to all orders in $g\mathcal{A}^{\mu}_{m}$ and order 0 in g. In the high energy limit, one neglects the quark mass. As usual in quantum field theory, one must first calculate the scattering amplitude $\mathcal{M}(p', p) \equiv \langle p'|p\rangle$. This amplitude depends also on the spins s, s' and colours j, j' of the incoming and outgoing quarks. Then, the differential cross-section is given by

$$\frac{\mathrm{d}^3\sigma}{\mathrm{d}p'^{+}\mathrm{d}^2p'_{\perp}} = \frac{1}{T_{\mathfrak{B}} 2p^0(2\pi)^3 2p'^{+}} \left(\frac{1}{2N_c} \sum_{s,s',j,j'} |\mathcal{M}(p', p)|^2 \right) \tag{3.43}$$

From the Lehmann-Symanzik-Zimmermann (LSZ) reduction formula, the amplitude $\langle p'|p\rangle$ is related to the truncated quark propagator in momentum space $D_{tc}(p, p'|\mathcal{A}_m)$ according to:

$$\langle p'|p\rangle = \lim_{p^2, p'^2 \to 0} \frac{1}{Z_\psi} \bar{u}_s(p') D_{tc}(p, p'|\mathcal{A}_m) u_s(p) \tag{3.44}$$

with Z_ψ the quark wave function renormalization constant. We keep the dependence of the quark propagator on the background field explicit (in the vacuum, this calculation would be pointless since $\langle p'|p\rangle \propto \delta^{(4)}(p' - p)$ for idealized quark asymptotic states). Hence, to calculate (3.43) to all orders in $g\mathcal{A}^{\mu}_{m}$, we need to calculate the truncated quark propagator $D_{tc}(p, p'|\mathcal{A}_m)$.

3.3.1.1 In-medium eikonal quark propagation

Calculating $D_{tc}(p, p'|\mathcal{A}_m)$ exactly is complicated. However, in the eikonal regime, there exist explicit analytic formulas. In this regime, the incoming quark moves along the light cone $+$ direction with a large $p^+ \to \infty$ component, i.e. $p^+ \gg |p_\perp|$ (and so $p^- \ll |p_\perp|$) which is conserved during the scattering process $p^+ \simeq p'^{+}$. This means that the momentum transferred by the background field, $q = p' - p$ is small: $-q^2 \ll p^{+2}$.

There are several methods to obtain the eikonal truncated quark propagator. The S-matrix element (3.44) in the high energy limit has been obtained for instance in [112] in light-cone quantization using the boost invariance of the S-matrix (see also [113] in conventional quantization). A pedestrian methods consists in calculating and resumming all the Feynman diagrams with external field insertions to all orders. The calculation is sketched in [114] and done precisely in [115, 116]. One can show that the coupling of the incoming particle with the external field is independent of the representation of the Lorentz group to which the particle belongs. In particular it is the same for scalar particles as for Dirac fermions. We note $\gamma^{\mu}_{\mathrm{cl}}(x^+) = \gamma^{\mu}_{\mathrm{cl}}(0) + u^{\mu}x^+$ the classical path of the incoming quark through the medium, parametrized by the x^+ coordinate along the quark trajectory with $\gamma^{\mu}_{\mathrm{cl}}(0) \equiv (0, x^-, x_\perp)$ and $u^{\mu} = p^{\mu}/p^+$ (u^{μ} in light cone coordinates). The result of this calculation in the scalar case is then:

$$\boxed{\mathcal{D}_{tc}\left(p, p'|\mathcal{A}_m\right) = 2p^+ \int \mathrm{d}^2x_\perp \mathrm{d}x^- \, e^{ix^-(p'^{+} - p^+) - ix_\perp(p_\perp - p'_\perp)} [W(\gamma_{\mathrm{cl}})]_{j'j}} \tag{3.45}$$

where $W(\gamma_{\mathrm{cl}})$ is the Wilson line along the path $\gamma^{\mu}(x^+)$:

$$W(x_{\mathrm{cl}}) = T\left[\exp\left(ig\int_{-\infty}^{\infty} \mathrm{d}x^+ \mathcal{A}_{m,\mu}(\gamma^{\mu}(x^+))u^{\mu}\right)\right] \tag{3.46}$$

The operator T is the usual time ordering operator: in expanding the exponential, the colour matrices $\mathcal{A}_{m,\mu}$ are ordered with decreasing time x^+ from the left to the right. For fermionic quarks, the truncated propagator reads $\bar{u}_s(p')D_{tc}(p, p'|\mathcal{A}_m)u_s(p) = \delta_{ss'}\mathcal{D}_{tc}(p, p'|\mathcal{A}_m)$, reflecting the fact that quarks conserve their spin in the eikonal limit.

Formula (3.45) enables to justify a posteriori why it is allowed to take a x^- independent 4-current and background gauge field (it is even more transparent in the derivation done in [112]). If we are interested in the regime $p'^+ \simeq p^+$, neglecting the x^- dependence of $\mathcal{A}_{m,\mu}$ in the integral (3.45) gives a $\delta(p'^+ - p^+)$ factor as requested. This is independent of the gauge choice. It turns out that $\mathcal{A}_{m,\mu}$ does not depend at all on x^- for a current of the form (3.23) in the light cone gauge $\mathcal{A}_m^+ = 0$. Hence, for $u_\perp = 0$:

$$\bar{u}_s(p')D_{tc}(p,p'|\mathcal{A}_m)u_s(p) = 4\pi p^+\delta_{ss'}\delta(p'^+ - p^+)\int \mathrm{d}^2x_\perp\, e^{-ix_\perp(p'_\perp - p_\perp)}[W(x_\perp)]_{j'j} \tag{3.47}$$

$$W(x_\perp) = T\Big[\exp\Big(ig\int_{-\infty}^{\infty}\mathrm{d}x^+\mathcal{A}_m^-(x^+,x_\perp)\Big)\Big] \tag{3.48}$$

An other approach is to use the worldline formalism to write an exact formal expression for the propagator. In the worldline formalism, the full *scalar* quark propagator in the background field $\mathcal{A}_m^\mu$ reads:

$$\mathcal{D}(p,p'|\mathcal{A}_m) = \int_0^\infty \mathrm{d}\tau \int \mathcal{D}x(\tau')\, e^{ip'x(\tau)-ipx(0)}T\left[\exp\left(i\int_0^\tau \mathrm{d}\tau'\,\frac{1}{2}\dot{x}^2 - g\mathcal{A}_{\mu,m}(x)\dot{x}^\mu\right)\right] \tag{3.49}$$

Then, in the eikonal approximation, the path integral (3.49) is calculated with the saddle-point method at the lowest order. The saddle point is the classical trajectory of the particle, and after truncation of the propagator, one gets formula (3.45). This technique explicitly shows that the eikonal approximation is equivalent to neglect quantum fluctuations around the classical path. For non-scalar particles, formula (3.49) can be modified to take into account the non-trivial Lorentz structure. However, in the eikonal/saddle-point approximation, these terms are irrelevant so Eq. (3.45) is very general.

3.3.1.2 Transverse momentum broadening

When taking the square of the amplitude $\langle p'|p\rangle$, this generates a Dirac delta $\delta(p'^+ - p^+)$ squared, which should be understood as:

$$\delta(p'^+ - p^+)^2 \equiv \delta(p'^+ - p^+)\frac{1}{2\pi}\int \mathrm{d}x^- \tag{3.50}$$

$$= \delta(p'^+ - p^+)\frac{1}{2\pi}\frac{T_{\mathfrak{B}}}{\sqrt{2}} \tag{3.51}$$

The second equality comes from the normalization of the one particle states. Indeed, using the result (3.48) in the vacuum, that is with $W(x_\perp) = 1$, and for $p' = p$ one gets:

$$\langle p|p\rangle = 4\pi p^+\delta(p^+ = 0)\int \mathrm{d}^2x_\perp \tag{3.52}$$

$$= 2p^+S_{\mathfrak{B}}\int \mathrm{d}x^- = \sqrt{2}p^+S_{\mathfrak{B}}T_{\mathfrak{B}} \tag{3.53}$$

The last equality is precisely (3.17). Hence, the volume factor $T_{\mathfrak{B}}$ cancels with the $1/T_{\mathfrak{B}}$ in the cross-section and using $2p^0 \simeq \sqrt{2}p^+$ with eikonal accuracy in (3.43), the two factors $1/\sqrt{2}$ gives a factor $1/2$. Finally, one gets

$$\frac{\mathrm{d}^3\sigma}{\mathrm{d}p'^+\mathrm{d}^2p'_\perp} = \frac{\delta(p'^+ - p^+)}{(2\pi)^2}\frac{1}{N_c}\int \mathrm{d}^2x_\perp\mathrm{d}^2y_\perp e^{-i(x_\perp - y_\perp)(p'_\perp - p_\perp)}\mathrm{Tr}\left(W(x_\perp)W^\dagger(y_\perp)\right) \tag{3.54}$$

The wave function renormalization constant is equal to one at this order (see [116]). The last step of the calculation is to average over all statistical configurations of $\mathcal{A}_m$ using the results of Section 3.2.3. Performing the trivial integration over p'^+, the previous equation becomes:

$$\frac{\mathrm{d}^2\sigma}{\mathrm{d}^2 p'_\perp} = \frac{1}{(2\pi)^2}\int \mathrm{d}^2 b_\perp \mathrm{d}^2 u_\perp e^{-iu_\perp(p'_\perp - p_\perp)} \frac{1}{N_c}\left\langle \mathrm{Tr}\, W\left(\frac{b_\perp + u_\perp}{2}\right) W^\dagger\left(\frac{b_\perp - u_\perp}{2}\right)\right\rangle \tag{3.55}$$

Thus, we are left with the calculation of the average of two Wilson lines with "impact parameter" $b_\perp$ and separated by a transverse distance $u_\perp$. The standard way to make this calculation to all orders in g is to expand the product of the two Wilson lines up to the first non trivial order in g (leading order in opacity), using the expression for the correlation between the medium gauge field (3.32). One easily finds, for a medium with constant density in the transverse plane,

$$\frac{1}{N_c}\left\langle \mathrm{Tr}\, W\left(\frac{b_\perp + u_\perp}{2}\right) W^\dagger\left(\frac{b_\perp - u_\perp}{2}\right)\right\rangle = 1 - g^2 C_R \int_{-\infty}^{\infty} \mathrm{d}x^+ n(x^+)[\Upsilon(0) - \Upsilon(u_\perp)] + \mathcal{O}(g^4) \tag{3.56}$$

C_R depends on the representation of $\mathfrak{su}(N_c)$ in the Wilson line ($C_R = C_F$ here). To all orders in $g\mathcal{A}^\mu_m$, the average of two Wilson lines exponentiates (see [117]):

$$\frac{1}{N_c}\left\langle \mathrm{Tr}\, W\left(\frac{b_\perp + u_\perp}{2}\right) W^\dagger\left(\frac{b_\perp - u_\perp}{2}\right)\right\rangle = \exp\left(-g^2 C_R \int_{-\infty}^{\infty} \mathrm{d}x^+\, n(x^+)\big(\Upsilon(0) - \Upsilon(u_\perp)\big)\right) \tag{3.57}$$

Dipole cross-section. In this chapter as well as in Chapter 4, we will often encounter the dipole cross-section appearing inside the exponential in (3.57) and defined by:

$$\sigma_d(u_\perp) \equiv 2\int \frac{\mathrm{d}^2 k_\perp}{(2\pi)^2}\Big(1 - e^{ik_\perp u_\perp}\Big)\tilde{\Upsilon}(k_\perp) \tag{3.58}$$

$$= 2\big(\Upsilon(0_\perp) - \Upsilon(u_\perp)\big) \tag{3.59}$$

with $\tilde{\Upsilon}$ defined in (3.34)-(3.35). In the case at hand, this dipole is the effective $q\bar{q}$ dipole formed by the quark in the amplitude and the "antiquark" in the complex conjugate amplitude. This dipole cross-section can be estimated in the regime where the transverse size of the dipole $u_\perp$ is smaller than the Debye length. In this case, the integral is controlled by small values of $k_\perp$ between μ_D and $1/u_\perp$ so that a Taylor expansion of the factor $(1 - \exp(ik_\perp u_\perp))$ up to the second order gives the leading behaviour of $\sigma_d(u_\perp)$:

$$u_\perp \ll \lambda_D \Longrightarrow \sigma_d(u_\perp) = \frac{g^2}{16\pi} u_\perp^2 \log\left(\frac{1}{\mu_D^2 u_\perp^2}\right) + \mathcal{O}(u_\perp^2) \tag{3.60}$$

With this estimate, one defines the quenching parameter $\hat{q}_R$ in colour representation R:

$$g^2 C_R n(x^+)\sigma_d(u_\perp) \equiv \frac{1}{2}\hat{q}_R(x^+, u_\perp)u_\perp^2 + \mathcal{O}(u_\perp^2) \tag{3.61}$$

Using (3.61) and (3.58), one gets:

$$\hat{q}_R(x^+, u_\perp) = 2\pi\alpha_s^2 C_R n(x^+) \log\left(\frac{1}{\mu_D^2 u_\perp^2}\right) \tag{3.62}$$

Thus, the quenching parameter depends on the size of the dipole crossing the medium.

Let us now come back to (3.57). In order to avoid complications due to the transverse modelling of the medium, let us consider the differential cross-section per impact parameter. The final result of this subsection is then:

$$\frac{\mathrm{d}^4\sigma}{\mathrm{d}^2b_\perp \mathrm{d}^2p'_\perp} = \frac{1}{(2\pi)^2}\int \mathrm{d}^2u_\perp \exp\left(-iu_\perp(p'_\perp - p_\perp) - \frac{g^2}{2}C_R\int_{-\infty}^{\infty} n(x^+)\sigma_d(u_\perp)\mathrm{d}x^+\right) \quad (3.63)$$

We now discuss the physical meaning of this equation. The outgoing quark acquires a transverse momentum after propagation through the medium. One can generally define the probability distribution $\mathcal{P}(k_\perp, t_1, t_2)$ for an incoming quark to end up with a transverse momentum $k_\perp$ after propagation through the medium between $x^+ = t_1$ and $x^+ = t_2$:

$$\mathcal{P}(k_\perp, t_1, t_2) = \frac{1}{(2\pi)^2}\int \mathrm{d}^2u_\perp \exp\left(-iu_\perp k_\perp - \frac{g^2}{2}C_R\int_{t_1}^{t_2} n(x^+)\sigma_d(u_\perp)\mathrm{d}x^+\right) \quad (3.64)$$

This probability is properly normalized as $\sigma_d(0_\perp) = 0$. It is also explicitly boost invariant in the sense that one can use the average density of colour charges n measured in the laboratory frame provided that t_1 and t_2 refer to the light cone time along the quark trajectory in this frame. This is a generic feature of all the cross-sections calculated in this chapter.

The harmonic approximation. The harmonic approximation for the quenching parameter is very well suited for analytic approximations and captures the mean features of the multiple soft scattering regime. In this approximation, one neglects the logarithmic dependence of the quenching parameter in (3.61), by fixing $u_\perp$ at the typical transverse size $R_\perp$ encountered in the calculation at hand,

$$\hat{q}_R(x^+) \equiv 2\pi\alpha_s^2 C_R n(x^+)\log\left(\frac{1}{\mu_D^2 R_\perp^2}\right) \quad (3.65)$$

In most of the calculation done in this chapter, the typical transverse size $R_\perp$ is given by the inverse of the maximal transverse momentum acquired via collisions during a propagation time L, namely $Q_s = \sqrt{\hat{q}L}$[2]. This enables to define the quenching parameter through the implicit relation:

$$\hat{q}_R = 2\pi\alpha_s^2 C_R n(x^+)\log\left(\frac{\hat{q}_R L}{\mu_D^2}\right) \quad (3.66)$$

From this equation, one sees that $\hat{q}$ is reduced by two powers of α_s, however, this reduction is compensated by the large value of n in a *dense* medium. This is characteristic of the calculations performed in this section, to all orders in $\alpha_s^2 n$. With a constant $\hat{q}_R$, the probability distribution (3.64) is Gaussian and accounts for the random diffusive walk in the transverse plane of the quark due to the "kicks" given by the medium constituents. In this thesis, one should keep in mind that the parameter $\hat{q}$ is always the *adjoint* $\hat{q}_A$. Whenever necessary, we restore the index to avoid any ambiguity. Finally, for an expanding medium, $\hat{q}_R$ depends on x^+. Using (3.42) in (3.66), this dependence is written $\hat{q}(x^+) = \hat{q}_0(x_0^+/x^+)^\gamma$ in the harmonic approximation.

[2]The antenna pattern in Section 3.4 is an exception, as $R_\perp \sim \theta_{q\bar{q}}L \leq 1/Q_s$ if the opening angle $\theta_{q\bar{q}}$ of the dipole is smaller than θ_c.

3.3.2 One-gluon emission spectrum

3.3.2.1 Effective generating functional for soft gluon emissions

Now, we turn to the calculation of the one-gluon emission spectrum from an on-shell or off-shell incoming quark. With respect to the previous section, we are now looking for the cross-section for producing one gluon with 4-momentum k^μ after the propagation of the highly energetic quark through the medium, to leading (first) order in g but all orders in $g\mathcal{A}_m$. We consider a quark, but as the eikonal propagator of a gluon has the same expression, with a Wilson line in the adjoint representation, all the calculations of this section are valid for a gluon emission from an eikonal gluon with the substitution $C_F \to C_A$.

The basic ingredient of this calculation is the amplitude $\mathcal{M}(k,p',p) \equiv \langle k,p'|p\rangle$ from which one gets the cross-section:

$$\frac{\mathrm{d}^6\sigma}{\mathrm{d}p'^+\mathrm{d}^2p'_\perp\mathrm{d}k^+\mathrm{d}^2k_\perp} = \frac{1}{T_{\mathfrak{B}}2p^0(2\pi)^6 2p'^+2k^+}\left(\frac{1}{2N_c}\sum_{s,s',\lambda,j,j',c}|\mathcal{M}(k,p',p)|^2\right) \tag{3.67}$$

where the sum runs over all initial and final colours j, j', c, spins s and s' and physical polarizations λ of the emitted gluon. We use the eikonal approximation for the quark propagation. This means that the emitted gluon cannot be too "hard". More explicitly, the constraints on the 4-momentum of the gluon are $k^+ \ll p^+ \simeq p'^+$ and $k_\perp \ll p_\perp, p'_\perp$.

From the LSZ reduction formula, the amplitude $\mathcal{M}(k,p',p)$ is related to the time ordered three-point Green function of the theory. The generating functional of these Green functions in QCD in the presence of the background field $\mathcal{A}_m$ is

$$Z[J^\mu,\bar\eta,\eta\mid\mathcal{A}_m] = \int \mathcal{D}A^\mu\mathcal{D}\bar\psi\mathcal{D}\psi\,\delta(G[A^\mu])\exp\left(iS_g[A^\mu|\mathcal{A}^\mu_m] + i\int \mathrm{d}^4x\,\bar\psi i\not{D}\psi \right.$$
$$\left. +i\int \mathrm{d}^4x\,(J^\mu A_\mu + \bar\eta\psi + \eta\bar\psi)\right) \tag{3.68}$$

where $S_g[A^\mu|A^\mu_m]$ is the part of the Yang-Mills action depending only on the gluon and medium fields and $\delta(G[A^\mu])$ is a gauge-fixing prescription. We work in the (physical) light cone gauge $A^+ = 0$. As we consider an energetic quark which propagates through the medium, we shall need to compute correlation functions with at least one $\bar\psi$ and one ψ. It is then convenient to introduce the following effective generating functional:

$$Z_{\mathrm{eff}}[J^\mu|\mathcal{A}_m] = \Big(-i\frac{\delta}{\delta\bar\eta^{j'}_{s'}(y)}\Big)\Big|_{\bar\eta=0}\Big(-i\frac{\delta}{\delta\eta^j_s(x)}\Big)\Big|_{\eta=0} Z[J^\mu,\bar\eta,\eta|A^\mu_m] \tag{3.69}$$

$$= \int \mathcal{D}\mathcal{A}^\mu\mathcal{D}\bar\psi\mathcal{D}\psi\,\delta(G[A^\mu])\psi^{j'}_{s'}(y)\bar\psi^j_s(x)\exp\Big(iS_g[A^\mu|\mathcal{A}^\mu_m]$$
$$+i\int \mathrm{d}^4x\,\bar\psi i\not{D}\psi + i\int \mathrm{d}^4x\,J^\mu A_\mu\Big) \tag{3.70}$$

In the eikonal propagation approximation, it is possible to integrate out exactly the fermionic degrees of freedom using the propagator $D(x,y|A+\mathcal{A}_m)$ discussed in the previous section. It is even more convenient to use the truncated propagator $\delta_{ss'}\mathcal{D}_{tc}(p,p'|A+\mathcal{A}_m)$ in order to reduce the initial and final quarks according to the LSZ procedure. Our effective generating functional is then:

$$Z_{\mathrm{eff}}[J^\mu|\mathcal{A}_m] = \int \mathcal{D}A^\mu\delta(G[A^\mu])\delta_{ss'}\mathcal{D}_{tc}(p,p'|A+\mathcal{A}_m)\exp\left(iS_g[A^\mu|\mathcal{A}^\mu_m] + i\int \mathrm{d}^4x J^\mu A_\mu\right) \tag{3.71}$$

with $\mathcal{D}_{tc}(p,p'|A^\mu+\mathcal{A}^\mu_m)$ given by (3.45).

From the LSZ reduction formula, the amplitude $\mathcal{M}(k,p',p)$ is now related to the one point function of this effective generating functional:

$$\mathcal{M}(k,p',p)=\lim_{k^2\to 0}\frac{k^2}{iZ_A^{1/2}Z_\psi}\langle A_{\mu,c}(k)\rangle\epsilon^\mu_\lambda(k) \tag{3.72}$$

$$\langle A^\mu_c(z)\rangle\equiv\frac{1}{Z_0}\Big(-i\frac{\delta}{\delta J_{\mu,c}(z)}\Big)Z_{\text{eff}}[J^\mu|\mathcal{A}_m]\Big|_{J=0} \tag{3.73}$$

In the light cone gauge $A^+=0$, only the transverse components of the polarization vector $\epsilon^\mu_\lambda(k)=(0,\epsilon_\perp\cdot k_\perp/k^+,\epsilon_\perp)$ and A^μ matter. Written explicitly, the above formula is

$$\langle A^i_c(z)\rangle\propto\frac{1}{Z_0}\int\mathcal{D}A^\mu\,\delta(G[A^\mu])e^{iS_g[A^\mu|\mathcal{A}^\mu{}_m]}A^i_c(z)T\Big[e^{ig\int_{-\infty}^{\infty}\mathrm{d}x^+\,(A^-(x^+,x^-,x_\perp)+\mathcal{A}^-_m(x^+,x_\perp))}\Big]_{j'j} \tag{3.74}$$

where the $\propto$ symbol abbreviates all the factors and integrals over $x_\perp$ and x^- in (3.45). As in the transverse momentum distribution calculation, we choose a coordinate system where x^- and $x_\perp$ are constant along the classical path of the incoming quark. We point out that the brackets in (3.74) refer to the *quantum expectation value* of the quantum operator A and should be distinguished from the statistical averages over background field configuration performed later on in this section.

3.3.2.2 Gluon propagators beyond the eikonal approximation

As we shall see after this short digression, the calculation of (3.74) at a given fixed order in gA^μ requires to know the gluon propagator $G^{\mu\nu}_{ab}(z,x)$ in the background field beyond the eikonal approximation discussed in (3.3.1.1):

$$G^{\mu\nu}_{ab}(z;x|\mathcal{A}_m)\equiv\frac{1}{Z_0}\int\mathcal{D}A^\mu\delta(G[A^\mu])e^{iS_g[A^\mu|\mathcal{A}^\mu_m]}A^\mu_a(z)A^\nu_b(x) \tag{3.75}$$

We focus here only on the $i-$ component of the gluon necessary to pursue this calculation. The other components are given in Appendix A and will be used mainly in Section 3.4.

Since the external field appearing in $S_g[A^\mu|\mathcal{A}^\mu_m]$ does not depend on x^-, the propagator $G^{\mu\nu}_{ab}(z,x)$ depends on z^- and y^- only through the difference z^--y^-. The linearisation of the Yang-Mills equations around the background field leads to the following formula for the $-i$ component[3] (see [103] or [118]):

$$G^{i-}_{ab}(z,x|\mathcal{A}_m)=\partial^i_{x_\perp}\int\frac{\mathrm{d}k^+}{2\pi}e^{-ik^+(z^--x^-)}\frac{i}{2k^{+2}}\mathcal{G}_{ab}(z^+,z_\perp;x^+,x_\perp|k^+) \tag{3.76}$$

with the scalar propagator $\mathcal{G}$ satisfying the Green equation

$$\left(i\delta^{ab}\partial^-+\delta^{ab}\frac{\nabla^2_{x_\perp}}{2k^+}+g\mathcal{A}^-_{m,d}T^d_{ab}\right)\mathcal{G}_{bc}(z^+,z_\perp;x^+,x_\perp|k^+)=i\delta_{ac}\delta(z^+-x^+)\delta^{(2)}(z_\perp-x_\perp) \tag{3.77}$$

This propagator satisfies also the Chapman-Kolmogorov relation:

$$\mathcal{G}_{ab}(z^+,z_\perp;x^+,x_\perp|k^+)=\int dw_\perp\mathcal{G}_{ad}(z^+,z_\perp;w^+,w_\perp|k^+)\mathcal{G}_{db}(w^+,w_\perp;x^+,x_\perp|k^+) \tag{3.78}$$

[3]We do not include the $k^++i\epsilon$ prescription for retarded propagators to keep our expressions compact.

if $x^+ < w^+ < z^+$.

The solution of the equation satisfied by $\mathcal{G}$ has an elegant representation in term of a path integral as in non-relativistic quantum mechanics. Indeed, Eq. (3.77) is formally a two-dimensional Schrödinger equation in a non-abelian potential for a particle with effective mass k^+. Its Green function reads:

$$\mathcal{G}(z^+, z_\perp; x^+, x_\perp|k^+) = \int_{r_\perp(x^+)=x_\perp}^{r_\perp(z^+)=z_\perp} \mathcal{D}r_\perp(\xi) \exp\left(\frac{ik^+}{2}\int_{x^+}^{z^+} \mathrm{d}\xi\, \dot{r}_\perp^2(\xi)\right) \mathcal{W}_{x^+}^{z^+}(r_\perp(\xi)) \tag{3.79}$$

In the strict eikonal approximation given by the saddle point evaluation of the path integral, this propagator reduces to a Wilson line over the classical path in the adjoint representation, in agreement with our calculation of the gluon *eikonal* propagator. The propagator (3.79) includes sub-eikonal corrections by averaging Wilson lines over random quantum motions in the transverse plane.

One may wonder why the eikonal approximation is not enough for our purposes. The eikonal approximation is given by the saddle point evaluation of (3.79), approximation valid when the phase in the exponential is large. For a gluon propagating over a distance L through the medium, this phase is parametrically of order $k^+(\Delta r_\perp/L)^2 L$, with $\Delta r_\perp$ the typical variation around the classical trajectory. By the uncertainty principle, $\Delta r_\perp$ is of the same order than $1/k_\perp$ where $k_\perp$ is the measured transverse momentum of the gluon. Consequently, the eikonal approximation is valid when:

$$k^+\Big(\frac{1}{k_\perp L}\Big)^2 L \gg 1 \Leftrightarrow \frac{k^+}{k_\perp^2} \gg L \tag{3.80}$$

In more physical terms, this inequality means that the variation of the gluon transverse coordinate $L\Delta\theta \sim Lk_\perp/k^+$ while propagating over a distance L is much smaller than the quantum fluctuation $\sim 1/k_\perp$ in the transverse motion. That said, we recognize in (3.80) the condition stating that the formation time of the gluon is larger than the gluon in-medium path length. This is a too strong condition, as we do not want to focus only on this kinematic regime: we will see later than many interesting physical phenomena happen when $k^+/k_\perp \ll L$. Therefore, we shall use the propagator (3.79) for the emitted gluon.

3.3.2.3 Details of the amplitude calculation

Now, we detail the general method for calculating $\langle A^i(z)\rangle$ at a given order in g and all orders in $g\mathcal{A}_m$. To proceed, we expand the time ordered Wilson line in $\mathcal{D}_{tc}(p, p'|A + \mathcal{A}_m)$ thanks to the following formula, obtained after discretization of the integral:

$$T\Big[e^{\int_{x_i}^{x_f} \mathrm{d}x^+ A(x^+)}\Big] = \lim_{N\to\infty} \prod_{n=N..1} e^{\epsilon A(x_n)} \tag{3.81}$$

with $\epsilon = (x_f - x_i)/N$, $x_n = x_i + \epsilon n$. Keeping only the first two lowest order terms in gA^μ, it is easy to see that

$$\prod_{n=N..1} e^{ig\epsilon(A^-(x_n^+)+\mathcal{A}_m^-(x_n^+))} = \prod_n e^{ig\epsilon\mathcal{A}_m^-(x_n^+)} + ig\sum_n \prod_{p=N..n+1}\Big[e^{ig\epsilon\mathcal{A}_m^-(x_p^+)}\Big]\epsilon A^-(x_n^+)\prod_{q=n-1..1}\Big[e^{ig\epsilon\mathcal{A}_m^-(x_q^+)}\Big]$$

Now, if we take the limit $N \to \infty$, we obtain

$$\begin{aligned} T\Big[e^{ig\int_{-\infty}^{\infty}\mathrm{d}x^+(A^-(x^+,x^-,x_\perp)+\mathrm{A}_{m,c}^-(x^+,x_\perp))}\Big] =& W_{-\infty}^{\infty}(x_\perp) \\ &+ ig\int_{-\infty}^{\infty}\mathrm{d}y^+ W_{y^+}^{\infty}(x_\perp)A^-(y^+,x^-,x_\perp)W_{-\infty}^{y^+}(x_\perp) \end{aligned} \tag{3.82}$$

where $W_{t_1}^{t_2}(x_\perp)$ is the Wilson line (3.48) for a path from $x^+ = t_1$ to $x^+ = t_2$ with $x_\perp$ fixed.

The first term cancels in the path integral over A^μ in (3.73) because the 1-point quantum correlation function is null by convention (no tadpoles). The second term involves the gluon propagator $G^{i-}(z;x|\mathcal{A}_m)$ determined in the previous paragraph beyond the eikonal approximation, which describes the propagation of the gluon inside the medium between the emission point $x = (y^+, x^-, x_\perp)$ and z. Gathering everything together with the colour indices explicit, one gets

$$\langle A_c^i(z)\rangle = ig\int_{-\infty}^{\infty} \mathrm{d}y^+ G_{cb}^{i-}(z^+, z^-, z_\perp; y^+, x^-, x_\perp|\mathcal{A}_m)\Big[W_{y^+}^{\infty}(x_\perp)t^b W_{-\infty}^{y^+}(x_\perp)\Big]_{j'j} \tag{3.83}$$

In this formula, the Wilson lines are in the fundamental representation of $\mathfrak{su}(N_c)$. To simplify the colour algebra, it is convenient to express the product of the three matrices inside the bracket as a colour rotation in the adjoint representation of $\mathfrak{su}(N_c)$:

$$W_{y^+}^{\infty}(x_\perp)t^b W_{-\infty}^{y^+}(x_\perp) = W_{-\infty}^{\infty}(x_\perp)W_{-\infty}^{\dagger,y^+}(x_\perp)t^b W_{-\infty}^{y^+}(x_\perp) \tag{3.84}$$

$$= W_{-\infty}^{\infty}(x_\perp)\mathcal{W}_{-\infty,bd}^{y^+}(x_\perp)t^d \tag{3.85}$$

In the first line, we have used the unitarity of the Wilson lines and in the second line, the definition of the adjoint representation. Calligraphic letters, as in $\mathcal{W}$, are used for Wilson lines in the adjoint representation. Inserting this relation and the representation (3.76) of the propagator into the Fourier transform with respect to z^- of the amplitude in coordinate space (3.83), one finds:

$$\int \mathrm{d}z^-\, e^{ik^+z^-}\langle A_c^i(z)\rangle = \frac{-g}{2k^{+2}}e^{ik^+x^-}W_{-\infty}^{\infty}(x_\perp) \times \int_{-\infty}^{\infty}\mathrm{d}y^+\,\partial_{y_\perp=x_\perp}^i \mathcal{G}_{cb}(z^+, z_\perp; y^+, y_\perp|k^+)\mathcal{W}_{-\infty,bd}^{y^+}(x_\perp)t^d \tag{3.86}$$

The last step consists in taking the Fourier transform with respect to the remaining z^+ and $z_\perp$ components of the final position of the gluon and to multiply by k^2 in order to follow the LSZ recipe. The multiplication by k^2 in Fourier space corresponds to the application of the operator $-2ik^+\partial_z^- - \nabla_\perp^2$ in the remaining space coordinates.

Now let's assume that the background field $\mathcal{A}_m$ goes to 0 at sufficiently large light cone time $y^+ \geq T$. Then we split the integral at $y^+ = T$. As T is arbitrary, we can take $T \to \infty$ at the end of the calculation so that the integral between T and $+\infty$ vanishes. In the $y^+ \leq T$ piece, we insert a Chapman-Kolmogorov relation for the propagator with intermediate time T and intermediate transverse momentum $w_\perp$:

$$\mathcal{G}_{cb}(z^+, z_\perp; y^+, y_\perp|k^+) = \int \mathrm{d}w_\perp \mathcal{G}_{ce}(z^+, z_\perp; T, w_\perp|k^+)\mathcal{G}_{eb}(T, w_\perp; y^+, y_\perp|k^+) \tag{3.87}$$

The propagator $\mathcal{G}(z^+, z_\perp; T, w_\perp|k^+)$ is free so the operator $-2ik^+\partial_z^- - \nabla_\perp^2$ gives $-2ik^+\delta_{ce}\delta(z^+ - T)\delta(w_\perp - z_\perp)$ leading to a trivial $w_\perp$ integral. After Fourier transform, one gets:

$$k^2\langle A_c^i(k)\rangle = \frac{ig}{k^+}e^{ik^+x^-}W_{-\infty}^{\infty}(x_\perp)e^{ik^-T} \times \int_{-\infty}^{T}\mathrm{d}y^+ \int \mathrm{d}^2z_\perp e^{-ik_\perp z_\perp}\,\partial_{y_\perp=x_\perp}^i \mathcal{G}_{cb}(T, z_\perp; y^+, y_\perp|k^+)\mathcal{W}_{-\infty,bd}^{y^+}(x_\perp)t^d \tag{3.88}$$

In order to have a meaningful mathematical expression in the limit $T \to \infty$, we should have deformed the light cone z^+ integration contour in the Fourier transform with respect to z^+ to ensure the adiabatic switching of the interactions. This amounts to add a small imaginary part $i\text{sign}(z^+)\varepsilon^4$ to the k^- component of the 4-momentum k in the previous expression. Using the following relation obtained after a trivial integration by part in y^+:

$$\lim_{\varepsilon\to 0} e^{-\varepsilon T}\int_{-\infty}^{T} \mathrm{d}y^+\, f(y^+) = \lim_{\varepsilon\to 0}\int_{-\infty}^{T} \mathrm{d}y^+\, e^{-\varepsilon y^+} f(y^+) \tag{3.89}$$

one shows that, apart from the pure phase e^{ik^-T} which cancels anyway in the amplitude squared, the limit $T \to \infty$ is given by:

$$\begin{aligned} k^2\langle A_c^i(k)\rangle = {} & \frac{ig}{k^+} e^{ik^+x^-} W_{-\infty}^{\infty}(x_\perp) \\ & \times \int_{-\infty}^{\infty} \mathrm{d}y^+\, e^{-\varepsilon|y^+|} \int \mathrm{d}^2 z_\perp e^{-ik_\perp z_\perp}\, \partial^i_{y_\perp = x_\perp} \mathcal{G}_{cb}(\infty, z_\perp; y^+, y_\perp|k^+) \mathcal{W}^{y^+}_{-\infty,bd}(x_\perp) t^d \end{aligned} \tag{3.90}$$

with the implicit limit $\varepsilon \to 0$ taken *after* the integration. This concludes the calculation of the amplitude for the one-gluon emission process at leading order in g. However, this result resums to all orders $g\mathcal{A}_m$ by means of Wilson lines. Recall also that the equality here is a small abuse of notation as one should integrate over $x_\perp$ and x^- according to (3.45).

3.3.2.4 The cross-section averaged over $\mathcal{A}_m$

The amplitude (3.90) involves three Wilson lines. This means that we should compute the average of six Wilson lines over background field configurations in order to get the cross-section, which is a very complicated task. However, in the full cross-section (3.67), we are not really interested any more on the distribution over the 4-momentum p' of the outgoing quark. If we integrate the cross-section (3.67) over p'^+ and $p'_\perp$, the integral yields a $\delta(x_\perp - \bar{x}_\perp)$ with $x_\perp$, $\bar{x}_\perp$ the transverse coordinate of the quark in the direct amplitude and in the complex conjugate amplitude respectively. This considerably simplifies the calculation of the *inclusive* one-gluon emission cross-section per impact parameter $x_\perp$:

$$\frac{\mathrm{d}^5\sigma_g}{\mathrm{d}^2x_\perp \mathrm{d}k^+ \mathrm{d}^2k_\perp} \equiv \int \mathrm{d}p'^+ \int \mathrm{d}^2p_\perp \frac{\mathrm{d}^8\sigma}{\mathrm{d}^2x_\perp \mathrm{d}p'^+ \mathrm{d}^2p'_\perp \mathrm{d}k^+ \mathrm{d}k_\perp} \tag{3.91}$$

since the transverse coordinate $x_\perp$ of the incoming quark is now frozen in the direct and complex conjugate amplitude. Summing over the polarization states λ and spin s, s' one gets:

$$k^+ \frac{\mathrm{d}^5\sigma_g}{\mathrm{d}^2x_\perp \mathrm{d}k^+ \mathrm{d}^2k_\perp} = \frac{1}{16\pi^3}\frac{1}{N_c}\sum_{j,j',c,i} |k^2\langle A_c^i(k)\rangle|^2 \tag{3.92}$$

The wave function renormalization constants in (3.72) are equal to 1 at this order and one checks that all the factors in formula (3.72) (and in particular the $1/T_{\mathfrak{B}}$) give a factor $1/(16\pi^3)$ using the same tricks as for the calculation of the transverse momentum distribution.

[4] ε should not be confused with ϵ defining *retarded* propagators.

Before writing explicitly the value of the modulus square, we need to perform the colour algebra:

$$\frac{1}{N_c}[W^{\infty}_{-\infty}(x_\perp)t^d]_{j'j}\times[W^{\star,\infty}_{-\infty}(x_\perp)t^{\star,\bar{d}}]_{j'j}=\frac{1}{N_c}[W^{\infty}_{-\infty}(x_\perp)t^d]_{j'j}\times[t^{\dagger,\bar{d}}W^{\dagger\infty}_{-\infty}(x_\perp)]_{jj'} \tag{3.93}$$

$$=\frac{1}{N_c}\mathrm{Tr}(W^{\infty}_{-\infty}(x_\perp)t^dt^{\bar{d}}W^{\dagger,\infty}_{-\infty}(x_\perp)) \tag{3.94}$$

$$=\frac{C_F}{N_c^2-1}\delta^{d\bar{d}} \tag{3.95}$$

It is convenient to make appear the $1/(N_c^2-1)$ factor for the future average of Wilson lines in the adjoint representation. Now, the cross-section (3.92) averaged over $\mathcal{A}_m$ reads:

$$k^+\frac{\mathrm{d}^5\sigma_g}{\mathrm{d}^2x_\perp\mathrm{d}k^+\mathrm{d}^2k_\perp}=\frac{\alpha_sC_F}{(2\pi)^2k^{+2}}2\mathfrak{Re}\int_{-\infty}^{\infty}\mathrm{d}y^+\int_{-\infty}^{y^+}\mathrm{d}\bar{y}^+e^{-\varepsilon(|y^+|+|\bar{y}^+|)}\int\mathrm{d}z_\perp\mathrm{d}\bar{z}_\perp e^{-ik_\perp(z_\perp-\bar{z}_\perp)}$$
$$\times\frac{1}{N_c^2-1}\Big\langle\mathrm{Tr}\,\partial^i_{y_\perp=x_\perp}\mathcal{G}^\dagger(\infty,\bar{z}_\perp;\bar{y}^+,y_\perp|k^+)\partial^i_{\bar{y}_\perp=x_\perp}\mathcal{G}(\infty,z_\perp;y^+,\bar{y}_\perp|k^+)\mathcal{W}^{y^+}_{\bar{y}^+}(x_\perp)\Big\rangle \tag{3.96}$$

with $\alpha_s\equiv g^2/(4\pi)$. We used the property $\mathcal{G}(y^+;\bar{y}^+)=\mathcal{G}^\dagger(\bar{y}^+;y^+)$ (following the equivalent property for Wilson lines) to write the integral over $\bar{y}^+\geq y^+$ as the complex conjugate of the one over $y^+\geq\bar{y}^+$. Note that the remaining colour precession associated with the Wilson line $\mathcal{W}^{y^+}_{\bar{y}^+}$ occurs between the creation time $\bar{y}^+$ in the complex conjugate amplitude and the absorption time y^+ in the direct amplitude.

The latter expression can be further simplified if we manage to use the locality in light cone time y^+ of the background field correlations. To do so, we use the Chapman-Kolmogorov relation to write the scalar propagator $\mathcal{G}^\dagger(\infty;\bar{y}^+)$ as the product of two propagators, one between $\bar{y}^+$ and y^+, followed by one between y^+ up to $+\infty$ with intermediate transverse momentum $u_\perp$. Then,

$$\frac{1}{N_c^2-1}\Big\langle\mathrm{Tr}\,\mathcal{G}^\dagger(\infty,\bar{z}_\perp;\bar{y}^+,\bar{y}_\perp|k^+)\mathcal{G}(\infty,z_\perp;y^+,y_\perp|k^+)\mathcal{W}^{y^+}_{\bar{y}^+}(x_\perp)\Big\rangle=$$
$$\frac{1}{N_c^2-1}\int\mathrm{d}^2u_\perp\Big\langle\mathrm{Tr}\,\mathcal{G}^\dagger(y^+,u_\perp;\bar{y}^+,\bar{y}_\perp|k^+)\mathcal{G}^\dagger(\infty,\bar{z}_\perp;y^+,u_\perp|k^+)\mathcal{G}(\infty,z_\perp;y^+,y_\perp|k^+)\mathcal{W}^{y^+}_{\bar{y}^+}(x_\perp)\Big\rangle$$
$$=\frac{1}{(N_c^2-1)^2}\int\mathrm{d}^2u_\perp\Big\langle\mathrm{Tr}\,\mathcal{G}^\dagger(y^+,u_\perp;\bar{y}^+,\bar{y}_\perp|k^+)\mathcal{W}^{y^+}_{\bar{y}^+}(x_\perp)\Big\rangle$$
$$\times\Big\langle\mathrm{Tr}\,\mathcal{G}^\dagger(\infty,\bar{z}_\perp;y^+,u_\perp|k^+)\mathcal{G}(\infty,z_\perp;y^+,y_\perp|k^+)\Big\rangle \tag{3.97}$$

Thanks to the locality in time of the background field correlations, the average of the four Wilson lines factorizes into the product of averages of only two Wilson lines. Now, let us define the following general quantities:

$$\tilde{S}_{gg}(k_\perp,a_\perp,b_\perp)\equiv\frac{1}{N_c^2-1}\int\mathrm{d}z_\perp\mathrm{d}\bar{z}_\perp\,e^{-ik_\perp(a_\perp-b_\perp)}e^{-ik_\perp(z_\perp-\bar{z}_\perp)}$$
$$\times\Big\langle\mathrm{Tr}\,\mathcal{G}^\dagger(\infty,\bar{z}_\perp;y^+,a_\perp|k^+)\mathcal{G}(\infty,z_\perp;y^+,b_\perp|k^+)\Big\rangle \tag{3.98}$$

$$\mathcal{K}_{qg}(y^+,a_\perp;\bar{y}^+,b_\perp|c_\perp)\equiv\frac{1}{N_c^2-1}\Big\langle\mathrm{Tr}\,\mathcal{G}^\dagger(y^+,a_\perp;\bar{y}^+,b_\perp|k^+)\mathcal{W}^{y^+}_{\bar{y}^+}(c_\perp)\Big\rangle \tag{3.99}$$

where $\tilde{S}_{gg}$ is the equivalent of the Fourier transform of the dipole S-matrix (3.54) with sub-eikonal corrections and $\mathcal{K}_{qg}$ is the effective qg dipole propagator inside the medium between $\bar{y}^+$ and y^+.

One can show (see Appendix A) that for Gaussian statistics, $\tilde{S}_{gg}$ is a function of $a_\perp - b_\perp$ only, that is $\tilde{S}_{gg}(k_\perp, a_\perp, b_\perp) = S_{gg}(a_\perp - b_\perp)$. On top of that, the Fourier transform of the "dipole S-matrix" S_{gg} is not modified by sub-eikonal corrections included in the scalar propagator, namely:

$$S_{gg}(u_\perp) = \exp\left(-\frac{g^2}{2} C_A \int_{y^+}^{\infty} n(x^+)\sigma_d(u_\perp)\mathrm{d}x^+\right) \tag{3.100}$$

From our calculation of the average of two Wilson lines for Gaussian correlations in (3.57), the function $\mathcal{K}_{qg}(a_\perp; b_\perp|c_\perp)$ can be written:

$$\mathcal{K}_{qg}(y^+, a_\perp; \bar{y}^+, b_\perp|c_\perp) = \mathcal{K}(y^+, a_\perp - c_\perp; \bar{y}^+, b_\perp - c_\perp) \tag{3.101}$$

with the general function $\mathcal{K}$ defined as a path integral:

$$\mathcal{K}(y^+, a_\perp; \bar{y}^+, b_\perp) = \int_{r_\perp(\bar{y}^+)=b_\perp}^{r_\perp(y^+)=a_\perp} \mathcal{D}r_\perp(\xi) \exp\left(-\int_{\bar{y}^+}^{y^+} \mathrm{d}\xi\, \frac{ik^+}{2}\dot{r}_\perp^2(\xi) + \frac{g^2 C_A}{2} n(\xi)\sigma(r_\perp)\right) \tag{3.102}$$

With these notations, and after a shift of the integration variable $u_\perp \to u_\perp + y_\perp$, the inclusive one-gluon medium-induced cross-section reads:

$$\begin{aligned} k^+\frac{\mathrm{d}^5\sigma_g}{\mathrm{d}^2x_\perp \mathrm{d}k^+ \mathrm{d}^2k_\perp} = \frac{\alpha_s C_F}{(2\pi)^2 k^{+2}} 2\mathfrak{Re}\int_{-\infty}^{\infty}\mathrm{d}y^+ \int_{-\infty}^{y^+}\mathrm{d}\bar{y}^+ e^{-\varepsilon(|y^+|+|\bar{y}^+|)} \\ \times \int \mathrm{d}^2u_\perp e^{ik_\perp u_\perp} S_{gg}(u_\perp)\partial^i_{y_\perp}\partial^i_{\bar{y}_\perp}\mathcal{K}(y^+, y_\perp + u_\perp - x_\perp; \bar{y}^+, \bar{y}_\perp - x_\perp) \end{aligned} \tag{3.103}$$

with the derivative taken at $y_\perp = \bar{y}_\perp = x_\perp$. This is the main result of this section. It has been obtained in this form by Armesto, Salgado and Wiedemnann in [62, 64, 69], Zakharov [59, 60] and BDMPS [56, 61].

Even if this cross-section has been obtained from a "CGC-like" formalism, it is actually very general and its applicability range goes beyond the traditional underlying assumption of this formalism. For example, it shown in [69, 72] that using (3.103) with the effective propagator $\mathcal{K}_{qg}$ calculated at the leading order in opacity (i.e truncating the calculation to the first order in $n\sigma_d$), one gets the GLV spectrum [67, 67, 68].

In the next section, we shall give some analytical results for the cross-section (3.103) in the multiple soft scattering regime and in the harmonic approximation, which are the main underlying assumptions leading to the BDMPS-Z spectrum. From now on, we shall forget about the dependence of the spectrum on $x_\perp$, the transverse coordinate of the incoming quark. Integrating over it gives the transverse surface of the target, but if we decide to normalize the cross-section σ_g by this surface, the factor cancels. We thus define the gluon spectrum as

$$k^+\frac{\mathrm{d}^3N}{\mathrm{d}k^+\mathrm{d}^2k_\perp} \equiv k^+\frac{\mathrm{d}^5\sigma_g}{\mathrm{d}^2x_\perp \mathrm{d}k^+\mathrm{d}^2k_\perp}_{|x_\perp=0_\perp} \tag{3.104}$$

and deal with this quantity for the rest of this section.

3.3.3 The multiple soft scattering regime

In this subsection, we focus on the harmonic approximation which captures the main features of the multiple soft scattering regime. The harmonic approximation enables to perform almost entirely analytically the calculation of the complicated formula (3.103).

3.3.3.1 Some useful analytic formulas

Within the harmonic approximation, S_{gg} becomes a simple two-dimensional Gaussian function:

$$S_{gg}(u_\perp) = \exp\left(-\frac{1}{4}\int_{y^+}^{\infty} \mathrm{d}x^+\, \hat{q}(x^+) u_\perp^2\right) \tag{3.105}$$

The in-medium effective propagator $\mathcal{K}$ is delicate to handle written in the form (3.102). Fortunately, exact analytical forms are known in the harmonic approximation. In this case, it reads (see [65] and Appendix A):

$$\mathcal{K}(y^+, u_\perp; \bar{y}^+, x_\perp) = \frac{-k^+}{2\pi i S(y^+, \bar{y}^+)} e^{\frac{-ik^+}{2S(y^+,\bar{y}^+)}\left[C(\bar{y}^+,y^+)u_\perp^2 + C(y^+,\bar{y}^+)x_\perp^2 - 2u_\perp x_\perp\right]} \tag{3.106}$$

with $C(t,\xi) \equiv \partial_\xi S(\xi, t)$ and $S(t,\xi)$ is the solution of the second-order linear differential equation:

$$\frac{\partial^2 S(t,\xi)}{\partial t^2} + \frac{i\hat{q}_A(t)}{2k^+} S(t,\xi) = 0 \tag{3.107}$$

$$S(\xi,\xi) = 0\,, \qquad \frac{\partial S(t,\xi)}{\partial t}_{|t=\xi} = 1 \tag{3.108}$$

The function S satisfies $S(t,\xi) = -S(\xi,t)$. The function C is also a solution of this differential equation, with different initial conditions though: $C(\xi,\xi) = 1$ and $\partial_{t=\xi} C(t,\xi) = 0$. Since the Wronskian $\mathrm{Wr}(t,\xi)$ of the differential equation is constant:

$$\mathrm{Wr}(t,\xi) \equiv \partial_t S(t,\xi) C(t,\xi) - S(t,\xi)\partial_t C(t,\xi) = 1 \tag{3.109}$$

one has [119],

$$-\partial_t\left(\frac{C(t,\xi)}{S(t,\xi)}\right) = \frac{1}{S^2(t,\xi)} \tag{3.110}$$

When $\hat{q}(t)$ is only piece-wise continuous, the solutions S and C must be chosen in such a way that they are continuous and derivable in their first argument at any points (however the second derivative may not exist everywhere).

In the limit $\hat{q} \to 0$ or $y^+ \to \bar{y}^+$, the effective propagator converges toward the adjoint of the free scalar propagator:

$$\lim_{\hat{q}\to 0} \mathcal{K}(y^+, u_\perp; \bar{y}^+, x_\perp) = \mathcal{G}_0^\dagger(y^+, u_\perp; \bar{y}^+, x_\perp) \tag{3.111}$$

$$\mathcal{K}(y^+, u_\perp; \bar{y}^+, x_\perp) \underset{y^+\to\bar{y}^+}{\sim} \mathcal{G}_0^\dagger(y^+, u_\perp; \bar{y}^+, x_\perp) \tag{3.112}$$

with the free scalar propagator given by

$$\mathcal{G}_0(y^+, u_\perp; \bar{y}^+, x_\perp) \equiv \frac{k^+}{2\pi i(y^+ - \bar{y}^+)} \exp\left(\frac{ik^+(u_\perp - x_\perp)^2}{2(y^+ - \bar{y}^+)}\right) \tag{3.113}$$

$$= \int \frac{\mathrm{d}^2 q_\perp}{(2\pi)^2} e^{iq_\perp(u_\perp - x_\perp)} \exp\left(\frac{-i(y^+ - \bar{y}^+)}{2(k^+ + i\epsilon)} q_\perp^2\right) \tag{3.114}$$

Using this property, one easily shows that the spectrum (3.103) vanishes in the limit $\hat{q} \to 0$. As expected, an on-shell incoming quark cannot radiate in the vacuum.

3.3.3.2 Importance of the adiabatic prescription

Before giving the analytic results for (3.103) using the expression of S_{gg} and $\mathcal{K}$, let us make few comments on the adiabatic regulator ε. In most calculations of the BDMPS-Z spectrum in the case of a finite path length L, the calculation of (3.103) is performed by cutting the integral over y^+ in pieces: $(-\infty, 0)$, $[0, L]$ and (L, ∞) in order to use the vacuum propagator $\mathcal{G}_0$ wherever it is necessary. For the in/in term, corresponding to $y^+ \in [0, L]$ and $\bar{y}^+ \in [0, y^+]$, the adiabatic regulator is not necessary since the integral is convergent on the compact domain. However, if there is no sharp boundary such as in an expanding infinite medium[5], this procedure is not allowed. As the limit $\varepsilon \to 0$ must be taken *after* the integration, this complicates the analytic calculation of the full cross-section in the expanding infinite medium case.

In order to highlight how the adiabatic switching works, we calculate the cross-section (3.103) in the vacuum for an off-shell quark created by a hard process occurring at $y^+ = 0$. We first take the limit $\hat{q} \to 0$ in the integral. There are two ways to proceed but in any cases, one has to keep track of the ε dependence. The first way is to calculate

$$k^+ \frac{\mathrm{d}N}{\mathrm{d}k^+ \mathrm{d}^2 k_\perp} = \frac{\alpha_s C_F}{4\pi^2 k^{+2}} 2\mathfrak{Re} \int_0^\infty \mathrm{d}y^+ \int_0^{y^+} \mathrm{d}\bar{y}^+ e^{-\varepsilon y^+ - \varepsilon \bar{y}^+} \times \int \mathrm{d}^2 u_\perp e^{ik_\perp u_\perp} \partial^i_{y_\perp = 0_\perp} \partial^i_{\bar{y}_\perp = 0_\perp} \mathcal{G}_0^\dagger(y^+, y_\perp + u_\perp; \bar{y}^+, \bar{y}_\perp) \tag{3.115}$$

integrating first over $u_\perp$. This gives $k_\perp^2 \exp(ik^-(y^+ - \bar{y}^+))$ so

$$k^+ \frac{\mathrm{d}^3 N}{\mathrm{d}k^+ \mathrm{d}^2 k_\perp} = 2\mathfrak{Re}\Big\{ \frac{\alpha_s C_F k_\perp^2}{4\pi^2 k^{+2}} \int_0^\infty \mathrm{d}y^+ \int_0^{y^+} \mathrm{d}\bar{y}^+ e^{-\varepsilon(y^+ + \bar{y}^+) + ik^-(y^+ - \bar{y}^+)} \Big\} \tag{3.116}$$

$$= \lim_{\varepsilon \to 0} \frac{\alpha_s C_F k_\perp^2}{4\pi^2 k^{+2}} \left(\frac{2}{\varepsilon^2 + k^{-2}} - \frac{1}{k^{-2} + \varepsilon^2} \right) \tag{3.117}$$

$$= \frac{\alpha_s C_F}{\pi^2} \frac{1}{k_\perp^2} \tag{3.118}$$

which is the standard Bremsstrahlung spectrum in the vacuum. Changing the time ordering in the double integral, one can also choose to integrate first over y^+, and even if the calculation is more difficult, it gives the same result:

$$k^+ \frac{\mathrm{d}N}{\mathrm{d}k^+ \mathrm{d}^2 k_\perp} = 2\mathfrak{Re}\Big\{ \frac{\alpha_s C_F k_\perp^2}{4\pi^2 k^{+2}} \int_0^\infty \mathrm{d}\bar{y}^+ e^{-2\varepsilon \bar{y}^+} \int \mathrm{d}^2 u_\perp e^{ik_\perp u_\perp} 2\varepsilon \mathrm{K}_0\Big[2\Big(\frac{ik^+ u_\perp^2}{2} \Big)^{1/2} \varepsilon^{1/2} \Big] \Big\} \tag{3.119}$$

$$= \lim_{\varepsilon \to 0} 2\mathfrak{Re}\Big\{ \frac{\alpha_s C_F k_\perp^2}{4\pi^2 \omega^2} \int \mathrm{d}^2 u_\perp e^{ik_\perp u_\perp} \mathrm{K}_0\Big[2\Big(\frac{ik^+ u_\perp^2}{2} \Big)^{1/2} \varepsilon^{1/2} \Big] \Big\} \tag{3.120}$$

$$= \frac{\alpha_s C_F}{\pi^2} \frac{1}{k_\perp^2} \tag{3.121}$$

where K_0 is the zeroth Bessel function of second kind.

Both ways of doing the calculation give the right answer. However, if we decide to forget about the ε dependence in the integral over $\bar{y}^+$ in (3.116) or in (3.119), we would have obtained the Bremsstrahlung spectrum with an incorrect factor 2! [63] We expect this kind of feature to appear also in the medium calculation with $\hat{q} \neq 0$, enlightening the importance of the adiabatic prescription.

[5]This academic situation is nonetheless considered in Chapter 5 Section 6.1 or Chapter 4, Section 4.3.4.

With a non zero $\hat{q}$, the best we can hope is this spurious factor 2 to be general. Fortunately it is, and we shall use the following lemma in the next section:

$$\lim_{\varepsilon\to 0}\mathfrak{Re}\int_0^\infty \mathrm{d}y^+\int_0^{y^+}\mathrm{d}\bar{y}^+\,e^{-\varepsilon(y^+-\bar{y}^+)}f(y^+,\bar{y}^+)=\lim_{\varepsilon\to 0}\mathfrak{Re}\int_0^\infty \mathrm{d}y^+\,e^{-\varepsilon y^+}\times\int_0^{y^+}\mathrm{d}\bar{y}^+ f(y^+,\bar{y}^+)-\frac{1}{2\phi^2} \quad (3.122)$$

for $f(y^+,\bar{y}^+)\sim\exp(i\phi(y^+-\bar{y^+}))$ as $y^+,\bar{y}^+\to\infty$, with ϕ a real phase. This lemma is important as it enables to forget about the ε dependence in the first integral over $\bar{y}^+$. In the medium, one can always find a primitive of the integral over $\bar{y}^+$ without the exponential adiabatic switching, thanks to the Wronskian relation (3.110). The remaining integral over y^+ is even often convergent so the limit $\varepsilon\to 0$ is trivial.

The proof of (3.122) goes this way: first, we re-order the integrals, integrating first over $\bar{y}^+$. This is allowed as *both* integrals are convergent as long as $\varepsilon>0$. Then, we cut the integral at $\bar{y}^+=T$ with T large enough so that the the difference $|f(y^+,\bar{y}^+)-\exp(i\phi(y^+-\bar{y}^+))|$ is as small as desired. This is possible since by assumption, $f(y^+,\bar{y}^+)\sim\exp(i\phi(y^+-\bar{y}^+))$ for large values of y^+ and $\bar{y}^+$. Then, one can remove the ε prescription in the piece with $\bar{y}^+\leq T$, since the integration domain is compact. On the other piece, one notices:

$$\int_T^\infty \mathrm{d}\bar{y}^+\int_{\bar{y}^+}^\infty \mathrm{d}y^+ e^{i\phi(y^+-\bar{y}^+)-\varepsilon(y^+-\bar{y}^+)}=\frac{i}{2\phi\varepsilon}+\frac{1-2iT\phi}{2\phi^2}+\mathcal{O}(\varepsilon) \quad (3.123)$$

$$\int_T^\infty \mathrm{d}\bar{y}^+\int_{\bar{y}^+}^\infty \mathrm{d}y^+ e^{i\phi(y^+-\bar{y}^+)-\varepsilon y^+}=\frac{i}{\phi\varepsilon}+\frac{1-iT\phi}{\phi^2}+\mathcal{O}(\varepsilon) \quad (3.124)$$

Taking the real part and then the limit $\varepsilon\to 0$ concludes the proof. We emphasize the importance of $\mathfrak{Re}$ in the lemma, as well as the condition $\phi\in\mathbb{R}$.

3.3.3.3 Transverse momentum dependence of the BDMPS-Z spectrum

Without loss of generality, let us assume that the density of scattering centers $n(x^+)$ has support only for $x^+\geq x_0^+$, so that the parton enters into the medium at this time. Then $\hat{q}(x^+)$ decreases smoothly with x^+. We split the integral over y^+ and $\bar{y}^+$ in three pieces $I^{b/b}$, $I^{b/i}$ and $I^{i/i}$ with $y^+,\bar{y}^+\in(-\infty,x_0^+]$, $y^+\in[x_0^+,\infty)$, $\bar{y}^+\in(-\infty,x_0^+]$ and $y^+,\bar{y}^+\in[x_0^+,\infty)$ respectively in order to use the expression (3.106):

$$k^+\frac{\mathrm{d}^3N}{\mathrm{d}k^+\mathrm{d}^2k_\perp}=\frac{\alpha_s C_F}{\pi^2}\big(I^{b/b}+I^{b/i}+I^{i/i}\big) \quad (3.125)$$

If the jet has a finite path length through the medium, meaning that $\hat{q}(t)$ suddenly vanishes for $t\geq L$, one can obtain even more transparent formulas in terms of L. The results for the brick problem or for an eikonal parton with finite path length through an expanding plasma are given in Appendix B. Equivalently, if the hard vertex location is distinct from x_0^+, one can use the junction method described in Appendix B to properly adapt the general formulas presented in this section.

In/in term. The in/in term is also the spectrum of an off-shell quark created at $y^+=x_0^+$. If we introduce the following quantity:

$$Q_s^2(y^+)=\int_{y^+}^\infty \hat{q}(\xi)\mathrm{d}\xi \quad (3.126)$$

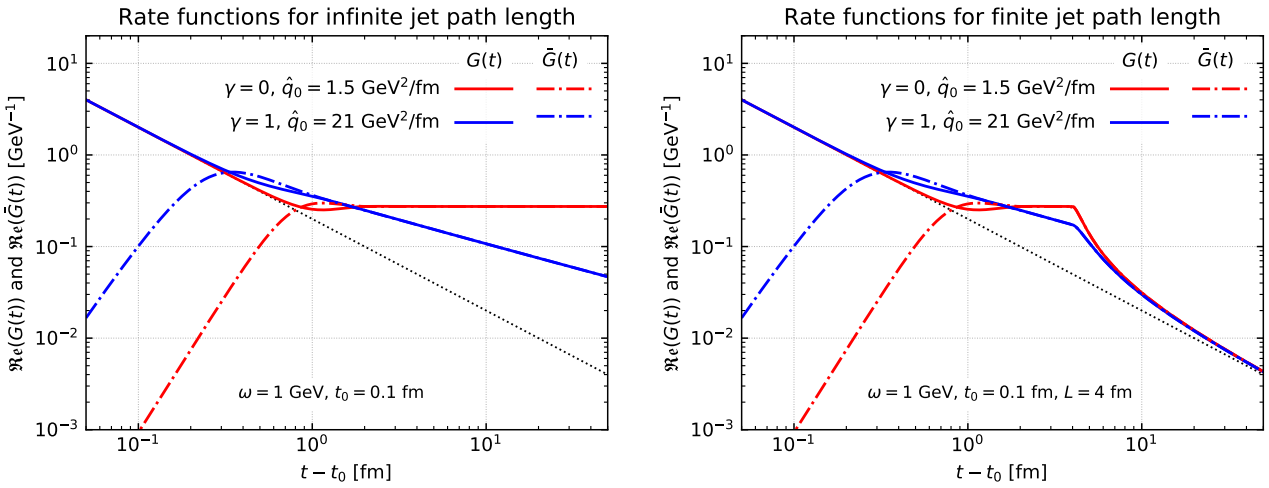

Figure 3.1: The functions G (plain curves) and $\bar{G}$ (dashed curves) for a static medium ($\gamma = 0$, red curves) and an ideal expanding plasma ($\gamma = 1$, blue curves). Only the real parts are represented. On the left hand side, the medium is infinite and G, $\bar{G}$ are solutions of (3.130) and (3.135) respectively. On the right hand side, $\hat{q}(t)$ suddenly vanishes for $t \geq L$. The functions G and $\bar{G}$ are the only *continuous* solutions of the equations (3.130) and (3.135) (see Appendix B). The black dotted curve is the $\hat{q} \to 0$ limit of G, i.e. $1/(t - t_0)$, which is also the solution of (3.130) when $\hat{q} = 0$.

which corresponds to the transverse momentum squared acquired by the gluon during its propagation after y^+, the $I^{i/i}$ reads:

$$I^{i/i} = 2\mathfrak{Re}\int_{x_0^+}^{\infty} \mathrm{d}y^+ \int_{x_0^+}^{y^+} \mathrm{d}\bar{y}^+ \frac{-e^{-\varepsilon(y^+ + \bar{y}^+)}}{S^2(y^+, \bar{y}^+)} \frac{Q_s^4 + 2ik^+ \frac{C(\bar{y}^+, y^+)}{S(y^+, \bar{y}^+)}(k_\perp^2 + Q_s^2)}{\left(Q_s^2 + 2ik^+ \frac{C(\bar{y}^+, y^+)}{S(y^+, \bar{y}^+)}\right)^3} e^{\frac{-k_\perp^2}{Q_s^2 + 2ik^+ \frac{C(\bar{y}^+, y^+)}{S(y^+, \bar{y}^+)}}} \tag{3.127}$$

Now, one can use our lemma (3.122) to integrate over $\bar{y}^+$. Indeed, if $\hat{q}(t)$ goes to 0 at large time, one sees that the integrand becomes a pure vacuum phase of the form $\exp(ik^-(y^+ - \bar{y}^+))$ and thus satisfies the condition of (3.122). Moreover, one can find a primitive with respect to $\bar{y}^+$ when there is no $\exp(-\varepsilon\bar{y}^+)$ factor using the change of variable $\bar{y}^+ \to C(\bar{y}^+, y^+)/S(y^+, \bar{y}^+)$. Naming the function

$$G(y^+) = \frac{C(x_0^+, y^+)}{S(y^+, x_0^+)} = \frac{\partial_{y^+} S(y^+, x_0^+)}{S(y^+, x_0^+)}, \tag{3.128}$$

the final remarkably simple formula for the in/in term, taking into account the correction due to (3.122) is:

$$I^{i/i} = 2\mathfrak{Re}\int_{x_0^+}^{\infty} \mathrm{d}y^+ e^{-\varepsilon y^+} \frac{G(y^+)}{Q_s^2(y^+) + 2ik^+ G(y^+)} \exp\left(\frac{-k_\perp^2}{Q_s^2(y^+) + 2ik^+ G(y^+)}\right) - \frac{1}{k_\perp^2} \tag{3.129}$$

To check this result, and in particular the presence of the corrective term in (3.129), one verifies easily that in the limit $\hat{q} \to 0$ where $Q_s^2(y^+) \to 0$ and $G(y^+) \to 1/(y^+ - x_0^+)$, one recovers the standard Bremsstrahlung spectrum $1/k_\perp^2$. The function G^{-1} satisfies the following non linear differential equation (of Riccati kind):

$$\frac{\mathrm{d}G^{-1}}{\mathrm{d}y^+} = 1 + \frac{i\hat{q}(y^+)}{2k^+}(G^{-1})^2\,, \qquad G^{-1}(x_0^+) = 0 \tag{3.130}$$

and is represented Fig. 3.1-left. For a static medium, with constant $\hat{q}(t) = \hat{q}_0$, the function G is:

$$G_{\rm brick}(y^+) = \Omega \,\mathrm{cotan}\Big(\Omega(y^+ - x_0^+)\Big)\,, \qquad \Omega^2 = \frac{i\hat{q}_0}{2k^+} \tag{3.131}$$

Before/in term. The calculation of the before/in term is more tedious because of the multiple transverse integrals. However, there is no subtlety due to the limit $\varepsilon \to 0$ as the integrals over y^+ and $\bar{y}^+$ decouple. To do the calculation, the trick consists in inserting a Chapman-Kolmogorov relation at intermediate time $y^+ = x_0^+$. The effective propagator between $\bar{y}^+$ and x_0^+ then reduces to a standard (adjoint) vacuum propagator. Introducing the function:

$$\bar{G}(y^+) = \frac{C(x_0^+, y^+)C(y^+, x_0^+) - 1}{S(y^+, x_0^+)C(y^+, x_0^+)} = \frac{\partial_{y^+} C(y^+, x_0^+)}{C(y^+, x_0^+)} \tag{3.132}$$

one gets:

$$I^{b/i} = 2\mathfrak{Re}\int_{x_0^+}^{\infty} \mathrm{d}y^+ e^{-\varepsilon y^+} \frac{\bar{G}(y^+)}{Q_s^2(y^+) + 2ik^+\bar{G}(y^+)} \exp\left(\frac{-k_\perp^2}{Q_s^2(y^+) + 2ik^+\bar{G}(y^+)}\right) \tag{3.133}$$

$$- 2\mathfrak{Re}\int_{x_0^+}^{\infty} \mathrm{d}y^+ e^{-\varepsilon y^+} \frac{G(y^+)}{Q_s^2(y^+) + 2ik^+G(y^+)} \exp\left(\frac{-k_\perp^2}{Q_s^2(y^+) + 2ik^+G(y^+)}\right) \tag{3.134}$$

Note the nice cancellation between the in/in term and the second term of the before/in term in the full on-shell spectrum. This term has also the right $\hat{q} \to 0$ limit $\sim -2/k_\perp^2$ since the function $\bar{G}(y^+)$ goes to zero in this limit.

Also, the function $\bar{G}$ satisfies again a Riccati differential equation:

$$\frac{\mathrm{d}\bar{G}}{\mathrm{d}y^+} + \bar{G}^2 + \frac{i\hat{q}(y^+)}{2k^+} = 0\,, \qquad \bar{G}(x_0^+) = 0 \tag{3.135}$$

The behaviour of $\bar{G}$ is very similar to the one of G since both G and $\bar{G}$ satisfy the same differential equation. The main difference lies in the initial condition and the behaviour at $y^+ = x_0^+$ since $G(y^+) \sim 1/(y^+ - x_0^+)$ whereas $\bar{G}(y^+) \to 0$. This is clear from Fig. 3.1. For a static medium, this function reads:

$$\bar{G}_{\rm brick}(y^+) = -\Omega \,\tan\Big(\Omega(y^+ - x_0^+)\Big)\,, \qquad \Omega^2 = \frac{i\hat{q}_0}{2k^+} \tag{3.136}$$

Before/before term. Last but not least, the before/before term requires also some care. In this term, the effective propagator $\mathcal{K}(y^+; \bar{y}^+)$ is a free propagator and the Fourier transform of the dipole cross-section S_{gg} is independent of y^+ and $\bar{y}^+$ since it is associated with the total transverse momentum acquired during the full propagation. Using the representation (3.114) of the free scalar propagator, this term reads:

$$I^{b/b} = \mathfrak{Re}\int \frac{d^2q_\perp}{(2\pi)^2}\frac{1}{q_\perp^2}\int \mathrm{d}^2u_\perp e^{i(k_\perp - q_\perp)u_\perp} S_{gg}(u_\perp) \tag{3.137}$$

$$= \mathfrak{Re}\int \frac{d^2q_\perp}{(2\pi)^2}\frac{1}{q_\perp^2}\int \mathrm{d}^2u_\perp \exp\left(iu_\perp(k_\perp - q_\perp) - \frac{g^2}{2}C_A\int_{x_0^+}^{\infty} n(x^+)\sigma_d(u_\perp)\mathrm{d}x^+\right) \tag{3.138}$$

In the harmonic approximation used so far in this section, the integral over $u_\perp$ is the Fourier transform of a Gaussian function giving:

$$I^{b/b} = \frac{4\pi}{Q_s^2}\int \frac{d^2q_\perp}{(2\pi)^2}\frac{1}{q_\perp^2}\exp\left(\frac{-(k_\perp - q_\perp)^2}{Q_s^2}\right) \tag{3.139}$$

with $Q_s^2 \equiv Q_s^2(x_0^+)$.

Full results and discussion. It turns out that the inclusive one gluon emission spectrum for an incoming on-shell quark has a very simple analytical form in the multiple soft scattering limit and harmonic approximation. We first give the result for an on-shell incoming quark. This situation is rather academic since the hard probes of the quark-gluon plasma produced in heavy-ion collisions are off-shell time-like quarks. However, this spectrum will help us to understand the physics contained in the off-shell one (cf. Chapter 5). This on-shell spectrum reads:

$$k^+\frac{\mathrm{d}^3N^{\text{on-shell}}}{\mathrm{d}k^+\mathrm{d}^2k_\perp} = \frac{\alpha_s C_F}{\pi^2}\left[\frac{4\pi}{Q_s^2}\int\frac{d^2q_\perp}{(2\pi)^2}\frac{1}{q_\perp^2}\exp\left(\frac{-(k_\perp-q_\perp)^2}{Q_s^2}\right)\right.$$
$$\left.+2\mathfrak{Re}\int_{x_0^+}^{\infty}\mathrm{d}y^+\frac{\bar{G}(y^+)}{Q_s^2(y^+)+2ik^+\bar{G}(y^+)}\exp\left(\frac{-k_\perp^2}{Q_s^2(y^+)+2ik^+\bar{G}(y^+)}\right)-\frac{1}{k_\perp^2}\right] \quad (3.140)$$

where we have removed the adiabatic prescription for compactness. As expected, this spectrum vanishes in the limit $\hat{q}\to 0$, since in this limit $\bar{G}(y^+)\to 0$, so that the last term cancels exactly the before/before term.

On the other hand, the spectrum of an off-shell quark from a hard-vertex located at light cone time x_i^+ is:

$$k^+\frac{\mathrm{d}^3N^{\text{off-shell}}}{\mathrm{d}k^+\mathrm{d}^2k_\perp} = \frac{2\alpha_s C_F}{\pi^2}\mathfrak{Re}\int_{x_i^+}^{\infty}\mathrm{d}y^+\,\frac{G(y^+)}{Q_s^2(y^+)+2ik^+G(y^+)}\exp\left(\frac{-k_\perp^2}{Q_s^2(y^+)+2ik^+G(y^+)}\right)$$
$$-\frac{\alpha_s C_F}{\pi^2}\frac{1}{k_\perp^2} \quad (3.141)$$

With respect to (3.129), note that the lower boundary is now x_i^+. If the medium "starts" at $x_0^+\geq x_i^+$, the function G is the only continuous function satisfying (3.130) for all $y^+\geq x_i^+$ with $G^{-1}(x_i^+)=0$. This off-shell spectrum is more generally considered in the literature, albeit never written under the simple form (3.141).

Whereas the "off-shell" spectrum is mathematically well defined, the first term of the on-shell spectrum corresponding to the before/before integral is ill-defined since the integral is divergent. An infrared cut-off $|q_\perp|\geq\mu$ is required for the integral over $q_\perp$ to make sense and then the question of how choosing this cut-off arises. Note that this feature is not related to the harmonic approximation. Indeed, the $1/q_\perp^2$ behavior when $q_\perp\to 0_\perp$ of (3.137) is independent of the value of σ_d.

As a matter of fact, as on-shell quarks do not exist in QCD because of confinement, it is natural for the on-shell spectrum to be ill-defined. The divergence of the before/before term corresponds to huge wave-length gluons with very long formation time formed before the interaction with the medium and that subsequently undergo transverse momentum broadening. In a confining theory, there is an upper limit on the formation time, or equivalently an upper limit on the wave-length of any emission that translates into a lower bound of order $\mu\sim\Lambda_{\text{QCD}}$ for the $q_\perp$ integral. Note that in the equivalent QED calculation, there is no such singularity as the emitted photon does not further interact with the medium: this divergence is specific to QCD [69]. In Section 3.4, where we deal with an initial colour singlet dipole instead of an on-shell incoming quark, we will see more precisely how the divergence of the before/before term is cured in pQCD.

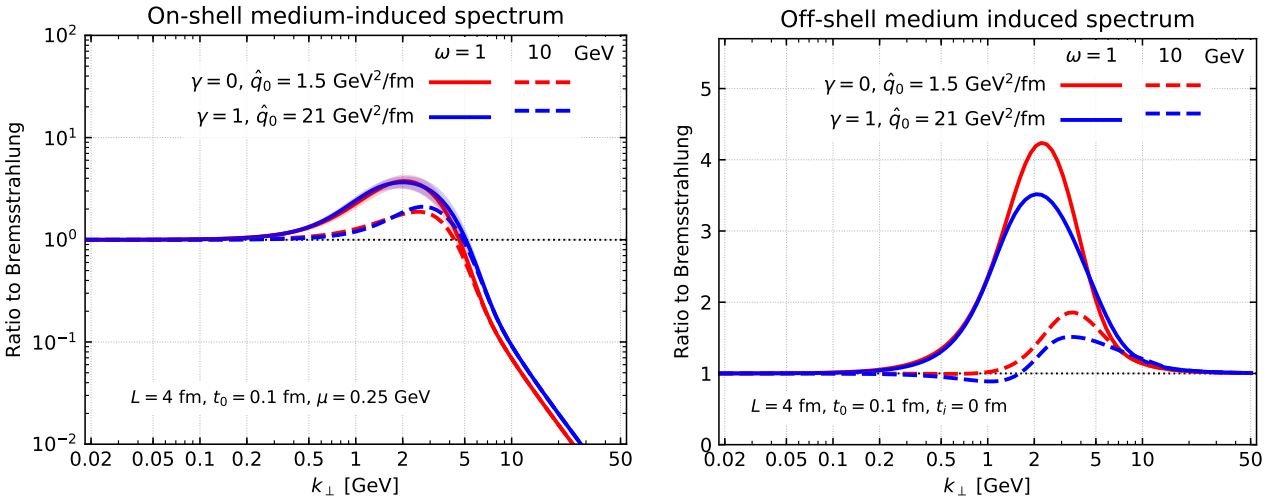

Figure 3.2: On-shell (left) and off-shell (right) medium induced spectra as a function of $k_\perp$ for several values of $\omega \equiv k^+$. The spectra are normalized by the leading order Bremsstrahlung spectrum. For the off-shell spectrum, the location of the hard vertex is $t_i = 0$ fm and the parton enters the medium at $t_0 = 0.1$ fm. For the on-shell spectrum, the bands correspond to the variation of the regularization scale μ by a factor 2. The red curves correspond to the "brick" medium with constant $\hat{q}_0$ density ($\gamma = 0$), whereas the blue curves correspond to the Bjorken expansion of an ideal relativistic plasma ($\gamma = 1$). For the ideal plasma, the value of $\hat{q}_0$ is chosen to scale with the brick calculation in the soft limit of the $k_\perp$-integrated BDMPS-Z spectrum (see Fig. 3.3 and discussion on this subject in Chapter 4-Section 4.3.4).

A curiosity. The μ regularization of the before/before term is of course not unique. It is interesting to notice that the adiabatic switching prescription provides another natural way to regularize the integral. A calculation of the before/before term leaving unintegrated the integral over $t \equiv y^+ - \bar{y}^+$ gives:

$$I^{b/b} = \frac{-1}{\varepsilon} \mathfrak{Re} \int_0^\infty \mathrm{d}t \, \frac{Q_s^4 t + 2ik^+(k_\perp^2 + Q_s^2)}{\left(Q_s^2 t + 2ik^+\right)^3} \exp\left(\frac{-k_\perp^2 t}{Q_s^2 t + 2ik^+} - \varepsilon t\right) \tag{3.142}$$

The integral is well defined as long as $\varepsilon > 0$ but of course, does not have a finite limit as $\varepsilon \to 0$. For any non-zero ε, the integral is cut for $t = |y^+ - \bar{y}^+| \geq 1/\varepsilon$. Since $|y^+ - \bar{y}^+|$ is also the formation time of the emission, it is clear that the μ regularization and the ε regularization are related by:

$$\mu^2 \sim 2k^+\varepsilon \tag{3.143}$$

3.3.3.4 Integrated medium-induced spectrum: LPM effect

Now, we investigate the medium-induced spectrum integrated over $k_\perp$. We first naively attempt to integrate the on-shell spectrum. Indeed, since in this section we are only interested in the purely medium-induced component and not the virtuality driven part, the on-shellness of the quark should prevent the existence of a $k_\perp$-divergent Bremsstrahlung component. However, this is not the case because the medium inevitably puts the quark out of its mass-shell, leading to a Bremsstrahlung tail at small $k_\perp$ (long formation time). We then consider the standard method encountered in the literature, where the $k_\perp$ integrated spectrum is defined as the integral of the off-shell spectrum minus its $\hat{q} \to 0$ limit. In this case, the collinear singularity of the off-shell spectrum is regularized by the vacuum limit.

Integral of the on-shell spectrum. Doing a brute force integration of (3.140), one notices that the two divergent pieces cancel each other exactly in the limit where the infrared cut-off defining the before/before term goes to 0. Indeed, the broadening probability (or the Fourier transform of the dipole cross-section in the more general case) is normalized to 1 once integrated over $k_\perp$. Thus, we are left with a purely medium induced component, that would vanish in the absence of the external field, given by:

$$k^+\frac{\mathrm{d}N^{\text{on-shell}}}{\mathrm{d}k^+} = \frac{2\alpha_s C_F}{\pi}\mathfrak{Re}\int_{x_0^+}^{\infty}\mathrm{d}y^+\bar{G}(y^+) \tag{3.144}$$

Using the Wronskian relation $C\partial_{y^+}S - S\partial_{y^+}C = 1$, one can perform the integral over y^+:

$$k^+\frac{\mathrm{d}N^{\text{on-shell}}}{\mathrm{d}k^+} = \frac{2\alpha_s C_F}{\pi}\lim_{T\to\infty}\log\left(\left|C(T,x_0^+)\right|\right) \tag{3.145}$$

As it is, this limit is not defined. We will prove this in Chapter 4, Section 4.3.4, but this can be understood from Fig. 3.1 as well. For a power law decrease of $\hat{q}(y^+) = \hat{q}_0(x_0^+/y^+)^\gamma$, $\bar{G}$ behaves like $1/y^+$ at large y^+ if $\gamma \geq 2$, and is therefore non-integrable. The physical reason for this divergence lies in the collinear singularity at small $k_\perp$. The interactions with the medium put the parton off-shell and thus, the incoming quark can radiate gluons according to the Bremsstrahlung spectrum. We shall also come back to this point in Chapter 5. If $\gamma < 2$, $G(y^+) \sim \sqrt{\hat{q}(y^+)/(2i\omega)}$ for $y^+ \to \infty$. In this case, $G(y^+)$ is non integrable for a different reason: the amount of radiations induced by the medium is infinite for an infinite jet path length because the medium dilutes too slowly. This suggests that one should integrate the function $\bar{G}$ up to $y^+ = x_0^+ + L$ (another argument based on the shape of the $k_\perp$ spectrum is given in Appendix B). This integral reads:

$$k^+\frac{\mathrm{d}\tilde{N}}{\mathrm{d}k^+} = \frac{2\alpha_s C_F}{\pi}\log\left(\left|C(x_0^+ + L, x_0^+)\right|\right) \tag{3.146}$$

This spectrum is perfectly well defined, whatever the value of γ is. If $\gamma \geq 2$, it includes a substantial amount of vacuum-like collinear emissions with $k_\perp^2 \gtrsim 2k^+/L$.

Integral of the (regularized) off-shell spectrum. As mentioned above, an alternative way to proceed consists in subtracting the genuine vacuum Bremsstrahlung contribution to the off-shell spectrum of a quark created at $y^+ = x_0^+$ (i.e we fix $x_i^+ = x_0^+$ in (3.141)):

$$k^+\frac{\mathrm{d}N}{\mathrm{d}k^+} \equiv \int \mathrm{d}k_\perp^2\left(k^+\frac{\mathrm{d}^3N^{\text{off-shell}}}{\mathrm{d}k^+\mathrm{d}^2k_\perp} - \frac{\alpha_s C_F}{\pi^2}\frac{1}{k_\perp^2}\right) \tag{3.147}$$

Both terms in the integral lead to a divergence but the full integral is convergent. The genuine vacuum spectrum can be written as an integral over y^+ using (3.129) in the limit $\hat{q} \to 0$. The integral over $k_\perp$ is easy and gives:

$$k^+\frac{\mathrm{d}N}{\mathrm{d}k^+} = \frac{2\alpha_s C_F}{\pi}\int_{x_0^+}^{\infty}\mathrm{d}y^+\left(G(y^+) - \frac{1}{y^+ - x_0^+}\right)e^{-\varepsilon y^+} \tag{3.148}$$

The vacuum regulator corresponds to the limit of G when $\hat{q} \to 0$, and can be directly derived from the defining differential equation (3.130) with $\hat{q} = 0$.

As the integral is convergent, one can now remove the adiabatic switching. In order to control the divergences for $y^+ \to x_0^+, \infty$, let us introduce two cut-offs ν and T:

$$k^+\frac{\mathrm{d}N}{\mathrm{d}k^+} = \frac{2\alpha_s C_F}{\pi}\lim_{\nu\to 0,T\to\infty}\mathfrak{Re}\int_{x_0^++\nu}^{T}\mathrm{d}y^+\left(G(y^+)-\frac{1}{y^+-x_0^+}\right) \tag{3.149}$$

$$= \frac{2\alpha_s C_F}{\pi}\lim_{\nu\to 0,T\to\infty}\mathfrak{Re}\int_{x_0^++\nu}^{T}\mathrm{d}y^+\frac{\partial_{y^+}S(y^+,x_0^+)}{S(y^+,x_0^+)}-\log\left((T-x_0^+)/\nu\right) \tag{3.150}$$

$$= \frac{2\alpha_s C_F}{\pi}\lim_{T\to\infty}\log\left(\frac{|S(T,x_0^+)|}{T-x_0^+}\right) = \frac{2\alpha_s C_F}{\pi}\lim_{T\to\infty}\log\left(\left|C(x_0^+,T)\right|\right) \tag{3.151}$$

where we used $S(x_0^+ + \nu, x_0^+) \sim \nu$ when ν goes to zero. This result has been obtained in [119] starting directly from the integral over $k_\perp$ of (3.103) with its vacuum limit subtracted.

As for (3.144) the limit (3.151) is not defined if the medium expands too slowly, with a power $\gamma \leq 2$. In this case, one must also take into account the finite path length L of the parton through the medium. We refer the reader to the calculations presented in Appendix B in this case. We show that formula 3.151 is still valid if the argument of the function C is changed:

$$k^+\frac{\mathrm{d}N}{\mathrm{d}k^+} = \frac{2\alpha_s C_F}{\pi}\log\left(\left|C(x_0^+,x_0^++L)\right|\right) \tag{3.152}$$

Note the nice symmetry between (3.152) and (3.146). On the contrary, if $\gamma > 2$, the integrand in (3.149) behaves like $\hat{q}(y^+)y^+/(2i\omega)$ at large y^+, and is therefore integrable (see again Section 4.3.4). The collinear divergence highlighted in the on-shell spectrum is cured by the vacuum subtraction of the same collinear divergence.

The brick case - LPM effect. To understand the specificity of the BDMPS-Z spectrum, let us consider the brick model where $\hat{q}(t) = \hat{q}$ for $t < L$ and vanishes for $t \geq L$. As shown in Appendix B where we find the solution C of (3.107) continuous and derivable for all $t \geq 0$, one gets:

$$C_{\text{brick}}(0,L) = C_{\text{brick}}(L,0) = \cos(\Omega L)\,, \qquad \Omega^2 = \frac{i\hat{q}}{2k^+} \tag{3.153}$$

so that the BDMPS-Z spectrum reads:

$$k^+\frac{\mathrm{d}N^{\text{brick}}}{\mathrm{d}k^+} = \frac{2\alpha_s C_F}{\pi}\log\left|\cos\left(\frac{1+i}{2}\sqrt{\frac{\hat{q}}{k^+}}L\right)\right| \approx \frac{2\alpha_s C_F}{\pi}\begin{cases}\sqrt{\frac{\omega_c}{2k^+}} & \text{for } k^+ \ll \omega_c\\ \frac{1}{12}\left(\frac{\omega_c}{k^+}\right)^2 & \text{for } k^+ \gg \omega_c\end{cases} \tag{3.154}$$

with $\omega_c \equiv \hat{q}L^2/2$. Note that for the brick model, the spectra (3.152) and (3.146) give the same result because the cosine function is even.

The $\sqrt{\omega_c/k^+}$ behaviour is a consequence of the so-called Landau-Pomerantchuk-Migdal (LPM) effect in QCD [120, 121]. The formation of the gluon is a quantum process which is not instantaneous. The formation time t_f as given by the uncertainty principle is $t_f \sim 2k^+/k_\perp^2$. During this time, if it is larger than the medium mean free path ℓ, the quark-gluon pair interacts coherently with many scattering centers so that the gluon acquires a typical transverse momentum of order $k_\perp^2 \sim \hat{q}t_f$ in the multiple soft scattering regime. Inserting the quantum relation for t_f, one gets the following relation for the formation time $t_{f,\text{med}}$ and transverse momentum $k_{f,\text{med}}$ of medium-induced radiations in the multiple soft scattering regime:

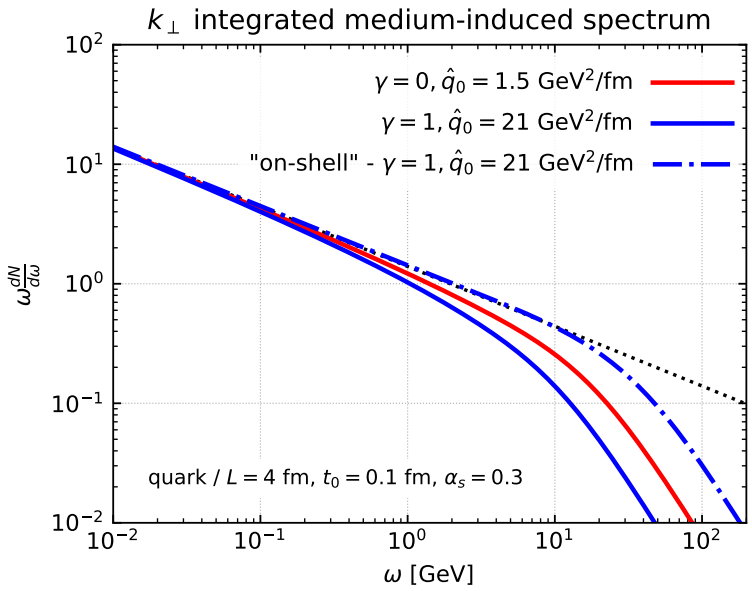

Figure 3.3: Integrated BDMPS-Z spectrum (formula (3.152)) as a function of $\omega \equiv k^+$, for a static medium ($\gamma = 0$) and an expanding ideal plasma ($\gamma = 1$). The value of $\hat{q}_0$ in the latter case is chosen so that both spectra scale exactly in the soft limit. The relation is given by (4.97). In this soft limit, the asymptote is $\propto \sqrt{\omega_c/\omega}$ (dotted black line). The dashed blue line is the integrated on-shell spectrum, i.e. formula (3.146) for comparison.

$$t_{f,\mathrm{med}} = \sqrt{\frac{2k^+}{\hat{q}}}\,, \qquad k^2_{f,\mathrm{med}} = \sqrt{2\hat{q}k^+} \tag{3.155}$$

Hence, for medium induced emissions, the formation time is fixed once the energy k^+ of the emission is fixed. The condition $t_f \geq \ell$ translates into a lower limit in k^+: $k^+ \geq \omega_{\mathrm{BH}} \sim \hat{q}\ell^2$ for the validity of our calculation.

The scale ω_c should be understood as the maximal energy of a medium induced emission that can develop over a time L from multiple scatterings. Indeed, $t_{f,\mathrm{med}} \leq L$ implies $k^+ < \omega_c$. Then ω_c is also the upper limit of validity of our calculation relying on the multiple soft scattering and harmonic approximation. This upper limit enables also to better constrain the validity of the eikonal approximation for the incoming quark: one should impose $p^+ \gg \omega_c$. One can find an equivalent calculation of the gluon emission spectrum relaxing the eikonal approximation for the incoming parton in [122, 123].

This concludes the study of the BDMPS-Z spectrum in QCD which encompasses the regime $\omega_{\mathrm{BH}} \leq k^+ \leq \omega_c$. In the Bethe-Heitler regime, $k^+ \leq \omega_{\mathrm{BH}}$, the spectrum $k^+\mathrm{d}N/\mathrm{d}k^+$ scales as $\alpha_s L/\ell$, i.e. an incoherent sum of radiation spectra. In the regime $k^+ \geq \omega_c$, it becomes dominated by the contribution coming from a single hard scattering (GLV spectrum, order 1 in opacity). This regime is captured by the present formalism [72] but requires to go beyond the harmonic approximation for the dipole cross-section σ_d.

3.4 Interferences in the multiple soft scattering regime

The last section was devoted to medium-induced emissions by an incoming eikonal quark or gluon either on its mass shell or infinitely off-shell since created at a vertex with some fixed

light cone time x_i^+. In this section we shall discuss the scattering of a dipole, i.e. a $q\bar{q}$ pair, off the medium, assuming that the dipole is initially in a colour singlet state. Considering an initial colour singlet state enables to study the effects of interferences on the emission spectrum.

This section is organized as follows: the first part sets up the formalism for the calculation of the emission spectrum from a colour dipole in the medium. The limit $\hat{q} \to 0$ of the result gives the eikonal factor presented in 3.1. In the second part, the effect of interferences is studied in details for medium-induced emissions, removing by hand the standard Bremsstrahlung emissions. Finally, in the third part, interferences are discussed for the vacuum-like emissions as well.

3.4.1 Effective generating functional for soft emissions from a colour-singlet dipole

3.4.1.1 General formalism

We have already developed the major part of the formalism necessary to set-up the calculation of a gluon emission from a $q\bar{q}$ pair. Hence, we shall give less details in this section and refer the reader to Section 3.3.2. Our starting point will be again an effective generating functional for soft gluon emissions where the fermionic degrees of freedom have already been integrated out using the eikonal propagators for the quark and antiquark in the presence of an external (quantized and/or classical) gauge field.

The main difference with respect to the previous section is the initial colour state of the $q\bar{q}$ pair. This state is the colour singlet state:

$$|\phi\rangle = \frac{1}{\sqrt{N_c}} \sum_\alpha |\alpha\rangle \otimes \overline{|\alpha\rangle} \tag{3.156}$$

with $\{|\alpha\rangle\}$ a basis of the fundamental representation of $\mathrm{SU}(N_c)$. It is the only normed state of a $q\bar{q}$ pair invariant under all colour rotations. The effective generating functional for processes involving a $q\bar{q}$ pair in the initial and in the final state is:

$$Z_{\text{eff}}[J^\mu|\mathcal{A}_m] = \frac{1}{\sqrt{N_c}} \sum_\alpha \int \mathcal{D}A^\mu \delta(G[A^\mu]) \mathcal{D}_{tc,\beta\alpha}(p,p'|A+\mathcal{A}_m) \overline{\mathcal{D}}_{tc,\bar{\gamma}\alpha}(\bar{p},\bar{p}'|A+\mathcal{A}_m) \times \exp\left(iS_g[A^\mu|\mathcal{A}_m^\mu] + i\int \mathrm{d}^4x J^\mu A_\mu \right) \tag{3.157}$$

where we have omitted the spin dependence $\delta_{ss'}$, $\delta_{\bar{s}\bar{s}'}$ and written explicitly the colour indices of the truncated propagators in order to highlight the fact that the initial state is fixed. This generating functional fully incorporates the quark degrees of freedom in the eikonal limit, via a colour rotation of the dipole from the state $|\phi\rangle$ to a generic state $|\beta\rangle \otimes \overline{|\gamma\rangle}$. Note that the Wilson line for the anti-quark truncated propagator is in the conjugate fundamental representation.

We are interested in the gluon emission cross-section with the $q\bar{q}$ pair in the final state, but we do not care about the dependence of this cross-section with respect to the final state momenta p' and $\bar{p}'$. If we integrate over the kinematic variables of the final $q\bar{q}$ pair, the classical paths in (3.45) of both partons will be frozen in the amplitude and in the complex conjugate amplitude, as noticed in Section 3.3.2.4. For the inclusive gluon emission cross-section, one can directly replace the truncated propagator $\mathcal{D}_{tc}$ in (3.157) by Wilson lines along the frozen classical paths.

Let us then call $\gamma_q^\mu(x^+)$ and $\gamma_{\bar{q}}^\mu(x^+)$ the respective classical path of the quark and the antiquark in Minkowski space. It is convenient the choose x^+ as the parameter along the path

of both particles because x^+ plays the role of time in light-cone coordinates for a right mover at the speed of light. In light cone coordinates, these paths are parametrised according to:

$$\gamma_q^\mu(x^+) = (x^+, \gamma_q^-(x^+), \gamma_\perp^q(x^+)) \tag{3.158}$$
$$\gamma_{\bar{q}}^\mu(x^+) = (x^+, \gamma_{\bar{q}}^-(x^+), \gamma_\perp^{\bar{q}}(x^+)) \tag{3.159}$$

so that the quark and antiquark Wilson lines read:

$$W^{q,\infty}_{-\infty,\beta\alpha}(\gamma_q|A+\mathcal{A}_m) = T\Big[\exp\Big(ig\int_{-\infty}^{\infty}\mathrm{d}x^+\big(A_a^\mu(\gamma_q)+\mathcal{A}^\mu_{m,a}(\gamma_q)\big)t^a u_\mu\Big)\Big]_{\beta\alpha} \tag{3.160}$$
$$\overline{W}^{\bar{q},\infty}_{-\infty,\bar{\gamma}\alpha}(\gamma_{\bar{q}}|A+\mathcal{A}_m) = T\Big[\exp\Big(-ig\int_{-\infty}^{\infty}\mathrm{d}x^+\big(A_a^\mu(\gamma_{\bar{q}})+\mathcal{A}^\mu_{m,a}(\gamma_{\bar{q}})\big)t^a \bar{u}_\mu\Big]\Big]_{\alpha\bar{\gamma}} \tag{3.161}$$

with $u^\mu = \mathrm{d}\gamma_q^\mu/\mathrm{d}x^+$, $\bar{u}^\mu = \mathrm{d}\gamma_{\bar{q}}^\mu/\mathrm{d}x^+$ constant "4-velocity" vectors. These 4-vectors are related to the 4-momentum of the quark and the antiquark by $p^\mu \simeq p'^\mu = p^+u^\mu$ and $\bar{p}^\mu \simeq \bar{p}'^\mu = \bar{p}^+\bar{u}^\mu$.

The inclusive one gluon emission probability is related to the one-point vacuum expectation value given by our effective generating functional through the LSZ reduction formula. In the light-cone gauge, only the transverse components A^i, $i = 1, 2$ contribute to the matrix elements for the gluon emission. Consequently, we consider

$$\langle A_a^i(z)\rangle = \frac{1}{Z_0}\left(-i\frac{\delta}{\delta J_{i,a}(z)}\right) Z_{\mathrm{eff}}[J^\mu|\mathcal{A}^\mu_m]\Big|_{J=0} \tag{3.162}$$

in order to obtain

$$k^+\frac{\mathrm{d}^3N}{\mathrm{d}k^+\mathrm{d}^2k_\perp} = \lim_{k^2\to 0}\frac{1}{16\pi^3}\Big\langle\sum_{\beta,\bar{\gamma}}\sum_{a,i}\Big|k^2\langle A_a^i(k)\rangle\Big|^2\Big\rangle \tag{3.163}$$

where the big brackets refer to a statistical average. All the spin sums have already been performed and there is no average over initial colours since the initial state is fixed. As in (3.104), the surface of the target has been integrated out.

3.4.1.2 Summary of the cross-section calculation

Amplitude. Then, we proceed in the same way as in the last section: we develop the generating functional up to the first order in gA^μ thanks to the following expansion of the Wilson line:

$$\begin{aligned}W^{q,\infty}_{-\infty,\beta\alpha}(\gamma_q|A+\mathcal{A}_m) =& W^{q,\infty}_{-\infty,\beta\alpha}\\ &+ ig\int_{-\infty}^{\infty}\mathrm{d}y^+\Big[W^{q,\infty}_{y^+}A_b^\mu(\gamma_q(y^+))t^b u_\mu W^{q,y^+}_{-\infty}\Big]_{\beta\alpha} + \mathcal{O}(g^2A^\mu A^\nu u_\mu u_\nu)\end{aligned} \tag{3.164}$$

where all the Wilson lines in the right hand side are Wilson lines over the external field only. The generalization for the antiquark Wilson line (3.161) is straightforward.

Consequently, to the first order in g but all orders in $g\mathcal{A}_m$, the vacuum expectation value of A_a^i reads (we have again omitted the tadpole terms):

$$\begin{aligned}\langle A_a^i(z)\rangle =& \frac{ig}{\sqrt{N_c}}\Big[W^{q,\infty}_{-\infty}\int_{-\infty}^{\infty}\mathrm{d}y^+ G^{i\mu}_{ab}(z,\gamma_q(y^+))u_\mu\mathcal{W}^{q,y^+}_{-\infty,bc}t^c\Big]_{\beta\alpha}\Big[W^{\bar{q},\infty\dagger}_{-\infty}\Big]_{\alpha\bar{\gamma}}\\ &- \frac{ig}{\sqrt{N_c}}\Big[W^{q,\infty}_{-\infty}\Big]_{\beta\alpha}\int_{-\infty}^{\infty}\mathrm{d}x^+ G^{i\nu}_{a\bar{b}}(z,\gamma_{\bar{q}}(x^+))\bar{u}_\nu\mathcal{W}^{\bar{q},x^+}_{-\infty,\bar{b}\bar{c}}\Big[t^{\bar{c}}W^{\bar{q},\infty\dagger}_{-\infty}\Big]_{\alpha\bar{\gamma}}\end{aligned} \tag{3.165}$$

In this expression, we have introduced the gluon propagator $G^{\mu\nu}(z,x)$ defined in (3.75). The sum over α associated with the colour singlet state is implicit. The y^+ coordinate corresponds to the emission time of the gluon from the quark, whereas x^+ is the emission time from the antiquark. We have also written the conjugation of the matrices t^b and $t^{\bar{b}}$ as colour rotations with Wilson lines in the adjoint representation $\mathcal{W}^{q,y^+}_{-\infty,bc}$ and $W^{\bar{q},\infty\dagger}_{-\infty}$, as in the calculation (3.84).

Using the representation of $G^{\mu\nu}(z,x)$ in terms of the scalar propagator in the background field and the generalization of formula (3.76) for the other Lorentz indices given in Appendix A, we perform the Fourier transform with respect to z^-:

$$\begin{aligned}
&\int \mathrm{d}z^-\, e^{ik^+z^-}\langle A^i_a(z)\rangle = \\
&\frac{ig}{2k^+\sqrt{N_c}}\int_{-\infty}^{\infty}\mathrm{d}y^+ e^{ik^+\gamma^-_q(y^+)}\Big(\frac{i\partial^i_{y_\perp}}{k^+}+u^i\Big)\mathcal{G}_{ab}(z^+,z_\perp;y^+,y_\perp|k^+)\mathcal{W}^{q,y^+}_{-\infty,bc}\times\Big[W^{q,\infty}_{-\infty}t^c\Big]_{\beta\alpha}\Big[W^{\bar{q},\infty\dagger}_{-\infty}\Big]_{\alpha\bar{\gamma}}\\
&-\frac{ig}{2k^+\sqrt{N_c}}\int_{-\infty}^{\infty}\mathrm{d}x^+ e^{ik^+\gamma^-_{\bar{q}}(x^+)}\Big(\frac{i\partial^i_{x_\perp}}{k^+}+\bar{u}^i\Big)\mathcal{G}_{a\bar{b}}(z^+,z_\perp;x^+,x_\perp|k^+)\mathcal{W}^{\bar{q},x^+}_{-\infty,\bar{b}\bar{c}}\Big[W^{q,\infty}_{-\infty}\Big]_{\beta\alpha}\Big[t^{\bar{c}}W^{\bar{q},\infty\dagger}_{-\infty}\Big]_{\alpha\bar{\gamma}}
\end{aligned}\tag{3.166}$$

In this formula, it is implicit that the transverse coordinates $y_\perp$ and $x_\perp$ are evaluated at the corresponding transverse position of the quark and the antiquark, i.e. $y_\perp=\gamma^q_\perp(y^+)$ and $x_\perp=\gamma^{\bar{q}}_\perp(x^+)$. With respect to Eq. (3.86), the main difference is in the pure phase $e^{ik^+\gamma^-_q(y^+)}$ (and similarly for the antiquark) that appears inside the integral over the emission time and not outside. Indeed, in the present calculation, one cannot generally find a coordinate system where both the quark and the antiquark have a classical path $\gamma(x^+)$ with constant transverse and minus components. These phases have important consequences as we shall see when discussing the result of this calculation.

Colour algebra. Before completing the Fourier transform of the vacuum expectation value of $A^i_a(z)$, it is convenient to perform the colour algebra when summing over all final colour indices β and $\bar{\gamma}$ of the $q\bar{q}$ pair in the amplitude squared. This amplitude squared contains four terms corresponding to a direct emission by the quark, by the antiquark and the two interferences terms. The choice of the initial state of the dipole (the summation over α) enables to simplify the colour algebra in the product between the amplitude and its complex conjugate. For instance, the algebra for the interference terms reads:

$$\frac{1}{N_c}\sum_{\alpha_1,\alpha_2,\beta,\bar{\gamma}}[W^{q,\infty}_{-\infty}t^c]_{\beta\alpha_1}[W^{\bar{q},\infty\dagger}_{-\infty}]_{\alpha_1\bar{\gamma}}[W^{q,\infty\dagger}_{-\infty}]_{\alpha_2\beta}[W^{\bar{q},\infty}_{-\infty}t^{\bar{c}}]_{\bar{\gamma}\alpha_2} \tag{3.167}$$

$$=\frac{1}{N_c}\sum_{\alpha_1,\alpha_2}t^c_{\alpha_2\alpha_1}t^{\bar{c}}_{\alpha_1\alpha_2}=\frac{1}{N_c}\mathrm{Tr}(t^ct^{\bar{c}}) \tag{3.168}$$

$$=\frac{C_F}{N_c^2-1}\delta^{c\bar{c}} \tag{3.169}$$

In fact, all the four terms give the same $\delta^{c\bar{c}}C_F/(N_c^2-1)$ factor, so we will not write explicitely the fundamental Wilson lines appearing in Eq. (3.166) in the following formulas.

Finally, the application of the k^2 operator in coordinate space $-2ik^+\partial^-_z-\nabla^2_\perp$ and the Fourier transform to momentum space work exactly as in the calculation of a soft gluon emission by a quark. It is again important not to forget the adiabatic switching of interactions, and the

analogous of formula (3.90) is:

$$k^2\langle A_a^i(k)\rangle = g\int_{-\infty}^{\infty}\mathrm{d}y^+ e^{-\varepsilon|y^+|+ik^+\gamma_q^-(y^+)}\int\mathrm{d}^2z_\perp e^{-ik_\perp z_\perp}\Big(\frac{i\partial^i_{y_\perp}}{k^+}+u^i\Big)\mathcal{G}_{ab}(z^+,z_\perp;y^+,y_\perp|k^+)\mathcal{W}^{q,y^+}_{-\infty,bc}$$
$$-g\int_{-\infty}^{\infty}\mathrm{d}x^+ e^{-\varepsilon|x^+|+ik^+\gamma_{\bar q}^-(x^+)}\int\mathrm{d}^2z_\perp e^{-ik_\perp z_\perp}\Big(\frac{i\partial^i_{x_\perp}}{k^+}+\bar u^i\Big)\mathcal{G}_{a\bar b}(z^+,z_\perp;x^+,x_\perp|k^+)\mathcal{W}^{\bar q,x^+}_{-\infty,\bar b\bar c} \quad (3.170)$$

The indices c and $\bar c$ are free but they will be contracted with $\delta^{c\bar c}$ once the amplitude is squared.

Amplitude squared. The last step consists in squaring this amplitude. We expect that the direct terms by the quark or the antiquark to be very close to (3.96), apart from the phase $e^{ik^+\gamma^-(y^+)}$. The full gluon cross-section is decomposed as:

$$\boxed{k^+\frac{\mathrm{d}^3N}{\mathrm{d}k^+\mathrm{d}^2k_\perp}=k^+\frac{\mathrm{d}^3N^{qq}}{\mathrm{d}k^+\mathrm{d}^2k_\perp}+k^+\frac{\mathrm{d}^3N^{q\bar q}}{\mathrm{d}k^+\mathrm{d}^2k_\perp}+(q\leftrightarrow\bar q)} \quad (3.171)$$

The two terms $(q\leftrightarrow\bar q)$ are calculated switching the quark and the antiquark in the formulas. The direct emission spectrum from the quark is:

$$k^+\frac{\mathrm{d}^3N^{qq}}{\mathrm{d}k^+\mathrm{d}^2k_\perp}=\frac{\alpha_sC_F}{(2\pi)^2}2\mathfrak{Re}\int_{-\infty}^{\infty}\mathrm{d}y^+\int_{-\infty}^{y^+}\mathrm{d}\bar y^+ e^{-\varepsilon(|y^+|+|\bar y^+|)}e^{ik^+(\gamma_q^-(y^+)-\gamma_q^-(\bar y^+))}\int\mathrm{d}z_\perp\mathrm{d}\bar z_\perp e^{-ik_\perp(z_\perp-\bar z_\perp)}$$
$$\Big(\frac{i\partial^i_{y_\perp}}{k^+}+u^i\Big)\Big(\frac{-i\partial^i_{\bar y_\perp}}{k^+}+u^i\Big)\frac{1}{N_c^2-1}\Big\langle\mathrm{Tr}\,\mathcal{G}^\dagger(\infty,\bar z_\perp;\bar y^+,\bar y_\perp|k^+)\mathcal{G}(\infty,z_\perp;y^+,y_\perp|k^+)\mathcal{W}^{q,y^+}_{\bar y^+}\Big\rangle \quad (3.172)$$

and the derivatives are taken at $y_\perp=\gamma_\perp^q(y^+)$, $\bar y_\perp=\gamma_\perp^q(\bar y^+)$.

The $q\bar q$ term is a sum of two terms from the amplitude (3.170) squared:

$$k^+\frac{\mathrm{d}^3N^{q\bar q}}{\mathrm{d}k^+\mathrm{d}^2k_\perp}\equiv\int_{-\infty}^{\infty}\mathrm{d}y^+\int_{-\infty}^{y^+}\mathrm{d}\bar x^+\ldots+\int_{-\infty}^{\infty}\mathrm{d}\bar y^+\int_{-\infty}^{\bar y^+}\mathrm{d}x^+\ldots=2\mathfrak{Re}\int_{-\infty}^{\infty}\mathrm{d}y^+\int_{-\infty}^{y^+}\mathrm{d}\bar x^+\ldots \quad (3.173)$$

with, as usual, the integration variable x^+ coming from the complex conjugate amplitude noted $\bar x^+$. Moreover, in the interference term, the product $\mathcal{W}^{q,y^+}_{-\infty}\mathcal{W}^{\bar q,\bar x^+\dagger}_{-\infty}$ cannot be simplified as easily as in the direct terms. This product is responsible for the effect that we will discuss in details in this section: decoherence.

$$k^+\frac{\mathrm{d}^3N^{q\bar q}}{\mathrm{d}k^+\mathrm{d}^2k_\perp}=\frac{-\alpha_sC_F}{(2\pi)^2}2\mathfrak{Re}\int_{-\infty}^{\infty}\mathrm{d}y^+\int_{-\infty}^{y^+}\mathrm{d}\bar x^+ e^{-\varepsilon(|y^+|+|\bar x^+|)}e^{ik^+(\gamma_q^-(y^+)-\gamma_{\bar q}^-(\bar x^+))}\int\mathrm{d}z_\perp\mathrm{d}\bar z_\perp e^{-ik_\perp(z_\perp-\bar z_\perp)}$$
$$\Big(\frac{i\partial^i_{y_\perp}}{k^+}+u^i\Big)\Big(\frac{-i\partial^i_{\bar x_\perp}}{k^+}+\bar u^i\Big)\frac{1}{N_c^2-1}\Big\langle\mathrm{Tr}\,\mathcal{G}^\dagger(\infty,\bar z_\perp;\bar x^+,\bar x_\perp|k^+)\mathcal{G}(\infty,z_\perp;y^+,y_\perp|k^+)\mathcal{W}^{q,y^+}_{-\infty}\mathcal{W}^{\bar q,\bar x^+\dagger}_{-\infty}\Big\rangle \quad (3.174)$$

and the derivatives are taken at $y_\perp=\gamma_\perp^q(y^+)$, $\bar x_\perp=\gamma_\perp^{\bar q}(\bar x^+)$. These results have been obtained independently in [124] and in [91].

3.4.1.3 Medium average

In order to go beyond the previous equations, we need to average over the background field describing the medium. The two basic ingredients are the medium average of two Wilson lines

calculated in (3.57) with equal initial and final times, and the fact that the background field correlations are local in time.

In Eq. (3.57) the two classical paths have a very simple dependence with x^+, namely $u^- = 0$ and $u_\perp = 0_\perp$. The generalization for generic paths is straightforward:

$$\frac{1}{N_c^2-1}\Big\langle \mathrm{Tr}\mathcal{W}_{y_1^+}^{y_2^+}(\gamma)\mathcal{W}_{y_1^+}^{y_2^+\dagger}(\gamma')\Big\rangle = \exp\left(-\frac{g^2}{2}C_A\int_{y_1^+}^{y_2^+}\mathrm{d}x^+\, n(x^+)\sigma_d\big(\gamma_\perp(x^+)-\gamma'_\perp(x^+)\big)\right)$$
$$\simeq \exp\left(-\frac{1}{4}\int_{y_1^+}^{y_2^+}\mathrm{d}x^+\,\hat{q}_A(x^+)\big(\gamma_\perp(x^+)-\gamma'_\perp(x^+)\big)^2\right) \tag{3.175}$$

We used the harmonic approximation for the dipole cross section σ_d in the second line.

The Chapman-Kolmogorov relation for $\mathcal{G}$ is inserted in (3.172) and (3.174) in order to use the locality property. In the direct term, this is done as in (3.97). In the interference term, one does the same trick without forgetting to decompose the adjoint Wilson line for the quark colour rotation: $\mathcal{W}_{-\infty}^{q,y^+} = \mathcal{W}_{\bar{x}^+}^{q,y^+}\mathcal{W}_{-\infty}^{q,\bar{x}^+}$. The final result involves then the Fourier transform of the dipole cross-section S_{gg} related to the broadening of the final state gluon defined in (3.98), the effective propagators $\mathcal{K}_{qg}$ and $\mathcal{K}_{\bar{q}g}$ which depends on the path of the $q\bar{q}$ pair and a colour dipole in the adjoint representation $S_{q\bar{q}}$:

$$\boxed{S_{q\bar{q}}(\bar{x}^+,z^+) \equiv \frac{1}{N_c^2-1}\Big\langle \mathrm{Tr}\mathcal{W}_{z^+}^{q,\bar{x}^+}\mathcal{W}_{z^+}^{\bar{q},\bar{x}^+\dagger}\Big\rangle} \tag{3.176}$$

It is interesting to notice that an adjoint dipole appears in relation with a $q\bar{q}$ dipole. This function describes the colour precession of the colour *currents* of the quark and antiquark and not that of their colour states. They are objects belonging to the adjoint representation contrary to the states, which are in the fundamental one. See [91] for more details.

This average can be calculated from the formula (3.175). With all these pieces, the direct and interference terms for the gluon emission cross-section read[6]:

$$k^+\frac{\mathrm{d}^3N^{qq}}{\mathrm{d}k^+\mathrm{d}^2k_\perp} = \frac{\alpha_s C_F}{(2\pi)^2}2\mathfrak{Re}\int_{-\infty}^{\infty}\mathrm{d}y^+\int_{-\infty}^{y^+}\mathrm{d}\bar{y}^+ e^{-\varepsilon(|y^+|+|\bar{y}^+|)}e^{ik^+(\gamma_q^-(y^+)-\gamma_q^-(\bar{y}^+))}$$
$$\times\Big(\frac{i\partial^i_{y_\perp}}{k^+}+u^i\Big)\Big(\frac{-i\partial^i_{\bar{y}_\perp}}{k^+}+u^i\Big)\int\mathrm{d}^2v_\perp e^{ik_\perp v_\perp}S_{gg}(v_\perp)\mathcal{K}_{qg}(y^+,y_\perp+v_\perp;\bar{y}^+,\bar{y}_\perp|\gamma_q) \tag{3.177}$$

$$k^+\frac{\mathrm{d}^3N^{q\bar{q}}}{\mathrm{d}k^+\mathrm{d}^2k_\perp} = \frac{-\alpha_s C_F}{(2\pi)^2}2\mathfrak{Re}\int_{-\infty}^{\infty}\mathrm{d}y^+\int_{-\infty}^{y^+}\mathrm{d}\bar{y}^+ e^{-\varepsilon(|y^+|+|\bar{y}^+|)}e^{ik^+(\gamma_q^-(y^+)-\gamma_{\bar{q}}^-(\bar{y}^+))}S_{q\bar{q}}(\bar{y}^+,-\infty)$$
$$\times\Big(\frac{i\partial^i_{y_\perp}}{k^+}+u^i\Big)\Big(\frac{-i\partial^i_{\bar{y}_\perp}}{k^+}+\bar{u}^i\Big)\int\mathrm{d}^2v_\perp e^{ik_\perp v_\perp}S_{gg}(v_\perp)\mathcal{K}_{qg}(y^+,y_\perp+v_\perp;\bar{y}^+,\bar{y}_\perp|\gamma_q) \tag{3.178}$$

with the derivative taken as explained above. Because of the non-trivial paths followed by the quark or the antiquark, the effective propagators $\mathcal{K}_{qg}$ (or $\mathcal{K}_{\bar{q}g}$) are a bit more complicated than

[6] We have renamed the bound variables $\bar{y}^+ = \bar{x}^+$ and $\bar{y}_\perp = \bar{x}_\perp$ in the interference term to highlight the symmetry with the direct term.

in (3.99) as they depend on the classical path $\gamma_{q/\bar{q}}$ followed by the quark or the antiquark.

$$\mathcal{K}_{qg}(y^+,y_\perp;\bar{y}^+,\bar{y}_\perp|\gamma_q) \equiv \frac{1}{N_c^2-1}\Big\langle \mathrm{Tr}\mathcal{G}^\dagger(y^+,y_\perp;\bar{y}^+,\bar{y}_\perp|k^+)\mathcal{W}^{q,y^+}_{\bar{y}^+}\Big\rangle \tag{3.179}$$

$$= e^{-ik^+(u_\perp(y_\perp-\bar{y}_\perp)-u^-(y^+-\bar{y}^+))}\mathcal{K}\big(y^+,y_\perp-\gamma^q_\perp(y^+);\bar{y}^+,\bar{y}_\perp-\gamma^q_\perp(\bar{y}^+)\big) \tag{3.180}$$

with $\mathcal{K}$ defined in (3.102). The phase appearing in front of the effective propagator used in the calculation of the BDMPS-Z cross-section is a consequence of the geometry of the dipole. Of course, this phase can be one in an adapted coordinate system, but as emphasized before, one cannot generally find a coordinate system where this phase is one for both the quark and the antiquark effective propagators.

3.4.1.4 Onium scattering with the medium

So far, we have deliberately not specified the forms of $\gamma^\mu_q(x^+)$ and $\gamma^\mu_{\bar{q}}(x^+)$ to keep the discussion as general as possible. In this subsection, as a warm up for the antenna calculation, we consider the scattering of an onium with a medium. The onium enters into the medium at light cone time x_0^+. This simple model for heavy mesons will provide a solution to the divergence of the on-shell spectrum encountered in Section 3.3.3.3.

The onium is defined as an highly energetic (i.e. eikonal) $q\bar{q}$ pair in colour singlet state with fixed transverse separation $X_\perp$. One can then choose a coordinate system such that:

$$\gamma^\mu_q(x^+) = (x^+,0,0_\perp) \tag{3.181}$$

$$\gamma^\mu_{\bar{q}}(x^+) = (x^+,0,X_\perp) \tag{3.182}$$

Hence, for an onium, $u^- = \bar{u}^- = 0$ and $u_\perp = \bar{u}_\perp = 0$ and all the new phases enlighten in the previous discussion disappear. Consequently, if the transverse size of the medium is much larger than $|X_\perp|$ and if one assumes that the density of scattering centers is slowly varying on typical scales of order $|X_\perp|$, it means that the calculation we have made in the previous section is correct also for the direct terms. We only need to calculate the interference term which simply reads:

$$k^+\frac{\mathrm{d}^3N^{q\bar{q}}}{\mathrm{d}k^+\mathrm{d}^2k_\perp} = \frac{-\alpha_sC_F}{(2\pi)^2k^{+2}}2\mathfrak{Re}\int_{-\infty}^{\infty}\mathrm{d}y^+\int_{-\infty}^{y^+}\mathrm{d}\bar{y}^+e^{-\varepsilon(|y^+|+|\bar{y}^+|)}S_{q\bar{q}}(\bar{y}^+,-\infty)$$
$$\times\int\mathrm{d}^2u_\perp\,e^{ik_\perp u_\perp}S_{gg}(u_\perp)\partial^i_{y_\perp=0_\perp}\partial^i_{\bar{y}_\perp=X_\perp}\mathcal{K}(y^+,y_\perp+u_\perp;\bar{y}^+,\bar{y}_\perp) \tag{3.183}$$

The before/before interference term. Now, we calculate the before/before component of the interference term, defined by $y^+,\bar{y}^+\in(-\infty,x_0^+]$. In this domain, the effective propagator $\mathcal{K}$ is free and the $q\bar{q}$ dipole factor $S_{q\bar{q}}$ is equal to 1. Using (3.114) to represent the free propagator, one ends up with the following result:

$$k^+\frac{\mathrm{d}^3N^{q\bar{q},b/b}}{\mathrm{d}k^+\mathrm{d}^2k_\perp} = \frac{-\alpha_sC_F}{\pi^2}\mathfrak{Re}\int\frac{\mathrm{d}^2q_\perp}{(2\pi)^2}\frac{e^{iq_\perp X_\perp}}{q_\perp^2}\int\mathrm{d}^2u_\perp e^{iu_\perp(k_\perp-q_\perp)}S_{gg}(u_\perp) \tag{3.184}$$

$$\simeq \frac{-\alpha_sC_F}{\pi^2}\left[\frac{4\pi}{Q_s^2}\int\frac{\mathrm{d}^2q_\perp}{(2\pi)^2}\frac{\cos(q_\perp X_\perp)}{q_\perp^2}\exp\left(\frac{-(k_\perp-q_\perp)^2}{Q_s^2}\right)\right] \tag{3.185}$$

where we use again the harmonic approximation to get the second line. Combined with the before/before direct terms calculated in (3.139), the divergence in $1/q_\perp^2$ due to the before/before

term of the on-shell spectrum is cured by the $\cos(q_\perp X_\perp)$ factor:

$$k^+\frac{\mathrm{d}^3N^{b/b}}{\mathrm{d}k^+\mathrm{d}^2k_\perp}=\frac{2\alpha_sC_F}{\pi^2}\left[\frac{4\pi}{Q_s^2}\int\frac{\mathrm{d}^2q_\perp}{(2\pi)^2}\frac{1-\cos(q_\perp X_\perp)}{q_\perp^2}\exp\left(\frac{-(k_\perp-q_\perp)^2}{Q_s^2}\right)\right] \tag{3.186}$$

which is a perfectly well defined integral. The factor $1-\cos(q_\perp X_\perp)$ now cuts the long wavelength emissions with $|q_\perp|\lesssim 1/|X_\perp|$ before scattering. Physically, the very soft gluons do not resolve the onium and are thus suppressed.

3.4.2 Medium-induced emissions from a colour singlet antenna

In this section, we consider a colour singlet $q\bar{q}$ antenna. We are interested only in the medium-induced spectrum from this antenna. We leave the study of the vacuum-like pattern to Section 3.4.3. As we are only interested in the medium-induced component, we shall subtract the vacuum limit $\hat{q}\to 0$ of our result as in the discussion of the LPM effect in the previous section.

Let us first define an antenna as an eikonal $q\bar{q}$ pair created at a fixed vertex with light cone time $x_i^+=x_0^+$[7] with fixed opening angle $\theta_{q\bar{q}}$. The corresponding classical trajectories are:

$$\gamma_q^\mu(x^+)=(x^+,u^-(x^+-x_0^+),u_\perp(x^+-x_0^+)) \tag{3.187}$$

$$\gamma_{\bar{q}}^\mu(x^+)=(x^+,\bar{u}^-(x^+-x_0^+),\bar{u}_\perp(x^+-x_0^+)) \tag{3.188}$$

Let us choose our z axis aligned with the direction of motion of the center of mass of the $q\bar{q}$ pair. The opening angle $\theta_{q\bar{q}}$ of the pair is related to the transverse velocities $u_\perp$ and $\bar{u}_\perp$ from the relation $p^2=2E\bar{E}(1-\cos(\theta_{q\bar{q}}))$ with $p=(p+\bar{p})\simeq(p'+\bar{p}')$ and E, $\bar{E}$ the respective energy of the quark and the antiquark. Thus, $2p^\mu\bar{p}_\mu=p^+\bar{p}^+(1-\cos(\theta_{q\bar{q}}))$. Finally, using the relation $p^\mu=p^+u^\mu$,

$$2u^\mu\bar{u}_\mu=1-\cos(\theta_{q\bar{q}})\simeq\frac{\theta_{q\bar{q}}^2}{2} \tag{3.189}$$

in the small angle approximation. The product $2u^\mu\bar{u}_\mu=2u^-+2\bar{u}^--2u_\perp\bar{u}_\perp$ is also equal to $(u_\perp-\bar{u}_\perp)^2$ since $u^2=\bar{u}^2=0$ or equivalently $2u^-=u_\perp^2$ and $2\bar{u}^-=\bar{u}_\perp$ (massless partons).

For an antenna, the $q\bar{q}$ dipole factor $S_{q\bar{q}}$ has a simple expression, in the small angle limit and harmonic approximation. From (3.175), one gets

$$S_{q\bar{q}}(\bar{y}^+)=\exp\left(-\frac{1}{8}\theta_{q\bar{q}}^2\int_{-\infty}^{\bar{y}^+}\mathrm{d}\xi\,\hat{q}_A(\xi)(\xi-x_0^+)^2\right) \tag{3.190}$$

3.4.2.1 The energy spectrum

In a first place, we are not interested in the transverse momentum dependence of the gluon spectrum. In the previous section, we have seen that the off-shell spectrum associated with the emission from a quark created at x_0^+ is divergent once integrated over $k_\perp$. To get a meaningful result, a subtraction of the vacuum radiation pattern is necessary. So, we aim at calculating:

$$k^+\frac{\mathrm{d}N}{\mathrm{d}k^+}=\int\mathrm{d}^2k_\perp\left(k^+\frac{\mathrm{d}^3N^{i/i}}{\mathrm{d}k^+\mathrm{d}^2k_\perp}-\lim_{\hat{q}\to 0}k^+\frac{\mathrm{d}^3N^{i/i}}{\mathrm{d}k^+\mathrm{d}^2k_\perp}\right) \tag{3.191}$$

[7] The generalization to any value of x_i^+ is straightforward.

where the i/i label refers to the in/in term where $y^+, \bar{y}^+ \geq x_0^+$, since the antenna is created at this time.

We work within the multiple soft scatterings and harmonic approximations. For symmetry reasons, the $k_\perp$-*integrated* spectrum for direct emissions by the quark or the antiquark is exactly the same as the one calculated in Section 3.3.3.4. It is given by the expression (3.151).

The interference term is more complicated as one cannot avoid the difficulties due to the phases. As the only dependence on $k_\perp$ is inside the Fourier transform factor $\exp(ik_\perp v_\perp)$, the integration over $k_\perp$ gives a Dirac delta function $(2\pi)^2\delta^{(2)}(v_\perp)$. The final result, for the interference term, is:

$$k^+\frac{\mathrm{d}N^{q\bar{q}}}{\mathrm{d}k^+} \equiv \int \mathrm{d}^2k_\perp \left(k^+\frac{\mathrm{d}^3N^{q\bar{q},i/i}}{\mathrm{d}k^+\mathrm{d}^2k_\perp} - \lim_{\hat{q}\to 0} k^+\frac{\mathrm{d}^3N^{q\bar{q},i/i}}{\mathrm{d}k^+\mathrm{d}^2k_\perp}\right) \tag{3.192}$$

$$= \frac{-\alpha_s C_F}{\pi} 2\mathfrak{Re}\int_{x_0^+}^{\infty}\mathrm{d}y^+\int_{x_0^+}^{y^+}\mathrm{d}\bar{y}^+ e^{-\varepsilon(y^+ + \bar{y}^+)}\left(\frac{-S_{q\bar{q}}(\bar{y}^+)}{S^2(y^+,\bar{y}^+)}e^{\phi(y^+,\bar{y}^+)}\big(1+\phi(y^+,\bar{y}^+)\big)\right.$$
$$\left. + \frac{1}{(y^+-\bar{y}^+)^2}e^{\phi_0(y^+,\bar{y}^+)}\big(1+\phi_0(y^+,\bar{y}^+)\big)\right) \tag{3.193}$$

with the functions ϕ and ϕ_0 defined as (in the small angle approximation):

$$\phi(y^+,\bar{y}^+) = \frac{-ik^+\theta_{q\bar{q}}^2(\bar{y}^+ - x_0^+)}{4}\left(1+\frac{C(y^+,\bar{y}^+)}{S(y^+,\bar{y}^+)}(\bar{y}^+-x_0^+)\right) \tag{3.194}$$

and

$$\phi_0(y^+,\bar{y}^+) \equiv \lim_{\hat{q}\to 0}\phi(y^+,\bar{y}^+) \tag{3.195}$$

$$= \frac{-ik^+\theta_{q\bar{q}}^2(\bar{y}^+ - x_0^+)}{4}\left(1+\frac{\bar{y}^+-x_0^+}{y^+-\bar{y}^+}\right) \tag{3.196}$$

From (3.193), one clearly sees that the unregularised interference term is divergent because of the $1/S^2$ with $S(y^+,\bar{y}) \sim y^+ - \bar{y}^+$ as $y^+ \to \bar{y}^+$.

Note that this expression is completely symmetric in the exchange $q \leftrightarrow \bar{q}$ so the other $\bar{q}q$ interference term is also equal to (3.193). The expression (3.193) can be further simplified using the Wronskian relation (3.110). The ε prescription can be removed as the integral is convergent, and one can switch the order of integration, integrating first over y^+. If we define the quantity:

$$G_\infty(\bar{y}^+) \equiv \lim_{T\to\infty}\frac{C(T,\bar{y}^+ + x_0^+)}{S(T,\bar{y}^+ + x_0^+)} \tag{3.197}$$

then, the full interference term can be expressed as a single integral over $\bar{y}^+$:

$$k^+\frac{\mathrm{d}N^{q\bar{q}}}{\mathrm{d}k^+} = \frac{-2\alpha_s C_F}{\pi}\mathfrak{Re}\int_0^\infty\frac{\mathrm{d}\bar{y}^+}{\bar{y}^+}\left(S_{q\bar{q}}(\bar{y}^+ + x_0^+)e^{-\frac{ik^+\theta_{q\bar{q}}^2\bar{y}^+}{4}\left(1+G_\infty(\bar{y}^+)\bar{y}^+\right)}\left(1+G_\infty(\bar{y}^+)\bar{y}^+\right)\right)$$
$$+ \frac{2\alpha_s C_F}{\pi}\mathfrak{Re}\int_0^\infty\frac{\mathrm{d}\bar{y}^+}{\bar{y}^+}e^{-\frac{ik^+\theta_{q\bar{q}}^2\bar{y}^+}{4}} \tag{3.198}$$

In the limit $\theta_{q\bar{q}} \to 0$, the interference term is exactly equal to minus the direct term. As expected, colour singlet antenna with vanishing opening angle do not radiate.

3.4.2.2 Time-scales in the interference term

Formula (3.198) is general and valid for any continuous function $\hat{q}(t)$. Combined with (3.151), it allows for a straightforward numerical calculation of the medium-induced spectrum generated by a colour singlet antenna. However, the different time scales involved in the integral are difficult to extract without assuming a particular time dependence of $\hat{q}$. In order to have an insight on the physical content of the interference term, let us consider an infinite medium with constant $\hat{q}(t) = \hat{q}$ created at $x_0^+ = 0$. In this simple model, the function $G_\infty(\bar{y}^+)$ is independent of $\bar{y}^+$, since the medium is invariant by light-cone + translation:

$$G_\infty(\bar{y}^+) = \frac{1+i}{2}\sqrt{\frac{\hat{q}}{k^+}} \tag{3.199}$$

Note that an infinite medium with constant $\hat{q}$ does not satisfy the assumptions made for the calculation of the direct terms in the previous section, as the function $\hat{q}(t)$ does not vanish at large times. Consequently, the direct terms are ill-defined in this model. Nevertheless, as we shall see, thanks to the suppression mechanism of interference due to decoherence, the following formula with the upper boundary set to the characteristic length of the medium is a good approximation for the interference term in a finite medium. That said, the present discussion for the interference term is meant to illustrate the time scales characteristic of the interference pattern. The complete formula (3.198) becomes:

$$\begin{aligned} k^+\frac{\mathrm{d}N^{q\bar{q}}}{\mathrm{d}k^+} = \frac{2\alpha_s C_F}{\pi}\int_0^\infty \frac{\mathrm{d}t}{t}\Bigg[\exp\left(-\frac{1}{24}\hat{q}\theta_{q\bar{q}}^2 t^3 - \frac{1}{8}\sqrt{\hat{q}k^+}t^2\theta_{q\bar{q}}^2\right)\times \\ \left(\sqrt{\frac{\hat{q}}{k^+}}\frac{t}{2}\sin\left(\frac{k^+t\theta_{q\bar{q}}^2}{4}+\frac{t^2\theta_{q\bar{q}}^2\sqrt{\hat{q}k^+}}{8}\right) - \left(1+\sqrt{\frac{\hat{q}}{k^+}}\frac{t}{2}\right)\cos\left(\frac{k^+t\theta_{q\bar{q}}^2}{4}+\frac{t^2\theta_{q\bar{q}}^2\sqrt{\hat{q}k^+}}{8}\right)\right) \\ +\cos\left(\frac{k^+t\theta_{q\bar{q}}^2}{4}\right)\Bigg] \end{aligned} \tag{3.200}$$

The last term is the vacuum subtraction required to have a well-defined integral because of the singularity at $t = 0$. One can now identify four time scales in the expression (3.200) (see also the detailed discussion at the level of the $k_\perp$ unintegrated spectrum in [91]).

1. The vacuum interference time $t_{i,\mathrm{vac}}$ is the characteristic time scale for interferences of vacuum-like emissions: interference occurs when the transverse size of the dipole $\theta_{q\bar{q}}t_{i,\mathrm{vac}}$ is shorter than the transverse wavelength $\sim 1/k_\perp$ of the emission. For vacuum-like emissions, $k_\perp \simeq k^+\theta$. Using $\theta = \theta_{q\bar{q}}$ in the relation $1/k_\perp = \theta_{q\bar{q}}t_{i,\mathrm{vac}}$, this gives the following expression for $t_{i,\mathrm{vac}}$:

$$\boxed{t_{i,\mathrm{vac}} = \frac{2}{k^+\theta_{q\bar{q}}^2}} \tag{3.201}$$

   This scale is the only one remaining in the limit $\hat{q} \to 0$ (that is why it is really a vacuum-like time scale), and corresponds to a purely imaginary phase in formula (3.198) or (3.200).

2. The medium induced interference time $t_{i,\mathrm{med}}$ is the characteristic time scale for interferences of medium induced emissions. Instead of using $k_\perp \simeq k^+\theta_{q\bar{q}}$ in the relation $1/k_\perp = \theta_{q\bar{q}}t_{i,\mathrm{med}}$, one uses the typical transverse momentum at formation $k_{f,\mathrm{med}} \sim (\hat{q}k^+)^{1/4}$

of medium-induced emissions, cf. (3.155):

$$\boxed{t_{i,\mathrm{med}} = \frac{2}{k_f \theta_{q\bar{q}}} = \frac{2^{3/4}}{(\hat{q}k^+)^{1/4}\theta_{q\bar{q}}}} \tag{3.202}$$

This time scale appears in the exponential suppression factor in (3.200) as well as in the imaginary phase seen in the sine and cosine functions.

3. The medium induced formation time $t_{f,\mathrm{med}}$ discussed in the previous section:

$$\boxed{t_{f,\mathrm{med}} = \sqrt{\frac{2k^+}{\hat{q}}}} \tag{3.203}$$

This time scale is the only one involved in the direct terms (besides the length L of the medium, see below).

4. The decoherence time coming from the dipole $q\bar{q}$ factor $S_{q\bar{q}}$. For a constant $\hat{q}$, $S_{q\bar{q}}$ can be calculated exactly:

$$S_{q\bar{q}}(t) = \exp\left(-\frac{1}{24}\hat{q}\theta_{q\bar{q}}^2 t^3\right) = \exp\left(-\frac{1}{6}(t/t_{\mathrm{coh}})^3\right), \tag{3.204}$$

$$\boxed{t_{\mathrm{coh}} = \left(\frac{4}{\hat{q}\theta_{q\bar{q}}^2}\right)^{1/3}} \tag{3.205}$$

It is independent of the energy k^+ of the emission.

The numerical prefactors for these time scales have been chosen so that they are equal at a special energy scale $\omega_0(\theta_{q\bar{q}})$ defined by:

$$\omega_0(\theta_{q\bar{q}}) \equiv \left(\frac{2\hat{q}}{\theta_{q\bar{q}}^4}\right)^{1/3} \tag{3.206}$$

The ordering of the four time scales is the following:

$$\begin{array}{ll} t_{f,\mathrm{med}} \le t_{\mathrm{coh}} \le t_{i,\mathrm{med}} \le t_{i,\mathrm{vac}} & \text{if } k^+ \le \omega_0(\theta_{q\bar{q}}) \\ t_{f,\mathrm{med}} \ge t_{\mathrm{coh}} \ge t_{i,\mathrm{med}} \ge t_{i,\mathrm{vac}} & \text{if } k^+ \ge \omega_0(\theta_{q\bar{q}}) \end{array} \tag{3.207}$$

with equality for $k^+ = \omega_0(\theta_{q\bar{q}})$. In terms of these time scales, the interference term for constant $\hat{q}$ in an infinite medium reads:

$$\begin{aligned} k^+\frac{\mathrm{d}N^{q\bar{q}}}{\mathrm{d}k^+} = \frac{2\alpha_s C_F}{\pi}\frac{1}{\sqrt{2}t_{f,\mathrm{med}}}\int_0^\infty \frac{\mathrm{d}t}{t}\Bigg\{ & \exp\Big(-\frac{1}{6}\Big(\frac{t}{t_{\mathrm{coh}}}\Big)^3 - \frac{1}{16\sqrt{2}}\Big(\frac{t}{t_{i,\mathrm{med}}}\Big)^2\Big) \times \\ & \Bigg[t\sin\Big(\frac{t}{2t_{i,\mathrm{vac}}} + \frac{1}{16\sqrt{2}}\Big(\frac{t}{t_{i,\mathrm{med}}}\Big)^2\Big) - \Big(\sqrt{2}t_{f,\mathrm{med}} + t\Big)\cos\Big(\frac{t}{2t_{i,\mathrm{vac}}} + \frac{1}{16\sqrt{2}}\Big(\frac{t}{t_{i,\mathrm{med}}}\Big)^2\Big)\Bigg] \\ & + \sqrt{2}t_{f,\mathrm{med}}\cos\Big(\frac{t}{2t_{i,\mathrm{vac}}}\Big)\Bigg\} \end{aligned} \tag{3.208}$$

3.4.2.3 Discussion

Now that we have identified the main time scales in the interference term, we would like to discuss the effect of this term on the full medium-induced spectrum as a function of the opening angle $\theta_{q\bar{q}}$ of the dipole and the energy k^+ of the medium-induced emission. Thus, we need to re-introduce a characteristic path length L of the antenna through the medium so that $\hat{q}(t)$ vanishes when $t \geq L$. We shall consider only emissions with $k^+ \ll \omega_c$, i.e $t_{f,\mathrm{med}} \ll L$, so that all the approximations made to derive the BDMPS-Z spectrum (direct terms) are valid.

As a first step, we need to understand how the four time scales involved in the unintegrated medium-induced spectrum are related with the length L. We now call this unintegrated medium-induced spectrum the "medium induced rate" for the following reason. In the regime $k^+ \leq \omega_c$, the BDMPS-Z spectrum is proportional to $L/t_{f,\mathrm{med}}$. Hence one can interpret $t_{f,\mathrm{med}}$ as a (constant) rate for medium-induced emissions that can occur everywhere over the characteristic length L:

$$k^+ \frac{\mathrm{d}^2 N^{qq}}{\mathrm{d}k^+ \mathrm{d}t} \simeq \frac{2\alpha_s C_F}{\pi} \sqrt{\frac{\hat{q}}{4k^+}} = \frac{2\alpha_s C_F}{\pi} \frac{1}{\sqrt{2} t_{f,\mathrm{med}}} \tag{3.209}$$

so that

$$k^+ \frac{\mathrm{d}N^{qq}}{\mathrm{d}k^+} = \int_0^L \mathrm{d}t \, k^+ \frac{\mathrm{d}^2 N^{qq}}{\mathrm{d}k^+ \mathrm{d}t} = \frac{2\alpha_s C_F}{\pi} \sqrt{\frac{\omega_c}{2k^+}} \tag{3.210}$$

as shown in (3.154). Thus, the direct emission rate depends on the medium induced formation time only, whereas the interference emission rate depends on the medium induced formation time and the three other time-scales $t_{i,\mathrm{vac}}$, t_{coh} and $t_{i,\mathrm{med}}$ appearing in the exponential, either as real or imaginary phases. These three phases depends on $\theta_{q\bar{q}}$.

Now, from the formula (3.200), the interference rate exactly cancels the direct rate for all $t \leq L$ if the exponential is equal to one for $t \leq L$, i.e if the three following conditions are satisfied: $t_{i,\mathrm{vac}} \gg L$, $t_{\mathrm{coh}} \gg L$ and $t_{i,\mathrm{med}} \gg L$. Fortunately, the conditions $t_{\mathrm{coh}} \gg L$ implies the other two. Indeed, the condition $t_{\mathrm{coh}} \geq L$ is equivalent to $\omega_0(\theta_{q\bar{q}}) \geq \omega_c$ since:

$$\frac{\omega_c}{\omega_0(\theta_{q\bar{q}})} = \left(\frac{L}{t_{\mathrm{coh}}}\right)^2 \tag{3.211}$$

As we consider only emissions such that $k^+ \leq \omega_c$, we see from (3.207) that the three time scales t_{coh}, $t_{i,\mathrm{vac}}$ and $t_{i,\mathrm{med}}$ are ordered as follows $t_{\mathrm{coh}} \leq t_{i,\mathrm{med}} \leq t_{i,\mathrm{vac}}$. Hence, if $t_{\mathrm{coh}} \gg L$, one has also $t_{i,\mathrm{vac}} \gg L$ and $t_{i,\mathrm{med}} \gg L$. The condition $t_{\mathrm{coh}} \gg L$ can be expressed more naturally as a condition on the dipole opening angle $\theta_{q\bar{q}}$. Defining the critical angle θ_c such that $t_{\mathrm{coh}}(\theta_c) = L$, the decoherence time is much larger than the characteristic length of the medium if $\theta_{q\bar{q}} \ll \theta_c$, with

$$\boxed{\theta_c \equiv \frac{2}{\sqrt{\hat{q} L^3}}} \tag{3.212}$$

To sum up, when $\theta_{q\bar{q}} \ll \theta_c$, there is no exponential suppression of interferences and the interference term cancels the direct terms: the medium-induced spectrum is strongly suppressed for a colour singlet dipole. The case $t_{\mathrm{coh}} \gg L \Leftrightarrow \theta_{q\bar{q}} \ll \theta_c$ is simple then: for a colour singlet initial state, the medium-induced spectrum vanishes. For a colour octet initial state, one can show that the medium-induced spectrum is equal to the medium-induced spectrum of a gluon. This leads to the following general statement: when the opening angle of the dipole is smaller than θ_c, the dipole emits medium-induced gluons as a single colour charge depending on the initial colour state of the dipole [91, 124, 125].

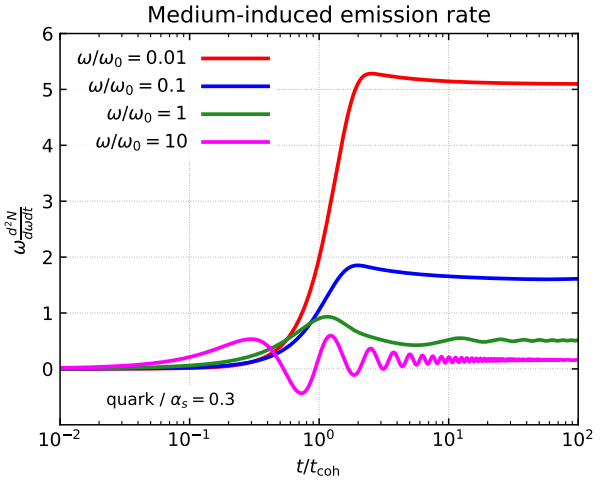

(a) Medium induced emission rate from a $q\bar{q}$ antenna.

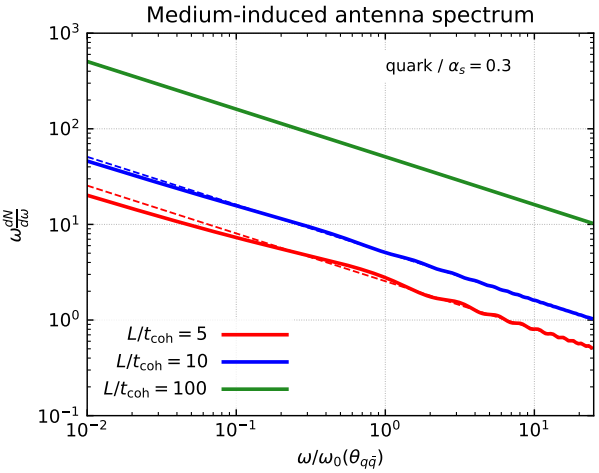

(b) BDMPS-Z spectrum from a $q\bar{q}$ antenna.

Figure 3.4: Interference effects in the medium-induced spectrum from a colour singlet antenna for a static medium, in the regime $\omega \ll \omega_c$. On the left plot, the medium-induced rate (3.213) is represented as a function of the dimensionless time $t/t_{\rm coh}$, for several values of $\omega \equiv k^+$. The large time limit of the rates is twice the constant BDMPS-Z rate for a single quark. On the right plot, the integrated rate (between 0 and L) is represented as a function of $\omega/\omega_0(\theta_{q\bar{q}})$. The dotted lines correspond to the soft limit of the BDMPS-Z spectrum for a static medium multiplied by a 2.

Let us now focus on the other regime $L \gg t_{\rm coh} \Leftrightarrow \theta_{q\bar{q}} \gg \theta_c$. These inequalities are also equivalent to $\omega_0(\theta_{q\bar{q}}) \ll \omega_c$. Consequently, the characteristic energy scale $\omega_0(\theta_{q\bar{q}})$ belongs well to the multiple soft scattering regime. One can trust formula (3.200) even when the medium has a finite length since the rate vanishes when $t > L > t_{\rm coh}$ due to the exponential decoherence suppression. Combining all the terms together, the full medium-induced rate from a colour singlet antenna in the regime $\theta_{q\bar{q}} \gg \theta_c$ and $k^+ \ll \omega_c$ reads:

$$k^+\frac{\mathrm{d}^2N}{\mathrm{d}k^+\mathrm{d}t} = \frac{4\alpha_s C_F}{\pi}\sqrt{\frac{\hat{q}}{4k^+}}\left\{1+\exp\left(-\frac{1}{24}\hat{q}\theta_{q\bar{q}}^2t^3-\frac{1}{8}\sqrt{\hat{q}k^+}t^2\theta_{q\bar{q}}^2\right)\times\right.$$
$$\left[\sin\left(\frac{k^+t\theta_{q\bar{q}}^2}{4}+\frac{t^2\theta_{q\bar{q}}^2\sqrt{\hat{q}k^+}}{8}\right)-\left(\sqrt{\frac{4k^+}{\hat{q}}}\frac{1}{t}+1\right)\cos\left(\frac{k^+t\theta_{q\bar{q}}^2}{4}+\frac{t^2\theta_{q\bar{q}}^2\sqrt{\hat{q}k^+}}{8}\right)\right]$$
$$\left.+\sqrt{\frac{4k^+}{\hat{q}}}\frac{1}{t}\cos\left(\frac{k^+t\theta_{q\bar{q}}^2}{4}\right)\right\} \quad (3.213)$$

In the regime $L \gg t_{\rm coh}$, since $\omega_0(\theta_{q\bar{q}}) \ll \omega_c$, one has to distinguish two cases: either $k^+ \leq \omega_0(\theta_{q\bar{q}})$ or $\omega_c \geq k^+ \geq \omega_0(\theta_{q\bar{q}})$. In the case $k^+ \leq \omega_0(\theta_{q\bar{q}})$, the interference rate vanishes for $t > t_{\rm coh}$ and the other time $t_{i,\rm med}$ and $t_{i,\rm vac}$ are irrelevant because of the ordering (3.207). In the limit $L \gg t_{\rm coh}$, after integrating the full rate between 0 and L, the net result is an incoherent sum of the emission spectrum by the quark and the antiquark. If $L \gtrsim t_{\rm coh}$, one observes numerically a small suppression due to the interference rate integrated for $t \leq t_{\rm coh}$.

The case $\omega_c \geq k^+ \geq \omega_0(\theta_{q\bar{q}})$ is more delicate, because the interpretation of (3.213) as a *formation rate* is ambiguous. Indeed, from the ordering (3.207), the interference rate is controlled by $t_{i,\rm vac}$ and thus becomes oscillatory. This is shown Fig. 3.4a. The exponential suppression of the interference is controlled by $t_{i,\rm med}$. The interference spectrum obtained after

integrating the interference rate between 0 and L gives the average of the oscillatory integral which is typically zero. Consequently, the full spectrum is again twice the spectrum of a single colour charge. Thus, even if the rate interpretation of (3.213) when $\omega_c \geq k^+ \geq \omega_0(\theta_{q\bar{q}})$ is not allowed, the integrated spectrum is still the incoherent sum of two BDMPS-Z spectra, as shown Fig.3.4b because the interference is a quantity proportional to $t_{i,\mathrm{med}} \ll L$ suppressed with respect to the direct terms.

3.4.3 Decoherence effects in the vacuum-like radiation pattern

In the previous subsection, we have discussed the effect of the interferences on the medium-induced radiations only, as the standard vacuum radiation pattern was subtracted off in order to have a convergent $k_\perp$ integral. The effect of the medium on the vacuum-like radiation pattern from a colour singlet antenna is the subject of this last subsection. We will comment the potential overlap between these two calculations in due course.

In the vacuum, we have seen in Section 3.1 that the radiation pattern of a colour singlet dipole presents the property of angular ordering: no radiations are allowed outside the opening angle of the dipole. This is a consequence of quantum interferences associated with the colour coherence of the dipole. In the medium, the $q\bar{q}$ dipole factor $S_{q\bar{q}}$ washes out the colour coherence of the dipole so we expect non trivial effects on the vacuum-like radiation pattern.

Calculating the full differential emission spectrum $\mathrm{d}^3N/\mathrm{d}k^+\mathrm{d}^2k_\perp$ from a colour singlet antenna is complicated and the final result is not as simple as the differential emission spectrum from a single quark. However, one can easily understand the effect of the factor $S_{q\bar{q}}$ on the vacuum radiation pattern with a simple calculation. This is the subject of the first subsection, where we explain the effect of decoherence with a simple toy model. In the second subsection, we consider the same antenna as in Section 3.4.2, but we constrain the gluon to be vacuum-like by choosing a kinematic regime in which the formation time is either very *short* or very *long*.

3.4.3.1 Shockwave limit of the emission cross-section from onium scattering

Let us first consider again the scattering of the onium briefly discussed in Section 3.4.1.4. However, the onium is now highly virtual, that is both the quark and the antiquark are created at light cone time $x_0^+ = 0$. This toy model enables to understand the main features of decoherence in the medium. Since the transverse size of the dipole is fixed to $|X_\perp|$, contrary to the antenna where the transverse size increases with time as $\theta_{q\bar{q}}t$, the interference criterium is simply $|X_\perp| \lesssim |1/k_\perp|$ and does not depend on time.

In the vacuum, the full double differential cross-section, after integration over the azimuthal angle is:

$$k^+\frac{\mathrm{d}^2N^{\mathrm{vac}}}{\mathrm{d}k^+\mathrm{d}k_\perp} = \frac{4\alpha_s C_F}{\pi}\frac{1}{k_\perp}\Big(1 - \mathrm{J}_0\big(X_\perp k_\perp\big)\Big) \tag{3.214}$$

When $k_\perp \gg 1/X_\perp$, the spectrum behaves as an incoherent sum of two Bremsstrahlung spectra. On the contrary, when $k_\perp \ll 1/X_\perp$, the spectrum is suppressed and vanishes in the limit $k_\perp \to 0$.

In the presence of the medium, the radiation pattern is modified. We are not interested in the medium-induced emission generated by the scattering. Consequently, we can take the shockwave limit of the full spectrum, that is $L \to 0$ with $Q_s^2 = \hat{q}L$ fixed. The medium is a brick with fixed length L and constant $\hat{q}$, starting at $x_0^+ = 0$. In this limit, only the out/out term with $y^+, \bar{y}^+ \geq L \to 0$ contributes to the spectrum for a $q\bar{q}$ pair created at $x_0^+ = 0$. The out/out direct terms are trivial and give one $1/k_\perp^2$ term for the quark and the antiquark. Let

us calculate the out/out interference term:

$$k^+\frac{\mathrm{d}^3N^{q\bar{q},o/o}}{\mathrm{d}k^+\mathrm{d}^2k_\perp}=\frac{-\alpha_sC_F}{(2\pi)^2k^{+2}}2\mathfrak{Re}\int_L^\infty \mathrm{d}y^+\int_L^{y^+}\mathrm{d}\bar{y}^+e^{-\varepsilon(y^++\bar{y}^+)}S_{q\bar{q}}(\bar{y}^+,-\infty) \tag{3.215}$$

$$\times\int \mathrm{d}^2u_\perp e^{ik_\perp u_\perp}\partial^i_{y_\perp=0_\perp}\partial^i_{\bar{y}_\perp=X_\perp}\mathcal{G}_0(y^+,y_\perp+u_\perp;\bar{y}^+,\bar{y}_\perp) \tag{3.216}$$

$$\underset{L\to 0}{=}\frac{-\alpha_sC_F}{\pi^2}\exp\Big(-\frac{1}{4}Q_s^2X_\perp^2\Big)\frac{\cos\big(X_\perp k_\perp\big)}{k_\perp^2} \tag{3.217}$$

The exponential is entirely due to the factor $S_{q\bar{q}}$ associated with the decoherence of the $q\bar{q}$ pair. The full off-shell onium spectrum in the shockwave limit reads, again after integration over the azimuthal angle:

$$k^+\frac{\mathrm{d}^2N}{\mathrm{d}k^+\mathrm{d}k_\perp}=\frac{4\alpha_sC_F}{\pi}\frac{1}{k_\perp}\Big(\Big(1-\mathrm{J}_0\big(X_\perp k_\perp\big)\Big)+\Big(1-e^{-\frac{1}{4}Q_s^2X_\perp^2}\Big)\mathrm{J}_0\big(X_\perp k_\perp\big)\Big) \tag{3.218}$$

This expression is very simple. For small dipole, with $X_\perp \ll 1/Q_s$, the decoherence factor has no effect as long as $k_\perp > Q_s$ and the spectrum becomes identical to the vacuum spectrum (3.214). However, if the dipole is large enough, namely $X_\perp \gtrsim 1/Q_s$, the long wavelength radiations, with $k_\perp \ll 1/X_\perp$ are not forbidden anymore by the interferences. Indeed, the spectrum behaves as $(1-\exp(-Q_s^2X_\perp^2/4))/k_\perp$. The factor $\exp(-Q_s^2X_\perp^2/4)$ can be interpreted as the survival probability of the dipole in a colour singlet state, configuration which forbids long wavelength emissions. A numerical evaluation of (3.218) is shown Fig. 3.5a.

3.4.3.2 Decoherence in the antenna radiation pattern

Let us now turn to a more physically relevant scenario: the emission of a vacuum-like gluon by a $q\bar{q}$ antenna inside a dense medium. On may wonder why the medium would play any role in the emission of a vacuum-like gluon. The situation is pretty much like for our off-shell onium: the decoherence of the pair may lead to a modification of the vacuum-like radiation pattern, destroying interferences and hence allowing extra radiations.

Vacuum-like emissions with very short formation time. To understand more precisely the effect of $S_{q\bar{q}}$, we try the following exercise: we replace the effective propagators $\mathcal{K}_{qg}$ and $\mathcal{K}_{\bar{q}g}$ by the free vacuum propagator $\mathcal{G}_0^\dagger$ and we neglect the subsequent transverse momentum broadening. As we are interested in vacuum-like emissions (VLEs), these simplifications do not drastically change the physical picture of the vacuum-like antenna radiation pattern for emissions such that:

$$\omega_c \ll k^+ \ll p^+,\bar{p}^+\,,\qquad Q_s \ll k_\perp \ll p_\perp,\bar{p}_\perp \tag{3.219}$$

Note that that this limit is different from the soft limit considered in [89, 90]. We focus here on vacuum-like emissions with a very short formation time, hence occurring inside the medium. The formation time is so short that the formation process cannot be triggered by the multiple soft collisions, as it would take at least a time $t_{f,\mathrm{med}}$ for producing it in this way. We will see in Chapter 5 that the kinematic constraints (3.219) are actually too strong: in-medium VLEs satisfy $k_\perp \gg (2\hat{q}k^+)^{1/4}$ instead of (3.219). We leave for further studies the question of whether the calculation below gives a good estimate of the in-medium VLE pattern also in this regime. As a last comment, we emphasize that this kinematic regime was not considered in our discussion of the medium-induced spectrum by an antenna since we assumed $k^+ \ll \omega_c$.

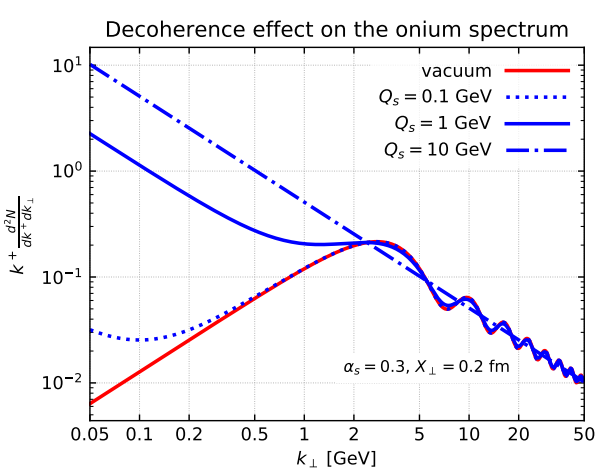

(a) Gluon spectrum from an off-shell onium in the shockwave limit. The red curve is the spectrum in the absence of decoherence effect: one observes a strong suppression for $k_\perp \ll 1/X_\perp$. The blue curves show the numerical evaluation of (3.218) for several values of Q_s. For large values of Q_s the interference pattern is destroyed, and small $k_\perp$ radiations are copiously emitted.

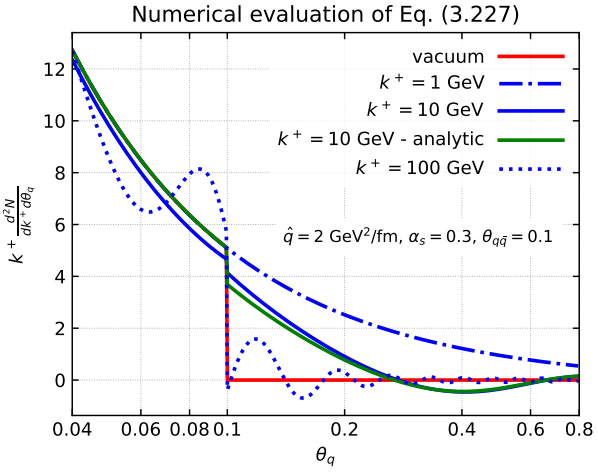

(b) Numerical evaluation of the formula (3.235). The green curve corresponds to the approximation (3.236). The medium parameters are fixed whereas the kinematic of the emission is varied, showing that decoherence induces out-of cone radiations with respect to the vacuum (red curve). We have deliberately chosen k^+ not in the regime (3.219) to highlight the effect. Actually, as shown in Chapter 5, out-of-cone radiations are always suppressed if (3.219) is enforced (dotted curve).

Figure 3.5: Decoherence effects on colour-singlet dipoles with two different geometries: the "onium" geometry (left) and the antenna (right).

In this limit, the sum of the direct terms is an incoherent sum of two Bremsstrahlung spectra:

$$k^+ \frac{\mathrm{d}^3 N^{\mathrm{direct}}}{\mathrm{d}k^+ \mathrm{d}^2 k_\perp} = \frac{\alpha_s C_F}{\pi^2} \left(\frac{1}{(k_\perp - k^+ u_\perp)^2} + \frac{1}{(k_\perp - k^+ \bar{u}_\perp)^2} \right) = \frac{\alpha_s C_F}{2\pi^2 k^+} \left(\frac{1}{k^\mu u_\mu} + \frac{1}{k^\mu \bar{u}_\mu} \right) \tag{3.220}$$

where the transverse momentum $k_\perp$ has been shifted to take into account the change of coordinate system due to the geometry of the antenna. The $q\bar{q}$ interference term has the following structure:

$$k^+ \frac{\mathrm{d}^3 N^{q\bar{q}}}{\mathrm{d}k^+ \mathrm{d}^2 k_\perp} = \frac{-\alpha_s C_F}{4\pi^2 k^{+2}} (k_\perp - k^+ u_\perp)(k_\perp - k^+ \bar{u}_\perp) \times 2\mathfrak{Re} \int_0^\infty \mathrm{d}\bar{y}^+ \int_{\bar{y}^+}^\infty \mathrm{d}y^+ e^{-\varepsilon(y^+ + \bar{y}^+)} S_{q\bar{q}}(\bar{y}^+) e^{ik^\mu u_\mu y^+ - ik^\mu \bar{u}_\mu \bar{y}^+} \tag{3.221}$$

with $2k^+ k^\mu u_\mu = (k_\perp - k^+ u_\perp)^2$. In the vacuum, i.e without the factor $S_{q\bar{q}}$, the $q\bar{q}$ and the $\bar{q}q$ terms combine to give the famous antenna radiation pattern discussed in Section 3.1:

$$k^+ \frac{\mathrm{d}^3 N^{\mathrm{vac}}}{\mathrm{d}k^+ \mathrm{d}^2 k_\perp} = \frac{\alpha_s C_F}{\pi^2} \left[\frac{1}{(k_\perp - k^+ u_\perp)^2} + \frac{1}{(k_\perp - k^+ \bar{u}_\perp)^2} - 2 \frac{(k_\perp - k^+ u_\perp)(k_\perp - k^+ \bar{u}_\perp)}{(k_\perp - k^+ u_\perp)^2 (k_\perp - k^+ \bar{u}_\perp)^2} \right] = \frac{\alpha_s C_F}{2\pi^2} \frac{p^\mu \bar{p}_\mu}{(p^\mu k_\mu)(\bar{p}^\mu k_\mu)} \tag{3.222}$$

If the medium has a size L and constant $\hat{q}$, the integral (3.221) is cut at $\bar{y}^+ = L$. The piece with $\bar{y}^+ \geq L$ gives the same contribution as (3.222) with an additional factor $S_{q\bar{q}}(L)$ [89, 90] corresponding to the survival probability of the dipole in a colour singlet state after a time L and a phase $\cos(k^\mu(u_\mu - \bar{u}_\mu)L)$. The piece with $\bar{y}^+ \leq L$ cannot be calculated analytically:

$$k^+\frac{\mathrm{d}^3N^{q\bar{q}+\bar{q}q}}{\mathrm{d}k^+\mathrm{d}^2k_\perp} = \frac{-2\alpha_s C_F}{4\pi^2k^{+2}}(k_\perp - k^+u_\perp)(k_\perp - k^+\bar{u}_\perp)\left[\frac{1}{(k^\mu u_\mu)(k^\mu\bar{u}_\mu)}\cos(k^\mu(u_\mu-\bar{u}_\mu)L)S_{q\bar{q}}(L)\right.$$
$$\left. + \left(\frac{1}{k^\mu u_\mu} - \frac{1}{k^\mu\bar{u}_\mu}\right)\int_0^L \mathrm{d}\bar{y}^+ \sin\Big(k^\mu(\bar{u}_\mu - u_\mu)\bar{y}^+\Big)\exp\Big(-\frac{1}{6}u^\mu\bar{u}_\mu\hat{q}\bar{y}^{+3}\Big)\right] \quad (3.223)$$

with $S_{q\bar{q}}(L) = \exp(-\frac{1}{6}u^\mu\bar{u}_\mu\hat{q}L^3) \simeq \exp(-(\theta_{q\bar{q}}/\theta_c)^2/6)$.

With this expression, the discussion is pretty much the same as in the onium case. When the opening angle of the dipole $\theta_{q\bar{q}}$ is small, i.e. $\theta_{q\bar{q}} \ll \theta_c$, the survival probability $S_{q\bar{q}}(L) \sim 1$ as well as the exponential inside the integral. Consequently, the two terms in (3.223) gives the standard vacuum interference spectrum so that the full spectrum is the vacuum one (3.222). Large angle soft emissions are suppressed (angular ordering) because of the interferences.

However, if $\theta_{q\bar{q}} \gg \theta_c$ or equivalently $L \gg t_{\mathrm{coh}}$, the factor $S_{q\bar{q}}(L)$ vanishes. One can safely take the limit $L \to \infty$ for the integral in the second term of (3.223). After the change of variable $k(\bar{u}-u)\bar{y}^+ \to t$, one gets:

$$k^+\frac{\mathrm{d}^3N^{q\bar{q}+\bar{q}q}}{\mathrm{d}k^+\mathrm{d}^2k_\perp} \simeq \frac{-2\alpha_s C_F}{4\pi^2k^{+2}}\frac{(k_\perp - k^+u_\perp)(k_\perp - k^+\bar{u}_\perp)}{(k^\mu u_\mu)(k^\mu\bar{u}_\mu)}\mathcal{I}_{q\bar{q}}(k^\mu) \quad (3.224)$$

and the integral $\mathcal{I}_{q\bar{q}}$ defined by:

$$\mathcal{I}_{q\bar{q}}(k^\mu) = \int_0^\infty \mathrm{d}t\ \sin(t)\exp\left(-\frac{1}{6}\frac{u^\mu\bar{u}_\mu}{(k^\mu(\bar{u}_\mu - u_\mu))^3}\hat{q}t^3\right) \quad (3.225)$$

With this form where the standard vacuum interference spectrum factorizes, it is clear that the $\mathcal{I}_{q\bar{q}}$ factor plays the same role as the factor $\exp(-Q_s^2X_\perp^2/4)$ for the decoherence of the onium in the shockwave limit. It induces a mismatch between the direct terms and the interference term which allows for large angle radiations outside the opening angle $\theta_{q\bar{q}}$. To see that, we write the full antenna radiation pattern in the limit $L \gg t_{\mathrm{coh}}$ as:

$$k^+\frac{\mathrm{d}^3N}{\mathrm{d}k^+\mathrm{d}^2k_\perp} \simeq \frac{\alpha_s C_F}{2\pi^2}\left(\frac{p^\mu\bar{p}_\mu}{(p^\mu k_\mu)(\bar{p}^\mu k_\mu)} + \big(1-\mathcal{I}_{q\bar{q}}(k^\mu)\big)\frac{k^\mu u_\mu + k^\mu\bar{u}_\mu - k^+u^\mu\bar{u}_\mu}{k^+(k^\mu u_\mu)(k^\mu\bar{u}_\mu)}\right) \quad (3.226)$$

Now, we want to show that the second term is precisely the large angle contribution due to the rapid decoherence of the $q\bar{q}$ pair while propagating through the medium. There is one difference with respect to the onium case: the factor $1-\mathcal{I}_{q\bar{q}}(k^\mu)$ is *dynamical* since it depends on the kinematic k^μ of the emission. To understand more precisely how, we estimate this factor neglecting the exponential inside the integral for $t \geq t_{\mathrm{coh}}$ and replacing it by one for $t \leq t_{\mathrm{coh}}$. One finds:

$$1 - \mathcal{I}_{q\bar{q}}(k^\mu) \simeq 1 - \int_0^{k\cdot(\bar{u}-u)t_{\mathrm{coh}}} \mathrm{d}t\ \sin(t) \quad (3.227)$$
$$= \cos\big(k\cdot(\bar{u}-u)t_{\mathrm{coh}}\big) \quad (3.228)$$

With this approximation, the antenna spectrum reads:

$$k^+\frac{\mathrm{d}^3N}{\mathrm{d}k^+\mathrm{d}^2k_\perp} \simeq \frac{\alpha_s C_F}{2\pi^2k^{+2}}\left[\frac{u^\mu\bar{u}_\mu}{(\tilde{k}^\mu u_\mu)(\tilde{k}^\mu\bar{u}_\mu)} + \cos\big(k\cdot(\bar{u}-u)t_{\mathrm{coh}}\big)\frac{\tilde{k}^\mu u_\mu + \tilde{k}^\mu\bar{u}_\mu - u^\mu\bar{u}_\mu}{(\tilde{k}^\mu u_\mu)(\tilde{k}^\mu\bar{u}_\mu)}\right] \quad (3.229)$$

with $\tilde{k} = k/k^+$. This spectrum can be decomposed symmetrically into two components, each component having a collinear singularity when k^μ is aligned with the quark or antiquark direction:

$$k^+\frac{\mathrm{d}^3N}{\mathrm{d}k^+\mathrm{d}^2k_\perp} = \left(k^+\frac{\mathrm{d}^3N^{k||q}}{\mathrm{d}k^+\mathrm{d}^2k_\perp} + k^+\frac{\mathrm{d}^3N^{k||\bar{q}}}{\mathrm{d}k^+\mathrm{d}^2k_\perp}\right) \tag{3.230}$$

with

$$k^+\frac{\mathrm{d}^3N^{k||q}}{\mathrm{d}k^+\mathrm{d}^2k_\perp} = \frac{\alpha_s C_F}{2\pi^2k^{+2}}\frac{1}{2}\left(\frac{u^\mu\bar{u}_\mu + \tilde{k}^\mu\bar{u}_\mu - \tilde{k}^\mu u_\mu}{(\tilde{k}^\mu u_\mu)(\tilde{k}^\mu\bar{u}_\mu)} + \cos\left(k^\mu(\bar{u}_\mu - u_\mu)t_{\mathrm{coh}}\right)\frac{\tilde{k}^\mu u_\mu + \tilde{k}^\mu\bar{u}_\mu - u^\mu\bar{u}_\mu}{(\tilde{k}^\mu u_\mu)(\tilde{k}^\mu\bar{u}_\mu)}\right) \tag{3.231}$$

and similarly for the antiquark term, with $u \leftrightarrow \bar{u}$ exchanged. Now, we average $\mathrm{d}^3N^{k||q}$ over the azimuthal angle ϕ around the quark direction. The following geometrical relations are useful:

$$2u^\mu\bar{u}_\mu = 1 - \cos(\theta_{q\bar{q}}) \tag{3.232}$$

$$2\tilde{k}^\mu u_\mu = 1 - \cos(\theta_q) \tag{3.233}$$

$$2\tilde{k}^\mu\bar{u}_\mu = 1 - \cos(\theta_{\bar{q}}) = (1 - \cos(\theta_{q\bar{q}})\cos(\theta_q)) - \sin(\theta_{q\bar{q}})\sin(\theta_q)\cos(\phi) \tag{3.234}$$

where $\theta_{q/\bar{q}}$ is the emission angle with respect to the quark/antiquark direction. After averaging over ϕ, the first piece gives the standard angular ordered spectrum, whereas the second is more complicated:

$$k^+\frac{\mathrm{d}^2N^{k||q}}{\mathrm{d}k^+\mathrm{d}\theta_q} = \frac{\alpha_s C_F}{\pi}\frac{\sin(\theta_q)}{1-\cos(\theta_q)}\Big(\Theta\big(\cos(\theta_q) - \cos(\theta_{q\bar{q}})\big) + \mathrm{J}_0(|x_2|)\cos(x_1) + \big(\cos(\theta_{q\bar{q}}) - \cos(\theta_q)\big)\int\frac{\mathrm{d}\phi}{2\pi}\frac{\cos(x_1 - x_2\cos(\phi))}{\lambda_1 - \lambda_2\cos(\phi)}\Big) \tag{3.235}$$

with $x_1 = \frac{1}{2}k^+t_{\mathrm{coh}}\cos(\theta_q)(1-\cos(\theta_{q\bar{q}}))$, $x_2 = \frac{1}{2}k^+t_{\mathrm{coh}}\sin(\theta_{q\bar{q}})\sin(\theta_q)$, $\lambda_1 = 1 - \cos(\theta_{q\bar{q}})\cos(\theta_q)$ and $\lambda_2 = \sin(\theta_{q\bar{q}})\sin(\theta_q)$. The remaining ϕ integral can be estimated neglecting the phase inside the numerator:

$$\int\frac{\mathrm{d}\phi}{2\pi}\frac{\cos(x_1 - x_2\cos(\phi))}{\lambda_1 - \lambda_2\cos(\phi)} \simeq \frac{\mathrm{J}_0(|x_2|)\cos(x_1)}{|\cos(\theta_q) - \cos(\theta_{q\bar{q}})|} \tag{3.236}$$

This approximation enables to put the antenna pattern in the following compact form:

$$k^+\frac{\mathrm{d}^2N^{k||q}}{\mathrm{d}k^+\mathrm{d}\theta_q} = \frac{\alpha_s C_F}{\pi}\frac{\sin(\theta_q)}{1-\cos(\theta_q)}\Big(\Theta\big(\cos(\theta_q) - \cos(\theta_{q\bar{q}})\big) + \mathrm{J}_0(|x_2|)\cos(x_1)\Theta\big(\cos(\theta_{q\bar{q}}) - \cos(\theta_q)\big)\Big) \tag{3.237}$$

With respect to (3.226), the latter formula is even more transparent because the geometry of the emission is explicit: the term proportional to $\Theta(\cos(\theta_{q\bar{q}}) - \cos(\theta_q))$ corresponds to the radiation outside the cone, which would be forbidden in the vacuum. The amount of radiation with $\theta_q \geq \theta_{q\bar{q}}$ is controlled by the factor $\mathrm{J}_0(|x_2|)\cos(x_1)$. In analogy with the factor $1 - \exp(-k_\perp^2/Q_s^2)$ for the onium toy model, we call it the decoherence factor $\Delta_{>\theta_{q\bar{q}}}$. In the small angle approximation:

$$\Delta_{>\theta_{q\bar{q}}} \simeq \mathrm{J}_0\left(\frac{1}{2}k^+t_{\mathrm{coh}}\theta_q\theta_{q\bar{q}}\right)\cos\left(\frac{1}{4}k^+t_{\mathrm{coh}}\theta_{q\bar{q}}^2\right) \tag{3.238}$$

$$= \mathrm{J}_0\left(\frac{t_{\mathrm{coh}}}{t_f}\frac{\theta_{q\bar{q}}}{\theta_q}\right)\cos\left(\frac{1}{2}\frac{t_{\mathrm{coh}}}{t_{i,\mathrm{vac}}}\right) \tag{3.239}$$

Out-of-cone radiations scale with $t_{\rm coh}\theta_{q\bar{q}}/(t_f\theta_q)$ in the short formation time limit, for $\theta_{q\bar{q}} \gg \theta_c$. Note the somehow unexpected $\theta_{q\bar{q}}/\theta_q$ geometric factor. In Chapter 5-Section 5.2 we will generalize this calculation to multiple emissions. We will show that the kinematic constraints (3.219) — and also the less strong condition $k_\perp \geq (2\hat{q}k^+)^{1/4}$ — actually impose that the factor $\Delta_{>\theta_{q\bar{q}}}$ vanishes, so that in-medium VLEs with short formation times remain angular ordered!

Vacuum-like emissions in the long formation time limit $t_f \gg L$. This is the limit considered in [89, 90]. For these emissions as well, one can approximate the effective propagators $\mathcal{K}_{qg}$ and $\mathcal{K}_{\bar{q}g}$ by the free vacuum propagator $\mathcal{G}_0^\dagger$ and remove the broadening factor S_{gg} because these emissions come from a time integration domain where there is no medium any more. More precisely, the out/out interference term where $y^+ \geq L$ and $\bar{y}^+ \geq L$ dominates in the infrared limit, and is precisely given by the first term of formula (3.223). Taking the limit $k^\mu(u^\mu - \bar{u}^\mu)L \to 0$ in this out/out term, corresponding to the regime $k^+\theta_q^2 L$, $k^+\theta_{\bar{q}}^2 L \ll 1$ i.e. $t_f \gg L$, one gets the full spectrum in this limit:

$$k^+\frac{{\rm d}^3N}{{\rm d}k^+{\rm d}^2k_\perp} \simeq \frac{\alpha_s C_F}{2\pi^2}\left(\frac{p^\mu\bar{p}_\mu}{(p^\mu k_\mu)(\bar{p}^\mu k_\mu)} + \big(1-S_{q\bar{q}}(L)\big)\frac{k^\mu u_\mu + k^\mu\bar{u}_\mu - k^+u^\mu\bar{u}_\mu}{k^+(k^\mu u_\mu)(k^\mu\bar{u}_\mu)}\right) \tag{3.240}$$

leading to the following spectrum, once averaged over the azimuthal angle around the quark direction for instance:

$$k^+\frac{{\rm d}^2N^{k||q}}{{\rm d}k^+{\rm d}\theta_q} = \frac{\alpha_s C_F}{\pi}\frac{\sin(\theta_q)}{1-\cos(\theta_q)}\Big(\Theta\big(\cos(\theta_q)-\cos(\theta_{q\bar{q}})\big) + \big(1-S_{q\bar{q}}(L)\big)\Theta\big(\cos(\theta_{q\bar{q}})-\cos(\theta_q)\big)\Big) \tag{3.241}$$

This time, the decoherence factor $\Delta_{>\theta_{q\bar{q}}} = 1 - S_{q\bar{q}}(L)$ is not *dynamical* (as in the onium toy model), in the sense that it does not depend on the kinematic of the emission in the soft limit. For large antenna $\theta_{q\bar{q}} \gg \theta_c$, $1 - S_{q\bar{q}}(L) \simeq 1$ whereas for small dipole $1 - S_{q\bar{q}}(L) \simeq 0$. The physical interpretation is the following: after propagation through the medium over a distance L, the antenna does not remain in a colour singlet state with a probability $1 - S_{q\bar{q}}(L)$. Thus, a gluon with formation time $t_f \gg L$ can be emitted at any angle, with a probability $1 - S_{q\bar{q}}(L)$ ("anti angular-ordering" effect [89, 90]). To conclude, we emphasize that these emissions *are* included in the calculation of Section 3.4.2 since the subtraction of the limit $\hat{q} \to 0$ removes only the angular-ordered vacuum-like pattern. The resummation of such emissions is considered in Chapter 5-Section 5.2.

Chapter 4

Jets in vacuum and jets from medium-induced emissions

With respect to the previous chapter, where we have computed cross-sections for *one* emission, this chapter deals with multiple emission cross-sections. At first sight, one may wonder why such cross sections are important at all, since multi-particle production comes with sub-leading powers of α_s, which is supposed to be small. This reasoning is true to some extent. In certain regions of the phase space for emissions, that we shall specify in this chapter, the smallness of α_s may be compensated by a large dimensionless parameter so that the standard perturbation theory breaks down. Consequently, being able to estimate such cross-sections is crucial to improve the precision of our calculations.

How is this related to jets? The concept of jets has originally been developed to give a precise meaning to non fully inclusive cross-sections in perturbative chromodynamics, without relying on the concept of *hadrons* which are not under control in this regime. Once a well-suited *jet definition* is provided, a theorist can calculate in pQCD any jet cross-section at a given order in α_s. Jets are object with a rich "internal structure", which can be defined either in terms of the hadronic content of the jets, or even better, in terms of subjets. There is now an increasing interest in such observables related to the internal structure of jets. As we shall see, once one knows how to calculate multiple emission cross-sections, it is straightforward to calculate jet substructure observables.

The first section of this chapter is a textbook recap on jets in the "vacuum", that is in electron-positron annihilation and proton-proton collisions. The second section makes the link between multi-particle cross-sections from an off-shell parton in the soft and collinear region of the phase space and jet substructure calculations in the vacuum. The third section is dedicated to the multiple branching regime for medium-induced radiations from an incoming on-shell parton. The emphasis is put on the mathematical similarities between these two distinct regimes.

4.1 Jets in e^+e^- annihilation and pp collisions: generalities

Perturbative quantum chromodynamics has quarks and gluons as elementary degrees of freedom. However, due to confinement, these degrees of freedom are never directly measured in experiments as they do not constitute the asymptotic states of the theory. Instead of dealing with quarks and gluons to calculate physical observables such as cross-sections, a way to circumvent this problem is to deal with jets.

4.1.1 IRC safety and jet definitions

A standard calculation and experimental test of pQCD is the *inclusive* e^+e^- annihilation into hadrons cross-section and its ratio with respect to $\mu^+\mu^-$ production. For this fully inclusive observable, there is a well defined and reliable α_s expansion of the cross-section written in terms of Feynman diagrams with *partonic* final states, even if the experimental final states are hadrons. This is a consequence of the Kinoshita-Lee-Nauenberg theorem [126, 127] which guarantees the cancellation of infrared divergences for inclusive observables over QCD degenerate states and thus, a reduced sensitivity to hadronisation corrections.

If one wants to go one step further and calculate more exclusive processes in pQCD, it is necessary to build observables which are protected by the Kinoshita-Lee-Nauenberg theorem. Such observables are generically called infrared and collinear (IRC) safe. The precise definition is the following: let us call $V_n(k_1, .., k_n)$ the functional constraints on the n-particle phase space (k_i is the 4-momentum of a particle) that define the value of this observable at a given order (related to n) in α_s. For the cross-section σ_V associated with this observable to be well defined, i.e. without infrared singularity, to all orders in perturbation theory, V must satisfy:

1. $\forall (i,j),\ V_{n+1}(k_1, .., k_i, .., k_j, .., k_{n+1}) \longrightarrow V_n(k_1, .., k_i + k_j, .., k_{n+1})$ as k_i and k_j become collinear, in the sense of (3.1).

2. $\forall i,\ V_{n+1}(k_1, .., k_i, .., k_{n+1}) \longrightarrow V_n(k_1, .., k_{i-1}, k_{i+1}, .., k_n)$ as $k_i^\mu \to 0$.

Sterman-Weinberg jets. Historically, the first IRC safe exclusive observable calculated in pQCD is the Sterman-Weinberg dijet cross-section in e^+e^- annihilation [128]. This dijet cross-section is defined as the cross-section for events such that all but a fraction $\xi\sqrt{s}$, $\xi \ll 1$ of the initial energy $\sqrt{s}$ is deposited within two cones of opening angles R. This cross-section is fully inclusive with respect to soft and collinear gluon emissions. The famous result for the differential cross-section per solid angle $\mathrm{d}^2\Omega = \sin(\theta)\mathrm{d}\phi\mathrm{d}\theta$ in the laboratory frame, obtained by Sterman and Weinberg, is

$$\frac{\mathrm{d}\sigma_{2-\mathrm{jet}}}{\mathrm{d}^2\Omega} = \frac{\mathrm{d}\sigma_0}{\mathrm{d}^2\Omega}\left(1 - \frac{\alpha_s C_F}{\pi}\left(4\log(R)\log(\xi) + 3\log(R) + \frac{\pi^2}{3} - \frac{5}{2} + \mathcal{O}(\xi, R)\right) + \mathcal{O}(\alpha_s^2)\right) \quad (4.1)$$

to first order in α_s, with α_s evaluated at $\sqrt{s}$. ($\mathrm{d}\sigma_0$ is the Born level cross-section.) Higher order corrections $\mathcal{O}(\alpha_s^2)$ have been calculated [129]. This observable is also the first *jet definition*. A jet definition is a systematic way of organizing the final state so that any exclusive *jet* cross-section is always IRC safe.

Modern jet algorithms. Nowadays, more practical jet definitions are used in the high energy community (see [130] for a modern review on jets). They have the advantage of being easily implemented in experiments and more convenient for higher order theoretical predictions. The most used are jet definitions from a sequential recombination algorithm, such as the k_t, Cambridge/Aachen and anti-k_t algorithms. The basic idea of these recombination algorithms is to cluster final state particles together iteratively, according to a given rule, until no particle remains. The final clusters are called jets.

A sequential recombination algorithm makes use of a distance measure between final state particles and a recombination rule when merging particle together. The distance measures are a little bit different in e^+e^- collisions and in pp or AA collisions, essentially because one does not know a priori the total energy of the collision of the two partons inside the protons. We

focus here on the more relevant pp or AA case, and we provide the definition of the "generalized k_t algorithm", based on the distance d_{ij} between two particles and a beam distance d_{iB}:

$$d_{ij} = \min(p_{T,i}^{2p}, p_{T,j}^{2p})\Delta R_{ij}^2\,, \qquad \Delta R_{ij}^2 = \Delta\eta_{ij}^2 + \Delta\phi_{ij}^2 \tag{4.2}$$

$$d_{iB} = p_{T,i}^{2p} R \tag{4.3}$$

where ΔR_{ij} is the distance between i and j in the rapidity-azimuth plane and (p, R) are free parameters. Starting from a list of final state particles — called *pseudo-jets* in this context — the algorithm then goes as follows,

1. Iteratively find the smallest distance among all the d_{ij} and d_{iB}:
   - If the smallest distance is of d_{ij} kind then pseudo-jets i and j are removed from the list and recombined using the recombination scheme into a new pseudo-jet k, which becomes part of the final state pseudo-jets.
   - If the smallest distance is a beam distance , pseudo-jet i is called a jet and removed from the list.
2. Go back to the previous step until all the pseudo-jets in the list have been exhausted.

The standard recombination scheme ("E-scheme") consists in simply adding the 4-momenta of particles i and j to get the 4-momentum of k.

For $p = 0$, this algorithm is called Cambridge/Aachen [131, 132]. The declustering sequence is ordered in angles. For $p = 1$, it is called the k_t algorithm [133] and the declustering sequence is ordered in k_t. For $p = -1$, this algorithm is known as the anti-k_t algorithm [134]. One can check that any n-jet cross-section in the sense of this jet definition is an IRC safe observable (provided that a lower cut-off is imposed on the transverse momenta of jets).

4.1.2 Resummation of large logarithms and matching

Even for IRC safe cross-sections with a well defined expansion in powers of α_s, each order of the perturbation may go with a large dimensionless parameter of the form $\log(Q/Q_0)$ where Q is a hard scale and Q_0 a soft scale (often introduced to make the observable IRC safe). Such large logarithms, remnants of the infrared singularity of the theory, may spoil the convergence of the perturbation series in the region of the phase space where $Q \gg Q_0$. Formula (4.1) exhibits this kind of behaviour: for very small jet radii R, $|\alpha_s \log(R)| \gg 1$ so that a fixed order calculation is not enough to get an accurate answer.

Under these circumstances, an all-order *resummation* is required to take into account all the terms in the full perturbation series which are enhanced by large logarithms (for jet cross-sections with small radii, this program has been carried out in [135]). In the next section, we will obtain resummed results for several jet substructure observables.

It is enlightening to understand more precisely the general structure of a resummed result. Let us first define the cumulative cross-section Σ_V for the observable defined by the $V_{n\in\mathbb{N}}$ constraints on the n-body phase space:

$$\Sigma_V(v) = \int_0^v \mathrm{d}v' \frac{1}{\sigma_{V,0}} \frac{\mathrm{d}\sigma_V}{\mathrm{d}v'} \tag{4.4}$$

where v is the value of the observable (without dimension for this discussion) and $\sigma_{V,0}$ is the Born level total cross-section for V. For a certain subclass of IRC safe observables (see [136, 137]

for more details), and in the region of the phase space where $L \equiv |\log(v)| \gg 1$, the resummation *exponentiates* with the following form:

$$\Sigma_V(x) \simeq \exp\Big(Lg_1(\alpha_s L) + g_2(\alpha_s L) + \alpha_s g_3(\alpha_s L) + \mathcal{O}\big(\alpha_s^{n+2} L^n\big)\Big) \tag{4.5}$$

where α_s is evaluated at the hard scale Q of the problem. The functions g_i are analytic functions that resum to all orders powers of $\alpha_s L \sim 1$. From this general structure, one defines the logarithmic accuracy as follows: at leading logarithmic (LL) accuracy, one keeps only the Lg_1 term, at next-to-leading logarithmic (NLL) accuracy, one keeps the $Lg_1 + g_2$ terms and so on. In this thesis, we define the double logarithmic accuracy as the leading logarithmic approximation where the strong coupling is fixed. This corresponds to the first order expansion of $g_1(x) \simeq g_1'(0)x$, so that:

$$\Sigma_V(x) = \sum_{n=0}^{\infty} \frac{(g_1'(0))^n}{n!} (\alpha_s L^2)^n \tag{4.6}$$

where the double-logarithmic all order resummation is explicit. The double logarithmic approximation is physically insightful because the resulting formulas are often very simple.

Matching with fixed order calculations. We emphasize that such a resummation is required only in a region of the phase space where logarithms are large. To obtain an accurate answer all over the phase space, resummed and fixed order results must be combined according to a matching scheme. Such a matching scheme must avoid double counting between terms included in the all order result and terms in the fixed order.

4.2 Jet substructure calculation

The previous discussion was rather abstract in order to keep things as general as possible. In this section, we would like first to make concrete this resummation for the special case of jet substructure observables. The "coherent branching algorithm" defined in the first subsection provides an intuitive way to resum multiple emissions thanks to an effective classical branching process. The second goal of this section is to give some vacuum benchmark results for the second part of this thesis where we analyse these observables in heavy-ion collisions.

4.2.1 The coherent branching algorithm

The coherent branching algorithm enables to calculate multi-partons QCD amplitude *squared* in the phase space where such emissions are enhanced by large collinear/soft logarithms, taking into account the coherence property of soft gluon emissions [138, 139, 140, 141]. Its precision depends on the process and the observable under consideration. For example, in e^+e^- annihilation, it is accurate at NLL in the relevant phase space region where the thrust or the jet mass distributions are enhanced by large logs [142]. Yet, it is generally accurate at LL, and some NLL corrections are included as well, but not all of them: single logarithms and non-global logarithms from multiple soft emissions at commensurate angles are missing for instance.

The algorithm relies on the following results, valid at least to LL accuracy:

1. The probability distribution for multi-particle production from a highly virtual parton in the soft and collinear regime can be generated by a classical Markovian branching process.

2. The evolution variable for this process is the angle of emission with respect to the parent particle, in order to account for the strict angular ordering of soft gluon emissions.

3. The rate of the branching process is given by the leading order $\mathcal{O}(\alpha_s)$ cross-section (differential in the transverse angle) for producing *one* other parton from a virtual parton, in the collinear regime. This cross-section is averaged over the azimuthal angle of the produced particle:
$$\mathrm{d}^2\mathcal{P}_a^{bc}(z,\theta) = \frac{\alpha_s(k_\perp)}{\pi}\Phi_a^{bc}(z)\mathrm{d}z\frac{\mathrm{d}\theta}{\theta} \tag{4.7}$$
with $\Phi_a^{bc}(z)$ the DGLAP splitting functions given in Appendix C, z the splitting fraction of parton b, and $k_\perp = z(1-z)p_T\theta$.[1]

To be useful in realistic applications, this algorithm has to be combined with fixed order calculations for producing the initial partons with transverse momentum p_T. Hence it is assumed implicitly the factorization between the exclusive hard cross-section and the decay of the produced partons into soft and/or collinear emissions. Note that because of the azimuthal average, informations about the direction of the produced particles in the transverse plane with respect to the initial parton 3-momentum are lost.

Let us define the generating functional for a jet initiated by a parton $i = q, \bar{q}, g$, with transverse momentum p_T and time-like virtuality squared $t^2 = z_0(1-z_0)p_T^2\theta^2$. z_0 and θ are the energy fraction and opening angle of the first splitting. Yet, the generating functional depends only upon θ,
$$Z_i(p_T,\theta \mid u(k)) = \sum_{n=0}^{\infty}\int \mathrm{d}^3k_1...\mathrm{d}^3k_n\, u(k_1)...u(k_n)P_i^{(n)}(k_1,...,k_n) \tag{4.8}$$
where $P_i^{(n)}(k_1,...,k_n)$ is the probability density for exclusive production of particles with 3-momenta k_1,...,k_n and $u(k)$ is an auxiliary profile function. Probability conservation ensures that $Z_i(p_T,\theta,\mid u(k)=1) = 1$. The complete knowledge of the generating functional enables to calculate any multi-parton inclusive cross-section. For example, the probability distribution $D_i(k)$ for measuring at least one parton with 3-momentum k in the final state is given by:
$$D_i(k) = \frac{\delta Z_i(p_T,\theta \mid u(k))}{\delta u(k)}\Big|_{u=1} \tag{4.9}$$

The Markovian property of the branching process leads to the following master equation in backward form, known as Modified Leading Logarithm Approximation (MLLA) equation [102, 143]:

$$\frac{\partial Z_i(p_T,\theta \mid u)}{\partial\log(\theta)} = \frac{1}{2!}\sum_{(a,b)}\int_0^1 \mathrm{d}z\,\Phi_i^{ab}(z)\frac{\alpha_s(k_\perp^2)}{\pi}\Big(Z_a(zp_T,\theta \mid u)Z_b((1-z)p_T,\theta \mid u) - Z_i(p_T,\theta \mid u)\Big) \tag{4.10}$$

where the sum runs over all *distinct* pairs of partons (a,b). This master equation has a simple probabilistic interpretation [144]. The first term is a gain term associated with the splitting of a i-jet into two subjets with splitting fraction z and $1-z$. The second term is a loss term associated with all possible splittings of the initial jet i. The factor $1/2!$ is a symmetry factor

[1] We assume a purely transverse initial parton and work in the small angle approximation.

to avoid a double counting of decays. The logarithmic derivative with respect to θ enforces the angular ordering. In order to regulate the collinear divergence as θ goes to 0, and to avoid the Landau pole in the running coupling, one puts by hand a transverse momentum cut-off $k_T > k_{\perp,\min}$ in this equation. Then, the initial condition for this differential equation is

$$Z_i(p_T, \theta \to 0 \mid u) = u(p_T) \tag{4.11}$$

in agreement with the fact that on-shell partons with $t = 0$ cannot radiate.

4.2.2 Jet fragmentation function

The jet fragmentation function $\mathcal{D}(x)$ is defined by the number $\mathrm{d}N$ of jets having one constituent with transverse momentum fraction $x = p_T/p_{T,\text{jet}}$ between x and $x + \mathrm{d}x$:

$$\mathcal{D}(x) \equiv \frac{1}{N_{\text{jets}}} \frac{\mathrm{d}N}{\mathrm{d}x} \tag{4.12}$$

normalized by the total number N_{jets} of selected jets. This observable is not IRC safe but it remains nonetheless a relatively simple observable. The price to pay is a strong sensitivity of any calculation in pQCD with respect to the infrared cut-offs involved in the calculation. Also, even if $\mathcal{D}(x)$ is itself IRC unsafe, its evolution with the hard scale (i.e. the p_T of the jet) can be obtained from pQCD.

In this section, we investigate the predictions of the coherent branching algorithm for this observable. We will ignore subtleties related to the fixed order calculation and matching with the resummed result. Hence, we focus on the following problem: starting with an off-shell parton with transverse momentum p_T decaying inside a cone of opening angle θ, what is the inclusive probability $D_i(x|p_T, \theta)$ of measuring a parton with transverse momentum fraction x in the final state?

This quantity is easily obtained from the generating functional:

$$D_i(x|p_T, \theta) \equiv \int \mathrm{d}^3k\, \delta(k^0 - xp_T) \frac{\delta Z_i(p_T, \theta|u(k))}{\delta u(k)}\Big|_{u(k)=1} \tag{4.13}$$

From (4.10), it is straightforward to write the corresponding evolution equation for $D_i(x, Q = p_T\theta)$ (the sum over pairs (a, b) is implicit):

$$\frac{\partial D_i(x,Q)}{\partial \log(Q)} = \int_0^1 \mathrm{d}z\, \frac{\alpha_s(k_\perp^2)}{2\pi} \Phi_i^{ab}(z) \left[\frac{1}{z} D_a\Big(\frac{x}{z}, zQ\Big) + \frac{1}{1-z} D_b\Big(\frac{x}{1-z}, (1-z)Q\Big) - D_i(x,Q)\right] \tag{4.14}$$

with initial condition $D_i(x, Q = 0) = \delta(1 - x)$ — recall that the condition $k_\perp > k_{\perp,\min}$ is enforced. Once the solution of this equation is found, it should be evaluated for $Q \simeq p_T R$ where R is the opening angle of the jet.

4.2.2.1 Solution for $x \sim 1$ with NLL corrections

In this subsection, we look for the asymptotic form of $D_i(x, Q = p_T R)$ when x is close to 1. In this regime, it is more convenient to consider the *cumulative* fragmentation distribution, defined as

$$\Sigma_i(x, p_T R) \equiv \int_x^1 \mathrm{d}x' D_i(x', p_T R) \tag{4.15}$$

When $x \sim 1$, the perturbative expansion of the cumulative fragmentation distribution receives contributions enhanced by two types of logarithms: the collinear logarithm $L_0 \equiv \log(p_{T0}R/k_{\perp,\min})$ generated by integrating over emission angles within the range $k_{\perp,\min}/p_{T0} < \theta < R$ and the soft logarithm $L \equiv \log\frac{1}{1-x}$ generated by integrating over soft gluon emissions with energy fractions z within the range $1-x < z < 1$. One has $L_0 \geq L$, since all emissions must obey $z\theta p_{T0} > k_{\perp,\min}$ for any $z \geq 1-x$ and any $\theta \leq R$. Taking the value of the running coupling at the largest scale as the small parameter, $\alpha_0 \equiv \alpha_s(p_T R) \ll 1$, the perturbative series can be organised as follows:

$$\log(\Sigma_i(x \mid p_T)) = Lg_{1,i}(\alpha_0 L, \alpha_0 L_0) + g_{2,i}(\alpha_0 L, \alpha_0 L_0) + \mathcal{O}(\alpha_0^{n+1}\log^n) \tag{4.16}$$

where $Lg_{1,i}$ and $g_{2,i}$ resum respectively all the leading-log (LL) terms $\alpha_0^n \log^{n+1}$ and the next-to-leading-log (NLL) terms $\alpha_0^n \log^n$ with $n \geq 1$, where log means either L, or L_0.

Now, let us sketch the strategy to find the functions g_1 and g_2. To the accuracy of interest, one can neglect the quark/gluon mixing terms. The MLLA equation for the quark fragmentation function reduces to

$$Q\frac{\partial D_i(x,Q)}{\partial Q} = \int_0^1 \mathrm{d}z\, \frac{\alpha_s(k_\perp)}{\pi}\Phi_i^{ig}(z)\Theta(k_\perp - k_{\perp,\min})\left[\frac{1}{z}D_i\Big(\frac{x}{z}, zQ\Big) - D_i(x,Q)\right] \tag{4.17}$$

The standard way to deal with Eq. (4.17) is to go to Mellin space $D_i(x,Q) \to \tilde{D}_q(j,Q)$ where the integro-differential equation is linear-differential. From the properties of the Mellin transform, x close to 1 corresponds to $j \to \infty$. More precisely, $\log(j) \sim -\log(1-x)$, so we keep all terms of the form $\alpha_0^n \log(j)^n \sim 1$ in the exact solution. The details of the calculation are given in Appendix D.

The results for the resumming functions g_1 and g_2 are

$$g_{1,i}(u,v) = \frac{C_i}{\pi\beta_0}\left[1 - \log\Big(\frac{1-2\beta_0 u}{1-2\beta_0 v}\Big) + \frac{\log(1-2\beta_0 u)}{2\beta_0 u}\right] \tag{4.18}$$

$$g_{2,i}(u,v) = \gamma_E\frac{\partial u g_{1,i}}{\partial u} - \log\left[\Gamma\Big(1 - \frac{\partial u g_{1,i}}{\partial u}\Big)\right] + \frac{C_i B_i}{\pi\beta_0}\log(1-2\beta_0 v) \tag{4.19}$$

where Γ is the Euler function, $\beta_0 = (11C_A - 2n_f)/(12\pi)$, $B_q = -3/4$ and $B_g = -11/12 + n_f T_R/(3N_c)$, with n_f the number of active quark flavours.

The LL piece is rather easy to understand: this is the would-be standard double-logarithmic (DL) approximation in which successive emissions are strongly ordered both in energy fraction z and in emission angle θ, however amended by the running of the coupling ($\alpha_s \to \alpha_s(k_\perp)$). To this LL accuracy, one can assume that a single emission — the first one in the DL series, which is soft relative to the leading parton, but much harder than all the other emissions — dominates the jet fragmentation function near $x = 1$. Indeed, the even softer emissions do not count for the energy balance of the leading parton, hence they are not probed by $D_i(x \mid p_T R)$. Accordingly, the probability (10.4) of finding the leading parton with an energy fraction $x' \geq x$ and x close to 1 is equal to the probability of having no emissions with an energy fraction larger than $1-x$, which is exactly the Sudakov factor at this accuracy:

$$\Sigma_i(x, p_T R) = \exp\left(-\frac{2C_i}{\pi}\int_{1-x}^1 \frac{\mathrm{d}z}{z}\int_0^R \frac{\mathrm{d}\theta}{\theta}\alpha_s(k_\perp)\Theta(k_\perp - k_{\perp,\min})\right) \tag{4.20}$$

with $k_\perp \simeq z\theta p_T$. Formula (4.20) gives precisely the function g_1 given in (4.18).

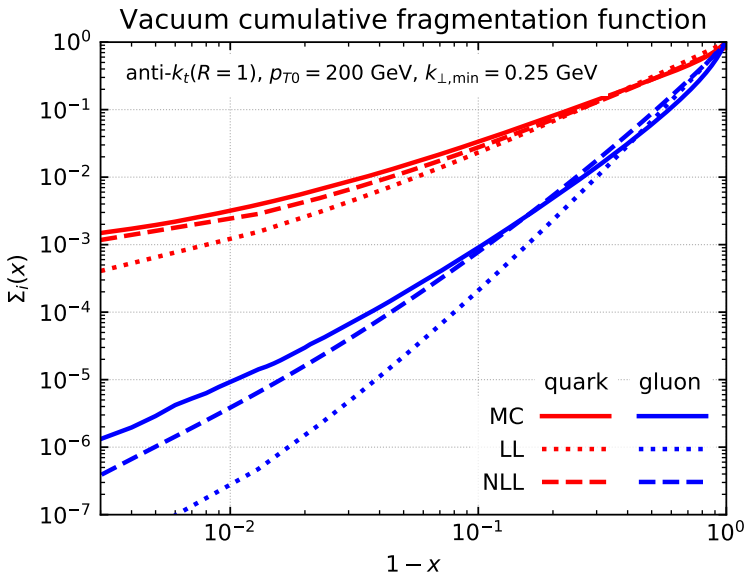

Figure 4.1: The cumulative fragmentation function $\Sigma_i(x|p_{T0})$ for quark ($i = q$) and gluon ($i = g$) initiated monochromatic jets in the vacuum. The MC calculations from `JetMed` (see Chapter 6) are shown with solid lines, and the two analytic approximations, LL and NLL, by dotted and dashed lines, respectively. Actually, the gluon NLL curve includes corrections due to quark/gluon mixing which are formally beyond NLL accuracy, as explained in Appendix D.

4.2.2.2 Solution at small x at DL

We now turn to the solution of (4.14) at small x to DL accuracy. This solution will be particularly useful when we will discuss the medium modifications of the jet fragmentation pattern. At DLA, one only resums logarithms of the form $\alpha_0 \log^2$ where this time, log means either $\log(1/x)$ or $\log(p_T R/k_{\perp,\min})$.

For later convenience, let us introduce the following function $T_i(\omega, \theta_0 \mid p_T, R)$:

$$T_i(\omega, \theta_0 \mid p_T, R) \equiv -\omega\theta_0 \frac{\mathrm{d}\bar{D}_{i,\theta_0}(\omega \mid p_T, R)}{\mathrm{d}\theta_0} \tag{4.21}$$

where $\bar{D}_{i,\theta_0}(\omega \mid p_T, R) \equiv D_{i,\theta_0}(\omega/p_T, p_T R)$ and D_{i,θ_0} is the solution of (4.14) with initial condition $D_i(x, p_T\theta_0) = \delta(1-x)$. The function T_i has a simple probabilistic interpretation: it is the number density of emissions with energy ω and angle θ_0 with respect to the *parent* parton in the branching process. Such a branching process is pictured on Fig. 4.2-left for a quark initiated jet. At DLA, energies and angles with respect to the emitter are strongly decreasing. It is also convenient to represent a given realization of the branching process on the (ω, θ) phase space for emissions, shown Fig. 4.2-right. In the vacuum, this phase space is only limited by the constraint $k_\perp \geq k_{\perp,\min}$.

To simplify the discussion, we focus on gluon initiated jets. The corresponding calculation for quark jets is similar. The integrand $I(z)$ in the right-hand side of equation (4.14) has the property $I(z) = I(1-z)$ so we can use the relation

$$\int_0^1 I(z)\mathrm{d}z = 2\int_0^1 (1-z)I(z)\mathrm{d}z$$

to put the singular behaviour of the splitting function Φ_g^{gg} at $z = 0$ only. At DLA, one neglects the energy recoil of the leading parton by setting $(1-z)p_T \simeq p_T$: the real term with argument

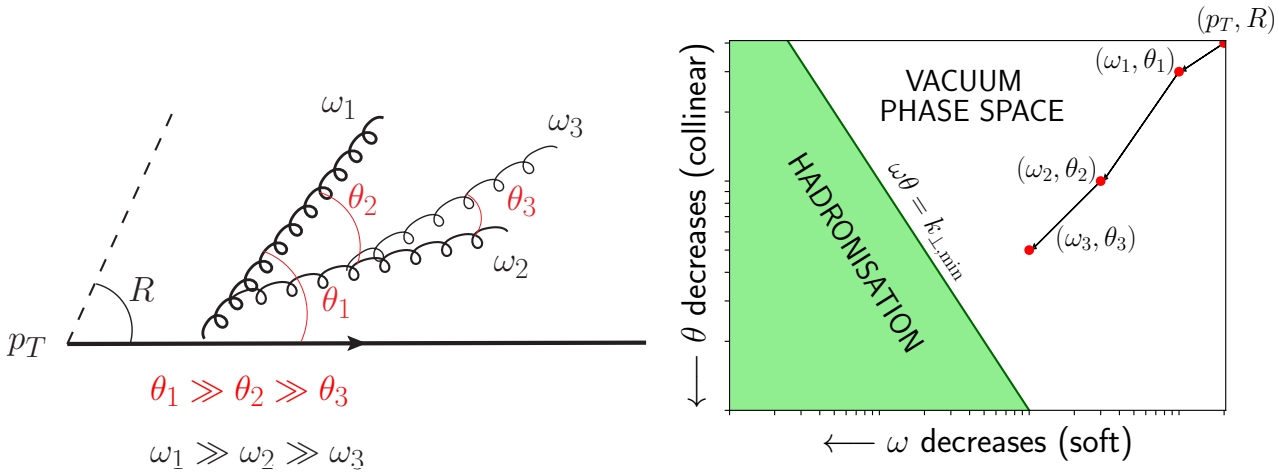

Figure 4.2: (Left) A given realization of the branching process that matters at DLA for the intrajet multiplicity. The parton sourcing the jet is a quark. (Right) The logarithmic (ω, θ) phase space for intrajet gluon emissions in the vacuum. Each emission in the cascade shown on the left is represented by a red circle with coordinates (ω_i, θ_i). The green line is the lower cut-off in the evolution, given by $k_\perp \simeq \omega\theta = k_{\perp,\min}$.

$(1-z)p_T\theta$ in (4.14) associated with the fragmentation of the hard-branch cancels against the virtual term. We approximate also $k_\perp \simeq zQ$ so that the evolution equation becomes simply:

$$\frac{\partial \bar{D}_{g,\theta_0}(\omega \mid p_T, \theta)}{\partial \log(\theta)} = \int_{\omega/p_T}^{1} \mathrm{d}z \, \frac{\alpha_s(zp_T\theta)}{\pi} \Phi_g^{gg}(z)(1-z) \bar{D}_{g,\theta_0}(\omega \mid zp_T, \theta) \tag{4.22}$$

The lower bound comes from the fact that $\bar{D}_g(\omega \mid p_T, \theta)$ obviously vanishes when $\omega > p_T$. Equation (4.22) is convenient to include corrections beyond DLA (see Chapter 5-Section 5.3.1.2). At DLA, it can be further simplified using $\alpha_s(k_\perp) = \alpha_0$ and $\Phi_g^{gg}(z)(1-z) \simeq 2C_A/z$. By definition, T_i satisfies the same evolution equation, with a different initial condition though: $T_i(\omega, \theta_0 \mid p_T, \theta_0) = 2\alpha_0 C_A/\pi \equiv 2\bar{\alpha}_s$. Integrating over θ between θ_0 and R, this equation can be written:

$$T_g(\omega, \theta_0 \mid p_T, R) = 2\bar{\alpha}_s + 2\bar{\alpha}_s \int_{\theta_0}^{R} \frac{\mathrm{d}\theta_1}{\theta_1} \int_{\omega/p_T}^{1} \frac{\mathrm{d}z_1}{z_1} T_g(\omega, \theta \mid z_1 p_T, \theta_1) \tag{4.23}$$

The series expansion in power of $\bar{\alpha}_s$ of the solution to (4.23) can be obtained iteratively using (4.23). One then recognizes the series expansion of the following function:

$$T_g(\omega, \theta_0 \mid p_T, R) = 2\bar{\alpha}_s \mathrm{I}_0\left(2\sqrt{2\bar{\alpha}_s \log(p_T/\omega)\log(R/\theta_0)}\right) \tag{4.24}$$

with I_n the modified Bessel function of rank n. Equation (4.24) is the building block for the calculation of the gluon distribution with a medium at DLA.

From (4.24), one can easily obtain the solution of (4.14) with the condition $k_\perp = xp_T\theta_0 > k_{\perp,\min}$ by inverting equation (4.21), [102, 145, 146]:

$$xD_g(x, p_T R) = \int_{k_{\perp,\min}/(xp_T)}^{R} \frac{\mathrm{d}\theta_0}{\theta_0} T_g(xp_T, \theta_0 \mid p_T, R) \tag{4.25}$$

$$= \sqrt{\bar{\alpha}_s} \sqrt{\frac{2\bar{\alpha}_s \log\frac{xp_T R}{k_{\perp,\min}} \log\frac{1}{x}}{\bar{\alpha}_s \log^2\frac{1}{x}}} \, \mathrm{I}_1\left(2\sqrt{2\bar{\alpha}_s \log\frac{1}{x} \log\frac{xp_T R}{k_{\perp,\min}}}\right) \tag{4.26}$$

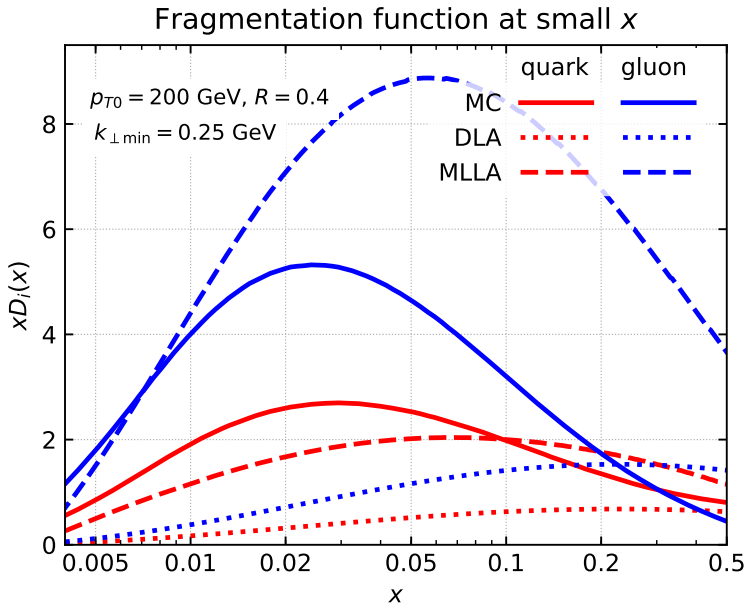

Figure 4.3: Fragmentation function at small x. The curves referred as "DLA" correspond to the double-logarithmic result (4.25) whereas the curves referred as "MLLA" include running coupling and hard-collinear contributions. The MLLA curve are obtained from a numerical resolution of the partial differential equation (5.94) equivalent to the MLLA evolution equation following the method developed in Section 5.3.1.2. The solid curves are `JetMed` calculations for comparison (see Chapter 6).

We have written the final result in a way that makes the double-logarithmic resummation clear. The most striking feature of $D_g(x, p_T R)$ is the maximum at $x_{\text{hump}} = \sqrt{k_{\perp,\min}/(p_T R)}$ and the collapse at small energies. One would naively expect that the multiplicity rises at small x due to the $1/x$ behaviour of the Bremsstrahlung spectrum but colour coherence forbids the multiplication of soft gluon emissions.

It is possible to include some NLL corrections to formula (4.26) such as those coming from the running coupling or from the hard collinear emissions. As in the $x \sim 1$ case, one possible method consists in going to Mellin space and solve the linear-differential equation. However, there is no known analytical solution in x space in terms of usual functions. In Chapter 5, Section 5.3.1.2, we use the partial differential equation method to obtain some NLL corrections shown in Fig. 4.3.

4.2.3 Subjet observables

As emphasised in the last section, the fragmentation function defined by Eq. (4.12) is not an IRC safe observable when computed in perturbative QCD. In the experiments, this observable is defined from final state hadrons whose theoretical description transcends pQCD. In our simplified treatment, which ignores hadronisation, the partonic cascades have been forced to terminate at a lowest transverse momentum $k_{\perp,\min}$, which mimics the QCD confinement scale Λ_{QCD}. The precise value of this scale is not well defined and results turn out to be rather strongly sensitive to its variations (see e.g. Eq. (4.25)).

In this section, we investigate a set of observables relying on the concept of subjets [147] (or [148] for a detailed review). Subjets, as jets, are IRC safe objects so there is a possibility to design an observable both IRC safe and sensitive to the intrajet structure. The analytical results obtained to LL accuracy will serve as benchmark formulas when we will discuss the

corresponding observables in heavy ion collisions.

4.2.3.1 The Soft Drop z_g distribution

For completeness, we first recall the definition of the Soft Drop (SD) procedure [149]. For a given jet of radius R, SD first reclusters the constituents of the jet using the Cambridge/Aachen (C/A) algorithm [131]. The ensuing jet is then iteratively declustered, i.e. the last step of the pairwise clustering is undone, yielding two subjets of transverse momenta p_{T1} and p_{T2} separated by a distance $\Delta R_{12} = \sqrt{\Delta y_{12}^2 + \Delta\phi_{12}^2}$ in rapidity-azimuth. This procedure stops when the SD condition is met, that is when

$$z_{12} \equiv \frac{\min(p_{T1}, p_{T2})}{p_{T1} + p_{T2}} > z_{\text{cut}} \left(\frac{\Delta R_{12}}{R}\right)^{\beta}, \tag{4.27}$$

where z_{cut} and β are the SD parameters. If the condition is not satisfied, the subjet with the smaller p_T is discarded and the declustering procedure continues with the harder. With the above procedure, θ_g and z_g are defined respectively as ΔR_{12} and z_{12} for the declustering which satisfied the SD condition. When the procedure exhausts all declusterings without meeting the SD condition, we set θ_g and z_g to zero. Furthermore, one can impose a lower cut-off $\theta_g > \theta_{\text{cut}}$. This is commonly used for Pb-Pb collisions at the LHC.

The distribution is IRC safe when $\beta < 0$. The limiting case $\beta = 0$, for which the SD procedure coincides with the modified MassDrop Tagger [147] is peculiar: the distribution is not IRC safe but "Sudakov safe" [150].

We then study the differential z_g distribution for a jet initiated by a parton of flavour i (quark or gluon). We can consider two possible normalisation for the z_g distribution: the "self-normalised" distribution, $p_i(z_g)$, and the "N_{jets}-normalised" distribution, $f_i(z_g)$. The former is defined such that

$$\int_{z_{\text{cut}}}^{1/2} \mathrm{d}z_g \, p_i(z_g) = 1. \tag{4.28}$$

which is equivalent to normalising the z_g distribution to the number of jets which pass the SD condition and the optional cut on θ_g. The latter is instead normalised to the total number of jets, i.e. the normalisation includes jets which fail either the SD condition or cut on the θ_g.

The coherent branching algorithm enables to calculate the z_g distribution in a intuitive way. Let us calculate this distribution to LL accuracy. At this order, the splitting functions (summed over final states) can be approximated by $2C_i/z$ where C_i is the Casimir factor of the representation of the leading parton. With this simplification, the branching rates (4.7) become

$$\mathrm{d}^2\mathcal{P}_i(z,\theta) = \frac{2C_i\alpha_s(zp_T\theta)}{\pi} \frac{\mathrm{d}z}{z} \frac{\mathrm{d}\theta}{\theta} \tag{4.29}$$

Then we introduce "Sudakov factor" $\Delta_i(R, \theta_g)$, which is the probability to have no emission at any angle between θ_g and R satisfying the Soft Drop constraint:

$$\Delta_i(R,\theta_g) = \exp\left(-\int_{\theta_g}^{R} \mathrm{d}\theta \int_0^{1/2} \mathrm{d}z \; \mathcal{P}_i(z,\theta)\Theta(z - z_{\text{cut}}(\theta/R)^{\beta})\right). \tag{4.30}$$

The z_g-distribution is obtained by considering the probability for both z_g and θ_g, marginalised over θ_g. The former is simply expressed as the probability to have no branching between θ_g and R times the probability of a branching with $\theta = \theta_g$ and $z = z_g$, so that

$$p_{i,\mathrm{vac}}(z_g) = \frac{1}{1-\Delta_i(R,\theta_{\mathrm{cut}})}\int_{\theta_{\mathrm{cut}}}^{R} \mathrm{d}\theta_g\, \mathcal{P}_i(z_g,\theta_g)\Delta_i(R,\theta_g)\Theta(z_g - z_{\mathrm{cut}}(\theta_g/R)^\beta), \qquad (4.31)$$

where we have included an optional cut $\theta_g > \theta_{\mathrm{cut}}$. The overall factor $(1-\Delta_i)^{-1}$ enforces the normalisation condition (4.28) and would be absent for $f_i(z_g)$.

To discuss the underlying physics of the z_g distribution, it is helpful to consider the fixed-coupling approximation. One can then easily perform the angular integration in (4.31). We give the results for $\beta \leq 0$ and $\theta_{\mathrm{cut}} = 0$ in such a way that the DL resummation is clear [150]:

$$z_g p_i(z_g) = \sqrt{\alpha_0} F_{\mathrm{DL}}^{z_g}\big(\alpha_0 \log^2(2z_g), \alpha_0 \log^2(2z_{\mathrm{cut}})\big)\Theta(z_g - z_{\mathrm{cut}}), \qquad (4.32)$$

$$F_{\mathrm{DL}}^{z_g}(u,v) = \sqrt{\frac{C_i}{\beta}} e^{\frac{C_i v}{\pi\beta}} \left[\mathrm{Erf}\left(\sqrt{\frac{C_i u}{\pi\beta}}\right) - \mathrm{Erf}\left(\sqrt{\frac{C_i v}{\pi\beta}}\right)\right] \qquad (4.33)$$

with $\mathrm{Erf}(x)$ the Gauss error function. The limiting case $\beta = 0$ is singular since there is no apparent α_0 dependence. A direct calculation of (4.31) when $\theta_{\mathrm{cut}} = 0$ or the limit $\beta \to 0$ of (4.32) give,

$$p_i(z_g) = \frac{1/z_g}{\log(1/(2z_{\mathrm{cut}}))}\Theta(z_g - z_{\mathrm{cut}}). \qquad (4.34)$$

This results makes clear that the z_g-distribution provides a direct measurement of the splitting function.

4.2.3.2 The n_{SD} distribution

The n_{SD} distribution $p_i(n_{\mathrm{SD}})$ relies on a generalization of the SD procedure called Iterated Soft Drop [151]. Iterated SD proceeds by iterating the Soft Drop procedure, still following the hardest branch in the jet, until all declusterings have been exhausted. n_{SD} is then defined as the number of declusterings passing the SD condition. It is a particular case of recursive SD (rSD) which is essentially the same technique: instead of following the hardest branch, rSD proceeds recursively through the full branching tree (see also [152]).

From the coherent branching algorithm, if we neglect the energy recoil of the leading parton — assumption which is valid to LL accuracy — the emission of *primary* partons is a Poisson process where the angle plays the role of time. Thus, the random variable n_{SD} follows a Poisson distribution whose parameter $\rho_{i,\mathrm{LL}}$ is simply given by the integrated rate (4.29) over the phase space available for emissions passing the SD cut [151].

$$p_i(n_{\mathrm{SD}}) = e^{-\rho_{i,\mathrm{LL}}}\frac{\rho_{i,\mathrm{LL}}^{n_{\mathrm{SD}}}}{n_{\mathrm{SD}}!} \qquad (4.35)$$

$$\rho_{i,\mathrm{LL}} = \frac{2C_i}{\pi}\int_0^R \frac{\mathrm{d}\theta}{\theta}\int_0^1 \frac{\mathrm{d}z}{z}\alpha_s(z p_T \theta)\Theta_{\mathrm{cut}} \qquad (4.36)$$

with $\Theta_{\mathrm{cut}} = \Theta(z - z_{\mathrm{cut}}(\theta/R)^\beta)$. This simple estimate of the n_{SD} distribution will be useful when we will discuss its nuclear modification in Section 9.3.1.

4.2.3.3 A new fragmentation function: the ISD fragmentation function

From the ISD procedure, one can build an IRC safe generalisation of the fragmentation function based on subjets and not on final state hadrons: the ISD jet fragmentation function, $\mathcal{D}_{\mathrm{ISD}}(z)$.

This new observable fixes IRC issues of the fragmentation function while keeping the same fundamental phenomenology. It is defined as the number $\mathrm{d}N_{\mathrm{ISD}}$ of subjets passing the SD cut through the ISD procedure, with a momentum fraction z between z and $z+\mathrm{d}z$ and normalized by the total number of jets integrated over a suitable range in $p_{T,\mathrm{jet}}$:

$$\mathcal{D}_{\mathrm{ISD}}(x) \equiv \frac{1}{N_{\mathrm{jets}}}\frac{\mathrm{d}N_{\mathrm{ISD}}}{\mathrm{d}z} \tag{4.37}$$

Note that this definition is directly similar to the primary Lund-plane density [153, 154], $\rho(\theta, k_\perp)$, integrated over all angles θ satisfying the $k_{\perp,\mathrm{cut}}$ condition at fixed $x = k_\perp/(\theta p_{T,\mathrm{jet}})$.

The way the ISD algorithm proceeds requires a slightly different master equation for the generating functional $\mathcal{Z}_i(p_T, \theta \mid u)$ of *primary* emissions than the one presented in (4.10). Indeed, ISD always follows the hardest branch in the declustering, so the subsequent branchings in the softer branch can be ignored. This leads to a simplification of the master equation, which now reads:

$$\frac{\partial \mathcal{Z}_i(p_T,\theta \mid u)}{\partial \log(\theta)} = \sum_{(a,b)}\int_0^{1/2}\mathrm{d}z\,\frac{\alpha_s(k_\perp)}{\pi}\Theta_{\mathrm{cut}}\Phi_i^{ab}(z)\Big(u(z)\mathcal{Z}_b((1-z)p_T,\theta \mid u) - \mathcal{Z}_i(p_T,\theta \mid u)\Big) \tag{4.38}$$

With respect to (4.10), note the integration range between 0 and 1/2 to account for the fact that ISD follows the hardest branch with splitting fraction $1-z$. Moreover, as we will be only interested in the *splitting* fraction z of the emissions, the probing functions u depend only on the splitting fraction z.

As for the fragmentation function analysed in details in Section 4.2.2, let us first consider the ISD fragmentation function $D_{i,\mathrm{ISD}}(z \mid p_T, \theta)$ of a leading virtual parton of type $i \in \{q, \bar{q}, g\}$ with initial transverse momentum p_T and decaying within an opening angle θ, together with its cumulative version $\Sigma_{i,\mathrm{ISD}}(z \mid p_T, \theta)$:

$$D_{i,\mathrm{ISD}}(z \mid p_T,\theta) \equiv \frac{\delta \mathcal{Z}_i(p_T,\theta \mid u)}{\delta u(z)}, \qquad \Sigma_{i,\mathrm{ISD}}(z \mid p_T,\theta) \equiv \int_z^{1/2}\mathrm{d}z'\,D_{i,\mathrm{ISD}}(z' \mid p_T,\theta) \tag{4.39}$$

At small z, we expect large logarithms of the form $L = \log(1/z)$ or $L_{\mathrm{cut}} = \log(1/z_{\mathrm{cut}})$ that must be resummed to all orders. This resummation is organised as usual:

$$\Sigma_{i,\mathrm{ISD}}(z \mid p_T, R) = L g_{\mathrm{LL}}^{\mathrm{ISD}}\big(\alpha_0 L, \alpha_0 L_{\mathrm{cut}}\big) + g_{\mathrm{NLL}}^{\mathrm{ISD}}\big(\alpha_0 L, \alpha_0 L_{\mathrm{cut}}\big) + O(\alpha_0^{n+1}\log^n) \tag{4.40}$$

but, interestingly, it does not exponentiate as in (4.5).

Leading-logarithmic analysis. At leading logarithmic accuracy, one neglects the energy recoil of the hard branch $\mathcal{Z}_b((1-z)p_T, \theta \mid u) \simeq \mathcal{Z}_b(p_T, \theta \mid u)$. However, contrary to the case of the fragmentation function at large x, the quark-gluon mixing terms matter to LL accuracy. At this level of precision, $k_\perp \simeq z p_T \theta$ when appearing in front of the singular part of the splitting functions and $k_\perp \simeq p_T\theta$ when appearing in front of the finite part of quark-gluon mixing terms.

From the master equation (4.38), one easily gets a set of three coupled differential equations for D_i which can be reduced to two coupled differential equations defining $\vec{D} \equiv (D_F, D_A)$ with $D_F = (D_q + D_{\bar{q}})/2$ and $D_A = D_g$. Using the standard variable $Q = p_T\theta$,

$$\frac{\partial \vec{D}_{\mathrm{ISD}}(z,Q)}{\partial \log(Q)} = \frac{2\vec{C}_R}{\pi}\frac{\alpha_s(zQ)}{z}\Theta_{\mathrm{cut}} + \frac{\alpha_s(Q)}{\pi}\begin{pmatrix} -f_F & f_F \\ f_A & -f_A\end{pmatrix}\vec{D}_{\mathrm{ISD}}(z,Q) \tag{4.41}$$

with f_R the finite part of the splitting functions:

$$f_F = \int_0^{1/2} \mathrm{d}z\, \Phi_q^{qg}(z) \qquad f_A = 2\int_0^{1/2} \mathrm{d}z\, \Phi_g^{q\bar{q}}(z) \tag{4.42}$$

The initial condition of (4.41) is $\vec{D}(z, Q=0) = 0$.

One can find a solution of this first order linear differential equation. The complete calculation is given in Appendix E. The full LL result is:

$$zD_{R,\mathrm{ISD}}(z \mid p_T, R) = \frac{C_F f_A + C_A f_F}{f_F + f_A} f_0(\alpha_0 L, \alpha_0 L_{\mathrm{cut}}) + \frac{C_R f_R - C_{\tilde{R}} f_R}{f_F + f_A} f_1(\alpha_0 L, \alpha_0 L_{\mathrm{cut}}) \tag{4.43}$$

$$f_0(u,v) = \frac{-1}{\pi\beta_0} \log\left(1 + \frac{2\beta_0}{\beta}(v + (\beta-1)u)\right) \tag{4.44}$$

$$f_1(u,v) = \frac{(2\beta_0 u)^{\frac{f_R+f_A}{2\pi\beta_0}}}{\pi\beta_0}\left[\mathcal{B}\left(\frac{1+\frac{2\beta_0}{\beta}(v-u)}{2\beta_0 u}, 1 + \frac{f_R+f_A}{2\pi\beta_0}, 0\right) - \mathcal{B}\left(\frac{1}{2\beta_0 u}, 1+\frac{f_R+f_A}{2\pi\beta_0}, 0\right)\right]$$

with $\mathcal{B}(x,a,b)$ the incomplete beta function and $\tilde{R} = A, F$ if $R = F, A$ respectively. With the full LL result (4.43), one can notice that the second term in Eq. (4.41) associated with quark-gluon mixing is not really numerically important. Consequently, when we will study the nuclear modifications of $D_{i,\mathrm{ISD}}(z \mid p_T, R)$, we will approximate the LL formula by:

$$zD_{R,\mathrm{ISD}} \simeq C_R f_0(\alpha_0 L, \alpha_0 L_{\mathrm{cut}}) = \frac{2C_R}{\pi}\int_0^R \frac{\mathrm{d}\theta}{\theta}\, \alpha_s(z p_T \theta)\Theta_{\mathrm{cut}} \tag{4.45}$$

This result has an interesting property: it coincides with a naive calculation in which one assumes that the jet is made of one soft collinear emission. This is a specificity of the LL approximation that we will extensively use in the rest of this thesis.

NLL corrections. For completeness, we have also analysed some NLL corrections to the LL result (4.43). At NLL, one cannot ignore the energy recoil of the hard branch but one can truncate to the first order the (logarithmic) Taylor expansion of $D_{R,\mathrm{ISD}}(z, (1-z)Q)$:

$$D_{R,\mathrm{ISD}}(z, \log((1-z)Q)) \simeq D_{R,\mathrm{ISD}}(z, \log(Q)) + \log(1-z)\frac{\partial D_{R,\mathrm{ISD}}(z, \log(Q))}{\partial \log(Q)} \tag{4.46}$$

The other NLL corrections included in the master equation (4.38) that can be easily added to the LL piece are the finite part of the splitting functions singular in $z = 0$ and the running coupling corrections when $k_\perp$ is small using $k_\perp = z p_T \theta$ in the pieces where we ignored the z dependence at LL. With these corrections, formula (4.41) has the following solvable form:

$$\frac{\partial \vec{D}_{\mathrm{ISD}}(z,Q)}{\partial \log(Q)} = \vec{C}_{\mathrm{NLL}}(z,Q) + \frac{\alpha_s(Q)}{\pi}\begin{pmatrix} -f_F & f_A \\ f_F & -f_A \end{pmatrix}\vec{D}_{\mathrm{ISD}}(z,Q) \tag{4.47}$$

There are also other NLL corrections which are not taken into account in the master equation (4.38). First of all, one should use the two loop running coupling and include the singular part at $z = 0$ of the two-loops splitting functions wherever it is necessary. This amounts to a simple modification of the function $C_{\mathrm{NLL}}(z,Q)$ in formula (4.47). The full function $C_{\mathrm{NLL}}(z,Q)$ and the solution of (4.47) from the variation of parameters method are given in Appendix E. Moreover, there are also NLL corrections related to clustering effects which occur when a non-primary emission is clustered with the hard branch. These corrections are beyond the scope of this simple analysis. Nevertheless, a complete NLL result would be very interesting for precision jet physics in pp collisions.

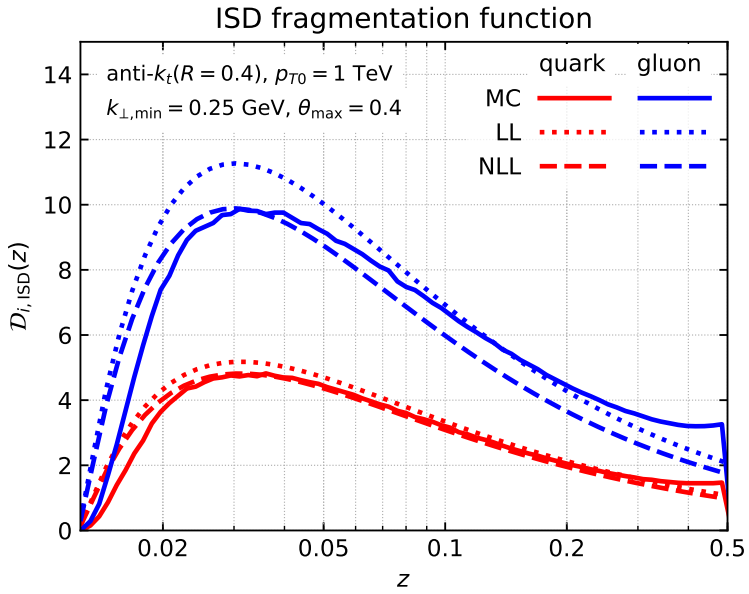

Figure 4.4: The ISD fragmentation function to LL accuracy (dotted curves) and with NLL corrections (dashed curves) compared to `JetMed` Monte Carlo calculations of this observable. The LL results are given by (4.43) whereas the NLL formula used for this plot is given by the solution (E.18) of (4.47).

4.3 Jets from medium-induced emissions

The first section of this chapter was dedicated to jets evolving in the vacuum via iteration of Bremsstrahlung emissions triggered by the virtuality of the initial parton coming from the hard event. From a mathematical point of view, iterating vacuum-like soft/collinear emissions is equivalent to an all-orders resummation of the large soft and collinear logarithms. We have seen a couple of examples of such resummations through jet observables that we will study also in heavy-ion collisions.

In this section, we present another kind of "jet" that happen specifically in a dense QCD medium and we call it "jet from medium-induced emissions" because the emission process which is iterated is not the Bremsstrahlung process associated with an off-shell parton but the medium-induced spectrum studied in Chapter 3 associated with an on-shell parton travelling through a dense medium (see [155] for a review).

4.3.1 The multiple branching regime: probabilistic picture

Before discussing the properties of jets from medium-induced emissions, we first review the main constructing stages of the effective field theory for multiple soft medium-induced emissions in a dense QCD medium [156].

4.3.1.1 The branching energy scale $\omega_{\mathbf{br}}$

In Section 3.3, we have calculated the medium-induced gluon spectrum from an on-shell quark or gluon travelling through the medium. Focusing on the behaviour at small energy $\omega = k^+$ (in light cone coordinates) in the case of a medium with fixed length L and constant density, this spectrum behaves like:

$$\omega \frac{\mathrm{d}N_{\mathrm{mie}}}{\mathrm{d}\omega} \sim \frac{\alpha_s C_A}{\pi} \sqrt{\frac{2\omega_c}{\omega}} \tag{4.48}$$

for an initial gluon. We recall that $\omega_c = \hat{q}L^2/2$ is typically the largest medium-induced radiation that can be formed over a time L. Without loss of generalities, we focus on gluon splittings in this subsection.

Comparing with the standard Bremsstrahlung spectrum, one notes first that the transverse momentum integral has been carried out: there is no collinear singularity associated with the medium-induced gluon spectrum. However, this spectrum remains singular at small ω. Of course, there are several assumptions that lead to formula (4.48). Among them, one must have $\omega > \omega_{\rm BH,}$ with $\omega_{\rm BH} \sim \hat{q}\ell^2$ the Bethe-Heitler frequency below which the formation time $t_f(\omega) = \sqrt{\omega/\hat{q}}$ of the medium-induced parton is smaller than the mean-free path ℓ in the medium.

Is there nothing more behind this soft singularity? Actually, the physics related to this singularity happens to be very rich. In the same way that the soft logarithmic singularity of the Bremsstrahlung spectrum must be taken into account beyond the leading order, to all orders in α_s, there is a regime in which medium-induced emissions have to be resummed beyond the leading order BDMPS-Z result. This regime occurs when the integrated BDMPS-Z spectrum becomes of order 1. This trivial integration defines a new energy scale, the branching energy $\omega_{\rm br}$:

$$N(\omega) = \int_{\omega}^{\omega_c} {\rm d}\omega' \, \frac{{\rm d}N_{\rm mie}}{{\rm d}\omega'} \sim \sqrt{\frac{\bar{\alpha}_s^2 \omega_c}{\omega}} = \mathcal{O}(1) \Rightarrow \omega \sim \omega_{\rm br} \equiv \bar{\alpha}_s^2 \omega_c \tag{4.49}$$

Even if $\omega_{\rm br}$ is smaller than ω_c by two powers of $\bar{\alpha}_s \equiv \alpha_s N_c/\pi$, this "branching" scale is still hard enough to be larger than $\omega_{\rm BH}$ provided that the medium is large enough: $\ell \ll \bar{\alpha}_s L$. When the latter condition is satisfied, there is a potentially large energy phase space such that $\omega_{\rm BH} \ll \omega \lesssim \omega_{\rm br}$ in which the emission probability $N(\omega)$ is larger than 1. In this regime, one should not interpret the integrated BDMPS-Z spectrum as a probability, but rather as an average *number* of emissions. Since this number is larger than 1 below $\omega_{\rm br}$, this means that one must also take into account the single BDMPS-Z process beyond the leading order: this is the so-called multiple branching regime.

To get more intuition on the parameter that will be resummed to all orders through this new branching process, we rewrite the condition (4.49) as a ratio of time-scales:

$$N(\omega) \sim \bar{\alpha}_s \frac{L}{t_f(\omega)} \tag{4.50}$$

Consequently, in the multiple branching regime, the parameter of order 1 which has to be resummed to all orders is $\bar{\alpha}_s L/t_f$.

4.3.1.2 Iteration of medium-induced emissions

Now that we have recognized the necessity of taking into account multiple medium-induced emissions, the next step is to understand how to calculate cross-sections in the multiple emission regime. The pedestrian method of computing Feynman diagrams with multiple external legs in the presence of the background field as in Chapter 3 would be a gigantic task. Actually, this task is greatly facilitated by doing a couple of parametrically well-controlled approximations that enable to calculate the multiple medium-induced emission probability from a classical Markovian branching process. In this context, there are mainly three approximations necessary to come up with this classical picture.

Colour coherence. The first one is related to the colour coherence of a medium-induced "antenna" that could significantly modify the interference term involved in the calculation of

the emission of one gluon by this antenna. By medium-induced antenna, we refers to a two-gluon system associated with a medium-induced branching. In the vacuum, we have seen that these interferences are responsible for the angular ordering constraint of the subsequent emission, but to LL accuracy at least, this was not an obstacle to see multiple vacuum-like emissions as a classical branching process (ordered in angle though).

For a medium-induced branching, we now show that the two offspring gluons lose their colour coherence during a time comparable to the duration of the branching $t_f(\omega)$. From the antenna calculation done in Section 3.4, we know that the (de)coherence time is given by $t_{\rm coh}(\theta) \sim (\hat{q}\theta^2)^{-1/3}$ where θ is the opening angle of the antenna. For a medium-induced branching, this angle is set by the transverse momentum k_f acquired during the branching process:

$$k_f^2 \simeq \omega^2\theta_f^2 \sim \hat{q}t_f(\omega) \Rightarrow \theta_f \sim \Big(\frac{\hat{q}}{\omega^3}\Big)^{1/4} \tag{4.51}$$

where we have assumed — without loss of generality — that one of the offspring gluon with energy ω is softer than the other. Thus, one has $t_{\rm coh}(\theta_f) \sim t_f$, equality which precisely means that the medium-induced antenna loses its colour coherence during its formation. Now, a subsequent gluon emission can occur with probability of order $(\bar{\alpha}_s L/t_f)^2 = \mathcal{O}(1)$ in the direct terms associated with independent emissions. However the interference term will be reduced by a factor t_f/L since the quantum colour coherence survives only during a time of order t_f. Hence, interferences are sub-leading in an calculation aiming at resumming all $\mathcal{O}((\bar{\alpha}_s L/t_f)^n)$ contributions [122, 123]. This is the solution to the first obstacle associated with quantum colour coherence.

Overlapping formation times. The second obstacle concerns the so-called problem of overlapping formation times [79]. If we now only focus on the direct term in the amplitude squared for producing two medium-induced gluons with energy ω, the two emissions may overlap in time, changing the naive estimate obtained by squaring the probability for producing one gluon. We would like to bring to light a physical regime enabling to neglect this possibility.

To do so, we would like to estimate the typical time $t_{\rm br}$ between two branchings in a regime where we can assume that they occur independently. Let us rewrite the leading soft behaviour of the BDMPS-Z spectrum (4.48) in a such a way that its interpretation as an emission *rate* is transparent:

$$\omega\frac{{\rm d}N_{\rm mie}}{{\rm d}\omega{\rm d}t} \sim \frac{\bar{\alpha}_s}{t_f(\omega)} \tag{4.52}$$

One recovers formula (4.48) integrating this constant rate over a time L. If the emissions are independent with each other, the no-emission probability $\Delta_{\rm mie}(\Delta t, \omega')$ during Δt of gluons with energies larger than some energy scale ω' follows the exponential law with parameter given by the rate (4.52) integrated over energies larger than ω':

$$\Delta_{\rm mie}(\Delta t, \omega') = \exp\Big(-\Delta t\int_{\omega'}\frac{{\rm d}\omega}{\omega}\,\frac{\bar{\alpha}_s}{t_f(\omega)}\Big) \tag{4.53}$$

The upper limit in the integration range, of order $\min(\omega, \omega_c)$, is left intentionally blank since the integral is controlled by the lower bound. ω' is a scale which will define the regime of validity of the independent emissions picture. The probability $\Delta_{\rm mie}(\Delta t, \omega')$ vanishes for $\Delta t \gg t_{\rm br}(\omega')$ with

$$t_{\rm br}(\omega') \sim t_f(\omega')/\bar{\alpha}_s \tag{4.54}$$

As suggested by our notations, $t_{\rm br}(\omega')$ is the survival time of our parton with energy ω without emitting any gluons with energies larger than ω' (but smaller than ω).

With this estimate at our disposal, one can neglect overlapping emissions if the formation time of the parton with energy ω is much smaller than $t_{\rm br}(\omega')$:

$$t_f(\omega) \ll t_{\rm br}(\omega') \Rightarrow \omega' \gg \bar{\alpha}_s^2 \omega \tag{4.55}$$

This inequality can be summarized as follows: given an emission with energy ω, the overlapping formation time problem is harmless if all other subsequent emissions have an energy much larger than $\bar{\alpha}_s^2\omega$. In terms of the splitting fraction $z = \omega'/\omega$, one must impose $z \geq \bar{\alpha}_s^2$. This seems to be a strong restriction since $\bar{\alpha}_s$ is not that small even in a weakly coupled medium. However, we will see that the evolution equation governing jets from medium-induced emissions favours "democratic" branchings instead of softer and softer branchings. Consequently, introducing a lower cut off for splitting fractions does not change this picture.

Collinear splitting approximation. The last main approximation that greatly simplifies the mathematical formulation of the multiple branching regime is the assumption of purely collinear splittings. To be more precise, after the splitting, the two offspring partons share equal fraction, respectively z and $1-z$, of both the initial energy and initial transverse momentum carried by the parent parton. This means that the transverse momentum acquired during the branching process is neglected and that all the transverse momentum of the emitted gluon is acquired during the propagation through the medium — between the emission and the decay — via collisions off the medium constituents.

We now find the regime of validity of this approximation. In the multiple soft scattering regime, the transverse momentum acquired during the formation is $k_f^2 = \hat{q}t_f$ whereas the transverse momentum acquired during propagation is $k_\perp^2 = \hat{q}t_{\rm br}$. Hence, the condition $k_\perp \gg k_f$ is equivalent to the condition (4.55) that we have already discussed. In order to obtain a typical value for the interval between two branchings which depends on ω only, we shall use $t_{\rm br} \equiv t_{\rm br}(\omega) = t_f/\alpha_s$. Hence, the transverse momentum acquired during formation is suppressed by one power of α_s with respect to the transverse momentum acquired after propagation. We point out that this argument rely on the fact that $t_{\rm br} < L \Leftrightarrow \omega < \omega_{\rm br}$ in agreement with the multiple branching regime that we are discussing now. However, even for relatively hard medium-induced emissions in the regime $\omega_{\rm br} < \omega < \omega_c$, this approximation remains valid since in this case, the transverse momentum acquired after emission is typically $Q_s = \sqrt{\hat{q}L}$ and the condition $\hat{q}t_f < Q_s^2$ is equivalent to $\omega < \omega_c$.

Thus, in the collinear splitting approximation, the transverse momentum broadening comes from multiple elastic collisions during propagation. It is worth mentioning that there is another indirect contribution to this transverse momentum coming from the recoil of the parton while radiating gluons [157, 158, 159]. This recoil effect is dominated by hard medium-induced emissions triggered by a single scattering with short formation time. For a parton propagating over a distance L, it amounts to an additive correction to the typical momentum transferred Q_s of the form $\alpha_s N_c Q_s \log^2(Lk_BT_{\rm p})/\pi$ where $T_{\rm p}$ is the plasma temperature and $k_BT_{\rm p}$, the thermal energy which is also the maximal energy that a medium constituent can transfer in a single scattering. It is possible to include these corrections to the probabilistic picture that we shall now expose in more details by a renormalization of the quenching parameter: these radiative corrections are local and universal, at least to leading logarithmic accuracy [111, 118, 160, 161].

4.3.1.3 Generating functional and master equation

We turn now to the construction of the master equation for the generating functional of the multiple medium-induced emissions. We choose first to focus on purely collinear processes, so

that transverse diffusions due to multiple rescatterings or elastic collisions are integrated out. For observables averaged over transverse coordinates, it generates the right distributions. We will discuss the angular (transverse) structure of jets from medium-induced emissions in the following section. Within the approximations listed in the previous section, one can calculate the cross-section for multiple medium-induced emissions using a classical and Markovian branching process with the following rules [156]:

1. Successive emissions are independent and ordered in time. By time, one refers to the light-cone "+" coordinates with the longitudinal axis defined by the direction of motion of the parton triggering the jet. We note E the (large) + component of the 4-vector of the leading parton.

2. The rate of the branching process is given by the BDMPS-Z spectrum rate (4.52) amended to take into account $q \to qg$ and $g \to gg$ splittings and finite z fractions,

$$\frac{\mathrm{d}^2\mathcal{P}^{bc}_{a,\mathrm{mie}}}{\mathrm{d}z\mathrm{d}t} = \frac{\mathcal{K}^{bc}_a(z)}{2\pi t_{\mathrm{br}}(z(1-z)E)}\Theta(\omega_c - z(1-z)E)\,, \qquad t_{\mathrm{br}}(\omega) \equiv \frac{1}{\alpha_s}\sqrt{\frac{\omega}{\hat{q}}} \tag{4.56}$$

   One can include running coupling corrections using $\alpha_s(k_{\mathrm{br}} = (\hat{q}zE)^{1/4})$. The rate is given for a medium with constant density (i.e. constant $\hat{q}$). The case of a longitudinally expanding medium will be discussed in Section 4.3.4. All the "in-medium" splitting functions $\mathcal{K}^{bc}_a(z)$ are given in Appendix C. Finally, the step function ensures that all medium-induced emissions have an energy smaller than ω_c as it should be.

We call $Z^{\mathrm{mie}}_i(t_0, E \mid u(k^+))$ the generating functional associated with this branching process, t_0 being the initial time. The definition is the same as the one given in Eq. (4.8), but the test functions $u(k^+)$ depends only on the + component of the 4-momentum of the emitted partons, since transverse informations have been integrated out. The generating functional Z^{mie} follows the master equation [156, 162]:

$$-\frac{\partial Z^{\mathrm{mie}}_i}{\partial t_0} = \frac{1}{2!}\sum_{(a,b)}\int_0^1 \mathrm{d}z\,\sqrt{\frac{\hat{q}}{E}}\frac{\alpha_s\mathcal{K}^{ab}_i(z)}{2\pi\sqrt{z(1-z)}}\Big[Z^{\mathrm{mie}}_a(t_0, zE)Z^{\mathrm{mie}}_b(t_0,(1-z)E) - Z^{\mathrm{mie}}_i(t_0,E)\Big] \tag{4.57}$$

The initial condition for it is $Z^{\mathrm{mie}}_i(t_0 = L, E) = u(E)$. As for Eq. (4.8), the endpoint singularities are regularized with a cut-off $z \geq \epsilon$. From the discussion in 4.3.1.2, ϵ should be of order α_s^2. Nevertheless, the observable that we will discuss thereafter are finite when $\epsilon \to 0$, and hence not sensitive to this cut-off.

In order to highlight the similarities and the differences between (4.57) and (4.8), we have written the former in backward form: $t_0 \Leftrightarrow \log(1/\theta)$. Besides the evolution parameter t_0 which accounts for the ordering in time of the process, an other important difference with respect to the MLLA evolution equation (4.8) is hidden in the endpoint singularities: contrary to the DGLAP splitting functions behaving like $1/z$ at small z, the singularity is stronger for the medium-induced evolution $\sim 1/z^{3/2}$. As we shall now see, this will drastically modify the picture of medium-induced cascades with respect to DGLAP cascades.

4.3.2 Democratic fragmentation and turbulent energy loss

In this section, we simplify the full process described by (4.57) in order to derive analytical results for medium-induced jet fragmentation and get some physical insights on the behaviour of the cascade. We first ignore quarks and assume that only gluons participate to the branching process. We also simplify the branching kernel $\mathcal{K}_g^{gg}(z)$ using:

$$\frac{1}{2C_A}\frac{\mathcal{K}_g^{gg}(z)}{\sqrt{z(1-z)}} \simeq \mathcal{K}_0(z) \equiv \frac{1}{(z(1-z))^{3/2}} \tag{4.58}$$

Finally, we assume that $E < \omega_c$ so that one can ignore the step function in (4.56). The forward evolution equation for the fragmentation function has a more simple form so we first rewrite (4.57) in forward form using the approximations specific to this section [156]:

$$\frac{\partial Z_g^{\rm mie}(t,E)}{\partial t} = \int_0^1 {\rm d}z \int {\rm d}k^+ \, \frac{\bar{\alpha}_s}{2}\sqrt{\frac{\hat{q}}{E}}\mathcal{K}_0(z)\Big(u(zk^+)u((1-z)k^+) - u(k^+)\Big)\frac{\delta Z_g^{\rm mie}(t,E)}{\delta u(k^+)} \tag{4.59}$$

with initial condition $Z_i^{\rm mie}(t=0,E) = u(E)$.

We want to find the evolution equation for the fragmentation function of medium-induced jets $D_{g,\rm mie}(x,t,E)$ defined by

$$D_{g,\rm mie}(x,t,E) = x\int {\rm d}k^+ \, \delta(k^+ - xE)\frac{\delta Z_g^{\rm mie}(t,E)}{\delta u(k^+)}\Big|_{u=1} \tag{4.60}$$

with the initial condition $D_{g,\rm mie}(x,0,E) = x\delta(1-x)$. From Eq. (4.57), it is straightforward to derive it, in terms of the dimensionless variable $\tau \equiv \bar{\alpha}_s t\sqrt{\hat{q}/E}$, [156, 163]

$$\frac{\partial D_{g,\rm mie}(x,\tau)}{\partial \tau} = \int_0^1 {\rm d}z\, \mathcal{K}_0(z)\left[\sqrt{\frac{z}{x}}D_{g,\rm mie}\Big(\frac{x}{z},\tau\Big) - \frac{z}{\sqrt{x}}D_{g,\rm mie}\Big(x,\tau\Big)\right] \tag{4.61}$$

This is the rate equation for the fragmentation function of medium-induced jets. The corresponding rate equation obtained from (4.57) is of course equivalent. This equation is well-defined without introducing any cut-off ϵ in z because there is no true endpoint singularity. For $z \to 0$, the first term is harmless because $D_{g,\rm mie}(x/z,\tau) = 0$ for $z < x$ and the second ("virtual") term is regularized by the z factor. For $z \to 1$, the two terms are singular when separately taken but the singularities cancel in the difference.

Physical discussion. This equation is particularly remarkable for several reasons [163].

- It admits a set of fixed point solutions $D(x,\tau) = c/\sqrt{x}$ for any constant c. In particular, the single-emission BDMPS-Z spectrum belongs to the set of fixed point solutions. They are called Kolmogorov–Zakharov fixed points and they naturally appear in phenomena associated with turbulence.

- It is exactly solvable given our initial condition. The solution is

$$D_{g,\rm mie}(x,\tau) = \frac{\tau}{\sqrt{x}(1-x)^{3/2}}e^{-\pi[\tau^2/(1-x)]} \tag{4.62}$$

  Using the final value $\tau_{\rm max} = \bar{\alpha}_s L/t_f(E)$, one recognises the all order resummation of the parameter $\bar{\alpha}_s L/t_f$ which defines the multiple branching regime.

- This solution has the following behaviour: at small times $t \ll t_{\rm br}(E)$ it is strongly peaked around $x = 1$. As time goes by, after $t_{\rm br}$, the leading gluon is progressively degraded into soft gluons that populate the soft modes of the spectrum. This soft part behaves like $\tau \exp(-\pi\tau^2)/\sqrt{x}$. The time dependence apart, the shape of the small x part of the spectrum is close to a fixed point solution. The story is not over though: because of the exponential factor, the amount of energy contained in every $x > 0$ bin of the spectrum vanishes in the limit $\tau \to \infty$. This is paradoxical: recall that energy is conserved along the branching process, even with the simplified kernel $\mathcal{K}_0$. Then, where does the initial energy go? It accumulates in a "condensate" located formally in the $x = 0$ bin.

- One can calculate the energy accumulated in this condensate at the end of the cascade, called $\epsilon_{g,\rm flow}(\tau_{\rm max})$, by energy conservation: it is the initial energy E minus the energy contained in the spectrum:

$$\epsilon_{g,\rm flow}(\tau_{\rm max}) = E - \int_0^1 {\rm d}x\, D_{g,\rm mie}(x, \tau_{\rm max}) = E\Big(1 - e^{-2\pi\omega_{\rm br}/E}\Big) \tag{4.63}$$

  This relation enlightens the physical role of $\omega_{\rm br}$. If $E \ll \omega_{\rm br}$, almost all the initial energy of the leading gluon will disappear in this condensate after propagation through the medium. On the contrary, for $E \gg \omega_{\rm br}$ (but smaller than ω_c by hypothesis), the initial energy is shared between the remnant of the leading gluon and the small x part of the spectrum: in this regime, the typical (event by event) energy loss by the leading gluon is $\omega_{\rm br}$. This is to be contrasted with the average energy loss as given by the BDMPS-Z spectrum which is of order $\bar{\alpha}_s\omega_c$. Note that $\epsilon_{\rm flow}$ has also been obtained in the regime $E > \omega_c$ not discussed in this section [164]. In this case, $\epsilon_{g,\rm flow} \simeq v\omega_{\rm br}$ with v a constant.

- The endpoint $x = 0$ is beyond the regime of validity of Eq. (4.61). Recall that we must impose at least $x > \omega_{\rm BH}/E$ for instance, since this analysis relies on the BDMPS-Z rate. One can also calculate the amount of energy that goes below the scale $\omega_{\rm BH}/E$. As $\omega_{\rm BH}$ is of the order of the temperature in a weakly coupled plasma, this is the amount of energy coming from the initial gluon that eventually "thermalizes" [165]. It happens that the result is very close to $\mathcal{E}_{\rm flow}$ so (4.63) is actually a good estimate of the thermalized energy loss.

- Equation (4.61) has an other interesting property, related to turbulence. Besides the energy accumulated in the condensate, one can calculate the energy flux $\mathcal{F}(x_0, \tau)$ transferred from modes with $x > x_0$ to modes with $x < x_0$ (counted positively in this direction):

$$\mathcal{F}(x_0, \tau) \equiv \frac{-\partial}{\partial\tau} \int_{x_0}^1 {\rm d}x\, D_{g,\rm mie}(x, \tau) = \underbrace{2\pi\tau e^{-\pi\tau^2}}_{\mathcal{F}_{\rm flow}} + \text{"non-flow"} \tag{4.64}$$

  For all x_0, there is always a non-zero component $\mathcal{F}_{\rm flow}$ of this flux which is independent of x_0 and that corresponds to the flow of energy transferred to the condensate. This is characteristic of *turbulent flows* in ideal cascades in which the energy flux at some energy is independent of the energy. This flow does not exist in DGLAP-like cascade such as the cascade describing vacuum-like branchings. A crucial physical ingredient for it is *democratic branching*: whereas DGLAP branchings strongly favour asymmetric splittings, in medium-induced jets, the two daughters partons have comparable energies. Turbulent flow constitutes a very efficient way to transport energy from high modes into

arbitrarily soft modes. This scenario is obviously particularly interesting for jet quenching physics.

4.3.3 Angular structure of medium-induced jets

So far, we have only discussed the longitudinal structure of medium-induced jets, ignoring its transverse structure. However, understanding this transverse structure is crucial to answer the following questions: what is the typical angle where the energy flow described in the previous section end up? For instance, if the energy accumulated in the condensate is also transferred to large angles with respect to the leading parton, then we have really an efficient mechanism for large angle energy loss by jets that could eventually explain the behaviour of the experimental data.

4.3.3.1 The general picture

In the collinear emission approximation (see Section 4.3.1.2), the transverse structure is dictated by the transverse momentum acquired during the propagation. Including this transverse momentum in the generating functional formalism as in (4.57) is straightforward. First of all, the generating functional $Z_i^{\rm mie}(t_0, E, p_\perp)$ and the test functions u depend now on the transverse component $p_\perp$ of the 4-momentum of an emission. Then, the master equation for $Z^{\rm mie}$ is amended by a term that can change the transverse momentum $p_\perp$ of the initial parton [156]:

$$-\frac{\partial Z_i^{\rm mie}}{\partial t_0} = \frac{1}{2!}\sum_{(a,b)}\int_0^1 {\rm d}z\,\sqrt{\frac{\hat{q}}{E}}\frac{\alpha_s \mathcal{K}_i^{ab}(z)}{2\pi\sqrt{z(1-z)}}\Big[Z_a^{\rm mie}(t_0, zE, zp_\perp)Z_b^{\rm mie}(t_0,(1-z)E,(1-z)p_\perp) - Z_i^{\rm mie}(t_0,E,p_\perp)\Big] + \int {\rm d}^2q_\perp\,\mathcal{C}_i(q_\perp,t_0)Z_i^{\rm mie}(t_0,E,p_\perp-q_\perp) \tag{4.65}$$

The collision kernel $\mathcal{C}_i(q_\perp, t_0)$ is related to the Fourier transform of the in-medium dipole cross-section σ_d, cf. Sections 3.2.3-3.3.1.2:

$$\mathcal{C}_i(q_\perp,t_0) = -\frac{g^2}{2}C_i n(t_0)\sigma_d(q_\perp) \tag{4.66}$$

In the multiple soft scattering regime and in the harmonic approximation, this collision kernel simplifies, $\mathcal{C}_i(q_\perp,t_0) \simeq -\frac{1}{4}\hat{q}_i(t_0)q_\perp^2$ and leads to the diffusion of emissions in the transverse plane. In this section, we will work within this simplified regime.

From (4.65), one can infer the evolution equation for the double-differential fragmentation function $D_{i,\rm mie}(x,k_\perp)$. Using the same kind of approximations as those used in the previous section, it is even possible to get analytical results [166]. As we will study this equation numerically via Monte Carlo methods in Chapter 6, we follow here a different path and give only the physical arguments enabling to get the angular picture of medium-induced jet evolution.

Actually, all the necessary ingredients for this discussion have already been given in Section 4.3.1.2. Let us pick a final parton in the distribution $D_{i,\rm mie}(x,k_\perp)$ with energy $\omega = xE$. We want to find its corresponding angle $\theta \simeq k_\perp/\omega$ with respect to the direction of the parton that has triggered the cascade. This angle is set by the time $t_{\rm prop}$ of propagation through the medium:

$$\theta(t_{\rm prop}) = \frac{k_\perp(t_{\rm prop})}{\omega} = \frac{\sqrt{\hat{q}t_{\rm prop}}}{\omega} \tag{4.67}$$

The different regimes will depend on the typical time $t_{\rm prop}$ of propagation. We assume a highly energetic initial parton with $E \gtrsim \omega_c$.

1. If $\omega \sim E$ corresponding to the leading parton case, the latter will most likely survive after the medium-induced evolution. Hence, its propagation time through the medium is $t_{\rm prop} = L$ and its final angle is typically $\theta = Q_s/E$.

2. For $\omega_{\rm br} \lesssim \omega \lesssim \omega_c$, the emission is not in the multiple branching regime. Hence, it corresponds to a single BDMPS-Z like emission emitted directly by the leading parton. We call it a *primary* medium-induced emission. This emission can occur everywhere inside the medium, but the typical propagation time remains the same as for the leading particle $t_{\rm prop} \sim L$, so that $\theta = Q_s/\omega$. One sees that if ω is hard-enough, such emissions can remain inside the jet which is defined through a typical opening angle R. The criterion is $\omega \geq Q_s/R$.

3. In the multiple branching regime $\omega \lesssim \omega_{\rm br}$, the propagation time is precisely the branching time $t_{\rm br}$ defined in 4.3.1.2. Hence, the typical angle of these emissions is

$$\theta(t_{\rm br}(\omega)) = \Big(\frac{\hat{q}}{\bar{\alpha}_s^2\omega^3}\Big)^{1/4} \tag{4.68}$$

   Thus, these soft emissions are most likely deviated at large angles, outside the jet cone. The corresponding criterion is $\omega \lesssim (\hat{q}/(\bar{\alpha}_s^2 R^4))^{1/3} \equiv \omega_s(R)$. This answers the question which started this section: the energy $\epsilon_{i,\rm flow}$ accumulated in the condensate (formally at $\omega = 0$) is an energy deviated at very large angles and is consequently always a component of the total energy loss by a medium-induced jet whatever its opening angle is.

From this general picture, one can find a better estimate of the energy loss $\epsilon_i(R)$ by a leading parton with energy $E \gtrsim \omega_c$ outside a given angle R, taking into account both the semi-hard primary large angle emissions and the soft emissions with $x_s(R) \geq \omega_s(R)/E$ [164]. Actually, one can perfectly neglect the latter contribution as the energy contained in the spectrum between 0 and $\omega_{\rm br}/E$ is much smaller than the energy accumulated in the condensate. Hence, to the "turbulent" component of the jet energy loss given by (4.63), one must add the (average) energy taken away by semi-hard gluons whose energies are larger than $\omega_{\rm br}$, yet small enough for the associated propagation angles $\theta \sim Q_s/\omega$ to be larger than R. The (average) semi-hard contribution to the energy loss is therefore obtained by integrating the emission spectrum over ω up to $\bar{\omega} \equiv c_* Q_s/R$, with c_* a number smaller than one. We will see later that an average value for it is $c_* = \sqrt{\pi}/3$.

$$\epsilon_{i,\rm spec}(E,R) \simeq \frac{\alpha_s C_i}{\pi}\int_0^{\bar{\omega}} {\rm d}\omega \sqrt{\frac{2\omega_c}{\omega}}\, {\rm e}^{-\upsilon_0 \frac{\omega_{\rm br}}{E}} = \frac{2\alpha_s C_i}{\pi}\omega_c\sqrt{\frac{2c_*\theta_c}{R}}\, {\rm e}^{-\upsilon_0 \frac{\omega_{\rm br}}{E}}\,, \tag{4.69}$$

where we have also used $Q_s = \theta_c\omega_c$. Note that the above expression uses the BDMPS-Z spectrum dressed by multiple branchings computed under the same assumptions as (4.63) yielding an extra exponential factor [163]. The R-dependence here is easy to understand: with increasing R, more and more semi-hard emissions are captured inside the jet so the energy loss is decreasing. Note that when R becomes as small as θ_c, all the MIEs are leaving the jet and the average energy loss by the jet coincides with that of the leading parton.

The total energy lost by the jet under the present assumptions is

$$\boxed{\epsilon_{i,\rm MIE} = \epsilon_{i,\rm flow} + \epsilon_{i,\rm spec}} \tag{4.70}$$

where the subscript "MIE" indicates that for the time being only MIEs are included. Formula (4.70) will be very important to understand the energy loss by a jet including both vacuum-like emissions and medium-induced emissions.

To conclude this discussion on the energy loss by a parton at large angles, let us comment on the Casimir i dependence of $\epsilon_{i,\text{flow}}$. The main observation of the previous section obtained for gluon-initiated jets can be generalized to quark-jets as well [167]: the small-x gluon distribution within a jet initiated by a parton of colour representation R develops a scaling behaviour with $1/\sqrt{x}$, the Kolmogorov-Zakharov (or "turbulent") fixed point. For large-enough initial jet energy E this scaling spectrum is identical to the BDMPS-Z spectrum created by a single emission, hence proportional to the colour representation of the initial parton and to $\hat{q} = \hat{q}_A$ which is the *gluonic* jet quenching parameter, proportional to C_A. Consequently, the scale ω_{br} that appears in Eq. (4.63) depends on i through the following relation:

$$\boxed{\omega_{\text{br}}^{(i)} = \frac{\alpha_s^2}{\pi^2} C_i C_A \hat{q} L^2} \tag{4.71}$$

One actually gets a factor $\alpha_s C_i/\pi$ associated with the emission from the leading parton, whereas the other coupling $\alpha_s C_A/\pi$ refers to the turbulent energy flux of the emitted gluons and carried away at large angles.

4.3.3.2 C/A declustering of medium-induced jets

As an exercise relying on the ideas exposed in the last paragraph, we want to show the following property for medium-induced jets dominated by *primary* medium-induced emissions, that is in the regime $\omega_s(R) \geq \omega_{\text{br}}$: the generating functional of a jet constituted by primary medium-induced emissions ordered in time is equal to the generating functional of a fictitious jet with primary emissions ordered in angle and emission rate properly found in order to satisfy this equivalence.

This fictitious ordering is exactly what a C/A declustering would reconstruct from final states particles. As many substructure observables in the vacuum rely on C/A declusterings, such as z_g or ISD, this statement provides an insight on the values of such observables for medium-induced jets, despite the lack of physical angular ordering.

To prove this statement, the first step is to rewrite (4.65) using the $z \leftrightarrow 1-z$ symmetry to integrate over z values between 0 and 1/2. As only primary emissions are considered, one replaces the generating functional of the soft subjet by another *independent* generating functional $Z_{a,\text{prim}}(t_0, zE, zp_\perp)$ describing primary emissions:

$$-\frac{\partial Z_i^{\text{mie}}}{\partial t_0} = \sum_{(a,b)} \int_0^{1/2} \mathrm{d}z \sqrt{\frac{\hat{q}}{E}} \frac{\alpha_s \mathcal{K}_i^{ab}(z)}{2\pi\sqrt{z(1-z)}} \Big[Z_{a,\text{prim}}(t_0, zE, zp_\perp) Z_b^{\text{mie}}(t_0, (1-z)E, (1-z)p_\perp) - Z_i^{\text{mie}}(t_0, E, p_\perp) \Big] + \int \mathrm{d}^2 q_\perp \, \mathcal{C}_i(q_\perp, t_0) Z_i^{\text{mie}}(t_0, E, p_\perp - q_\perp) \tag{4.72}$$

To simplify the discussion, we ignore quark/gluon mixing. We then neglect both the longitudinal and the transverse recoils of its 4-momentum, that is $(1-z)E \simeq E$, $(1-z)p_\perp \simeq p_\perp$ and $q_\perp \ll p_\perp$. This is valid as long as $E \gg \omega_c$ since in this case, the splitting fraction z carried away by a primary medium-induced emission is at most $\omega_c/E \ll 1$. In the multiple soft scattering approximation, neglecting $q_\perp \sim Q_s$ amounts to neglect Q_s in front of $p_\perp$. As the integral of $\mathcal{C}_i(q_\perp, t_0)$ over $q_\perp$ is 0 by symmetry, the collision term for the hard branch vanishes. Note that

it is relatively easy to take into account the transverse multiple collisions for the hard branch as well, but it is beyond the goal of this calculation.

With these approximations, the master equations (4.72) for $Z^{\rm mie}$ is exactly solvable given the initial condition $Z_i^{\rm mie}(L,E,p_\perp)=u(E,p_\perp)$:

$$Z_i^{\rm mie}=u(E,p_\perp)\exp\left(\int_0^L {\rm d}t_0\int_0^{1/2}{\rm d}z\,\sqrt{\frac{\hat q}{E}}\frac{\alpha_s\mathcal{K}_i^{gi}(z)}{2\pi\sqrt{z(1-z)}}\big(Z_{g,\rm prim}(t_0,zE,zp_\perp)-1\big)\right) \tag{4.73}$$

where we have set $t_0=0$. We must find the generating functional $Z_{g,\rm prim}(t_0,E,p_\perp)$. By definition of primary emissions, we can ignore subsequent splittings. Consequently, $Z_{g,\rm prim}$ follows (4.65) without the first term associated with branchings:

$$-\frac{\partial Z_{g,\rm prim}(t_0,E,p_\perp)}{\partial t_0}=\int {\rm d}^2q_\perp\,\mathcal{C}_g(q_\perp,t_0)Z_{g,\rm prim}(t_0,E,p_\perp-q_\perp) \tag{4.74}$$

The solution of this equation with the initial condition $Z_{g,\rm prim}(L,E,p_\perp)=u(E,p_\perp)$ is

$$Z_{g,\rm prim}(t_0,E,p_\perp)=\int {\rm d}^2k_\perp u(E,k_\perp)\mathcal{P}(k_\perp-p_\perp,t_0,L) \tag{4.75}$$

where $\mathcal{P}(q_\perp,t,L)$ is the probability density for a gluon to acquire a transverse momentum $q_\perp$ during its propagation between t_0 and L. An explicit calculation of $\mathcal{P}(q_\perp,t,L)$ is given in Section 3.2.3, Eq. (3.64). As $\mathcal{P}$ is normalized to 1, one can write (4.73) as

$$Z_i^{\rm mie}(E,0\mid u)=u(E,0)\exp\left(\int {\rm d}\theta\int_0^{1/2}{\rm d}z\frac{{\rm d}^2K_{i,C/A}^{\rm mie}}{{\rm d}\theta{\rm d}z}\big(u(zE,k_\perp)-1\big)\right) \tag{4.76}$$

This form is precisely the generating functional for a Poisson process ordered in angles, provided that the corresponding rate $K_{C/A}^{i,\rm mie}$ verifies the relation:

$$\frac{{\rm d}^2K_{i,C/A}^{\rm mie}}{{\rm d}\theta{\rm d}z}=\int_0^L {\rm d}t_0\int {\rm d}^2k_\perp\,\mathcal{P}(k_\perp,t_0,L)\sqrt{\frac{\hat q}{E}}\frac{\alpha_s\mathcal{K}_i^{gi}(z)}{2\pi\sqrt{z(1-z)}}\delta\left(\theta-\frac{|k_\perp|}{z(1-z)E}\right) \tag{4.77}$$

This relation shows the correspondence between the time-average of the probability density for a parton to get a given angle and the angular rate associated with the fictitious angular-ordered branching process. In the multiple soft scattering regime, and within the harmonic approximation, one can calculate exactly the rate $K_{C/A}^{i,\rm mie}$ for a medium with constant $\hat q$:

$$\frac{{\rm d}^2K_{i,C/A}^{\rm mie}}{{\rm d}\theta{\rm d}z}=\frac{\alpha_s}{2\pi}\sqrt{\frac{\hat qL^2}{E}}\frac{\mathcal{K}_i^{gi}(z)z^2(1-z)^2E^2}{\sqrt{z(1-z)}}\frac{2\theta}{Q_s^2}\Gamma\left(0,\frac{z^2(1-z)^2E^2\theta^2}{Q_s^2}\right) \tag{4.78}$$

$$\simeq\frac{\alpha_sC_i}{\pi}\sqrt{\frac{2\omega_c}{E}}\frac{1}{z^{3/2}}\frac{2z^2E^2\theta}{Q_s^2}\Gamma\left(0,\frac{z^2E^2\theta^2}{Q_s^2}\right),\qquad\text{for } z\ll1 \tag{4.79}$$

The function $\Gamma(0,x)$ is the incomplete gamma function. In Chapter 9, we will use this expression in the soft $z\ll1$ approximation to understand the phenomenological consequences of relatively hard intrajet medium-induced emissions on substructure observables, as in [168]. Finally, one can easily find the average angle $\bar\theta$ of a primary medium-induced emission with respect to the leading parton by calculating the first angular moment of (4.78). The result is $\bar\theta=c_\star Q_s/\omega$ with $c_\star=\sqrt{\pi}/3$.

4.3.4 Longitudinally expanding medium

To conclude this chapter, we discuss how to include the longitudinal expansion of the medium to the medium induced cascade picture. The naive way of adding the expansion is to modify the emission rate (4.56) using $\hat{q}(t)$ instead of a fixed $\hat{q}$:

$$\frac{\mathrm{d}^2\mathcal{P}^{bc}_{i,\mathrm{mie}}}{\mathrm{d}z\mathrm{d}t} = \frac{\alpha_s}{2\pi}\frac{\mathcal{K}^{bc}_i(z)}{(z(1-z))^{1/2}}\sqrt{\frac{\hat{q}(t)}{E}} \underset{z\ll 1}{\simeq} \frac{\alpha_s C_i}{\pi}\frac{1}{z^{3/2}}\sqrt{\frac{\hat{q}(t)}{E}} \tag{4.80}$$

4.3.4.1 The medium-induced formation rate in expanding media

We would like to show first that this procedure is legitimate under some circumstances. First of all, we recall that the medium-induced rate comes from the following procedure. Once one knows the medium induced spectrum of an incoming parton propagating over a path length L through the medium, the rate is obtained by differentiating this spectrum with respect to L (see (4.52)). As we work within the regime $\omega \ll \omega_c \sim \hat{q}L^2/2$, the rate relevant for the master equation (4.57) is obtained in the limit $L \to \infty$. This large path length limit corresponds to the physical situation $L \gg t_f(\omega) \sim \sqrt{2\omega/\hat{q}}$. We have calculated in Chapter 3 the medium induced gluon spectrum in longitudinally expanding media for a finite jet path length, see (3.152) and Appendix B:

$$\omega\frac{\mathrm{d}N_{\mathrm{mie}}}{\mathrm{d}\omega} = \frac{2\alpha_s C_R}{\pi}\mathfrak{Re}\log\Big(|C(t_0, t_0+L|\Big) \tag{4.81}$$

where t_0 is the light cone time at which the medium is created.

As mentioned when we did this calculation, the limit $L \to \infty$ of (4.81) is generally not defined. However, the rate can always be defined after differentiation with respect to L:

$$\omega\frac{\mathrm{d}^2N_{\mathrm{mie}}}{\mathrm{d}\omega\mathrm{d}t} = \frac{2\alpha_s C_R}{\pi}\mathfrak{Re}\,\frac{-i\hat{q}(t)G^{-1}(t)}{2\omega} \tag{4.82}$$

From the definition of the function G, one shows that it satisfies the following first order (non linear) differential equation, of Riccati kind:

$$G' + G^2 + \frac{i\hat{q}(t)}{2\omega} = 0 \tag{4.83}$$

The initial condition for G is $G(t) \sim 1/(t-t_0)$ for $t \to t_0$. We just have to extract from this defining differential equation the asymptotic behaviour of $G(t)$.

As a comment before finding an equivalent of G as $t \to \infty$, we recall that one could also perfectly define the medium induced spectrum from the on-shell spectrum as in Section 3.3.3.4, leading to (see also Appendix B):

$$\omega\frac{\mathrm{d}\tilde{N}_{\mathrm{mie}}}{\mathrm{d}\omega} = \frac{2\alpha_s C_R}{\pi}\mathfrak{Re}\log\Big(|C(t_0+L, t_0|\Big) \tag{4.84}$$

from which one easily deduces the corresponding rate:

$$\omega\frac{\mathrm{d}^2\tilde{N}_{\mathrm{mie}}}{\mathrm{d}\omega\mathrm{d}t} = \frac{2\alpha_s C_R}{\pi}\mathfrak{Re}\,\bar{G}(t) \tag{4.85}$$

The function $\bar{G}$ satisfies the same non-linear differential equation as G, with a different initial condition $\bar{G}(t_0) = 0$. For large values of t, the asymptotic behaviour of $\bar{G}$ is the same as the one of G. We will comment on the differences between (4.85) and (4.82) after having found the common asymptotic behaviour of these two functions.

Asymptotic behaviour of G and $\bar{G}$. We do not claim full mathematical rigour in the demonstration of the following results. Instead, we shall give hand-waving arguments to convince of their validity. In order to make the discussion also more concrete, we use the following form for the time dependence of $\hat{q}$, inspired by the Bjorken expansion model:

$$\hat{q}(t) = \hat{q}_0 \Big(\frac{t_0}{t}\Big)^\gamma \tag{4.86}$$

In the Bjorken model, $0 < \gamma \leq 1$. In this discussion, γ can take any non-negative values: $\gamma \geq 0$. We also invite the reader to look at Fig. 3.1 to guide the eye through the following mathematical discussion: on the left figure, the asymptotes of the rates are clear. We first define the following functions:

$$g(x) = \sqrt{\frac{2\omega}{i\hat{q}_0}} G\left(\sqrt{\frac{2\omega}{i\hat{q}_0}} x\right), \qquad u(x) = g(1/x) \tag{4.87}$$

The function g enables to nondimensionalize the differential equation (4.83), and the function u is useful to study the large x asymptote of $g(x)$ by looking at the $x \to 0^+$ behaviour of $u(x)$. They satisfy the following differential equations:

$$g'(x) + g^2(x) + \kappa^\gamma x^{-\gamma} = 0 \qquad \kappa = \sqrt{\frac{i\hat{q}_0 t_0^2}{2\omega}} \tag{4.88}$$

$$u'(x) = \left(\frac{u(x)}{x}\right)^2 + \kappa^\gamma x^{\gamma-2} \tag{4.89}$$

Considering Eq. (4.89), it is natural to distinguish two cases, either $\gamma < 2$ or $\gamma > 2$:[2]

1. If $\gamma > 2$, the second term in (4.89) proportional to $x^{\gamma-2}$ goes gently to 0 as $x \to 0^+$. We then expect to find the behaviour of $u(x)$ in this limit by solving the vacuum differential equation $u' = (u/x)^2$. The general solution is $u(x) = x/(1-bx)$ with b a constant, so that $u(x) \sim x$ at small x. Thus, for $\gamma > 2$, $g(x) \sim 1/x$ at large x and $G(t) \sim 1/t$ at large times. This is the typical vacuum-like behaviour since $G(t) = 1/(t - t_0)$ when $\hat{q} = 0$, meaning that the rate in the presence of a medium with $\gamma > 2$ decreases as in the vacuum at large times. We point out that neglecting the $(u/x)^2$ term in (4.89) instead of the $x^{\gamma-2}$ term would reduce to an absurdity. Indeed, one would get $u'(x) \sim \kappa^\gamma x^{\gamma-2}$. However, in the limit $\kappa \to 0$, this gives $u'(0) = 0$ (u is continuous as a function of κ) in contradiction with the exact solutions found for $\kappa = 0$ which predict $u'(0) = 1$. Thus, the vacuum solution of (4.89) strongly constrains the small x asymptote of u when $\gamma > 2$.

2. If $\gamma < 2$, the second term on the right hand side of (4.89) explodes as $x \to 0^+$. Let us *assume* that there exists some power $\alpha \geq 0$ such that $u(x) \sim c(\kappa)\, x^\alpha$ at small x, with $c(\kappa)$ a number without dimension. To say it differently, we assume that the rate functions G and $\bar{G}$ decrease like a power law at large times. Plugging this power law behaviour inside the differential equation satisfied by u, one finds:

$$c(\kappa)\, x^{\alpha-1} - c^2(\kappa)\, x^{2(\alpha-1)} \simeq \kappa^\gamma x^{\gamma-2}, \qquad x \ll 1 \tag{4.90}$$

One cannot have $\alpha \geq 1$, otherwise the left hand side is convergent in the limit $x \to 0^+$ whereas the left hand side diverges. Moreover, for $\alpha < 1$, $x^{\alpha-1}$ is negligible in front of $x^{2(\alpha-1)}$ in the same limit. Consequently, the small x behaviour of u satisfies

$$-c(\kappa)^2 x^{2(\alpha-1)} \sim \kappa^\gamma x^{\gamma-2} \Longrightarrow u(x) \sim (-\kappa x)^{\gamma/2} \tag{4.91}$$

[2]For $\gamma = 2$, it is possible to solve exactly (4.88) and one finds that $g(x) \sim (1 + \sqrt{1-4\kappa^2})/(2x)$ for $x \to \infty$.

This gives the following large time asymptote for G:

$$G(t) \sim \sqrt{-\frac{i\hat{q}_0}{2\omega}}\left(\frac{t_0}{t}\right)^{\gamma/2} \tag{4.92}$$

Conclusion. To sum up, if $\gamma > 2$, the medium dilutes too fast so $G(t) \sim 1/t$ has a vacuum-like decay law, whereas if $\gamma < 2$, $G(t) \sim \sqrt{-i\hat{q}_0/(2\omega)}(t_0/t)^{\gamma/2}$. The function $\bar{G}(t)$ follows the same property since it satisfies the same differential equation and the arguments presented above do not rely on the initial condition for G. Therefore, if $\hat{q}(t)$ decreases at large times slower than $1/t^2$, the large time behaviour of the medium-induced rate using (4.92) in (4.82) or (4.85) is of the form:

$$\omega\frac{\mathrm{d}^2 N_{\mathrm{mie}}}{\mathrm{d}\omega \mathrm{d}t} \underset{t\to\infty}{\simeq} \frac{\alpha_s C_R}{\pi}\sqrt{\frac{\hat{q}(t)}{\omega}} \tag{4.93}$$

which is precisely the form conjectured from our naive modification of the rate in (4.80).

We point out that if $\gamma > 2$, the integral of the rate (4.85) defined from the on-shell spectrum is divergent due to the vacuum-like $1/t$ tail at large times whereas the rate (4.82) is convergent because of the additional $\hat{q}(t)$ factor. If $\gamma < 2$, both rates agree at large times but they give a divergent time integral. In any case, for finite jet path length L, such considerations are meaningless since the time integral is naturally cut at $t = L$.

The exponential case. In an exponentially decaying medium with $\hat{q}(t) = \hat{q}_0 e^{-t/\lambda}$ (a rather academic situation), the functions $G(t)$ and $\bar{G}(t)$ behave like $1/t$ at large times since the exponential vanishes faster than any power law. The integral of (4.82) over *all times* is convergent because the additional factor $\hat{q}(t)$ cuts the integral for $t \geq \lambda$. However, the finite jet path length L is a priori different from the time scale λ and the medium induced spectrum should be obtained by integrating the rate up to $t = L$ and not over all times. This can give substantial differences for the medium-induced spectrum if $\lambda \gg L$, a situation where the jet path length is much smaller than the typical decaying time λ of the medium. In this case, one can of course use $\hat{q}(t) \simeq \hat{q}_0$ in (4.83) as long as $t \ll \lambda$. The emission rate for $\sqrt{2\omega/\hat{q}_0} \ll t \ll \lambda$ behaves like the rate of a static medium with $\hat{q}$ given by $\hat{q}_0$.

4.3.4.2 Scaling properties of medium-induced jet fragmentation

Now, we assume that $\hat{q}(t)$ vanishes slower than $1/t^2$ ($\gamma < 2$) as this is the most phenomenologically relevant scenario. Using the dimensionless time τ_{exp} defined such that:

$$\frac{\mathrm{d}\tau_{\mathrm{exp}}}{\mathrm{d}t} = \bar{\alpha}_s\sqrt{\frac{\hat{q}(t)}{E}} \Longrightarrow \tau_{\mathrm{exp}} = \int_{t_0}^{t}\mathrm{d}t'\,\bar{\alpha}_s\sqrt{\frac{\hat{q}(t')}{E}} \tag{4.94}$$

in the master equation (4.57) or (4.59) with the modified rate (4.80), these equations reduce to those of a static medium written in terms of the dimensionless time $\tau = \bar{\alpha}_s t\sqrt{\hat{q}_0/E}$. This means, for instance, that the solution of (4.61) given by (4.62) is still valid, provided that τ is replaced by τ_{exp}.

The equation (4.94) enables to answer easily the following question: for a given longitudinal expansion (that is a given $\hat{q}(t)$ dependence), what is the equivalent static medium with constant $\hat{q}_{\mathrm{eff}}$ such that the fragmentation of medium-induced jet is the same in both cases? This equivalent $\hat{q}_{\mathrm{eff}}$ is obtained in order to satisfy the following scaling identity:

$$\boxed{\tau_{\mathrm{exp}}(t_0 + L) = \tau(L)} \tag{4.95}$$

so that $\hat{q}_0$ reads:

$$\hat{q}_{\text{eff}} = \left(\frac{1}{L}\int_{t_0}^{t_0+L} \mathrm{d}t'\, \hat{q}(t')^{1/2}\right)^2 \tag{4.96}$$

Mathematically, $\hat{q}_{\text{eff}}$ is equal to the 1/2-norm of the function $\hat{q}(t)$. This allows for a straightforward generalization of all our analytical results obtained in the static case, provided that one uses $\hat{q}_{\text{eff}}$ defined by (4.96) in these results. Written explicitly, the relation between $\hat{q}_{\text{eff}}$ and $\hat{q}_0$ for a given path length L is:

$$\hat{q}_{\text{eff}} = \frac{4\hat{q}_0 t_0^\gamma}{L^2(2-\gamma)^2}\left((t_0+L)^{\frac{2-\gamma}{2}} - t_0^{\frac{2-\gamma}{2}}\right)^2 \tag{4.97}$$

$$\simeq \frac{4\hat{q}_0}{(2-\gamma)^2}\left(\frac{t_0}{L}\right)^\gamma \qquad \text{if } L \gg t_0 \tag{4.98}$$

We emphasize that these results are valid as long as one focuses on soft emissions in the medium-induced cascades with $\omega \ll \omega_{c,\text{eff}} = \hat{q}_{\text{eff}} L^2/2$. Beyond this approximation, there exists anoter effective $\hat{q}$ found numerically in [66] defined as

$$\hat{q}'_{\text{eff}} = \frac{2}{L^2}\int_{t_0}^{t_0+L} \mathrm{d}t'(t'-t_0)\hat{q}(t') \tag{4.99}$$

that provides a better scaling of the BDMPS-Z spectrum in the hard regime $\omega \gtrsim \omega_c$. Consequently, if the full BDMPS-Z rate (4.82) or (4.85) is used in the master equation (4.57), instead of its soft singular limit, the scaling properties of medium-induced cascades are better when considering this effective quenching parameter $\hat{q}'_{\text{eff}}$ [169].

Chapter 5

A new factorised picture for jet evolution in a dense medium

In Chapter 4, we have treated separately the vacuum-like emissions triggered by the virtuality, or "off-shellness", of the incoming parton and the medium-induced emissions. The leading order calculations as those done in Chapter 3 combine them on equal footing, but their associated resummation schemes described in Chapter 4 are intrinsically different for the following reasons:

1. the large parameter which needs to be resummed to all orders is not the same. It is typically $\alpha_s \log^2(Q_{\rm hard}/Q_{\rm min})$ for a vacuum-like shower between the hard virtuality scale $Q_{\rm hard}$ and a soft virtuality scale $Q_{\rm min}$ — depending on the observable — whereas it is typically $\alpha_s(L/t_{f,\rm med})$ for a medium-induced cascade, with $t_{f,\rm med}$ the formation time of a medium-induced emission.

2. the variable playing the role of time in the classical branching process which effectively resums to all orders the large parameter is the angle for vacuum-like emissions and the light-cone time for medium-induced radiations.

In this chapter, we develop a resummation scheme combining both vacuum-like and medium-induced emissions. This scheme relies on physical arguments which are based on the double logarithmic approximation for the vacuum-like series. Beyond the double logarithmic approximation (DLA), one argues that vacuum-like and medium induced emissions factorise in time from each other.

Throughout this chapter, we assume that the dominant medium induced processes are multiple soft collisions so we work within the multiple soft scattering regime and harmonic approximation. This amounts to neglect hard collisions with medium constituents and assume that the mean free path of the medium is small enough compared to the typical formation time of medium-induced emissions.

5.1 The veto constraint

At double-logarithmic accuracy, one aims at resumming to all-orders contributions to a given observable enhanced by both large collinear and soft logarithms. These logarithms are generated by multiple Bremsstrahlung processes with characteristic spectrum:

$$\mathrm{d}^3 N^{\rm brem} = \frac{\alpha_s C_R}{\pi^2} \frac{\mathrm{d}\omega}{\omega} \frac{\mathrm{d}^2 k_\perp}{k_\perp^2} \tag{5.1}$$

for an emission with transverse momentum $k_\perp$ with respect to the emitter, and energy ω[1].

Consequently, in the presence of a dense QCD medium, the first task to do before any resummed calculation is to understand where the contributions to the N-particle production cross-section enhanced by large soft and collinear logarithms come from. This is the topic of this section.

The main result of this analysis is the existence of a so-called veto constraint in the phase space for gluon emissions inside the medium. This veto constraint marks the transition between the virtuality driven initial shower and the regime where the partons in the shower can be considered as on their mass shell. We first give a qualitative but physically insightful argument for the existence of this veto constraint before providing a more mathematically grounded formulation of the proof.

5.1.1 Qualitative discussion

To simplify the discussion, we shall consider that the cross-section for multi-particle production is controlled by only two medium parameters: the distance L travelled by the jet inside the medium and the jet quenching parameter $\hat{q}$ related to the average transverse momentum acquired by multiple collisions during time Δt by $\langle k_\perp^2 \rangle = \hat{q}\Delta t$. The BDMPS-Z spectrum $\mathrm{d}N^{\mathrm{mie}}$ can be approximated by the formula (3.154),

$$\mathrm{d}N^{\mathrm{mie}} \simeq \frac{\alpha_s C_R}{\pi}\sqrt{\frac{2\omega_c}{\omega^3}}\mathrm{d}\omega \tag{5.2}$$

with $\omega_c = \hat{q}L^2/2$. With respect to the Bremsstrahlung spectrum, the obvious property of the BDMPS-Z spectrum is that collinear and soft radiations are not *logarithmically* enhanced (the angular dependence of the spectrum is roughly a Gaussian distribution with width of order Q_s). This will have important consequences since working at the double-log accuracy enables to simply ignore such emissions in the multi-particle cross-section.

Vacuum-like emissions inside the medium: the veto constraint. Medium induced radiations provide a natural constraint on the phase space available for one emission inside the medium.

To see that, we first consider that the medium is very large $L \gg 1/\Lambda_{\mathrm{QCD}}$ so that one first neglects all effects related to the finite path length of the jet. We recall that t_f is determined by the uncertainty principle, namely the condition that the transverse separation $\Delta r \sim \theta t_f$ between the gluon and its parent parton at the time of emission to be as large as the gluon transverse wavelength $2/k_\perp$, with $k_\perp \simeq \omega\theta$ its transverse momentum with respect to its parent. This argument applies to both vacuum-like and medium-induced emissions and implies $t_f \simeq 2\omega/k_\perp^2 \simeq 2/(\omega\theta^2)$. Then, gluons emitted inside the medium have a minimum $k_\perp$ set by the momentum acquired via multiple collisions during its formation, $k_{f,\mathrm{med}}^2 = \hat{q}t_f$. Gluons produced inside the medium with a transverse momentum smaller than $\hat{q}t_f$ cannot exist. This translates into an upper limit $t_f \leq \sqrt{2\omega/\hat{q}}$ on the formation time of any gluon inside the medium. That said, medium induced gluons for which $k_\perp \simeq k_{f,\mathrm{med}}$ are excluded because the emission probability is not enhanced by double logarithms. Consequently, at DLA, the only contribution to the intrajet activity inside the medium comes from vacuum-like (Bremsstrahlung) emissions with $k_\perp \geq k_{f,\mathrm{med}}$, inequality which becomes strong to our level of accuracy: $k_\perp \gg k_{f,\mathrm{med}}$ or

[1] In this chapter, we shall generically call ω the light cone k^+ component of a 4-momentum k^μ and identify it with its energy.

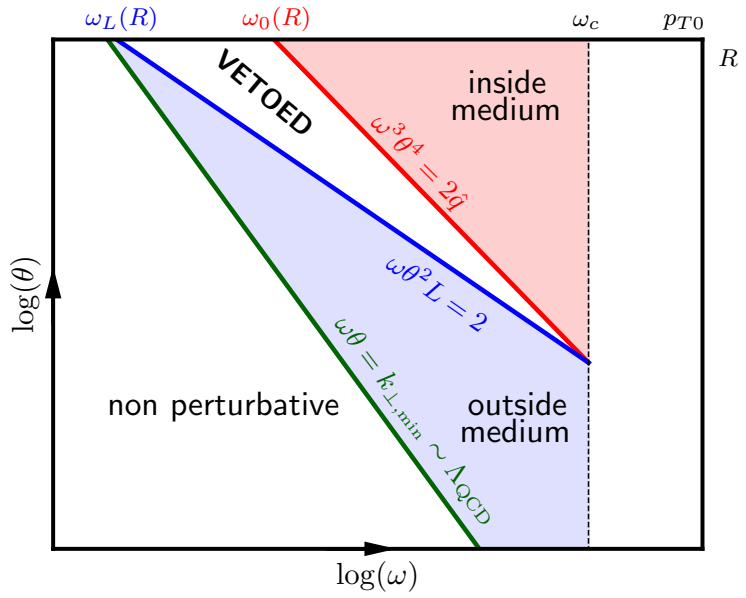

Figure 5.1: Phase space for vacuum-like emissions at DLA considered in this thesis, represented in terms of the energy ω and the angle θ (with respect to the parent) of emission. The red line is the lower boundary of the "in-medium" region defined by the veto constraint $k_\perp \geq k_{f,\rm med}$. The blue line is the line of vacuum formation time equal to the jet path length L through the medium: $t_f = L$. The green line is the hadronisation line $k_\perp = \Lambda_{\rm QCD}$ providing the lower boundary of the perturbative phase space. Between the red and the blue line, the phase space gap appearing is the vetoed region discussed in the main text.

equivalently $t_f \ll \sqrt{2\omega/\hat{q}}$. This means that VLEs occur much faster than medium-induced radiations with the same energy. This is the condition for an emission *inside* the medium to be vacuum-like. Thereafter, we shall refer to this condition as the "in-medium veto constraint".

Finite path length effects. Strictly speaking, the veto constraint $k_\perp \gg k_{f,\rm med}$ applies for very large path length $L \gg 1/\Lambda_{\rm QCD}$. For a realistic path length L in the medium, one should also take into account emissions *triggered by the initial virtuality* but occurring directly outside with a formation time *measured from the hard process* larger than L: $t_f \geq L$. Note also that emissions with energies larger than ω_c, $\omega \geq \omega_c = \hat{q}L^2/2$, behave exactly as in the vacuum: their emission angle can be arbitrarily small in the perturbative domain and their formation time can be larger than L.

These two conditions for VLEs, either inside with $t_f \ll \sqrt{2\omega/\hat{q}}$ or outside with $t_f \gg L$ can be written in terms of their energies ω and angles with respect to the emitter θ:

$$\text{In-medium veto constraint:} \quad t_f \ll \sqrt{2\omega/\hat{q}} \iff \omega \gg \omega_0(\theta) = (2\hat{q}/\theta^4)^{1/3} \tag{5.3}$$

$$\text{Medium size constraint:} \quad t_f \gg L \iff \omega \ll \omega_L(\theta) = 2/(\theta^2 L) \tag{5.4}$$

It is enlightening to represent these conditions on a (ω, θ) phase space as in Fig. 5.1. The red curve is the line $k_\perp = k_{f,\rm med}$ and the blue curve is the line $t_f = L$. Compared to the vacuum case for which the phase space is only restricted by the hadronisation line $k_\perp \simeq \omega\theta = \Lambda_{\rm QCD}$, the effect of the medium on the phase space available for VLEs is the presence of a gap or "vetoed region".

5.1.2 Derivation of the veto constraint from leading order calculations

Now, we would like to give a more formal proof of the existence of a veto constraint in the phase space for VLEs. The ultimate goal of this subsection are formulas (5.15) and (5.24).

We have seen in Chapter 3 that the spectrum of an off-shell quark can be written:

$$\omega\frac{\mathrm{d}^3N^{\text{off-shell}}}{\mathrm{d}\omega\mathrm{d}^2k_\perp}=\frac{\alpha_sC_F}{\pi^2}\frac{1}{k_\perp^2}+\omega\frac{\mathrm{d}^3N^{\text{mie}}}{\mathrm{d}\omega\mathrm{d}^2k_\perp} \tag{5.5}$$

where the second piece is perfectly integrable over all $k_\perp$ and gives precisely the BDMPS-Z spectrum. Even if such a decomposition is not unique, the integral of $\mathrm{d}^3N^{\text{off}}$ gives always the logarithmic area of the full perturbative phase space plus a piece without collinear logarithms corresponding to the integrated medium-induced spectrum.

We will argue that the $1/k_\perp^2$ term in the expression (5.5) comes from different physical mechanisms, not necessarily related to the initial virtuality of the process. Through detailed analytical calculations which have been put in Appendix F for the sake of brevity, we disentangle these different contributions. We show that `(i)` in an infinite static medium, the transverse momenta of emissions *at formation* is bounded by $k_{f,\text{med}}$, `(ii)` it is physically more insightful to decompose the off-shell spectrum (5.5) in another way. In this new decomposition, the first term corresponds to the VLEs with short formation time constrained by the veto $k_\perp > k_{f,\text{med}}$ whereas the second term is "medium-induced". We finally argue that Bremsstrahlung emissions with $t_f \gg L$ contained in the latter component are the only one that must be resummed to all orders in a leading twist approximation.

In all this subsection, we assume a static medium and $\omega \leq \omega_c$ since all the interesting features of the medium appear in this regime.

5.1.2.1 The off-shell spectrum at formation in the infinite path length limit

We first emphasize that the above discussion of the phase space for vacuum-like emissions refers only to their kinematic at formation. Final state broadening and energy loss subsequently move the emissions on this phase space. This leads to the concept of off-shell spectrum *at formation*: in this spectrum, one removes by hand the final state broadening of the emitted gluon by setting:

$$\mathcal{P}(k_\perp-q_\perp,t_1,t_2)=\delta(k_\perp-q_\perp) \tag{5.6}$$

In the next subsection, we will relax this approximation and take also into account the final state broadening.

Let us then rewrite the off-shell spectrum obtained in (3.141) (more precisely (3.127)) where the final state broadening appears as a convolution:

$$\omega\frac{\mathrm{d}^3N^{\text{off-shell}}}{\mathrm{d}\omega\mathrm{d}^2k_\perp}=\frac{\alpha_sC_F}{\pi^2}2\mathfrak{Re}\int_0^\infty\mathrm{d}y^+\,e^{-\varepsilon y^+}\int\mathrm{d}^2q_\perp\mathcal{P}(k_\perp-q_\perp,y^+,\infty)\\ \times\frac{q_\perp^2}{(2i\omega)^2}\int_0^{y^+}\mathrm{d}\bar{y}^+\,\frac{-e^{-\varepsilon\bar{y}^+}}{C^2(\bar{y}^+,y^+)}e^{\frac{-q_\perp^2S(y^+,\bar{y}^+)}{2i\omega C(\bar{y}^+,y^+)}} \tag{5.7}$$

where the position of the hard vertex is here 0. Using (5.6) in (5.7), one finds:

$$\omega\frac{\mathrm{d}^3N^{\text{off-shell,f}}}{\mathrm{d}\omega\mathrm{d}^2k_\perp}=\frac{\alpha_sC_F}{\pi^2}\frac{k_\perp^2}{(2\omega)^2}2\mathfrak{Re}\int_0^\infty\mathrm{d}y^+\int_0^{y^+}\mathrm{d}\bar{y}^+\,e^{-\varepsilon(y^++\bar{y}^+)}\frac{1}{C^2(\bar{y}^+,y^+)}e^{\frac{-k_\perp^2S(y^+,\bar{y}^+)}{2i\omega C(\bar{y}^+,y^+)}} \tag{5.8}$$

where the superscript "f" is put to highlight the difference between this off-shell spectrum at formation and the complete off-shell spectrum.

Instead of elucidating the functions S and C for a static medium (they are given in Appendix B though), we show that for $y^+ - \bar{y}^+ \ll t_{f,\text{med}} \equiv \sqrt{2\omega/\hat{q}}$, these two functions have their vacuum-like form, that is:

$$S_{\text{vac}}(y^+, \bar{y}^+) = y^+ - \bar{y}^+ \tag{5.9}$$

$$C_{\text{vac}}(\bar{y}^+, y^+) = 1 \tag{5.10}$$

To proceed, we find, thanks to the defining differential equation (3.107) the Taylor expansion of these functions when y^+ is close to $\bar{y}^+$ (short formation times). We will use the same method to derive the veto constraint in an expanding plasma. From the differential equation (3.107), the Taylor expansion of S and C around $y^+ = \bar{y}^+$ gives:

$$S(y^+, \bar{y}^+) = (y^+ - \bar{y}^+) - \frac{1}{6}\frac{i\hat{q}}{2\omega}(y^+ - \bar{y}^+)^3 + \mathcal{O}\big((y^+ - \bar{y}^+)^4\big) \tag{5.11}$$

$$C(\bar{y}^+, y^+) = 1 - \frac{1}{2}\frac{i\hat{q}}{2\omega}(y^+ - \bar{y}^+)^2 + \mathcal{O}\big((y^+ - \bar{y}^+)^3\big) \tag{5.12}$$

Thus, when $t_f = |y^+ - \bar{y}^+| \ll t_{f,\text{med}}$ one can use $C(\bar{y}^+, y^+) \simeq 1$ and $S(y^+, \bar{y}^+) \simeq y^+ - \bar{y}^+$, and neglect the sub-leading terms in the Taylor expansion. In the off-shell spectrum at formation, one then split the integral into two pieces: one with $y^+ \leq t_{f,\text{med}}$ (where $y^+ - \bar{y}^+ \leq t_{f,\text{med}}$ since $\bar{y}^+ \leq y^+$), and the other with $y^+ \geq t_{f,\text{med}}$ but $y^+ - t_{f,\text{med}} \leq \bar{y}^+ \leq y^+$. Using the vacuum approximations for the functions S and C and keeping only the terms with a leading $1/k_\perp^2$ singularity, this calculation gives:

$$\begin{aligned}\omega\frac{\mathrm{d}^3 N^{\text{off-shell,f } t_f \leq t_{f,\text{med}}}}{\mathrm{d}\omega \mathrm{d}^2 k_\perp} \simeq{}& \frac{\alpha_s C_F}{\pi^2} 2\mathfrak{Re}\int_0^{t_{f,\text{med}}} \mathrm{d}y^+ \frac{1}{2i\omega}\Big(-1 + e^{\frac{-k_\perp^2 y^+}{2i\omega}}\Big) \\ &+ \frac{\alpha_s C_F}{\pi^2} 2\mathfrak{Re}\int_{t_{f,\text{med}}}^{\infty} \mathrm{d}y^+ \, e^{-2\varepsilon y^+} \frac{\varepsilon}{k_\perp^2}\Big(-1 + e^{\frac{-k_\perp^2 t_{f,\text{med}}}{2i\omega}}\Big)\end{aligned} \tag{5.13}$$

In this calculation, it is again very important to keep track of the ε dependence up to the first order in the piece with y^+ unbounded. The second integral over y^+ then gives a factor $1/2$ in the limit $\varepsilon \to 0$. The first integral is easy and gives the same value as the second piece with an extra factor -2, leading to the final result:

$$\omega\frac{\mathrm{d}^3 N^{\text{off-shell,f } t_f \leq t_{f,\text{med}}}}{\mathrm{d}\omega \mathrm{d}^2 k_\perp} \simeq \frac{\alpha_s C_F}{\pi^2}\frac{1}{k_\perp^2}\mathfrak{Re}\Big(1 - e^{\frac{-k_\perp^2 t_{f,\text{med}}}{2i\omega}}\Big) \tag{5.14}$$

in the collinear limit. This spectrum is suppressed for $|k_\perp^2 t_{f,\text{med}}/(2i\omega)| \ll 1$ and averages to 1 for $|k_\perp^2 t_f/(2i\omega)| \gg 1$, giving precisely the in-medium veto constraint:

$$\omega\frac{\mathrm{d}^3 N^{\text{off-shell,f } t_f \leq t_{f,\text{med}}}}{\mathrm{d}\omega \mathrm{d}^2 k_\perp} \simeq \frac{\alpha_s C_F}{\pi^2}\frac{1}{k_\perp^2}\Theta(k_\perp - k_{f,\text{med}}) \tag{5.15}$$

To sum up, the off-shell spectrum at formation has a Bremsstrahlung component for $k_\perp \gg k_{f,\text{med}}$ coming from the short formation time emissions with $t_f = y^+ - \bar{y}^+ \ll t_{f,\text{med}}$. To prove the result asserted in our qualitative discussion of the in-medium veto constraint, one should also show that in the infinite path length limit, it is the *only* Bremsstrahlung-like component. This is easy. In the infinite path length limit, the function S and C for a static medium are given by

$$S(y^+, \bar{y}^+) = \Omega^{-1}\sin\Big(\Omega(y^+ - \bar{y}^+)\Big) \tag{5.16}$$

$$C(\bar{y}^+, y^+) = \cos\Big(\Omega(y^+ - \bar{y}^+)\Big) \tag{5.17}$$

with $\Omega^2 = i\hat{q}/(2\omega)$. Thus, the phase inside the exponential of formula (5.8) reads:

$$\frac{S(y^+,\bar{y}^+)}{C(\bar{y}^+,y^+)} = \bar{\Omega}^{-1}\tanh\Big(\bar{\Omega}(y^+-\bar{y}^+)\Big) \underset{y^+-\bar{y}^+\geq t_{f,\mathrm{med}}}{\simeq} \bar{\Omega}^{-1} \tag{5.18}$$

which does not lead to a collinear singularity at small $k_\perp$:

$$\omega\frac{\mathrm{d}^3N^{\text{off-shell,f } t_{f,\mathrm{med}}\leq t_f}}{\mathrm{d}\omega\mathrm{d}^2k_\perp} \simeq \frac{\alpha_s C_F}{\pi^2}\frac{k_\perp^2}{(2\omega)^2} 2\mathfrak{Re}\left[\frac{\mathcal{N}}{\Omega^2}\exp\left(-\frac{1-i}{\sqrt{2}}\frac{k_\perp^2}{k_{f,\mathrm{med}}}\right)\right] \tag{5.19}$$

$$\mathcal{N} = \Omega^2\int_{t_{f,\mathrm{med}}}^{\infty}\mathrm{d}y^+\int_0^{y^+-t_{f,\mathrm{med}}}\mathrm{d}\bar{y}^+\frac{e^{-\varepsilon(y^++\bar{y}^+)}}{C^2(\bar{y}^+,y^+)} \tag{5.20}$$

where $\mathcal{N}$ is a $k_\perp$ independent dimensionless factor which diverges in the limit $\varepsilon\to 0$ since for an infinite medium path length, the amount of induced radiations blows up in a static medium[2]. Thus, for $t_f > t_{f,\mathrm{med}}$, the off-shell spectrum at formation is strongly peaked around $k_\perp \simeq k_{f,\mathrm{med}}$ due to the exponential suppression of the form $\exp(-k_\perp^2/k_{f,\mathrm{med}})$ in (5.8). In physical terms, in the infinite medium length limit: either the emission spectrum is vacuum-like with a double logarithmic singularity at small $k_\perp$ and ω but constrained by $k_\perp \gg k_{f,\mathrm{med}}$, or it saturates the condition $k_\perp = k_{f,\mathrm{med}}$. However, in the latter case, the spectrum has no collinear singularity. In this formal limit, no emission occurs with $k_\perp \leq k_{f,\mathrm{med}}$.

5.1.2.2 Broadening and finite path length effects

The previous discussion aimed at proving the existence of the red line in the phase space (at formation) for vacuum-like emissions shown in Fig. 5.1. To discuss the rest of this phase space, beyond the infinite path length limit, we find extremely convenient to define the following quantity, that we call "vacuum-like spectrum in a dense medium":

$$\omega\frac{\mathrm{d}^3N^{\mathrm{VL}}}{\mathrm{d}\omega\mathrm{d}^2k_\perp} \equiv \omega\frac{\mathrm{d}^3N^{\text{off-shell}}}{\mathrm{d}\omega\mathrm{d}^2k_\perp} - \omega\frac{\mathrm{d}^3N^{\text{on-shell}}}{\mathrm{d}\omega\mathrm{d}^2k_\perp} \tag{5.21}$$

This definition naturally subtracts all the emissions which are not related to the initial virtuality of the parton. Then, the off-shell spectrum is rewritten:

$$\omega\frac{\mathrm{d}^3N^{\text{off-shell}}}{\mathrm{d}\omega\mathrm{d}^2k_\perp} = \omega\frac{\mathrm{d}^3N^{\mathrm{VL}}}{\mathrm{d}\omega\mathrm{d}^2k_\perp} + \omega\frac{\mathrm{d}^3N^{\text{on-shell}}}{\mathrm{d}\omega\mathrm{d}^2k_\perp} \tag{5.22}$$

This expression has a clear physical interpretation: the first term is to be associated with emissions triggered by the virtuality of the leading parton, whereas the second term corresponds to emissions which are all "medium-induced" since an on-shell quark would not radiate in the vacuum. Nevertheless, in spite of being medium-induced, they could have a Bremsstrahlung-like form. This is what we want to understand.

The expression (5.21) has an explicit μ regularization dependence, remnant of the μ dependence of the on-shell cross section discussed in Chapter 3, Section 3.3.3.3. Of course, by

[2]Rigorously speaking, we have made the assumption that $\hat{q}$ vanishes at sufficiently large times to derive the off-shell spectrum derived in Chapter 3, so one may wonder if our reasoning and especially formula (5.7) remain valid for an infinite path length through a static medium. Actually, one can assume that $\hat{q}(t)$ vanishes very slowly (the criterion is slower than $1/t^2$ at large times, see Section 4.3.4), so that formula (5.7) applies as well as the results (5.15) and (5.19) with $t_{f,\mathrm{med}}$ and $k_{f,\mathrm{med}}$ calculated in Section 5.1.3. Of course, even in this case, the factor $\mathcal{N}$ is still divergent when $\varepsilon\to 0$, but the $k_\perp$ dependence of the spectrum we find is right.

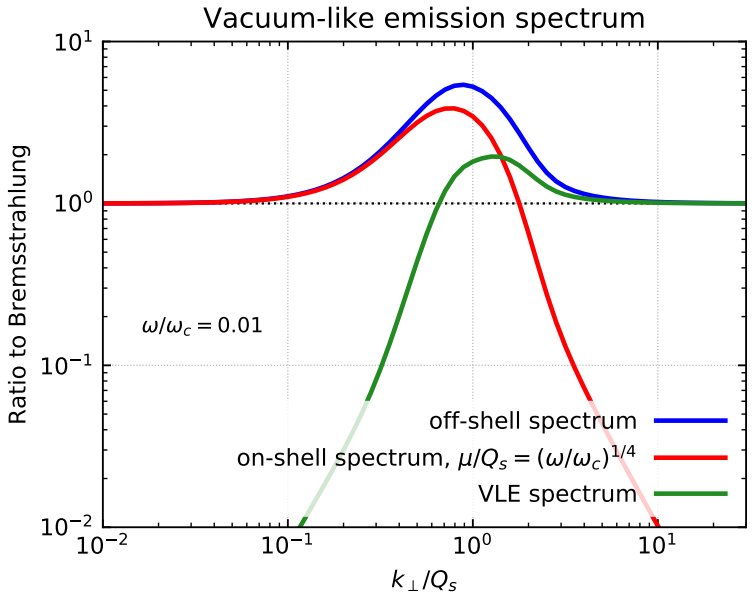

Figure 5.2: Vacuum-like emission spectrum (5.21) (green curve) as a function of $k_\perp/Q_s$ for a static medium, compared to the off-shell (blue curve) and on-shell (red curve) spectra. The spectra are normalized by the vacuum Bremsstrahlung spectrum. The choice $\mu/Q_s = (\omega/\omega_c)^{1/4}$ for the regularisation of the on-shell cross-section corresponds to $\mu = k_{f,\text{med}}$. At small $k_\perp$, the off-shell and the on-shell spectra coincide.

construction this μ dependence cancels in the off-shell spectrum (5.22) so we could choose μ as we want. The crucial point here is that there is a choice of μ which makes the physical content of (5.22) transparent. We now justify this choice of μ.

In QCD, as strictly on-shell partons do not exist, the meaning of "on-shellness" is *relative to a given virtuality scale*. For instance, if the virtuality of an incoming parton is much smaller than the hard scattering scale, it makes sense to consider it as an idealized on-shell asymptotic state. In the scattering of an on-shell quark with a dense medium that we are discussing now, the minimal momentum transferred in the process is of order $k_{f,\text{med}}$ so the "on-shellness" of the quark is relative to this scale.

With this perspective, we point out that μ is of order of the small virtuality of the incoming almost on-shell parton. This is clear from the "onium regularization" studied in Section 3.4.1.4. The divergence is regulated by the frozen transverse size $X_\perp$ of the onium: $\mu \sim 1/X_\perp$, itself related to the virtuality Q of the photon sourcing the onium by $X_\perp \sim 1/Q$. Consequently, for the calculation (5.21) to make sense, the small virtuality μ of the on-shell incoming quark should not be larger than $k_{f,\text{med}}$. For reasons that will become clear afterwards, we choose μ that saturates this constraint, i.e. $\mu = k_{f,\text{med}}$:

$$\omega \frac{\mathrm{d}^3 N^{\text{VL}}}{\mathrm{d}\omega \mathrm{d}^2 k_\perp} \equiv \omega \frac{\mathrm{d}^3 N^{\text{off-shell}}}{\mathrm{d}\omega \mathrm{d}^2 k_\perp} - \omega \frac{\mathrm{d}^3 N^{\text{on-shell}}}{\mathrm{d}\omega \mathrm{d}^2 k_\perp}\Big|_{\mu = k_{f,\text{med}}} \tag{5.23}$$

This is somehow our working hypothesis: *the scale $k_{f,med}$ must be considered as the transition scale between "offshellness" and "onshellness" in the presence of a dense medium.*

With this definition, we show in Appendix F that the leading behaviour of (5.21) in the soft and collinear limit is:

$$\omega\frac{\mathrm{d}^3N^{\mathrm{VL}}}{\mathrm{d}\omega\mathrm{d}^2k_\perp}\simeq\frac{\alpha_sC_F}{\pi^2}\int\frac{\mathrm{d}^2q_\perp}{q_\perp^2}\mathcal{P}(k_\perp-q_\perp,0,L)\Theta(|q_\perp|-k_{f,\mathrm{med}}) \tag{5.24}$$

This expression has a clear probabilistic picture for vacuum-like emissions in a dense medium in agreement with our initial qualitative discussion. These emissions have a very short formation time $t_f \ll \sqrt{2\omega/\hat{q}}$ and are created *inside* so that they subsequently undergo momentum broadening over the full path length L. The medium only restricts the phase space so that only emissions with $k_\perp > k_{f,\mathrm{med}}$ are allowed. This is precisely the veto constraint on in-medium vacuum-like emissions discussed in the previous subsection, with the final state broadening of the emitted gluon included.

The spectrum 5.24 does not account for the finite path length L of the off-shell parton in the medium and especially the vacuum-like radiations outside with $t_f \gg L$ discussed in section (5.1.1). Actually, these emissions are all included in the on-shell term in (5.22)! In mathematical terms, the on-shell spectrum with $\mu = k_{f,\mathrm{med}}$ reads (see Appendix F for the detailed calculations):

$$\omega\frac{\mathrm{d}^3N^{\text{on-shell}}}{\mathrm{d}\omega\mathrm{d}^2k_\perp}\simeq\text{“BDMPS-Z”}+\frac{\alpha_sC_F}{\pi^2}\frac{1}{k_\perp^2}\Theta(k_{f,\mathrm{med}}-k_\perp) \tag{5.25}$$

The BDMPS-Z term is a $k_\perp$ integrable term that gives the BDMPS-Z spectrum once integrated over $k_\perp$. The second term has the Bremsstrahlung form, but is bounded from above by $k_\perp \leq k_{f,\mathrm{med}}$. Such a contribution is expected, as the interactions with the medium put the initially on-shell quark off its mass-shell, so that it radiates afterwards according to the Bremsstrahlung law. What is somehow unexpected is that the upper boundary is given by $k_{f,\mathrm{med}}$ and not Q_s, the maximal transverse momentum acquired via multiple soft collisions during the propagation of the quark through the medium over a time L.

Now the question of the *iteration* or resummation of these Bremsstrahlung-like emissions appearing in (5.25) arises. We remind the reader that we are looking for *leading twist* modifications of the intrajet radiation pattern, that is emissions triggered by the virtuality of the parent parton and not by the scattering with the medium. In this sense, the spectrum (5.25) *alone* is not leading-twist since the initial quark is on its mass shell, and therefore should not be iterated. However, in (5.22), this on-shell spectrum is a component of the off-shell one. This suggests that there are also leading twist emissions in the second term of (5.22).

We now justify that only the contributions with $t_f \gg L$, that is $k_\perp^2 \ll 2\omega/L$ should be considered as leading twist in the second term of (5.25). There is clearly a competition between two kinds of Bremsstrahlung in the single gluon emission spectrum from an off-shell quark:

- the Bremsstrahlung associated with the initial large virtuality of the quark,
- the Bremsstrahlung associated with the scattering of the quark with the medium, giving a smaller virtuality of order $k_{f,\mathrm{med}}$ to the quark. This explains the presence of the scale $k_{f,\mathrm{med}}$ in (5.25).

In our language, the former is said “leading twist”, the latter is “higher twist”. To simplify the discussion, let us consider that the full medium acts as a *single scattering center* transferring a typical momentum $k_{f,\mathrm{med}}$ and located at light cone time L. One knows that there exist two regimes according to the ratio between L and $t_f = 2\omega/k_\perp^2$:

1. If $t_f \ll L$, the Bremsstrahlung radiations associated with the initial virtuality and the final state radiations associated with the scattering add up *incoherently*. With the constraint

$t_f \ll L$, the support of the Bremsstrahlung spectrum associated with the initial virtuality is $k_\perp \gg k_{f,\mathrm{med}}$ since we have just shown that in-medium leading twist Bremsstrahlung are bounded from below by $k_{f,\mathrm{med}}$. The support of the Bremsstrahlung associated with the scattering is constrained by $(2\omega/L)^{1/2} \ll k_\perp \ll k_{f,\mathrm{med}}$. Hence, there is no overlap between the two mechanisms in the phase space $k_\perp^2 \gg 2\omega/L$.

2. If $t_f \gg L \Leftrightarrow k_\perp^2 \ll 2\omega/L$, the two Bremsstrahlung *interferes*, as in the LPM effect, and cannot be distinguished from each other. Physically, the wavelength of the gluon is so large that it does not resolve the source of the virtuality of its parent. Nevertheless, this is a leading twist effect which must be iterated.

The interested reader should go to Appendix F to check these results in the simple case of the shockwave limit of the off-shell spectrum. In this calculation, the medium-induced spectrum defined as in (5.5) reads:

$$\omega\frac{\mathrm{d}N^{\mathrm{mie,\ SW}}}{\mathrm{d}\omega} \simeq \frac{2\alpha_s C_F}{\pi}\log\left(\frac{LQ_s^2}{2\omega}\right) \tag{5.26}$$

with L the light-cone time location of the shockwave. This is precisely the logarithmic area of the vetoed region in the shockwave limit where the transverse scale $k_{f,\mathrm{med}}$ is replaced by Q_s. This shows that a higher twist effect can produce logarithms in the multiple soft scattering approximation, at the level of the single gluon spectrum.

The final decomposition of the off-shell spectrum relevant for the resummation performed in the next section is then:

$$\omega\frac{\mathrm{d}^3N^{\text{off-shell}}}{\mathrm{d}\omega\mathrm{d}^2k_\perp} = \underbrace{\frac{\alpha_s C_F}{\pi^2}\int\frac{\mathrm{d}^2q_\perp}{q_\perp^2}\mathcal{P}(k_\perp-q_\perp,0,L)\Theta(|q_\perp|-k_{f,\mathrm{med}}) + \frac{\alpha_s C_F}{\pi^2}\frac{1}{k_\perp^2}\Theta(2\omega/L-k_\perp^2)}_{\text{leading-twist}}$$
$$+\underbrace{\text{“BDMPS-Z”} + \frac{\alpha_s C_F}{\pi^2}\frac{1}{k_\perp^2}\Theta(k_{f,\mathrm{med}}-k_\perp)\Theta(k_\perp^2-2\omega/L)}_{\text{higher twist}} \tag{5.27}$$

We believe that this decomposition is much more physical (as far as one is concerned with the resummation of vacuum-like emissions in the presence of a dense medium) than the naive one (5.5) from which we have started this section.

The conclusion to drawn from this discussion is that an apparent “Bremsstrahlung” form for an emission spectrum is not a sufficient condition to iterate such emissions in the leading twist approximation. The latter condition imposed, i.e. if one aims at resumming only emissions driven by the high virtuality of the process, the phase space for vacuum-like emissions is the one described in Section 5.1.1. That said, we leave for further studies the incorporation of this medium-induced Bremsstrahlung component in the phase space $2\omega/L \ll k_\perp^2 \ll k_{f,\mathrm{med}}^2$ to our global pQCD picture (see discussion in 5.2.5).

5.1.3 Veto constraint in longitudinally expanding media

5.1.3.1 The general case

The calculations made in the previous subsection in order to obtain the veto constraint for VLEs in a dense static medium can be easily generalised for longitudinally expanding media. The method is straightforward: in the leading order off-shell spectrum *at formation*, one finds the leading soft and collinear singularity coming from the integration domain $|y^+ - \bar{y}^+| \leq t_{f,\mathrm{med}}$, for

some $t_{f,\mathrm{med}}$, where the functions S and C have their vacuum form. The leading $1/k_\perp^2$ behaviour extracted in this way will have the signature of the constraints on VLEs inside the medium.

We first consider the case where the off-shell parton is created at light cone time t_0 inside the medium. Then the medium expands longitudinally. The easiest way to do the calculation is to use the expression (5.8) and the Taylor expansion method. In an expanding medium, $\hat{q}$ depends on y^+:

$$S(y^+,\bar{y}^+) = (y^+-\bar{y}^+) - \frac{1}{6}\frac{i\hat{q}(\bar{y}^+)}{2\omega}(y^+-\bar{y}^+)^3 + \mathcal{O}\big((y^+-\bar{y}^+)^4\big) \tag{5.28}$$

$$C(\bar{y}^+,y^+) = 1 - \frac{1}{2}\frac{i\hat{q}(y^+)}{2\omega}(\bar{y}^+-y^+)^2 + \mathcal{O}\big((\bar{y}^+-y^+)^3\big) \tag{5.29}$$

Note that one can also use $\hat{q}(y^+)$ in the Taylor expansion of S since the difference $\hat{q}(y^+)-\hat{q}(\bar{y}^+)$ is of order $\mathcal{O}((y^+-\bar{y}^+))$ if $\hat{q}(t)$ is derivable.

The condition to use $C(y^+,\bar{y}^+)\simeq 1$ and $S(y^+,\bar{y}^+)\simeq y^+-\bar{y}^+$ is:

$$(y^+-\bar{y}^+)^2 \le (2\omega)/\hat{q}(y^+) \equiv t_{f,\mathrm{med}}^2(y^+) \tag{5.30}$$

In the expanding case, the only extra difficulty is that the medium induced formation time depends on time. Let us call $t^\star_{f,\mathrm{med}}(\omega)$ the smallest solution of the equation $y^+ = t_0 + t_{f,\mathrm{med}}(y^+)$ larger than t_0 (if such solution exists):

$$t^\star_{f,\mathrm{med}} - t_0 = \sqrt{\frac{2\omega}{\hat{q}(t^\star_{f,\mathrm{med}})}} \tag{5.31}$$

By construction, one has $y^+ - t_{f,\mathrm{med}}(y^+) \le t_0$ for $y^+ \le t^\star_{f,\mathrm{med}}$ and $y^+ - t_{f,\mathrm{med}}(y^+) \ge t_0$ for $y^+ \ge t^\star_{f,\mathrm{med}}$ (at least in a neighbourhood of $t^\star_{f,\mathrm{med}}$).

Consequently, coming back to (5.7), the integral over y^+ can be split into two pieces: $y^+ \le t^\star_{f,\mathrm{med}}$ and $y^+ \ge t^\star_{f,\mathrm{med}}$. The two pieces give the following result in the soft and collinear limit:

$$\begin{aligned}\omega\frac{\mathrm{d}^3N^{\text{off-shell,f } t_f\le t_{f,\mathrm{med}}}}{\mathrm{d}\omega\mathrm{d}^2k_\perp} \simeq{}& \frac{\alpha_s C_F}{\pi^2}2\mathfrak{Re}\int_{t_0}^{t^\star_{f,\mathrm{med}}}\mathrm{d}y^+\frac{1}{2i\omega}\Big(-1+e^{\frac{-k_\perp^2(y^+-t_0)}{2i\omega}}\Big)\\ &+\frac{\alpha_s C_F}{\pi^2}2\mathfrak{Re}\int_{t^\star_{f,\mathrm{med}}}^{\infty}\mathrm{d}y^+\,e^{-2\varepsilon y^+}\frac{\varepsilon}{k_\perp^2}\Big(-1+e^{\frac{-k_\perp^2 t_f(y^+)}{2i\omega}}\Big)\end{aligned} \tag{5.32}$$

With respect to the static case, the second term is weird because $t_{f,\mathrm{med}}(y^+)\to\infty$ at large times in a diluting medium. This is because the condition $y^+-\bar{y}^+\le t_{f,\mathrm{med}}(y^+)$ does not make sense when y^+ is large. To avoid this difficulty, we take our cue from the static calculation and fix $t_{f,\mathrm{med}}(y^+)$ to $t_{f,\mathrm{med}}(t^\star_{f,\mathrm{med}}) = t^\star_{f,\mathrm{med}} - t_0$ in the second term of (5.32)[3]. Then, as in the fixed $\hat{q}$ case, the piece with $y^+\ge t^\star_{f,\mathrm{med}}(\omega)$ gives a factor 1/2 and the first term can be integrated explicitly:

$$\omega\frac{\mathrm{d}^3N^{\text{off-shell,f } t_f\le t_{f,\mathrm{med}}}}{\mathrm{d}\omega\mathrm{d}^2k_\perp} \simeq \frac{\alpha_s C_F}{\pi^2}\frac{1}{k_\perp^2}\Theta\left(k_\perp - \Big(\frac{2\omega}{t^\star_{f,\mathrm{med}}-t_0}\Big)^{1/2}\right) \tag{5.33}$$

The step function in (5.33) gives the veto constraint on vacuum-like emissions in an expanding medium. This can be rewritten in a form similar to the static case:

$$k_\perp \ge (2\hat{q}^\star\omega)^{1/4} \tag{5.34}$$

with $\hat{q}^\star = \hat{q}(t^\star_{f,\mathrm{med}})$.

[3]For a cleaner proof, we show in Appendix F that the second term in (5.32) is actually irrelevant to get the veto constraint. The latter can always be read in the first term alone. The price to pay is that a factor 2 appears in front of the spectrum, but this factor 2 cancels when using the spectrum (5.21).

Illustrative example: exponential decay The most simple time dependent $\hat{q}$ is the exponential decay, with $t_0 = 0$:

$$\hat{q}(t) = \hat{q}_0 \exp(-t/\lambda) \tag{5.35}$$

In this case, the scale $t^\star_{f,\mathrm{med}}(\omega)$ is solution of the implicit equation:

$$\exp(-t^\star_{f,\mathrm{med}}/\lambda) t^{\star 2}_{f,\mathrm{med}} = 2\omega/\hat{q}_0 \tag{5.36}$$

When $\omega \ll \hat{q}_0\lambda^2$, i.e $t^\star_{f,\mathrm{med}} \ll \lambda$, one can approximate the exponential by one, so that

$$t^\star_{f,\mathrm{med}}(\omega) \sim \sqrt{\frac{2\omega}{\hat{q}_0}} \tag{5.37}$$

and then, the transverse momentum of vacuum-like emissions inside the medium is such that $k_\perp \geq (2\hat{q}_0\omega)^{1/4}$. Note than one would obtain the same result using the argument given in Section 5.1.1 amended to take into account the time dependence of $\hat{q}$. During its formation $t_f = 2\omega/k_\perp^2$, an emission acquires a typical transverse momentum $k_{f,\mathrm{med}}$ given by:

$$k^2_{f,\mathrm{med}} = \int_0^{t_f} \mathrm{d}t\, \hat{q}(t) = \hat{q}_0\lambda(1 - \exp(-t_f/\lambda)) \underset{t_f \ll \lambda}{\simeq} \hat{q}_0 t_f \tag{5.38}$$

so that the condition $k_\perp^2 \geq k^2_{f,\mathrm{med}}$ gives also $k_\perp \geq (2\hat{q}_0\omega)^{1/4}$.

5.1.3.2 Bjorken expansion

For a Bjorken expansion, the time dependence of $\hat{q}$ is:

$$\hat{q}(t) = \hat{q}_0 \Big(\frac{t_0}{t}\Big)^\gamma \Theta(t - t_0) \tag{5.39}$$

with $0 \leq \gamma \leq 1$ for realistic expansion, and $t_0 > 0$ by convention (one cannot take $t_0 = 0$ in the general case). One must consider two different scenarii according to the location of the hard vertex: either $t_i = t_0$ or $t_i < t_0$.

Hard vertex at $t_i = t_0$. The first scenario is more simple as one can directly rely on the calculation made above. The characteristic medium formation time satisfies:

$$t^\star_{f,\mathrm{med}} - t_0 = \sqrt{\frac{2\omega}{\hat{q}_0 t_0^\gamma}} t^{\star\gamma/2}_{f,\mathrm{med}} \tag{5.40}$$

The extreme case $\gamma = 0$, where one can safely use $t_0 = 0$, corresponds to a static medium. One finds again the familiar relation $t^\star_{f,\mathrm{med}} = \sqrt{2\omega/q_0}$. The other extreme $\gamma = 1$ is the ideal relativistic plasma. The solution of (5.40) is, for $\gamma = 1$,

$$t^\star_{f,\mathrm{med}} - t_0 = \frac{1}{\hat{q}_0 t_0}\Big(\omega + \sqrt{\omega^2 + 2\hat{q}_0 t_0^2 \omega}\Big) \tag{5.41}$$

One can then distinguish two different regimes according to the ratio between ω and the energy scale $\hat{q}_0 t_0^2/2$:

1. If $\omega \gg \hat{q}_0 t_0^2/2$, then one can neglect the second term under the square root and one gets $t^\star_{f,\mathrm{med}} - t_0 \simeq 2\omega/(\hat{q}_0 t_0)$. The veto constraint is then:

   $$k_\perp \geq \sqrt{\hat{q}_0 t_0} \tag{5.42}$$

   This non trivial result comes entirely from the study of the off-shell spectrum for short formation times.

2. On the other hand, if $\omega \ll \hat{q}t_0^2/2$, one gets $t_{f,\mathrm{med}} - t_0 \simeq \sqrt{2\omega/\hat{q}_0}$ which has the same form as in the static case with constant $\hat{q}_0$. Physically, these emissions have such a short formation time that they do not "see" the expansion of the medium. Hence, the veto constraint is the same as for a static medium with constant $\hat{q}_0$.

The condition $k_\perp^2 \geq \hat{q}_0 t_0$ for $\omega \geq \hat{q}_0 t_0^2$ is interesting as the transverse momentum scale $\sqrt{\hat{q}_0 t_0}$ is naturally related to the saturation scale $Q_{s,A}$ of the incoming nuclei in $A-A$ collisions.

In the general $\gamma > 0$ case, it also possible to get the boundary of the in-medium region for vacuum-like emissions in the two regimes elucidated for $\gamma = 1$. For this, it is more convenient to write (5.41) as an equation for $\hat{q}^\star$:

$$\left(\frac{\hat{q}_0}{\hat{q}^\star}\right)^{1/\gamma} - \sqrt{\frac{2\omega}{\hat{q}_0 t_0^2}}\left(\frac{\hat{q}_0}{\hat{q}^\star}\right)^{1/2} - 1 = 0 \tag{5.43}$$

When $\omega \ll \hat{q}_0 t_0^2/2$, one can neglect the second term in this equation, so that the solution is $\hat{q}^\star = \hat{q}_0$. The constraint on $k_\perp$ is the same as in a static medium with constant $\hat{q}_0$: $k_\perp \geq (2\hat{q}_0\omega)^{1/4}$. When $\omega \gg \hat{q}_0 t_0^2/2$, one can neglect the minus 1 term and the solution is:

$$\hat{q}^\star = \hat{q}_0 \left(\frac{\hat{q}_0 t_0^2}{2\omega}\right)^{\frac{\gamma}{2-\gamma}} \tag{5.44}$$

Plugging this relation into (5.34) gives the boundary of the veto region for $\omega \gg \hat{q}_0 t_0^2/2$.

As a last comment, we point out that the generalisation of the condition $k_\perp \geq \hat{q}t_f$ for expanding media:

$$k_\perp^2 \geq \int_{t_0}^{t_f} \mathrm{d}t\, \hat{q}(t) \tag{5.45}$$

gives the same power dependence of the in-medium boundary as a function of ω. Indeed, for $\gamma < 1$,

$$\int_{t_0}^{t_f} \mathrm{d}t\, \hat{q}(t) = \frac{\hat{q}_0 t_0^\gamma}{1-\gamma}\left(t_f^{1-\gamma} - t_0^{1-\gamma}\right) \tag{5.46}$$

Then, when $t_f \simeq t_0$, one can use $t_f^{1-\gamma} - t_0^{1-\gamma} \simeq (1-\gamma)t_0^{-\gamma}(t_f - t_0)$. One can then take the limit $t_0 \to 0$, and one recovers the condition $k_\perp \geq (2\hat{q}_0\omega)^{1/4}$ corresponding to the regime $\omega \ll \hat{q}_0 t_0^2/2$. This also means that this regime is the regime of formation times of the same order as t_0. If $t_f \gg t_0$, one can neglect the minus term in (5.46) leading to

$$k_\perp^2 \geq \frac{1}{1-\gamma}\hat{q}_0 t_0^\gamma t_f^{1-\gamma} \tag{5.47}$$

As emphasized, once t_f is replaced by $\sim 2\omega/k_\perp^2$, this leads to the same dependence in ω of the $k_\perp$ boundary (except the uninteresting prefactor). Nevertheless, the case $\gamma = 1$ is ambiguous from the condition (5.45) because of a logarithmic prefactor of the form $\log(t_f/t_0)$.

Hard vertex at $t_i < t_0$. We would like to understand how these results are modified once the position of the hard vertex creating the off-shell parton is located at $0 < t_i < t_0$. In the limit $t_i \to t_0$, one should recover the results obtained above.

More precisely, when $\Delta t \equiv t_0 - t_i \ll \sqrt{2\omega/\hat{q}_0}$, we expect the boundary found in the previous paragraph not to be modified since $\sqrt{2\omega/\hat{q}_0}$ is the medium-induced time scale when $t_f \sim t_0$. Consequently, we focus on the regime $\Delta t \gg \sqrt{2\omega/\hat{q}_0} \Leftrightarrow \omega \ll \hat{q}_0 \Delta t^2/2$.

There are two possible ways to do the calculation. The first method consists in cutting the off-shell cross-section in three pieces with $t_i \leq y^+, \bar{y}^+ \leq t_0$ or $y^+, \bar{y}^+ \geq t_0$ or $y^+ \geq t_0$, $t_i \leq \bar{y}^+ \leq t_0$. The other method consists in finding a continuous and derivable solution over the full range $[t_i, \infty]$ of the differential equation satisfied by S and C. If this is possible, the calculation leading to (5.7) and (5.8) remains valid. It happens that such solutions exist and can be built explicitly (cf. Appendix B for a discussion of the junction method). In this paragraph, γ is arbitrary and all the conclusions drawn are independent of the value of γ. Performing the integral over $\bar{y}^+$ in (5.8) using lemma (3.122), one finds:

$$\omega \frac{\mathrm{d}^3 N^{\text{off-shell,f}}}{\mathrm{d}\omega \mathrm{d}^2 k_\perp} = \frac{\alpha_s C_F}{\pi^2} \left[2\mathfrak{Re} \frac{1}{2i\omega} \int_{t_i}^{\infty} \mathrm{d}y^+ \exp\left(\frac{-k_\perp^2 G^{-1}(y^+)}{2i\omega} \right) - \frac{1}{k_\perp^2} \right] \tag{5.48}$$

The function $G(y^+) = C(t_i, y^+)/S(y^+, t_i)$ is continuous and derivable even in $y^+ = t_0$ and verifies:

$$G^{-1}(y^+) = y^+ - t_i \qquad \text{if } t_i \leq y^+ \leq t_0 \tag{5.49}$$

For $y^+ \geq t_0$, one can approximate the functions $S(y^+, t_i)$ and $C(y^+, t_i)$ by their Taylor expansion around $y^+ = t_0$:

$$S(y^+, t_i) = y^+ - t_i - \frac{i\hat{q}_0 \Delta t}{4\omega}(y^+ - t_0)^2 + \mathcal{O}\big((y^+ - t_0)^3\big) \tag{5.50}$$

$$C(t_i, y^+) = 1 - \frac{i\hat{q}_0 \Delta t}{2\omega}(y^+ - t_0) + \mathcal{O}\big((y^+ - t_0)^2\big) \tag{5.51}$$

The continuity and derivability of the solutions C and S in $y^+ = t_0$ are essential to get this result. Let us comment these relations. First of all, when $\Delta t \to 0$, the sub-leading term vanishes, meaning that one should go beyond the first order calculation to obtain the range of validity of the vacuum-like expressions for S and C. This is precisely the situation studied in the case $t_i = t_0$ in the previous paragraph. Our assumption $\Delta t \gg \sqrt{2\omega/\hat{q}_0}$ is in agreement with the fact that Δt cannot be too small for this calculation to make sense.

That said, when

$$\frac{\hat{q}_0 \Delta t}{2\omega}(y^+ - t_0) \ll 1 \Leftrightarrow y^+ \ll t^\star_{f,\text{med}} \equiv t_0 + \frac{2\omega}{\hat{q}_0 \Delta t} \tag{5.52}$$

one can neglect the $\mathcal{O}(y^+ - t_0)$ terms and the calculation of (5.48) in the integration domain $y^+ \leq t^\star_{f,\text{med}}$ gives[4]:

$$\omega \frac{\mathrm{d}^3 N^{\text{off-shell,f } t_f < t_{f,\text{med}}}}{\mathrm{d}\omega \mathrm{d}^2 k_\perp} = \frac{\alpha_s C_F}{\pi^2} \frac{1}{k_\perp^2} \Theta\left(k_\perp - \left(\frac{2\omega}{t^\star_{f,\text{med}} - t_i} \right)^{1/2} \right) \tag{5.53}$$

The step function is the signature of the constraint on in-medium Bremsstrahlung emissions. As $\Delta t \gg \sqrt{2\omega/\hat{q}_0}$ by assumption, $t^\star_{f,\text{med}} - t_i = \Delta t + 2\omega/(\hat{q}_0 \Delta t) \simeq \Delta t$. The veto constraint reads then:

$$k_\perp \geq \sqrt{\frac{2\omega}{\Delta t}} \tag{5.54}$$

[4]As we have integrated over all $\bar{y}^+$, the final result is asymmetric (see also Appendix F for a discussion of this peculiarity). Anyway, the $-1/k_\perp^2$ should be decomposed into two pieces, one cancelling the factor 2 in (5.48) and another with $k_\perp \leq (2\omega)/(t^\star_{f,\text{med}} - t_i)$ which is not related to short formation times vacuum-like emissions.

In this case, the vacuum-like emissions have a formation time short enough to happen entirely in the vacuum before entering into the medium, so that the veto does not depend on $\hat{q}_0$. When $\omega \ll \hat{q}\Delta t^2/2$, the scale $\sqrt{2\omega/\hat{q}_0}$ has disappeared in this scenario, contrary to the situation where the hard scattering occurs directly inside the medium.

To sum up, in a Bjorken expanding plasma, the transverse momentum of vacuum-like emissions is constrained by:

$$k_\perp \geq \min\Big((2\hat{q}^\star(\omega)\omega)^{1/4}, (2\omega/\Delta t)^{1/2}\Big) \tag{5.55}$$

for $\Delta t \leq t_0$ and $\hat{q}^\star(\omega)$ given by $\hat{q}_0$ for $\omega \leq \hat{q}_0 t_0^2/2$ and (5.44) for $\omega \geq \hat{q}_0 t_0^2/2$.

5.2 Resummation at double logarithmic accuracy and in the large N_c limit

In the previous section, we have identified the phase space for one vacuum-like emission in the presence of a dense QCD medium. In this section, we explain how such emissions are iterated. The main obstacle with respect to a straightforward generalisation of the coherent branching algorithm is the decoherence induced by the medium, studied in Section 3.4.3. As we have seen, decoherence does not forbid soft emissions outside the opening angle of a colour singlet antenna. This means that the coherent branching algorithm fails to correctly resum to all orders soft and collinear emissions for a jet evolving in the medium.

We shall see, however, that one can build an effective branching algorithm for VLEs amended to take into account the effect of medium decoherence. The main results are:

1. the branching process is angular ordered inside the medium,

2. angular ordering can be violated for the first emission outside the medium.

These statements are demonstrated within the double logarithmic approximation (DLA) of pQCD and in the large N_c limit. In the last section of this chapter, we provide arguments in order to extend the validity of the branching process beyond DLA and the large N_c limit.

5.2.1 Angular ordering inside the medium

For simplicity, we consider a jet which starts as a colour-singlet quark-antiquark antenna with a small opening angle $\theta_{q\bar{q}} \ll 1$, e.g. produced by the decay of a boosted W/Z boson or a virtual photon. It also applies to the evolution of a quark or gluon jet, provided one replaces $\theta_{q\bar{q}}$ by either the jet radius or the angle of the first emission. The quark and the antiquark are assumed to have equal energies: $E_q = E_{\bar{q}} \equiv E$. As emphasized, we focus on the double-logarithmic approximation (DLA) where subsequent emissions are strongly ordered in both energies and emission angles. Furthermore, in the large N_c limit, the antenna is the only degree of freedom in this context as the emission of gluon from the initial $q\bar{q}$ antenna is equivalent to the splitting of this antenna into two other antennae.

In this subsection, we assume that the medium is infinite, with constant quenching parameter $\hat{q}_0$. We relax this approximation in the next subsection. In this limit, the phase space available for vacuum-like splittings from the initial $q\bar{q}$ pair is (see (I.9) or (5.24)):

$$k_\perp^2 \gg \sqrt{\hat{q}_0\omega} \quad \Longleftrightarrow \quad \omega \gg \left(\frac{2\hat{q}_0}{\theta^4}\right)^{1/3} \equiv \omega_0(\theta) \tag{5.56}$$

where the inequalities are stong at DLA. ω is the energy of the soft daughter antenna and θ its opening angle.

Colour decoherence. For emissions by a colour-singlet antenna, even a vacuum-like emission obeying (5.56) could be still affected by the medium, via *colour decoherence* [89, 90, 91, 92]. In the vacuum, gluon emissions at large angles $\theta \gg \theta_{q\bar{q}}$ are suppressed by the destructive interferences between the quark and the antiquark. This argument can be iterated to conclude that successive emissions in the vacuum are *ordered in angles*, $\theta_{i+1} \lesssim \theta_i$, an ordering which becomes *strong* ($\theta_{i+1} \ll \theta_i$) at DLA. But, as seen in Chapter 3-Section 3.4.3, an antenna propagating through a dense quark-gluon plasma can lose its coherence via rescattering off the medium: the quark and the antiquark suffer independent colour rotations, hence the probability that the antenna remains in a colour singlet state decreases with time. The two legs of the antenna start behaving like independent colour sources after the time $t \sim t_{\rm coh}$ defined in (3.204)

$$t_{\rm coh}(\theta_{q\bar{q}}) \equiv \left(\frac{4}{\hat{q}\theta_{q\bar{q}}^2}\right)^{1/3} \tag{5.57}$$

In principle, then, emissions with formation time $t_f = 2/(\omega\theta^2)$ larger than $t_{\rm coh}$ could violate the angular ordering property.

Now comes the crucial point. We show that to the order of interest, the first emission by the leading $q\bar{q}$ still has an angle θ smaller than $\theta_{q\bar{q}}$, despite the potential decoherence of the parent antenna. To see this, note that

$$\frac{t_f}{t_{\rm coh}} = \frac{(2\hat{q}\theta_{q\bar{q}}^2)^{1/3}}{\omega\theta^2} = \frac{\omega_0(\theta)}{\omega}\left(\frac{\theta_{q\bar{q}}}{\theta}\right)^{2/3} \tag{5.58}$$

where t_f is the formation time of the daughter antenna. The loss of colour coherence may only affect the emissions at sufficiently large angles, $\theta \gtrsim \theta_{q\bar{q}}$, which overlap with both sources. For VLEs satisfying (5.56), this implies $t_f \ll t_{\rm coh}$ meaning that the antenna is still coherent at the time of the emission and the would-be large-angle emissions are killed by the interference. In fine, only emissions with $\theta \lesssim \theta_{q\bar{q}}$ are allowed whether or not they occur at times larger than the decoherence time (5.57).

The attentive reader will notice that this time scale argument is based on the ratio $t_f/t_{\rm coh}$ and not $t_f\theta/(t_{\rm coh}\theta_{q\bar{q}})$ as one would expect from our discussion of the decoherence factor calculated in Section 3.4.3 (see (3.237) and (3.238)). Nevertheless, this more refined order parameter was derived in the regime $\omega \gg \omega_c$ and $k_\perp \gg Q_s$. In this regime, using the equality

$$\frac{t_{\rm coh}}{t_f}\frac{\theta_{q\bar{q}}}{\theta} = \frac{\omega}{\omega_c}\left(\frac{L}{t_{\rm coh}}\right)^2\left(\frac{\theta}{\theta_{q\bar{q}}}\right), \tag{5.59}$$

one shows that the argument inside the Bessel function in (3.238) is large for in-medium VLEs with $\theta \gtrsim \theta_{q\bar{q}}$, and thus large angle emissions are suppressed ($L/t_{\rm coh} \gg 1$ in the formal infinite medium length limit we are discussing). The question of whether the right order parameter is $t_f/t_{\rm coh}$ or $t_f\theta/(t_{\rm coh}\theta_{q\bar{q}})$ in the regime $\omega_0(\theta) \ll \omega \ll \omega_c$ deserves further studies from first principle calculations as those performed in Section 3.4.3.

These arguments, given for the first emission from the leading $q\bar{q}$ pair, can be easily generalised by induction for any vacuum-like cascade in the phase space (5.56). The leading logarithmic behaviour of in-medium parton showers comes from cascades which are strongly ordered in energies and angles, i.e. from cascades with n VLE's satisfying $\theta_{q\bar{q}} \gg \theta_1 \gg \cdots \gg \theta_n$

and $E \gg \omega_1 \gg \cdots \gg \omega_n \gg \omega_0(\theta_n)$. First, note that the formation times $t_i = 2/(\omega_i \theta_i^2)$ are strongly increasing from one emission to the next. It means that the condition (5.56) is satisfied by all the gluons in the cascade if it is satisfied by the last one. To validate the above picture, we now show by induction that colour coherence guarantees the angular ordering.

For any antenna in the cascade, say with opening angle θ_i, $i \in \mathbb{N}^\star$, one can apply the same argument about angular ordering as for the original antenna with angle $\theta_{q\bar{q}}$: VLEs at larger angles $\theta > \theta_i$ are strongly suppressed because their formation times are smaller that the decoherence time $t_{\rm coh}(\theta_i)$ of that antenna.

Energy loss during formation. Besides colour decoherence, another difficulty due to the medium is the potential energy loss during the formation of emissions. This effect could change the energy ω in such a way that they could get out of the phase space (5.56). As our conclusions strongly relies on the condition (5.56), one must show that the energy lost via medium-induced radiation remains negligible during the development of a vacuum-like cascade.

The hardest medium-induced emission that can occur over the time t has an energy $\omega_c(t) \simeq \hat{q}t^2/2$ and a probability of order α_s. For $t = t_n \equiv 2/(\omega_n \theta_n^2)$ (5.56) implies $\omega_c(t_n) \ll \omega_n$, i.e. the maximal energy loss is small compared to the energy of the *softest* gluon in the cascade. The *average* energy loss, of order $\alpha_s \omega_c(t_n)$, is even smaller. This argument also shows that, over their formation time, the gluons from the vacuum-like parton showers do not contribute to the energy loss of the jet. However, at the end of the in-medium partonic cascade, each of the final emissions will act as an additional source for medium-induced radiations and loses energy. We shall return to this point in the next subsection as it intimately related to the finite path length of the jet in the medium.

5.2.2 Angular ordering violation and finite length effects

Before exploring the consequences of the finite path length L of the jet through the medium, let us summarize the resummation scheme of VLEs in an infinite medium: the coherent branching algorithm still correctly resums to all orders the soft and collinear double logarithms provided that all the emissions belong to phase space (5.56). Introducing the path length scale L changes this picture in two respects:

1. the phase space for VLEs is extended to emissions with $t_f \gg L$,

2. two other scales come into play: the energy $\omega_c = \hat{q}L^2/2$ of the hardest medium-induced emission that develops over a time L and its corresponding angle $\theta_c = 2/\sqrt{\hat{q}L^3}$.

When discussing the shape of the phase-space for VLEs in Section 5.1.1, we have said that emissions with $\omega \geq \omega_c$ are necessarily vacuum-like since the maximal energy of a medium-induced emission in the multiple soft scattering regime is ω_c. Similarly, the angular scale θ_c should be thought as the minimal angle of an antenna resolvable by the medium. Indeed, the coherence time scale $t_{\rm coh}$ becomes comparable to L when $\theta_{q\bar{q}} \sim \theta_c$. Antennas with smaller opening angles $\theta_{q\bar{q}} \lesssim \theta_c$ cannot lose their coherence, hence their radiation pattern within the medium is exactly the same as in the vacuum. For this reason, the phase space for vacuum-like emissions shown in Fig 5.1 is amended to take into account this property: any antenna with opening angle smaller than θ_c is considered as "outside" (i.e. as in the vacuum), even if the emission occurs physically inside. This modification of the phase space is shown in Fig. 5.3.

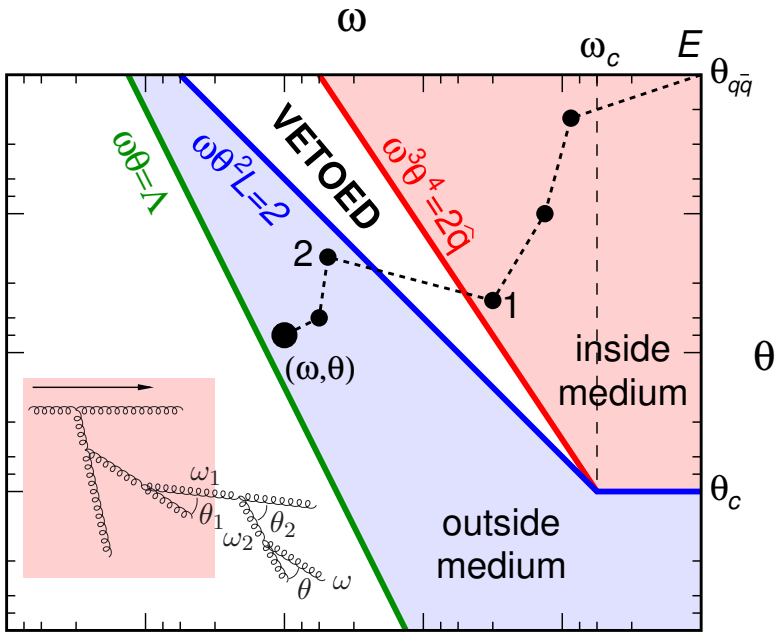

Figure 5.3: Complete double-logarithmic phase space taking into account the decoherence of large angle antennae during their propagation through the medium. With respect to Fig. 5.1, the only difference is the introduction of the angular scale θ_c that modifies the shape of the in-medium region for energies larger than ω_c. The figure includes an example of a cascade with "1" the last emission inside the medium and "2" the first emission outside. This cascade is pictured on the left. This figure should also be compared to the corresponding vacuum phase space for emissions shown Fig. 4.2.

Violation of angular ordering for the first emission outside the medium We remind that the gluons produced inside the medium are not yet on-shell: their virtualities are as large as their transverse momenta, themselves bound by the multiple scattering inside the medium: $k_\perp^2 \gg \sqrt{\omega\hat{q}} \gg \Lambda_{\rm QCD}^2$, with $\Lambda_{\rm QCD}$ the QCD confinement scale. These partons will thus continue radiating. Their next VLE must occur *outside* the medium, with a large formation time $2/(\omega\theta^2) \gg L$, i.e. with an energy $\omega \ll \omega_L(\theta) \equiv 2/(L\theta^2)$, as discussed in Section 5.1. As seen in the first section, this implies the existence of a gap in the energy of the VLEs, between the lower limit $\omega_0(\theta)$ on the last gluon emitted *inside* the medium, and the upper limit $\omega_L(\theta)$ on the first gluon emitted *outside* the medium. Since $\omega_0(\theta) = \omega_L(\theta) = \omega_c$ for $\theta = \theta_c$ the gap exists only for $\omega < \omega_c$, as shown Fig. 5.3.

As explained in Chapter 3, Section 3.4.3, the medium has an important effect on emissions with $t_f \gg L$: this first emission outside the medium can violate angular ordering [93]. Approximating the decoherence factor $1 - S_{q\bar{q}}(L)$ that appears in (3.240) by $\Theta(\theta - \theta_c)$, one sees that if the parent antenna of the emission with $t_f \gg L$ has an angle θ larger than θ_c, the angle of the emission is not bounded any more by θ. In physical terms, all the in-medium sources with $\theta \gg \theta_c$ satisfy $t_{\rm coh}(\theta) \ll L$ and thus lose colour coherence after propagating over a distance L in the medium. These sources can then radiate at *any* angle.

Energy loss and broadening after formation. After being created inside the medium via VLEs, the partons cross the plasma over a distance of order L and hence lose energy via medium-induced radiations and undergo $p_\perp$-broadening. The pattern of fragmentation produced by the in-medium VLEs, serving as multiple sources for medium-induced emissions and energy loss, is a cornerstone of many phenomenological observations made in Part II.

Emissions from sources created outside the medium. After a first emission outside the medium, the subsequent emissions follow, of course, the usual pattern of vacuum-like cascades, with angular ordering (and energy ordering in our DLA approximation). The evolution stops when the transverse momentum $k_\perp \simeq \omega\theta$ becomes comparable to the hadronisation scale $\Lambda_{\rm QCD}$. This implies a lower boundary, $\omega \gtrsim \Lambda_{\rm QCD}/\theta$, on the energy of the produced gluons, shown in Fig. 5.3 (green curve) together with the other boundaries introduced by the medium. The most interesting region for gluon production — the most sensitive to medium effects highlighted above — is the "outside medium" region at energies $\omega < \omega_c$.

5.2.3 Summary of the fundamental QCD picture

A very simple picture for the development of a partonic cascade in the medium emerges from the above observations and within our approximations. The full cascade can be factorised in three major steps.

1. *in-medium vacuum-like cascade*: an angular-ordered vacuum-like cascade governed by the standard DGLAP splitting functions occurs inside the medium up to $t_f(\omega,\theta) = t_{f,\rm med}(\omega)$. During this process, the only effect of the medium is to set the constraint (5.56) on the formation time;

2. *medium-induced emissions and broadening*: every parton resulting from the in-medium cascade travels through the medium, possible emitting (a cascade of) MIEs and acquiring momentum broadening;

3. *outside-medium vacuum-like cascade*: each parton exiting the medium at the end of the previous step initiates a new vacuum-like cascade outside the medium, down to a non-perturbative cut-off scale. The first emission in this cascade can happen at an arbitrary angle.

5.2.4 The double-logarithmic picture in Bjorken expanding media

In this subsection, we generalise the double logarithmic picture for a Bjorken expanding medium. More precisely, we show that the all-order factorised picture summarized above holds for a medium in expansion. We check that the boundaries of the veto region found in Section 5.1.3.2 lead to the same properties for the in-medium parton shower: angular ordering is preserved and energy loss during formation is negligible. Transverse momentum broadening during formation is negligible *by construction* of the veto region, see (5.45).

Angular ordering. As in the brick case, we first consider a leading $q\bar{q}$ pair with opening angle $\theta_{q\bar{q}}$. We also simplify the discussion of subsection 5.1.3.2 assuming that this antenna is created at $t_i = 0$, meaning that $\Delta t = t_0 - t_i = t_0$. In this situation, the constraint on short formation times VLEs is

$$\omega \geq \frac{2}{t_0\theta^2} \qquad \text{if } \omega \leq \frac{1}{2}\hat{q}_0 t_0^2 \tag{5.60}$$

$$\omega \geq \omega_0(\theta) \equiv \left(\frac{2\hat{q}_0(t_0/2)^\gamma}{\theta^{4-2\gamma}}\right)^{1/(3-\gamma)} \qquad \text{if } \omega \geq \frac{1}{2}\hat{q}_0 t_0^2 \tag{5.61}$$

The first condition is not really relevant in practice since the energy scale $\frac{1}{2}\hat{q}_0 t_0^2$ is very small for typical values of $t_0 \sim 0.1$ fm.

We want to extract the characteristic decoherence time as a function of t_i. It is given by the calculation of the $q\bar{q}$ dipole S-matrix $S_{q\bar{q}}(t)$ defined by (3.190):

$$S_{q\bar{q}}(t) = \exp\left(-\frac{1}{8}\theta_{q\bar{q}}^2 \int_{t_0}^{t} \mathrm{d}\xi\, \hat{q}(\xi)(\xi - t_i)^2\right) \tag{5.62}$$

$$= \exp\left(-\frac{1}{8(3-\gamma)}\theta_{q\bar{q}}^2 \hat{q}_0 t_0^\gamma \left(t^{3-\gamma} - t_0^{3-\gamma}\right)\right) \tag{5.63}$$

for $t_i = 0$. Clearly, this calculation is interesting in the regime where $t_f \geq t_0$. Otherwise, the emission happens before t_0, i.e in the vacuum where angular ordering holds. At DLA, one can further consider $t_f \gg t_0$. Neglecting the $-t_0^{3-\gamma}$ term in the result (5.63), one finds the characteristic (de)coherence time:

$$\boxed{t_{\mathrm{coh}} = \left(\frac{4}{\theta_{q\bar{q}}^2 \hat{q}_0 t_0^\beta}\right)^{1/(3-\gamma)}} \tag{5.64}$$

For $t_f \gg t_0$, one has then:

$$\frac{t_f}{t_{\mathrm{coh}}} = \frac{\omega_0(\theta)}{\omega}\left(\frac{\theta_{q\bar{q}}}{\theta}\right)^{2/(3-\gamma)} \tag{5.65}$$

which looks pretty much like (I.11) except for the exponent which is positive for $\gamma \leq 1 < 3$. This means that for emissions satisfying $\omega \geq \omega_0(\theta)$, the antenna is still coherent at t_f so that large angle emissions are forbidden.

In this reasoning, which is a simple transposition of the argument given for the brick medium, we have used $t_f \gg t_0 = \Delta t$. This means that the emission should not be sensitive to position of the hard vertex t_i. For consistency, we thus need to check that the angular ordering property remains valid also when $t_i = t_0$, that is when the antenna is created at the same time as it enters into the medium. The calculation of (5.62) gives in this case, for $\gamma < 1$:

$$S_{q\bar{q}}(t) = \exp\left(-\frac{1}{8}\theta_{q\bar{q}}^2 \hat{q}_0 t_0^\gamma \left[\xi^{1-\gamma}\left(\frac{t_0^2}{1-\gamma} - \frac{2t_0\xi}{2-\gamma} + \frac{\xi^2}{3-\gamma}\right)\right]_{\xi=t_0}^{\xi=t}\right) \tag{5.66}$$

According to our discussion in Section 5.1.3.2, there are two regimes that we should discuss: either $t \simeq t_0$ or $t \gg t_0$. When $t_f \simeq t_0$, the dipole S-matrix reads:

$$S_{q\bar{q}}(t) \underset{t\simeq t_0}{\simeq} \exp\left(-\frac{1}{24}\theta_{q\bar{q}}^2 \hat{q}_0 (t - t_0)^3\right) \tag{5.67}$$

The limit $t_0 \to 0$ is not singular any more, and the characteristic coherence time is the same as in the fixed $\hat{q}$ case: $t_{\mathrm{coh}} = (\hat{q}_0 \theta_{q\bar{q}}^2/4)^{-1/3}$. We have seen that for $t_f \simeq t_0$, the constraint on $k_\perp$ is not given by (5.60) but rather by $k_\perp \geq (2\hat{q}_0\omega)^{1/4}$ when $\omega \leq \hat{q}_0 t_0^2/2$. Consequently, for emissions in this phase space, the argument for angular ordering developed in the previous section when $\hat{q}$ is constant applies in the same way.

In the second regime $t \gg t_0$, the exponent in (5.66) is dominated the leading power in t:

$$S_{q\bar{q}}(t) \underset{t\gg t_0}{\simeq} \exp\left(-\frac{1}{8(3-\gamma)}\theta_{q\bar{q}}^2 \hat{q}_0 t_0^\gamma t^{3-\gamma}\right) \tag{5.68}$$

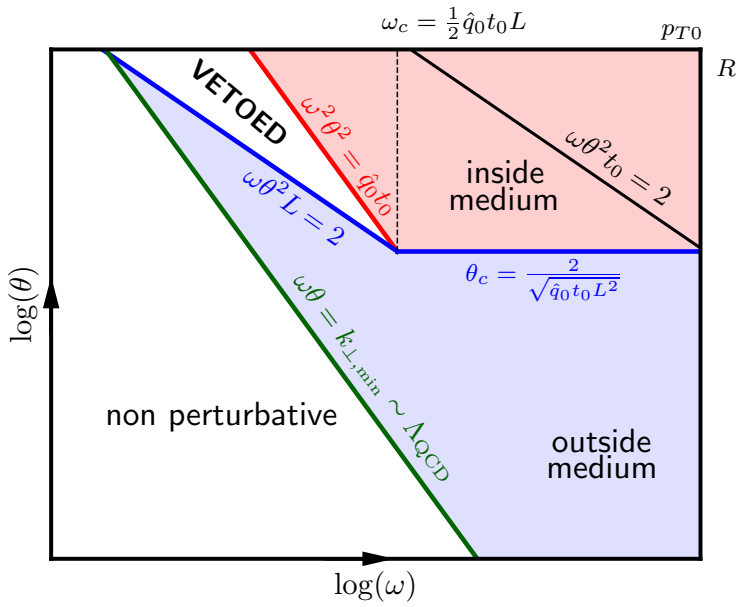

Figure 5.4: Phase space for vacuum-like emissions at DLA in a Bjorken expanding medium with $\gamma = 1$

One recovers the characteristic coherence time (5.64), so that the calculation in 5.65 remains valid.

To sum up, whatever the position of the hard-vertex with respect to the parameter t_0 is, the angular ordering property for the first emission by the leading $q\bar{q}$ pair holds, as long as this emission belongs to the in-medium phase space. The generalisation for a sequence of n emissions in this phase space proceeds by mathematical induction.

Energy loss during t_f. In a Bjorken expanding medium, the hardest medium-induced emission that can develop during the formation time t_f of an in-medium vacuum-like emission has an energy

$$\omega_c(t_f) \simeq \frac{1}{2}\hat{q}(t_f)t_f^2 = \frac{1}{2}\hat{q}_0 t_0^\gamma t_f^{2-\gamma} \tag{5.69}$$

As in static media, the condition $\omega \gg \omega_0(\theta)$ for $t_f \gg t_0$ implies $\omega_c(t_f) \ll \omega$ meaning that one can neglect the energy loss via medium-induced radiations during the formation of an in-medium vacuum-like emission.

Angular ordering violation and critical angle θ_c. From the definition (5.64) of the coherence time in a Bjorken expanding medium, one can easily deduces the parametric dependence of the critical angle θ_c for a jet getting out of the medium at time $t_L = t_0 + L \gg t_0$. This critical angle is given by the condition $t_{\rm coh}(\theta_c) = t_L$:

$$\boxed{\theta_c = \frac{2}{\sqrt{\hat{q}_0 t_0^\gamma t_L^{3-\gamma}}} = \frac{2}{\sqrt{\hat{q}(t_L)t_L^3}}} \tag{5.70}$$

An antenna with an angle smaller than θ_c does not lose its colour coherence when travelling through the diluting medium. As in the static case, a source inside the medium with $\theta \geq \theta_c$ can then radiate at any angle in the out-medium phase space.

5.2.5 Beyond the double-logarithmic picture

Now that we have exposed the basic picture for the development of parton showers in the presence of a medium, we show that several sub-leading corrections, beyond DLA, can easily be taken into account. First of all, the large N_c limit can be easily relaxed (in the collinear limit) taking into account the color representation of the emissions thanks to the usual DGLAP splitting functions.

The validity of our factorisation between VLEs and MIEs relies on strong inequalities between the formation times. Clearly, these inequalities do still hold if the strong ordering refers only to the emission angles ($\theta_n \ll \theta_{n-1}$) but not to the parton energies (as is the case beyond the soft limit $z \ll 1$). There is nevertheless some loss of accuracy with respect to a strict single logarithmic approximation associated with the uncertainties in the boundaries of the vetoed region in phase-space. Notably the condition $t_f(\omega,\theta) = t_{f,\mathrm{med}}(\omega)$ defining the upper boundary is unambiguous only at DLA. For a generic splitting fraction z, the formation times also depend upon the energy xE of the parent parton and not just upon the energy $\omega = xzE$ of the soft daughter gluon. For a generic $1 \to 2$ splitting where the "vacuum-like" formation time $t_f \equiv t_f(x,z,\theta)$ is given by

$$t_f(x,z,\theta) \simeq \frac{2xE}{Q^2} \simeq \frac{2}{z(1-z)xE\theta^2} \simeq \frac{2z(1-z)xE}{k_\perp^2}\,, \tag{5.71}$$

where z and θ (assuming $\theta \ll 1$) are the energy fraction and opening angle of the partonic decay and $k_\perp \simeq z(1-z)\theta xE$ is the (relative) transverse momentum of any of the two daughter partons with respect to the direction of the leading parton.

The corresponding "medium" formation time $t_{f,\mathrm{med}}(x,z)$ is different for different partonic channels. For example, for a $g \to gg$ splitting, it reads

$$t_{f,\mathrm{med}}(x,z)\big|_{g\to gg} = \sqrt{\frac{2z(1-z)xE}{\hat{q}_{\mathrm{eff}}(z)}} \overset{z\ll 1}{\approx} \sqrt{\frac{2\omega}{\hat{q}}}\,, \qquad \hat{q}_{\mathrm{eff}}(z) \equiv \hat{q}\big[1-z(1-z)\big], \tag{5.72}$$

with $\omega = zxE$. One could in principle use these more accurate estimates for t_f and $t_{f,\mathrm{med}}$ in (5.56). One would then need to deal with the difficulty that the evolution phase-space depends explicitly on xE, z and θ and not just on ω and θ. The corresponding generalisation of (5.56) would also be different for different partonic channels. Last but not least, the distinction between VLEs and MIEs according to their formation times only holds so long as the *strong* inequality $t_f \ll t_{\mathrm{med}}$ is satisfied, meaning that the precise form of the boundary could also be sensitive to subleading corrections. In practice, our strategy to deal with this ambiguity (notably, in the Monte Carlo simulations presented in Part II) is to stick to the simpler form of the boundary in (5.56). In phenomenological applications, one should keep in mind that the dependence on $\hat{q}$ and L of the VLEs is only leading-logarithmic.

Limitations. The resummation scheme developed in this chapter has of course its own limitation and domain of applicability. We will not discuss here the limitations due to our simple modelling of the medium and geometry of the collision. This will be detailed in the next chapter about the Monte Carlo parton shower built from the present picture. However, there are intrinsic theoretical limitations in our approach. We provide an non-extensive list here.

1. The multiple soft scattering approximation is maybe the strongest assumption in the perturbative treatment of the parton shower. Hard scattering off medium scattering centers are neglected. Combining consistently such scatterings with both the initial virtuality

and the multiple soft collisions is beyond the scope of the present thesis, but should not be too difficult to include in a Monte Carlo framework. This is also a widely developed topic in the literature.

2. Even in the multiple soft scattering regime, there are other emissions which are not taken into account in the double-logarithmic cascade: the BDMPS-Z emissions and the "Bremsstrahlung-like" emissions triggered by the medium discussed in Section 5.1. A complete picture should include the medium-induced emissions à la BDMPS-Z and the medium-induced emissions à la Bremsstrahlung appearing in (5.25). The former are currently included in the Monte Carlo `JetMed` presented in Chapter 6, but not the latter.

3. The double logarithmic resummation performed so far does not account for running coupling single logarithmic corrections. Including such corrections is straightforward. This is done semi-analytically in the next section for the jet fragmentation from vacuum-like emissions and numerically in the Monte Carlo parton shower `JetMed` presented in Chapter 6.

4. While crossing the medium, the hard parton sourcing the jet can transfer energy and momentum to the medium constituents that may finally belongs to the reconstructed jet. This is the so-called medium response effect [170, 171, 172, 173, 174] (see [175] for a review). This requires a detailed modelling of the medium itself which clearly goes beyond our current simple approach.

5.3 Analytic fragmentation function and jet energy loss

In this section, as a first step towards the detailed phenomenological study made in Part II, we provide analytic results for the fragmentation function and the jet energy loss obtained directly from our new factorised picture. This results are important since they enable to understand the important physical mechanisms at play in the modification of the jet fragmentation pattern.

5.3.1 Fragmentation function from vacuum-like emissions

Our first calculation is the intrajet multiplicity for a jet evolving in the medium with constant $\hat{q}$. As usual, we note L the path length of the jet through the medium. This calculation is a double logarithmic resummation in the strict sense, meaning that one completely neglects medium-induced emissions even for the last vacuum-like emission at the end of the in-medium shower. We recall that medium-induced emissions do not *formally* matter at DLA as the process is not enhanced by collinear logarithms.

Also, $p_\perp$-broadening effects, while important in general, can safely be neglected when computing the gluon multiplicity since the latter is only sensitive to the angle of emission and not to a change in the direction of the emitter.

5.3.1.1 Strict double logarithmic calculation

Within the present approximation, and in the large N_c limit, it is straightforward to compute the gluon distribution generated by VLEs. To that aim we compute the double differential distribution,

$$T(\omega, \theta | E, R^2) \equiv \omega\theta^2 \frac{\mathrm{d}^2 N}{\mathrm{d}\omega \mathrm{d}\theta^2}\,, \tag{5.73}$$

which describes the gluon distribution in both energies and emission angles. We note R the opening angle of the jet that we identify with the opening angle $\theta_{q\bar{q}}$ of the leading $q\bar{q}$ pair. In the vacuum, this distribution has been calculated in Section 4.2.2.2, Eq. (4.24) thanks to the coherent branching algorithm. At DLA, successive gluon emissions are strongly ordered in both energy and emission angle and one finds

$$T_i^{\rm vac}(\omega,\theta^2|E,R^2) = \frac{\alpha_s C_i}{\pi}\,\mathrm{I}_0\left(2\sqrt{\bar{\alpha}_s \log\frac{E}{\omega}\,\log\frac{R^2}{\theta^2}}\right) + \omega\theta^2\delta(E-\omega)\delta(R^2-\theta^2) \tag{5.74}$$

where $\bar{\alpha}_s = \alpha_s C_A/\pi$ and $\mathrm{I}_0(x)$ is the modified Bessel function of rank 0 which increases exponentially for $x \gg 1$. The second term in the r.h.s. which is not present in 4.2.2.2 represents the leading parton and the first term is associated with subsequent gluon emissions. The fragmentation function can be obtained from T_i by integrating over all the angles in the jet, as explained in Section 4.2.2.2 (with $\theta_{\rm min} = k_{\perp,\rm min}/\omega$)

$$\omega D_i(\omega,\theta^2|E,R^2) = \int_{\theta^2_{\rm min}}^{R^2} \frac{\mathrm{d}\theta_1^2}{\theta_1^2}\,T_i(\omega,\theta_1^2|E,R^2) \tag{5.75}$$

with $\theta_{\rm min} = k_{\perp,\rm min}/\omega$.

We want to do the same calculation taking into account the modifications of the branching process due to the medium. In the presence of the medium, the DLA calculation is modified by two effects: the presence of a vetoed phase-space for VLEs inside the medium, and the colour decoherence allowing for the violation of angular ordering by the first emission outside the medium. It is helpful to split the medium fragmentation function $T_i^{\rm med}$ in two contributions:

$$T_i^{\rm med}(\omega,\theta^2|E,R^2) = \Theta_{\rm in}(\omega,\theta^2)T_i^{\rm vac} + \Theta_{\rm out}(\omega,\theta^2)T_{i,\rm out} \tag{5.76}$$

where the step functions $\Theta_{\rm in/out}$ enforces that an emission (ω,θ^2) belongs to the "inside" or "outside" region. The first term, $\Theta_{\rm in}(\omega,\theta^2)T_i^{\rm vac}$, corresponding to the in-medium contribution, is unmodified compared to the vacuum. The outside-medium, $T_{i,\rm out}$, contribution can be expressed as the product of a vacuum-like cascade inside the medium, up to an intermediate point (ω_1,θ_1^2), followed by a first emission outside the medium at (ω_2,θ_2^2) (possibly violating angular ordering), and by a standard vacuum cascade from (ω_2,θ_2^2) to the final point (ω,θ^2):

$$T_{i,\rm out}(\omega,\theta^2|p_{T0},R^2) = \bar{\alpha}_s\int_\omega^{p_{T0}}\frac{\mathrm{d}\omega_1}{\omega_1}\int_{\theta_c^2}^{R^2}\frac{\mathrm{d}\theta_1^2}{\theta_1^2}\,\Theta_{\rm in}(\omega_1,\theta_1^2)\int_\omega^{\omega_1}\frac{\mathrm{d}\omega_2}{\omega_2}\int_{\theta^2}^{R^2}\frac{\mathrm{d}\theta_2^2}{\theta_2^2}\,\Theta_{\rm out}(\omega_2,\theta_2^2)$$
$$T_i^{\rm vac}(\omega_1,\theta_1^2|p_{T0},R^2)T_g^{\rm vac}(\omega,\theta^2|\omega_2,\theta_2^2) \tag{5.77}$$

The integral over θ_2^2 is not constrained by the angle θ_1^2 of the previous emission due to absence of angular ordering for the first emission outside the medium.

The two angular integrations in (5.77) can be performed analytically. The resulting formula is well suited for numerical evaluation of the double differential gluon distribution T as well as the fragmentation function D.

To gain more physical intuition, we now develop an analytic approximation, which is valid when both the energy and angular logarithms are larger than $1/\sqrt{\alpha_s}$. We give here the main ingredients of the calculation and defer details to Appendix G.

In the limit of interest, the δ contribution to $T^{\rm vac}$ (the second term in (5.74)) can be neglected in both $T^{\rm vac}$ factors in (5.77), the Bessel functions can be approximated by their (exponential) asymptotic behaviour and the integrations can be evaluated in the saddle-point approximation.

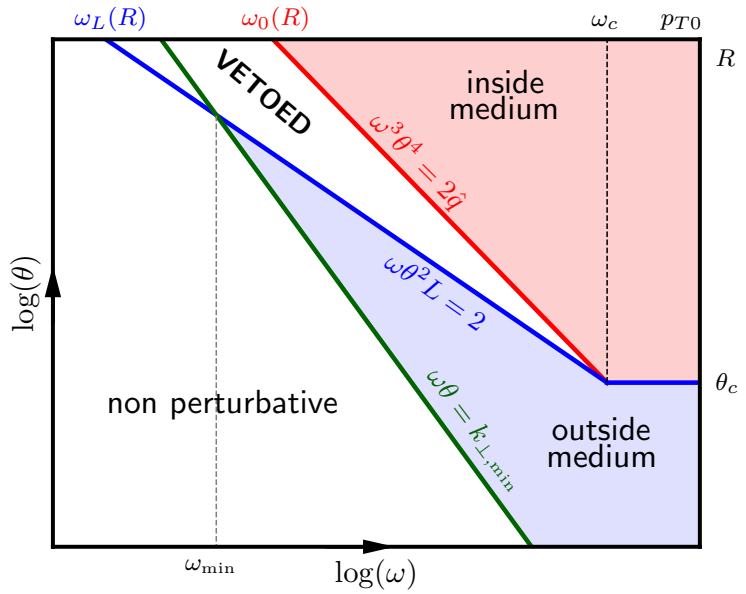

Figure 5.5: The phase space considered in our double-logarithmic resummation of vacuum-like emissions in the presence of a dense QCD medium. The relevant energy scales for the calculation of the vacuum-like fragmentation function are represented.

For definiteness, let us consider parameters such that $\omega_L(R) < k_{\perp,\min}/R$, meaning that the hadronisation line $\omega\theta = k_{\perp,\min}$ and the medium boundary $\omega_L(\theta) = 2/(L\theta^2)$ intersect at $\omega_{\min} = Lk_{\perp,\min}^2/2$. In practice we are interested in the fragmentation function at energies ω within the range $\omega_{\min} \ll \omega \ll \omega_c$. The saddle points for ω_1 and ω_2 integrals are respectively found to be

$$\omega_1^\star = \sqrt{\frac{p_{T0}(2\hat{q})^{1/3}}{R^{4/3}}} = \sqrt{p_{T0}\omega_0(R)}\,, \qquad \omega_2^\star = \sqrt{\frac{2\omega}{L\theta^2}} = \sqrt{\omega\omega_L(\theta)}\,, \tag{5.78}$$

with $\omega_0(\theta) \equiv (2\hat{q}/\theta^4)^{1/3}$ such that $\omega_0(R)$ is the lowest possible energy for a VLE inside the medium.

Several conditions are needed for these saddle points to control the energy integrations. First, the integration ranges must be wide enough, $p_{T0} \gg \omega_0(R)$ and $\omega_L(\theta) \gg \omega$, to allow for large enough logarithmic contributions. This translates into the following conditions:

$$\sqrt{\bar{\alpha}_s}\,\log\frac{p_{T0}}{\omega_0(R)} \gtrsim 1 \qquad \text{and} \qquad \sqrt{\bar{\alpha}_s}\,\log\frac{\omega_L(\theta)}{\omega} \gtrsim 1 \tag{5.79}$$

Second, for $\omega_1^\star$ to be a genuine saddle point, it must remain smaller than ω_c, meaning

$$p_{T0} < \omega_c\left(\frac{R}{\theta_c}\right)^{4/3} = \frac{\hat{q}^{5/3}L^4R^{4/3}}{2^{7/3}} \tag{5.80}$$

When this condition is satisfied (which is always the case in practice), the integral over ω_1 is dominated by relatively low-energy emissions with $\omega_0(\theta) < \omega_1 < \omega_c$, i.e. by the triangular region of the "inside medium" phase-space with energies below ω_c, see Fig. 5.5. In the opposite situation, which would occur for sufficiently large p_{T0}, the dominating region in phase-space is the rectangular region at $\omega_c \leq \omega_1 \leq p_{T0}$ and $\theta_c < \theta_1 < R$; see Appendix G for details.

Third, energy conservation in Eq. (5.77) requires $\omega_2^\star \leq \omega_1^\star$ which implies a θ-dependent upper limit on ω. When computing the fragmentation function using Eq. (5.75), this condition must be satisfied for all the angles θ that are integrated over, including lower bound $\theta_{\rm min} = k_{\perp,\rm min}/\omega$. This defines a critical energy ω_{cr}, obtained for $\theta = \theta_{\rm min}$, below which the saddle point method works:

$$\omega < \omega_{cr} = \left(p_{T0}\omega_0(R)\omega_{\rm min}\right)^{1/3} = \left(\frac{p_{T0}Lk_{\perp,\rm min}^2(2\hat{q})^{1/3}}{2R^{4/3}}\right)^{1/3} = \left(\frac{p_{T0}k_{\perp,\rm min}^2}{R^2}\right)^{1/3}\left(\frac{R}{\theta_c}\right)^{2/9}. \quad (5.81)$$

When the conditions in Eqs. (5.79)–(5.81) are satisfied, the saddle point method gives a meaningful approximation for the double differential gluon distribution in (5.77), which reads

$$T_{i,\rm out}(\omega,\theta^2|p_{T0},R^2) \simeq \frac{\alpha_s C_i}{4\pi}\exp\left\{\sqrt{\frac{3\bar{\alpha}_s}{2}}\,\log\frac{p_{T0}}{\omega_0(R)}\right\}\exp\left\{\sqrt{\bar{\alpha}_s}\,\log\frac{\omega_L(\theta)}{\omega}\right\} \quad (5.82)$$

The first exponential comes from the integrations over θ_1^2 and ω_1, i.e. over the "inside" region, and can be interpreted as the number of partonic sources generated via VLEs. The second exponential represents the number of gluons generated by each of these sources via gluon cascades developing outside the medium. This simple factorisation between the "inside" and the "outside" jet dynamics holds strictly speaking only in the saddle point approximation (and for energies $\omega \leq \omega_{cr}$) and is ultimately a consequence of the colour decoherence which washes out any correlation between the emission angles outside and inside the medium.

Integrating (5.76) over θ using Eq. (5.75) we find the fragmentation function for $\omega \leq \omega_{cr}$:

$$\omega D_i^{\rm med}(\omega) \simeq \frac{\sqrt{\bar{\alpha}_s}C_i}{4C_A}\exp\left\{\sqrt{\bar{\alpha}_s}\left(\sqrt{\frac{3}{2}}\log\frac{p_{T0}R^{4/3}}{(2\hat{q})^{1/3}} + \log\frac{2\omega}{k_{\perp,\rm min}^2 L}\right)\right\}. \quad (5.83)$$

The integration is dominated by the lower limit, $\theta = k_{\perp,\rm min}/\omega$. The respective contribution of the first term $\propto T_i^{\rm vac}$ in (5.76), that would be non-zero only for $\omega > \omega_0(R)$, is comparatively small, since it lacks the evolution outside the medium. Since $2\omega/k_{\perp,\rm min}^2 L = \omega/\omega_{\rm min} \gg 1$, the second logarithm in (5.83) is positive and $\omega D_i^{\rm med}(\omega)$ decreases when decreasing ω.

Our predictions are shown in Fig. 5.6 for the fragmentation function in Fig.5.6a and the nuclear modification factor $R_i(x|p_{T0})$ in Fig. 5.6b. This nuclear modification factor is defined by:

$$R_i(x|p_{T0}) = \frac{D_i^{\rm med}(\omega)}{D_i^{\rm vac}(\omega)} \quad (5.84)$$

with $D_i^{\rm vac}(\omega)$ given by (4.25) (or (5.75)). These plots compare the exact results at DLA based on Eq. (5.74) and the numerical integration of Eq. (5.77) for the vacuum and medium results respectively, to their asymptotic counterparts. The latter are obtained by taking the asymptotic behaviour of (5.74) in the vacuum case and by using the saddle-point approximation Eq. (5.83) for the medium results. In Fig. 5.6b we consider two different values for the IR cut-off $k_{\perp,\rm min}$ (blue: $k_{\perp,\rm min} = 200$ MeV, red: $k_{\perp,\rm min} = 100$ MeV). Overall we see a good agreement, which is moreover improving when $k_{\perp,\rm min}$ decreases, i.e. when the phase-space increases and the saddle point method becomes more reliable.

The fact that the ratio $R_i(x|p_{T0})$ increases at small ω can be traced back to angular ordering and the associated humpback plateau. Unlike the double-differential gluon distribution

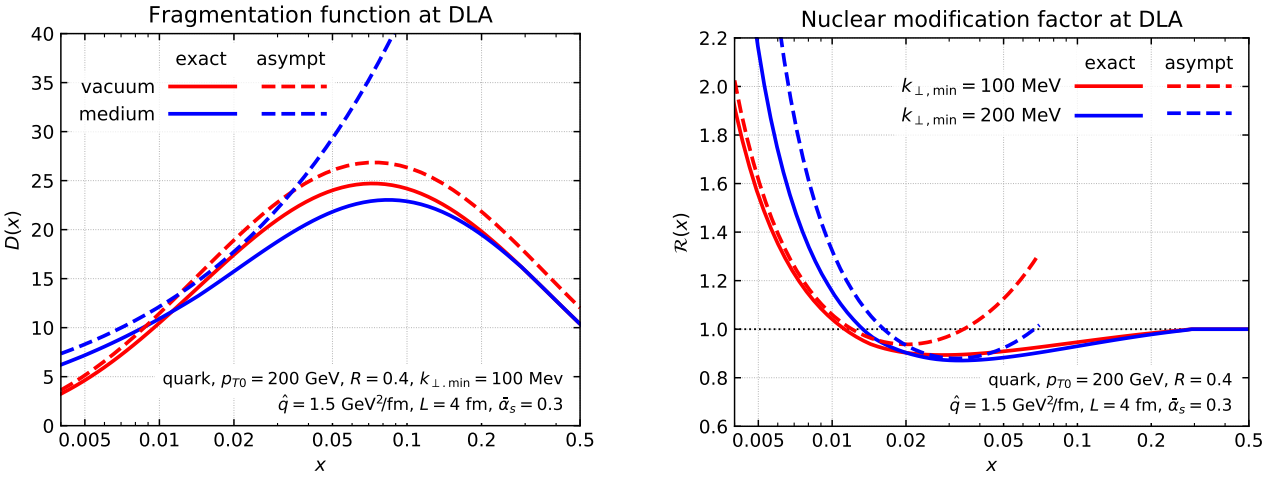

(a) Fragmentation function at DLA

(b) Nuclear modification $\mathcal{R}(x)$ at DLA

Figure 5.6: Comparison of the exact calculation of fragmentation functions (solid lines) and the asymptotic approximations (dashed lines).

(5.74) which keeps increasing when decreasing ω at fixed θ, the vacuum fragmentation function $\omega D_i^{\rm vac}(\omega)$ in (4.25) develops a maximum at $\omega \simeq \omega_{\rm hump} = (Ek_{\perp,\min}/R)^{1/2}$ and decreases very fast for ω below $\omega_{\rm hump}$. This is due to the fact that the angular phase-space at $k_{\perp,\min}/\omega < \theta < R$ permitted by angular ordering shrinks to zero when decreasing ω. For sufficiently small ω, namely such that[5] $\omega^3 \lesssim p_{T0}k_{\perp,\min}^2/R^2$, the denominator $\omega D_i^{\rm vac}(\omega)$ in the medium/vacuum ratio $R_i(x|p_{T0})$ decreases faster with $1/\omega$ than the respective numerator $\omega D_i^{\rm med}(\omega)$ (see also Fig. 5.6a), so the ratio is increasing.

5.3.1.2 Including running coupling and hard collinear corrections

The calculation made in the previous subsection does not take into account single logarithmic corrections coming from the running of the coupling constant and the hard collinear splittings. We briefly discuss two ways of including semi-analytically such corrections. Each one has its own advantages and drawbacks.

The first way is to calculate the convolution (5.77) in Mellin space. In Mellin space, the fixed coupling fragmentation function (5.75) or (4.25) in vacuum reads:

$$\omega D_g(\omega|E,R^2) = \int \frac{{\rm d}j}{2\pi i} C_j(\bar{\alpha}_s) \exp\left(\int_{k_{\perp,\min}^2}^{(ER)^2} \frac{{\rm d}Q^2}{Q^2} \gamma_j(\bar{\alpha}_s) + (j-1)\log(E/\omega) \right) \tag{5.85}$$

with γ_j the anomalous dimension, and C_j the coefficient function such that:

$$\begin{aligned} \gamma_j(\bar{\alpha}_s) &= \tfrac{1}{4}\left(-(j-1) + \sqrt{(j-1)^2 + 8\bar{\alpha}_s} \right) \\ C_j(\bar{\alpha}_s) &= \tfrac{1}{2}\left(1 + \tfrac{j-1}{\sqrt{(j-1)^2+8\bar{\alpha}_s}} \right) \end{aligned} \tag{5.86}$$

From this expression, running coupling corrections can be included using $\bar{\alpha}_s(Q^2)$ instead of $\bar{\alpha}_s$ in the Q^2 integral corresponding to the evolution, while $\bar{\alpha}_s$ remains fixed (evaluated at $Q = ER$) inside the coefficient function. Corrections from hard collinear splittings are added using:

$$\gamma_j^{\rm MLLA}(\bar{\alpha}_s) = \gamma_j(\bar{\alpha}_s(Q^2)) + 2B_g \frac{\bar{\alpha}_s}{j^2 + 8\bar{\alpha}_s} \tag{5.87}$$

[5] The upper limit $p_{T0}k_{\perp,\min}^2/R^2$ is smaller than ω_{cr}^3 guaranteeing the validity of the saddle-point method.

instead of γ_j in the evolution integral. B_g is the finite part of the gluon splitting function.

Then the convolution (5.77) between the inside evolution and the outside evolution is made using (5.85) amended as explained. In the evolution inside the medium, the lower limit of the Q^2 integration is the in-medium boundary of the veto region, while for the outside evolution, the upper limit is the out-medium boundary. Such a calculation is complicated, especially because of the convolution and the final inverse Mellin transform. However, as in the fixed coupling case, one may obtain a good approximation using the saddle point method. Instead of taking this path, we explain now a different approach more suitable for a final numerical evaluation.

The idea is to start with (4.22) where running coupling effects and hard-collinear contributions are already included [176]. From this equation, one obtains the following equation for the function T [145, 177]:

$$T(\omega,\theta^2 \mid E,R^2) = \bar{\alpha}_s(\omega^2\theta^2)\frac{\omega}{E}P_{gg}(\frac{\omega}{E}) + \int_{\theta^2}^{R^2}\frac{d\theta_1^2}{\theta_1^2}\int_{\omega/E}^{1} dz_1 \bar{\alpha}_s(z_1^2E^2\theta_1^2)P_{gg}(z_1)T(\omega,\theta^2 \mid z_1E,\theta_1^2) \tag{5.88}$$

with $P_{gg}(z) = (1-z)\Phi_g^{gg}(z)/(2C_A)$. Note that we still work within the large N_c limit in order to avoid complications due to quark/gluon mixing.

Let us first take into account the running of the coupling at one loop, while $P_{gg}(z)$ is approximated by its soft behaviour $P_{gg}(z) \simeq 1/z$. The Landau pole in the running coupling is regularised by adding a constant $C_{\rm reg}$ such that

$$\bar{\alpha}_s(k_\perp^2) = \bar{\alpha}_s(\omega^2\theta^2) = \frac{1}{\bar{\beta}_0}\frac{1}{\log(\omega^2\theta^2/\Lambda^2 + C_{\rm reg})} \tag{5.89}$$

where $\bar{\beta}_0 = \beta_0\pi/N_c$. In intermediate steps, we shall use $C_{\rm reg} = 0$. Taking the logarithmic derivative with respect to E and R^2, one finds the following partial differential equation

$$ER^2\frac{\partial^2 T}{\partial E\partial R^2} = \frac{1}{\bar{\beta}_0}\frac{T}{\log(ER^2/\Lambda^2)} \tag{5.90}$$

Then, changing to the variables $\kappa = \log(E/\omega)$ and $\lambda = \log(R^2/\theta^2)$ so that

$$\mathcal{T}(\kappa,\lambda,\mu) \equiv T(\omega,\theta^2 \mid E,R^2) \tag{5.91}$$

one gets

$$\frac{\partial^2\mathcal{T}}{\partial\kappa\partial\lambda} = \frac{1}{\bar{\beta}_0}\frac{\mathcal{T}}{2\kappa+\lambda+\mu} \tag{5.92}$$

with $\mu = \log(\omega^2\theta^2/\Lambda^2)$ and the initial conditions $\mathcal{T}(0,\lambda) = \mathcal{T}(\kappa,0) = 1/(\bar{\beta}_0\mu)$.

Including hard collinear splittings consists in adding the integral between 0 and 1 of the finite part of the splitting function, namely using

$$P_{gg}(z) \simeq \frac{1}{z} + \int_0^1 \mathrm{d}z\,\left(P_{gg}(z) - \frac{1}{z}\right) = \frac{1}{z} - \frac{11}{12} \equiv \frac{1}{z} + B_g \tag{5.93}$$

With this approximated splitting function and the running of the coupling, the evolution equation for $T(\omega,\theta^2 \mid E,R^2)$ or equivalently $\mathcal{T}(\kappa,\lambda,\mu)$ can also be put into a partial differential equation form,

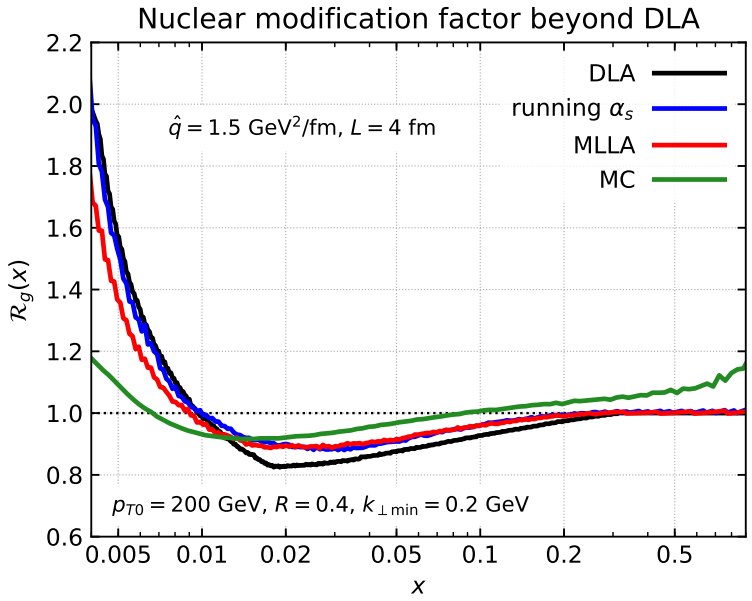

Figure 5.7: Nuclear modification factor for the fragmentation function beyond DLA

$$\frac{\partial^3 \mathcal{T}}{\partial \kappa^2 \partial \lambda} + \frac{\partial^2 \mathcal{T}}{\partial \kappa \partial \lambda} = (1 + B_g)\frac{\partial \bar{\alpha}_s \mathcal{T}}{\partial \kappa} + \bar{\alpha}_s \mathcal{T} \tag{5.94}$$

with the initial conditions

$$\mathcal{T}(\kappa, 0) = \frac{1}{\bar{\beta}_0 \mu}(1 + B_g e^{-\kappa}) \tag{5.95}$$

$$\mathcal{T}(0, \lambda) = \frac{1}{\bar{\beta}_0 \mu}(1 + B_g) \tag{5.96}$$

$$\frac{\partial \mathcal{T}}{\partial \kappa}(0, \lambda) = \frac{1}{\bar{\beta}_0 \mu}\Big(- B_g + \frac{(1 + B_g)^2}{\bar{\beta}_0} \log\left(1 + \lambda/\mu\right)\Big) \tag{5.97}$$

$$\frac{\partial \mathcal{T}}{\partial \lambda}(\kappa, 0) = \frac{1}{\bar{\beta}_0^2 \mu} \int_0^\kappa d\kappa_1 \frac{(1 + B_g e^{-\kappa_1})(1 + B_g e^{\kappa_1 - \kappa})}{2(\kappa - \kappa_1) + \mu} \tag{5.98}$$

since equation (5.88) gives not only the differential equation but also the initial conditions. The partial differential equation (PDE) is then solved numerically on a two-dimensional grid, to get the function $\mathcal{T}(\kappa, \lambda, \mu)$ for several values of μ.

This PDE is similar to the one given in Gerwick et al [178] in term of logarithmic accuracy but it has the advantage of being mathematically equivalent to the master equation (5.88) so that the solution T satisfies the Chapman-Kolmogorov relation. This enables to use (5.76) and (5.77) in order to calculate the medium-modified version of T.

Numerical results are shown Fig. 5.7 for the nuclear modification factor of the jet fragmentation function. Four calculations are compared: `(i)` the DLA result already shown above, `(ii)` the effect of the running coupling alone using the solution of (5.92), `(iii)` the MLLA approximation including both running coupling and hard collinear radiations thanks to the PDE (5.94), `(iv)` a MC calculation with full DGLAP splitting function and energy conservation (see Chapter 6). As expected, DLA overestimates the number of soft gluons inside the jet but the enhancement at small energies is still significant if we include the effects of the running coupling and the hard-collinear emissions. This shows the robustness of decoherence to generate soft

gluons inside jets in the presence of a medium.

5.3.2 Jet average energy loss

As the last exercise of this chapter, we estimate the jet energy loss within our factorised picture. So far, we have focused on the vacuum-like emissions since our arguments were grounded at DLA where one neglects the medium induced radiations. As explained in Section 5.2.2, this is correct for the vacuum-like series inside the medium, except for the set of partons at the end of the VLE cascade inside the medium which *by definition* cross all the medium before radiating outside. During this travel, such emission triggers medium-induced jets as those studies in Chapter 4, Section 4.3 so that the jet loses energy from large angles radiations.

For the intrajet multiplicity, at first sight, it is legitimate to neglect this energy loss since it does not change the number of partons produced but merely shifts their final energy in the spectrum (recall also that a double-logarithmic cascade does not satisfy energy conservation anyway). It is certainly not correct for jet observables which are strongly sensitive to the energy of the final state particles. For such quantities, one cannot ignore medium-induced processes. However, one can often rely on the factorisation between vacuum-like emissions and medium-induced jets to estimate them.

Jet cross-section in A-A collisions. In this subsection, we deal with the average jet energy loss $\mathcal{E}$. This quantity is ambiguous as it is not generally a well defined quantity in pQCD. It is not even measurable in experiments. The reason for this is that measuring an energy loss requires the knowledge of the energy of the leading parton sourcing the jet or some "vacuum-equivalent" jet. From a theoretical point of view, this is not a well defined problem whereas it is clearly not experimentally realisable.

Nevertheless, one can use this quantity as an intermediate tool in order to obtain an estimation of a well defined observable: the jet cross-section. We start then by explaining how the average jet energy loss enters into the calculation of the jet cross-section in nucleus-nucleus collisions. Jets are defined in this subsection with a single parameter $R \lesssim 1$, which should be thought as the jet radius in the anti-k_t algorithm or the opening angle of the effective cone in cone-based jet definitions.

We call $\mathrm{d}\sigma_{q/g}/\mathrm{d}p_{T0}$ the Born level cross-section for producing respectively a quark or a gluon with transverse momentum p_{T0} at central rapidity in pp collision. At the lowest order in α_s, the inclusive jet cross-section in pp collisions can be approximated by:

$$\frac{\mathrm{d}\sigma^{pp}_{\mathrm{jet}}}{\mathrm{d}p_T} = \frac{\mathrm{d}\sigma_q}{\mathrm{d}p_T} + \frac{\mathrm{d}\sigma_g}{\mathrm{d}p_T} + \mathcal{O}(\alpha_s^3) \tag{5.99}$$

At this order, it is independent of R.

Now, let us assume that energy loss is the dominant effect of the medium in the calculation of the inclusive jet cross section in A-A collisions (this is of course a very strong assumption). A jet initially made of a single leading parton $i \in \{q, g\}$ with energy p_{T0} evolves via vacuum-like and medium-induced emissions in the medium. We introduce the probability $P_i(\mathscr{E}|p_{T0}, R)$ for the reconstructed jet to have an energy $p_{T0} - \mathscr{E}$. In principle, this probability is non trivial even in the vacuum as the leading parton can radiate many soft gluons at angles larger than R. However, if R is large enough, such contributions can be neglected. Therefore, p_{T0} can be thought as the energy of an equivalent jet which would have evolved in the vacuum, so that $P_i(\mathscr{E}|p_{T0}, R)$ is the probability for a jet to loose an energy $\mathscr{E}$.

From the probability P, one can calculate the jet yield in A-A collisions as follows:

$$\frac{1}{\mathrm{T}_{AA}}\frac{\mathrm{d}\sigma_{\mathrm{jet}}^{AA}}{\mathrm{d}p_T} \simeq \sum_{i\in\{q,g\}} \int_0^\infty \mathrm{d}p_{T0} \int_0^\infty \mathrm{d}\mathscr{E}\, \delta(p_T - p_{T0} + \mathscr{E}) P_i(\mathscr{E}|p_{T0}, R) \frac{\mathrm{d}\sigma_i}{\mathrm{d}p_{T0}} \tag{5.100}$$

The factor T_{AA} accounts for the geometric enhancement of the jet yield due to the larger number of nucleons in a nucleus A. It depends only on the centrality of the collision and on the nature of the nucleus. Equation (5.100) states that the initial *parton* with transverse momentum p_{T0} ends up as final state jet with energy $p_{T0} - \mathscr{E}$ with probability P. An other underlying assumption of (5.100) is the absence of nuclear parton distribution function effects since we use the same Born-level quark/gluon cross-section as in the *pp* baseline. This formula is hence an estimation for phenomenological applications rather than a rigorous pQCD calculation with a controlled α_s expansion.

Performing the p_{T0} integration in (5.100) and a Taylor expansion of $P_i\sigma_i$ for $\mathscr{E}/p_T \ll 1$, one gets:

$$\frac{1}{\mathrm{T}_{AA}}\frac{\mathrm{d}\sigma_{\mathrm{jet}}^{AA}}{\mathrm{d}p_T} = \sum_{i\in\{q,g\}} \frac{\mathrm{d}\sigma_i}{\mathrm{d}p_T} + \frac{\partial}{\partial p_T}\Big(\mathcal{E}_i(p_T, R)\frac{\mathrm{d}\sigma_i}{\mathrm{d}p_T}\Big) + \mathcal{O}\big((\mathscr{E}/p_T)^2\big) \tag{5.101}$$

$$\simeq \sum_{i\in\{q,g\}} \frac{\mathrm{d}\sigma_i(p_T + \mathcal{E}_i(p_T, R))}{\mathrm{d}p_T} \tag{5.102}$$

where the $\mathcal{O}\big((\mathscr{E}/p_T)^2\big)$ term makes sense only if the probability P as a finite support $\mathcal{E} < \mathcal{E}_{\max} \leq p_{T0}$ so that $\mathcal{O}\big((\mathscr{E}/p_T)^2\big) = \mathcal{O}\big((\mathscr{E}_{\max}/p_T)^2\big)$. This means that if the typical maximal energy loss is negligible in front the initial p_{T0} of the parton, the jet cross-section in A-A can be understood as a simple shift of the partonic cross-section. Yet, this shift is different according to the "flavour" of the leading parton and is given by the average jet energy loss $\mathcal{E}_i(p_{T0}, R)$:

$$\mathcal{E}_i(p_{T0}, R) \equiv \int_0^\infty \mathrm{d}\mathscr{E}\, \mathscr{E} P_i(\mathscr{E}|p_T, R) \tag{5.103}$$

To get the second line, we have neglected the logarithmic derivative of $\mathcal{E}$ with respect to p_T in front of the logarithmic derivative of the differential cross-section. This is allowed because the differential cross-section $\mathrm{d}\sigma_i$ is a steeply falling function of p_T whereas we will see that $\mathcal{E}_i(p_T)$ increases with a α_s suppressed power of p_T. This steeply falling property of $\mathrm{d}\sigma_i$ as a function of p_T implies that $R_{AA} \leq 1$.

Calculation of $\mathcal{E}_i$ at DLA for the vacuum-like series. Let us now turn to an analytic estimation of the quantity $\mathcal{E}_i(p_{T0}, R)$. In Sections 4.3.2 and 4.3.3.1, we have investigated the energy loss by a leading parton via medium-induced jets. We have argued that the energy lost by the jet via medium-induced radiations at large angles ($\theta > R$) is controlled by multiple branchings (resummed to all orders) and the associated characteristic scale is ω_{br}. The results of (4.70) are summarized as follows:

- For jets with energies $p_{T0} \gg \upsilon\omega_{\mathrm{br}}$, the jet energy loss via MIEs becomes independent of p_{T0}:

$$\epsilon_{i,\mathrm{MIE}}(R) \simeq \upsilon\omega_{\mathrm{br}} + 2\bar{\alpha}_s\omega_c\sqrt{\frac{2c_*\theta_c}{R}} \qquad \text{when} \quad p_{T0} \gg \upsilon\omega_{\mathrm{br}}\,. \tag{5.104}$$

- Jets with $p_{T0} \lesssim \upsilon\omega_{\mathrm{br}}$ lose their whole energy via democratic branchings: $\epsilon_{i,\mathrm{MIE}}(R) \simeq \epsilon_{i,\mathrm{flow}} \simeq p_{T0}$.

- For a large jet radius $R \gtrsim \theta_c/\bar{\alpha}_s^2$, the flow component dominates over the spectrum component, $\epsilon_{i,\text{flow}} \gg \epsilon_{i,\text{spec}}$, for any energy E, and the energy loss $\epsilon_{i,\text{MIE}} \simeq \epsilon_{i,\text{flow}}$ becomes independent of R.

We can now consider the generalisation of the above results to the full parton showers, including both VLEs and MIEs. In the sequential picture described in Section 5.2, in which the two kinds of emissions are factorised in time, each VLE occurring inside the medium acts as an independent source of MIEs and hence the energy loss by the full jet can be computed by convoluting the distribution of partonic sources created by the VLEs in the medium with the energy loss via MIEs by any of these sources. Assuming that all the in-medium VLEs are collinear with the jet axis (which is the case in the collinear picture described in Section 5.2), the energy lost by the *full* jet is computed as

$$\begin{aligned}\mathcal{E}_i(p_{T0},R) &\simeq \int_{\omega_0(R)}^{p_{T0}} \mathrm{d}\omega\, \frac{\mathrm{d}N_{\text{VLE}}}{\mathrm{d}\omega}\, \epsilon_{\text{MIE}}(\omega,R)\,, \\ &\simeq \epsilon_{i,\text{MIE}}(p_{T0},R) + \frac{2\alpha_s C_i}{\pi}\int_{\theta_c}^{R}\frac{\mathrm{d}\theta}{\theta}\int_{\omega_0(\theta)}^{p_{T0}}\frac{\mathrm{d}\omega}{\omega}\,\mathrm{I}_0\left(2\sqrt{\bar{\alpha}_s\log\frac{p_{T0}}{\omega}\,\log\frac{R^2}{\theta^2}}\right)\epsilon_{g,\text{MIE}}(\omega,R)\end{aligned} \tag{5.105}$$

where $\mathrm{d}N_{\text{VLE}}/\mathrm{d}\omega$ is the energy distribution of the partons created via VLEs inside the medium. The second line follows after using the DLA result for the gluon multiplicity, (4.24). This is of course a rough approximation which overestimates the number of sources, but it remains useful to get a physical insight. Similarly, for qualitative purposes, one can use the simple estimate for $\epsilon_{i,\text{MIE}}(\omega,R)$ given by the sum of Eqs. (4.63)–(4.69).

In Fig. 5.8, we show the numerical results of Eq. (5.105) as a function of the initial p_{T0} of the parton and the jet opening angle R[6]. As expected, $\mathcal{E}_i(p_{T0},R)$ rises significantly as p_{T0} increases, as a consequence of the in-medium fragmentation. More surprisingly, we observe a very mild increase of the jet energy loss as R increases. One would naively expect that the more the jet opening angle is large, the more the energy loss is recovered at large angles (or equivalently, the spectrum component (4.69) decreases). However, this effect is compensated by the increase of the in-medium phase space for radiations. This compensation phenomenon has also been pointed out in [179] within the hybrid strong/weak coupling model with medium response included. The figure 5.8 should also be compared with the Monte Carlo calculations of this function made in Chapter 8. There is a very nice qualitative agreement between the simple analytic estimate (5.105) and these Monte Carlo results.

It is enlightening to understand the asymptotic behaviour of (5.105) at large p_{T0}. This is straightforward from the analysis made for the double-logarithmic fragmentation function. Recall that when $p_{T0} \leq \omega_c(R/\theta_c)^{4/3}$, the in-medium multiplicity is controlled by the position of saddle point $\omega_1^\star$. If this saddle point is larger than ω_{br}, one can approximate $\epsilon_{i,\text{MIE}}$ by ω_{br} in (5.105) meaning that the typical energy loss of an in-medium source is ω_{br} since its initial energy satisfies $\omega \gg \omega_{\text{br}}$. The condition $\omega_1^\star \geq \omega_{\text{br}}$ is equivalent to $p_{T0} \geq \bar{\alpha}_s^4\omega_c(\theta_c/R)^{4/3}$. Thus, (5.105) has the following large p_{T0} behaviour:

$$\mathcal{E}_i(p_{T0},R) \sim \omega_{\text{br}}^{(A)}\frac{C_i}{2C_A}\left(\frac{p_{T0}}{\omega_0(R)}\right)^{\sqrt{\frac{3\bar{\alpha}_s}{2}}} \qquad \text{if } \bar{\alpha}_s^4\omega_c\left(\frac{R}{\theta_c}\right)^{4/3} \ll p_{T0} \leq \omega_c\left(\frac{R}{\theta_c}\right)^{4/3} \tag{5.106}$$

[6]The precise description of the R dependence of the jet energy loss for $R \sim 1$ would require a proper treatment of initial state radiations, which is beyond our current framework.

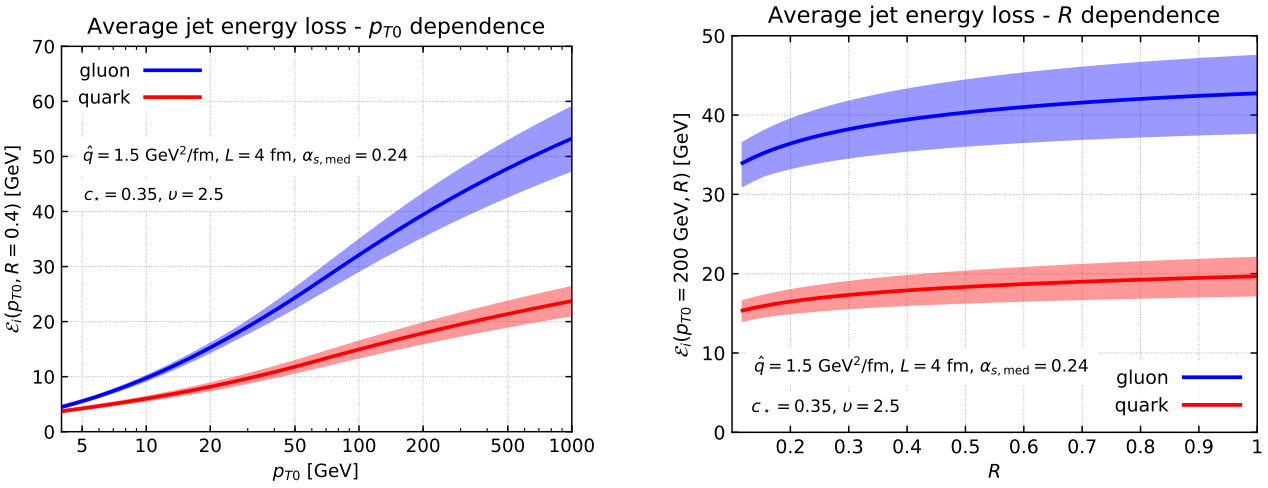

Figure 5.8: Double-logarithmic estimate of the jet energy loss as a function of p_{T0} and R, obtained from a numerical integration of (5.105). The bands correspond to 25% variations of the parameter $c_\star$ and υ around $c_\star = 0.35$ and $\upsilon = 2.5$. Note that (5.105) predicts an exact Casimir scaling of the quark and gluon jet energy loss.

This power-like increase of the energy loss with p_T is a simple consequence of the larger phase space available for radiations inside the medium as p_{T0} increases. It is a crucial ingredient to explain the flatness of the R_{AA} ratio for jet cross-section even at large p_T. Last but not least, (5.105) and (5.106) predicts that the jet energy loss is proportional to the Casimir of the initial parton.

The condition $p_{T0} \leq \omega_c (R/\theta_c)^{4/3}$ is not very restrictive for phenomenological applications as $\omega_c (R/\theta_c)^{4/3} = \mathcal{O}(1\text{ TeV})$ for typical values of $\hat{q}$ and L. For completeness we give also the asymptotic behaviour of (5.105) when p_{T0} is larger than $\omega_c (R/\theta_c)^{4/3}$. In this case, the multiplicity is controlled by the phase space above ω_c and θ_c so that the energy loss increases like:

$$\mathcal{E}_i(p_{T0}, R) \sim \omega_{\mathrm{br}}^{(A)} \frac{C_i}{\sqrt{4\pi} C_A} \frac{\exp\left(2\sqrt{\bar{\alpha}_s \log(p_{T0}/\omega_c)\log(R/\theta_c)}\right)}{(\bar{\alpha}_s \log(p_{T0}/\omega_c)\log(R/\theta_c))^{1/4}} \qquad \text{if } p_{T0} \geq \omega_c \left(\frac{R}{\theta_c}\right)^{4/3} \tag{5.107}$$

Jet quenching vs. hadron quenching. To conclude, let us comment about the difference between the jet yield and the *hadron* yield in nucleus-nucleus collisions. For a steeply falling cross-section, the method (5.101) would give a wrong answer if the probability P is such that the mean $\mathcal{E}$ is significantly larger than the typical energy loss corresponding to the energy where P is maximal [84]. This is a consequence of the steeply falling cross-section which favours typical events rather than the mean scenario. In this situation, one cannot truncate the Taylor expansion up to the first order derivative. The alternative strategy is to expand (5.100) as a function of $1/n$ where n is the (large) power of the power suppressed cross-section $\mathrm{d}\sigma_i$ [84]. For the hadron cross-section, such scenario occurs since we have seen in Chapter 4, Section 4.3 that the mean *parton* energy loss is of order $\alpha_s \omega_c$ whereas the typical event by event energy loss is $\omega_{\mathrm{br}} = \alpha_s^2 \omega_c \ll \alpha_s \omega_c$.

For jets, this is different though. Introducing the parameter R enforces the energy loss by the jet to be of the order of the event by event energy loss ω_{br} so that the gluons carrying away this energy end up at angles larger than R. For jets, the typical and the mean energy loss

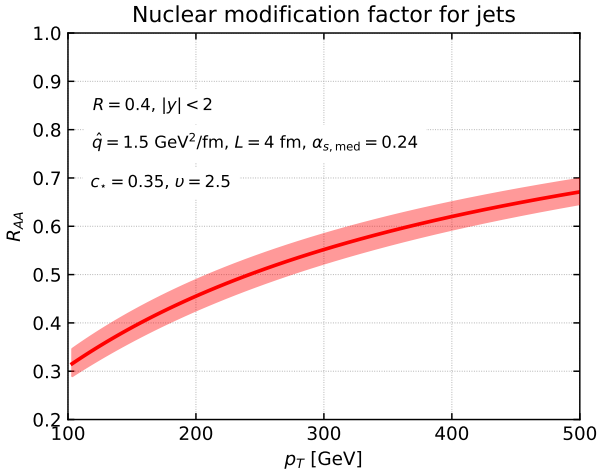

Figure 5.9: Analytic estimation of the nuclear modification factor for jets R_{AA}. The bands correspond to 25% variations of the parameter $c_\star$ and υ around $c_\star = 0.35$ and $\upsilon = 2.5$. For the quark and gluon Born level cross-sections, we used a power law decrease $A_i(\hat{p}_T/p_T)^{n_i+m_i \log(p_T/\hat{p}_T)}$ from a fit of the numerical cross-sections over $p_T \in [100, 500]$ GeV and $|y| < 2$ with LHAPDF6 parton distribution functions [180].

are of the same order so that one could expect Eq. (5.101) to give a good estimate of the *jet* cross-section in AA.

In Fig. (5.9), we show an analytic estimation of the R_{AA} ratio based on Eqs. (5.101) and the average energy loss function (5.105). The general trend is good, namely a strong suppression, slightly increasing with p_T. However, the suppression is largely overestimated with respect to the data and the Monte Carlo results obtained in Chapter 8. One explanation is that the assumption $\mathcal{E}_i \ll p_{T0}$ is not really realised as one can see from Fig. 5.8. Another explanation is that large angle energy loss fluctuations are as large as the mean $\sim \omega_{\mathrm{br}}$. Moreover, for jets, this energy loss is enhanced by the multiplicity of vacuum-like sources, and this multiplicity has also large p_T-dependent event-by-event fluctuations. Thus, the first order truncation in (5.101) is not a good approximation and the quenching weight method would be a better option if we knew the full probability distribution $P_i(\mathscr{E}|p_T, R)$.

Chapter 6

JetMed: a Monte Carlo parton shower for jets in the medium

Chapter 5 was dedicated to the theoretical foundation of our factorised picture for the parton showers in the presence of a dense QCD medium. In the last section of this chapter, we have tried to include analytically the sub-leading single logarithmic corrections for the vacuum-like shower as well as the medium-induced emissions in order to quantify the energy lost by jets in the plasma. Another approach consists in numerically implementing the classical branching process in a so-called Monte Carlo event generator that mimics the evolution of the jet. This numerical approach is equivalent to the resolution of the evolution equation for the generating functional of the exclusive multi-particle production cross-sections so that the large terms in the α_s expansion of the cross-section — due to either large soft/collinear logarithms for the vacuum-like emissions or large medium path length over formation time ratio for the medium-induced emissions —are correctly resummed to all orders.

In this chapter, we describe the Monte Carlo parton shower for jet fragmentation in a dense QCD medium as it emerges from the ideas developed in the two previous chapters. The first Section 6.1 recalls the basics of the Sudakov veto algorithm used to generate the "times" in the branching processes. The two following Sections 6.2 and 6.3 describe in details the two main modules of the full parton shower: the vacuum shower which solves the coherent branching evolution equation (4.10) and the medium induced shower which solves the evolution equation for medium-induced jets (4.65). These two modules are combined in the full medium shower according to the principles exposed in Chapter 5: this is the topic of Section 6.4. In this section, we also briefly present the code architecture. The last section 6.5 compares our parton shower with other Monte Carlo generators.

6.1 The Sudakov veto algorithm

A Monte Carlo parton shower simulates a classical branching process. In this section, we call t or "time" the ordering variable of the process, while keeping in mind that the physical sense of t may change according to the branching process at hand. The building block of a branching process is a time branching rate that we call $\Gamma(t)$. The probability $\mathrm{d}P$ for a branching to occur between t and $t + \mathrm{d}t$ is, by definition:

$$\mathrm{d}P \equiv \Gamma(t)\mathrm{d}t \tag{6.1}$$

From Γ, one can calculate the probability density $\mathcal{B}(t)$ for a branching to occur at time t, *knowing that* no branching occurred between t_0 and t. This is given by the exponential decay

law:

$$\mathcal{B}(t) = \Gamma(t) \exp\left(- \int_{t_0}^{t} \mathrm{d}t' \, \Gamma(t') \right) \Theta(t - t_0) \tag{6.2}$$

This probability density is properly normalised over the time interval $[t_0, \infty]$. If the branching process has an intrinsic maximal time $t_{\max}$, the normalised probability density $\mathcal{B}$ is given by (6.2) divided by its integral between t_0 and $t_{\max}$.

In a Monte Carlo parton shower, one must be able to select a time according to the probability density $\mathcal{B}$. This gives the time of the subsequent splitting, if the previous one occurred at time t_0. The purpose of this section is to recall the standard methods used to sample $\mathcal{B}$.

6.1.1 Basics of random variable sampling

We assume that we are able to generate numerically random numbers following the uniform distribution $\mathcal{U}(0,1)$ over $[0,1]$. We give here two general methods to sample x according to the density $\mathcal{B}(x)$ for $x \in [x_0, x_{\max}]$.

Inverse transform method. If the repartition function $B(x)$

$$B(x) = \int_{x_0}^{x} \mathrm{d}x' \, \mathcal{B}(x') \tag{6.3}$$

is strictly increasing and if one can find its inverse B^{-1}, then it is straightforward to generate x according to the probability density $\mathcal{B}$:

$$x = B^{-1}(u) \tag{6.4}$$

with u following $\mathcal{U}(0,1)$. For $\mathcal{B}$ of the form (6.2), if one knows a primitive γ of Γ and its inverse γ^{-1}, then the inversion methods reads:

$$t = \gamma^{-1}\Big(\gamma(t_0) - \log(u)\Big) \tag{6.5}$$

Hit-or-miss (rejection) method. When one cannot find analytically either the repartition function or its inverse, one can rely on the hit-or-miss method. If one finds a function $\mathcal{S}(x)$ and a constant $M \geq 1$ such that:

$$\mathcal{B}(x) \leq M\mathcal{S}(x) \tag{6.6}$$

for all x in $[x_0, x_{\max}]$, and such that one knows how to sample x following the density $\mathcal{S}(x)$, the variable x is selected according to the following procedure:

- Step 1: select x according to $\mathcal{S}$, and u according to $\mathcal{U}(0,1)$ independently,
- Step 2: while

$$u > \frac{\mathcal{B}(x)}{M\mathcal{S}(x)} \tag{6.7}$$

  go back to step 1, otherwise stop and select x.

The final x that comes out of this algorithm follows the density $\mathcal{B}$.

Note that if the function $\mathcal{B}$ is bounded by M on $[x_0, x_{\max}]$, one can use $\mathcal{S} = \mathcal{U}(x_0, x_{\max})$. Of course, the more M is small, the more the hit-or-miss algorithm is efficient (one can show that the expected value of the number of iteration is precisely M), so that it is advantageous to choose the envelop function $\mathcal{S}$ as close of $\mathcal{B}$ as possible.

6.1.2 Sudakov veto method

The hit-or-miss method is very general. Actually, we did not use the fact that the density $\mathcal{B}$ is of the form (6.2). The Sudakov veto method is a generalisation of the hit-or-miss method that makes use of the specific form (6.2) of the branching density probability.

We first consider the case where there is no maximal time $t_{\max} = +\infty$. The veto algorithm relies also on an envelop function $R(t)$, yet directly for the branching *rate* and not the full probability density (6.2). That is, we assume that there exists a function $R(t)$ such that:

$$\Gamma(t) \leq R(t) \qquad \text{for } t_0 \leq t \tag{6.8}$$

and such that one knows how to generate t following the probability density $\mathcal{S}_i(t)$:

$$\mathcal{S}_i(t) = R(t) \exp\left(- \int_{t_i}^{t} \mathrm{d}t' \, R(t') \right) \Theta(t - t_i) \tag{6.9}$$

where the index i refers to the initial time in the lower boundary of the integral and have been introduced for future convenience. From our discussion of the inversion method, one sees that it is interesting to look for a function R such that its primitive r and its inverse r^{-1} are analytically known.

Now, let us give the veto algorithm that generates t following the density $\mathcal{B}$:

- Step 1: Initialize the index $i = 0$, and $t_{i=0} = t_0$,
- Step 2: While $i \geq 0$, select t_{i+1} according to $\mathcal{S}_i$ (hence $t_{i+1} > t_i$) and u_{i+1} in $\mathcal{U}(0,1)$. If

$$u_{i+1} > \frac{\Gamma(t_{i+1})}{R(t_{i+1})} \tag{6.10}$$

  continue, otherwise stop and select $t = t_{i+1}$.

With respect to the hit-or-miss algorithm, one notices two main differences: firstly, the veto condition is on the ratio of the rates and not on the probability densities, and secondly the candidates t_i are picked according to a probability density that changes from one step to another. A proof of the validity of this method can be found in [181].

Finite $t_{\max}$ values are handled by stopping the veto algorithm if $t_{i+1} > t_{\max}$. Also, in all the applications of the veto algorithm discussed in this chapter, the rate $\Gamma(t)$ has the following general form:

$$\Gamma(t) = \int \mathrm{d}x \, \tilde{\Gamma}(t, x) \tag{6.11}$$

where the boundaries of the x integral may depend on t. Here, x is an other random variable over which the rate $\tilde{\Gamma}(t, x)$ is marginalised. In principle, if one knows how to select a time t distributed according to Γ, the generation of the other random variable x proceeds afterwards. One first selects t and then x following the distribution $\tilde{\Gamma}(t, x)$ properly normalised over the allowed x-range. If one does not know how to generate t directly, one can use an extension of the veto algorithm relying on an envelop rate $\tilde{R}(t, x)$ such that

$$\tilde{\Gamma}(t, x) \leq \tilde{R}(t, x) \qquad \text{for all } x \text{ and } t_0 \leq t \tag{6.12}$$

and such that the associated probability density $\mathcal{S}_i(t)$ given by (6.9) — with R given by $\tilde{R}(t, x)$ marginalised over x — is easy to generate. The properly adapted veto algorithm becomes:

- Step 1: Initialize the index $i = 0$, and $t_{i=0} = t_0$,
- Step 2: While $i \geq 0$, select t_{i+1} according to $\mathcal{S}_i$, x_{i+1} following the (normalised) density $\tilde{R}(t_{i+1}, x)$, and u_{i+1} in $\mathcal{U}(0, 1)$. If

$$u_{i+1} > \frac{\tilde{\Gamma}(t_{i+1}, x_{i+1})}{\tilde{R}(t_{i+1}, x_{i+1})} \tag{6.13}$$

  continue,
- Step 3: else, select $t = t_{i+1}$ and $x = x_{i+1}$ and stop.

This algorithm is the standard tool in Monte Carlo parton showers. In the following sections, we shall describe more precisely how this algorithm is used to generate the splitting angles in the vacuum shower and the splitting times in the medium-induced shower.

6.2 Vacuum shower

We start by describing the implementation of the vacuum-like shower. This shower serves first as a vacuum baseline for quantifying jet quenching when medium effects are introduced. Most importantly, this module enters into the full medium shower to iterate vacuum-like emissions both in the inside and outside phase space.

Generic kinematic. We will represent the massless 4-vectors corresponding to emissions using their transverse momentum p_{Ti}, their rapidity y_i and their azimuth ϕ_i. Since our physical picture is valid in the collinear limit, we will often neglect differences between physical emission angles θ and distances $\Delta R = \sqrt{\Delta y^2 + \Delta\phi^2}$ in the rapidity-azimuth plane. All showers are considered to be initiated by a single parton of given transverse momentum p_{T0}, rapidity y_0 and azimuth ϕ_0, and of a given flavour (quark or gluon).

Implementation of the shower. Still working in the collinear limit, we will generate our partonic cascades using an angular-ordered approach, starting from an initial opening angle $\theta_{\max}$. Hence the "time" variable of the branching process in the sense of the previous section is the angle θ always decreasing, or equivalently $\log(1/\theta)$. The initial parton can thus be seen as having $\theta = \theta_{\max}$ and a relative transverse momentum $k_\perp = p_{T0}\theta_{\max}$. To regulate the soft divergence of the splitting functions, we introduce a minimal relative transverse momentum cut-off $k_{\perp,\min}$. This corresponds to the transition towards the non-perturbative physics of hadronisation. Note that for a particle of transverse momentum p_{T0}, the condition $k_\perp > k_{\perp,\min}$ imposes a minimal angle $\theta > \theta_{\min} = k_{\perp,\min}/p_{T0}$, and a minimal transverse momentum $p_T > p_{T,\min} = k_{\perp,\min}/\theta_{\max}$ for the next emission.

The shower is then generated using the Sudakov veto algorithm described in Section 6.1. For the purposes of the subsequent discussion, p_{T0} and θ_0 denote respectively the transverse momentum and the angle of a *generic* parent parton, which is not necessarily the *leading* parton. Its relative transverse momentum is defined by $k_{\perp 0} = p_{T0}\theta_0$.

With the notation used in Section 6.1, the rate of the branching process is (see also (4.7) for the description of the coherent branching algorithm) reads

$$\tilde{\Gamma}_i^{\text{vac}}(\theta, z) = \frac{\alpha_s(k_\perp)}{\pi} P_i(z) \frac{1}{\theta} \tag{6.14}$$

where $i = (\mathrm{g}, \mathrm{q})$ is a flavour index, $z \equiv p_T/p_{T0}$ is the p_T fraction of the softest emission with respect to the transverse momentum p_{T0} of the parent and $k_\perp = z p_{T0}\theta = p_T\theta$ the relative transverse momentum of the emission. $P_i(z)$ is the splitting function of the parton i defined in Appendix C. z and θ are random variables, and we aim at first generating $\theta \leq \theta_0$ according to the probability density:

$$\mathcal{B}_i^{\mathrm{vac}}(\theta) = \frac{1}{\theta}\int_{p_{T,\min}/p_{T0}}^{1} \mathrm{d}z\, \frac{\alpha_s(z p_{T0}\theta)}{\pi} P_i(z) \exp\left(-\int_\theta^{\theta_0} \frac{\mathrm{d}\theta'}{\theta'} \int_{p_{T,\min}/p_{T0}}^{1} \mathrm{d}z\, \frac{\alpha_s(z p_{T0}\theta)}{\pi} P_i(z)\right) \tag{6.15}$$

and then, z is generated with probability density $\tilde{\Gamma}_i^{\mathrm{vac}}(\theta, z)$ normalised over $z \in [p_{T,\min}/p_{T0}, 1]$.

The envelop rate used for the veto algorithm is:

$$\tilde{R}_i^{\mathrm{vac}}(\theta, z) = \frac{2C_i}{\pi}\frac{\alpha_s(z p_{T0}\theta)}{\theta}\frac{1}{z} \tag{6.16}$$

where $C_\mathrm{g} \equiv C_A$, $C_\mathrm{q} \equiv C_F$. After the change of variable $k_\perp = z p_{T0}\theta$, the marginalisation of $\tilde{R}(\theta, z)$ over z gives:

$$R_i^{\mathrm{vac}}(\theta) = \frac{1}{\theta}\int_{k_{\perp,\min}}^{k_{\perp 0}} \frac{\mathrm{d}k'_\perp}{k'_\perp}\frac{2\alpha_s(k'_\perp)C_i}{\pi} \tag{6.17}$$

$$= \frac{1}{\theta}\frac{C_i}{\pi\beta_0}\log\left(\frac{1 - 2\alpha_s\beta_0\log(k_{\perp 0}/M_Z)}{1 - 2\alpha_s\beta_0\log(k_{\perp,\min}/M_Z)}\right) \tag{6.18}$$

To obtain the second line, we used a 1-loop running coupling $\alpha_s(k_\perp) = \frac{\alpha_s}{1-2\alpha_s\beta_0\log(k_\perp/M_Z)}$ with $\alpha_s \equiv \alpha_s(M_Z)$ the running coupling at the Z mass, fixed to 0.1265, and $\beta_0 = (11C_A - 2n_f)/(12\pi)$ the 1-loop QCD β function. We consider a fixed $n_f = 5$ flavours of massless quarks. The probability density $\mathcal{S}^{\mathrm{vac}}(\theta)$ given by this rate and (6.9) is sampled using the inversion method since one can easily find the primitive of R_i^{vac} with respect to θ and its inverse. In equations, given u uniformly distributed over $[0, 1]$, θ is picked using:

$$\theta = \theta_0 \exp(\log(u)/R_i^{\mathrm{vac}}(1)) \tag{6.19}$$

The $k_\perp$ of the emission is then generated between $k_{\perp,\min}$ and $k_{\perp 0}$ following the distribution $\alpha_s(k_\perp)\mathrm{d}k_\perp/k_\perp$. The allowed range for $k_\perp$ in (6.17) has been chosen in order to simplify the analytic calculation of the θ integration and does not correspond to the z physical boundaries $p_{T,\min}/p_{T0} \leq z \leq 1$. This procedure thus neglects finite effects in the splitting function and momentum conservation as the splitting fraction $z \equiv \frac{p_T}{p_{T0}} = \frac{k_\perp}{k_{\perp 0}}\frac{\theta_0}{\theta}$ associated with the emission of the gluon θ and $k_\perp$ in (6.17) can take values larger than one. This is simply taken into account by vetoing emissions with $z > 1$ and accepting those with $z \leq 1$ with a probability $\frac{z}{2C_i}P_i(z)$ with $P_i(z)$ the targeted splitting function. A similar trick allows us to select between the $g \to gg$ and $g \to q\bar{q}$ channels for gluon splittings. This trick is detailed in the next section as it is also used in the medium-induced shower. If any of these vetoes fails, we set $\theta \to \theta_0$ and $k_\perp\theta/\theta_0 \to k_{\perp 0}$ — so that $p_{T0} = k_{\perp 0}/\theta_0$ is preserved — and reiterate the procedure, following the Sudakov veto algorithm.

After a successful parton branching, both daughter partons are further showered. The procedure stops when the generated angle θ is smaller than the minimal angle $\theta_{\min}$.

4-vectors reconstruction. To fully specify the procedure we still need to specify how to reconstruct the daughter partons from the parent. For this, we use $z \equiv \frac{p_T}{p_{T0}} = \frac{k_\perp}{k_{\perp 0}}\frac{\theta_0}{\theta}$ and also

generate an azimuthal angle φ around the parent parton, randomly chosen between 0 and 2π. We then write

$$\text{parent: } (p_{T0}, y_0, \phi_0) \longrightarrow \begin{cases} \text{daughter 1: } \big(z\, p_{T0}, y_0 + (1-z)\theta\cos(\varphi), \phi_0 + (1-z)\theta\sin(\varphi)\big) \\ \text{daughter 2: } \big((1-z)p_{T0}, y_0 - z\,\theta\cos(\varphi), \phi_0 - z\,\theta\sin(\varphi)\big) \end{cases} . \tag{6.20}$$

This is strictly valid in the small-angle limit and power corrections in θ would appear beyond our small-angle approximation.

For examples of use of the vacuum shower, we refer the reader to Chapter 4 where the fragmentation function and other jet substructure observables are calculated using the vacuum module of `JetMed`. These calculations are compared to analytical predictions.

6.3 Medium-induced shower

The medium-induced module develops a medium-induced parton shower from a leading parton with transverse momentum p_{T0}, as those described in Section 4.3. The evolution parameter in the case of medium induced cascades is the "time" $t = x^+$ in light-cone coordinates with the longitudinal axis defined by the direction of motion of the leading particle. The generation of the shower is made in two steps. In the first step, all the partons produced are exactly collinear to the leading parton. In the second step, an angle is assigned to each parton produced by the collinear cascade assuming that all their relative transverse momentum comes from momentum broadening.

6.3.1 Implementation of the collinear shower

The collinear shower is mathematically equivalent to the resolution of the equation (4.57).

The splitting time probability density. The rate $\tilde{\Gamma}_i^{\text{med}}(t,z)$ of the Markovian branching process is given

$$\tilde{\Gamma}_i^{\text{med}}(t,z) = \frac{\alpha_{s,\text{med}}}{2\pi}\sqrt{\frac{\hat{q}}{p_T}}\frac{\mathcal{K}_i(z)}{(z(1-z))^{1/2}} \tag{6.21}$$

as in (4.56). The functions $\mathcal{K}_i$ are given in Appendix C. Here $i \in \{q, g\}$ and p_T are respectively the flavour and the transverse momentum of the parent that splits, which is *a priori* different from the leading parton p_{T0} which defines the direction of the light cone coordinate t. In `JetMed`, the coupling constant $\alpha_{s,\text{med}}$ is frozen during the medium induced evolution and is a parameter of the Monte Carlo. A straightforward extension of the rate (6.21) consists in evaluating α_s at the typical branching transverse momentum $k_{\text{br}} = (\hat{q}z(1-z)p_T)^{1/4}$. The rate (6.21) is constant with time since there is no explicit time dependence. The soft divergence in $\mathcal{K}_i$ is regulated with a minimal *energy fraction* $zp_T/p_{T0} > z_{\min}$. With respect to (4.56), we have dropped the step function $\Theta(\omega_c - z(1-z)p_T)$. This constraint is handled directly by the veto algorithm.

It is convenient to use a dimensionless evolution variable, so we promote the "reduced time" τ defined by

$$\tau \equiv \frac{\alpha_{s,\text{med}}}{\pi}\sqrt{\frac{\hat{q}/C_A}{p_{T0}}}t \tag{6.22}$$

as our new evolution variable. (We recall that, by convention, we use the adjoint quenching parameter to define $\hat{q} \equiv \hat{q}_A$.) The evolution is made from some τ_0, the reduced splitting time of the parent parton to τ_L when $t = L$, that is when the leading parton escapes the medium. For the leading parton triggering the cascade, we set $\tau_0 = 0$.

If τ_0 is the splitting of the parent parton, the targeted probability distribution for the subsequent splitting time $\tau > \tau_0$ is:

$$\mathcal{B}_i^{\rm med}(\tau) = \int_{x_{\rm min}}^{1-x_{\rm min}} {\rm d}z\, \frac{\sqrt{C_A}}{2\sqrt{x}} \frac{\mathcal{K}_i(z)}{(z(1-z))^{1/2}} \exp\left(- \int_{\tau_0}^{\tau} {\rm d}\tau' \int_{x_{\rm min}}^{1-x_{\rm min}} {\rm d}z\, \frac{\sqrt{C_A}}{2} \frac{\mathcal{K}_i(z)}{(z(1-z))^{1/2}} \right) \tag{6.23}$$

with $x = p_T/p_{T0}$ and $x_{\rm min} = z_{\rm min}/x$. The z-fraction of the splitting is chosen with probability $\tilde{\Gamma}_i(\tau, z)$ with z between $x_{\rm min}$ and $1 - x_{\rm min}$. Since it is not possible to use the inversion method for the probability density (6.23), we use the Sudakov veto method.

Sudakov veto method for gluon splittings. The envelop rate $\tilde{R}_g^{\rm med}(\tau, z)$ for gluons makes use of the approximated kernel $\mathcal{K}_0(z)$ (4.58) for which analytical solutions from the generating functional method are known. For convenience, the rate (6.23) is symmetrised so that z can be chosen between $x_{\rm min}$ and $1/2$. This cancels the factor $1/2$ in (6.21). Then, one checks that

$$\frac{\sqrt{C_A}}{\sqrt{x}} \frac{\mathcal{K}_g(z)}{(z(1-z))^{1/2}} \leq \tilde{R}_g^{\rm med}(\tau, z) \equiv \frac{C_A^{3/2}}{\sqrt{x}} \mathcal{K}_0(z), \qquad \mathcal{K}_0(z) = (z(1-z))^{-3/2} \tag{6.24}$$

Marginalising over $z \in [x_{\rm min}, 1/2]$ this envelop rate, one finds the following expression:

$$R_g^{\rm med}(\tau) = \frac{C_A^{3/2}}{\sqrt{x}} \frac{2 - 4x_{\rm min}}{\sqrt{x_{\rm min}(1 - x_{\rm min})}} \tag{6.25}$$

The probability density $S_i^{\rm med}(\tau)$ built from this rate is sampled by the inversion method using:

$$\tau = \tau_i - \log(u)/R_g^{\rm med}(0) \tag{6.26}$$

with u distributed as $\mathcal{U}(0, 1)$. Then, z is randomly chosen with probability density $\mathcal{K}_0(z)$ normalised between $x_{\rm min}$ and $1/2$, again using the inversion method

$$z = \frac{v}{2\sqrt{16 + v^2}}, \qquad v = u' \left(\frac{2 - 4x_{\rm min}}{\sqrt{x_{\rm min}(1 - x_{\rm min})}} \right) \tag{6.27}$$

with u' following $\mathcal{U}(0, 1)$. With these expressions, one knows how to generate the branching process with the simplified kernel $\mathcal{K}_0(z)$. We are left with the implementation of the veto algorithm, that we detail to highlight how the condition $\omega \leq \omega_c$ for medium-induced emissions is imposed and how the gluon/gluon and quark/antiquark splittings are handled:

- Initialize $\tau_{i=0} = \tau_0$.
- While $i \geq 0$:
  - select τ_{i+1} distributed as $S_i^{\rm med}(\tau)$, z_{i+1} between $x_{\rm min}$ and $1/2$ distributed as $\mathcal{K}_0(z)$ and u_{i+1} in $\mathcal{U}(0, 1)$.
  - If $\tau_{i+1} \geq \tau_L$, stop.

– Else if

$$z_{i+1} x p_{T_0} \geq \omega_c \tag{6.28}$$

continue,

– Else if

$$u_{i+1} \leq \frac{\mathcal{K}_g^{q\bar{q}}(z_{i+1})/\sqrt{z_{i+1}(1-z_{i+1})}}{C_A \mathcal{K}_0(z_{i+1})} \tag{6.29}$$

stop, and select τ_{i+1} as the next branching time. The branching is a $q\bar{q}$ splitting with momentum fraction z_{i+1}.

– Else if

$$u_{i+1} \leq \frac{\mathcal{K}_g^{gg}(z_{i+1})/\sqrt{z_{i+1}(1-z_{i+1})}}{2C_A \mathcal{K}_0(z_{i+1})} \tag{6.30}$$

stop, and select τ_{i+1} as the next branching time. The branching is a gluon-gluon splitting with momentum fraction z_{i+1}.

– Else continue.

The first condition guarantees that the subsequent branching time is well smaller than L whereas the second veto condition ensures that the energy of the soft emission is smaller than $\omega_c = \hat{q}_A L^2/2$.

Sudakov veto method for quark splittings. For quark, one puts the singular behaviour of the splitting function in $z = 0$ only using:

$$\mathcal{K}_q(z) = \mathcal{K}_q^{gq}(z) \tag{6.31}$$

thanks to the $z \leftrightarrow 1-z$ symmetry. z is then generated between $x_{\min}$ and 1 with the envelop rate $\tilde{R}_q^{\rm med}(\tau, z)$ such that:

$$\frac{\sqrt{C_A}}{2\sqrt{x}} \frac{\mathcal{K}_q(z)}{(z(1-z))^{1/2}} \leq \tilde{R}_q^{\rm med}(\tau, z) \equiv \frac{C_F C_A^{1/2}}{\sqrt{x}} \frac{1}{z(z(1-z))^{1/2}} \tag{6.32}$$

The marginalisation of $\tilde{R}_q^{\rm med}(\tau, z)$ over $z \in [x_{\min}, 1]$ gives:

$$R_q^{\rm med}(\tau) = \frac{C_F C_A^{1/2}}{\sqrt{x}} 2\sqrt{\frac{1-x_{\min}}{x_{\min}}} \tag{6.33}$$

Then, as for gluons, the branching time τ_i following $\mathcal{S}_i^{\rm med}(\tau)$ is picked using, with u distributed as $\mathcal{U}(0,1)$:

$$\tau = \tau_i - \log(u)/R_q^{\rm med}(0) \tag{6.34}$$

Finally z is randomly chosen between $x_{\min}$ and 1 using (with again u' given by $\mathcal{U}(0,1)$):

$$z = \frac{1}{1+v^2/4}\,, \qquad v = u' \left(2\sqrt{\frac{1-x_{\min}}{x_{\min}}}\right) \tag{6.35}$$

These formulas enable to generate the branching process given by the envelop rate $\tilde{R}_q^{\rm med}(\tau, z)$. The Sudakov veto algorithm is run to generate the branching given by the true rate $\tilde{\Gamma}_q^{\rm med}(\tau, z)$. This goes as for gluon splittings with the further simplification that there is only one decay channel for quarks.

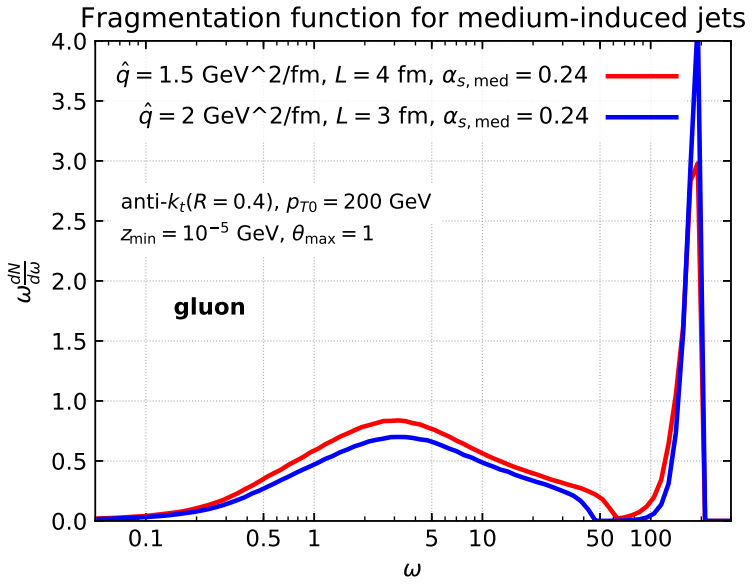

Figure 6.1: The energy spectrum of particles produced by medium-induced splittings from a leading gluon with $p_{T0} = 200$ GeV resulting from the module `MediumInducedShower`, for two different values of $\hat{q}$ and L. The parameters z_c and θ_{max} are fixed respectively to 10^{-5} and 1.

6.3.2 Implementation of the angular structure

In the cascade described above, all the splittings are considered to be exactly collinear. The angular pattern is generated afterwards via transverse momentum broadening, cf. Sect. 4.3.3. For this, we go over the whole cascade and, for each parton, we generate an opening angle θ and azimuthal angle φ according to the two-dimensional Gaussian distribution:

$$\frac{\mathrm{d}^2\mathcal{P}_{\mathrm{broad}}}{\mathrm{d}^2 k_\perp} = \frac{1}{\pi \hat{q}_R \Delta t} \exp\left(-\frac{k_\perp^2}{\hat{q}_R \Delta t}\right) \tag{6.36}$$

where Δt is the lifetime of the parton with colour representation R in the cascade, and $k_\perp \simeq \omega\theta$. Once we have the transverse momenta and angles of each parton in the cascade, we use (6.20) to reconstruct the kinematics. Partons which acquire an angle larger than θ_{max} via broadening are discarded together with their descendants. We could study more involved broadening distributions in the future, taking into account hard scattering contributions beyond the Gaussian approximation (see e.g. [182, 183]).

As an example, we show on figure 6.1, the resulting energy spectrum (or fragmentation function) of a medium-induced jet triggered by an initial gluon with energy $p_{T0} = 200$ GeV. After the evolution of the leading gluon via the medium-induced shower, all the produced particles are clustered with the anti-$k_\perp$ algorithm with $R = 0.4$ and only the hardest resulting jet is taken into account into the calculation of the fragmentation pattern. The large narrow peak near $\omega = 200$ GeV is obviously the remnant of the leading particle. The second broad peak is due to the suppression of soft medium-induced emissions, with energies smaller than the characteristic energy scale $\min(Q_s/R, \omega_s(R))$ (with $Q_s^2 = \hat{q}L$ and $\omega_s(R) = (\hat{q}/(\bar{\alpha}_s^2 R^4))^{1/3}$), see Section 4.3.3.1), because such soft emissions are deviated out of the jet cone via transverse momentum broadening. This spectrum agrees with our study of the fragmentation of medium-induced jets in Chapter 4, Section 4.3.

6.4 Full medium shower

6.4.1 The global picture

The in-medium shower is generated in three stages, according to the factorisation discussed in Section 5.2.3.

1. The first step is to generate in-medium VLEs. This is done exactly as for the full vacuum shower except that each emission is further tested for the in-medium conditions $k_\perp^3\theta > 2\hat{q}$ and $\theta > \theta_c$. If any of these two conditions fails, the emission is vetoed.

2. The second step is to generate MIEs for each of the partons obtained at the end of the first step, following the procedure described above. We neglect the formation time of the vacuum-like sources since for them, $t_f \ll L$. Consequently, all the medium-induced cascades triggered by the in-medium vacuum-like emissions develop over a time L.

3. The third step is to generate the VLEs outside the medium. For this, each parton at the end of the MIE cascade is taken and showered outside the medium. This uses again the vacuum shower, starting from an angle $\theta_{\max}$ since decoherence washes out angular ordering for the first emission outside the medium. Each emission which satisfies either $k_\perp\theta < 2/L$ or $\theta < \theta_c$ is kept, the others are vetoed.

The full parton shower can be converted to 4-vectors suited for any analysis. Final-state (undecayed) partons are taken massless with a kinematics taken straightforwardly from Eq. (6.20). If needed, the 4-vectors of the other partons in the shower are obtained by adding the 4-momenta of their daughter partons. This requires traversing the full shower backwards.

Whenever an observable requires to cluster the particles into jets and manipulate them, we use the `FastJet` program (v3.3.2) [184] and the tools in `fjcontrib` [185]. In particular, the initial jet clustering is always done using the anti-$k_\perp$ algorithm [134] with $R = 0.4$ unless explicitly mentioned otherwise.

6.4.2 Code architecture

The code is written in `C++` (v3 or higher). It requires the installation of the `FastJet` program (v3.3.2) [184].

Event classes. Besides generating the branching of a given parton described in the previous sections, the Monte Carlo records the full history of the branching process. One can access to any branching information thanks to the three following classes:

1. the class `Parton` which handles the leaves in the shower. This class gathers all the necessary informations about the partons generated during the cascade. These informations can be physical: one can access to the kinematic or the "flavour" of any given `Parton`. There are also unphysical informations related to the location of the `Parton` in the full `Event`.

2. the class `Vertex` which handles the nodes of the branching process. This class records the physical informations associated with the splitting at the node, as well as the location of the parent and daughters `Parton` in the `Event`.

3. the class `Event` contains a vector of `Vertex`, `Parton` and `PseudoJet` (class from `FastJet`) corresponding to the full tree of the branching process. A set of methods enables to handle the branching of a parton coming from a given shower to the full event or to access to the final states partons.

Shower classes. The two kind of showers described in the previous sections, vacuum-like or medium-induced constitute two independent classes `VacuumShower` and `MediumInducedShower`. A final class `MediumShower` combines together the vacuum-like shower and the medium-induced shower according to the principles of our factorisation. In order to highlight the specificity of this `MediumShower` with respect to other possible implementation, it is interesting to develop fictitious unphysical showers where one of the important ingredients of our picture is missing. Thus, a parton can be showered also via:

1. the class `HardMediumInducedShower`: in this shower, the angular pattern of the medium induced shower is not generated. All the medium-induced partons produced via the purely collinear shower are discarded in the event (and not further showered), because their angles are set to a value larger than $\theta_{\max}$ by hand. Only the resulting energy loss of the leading parton is recorded. This class enables to isolate the effects of the energy loss via medium-induced radiations, and by contrast, to understand the effect of the medium-induced emissions with relatively small angles.

2. the class `MediumAOShower`: this shower is the same as `MediumShower` except that there is no reopening of the phase space for the first decay given by the `VacuumShower` in the outside phase space. The angle of this emission is constrained by the opening angle of the previous one, so that all *vacuum-like* branchings are angular ordered.

6.4.3 `JetMed` free parameters

We give here the list of parameters that enter into a `JetMed` calculation. These parameters can be divided into two sets: the physical parameters that are, in principle, measurable and the unphysical parameters which enter into the calculation in order to regulate the soft or collinear singularities.

Shower	Unphysical parameters	Physical parameters
`VacuumShower`	$\theta_{\max}$, $k_{\perp,\min}$	$\alpha_s(M_Z)$
`MediumInducedShower`	$\theta_{\max}$, $z_{\min}$	$\hat{q}$, L, $\alpha_{s,\mathrm{med}}$

Table 6.1: Parameters of the Monte Carlo `JetMed`. The unphysical parameters $k_{\perp,\min}$ and $z_{\min}$ are used to regulate the infrared divergences in the probability distribution for generating a given emission. They are not measurable quantities contrary to the the physical parameters listed in the second column.

Among these parameters, one could easily avoid the use of the frozen coupling $\alpha_{s,\mathrm{med}}$ using the value of α_s at the transverse momentum scale k_{br} (see Section 6.3).

6.5 Limitations and comparison with other Monte Carlo event generators

6.5.1 The missing ingredients

The Monte Carlo generator that is described above is of course very simplistic and has a series of limitations. We list them here for the sake of completeness.

Hadronisation and initial state radiations. First of all, we only generate a partonic cascade, neglecting non-perturbative effects like hadronisation. Even if one can hope that these effects are limited — especially at large p_T — our description remains incomplete and, for example, track-based observables are not easily described in our current framework. Additionally, our partonic cascade only includes final-state radiation. Including initial-state radiation is left for future work. This would be needed, for example, to describe the transverse momentum pattern of jets recoiling against a high-energy photon.

Medium and nucleus-nucleus collision modelling. Our description of the medium is also simplified: several effects like medium expansion, density non-uniformities and fluctuations, and the medium geometry are neglected. The geometry of the collision is a crucial missing ingredient if we aim at understanding the dependence of Monte Carlo calculations with the centrality and the energy of the collision. This can to a large extent be hidden into an adjustment of the few parameters we have left, but we would have to include all these effects to claim a full in-medium generator.

Hard scatterings off medium constituents and medium response. As discussed in Section 5.2.5, there are other medium effects which are not included in the current implementation of `JetMed`. First of all, the medium response of the jet propagation is known to produce sizeable effects on medium modified jet shapes. Including the medium response of the jet at the level of our Monte Carlo would require a complete knowledge of the hydrodynamic evolution of the medium.

Hard scatterings between the leading parton that triggers the jet (or any of its descendent) and a medium scattering center are also neglected in the multiple soft scattering approximation. In terms of Monte Carlo modelling, i.e. without relying on a theoretical proof of the validity of the Monte Carlo calculation in a given approximation scheme, hard scattering contributions could be added using the full transverse momentum probability distribution $\mathcal{P}(k_\perp, \Delta t)$ defined in (3.64) instead of its Gaussian approximation (6.36) used to generate the angular pattern of the medium induced shower (or equivalently, using the analytic approach of [77]). This should at least correct the angular distributions, so that the Monte Carlo would really solve (4.65) with the right collision kernel. Note that the Monte Carlo implementation of the branching process associated with (4.65) for gluons only has also been pursued in the parton shower `MINCAS` [182].

Furthermore, hard scattering also modifies the emission rate. Hence, a complementary improvement would be to use the recent results of [73]. In this paper, the authors provide a rate for medium induced splittings that encompasses at the same time the Bethe-Heitler regime, the multiple soft scattering regime and the single hard scattering regime.

Shortcoming improvements. Among all of these approximations, some of them could easily be circumvented. As argued, the longitudinal expansion of the medium requires a modification of the veto region for vacuum-like emissions. This veto region has been calculated in Chapter 5,

so the implementation should be straightforward. Moreover, the effect of the longitudinal expansion on the medium-induced cascade discussed in 4.3.4 amounts to a change in the relation between the dimensionless parameter τ and the proper time t along the direction of motion of the leading parton.

6.5.2 JetMed in the landscape of in-medium event generators

Over the past few years, a large variety of Monte Carlo parton showers and event generators has appeared in the heavy-ion community, stimulated by the large amount of data associated with jet quenching effects. In this subsection, we would like to precise the location of JetMed among all these parton showers. JetMed is based on the factorised picture exposed in Chapter 5, which allows for a fast implementation of an in-medium parton shower. With this perspective, JetMed is unique as it is the only parton shower that includes decoherence effects in the vacuum-like cascade and the multiple branching regime for medium-induced radiations as predicted by perturbative QCD.

The factorisation between the vacuum-like shower and the medium effects is not unique. Actually, many in-medium parton showers start with a shower triggered by the virtuality of the hard-process up to some cut-off virtuality scale Q_{med} where medium effects take over. This is the case for MARTINI [186] for instance, for which the vacuum-like shower is generated by Pythia 8.1. Nevertheless, in our approach, this virtuality scale Q_{med} is dictated by the physical parameters of the medium. Besides the treatment of the vacuum-like cascade, it is not clear whether the MARTINI approach encompasses the multiple branching regime discussed in Chapter 4, Section 4.3, even if the transition rates used in MARTINI account for both the Bethe-Heitler and LPM regimes.

In the framework MATTER+LBT [187, 188, 189, 190], there is also a virtuality transition scale between the virtuality-driven shower and the outgoing partons-medium interactions. This transition scale is chosen of order $\mathcal{O}(1\text{ GeV})$. The MATTER shower includes the so-called higher twist (HT) contributions to the one-gluon emission cross-section from a single scattering, generalised to include multiple emissions in a DGLAP-like formalism with medium-modified splitting functions. When the shower reaches the typical virtuality scale generated by medium scatterings, the LBT shower takes over. This shower implements a kinetic rate equation, whose rates are again given by a higher-twist approach. In JetMed, higher-twist contributions to emission cross-sections and rates are neglected.

In the way the dominant medium effects are implemented, MATTER is close to the Q-PYTHIA and Q-HERWIG implementations of the in-medium parton shower [87, 191, 192, 193] (or [194] which uses a similar idea) since medium-modified splitting functions are used. These medium-modified splitting functions incorporate the effect of medium-induced emissions via an additive term to the usual DGLAP splitting functions. This additive term is given by the off-shell spectrum calculated in Chapter 3 (with the vacuum limit subtracted). This implementation is different from the one in JetMed since our factorisation enables to ignore either the vacuum or the medium-induced component according to the stage of the evolution. That said, at the level of a single emission, both calculations agree in the soft limit.

Our factorised approach is in principle closer to the implementation of the Monte Carlo JEWEL [88] in which "the interplay between competing radiative processes is governed by the formation times of the emissions" meaning that, for instance, in the generation of a splitting, the choice between a vacuum-like and a medium-induced one is made according to the criterion of shortest formation time. This is precisely the argument made to derive the veto region in Section 5.1.1. Hence, JetMed focuses somehow on the drastic scenario where the in-medium vacuum-

Monte Carlo	JetMed	MARTINI	MATTER+LBT	Q-PYTHIA	JEWEL	Hybrid
Factorisation scale	✓	✓	✓	✗	✗	✗
Decoherence	✓	✗	✗	✗	✗	✗
LPM effect	✓	✓	✗(1)	✓	✓	✗
Multiple branching regime	✓	?	✗	✗	?	✗
Hadronisation	✗	✓	✓	✓	✓	✓
Medium geometry/expansion	✗	✓	✓	✗(2)	✓	✓
Hard single scatterings	✗	✓	✓	✗	✓	✗
Medium response	✗	✗	✓	✗	✓	✓
HT splitting functions	✗	✗	✓	✗	✗	✗
Strongly coupled energy loss	✗	✗	✗	✗	✗	✓

Table 6.2: A personal comparison of several Monte Carlo in-medium parton showers. We apologize if they are not faithfully represented as it can be sometimes difficult to disentangle the physical ingredients behind the numerical implementations. Notes: (1) A modified-Boltzmann approach is proposed in [197] to take into account the LPM regime. (2) Q-PYTHIA can be interfaced to an optical Glauber model [198].

like cascade happens very shortly before triggering a bunch of medium-induced emissions. Since this scenario is the dominant one to single logarithmic accuracy for vacuum-like emissions, the JetMed approach is considerably simplified.

Last but not least, JetMed is completely orthogonal to the hybrid strong/weak coupling model [195], as the underlying medium in JetMed is assumed to be weakly coupled. Nevertheless, there are some physical similarities since the hybrid model takes into account a characteristic resolution length [196] of the plasma, a concept which is closed to the coherence angle derived in weak coupling calculation in Chapter 3.

To summarise, we provide a *non-exhaustive* Table 6.2 recapitulating the main ingredients of all the parton showers discussed in this subsection.

Part II

Phenomenology: jet quenching at the LHC

Chapter 7

Introduction: jet quenching observables

In this introductory chapter, we first aim at giving a large (but of course non exhaustive) survey of the measurements related to jet quenching phenomena which will be studied in more details in the following chapters. Furthermore, we explain qualitatively how the physical picture for jet evolution in a dense QCD medium discussed in Part I enables to understand the salient features of these experimental data.

So far, there are still important missing ingredients in this picture. These missing ingredients do not allow for a complete description of all the current data. Each time we discuss a measurement, we explain why we expect this measurement to be or not to be properly understood (at least qualitatively) within our theory.

As usual in jet physics, we also expect better agreement between the theory and the data when there is a large separation of scales between the hard process and the soft sector: hadronisation, underlying event, flow in heavy-ion collisions, etc. That is why we focus mainly on LHC data, as the center of mass energy is large enough to produce high $p_T \gtrsim 100$ GeV jets in the final state. A non-exhaustive list of references regarding jet measurements at RHIC is given in the first section.

One can divide the measurements done so far regarding jets in heavy-ion collisions into two main categories: global and substructure observables. For global jet observables, all the informations about the inner properties of jets are discarded, and only the global properties (transverse momentum, mass, etc) are compared to the proton-proton collision case. On the contrary, for substructure observables, one looks for modifications of the inner properties of jets after propagation through the quark-gluon plasma. Therefore, this chapter is divided into three sections. The first two discuss these global and substructure observables independently. In the last section, we argue that one can get substantial physical informations by correlating these two classes.

7.1 Global jet observables

7.1.1 Inclusive jet cross-sections

The first natural jet observable to look at in nuclei-nuclei collisions is the total jet cross-section. Since the seminal suggestion of Bjorken [43], such quantities have been extensively measured both at RHIC [199, 200, 201, 202, 203, 204, 205, 206, 207, 208, 209, 210, 211, 212, 213, 214, 215] and at the LHC [19, 216, 217, 218, 219, 220, 221, 222, 223, 224, 225, 226, 227, 228, 229, 230] (and other references below). We do not discuss the inclusive hadron cross section which has been the first historical evidence for jet quenching in heavy-ion collisions at RHIC. Instead we

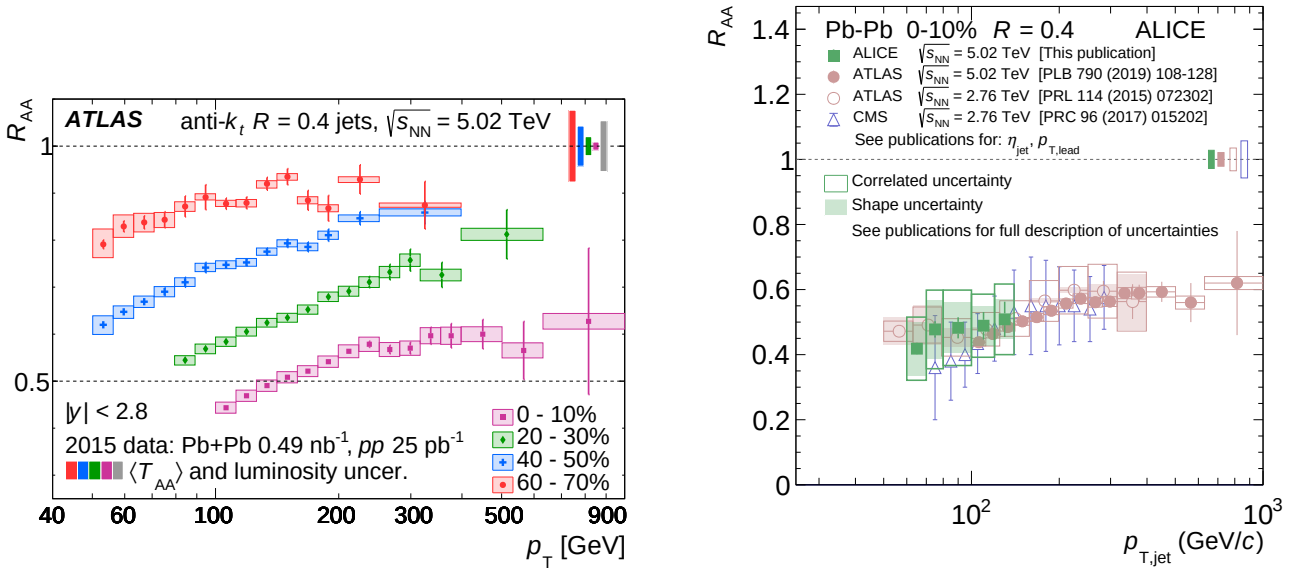

(a) ATLAS - Centrality dependence. Figure from [232].

(b) ALICE data [233] compared to ATLAS [232, 234] and CMS [235]. Figure from [233].

Figure 7.1: Measurements of the nuclear modification factor for jets. The left plot shows the dependence of the observable with the centrality of collisions. The right plot compares several jet R_{AA} measurements at the LHC from different detectors and collision energy $\sqrt{s_{NN}}$.

focus on the inclusive *jet* cross section and its nuclear modification factor as a function of the transverse momentum p_T and the rapidity y, defined by:

$$R_{AA}(p_T, y) \equiv \frac{1}{\langle T_{AA} \rangle} \frac{\left.\frac{\mathrm{d}^2\sigma_{\mathrm{jet}}}{\mathrm{d}p_T \mathrm{d}y}\right|_{AA}}{\left.\frac{\mathrm{d}^2\sigma_{\mathrm{jet}}}{\mathrm{d}p_T \mathrm{d}y}\right|_{pp}} \tag{7.1}$$

The normalisation factor $\langle T_{AA} \rangle$ is the mean nuclear thickness function which accounts for the geometric enhancement of the hard scattering rate [231]. In the absence of nuclear effect, this normalisation factor guarantees $R_{AA}(p_T, y) = 1$. Jets are usually reconstructed using the anti-k_t algorithm with parameter R [134].

In Fig. 7.1-left, we show the experimental results obtained by the ATLAS collaboration [232]. The R_{AA} ratio is plotted as a function of p_T for several centrality classes. For the most central collisions, one observes a strong suppression of the jet yield over all the p_T range, i.e even for very large p_T. This suppression is understood as a consequence of jet energy loss: jets produced with a final p_T come from hard partons with a larger transverse momentum in AA collisions than in pp collisions. As the hard scattering cross-section is steeply falling with p_T, producing such hard partons is less likely, leading to a suppression of the jet yield in AA with respect to pp.

This simple explanation hides two subtleties, which are easily explained within our theory for in-medium jet fragmentation:

- contrary to hadrons, jets are reconstructed with a parameter R, the jet radius. Thus, the energy flow must be deviated at large angles, larger than this jet radius, to effectively yields a jet suppression. The multiple branching regime, which occurs in the second step of the jet evolution inside the medium is a natural mechanism for such a large angle

energy loss. *Event by event*, the leading parton loses an energy of order $\omega_{\rm br} = \alpha^2 \hat{q} L^2$ deviated and thermalized outside the jet cone.

- this is not the end of the story, as a constant energy loss independent of p_T would not account for the flatness of R_{AA} over such a large range of p_T. This is where the *in-medium* vacuum-like evolution comes into play: this evolution increases the number of sources that subsequently lose a typical energy $\omega_{\rm br}$. The higher p_T is, the higher the number of these sources is.

Combining together these two mechanisms explains the behaviour of the ATLAS data, as we shall see with more quantitative arguments in the next chapter. We expect our approach to give reasonable results for the jet R_{AA} because the inclusive jet cross-section is an IRC safe observable, which is qualitatively well described by leading order pQCD calculations in e^+e^- or pp collisions. Moreover, one expects that for the most central collisions, all the distinct geometries of collision can be averaged and thus absorbed into our single parameter L. Therefore, it is a natural observable to compute in a first place.

7.1.2 Dijet asymmetry and γ-jet correlations

Among global jet quenching observables, another important class corresponds to the correlations between the global properties of a jet and its recoil partner in two-jets or γ-jet events. Typical quantities related to this class are the dijet asymmetry distribution σ_{A_J} and the $x_{\gamma J}$ distribution $\sigma_{x_{\gamma J}}$ defined respectively by:

$$\sigma_{A_J} \underset{\text{2-jets ev.}}{\equiv} \frac{1}{N_{\rm jets}} \frac{\mathrm{d}N}{\mathrm{d}A_J}, \qquad A_J = \frac{p_{T1} - p_{T2}}{p_{T2} + p_{T1}} \tag{7.2}$$

$$\sigma_{x_{\gamma J}} \underset{\gamma\text{-jets ev.}}{\equiv} \frac{1}{N_{\rm jets}} \frac{\mathrm{d}N}{\mathrm{d}x_{\gamma J}}, \qquad x_{\gamma J} = p_{T,\rm jet}/p_{T,\gamma} \tag{7.3}$$

where $p_{T1} > p_{T2}$ and p_{T2} are the transverse momenta of the two jets in a dijet event, and $p_{T,\rm jet}$ and $p_{T,\gamma}$ are respectively the transverse momenta of the jet and photon in a γ-jet event.

By energy conservation, we expect these distributions in pp collisions to be peaked around 0 for σ_{A_J} and 1 for $\sigma_{x_{\gamma J}}$. The results from the ATLAS experiment [236, 237, 238] are shown in Fig. 7.2. Both distributions are modified, and the expected peak is no longer visible. One observes a strong suppression of symmetric dijet and γ-jet events in PbPb collisions. The CMS collaboration has made a similar measurement for the photon-jet correlations [239, 240] and the dijet asymmetry [241] which shows the same trend.

For dijet events in AA collisions, there are two possible mechanisms (not necessarily incompatible with each other) explaining the observed dijet asymmetry.

- The geometry of the collision may lead to the following situation: one of the two jet has a shorter path length through the medium and thus loses less energy, whereas the other has a much longer path length and loses a substantial amount of its initial energy.

- Even if the geometry is perfectly symmetrical, the event by event fluctuations in the jet substructure and its energy loss induce also a dijet asymmetry.

Making predictions for the dijet asymmetry taking into account both possible mechanisms requires a good modelling of the geometry of the nucleus-nucleus collision. This is currently not included in `JetMed`. Note however that event by event fluctuations in jet substructure and

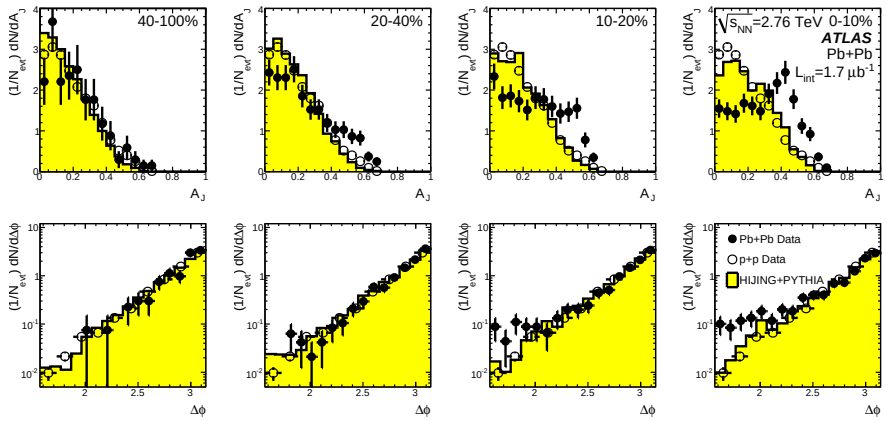

(a) ATLAS - dijet asymmetry. Figure from [236]

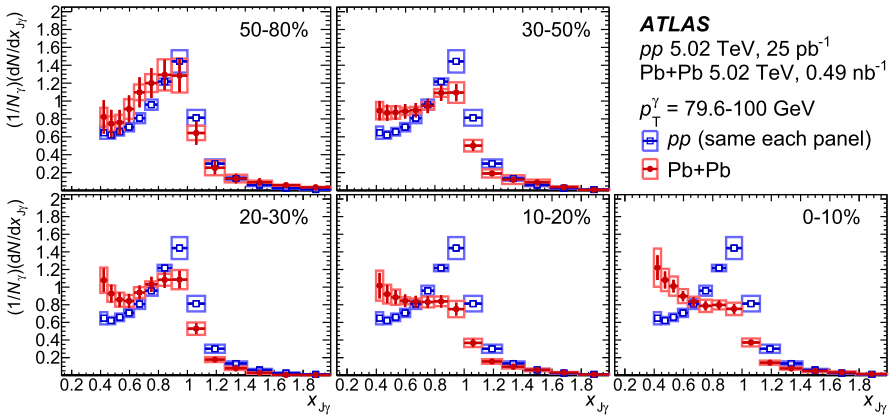

(b) ATLAS - γ-jet correlation. Figure from [238]

Figure 7.2: Dijet and γ-jet correlations measured by the ATLAS experiment. The upper panel of Fig. 7.2a corresponds to the definition of σ_{A_J} given in (7.2). The results are provided for four centrality selections in *pp* and PbPb. The lower panel of Fig. 7.2a is a measurement of azimuthal correlations ($\Delta\phi$ is defined as the azimuthal separation between the two jets). The bottom figure shows the distribution defined in (7.3) for five centrality classes in *pp* and PbPb. In most central collisions ($0-10\%$ centrality), all these distributions are strongly modified.

energy loss are included in our picture, so we expect to see a dijet asymmetry in our calculation. As other models predict a minor effect of the geometry fluctuation [242, 243], this might suggest that dijet asymmetry would be also qualitatively well described by a `JetMed` calculation.

For γ-jet events in AA, the underlying physics is even more simple to understand as the highly energetic photon does not interact with the plasma so the quantity $x_{\gamma J}$ can be thought as the fraction of energy lost by the leading parton at large angles (either via vacuum-like or medium-induced emissions). Unfortunately, the $x_{\gamma J}$ distribution is very sensitive to initial state radiations. That is why this observable lies (so far) beyond the regime of validity of our calculation.

7.2 Substructure jet observables

In this section, we discuss jet measurements related to their substructure properties. Again, it is enlightening to divide the actual set of data into two classes: the IRC unsafe substructure observable and the IRC safe substructure observables. While IRC unsafe observable are

interesting to have an insight on the main qualitative differences between the fragmentation pattern of jets in AA with respect to *pp*, their very definition does not allow for controlled comparisons between pQCD and data, or to say it differently, any prediction becomes highly model-dependent. On the contrary, IRC safe observable are often more delicate to interpret physically (we shall spend a lot of time in Chapter 9 doing it) but are much more robust for quantitative comparisons with pQCD predictions.

7.2.1 IRC unsafe

Definitions. Given a reconstructed jet, one can always define the following two-dimensional distribution of its hadron content:

$$f_h(x, \Delta R) = \frac{1}{N_{\text{jets}}} \frac{\mathrm{d}^2 N_h}{\mathrm{d}x \mathrm{d}\Delta R} \tag{7.4}$$

where $\mathrm{d}N_h$ is the number of hadrons inside the jet with "energy fraction" between x and $x + \mathrm{d}x$ and "angle" with respect to the jet axis between ΔR and $\Delta R + \mathrm{d}\Delta R$:

$$x \equiv \frac{p_T \cos(\Delta R)}{p_{T,\text{jet}}}, \qquad \Delta R \equiv \sqrt{(\Delta\eta)^2 + (\Delta\phi)^2} \tag{7.5}$$

This two-dimensional distribution carries all the informations about the longitudinal and transverse structure of the hadron content within jets. Marginalising over the angle ΔR, one gets the so-called jet fragmentation function, while marginalising over x gives the jet shape:

$$\mathcal{D}(x) = \frac{1}{N_{\text{jets}}} \frac{\mathrm{d}N_h}{\mathrm{d}x}, \qquad P(\Delta R) = \frac{1}{N_{\text{jets}}} \frac{\mathrm{d}N_h}{\mathrm{d}\Delta R} \tag{7.6}$$

Such substructure observables are not IRC safe. They are built from final state *hadrons* which are not under control in pQCD. In Chapter 4, Section 4.2.2, we have seen that a transverse momentum cut-off is required in order to regulate the collinear divergence in the calculation of the fragmentation function. The need for such a cut-off is a consequence of non IRC safety.

The experimental data. Before discussing what we can say about these observables with our Monte Carlo and its limitations, let us present some experimental data available. For the fragmentation function, the nuclear modification factor measured by ATLAS [244] and shown Fig. 7.3 has an interesting pattern. There is a significant excess of soft and hard hadrons within jets produced in Pb-Pb collisions with respect to jets produced in *pp* collisions. A similar pattern is observed (at least for the enhancement of soft constituents) in γ-jet events [246, 247] and at lower $\sqrt{s}$ [248, 249]. Regarding the jet shape, the CMS data [245, 250, 251], as those shown in 7.4, show an excess of intrajet *very soft* particles at large angles in PbPb for the most central collisions. This excess is stronger around the edges of the jets. Note that the ALICE collaboration also measured jet radial profiles in qualitative agreement with the CMS results [252, 253].

The main obstacle for quantitative comparisons between our MC calculations and these experimental data is the lack of hadronisation model in `JetMed`. Hadronisation has a large impact on the jet shape [254], especially for large ΔR where the medium effects are known to be important from the CMS data. This large ΔR enhancement comes mainly from hadrons with $0.5 \lesssim p_T \lesssim 2$ GeV, a kinematic region which is dangerously close to the hadronisation scale. Note that such effects also limit our predictive power for the large R dependence of the R_{AA} ratio.

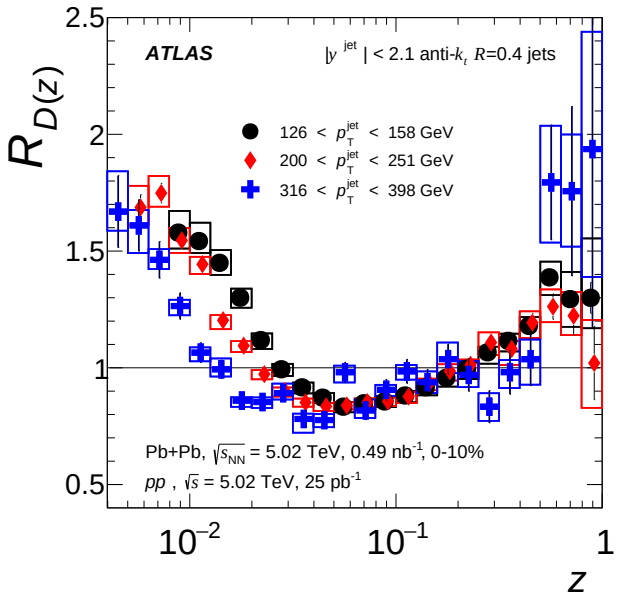

Figure 7.3: ATLAS - fragmentation function. Note that the variable z is called x in this thesis and especially in Chapter 10. Three jet p_T ranges are shown, suggesting an approximate scaling of the large x part of the fragmentation function with the jet transverse momentum. Figure from [244].

The fragmentation function is also sensitive to hadronisation effects even if the local parton-hadron duality hypothesis has been proven to give reasonably good descriptions of multiplicity distributions within jets produced in e^+e^- annihilation. Furthermore, one sees already substantial nuclear effects for hadron constituents with $p_T \gtrsim 2$ GeV well beyond the $\Lambda_{\rm QCD}$ scale. That is why we believe that our calculation for the partonic fragmentation function in PbPb collisions captures at least qualitatively the trend of the hadronic fragmentation function. This observable is explored in Chapter 10. Nevertheless, this study would not be complete without a detailed investigation of hadronisation corrections on the nuclear modification factor.

Physics of in-medium fragmentation. Regarding the physics of the fragmentation function, we argue in Chapter 10 that the enhancement seen at large x in the fragmentation function is essentially a filter effect caused by the medium. Indeed, looking at the large x part of this observable means looking at jets with a hard constituent inside. Such jets have a reduced evolution (otherwise, the leading particle would not carry a large $x \sim 1$ value), and thus lose less energy. Then, there is this generic property of the energy loss effect combined with the steeply falling cross-section: jets losing less energy are favoured. Consequently, hard fragmenting jets are preferably produced in AA relatively to other classes, simply because they lose less energy. This mainly explains the enhancement seen at large x.

The low x part is less trivial. As this enhancement is already present for tracks with $p_T \sim$ 3-4 GeV $\gg \Lambda_{\rm QCD}$ at the LHC, we expect a pQCD mechanism to explain this pattern. In Chapter 5, we have seen that the violation of angular ordering leading to a reopening of the angular phase space for radiations is a powerful mechanism to produce soft intrajet particles. Indeed, we confirm in Chapter 10 that this is a crucial ingredient for the nuclear enhancement of the fragmentation function at low x. On top of that, relatively hard medium-induced emissions with energies between $\omega_{\rm br}$ and ω_c also play an important role. Whereas medium induced emissions with $\omega \lesssim \omega_{\rm br}$ account for the event by event jet energy loss (at large angles), hard medium induced emissions are rare events, but they remain inside the jet cone and contribute to the

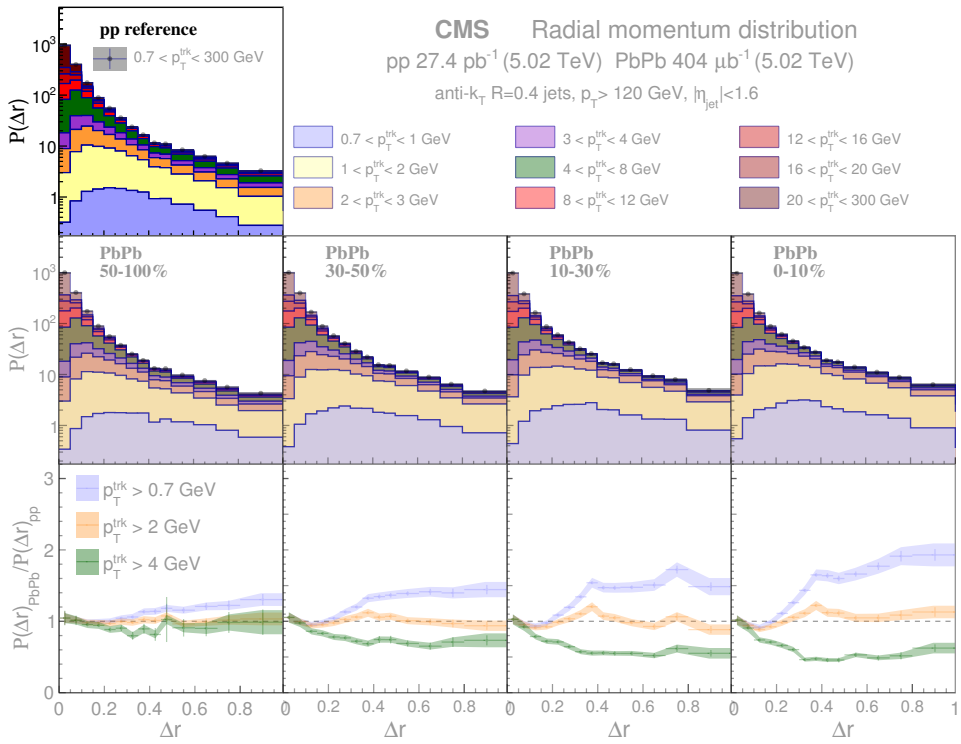

Figure 7.4: CMS - jet radial profile. The upper panel is the *pp* reference. The middle panels show the radial distribution of jet constituents binned in terms of the transverse momenta of these constituents. The lower panels present the nuclear modification factor for the jet angular shape. Each distribution is given for three centrality classes. Figure from [245].

fragmentation function at low x.

7.2.2 IRC safe

We turn now to IRC safe substructure observables. A common feature of these observables is to rely on subjets (in a given declustering procedure) and not on hadrons. There are a lot of possibilities for defining such observables. Among them, an interesting class relies on the primary Lund plane density [153]. The Lund plane density is defined as the number density of primary subjet emissions obtained after a C/A declustering of the jets:

$$\rho(\theta, k_\perp) = \frac{1}{N_{\text{jets}}} \frac{\mathrm{d}^2 N_{\text{sub}}}{\mathrm{d}\log(1/\theta)\mathrm{d}\log(k_\perp)} \tag{7.7}$$

with θ the angle of the subjet with respect to the hard branch and $k_\perp$ its transverse momentum. Choosing a kinematic cut on this Lund plane which avoids the non-perturbative region enables to build IRC safe observables. We refer the reader to Chapter 4, Section 4.2.3 for the definitions of the z_g and n_{SD} distributions and the subjet fragmentation function. One can easily check that such distributions are built from the Lund plane density with an IRC safe kinematic cut.

A glimpse at the experimental data. There is a lot of experimental activity around the measurement of substructure observables from grooming techniques [257, 258]. There is a measurement by the CMS collaboration of the z_g distribution in PbPb collisions [255]. Unfortunately, this measurement is not unfolded and fully corrected from detector effects. This

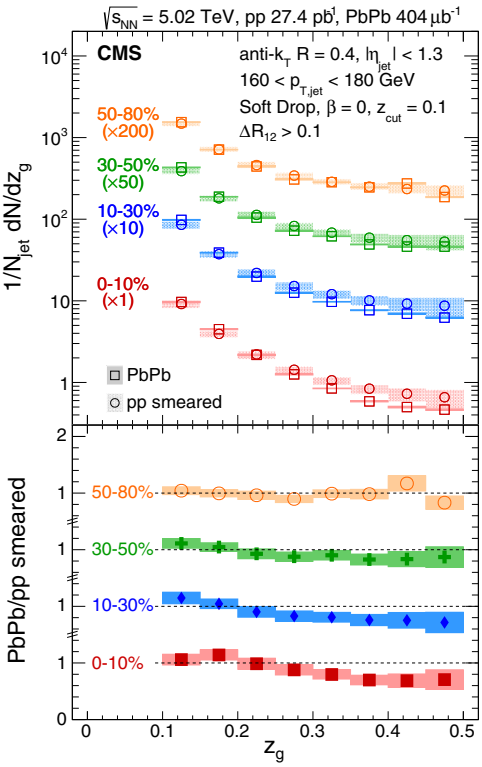

(a) CMS - self normalised z_g distribution. Figure from [255].

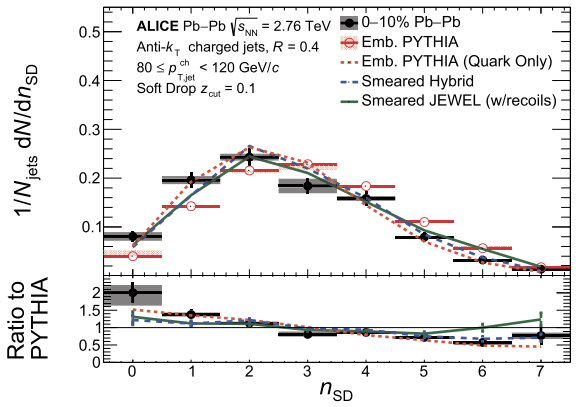

(b) ALICE - n_{SD} distribution. Figure from [256].

Figure 7.5: Substructure jet observables measured in heavy-ion collisions at the LHC. The figure on the left shows the self normalised z_g distributions defined in section (**??**) measured by the CMS collaboration for four centrality classes, and their nuclear modification factors PbPb/(*pp smeared*). The smearing of *pp* data takes into account detector effects. The figure on the right is a measurement of the Iterative Soft Drop multiplicity distribution (see section 4.2.3.2) in PbPb central collisions by the ALICE collaboration and its ratio to Pythia embedded in heavy-ion collisions. The measurement is compared to theoretical predictions from the Hybrid model and `Jewel`.

prevents a quantitative comparison between theory and data. Nevertheless, the results are shown in Fig. 7.5. The ratio is decreasing with z_g for most central collisions. Note that in this CMS measurement, z_g distributions are normalised to unity, so that if the ratio is larger than 1 in some z_g range, it has to be smaller than 1 in another range. Consequently, one can not conclude that there is an enhancement of soft splitting in the medium, or a reduction of symmetric splittings since it could just be a normalisation artefact.

The ALICE measurement for this observable shown Fig. 7.6 uses the N_{jets}-normalisation prescription. Also, additional cuts on the splitting angles are applied. For $\Delta R_{12} = \theta_g \geq 0.1$ or 0.2, the decreasing behaviour is still visible but the overall normalisation leads to a reduction in the number of wide angles SD splitting in PbPb with respect to pp. Again these measurements must be interpreted with care as they are not unfolded from detector effects. More recent measurements of the z_g distribution by the ALICE collaboration without cut on ΔR_{12} and fully corrected from detector effects show a very mild medium modification, even if the uncertainties are quite large.

ALICE also measured the nuclear modification factor of the n_{SD} distribution [256]. The result is shown 7.5b. They measure a relative increase in the number of jets with few SD

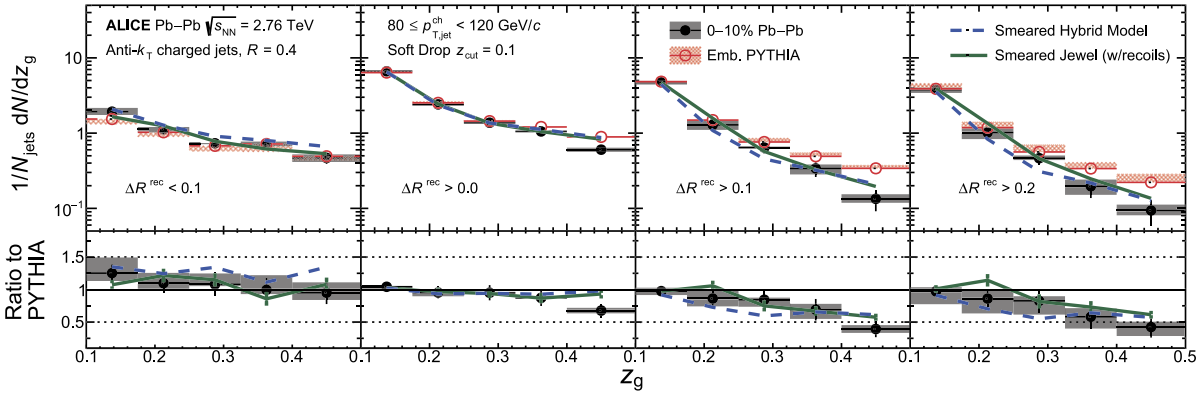

Figure 7.6: ALICE - N_{jets}-normalised z_g distribution in PbPb central collisions. As in Fig. 7.5b, the ratio shown in the bottom panel is taken with Pythia predictions embedded in heavy-ion collisions. The difference between the four panels lies in the angular cut (called θ_{cut} in Section 4.2.3.1) imposed for the Soft Drop procedure. Figure from [256].

splittings in PbPb collision and a relative reduction of jets with a large number of SD splittings.

Brief physics discussion. Thanks to their IRC safety, these observables are less sensitive to hadronisation corrections. Moreover, the geometry of the collision is not the driven mechanism that would explain a nuclear modification. The underlying event is groomed away in the Soft Drop or Iterative Soft Drop procedure. Consequently, this improves the reliability of our calculations. The physics a play in these Lund plane based observables consists in the following four ingredients:

- jets with a hard substructure are more suppressed because they have a larger in-medium evolution, and hence lose more energy.
- As for the fragmentation function, the small angle (hard) medium-induced emissions contribute to the Lund plane density at small z and $k_\perp \sim Q_s$. As the single BDMPS-Z emission spectrum is more singular at small z than the standard Bremsstrahlung spectrum, this often produces a peak at small z in the PbPb/pp ratio of integrated distributions.
- On the contrary, the veto region induces a suppression of the density of vacuum-like splittings in this region of the Lund plane.
- Finally, for in-medium splittings, subsequent energy loss changes the value of the kinematic associated with that spitting. Thus the difference between the physical kinematic of this emission and the *measured* one must be taken into account when calculating the probability of emission.

Such effects will be discussed in details in Chapters 9 and 10.

7.2.3 Correlating global and substructure jet measurements

Whereas we were dealing so far with global and substructure jet observables rather independently, we discuss here the correlation between these two kinds of measurement. The idea that the jet energy loss is strongly correlated with jet substructure can be tested experimentally by measuring the nuclear modification factor for different classes of jets according to their substructure. A proposal for such a measurement is presented in Chapter 9, Section 9.3.2. On

the experimental side, a measurement at the LHC correlating R_{AA} and substructure has been performed by the ATLAS collaboration [259], but is still preliminary.

Beyond the correlation of R_{AA} and substructure, one can correlate dijet or γ-jet asymmetry with substructure, in the spirit of the correlation between jet shape and leading versus subleading jet in dijet events as done in [260]. Such measurements could disentangle the two mechanisms discussed in Section 7.1.2 for the dijet asymmetry and understand the relative importance of the path length dependence mechanism versus the jet substructure/energy loss event by event fluctuation.

Chapter 8

Jet energy loss and the jet nuclear modification factor R_{AA}

In this chapter we present our Monte Carlo results for the jet nuclear modification factor R_{AA}. We first discuss the case of a monochromatic leading parton, for which we compute the jet average energy loss defined in Chapter 5, Section 5.3.2, and then turn to R_{AA} itself, using a Born-level jet spectrum for the hard process producing the leading parton.

8.1 Choice of parameters

The implementation of in-medium partonic cascades described in Chapter 6 has 5 free parameters: two unphysical ones, $\theta_{\max}$ and $k_{\perp,\min}$, essentially regulating the soft and collinear divergences, and three physical parameters, $\hat{q}$, L and $\alpha_{s,\mathrm{med}}$, describing the medium. In our phenomenological studies, we will make sure that our results are not affected by variations of the unphysical parameters and we will study their sensitivity to variations of the medium parameters.

The different sets of parameters we have used are listed in Table 8.1. The first line is our default setup. It has been chosen to give a reasonable description of the R_{AA} ratio measured by the ATLAS collaboration (see Sect. 8.3 below). The next 3 sets are variants which give a similarly good description of R_{AA} and can thus be used to test if other observables bring an additional sensitivity to the medium parameters compared to R_{AA}. The last 6 lines are variations that will be used to probe which physical scales, amongst θ_c, ω_c and ω_{br}, influence a given observable.

8.2 The jet average energy loss

To study the jet energy loss we start with a single hard parton of transverse momentum p_{T0} and shower it with the Monte Carlo including either MIEs only, or both VLEs and MIEs. The jet energy loss is defined as the difference between the energy of the initial parton and the energy of the reconstructed jet. To avoid artificial effects related to emissions with an angle θ between the jet radius R and the maximal opening angle $\theta_{\max}$ of the Monte Carlo, we have set $\theta_{\max} = R$. Furthermore, for the case where both VLEs and MIEs are included, we have subtracted the pure-vacuum contribution (which comes from clustering and other edge effects and is anyway small for $\theta_{\max} = R$).

Our results for the energy loss are shown in Fig 8.1 as a function of $E \equiv p_{T0}$ and in Fig. 8.2

	parameters			physics constants		
Description	$\hat{q}$ [GeV^2/fm]	L [fm]	$\alpha_{s,\mathrm{med}}$	θ_c	ω_c [GeV]	ω_{br} [GeV]
default	1.5	4	0.24	0.0408	60	3.456
similar R_{AA}	1.5	3	0.35	0.0629	33.75	4.134
	2	3	0.29	0.0544	45	3.784
	2	4	0.2	0.0354	80	3.200
vary θ_c	0.667	6	0.24	0.0333	60	3.456
	3.375	2.667	0.24	0.05	60	3.456
vary ω_c	0.444	6	0.294	0.0408	40	3.456
	5.063	2.667	0.196	0.0408	90	3.456
vary ω_{br}	1.5	4	0.196	0.0408	60	2.304
	1.5	4	0.294	0.0408	60	5.184

Table 8.1: Table of medium parameters used in this paper. The default set of parameters is given in the first line. The next 3 lines are parameters which give a similar prediction for R_{AA}. The last 6 lines are up and down variations of θ_c^2, ω_c and ω_{br} by 50%, keeping the other two physics constants fixed.

as a function of R, for both gluon- and quark-initiated jets. For these plots we have used the default values for the medium parameters (see the first line of Table 8.1). Overall, we see a good qualitative agreement with the features expected from the theoretical discussion in Sections 4.3.3 and 5.3.2.

For the jets involving MIEs only, we see that the energy loss first increases with p_{T0} and then saturates, as predicted by Eqs. (4.63)–(4.69). Also, as a function of R for fixed $p_{T0} =$ 200 GeV, it decreases according to the expected $1/\sqrt{R}$ behaviour, cf. (4.69). The agreement is even quantitatively decent. Indeed, with the physical parameters given in Table 8.1, the fitted R-dependence for gluon-initiated jets, $\epsilon_{\mathrm{MIE}}(R) \simeq \epsilon_0 + \epsilon_1/\sqrt{R}$, with $\epsilon_0 = 10.2$ GeV and $\epsilon_1 = 4.0$ GeV, corresponds to the prediction in (5.104) provided one chooses $\upsilon \simeq 2.95$ and $c_* \simeq 0.38$, which are both reasonable.

Consider now the full parton showers, with both VLEs and MIEs. Although we do not have accurate-enough analytic results to compare with (only the DLA estimate (5.105)), the curves "MI+VLEs" in Figs. 8.1 and 8.2 show the expected trend: the energy loss increases with both p_{T0} and R, due to the rise in the phase-space for VLEs. For later use, we have fitted the dependence on p_{T0} with a quadratic polynomial in $\ln(p_{T0}/\omega_c)$ and the resulting coefficients are shown on Fig. 8.1.

It is also striking from Figs. 8.1 and 8.2, that the average energy loss obeys a surprisingly good scaling with the Casimir colour factor of the leading parton: the energy loss by the quark jet is to a good approximation equal to $C_F/C_A = 4/9$ times the energy loss by the gluon jet. Such a scaling, natural in the case of a single-gluon emission, is very non-trivial in the presence of multiple branchings. Let us first recall the explanation of this scaling for the case of MIEs alone. We have seen that the branching scale that appears in (4.63) depends on the Casimir of the leading parton through the relation (4.71):

$$\omega_{\mathrm{br}}^{(R)} \equiv \frac{\alpha_s^2}{\pi^2}\, C_A C_R\, \frac{\hat{q}L^2}{2}\,, \tag{8.1}$$

where $\hat{q}$ is the gluonic jet quenching parameter, proportional to C_A.

From (8.1) it is easy to show the energy loss (5.104) of a jet initiated by a parton in an arbitrary colour representation R scales linearly with C_R: the first term in (5.104) is proportional to C_R as it is proportional to $\omega_{\mathrm{br}}^{(R)}$ and the second term is also proportional to C_R in the general

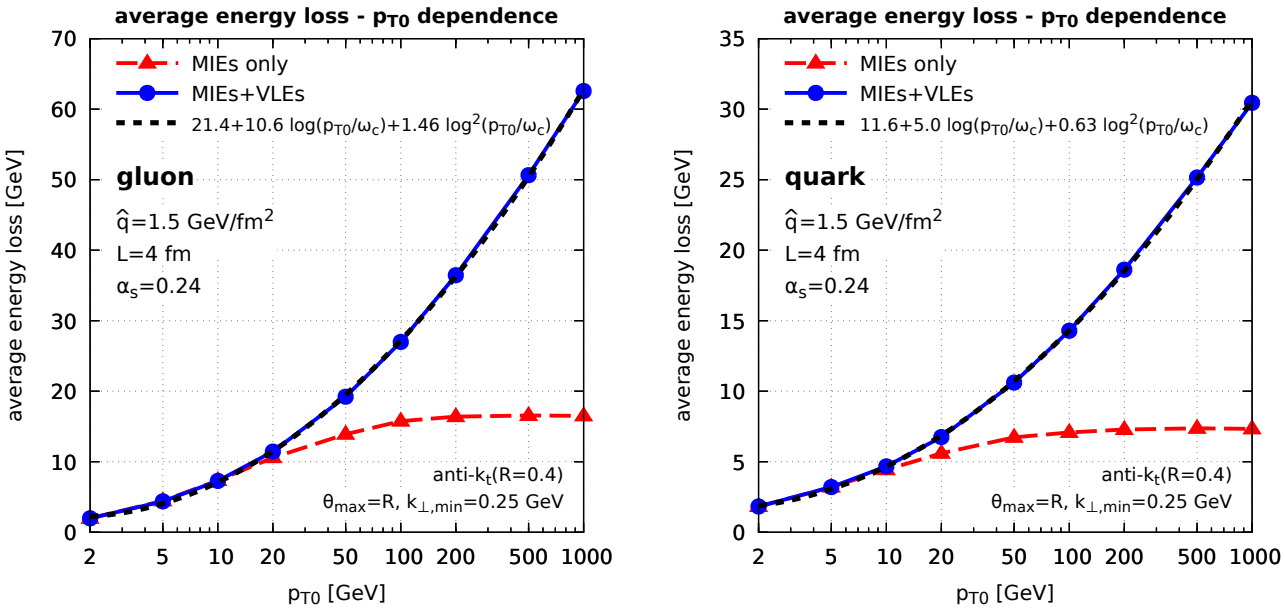

Figure 8.1: The MC results for the average energy loss by a gluon-initiate jet (left), respectively, a quark-initiated one (right), is displayed as a function of the initial energy p_{T0} of the leading parton, for two scenarios for the jet evolution: jets with MIEs only (triangles) and full showers with both MIEs and VLEs (circles). The dashed line shows the quadratic fit to the energy loss by the full parton shower.

case. All the other factors only refer to gluons and are independent of R. This justifies the Casimir scaling visible in Figs. 8.1 and 8.2 for the cascades with MIEs only. For the full cascades including VLEs, the linear dependence on C_R can be argued based on (5.105), assuming $p_{T0} \gg \omega_{\rm br}$. The first term in the r.h.s. of (5.105) is the energy lost by the leading parton and is by itself proportional to C_R, as just argued. The second term in (5.105), which refers to the additional "sources" created via VLEs, one can assume that most of these "sources" are gluons, so they all lose energy (via MIEs) in the same way; the only reference to the colour Casimir of the leading parton is thus in the overall number of sources, which is indeed proportional to $\alpha_s C_R/\pi$ as it is clear from Eq. (5.106).

8.3 The nuclear modification factor R_{AA}

We now consider the physically more interesting jet nuclear modification factor R_{AA}, which is directly measured in the experiments. In order to compute this quantity, we have considered a sample of Born-level $2 \to 2$ partonic hard scatterings. We have used the same hard-scattering spectrum for both the pp baseline and the PbPb sample. This means that we neglect the effects of nuclear PDF, which can sometimes be as large as 15-20% and can be added in a more phenomenologically-oriented study. For each event, both final partons are showered using our Monte Carlo. Jets are reconstructed using the anti-$k_\perp$ algorithm [134] as implemented in `FastJet` v3.3.2 [184]. All the cuts are applied following the ATLAS measurement from Ref. [232].

Figs. 8.3–8.4 show our predictions together with the LHC (ATLAS) data [232] as a function of the transverse momentum $p_{T,\rm jet}$ of the jet (that we shall simply denote as p_T in this section). As discussed in Sect. 6.4.3, our calculation involves 5 free parameters: the 3 "physical" parameters $\hat{q}$, L and $\alpha_{s,\rm med}$ which characterise the medium properties and 2 "unphysical" parameters

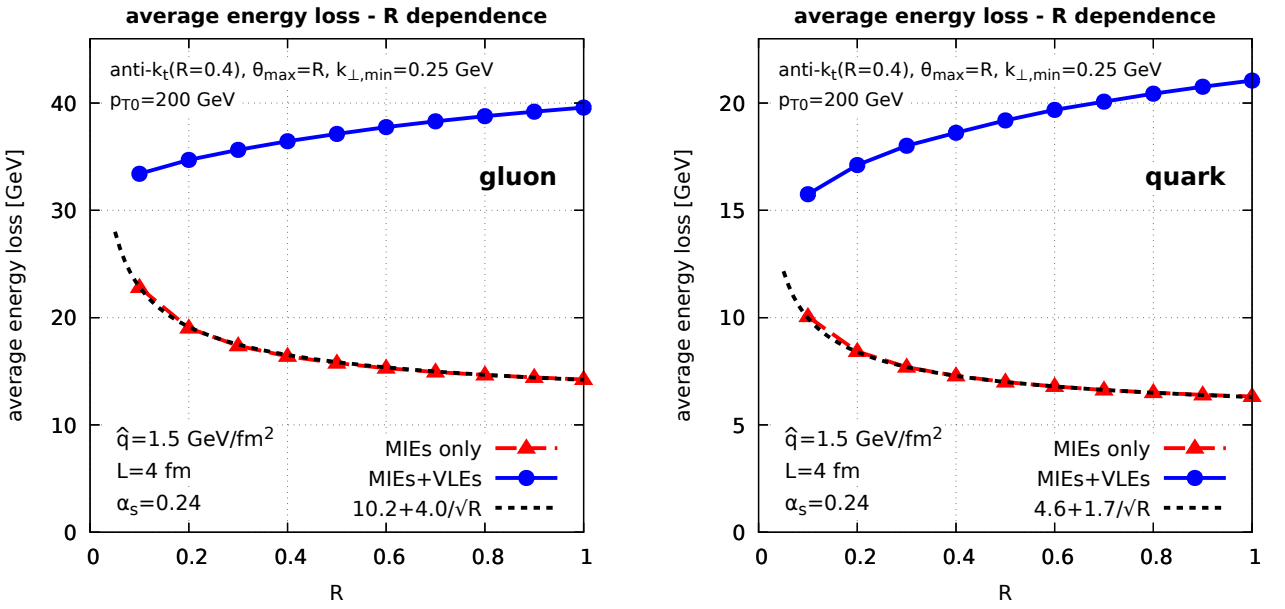

Figure 8.2: The MC results for the average energy loss by the jet are displayed as a function of the jet angular opening R, for the same choices as in Fig. 8.1. We also show in dashed line a fit (inspired by the theoretical estimate in (4.69)) for the jet built with MIEs alone.

$\theta_{\rm max}$ and $k_{\perp,\rm min}$ which specify the boundaries of the phase-space for the perturbative parton shower. Our aim is to study the dependence of our results under changes of these parameters.

The first observation, visible in Fig. 8.3 (left) is that the R_{AA} ratio appears to be very little sensitive to variations of the "unphysical" parameters $\theta_{\rm max}$ and $k_{\perp,\rm min}$. Although our results for the inclusive jet spectrum do depend on these parameters,[1] the impact on $R_{\rm AA}$ remains well within the experimental error bars when changing $\theta_{\rm max}$ by a factor 2 and $k_{\perp,\rm min}$ by a factor larger than 3.

In Fig. 8.3 right and in the two plots of Fig. 8.4 we fix the "unphysical" parameters and vary the medium ones. The variations are done, following Table 8.1, so as to keep two of the three physical scales $\omega_{\rm br}$, ω_c and θ_c fixed while varying the third. It is obvious from the figures that $R_{\rm AA}$ is most sensitive to variations of $\omega_{\rm br}$ (Fig. 8.3, right) and shows only a small dependence on ω_c and θ_c. This is in perfect agreement with the expectations from section 5.3.2 that the jet energy loss is mostly driven by the scale $\omega_{\rm br}$. Furthermore, the small variations of $R_{\rm AA}$ with changes in ω_c and θ_c can be attributed to the slight change in the phase-space for VLEs leading to a corresponding change in the number of sources for energy loss (see section 5.3.2 and, in particular, (5.105)).

One remarkable fact about the LHC measurements is the fact that $R_{\rm AA}$ increases very slowly with the jet p_T. This implies that the jet energy loss $\mathcal{E}_{\rm jet}$ must itself increase with p_T to avoid a fast approach of $R_{\rm AA}$ towards unity. In our picture, such an increase is indeed present, as manifest in Fig. 8.1, and is associated with the steady rise of the phase-space for VLEs leading to an increase in the number of sources for MIEs (cf. (5.105)).

[1] In particular on $\theta_{\rm max}$ as the parton shower would generate collinear logarithms of $\theta_{\rm max}/R$ to all orders.

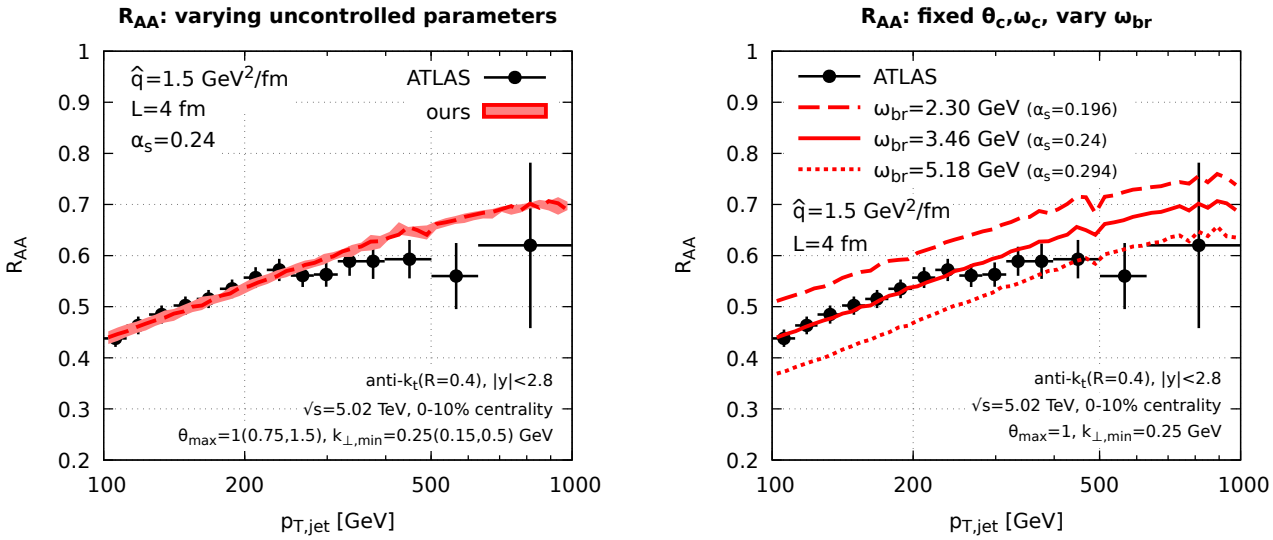

Figure 8.3: Our MC predictions for $R_{\rm AA}$ are compared with the results of an experimental analysis by ATLAS [232] (shown as dots with error bars). Left: the sensitivity of our results to changes in the kinematic cuts $\theta_{\rm max}$ and $k_{\perp,\rm min}$. Right: the effect of varying $\omega_{\rm br}$ (by $\pm 50\%$) at fixed values for ω_c and θ_c.

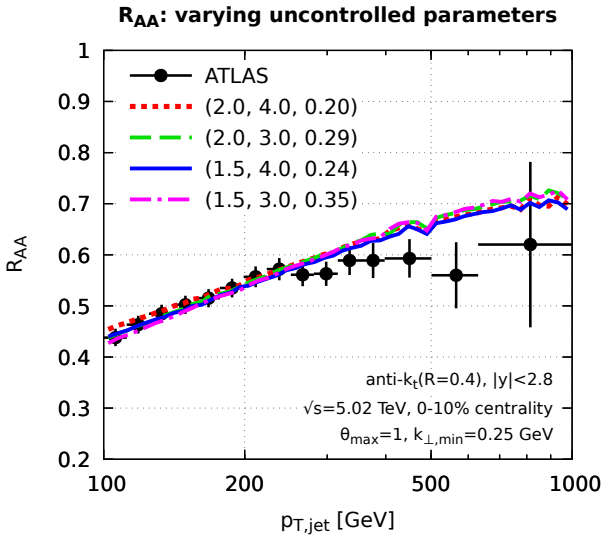

(a) Our MC results for jet R_{AA} and for 4 sets of medium parameters which give quasi-identical predictions are compared to the ATLAS data [232].

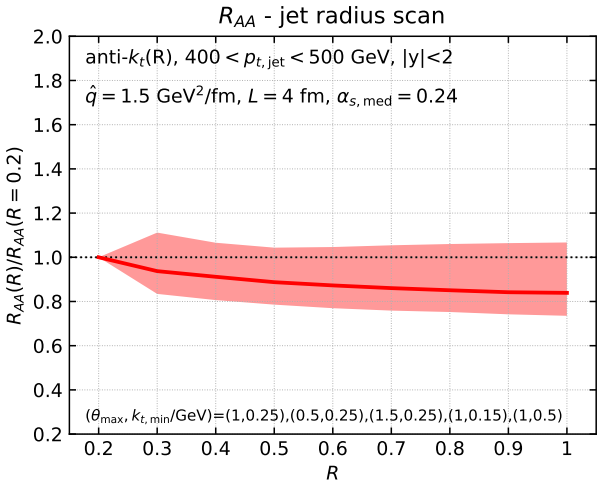

(b) Dependence of R_{AA} with the jet reconstruction radius R in a "CMS-like" set-up.

Figure 8.5: Phenomenology of the nuclear modification factor for jets with `JetMed`.

8.3.1 Medium parameters degeneracy

In Fig. 8.5a, we show a selection of 4 sets of medium parameters, $\hat{q}$, L and $\alpha_{s,\rm med}$ which provide a good description of the LHC data [232] for the jet R_{AA} ratio. We see that our 4 choices of medium parameters correspond to somewhat different values for the physical medium scales

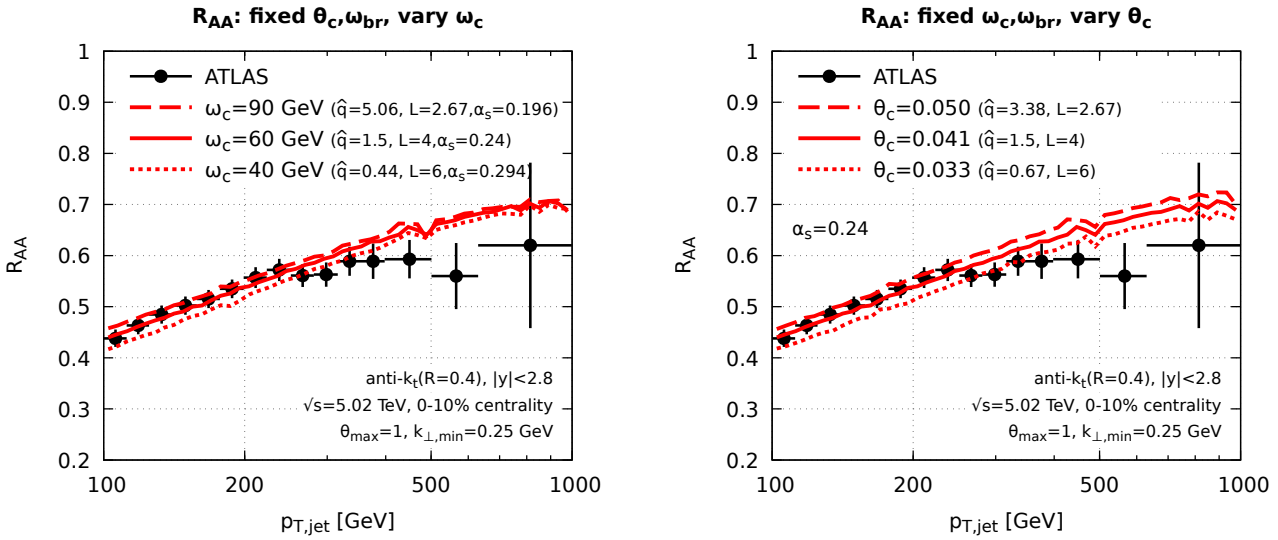

Figure 8.4: The effects of varying the medium parameters $\hat{q}$, L and $\alpha_{s,\mathrm{med}}$ in such a way to keep a constant value for ω_{br} (the same as the central value in the right plot in Fig. 8.3, i.e. $\omega_{\mathrm{br}} = 3.46$ GeV). Left: we vary ω_c by $\pm 50\%$ at fixed θ_c. Right: we vary θ_c^2 by $\pm 50\%$ at fixed ω_c.

ω_{br}, ω_c and θ_c. They therefore lead to different predictions both for the average energy lost *by a single parton* at large angles, dominated by ω_{br}, and for the number and distribution of sources, which is controlled via the phase-space boundaries for VLEs by ω_c and θ_c. While the R_{AA} ratio is most sensitive to variations in ω_{br}, small variations in ω_{br} ($\sim 30\%$ between our extreme values) can be compensated by larger variations of ω_c and θ_c (a factor ~ 2 between our extreme values).

8.3.2 Dependence on the jet reconstruction parameter R

In the last subsection of this chapter, we would like to comment on the R dependence of the R_{AA} ratio predicted by `JetMed`. The dependence of R_{AA} with the jet reconstruction radius has driven a lot of experimental and theoretical activities over the past few months. Indeed, it has been realised that this measurement has an interesting discriminatory power between jet quenching models. At the time we are writing these lines, the preliminary results of the CMS collaboration show a very mild increase of the jet cross-section ratio $\mathscr{R}(R)$ defined by

$$\frac{R_{AA}(R)}{R_{AA}(0.2)} = \frac{\sigma^{R}_{\mathrm{jet,PbPb}}}{\sigma^{R=0.2}_{\mathrm{jetPbPb}}} \tag{8.2}$$

where $\sigma^{R}_{\mathrm{jet}}$ is the integrated jet cross-section over $p_T = [400, 500]$ GeV and pseudo-rapidity $|\eta| < 2$ for jets reconstructed with anti-$k_t(R)$.

From the analytic estimations of the R dependence of the average jet energy loss made in Chapter 5, Section 5.3.2 and from the corresponding Monte Carlo calculations in Section 8.2, we expect also to observe a very mild modification of the function $R_{AA}(R)/R_{AA}(0.2)$. Indeed, the average energy loss is only slightly increasing with R. As explained in Section 5.3.2, this is a consequence of the competition between the recovered energy loss and the increase of in-medium vacuum-like sources. This slight increase explains the slight *decrease* of $R_{AA}(R)/R_{AA}(0.2)$ seen in the central curve of Fig. 8.5b.

That said, the way the large angle energy loss is recovered is strongly model dependent and not really under control in the Monte Carlo. By varying the parameter $\theta_{\max}$ of `JetMed` which should be thought as the angle where the turbulent medium-induced flow ends up, one can access to the uncertainty related to the lack of modelling of thermalization and plasma-jet interactions (e.g. medium response.) As shown in Fig. 8.5b with the red band, this uncertainty is quite large. We have checked that the more $\theta_{\max}$ is small, the more the energy loss recovery effect is important, so that the upper boundary of the bands in Fig. 8.5b corresponds to the minimal value of $\theta_{\max}$. Thus, one must be cautious when interpreting these `JetMed` results, as the physics at play in the R dependence of R_{AA} certainly involves a lot of non perturbative modelling which are not currently included in the Monte Carlo.

Chapter 9

The Soft Drop z_g distribution in heavy-ion collisions

Nowadays, there is an increasing interest in jet observables dealing with the inner structure of jets [261]. By requiring infrared and collinear safety for these substructure observables, one can hope for controlled calculations in pQCD even in the complex environment of a nucleus-nucleus collision and therefore quantitative comparisons with experiments. In this chapter, we explore jet substructure, and in particular the Soft Drop z_g distribution within our picture of jet fragmentation in a dense QCD medium. The emphasis is put on the main physical ingredients that explain the behaviour of our results. Thus, all the numerical results obtained from the Monte Carlo `JetMed` are supported by analytical phenomenological formulas that capture these ingredients.

To understand the nuclear modifications of a jet observable, it is often enlightening to adopt the following methodology:

- starting with a leading parton with *fixed* initial transverse momentum p_{T0}, one first tries to understand the effects of the medium on this observable. In this configuration, one looks for effects coming from the modification of the jet fragmentation pattern itself. This first approach also enables to use simple analytical estimates.
- Then, one adds a realistic initial hard scattering spectrum. This causes additional effects, mostly because large angle energy loss changes the statistics in the transverse momentum of the initial partons.

Therefore, our discussion is divided into two main sections. Section 9.1 only investigates the monochromatic hard spectrum case, whereas Section 9.2 deals with the `JetMed` calculations with a realistic initial spectrum. In the last section, we discuss other Soft Drop related observables, such as the Iterated Soft Drop multiplicity.

9.1 The z_g distribution for monochromatic hard spectra

For the benchmark vacuum results, definitions of the z_g distribution and notations, we refer the reader to Chapter 4, section 4.2.3.1.

9.1.1 Two regimes: high-p_T and low-p_T jets

Let us start with a presentation our Monte Carlo results for the z_g-distribution created by "monochromatic" jets which propagates through the quark-gluon plasma. From these results,

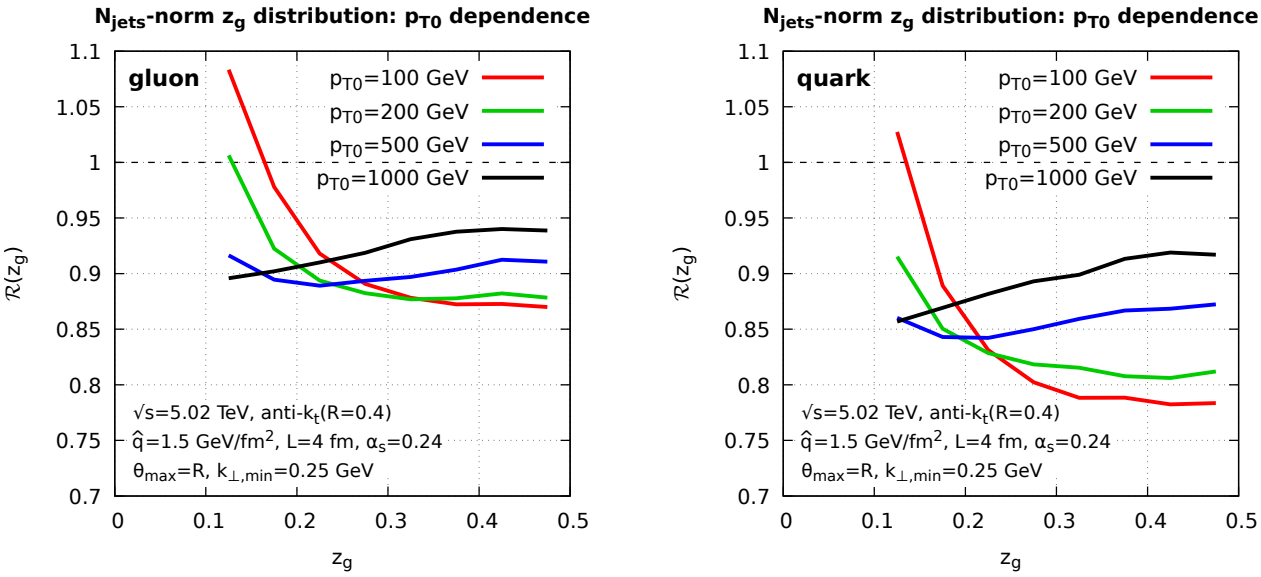

Figure 9.1: A summary of our MC results for the medium/vacuum ratio $\mathcal{R}_i(z_g)$ of the N_{jets}-normalised distributions, for monochromatic jets initiated either by a gluon (left figure), or by a quark (right figure), and for 4 different values for the initial transverse momentum p_{T0}.

we will have to distinguish two regimes — high p_T and low p_T — according to the value of the transverse momentum p_{T0} of the leading parton with respect to the medium-induced scale $\omega_c = \hat{q}L^2/2$. Detailed analytic calculations are presented in Sections 9.1.2 for high-energy jets and 9.1.3 for lower-energy jets.

We focus on the N_{jets}-normalised distribution $f_{i,\text{med}}(z_g)$ (see 4.2.3.1), which carries more information. We define the corresponding nuclear modification factor, $\mathcal{R}_i(z_g) \equiv f_{i,\text{med}}(z_g)/f_{i,\text{vac}}(z_g)$. Similarly we define $\mathcal{R}_i^{(\text{norm})}(z_g) \equiv p_{i,\text{med}}(z_g)/p_{i,\text{vac}}(z_g)$ as the nuclear modification factor of the self-normalised z_g distributions. We study four different values for the initial p_{T0} spanning a wide range in p_{T0}, from 100 GeV to 1 TeV. We use the same SD parameters as in the CMS analysis [255], namely $\beta = 0$ and $z_{\text{cut}} = 0.1$, together with a cut $\theta_g > \theta_{\text{cut}} = 0.1$.

Our results are shown in Fig. 9.1, separately for jets initiated by a gluon (left plot) and by a quark (right plot), using our default MC parameters (cf. Table 8.1). As for our study of energy loss for monochromatic jets in Section 10.2.2.1, we set the angular cutoff scale of our Monte Carlo to $\theta_{\text{max}} = R$ with $R = 0.4$ the jet radius. Each of the plots in Fig. 9.1 show qualitatively different behaviours between our lowest p_{T0} (100 GeV) value and the largest one (1 TeV). More precisely, for the highest energy jets, $p_{T0} = 1$ TeV, the ratio $\mathcal{R}(z_g)$ is always smaller than one, indicating a nuclear suppression, and it increases monotonously with z_g, meaning that the nuclear suppression is larger at small z_g. Conversely, for lower p_{T0}, while the nuclear suppression becomes stronger at large z_g, a peak develops at small z_g where $\mathcal{R}(z_g)$ can even become larger than one, indicating a nuclear *enhancement*.

Let us first discuss the behaviour at large p_{T0}, focusing on $p_{T0} = 1$ TeV. In this case, the softest radiation that can be captured by Soft Drop has an energy $z_{\text{cut}} p_{T0} = 100$ GeV which is still larger than the hardest medium-induced emissions which have energies $\omega \sim \omega_c = 60$ GeV. Hence, for jets with high-enough p_{T0}, SD can only select vacuum-like emissions. To illustrate this, we show in the left plot of Fig. 9.2 the phase-space selected by SD. Under these circumstances, the only nuclear effect on the z_g-distribution is the energy lost by the two (hard, $z_g > z_{\text{cut}}$) subjets passing the SD condition. Due to this energy loss, the *effective*

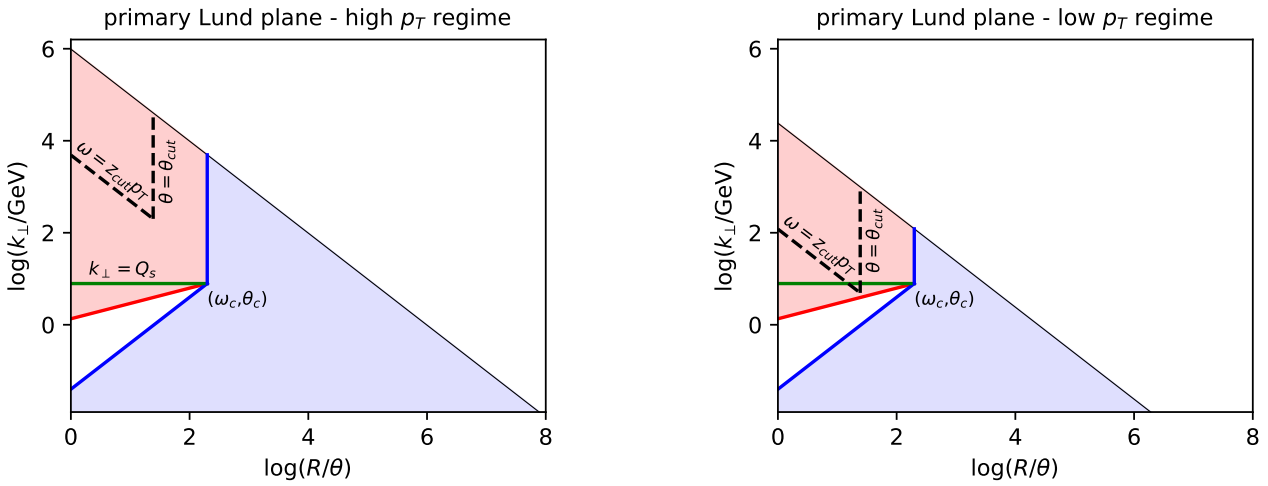

Figure 9.2: The kinematic regions in the Lund plane that are covered by the SD algorithm in the case of a high-energy jet ($z_{\mathrm{cut}} p_T > \omega_c$) in the left figure and of a low-energy jet ($z_{\mathrm{cut}} p_T < \omega_c$) in the right figure. As suggested by the pictorial representation in the right figure, the most interesting situation for "low-energy jets" is such that there is only little overlap between the kinematic region for SD and the phase-space for MIEs.

splitting fraction z_g measured by SD turns out to be slightly smaller than the *physical* splitting fraction z at the branching vertex (see Sect. 9.1.2 for details). If we call for now this shift $\Delta z = z - z_g > 0$, we have (cf. (4.34))

$$\mathcal{R}(z_g) \approx \frac{\bar{P}_g(z = z_g + \Delta z)}{\bar{P}_g(z_g)} \simeq \frac{z_g}{z_g + \Delta z} \simeq 1 - \frac{\Delta z}{z_g} \quad \text{for} \quad \Delta z \ll z_g \ll 1\,, \tag{9.1}$$

which explains the pattern (smaller than one and increasing with z_g) observed at large p_{T0} in Fig. 9.1.

The above discussion also suggests what changes when moving to the opposite regime of (relatively) low energy jets, say $p_{T0} = 100$ GeV. In this case, the energy interval covered by SD, that is ω between $z_{\mathrm{cut}} p_{T0} = 10\,\mathrm{GeV}$ and $p_{T0}/2 = 50$ GeV, fully overlaps with the BDMPS-Z spectrum for medium-induced radiation which has $\omega \lesssim \omega_c = 60$ GeV (cf. the right plot of Fig. 9.2). Consequently, the SD condition can now be triggered either by a vacuum-like splitting, or by a medium-induced one. Since the BDMPS-Z spectrum increases rapidly at small z (faster than the vacuum splitting function), this naturally explains the peak in the ratio $\mathcal{R}(z_g)$ at small z_g, visible in Fig. 9.1. The nuclear suppression observe at large z_g suggests that in this region, the energy loss effects dominate over the BDMPS-Z emissions.

The above arguments show that the z_g distribution is best discussed separately for high-energy and low-energy jets, where the separation between the two regimes is set by the ratio $z_{\mathrm{cut}} p_{T0}/\omega_c$. The high-energy jets, for which $p_{T0} > \omega_c/z_{\mathrm{cut}}$, are conceptually simpler as the in-medium z_g distribution is only affected by the energy loss via MIEs. For low-energy jets, i.e. jets with $p_{T0} < \omega_c/z_{\mathrm{cut}}$, the z_g distribution is affected by the medium both *directly* when the SD condition is triggered by a MIE, and *indirectly* via the energy loss of the two subjets emerging from the hard splitting. This second case is more complex for a series of reasons and notably because MIEs do not obey angular ordering.

Since z_g is intrinsically tied to energy loss effects, it is interesting to study how the average jet energy loss correlates with z_g. Our numerical results are presented in Fig. 9.3. The dashed curve shows the MC results for the inclusive jets (all values of z_g), the one denoted "no z_g" refers

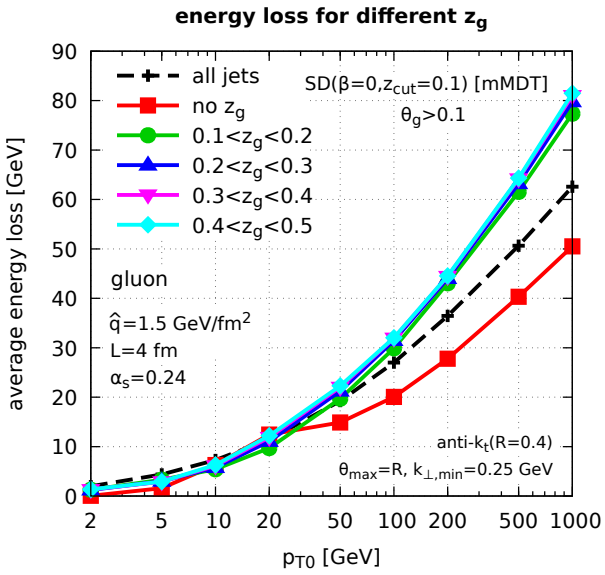

Figure 9.3: Our MC results for the average energy loss by a gluon-initiated jet are displayed as a function of the initial gluon energy p_{T0} in bins of z_g. The inclusive (all jets) result is also shown, by the dashed line.

to jets which did not pass the SD criterion or failed the cut $\theta_g > \theta_{\rm cut}$, and the other curves correspond to different bins of z_g. One clearly sees a distinction between the "no z_g" jets, which lose much less energy than the average jet, and those which passed SD, whose energy loss is larger than the average and quasi-independent of z_g. The main reason for this behaviour is that jets passing the SD condition are effectively built of two relatively hard subjets. Since the angular separation between these two hard subjets is larger than $\theta_{\rm cut} = 0.1 > \theta_c \simeq 0.04$, they lose energy (via MIEs) as two independent jets, giving a larger-than-average energy loss. This is mostly controlled by the geometry of the system, with only a limited sensitivity to the precise sharing of the energy between the subjets. On the other hand, the jets which did *not* pass SD are typically narrow one-prong jets with either no hard substructure or with some substructure at an angle smaller that $\theta_{\rm cut} = 0.1$ (i.e. at an angle $\simeq \theta_c$). These jet therefore lose less energy that an average jet. The fact that the angular cut-off $\theta_{\rm cut} = 0.1$ is close to the critical value $\theta_c \simeq 0.04$ is clearly essential for the above arguments.

A last comment concerns the difference between the z_g-distributions for gluon- and quark-initiated jets, as shown in the left and right plots of Fig. 9.1, respectively. The deviation of the medium/vacuum ratio from unity appears to be larger for quark jets than for gluon jets. This might look surprising at first sight given that the average energy loss is known to be larger for the gluon jet than for the quark one (cf. Figs. 8.1 and 8.2). However we will show in Section 9.1.2 that the z_g distribution is mostly controlled by the energy loss of the softest subjet, which is typically a *gluon* jet even when the leading parton is a quark. The difference between quark and gluon jets in Fig. 9.1 is in fact controlled by "non-medium" effects, like the difference in their respective splitting functions.

9.1.2 High p_T jets: VLEs and energy loss

We begin our investigations of the nuclear effects on the z_g distribution with the case of a high-energy jet, $p_{T0} > \omega_c/z_{\rm cut}$ In this case, the SD condition is triggered by an in-medium VLE

that we call the "hard splitting" in what follows. This splitting occurs early (since $t_f \ll L$, cf. Eq. (5.56)) and the daughter partons propagate through the medium over a distance of order L. During their propagation, they evolve into two subjets, both via VLEs (which obey angular ordering, except possibly for the first emission outside the medium) and via MIEs (which can be emitted at any angle).

Since the C/A algorithm is used by the SD procedure, both subjets have an opening angle of order[1] θ_g, with θ_g the angle of the hard splitting. Consequently, the emissions from the two subjets with angles larger than θ_g — either MIEs, or VLEs produced outside the medium — are *not* clustered within the two subjets. Accordingly, their reconstructed transverse momenta p_{T1} and p_{T2} are generally lower than the initial momenta, ω_1 and ω_2, of the daughter partons produced by the hard splitting. This implies a difference between the *reconstructed* splitting fraction $z_g = p_{T,1}/(p_{T,1} + p_{T,2})$ and the *physical* one, $z \equiv \omega_1/(\omega_1 + \omega_2)$. This difference is controlled by the energy lost by the two subjets.

Let us first mention that the energy loss via VLEs outside the medium at angles $\theta > \theta_g$ can be neglected. Indeed, since these emissions have $t_f \sim 1/(\omega\theta^2) > L$, they are soft and only give very small contributions to the energy loss. We have checked this explicitly with MC studies of the VLEs *alone*: we find that the effect on the z_g distribution of the vetoed region and of the violation of angular ordering for the first emission outside the medium are much smaller than those associated with the energy loss via MIEs.

We then discuss the role of *colour coherence* for the energy loss via MIEs. If the splitting angle θ_g is smaller than θ_c the daughter partons are not discriminated by the medium. This is a case of *coherent* energy loss where the MIEs at angles $\theta > \theta_g$ are effectively sourced by their parent parton [89, 90, 91, 92, 168], so that $z = z_g$. On the other hand, for larger splitting angles $\theta_g \gg \theta_c$, the colour coherence is rapidly washed out, so the two daughter partons act as independent sources of MIEs. In this case, one can write $\omega_i = p_{Ti} + \mathcal{E}_i(\omega_i, \theta_g)$, where $i = 1, 2$ and $\mathcal{E}_i(\omega_i, \theta_g)$ is the average energy loss for a jet of flavour i, initial energy ω_i and opening angle θ_g (cf. e.g. Eq. (5.105)). It would be relatively straightforward to deal with generic values of θ_g, both coherent and incoherent. In practice, all existing measurements at the LHC imposes a minimal angle $\theta_g \geq \theta_{\rm cut}$, with $\theta_{\rm cut} = 0.1$. Since $\theta_{\rm cut}$ is larger than θ_c for all our choices of parameters, we only consider the incoherent case $\theta_g > \theta_{\rm cut}$ in what follows.

That said, the relation between the measured z_g and the physical splitting fraction z can be written as (assuming $p_{T1} < p_{T2}$)

$$z_g = \frac{p_{T1}}{p_{T1} + p_{T2}} = \frac{z p_T - \mathcal{E}_1(z p_T, \theta_g)}{p_T - \mathcal{E}_1(z p_T, \theta_g) - \mathcal{E}_2((1-z) p_T, \theta_g)} \equiv \mathcal{Z}_g(z, \theta_g)\,, \tag{9.2}$$

where $p_T \equiv \omega_1 + \omega_2$ is the energy (or transverse momentum) of the parent parton at the time of the "hard" branching. In what follows we approximate $p_T \simeq p_{T,0}$. This is valid as long as one can neglect two effects: `(i)` the transverse momentum of the partons which have been groomed away during previous iterations of the SD procedure, and `(ii)` MIEs prior to the hard branching. The former is indeed negligible as long as we work in the standard limit $z_{\rm cut} \ll 1$, and the latter is also negligible based on our short formation time arguments in Chapter 5.

For a given average energy loss $\mathcal{E}(p_T, \theta_g)$ one can, at least numerically, invert Eq. (9.2) to obtain the physical splitting fraction $z = \mathcal{Z}(z_g, \theta_g)$ corresponding to the measured z_g. The

[1] On average, the two subjets have an (active) area $\approx 0.69\pi\theta_g^2$, while a single jet of radius θ_g has an area $\approx 0.81\pi\theta_g^2$, cf. Fig 8 of Ref. [262]. Each subjet thus have an effective radius of order $\sqrt{0.69/0.81}\theta_g \approx 0.92\theta_g$ which is very close to θ_g.

kinematic constraint $z_g > z_{\rm cut}$ thus implies a constraint on z, $z \geq \mathcal{Z}(z_{\rm cut}, \theta_g)$,[2] and the in-medium z_g distribution in this high-energy regime becomes a straightforward generalisation of Eq. (4.31)

$$p_{i,\rm med}(z_g) = \mathcal{N} \int_{\theta_{\rm cut}}^{R} {\rm d}\theta_g \, \Delta_i^{\rm VLE}(R, \theta_g) \int_0^{1/2} {\rm d}z \, \mathcal{P}_{i,\rm vac}(z, \theta_g) \, \delta\big(z_g - \mathcal{Z}_g(z, \theta_g)\big) \Theta(z_g - z_{\rm cut}), \tag{9.3}$$

where the Sudakov factor is formally the same as in the vacuum, Eq. (4.30), but with the new, medium-dependent, lower limit $\mathcal{Z}(z_{\rm cut}, \theta)$ on z:

$$\Delta_i^{\rm VLE}(R, \theta_g) = \exp\left(- \int_{\theta_g}^{R} {\rm d}\theta \int_0^{1/2} {\rm d}z \; \mathcal{P}_{i,\rm vac}(z, \theta) \, \Theta\big(z - \mathcal{Z}(z_{\rm cut}, \theta)\big) \right) \tag{9.4}$$

The normalisation factor $\mathcal{N}$ in (9.3) is given by $(1 - \Delta_i^{\rm VLE})^{-1}$. The $N_{\rm jets}$-normalised distribution $f_{i,\rm med}(z_g)$ is obtained by simply removing this factor $\mathcal{N}$.

In practice we will replace θ_g by R in the argument of the energy loss. This is motivated by two facts. Firstly, due to the SD procedure, we know that the jet is free of emissions with $\omega > z_{\rm cut} p_{T0}$ at angles between θ_g and R, simply because such an emission would have triggered the SD condition. The remaining emissions between θ_g and R are therefore soft and we neglect them. Secondly, the angular phase-space $\theta_{\rm cut} < \theta < R$ is relatively small and $\mathcal{E}$ is slowly varying over this domain. With this approximation, both $\mathcal{Z}_g$ and $\mathcal{Z}$ becomes independent of θ_g and the Sudakov factor (9.4) simplifies to the vacuum one, Eq. (4.30), evaluated at $z_{\rm cut} \to \mathcal{Z}(z_{\rm cut})$.

The above picture can be further simplified by noticing that the energy losses are typically much smaller than zp_T and $(1-z)p_T$. This means that the difference between z and z_g is parametrically small and we can replace z by z_g in the arguments of the energy loss in (9.2) so that

$$z \equiv \mathcal{Z}(z_g, \theta_g) \simeq \; z_g + \; \frac{\mathcal{E}_1 - z_g(\mathcal{E}_1 + \mathcal{E}_2)}{p_T} \,, \tag{9.5}$$

with $\mathcal{E}_1 \equiv \mathcal{E}_1(z_g p_T)$ and $\mathcal{E}_2 \equiv \mathcal{E}_2((1-z_g)p_T)$. Since $z_g < 1/2$, this shows that the physical z is typically[3] larger than z_g.

As before, it is useful to consider the fixed-coupling scenario where the z_g-dependence of Eq. (9.3) factorises from the integral over θ_g. After dividing out by the vacuum distribution $\propto \bar{P}_i(z_g)$, we find

$$\mathcal{R}(z_g) \equiv \frac{f_{\rm med}(z_g)}{f_{\rm vac}(z_g)} \simeq \mathcal{J}(z_g) \, \frac{\bar{P}_g(\mathcal{Z}(z_g))}{\bar{P}_g(z_g)} \,, \qquad \text{with} \quad \mathcal{J}(z_g) \equiv \left| \frac{{\rm d}\mathcal{Z}(z_g)}{{\rm d}z_g} \right| \simeq 1 - \frac{\mathcal{E}_1 + \mathcal{E}_2}{p_T} \,, \tag{9.6}$$

where $\mathcal{J}$ is a Jacobian and the last equality in (9.6) is obtained using the simplified expression (9.5).

At this level, it becomes necessary to specify the energy lost by a subjet. At high energy, both zp_T and $(1-z)p_T$ are large and the energy lost by the subjets is sensitive to the increase in the number of partonic sources for MIEs (cf. Sections 5.3.2-8.2 and Fig. 8.1). To test this picture, we consider two energy loss scenarios. First, the case of an energy loss which captures

[2]Here we assume that $\mathcal{Z}_g(z, \theta_g)$ is a monotonously increasing function of z.

[3]Small deviations from this behaviour can happen close to $z_g = 1/2$ when $\mathcal{E}_2 \neq \mathcal{E}_1$. In this limit, our assumption that the softer physical parton ($z < 1/2$) matches with the softer measured subjet ($z_g < 1/2$) has to be reconsidered anyway.

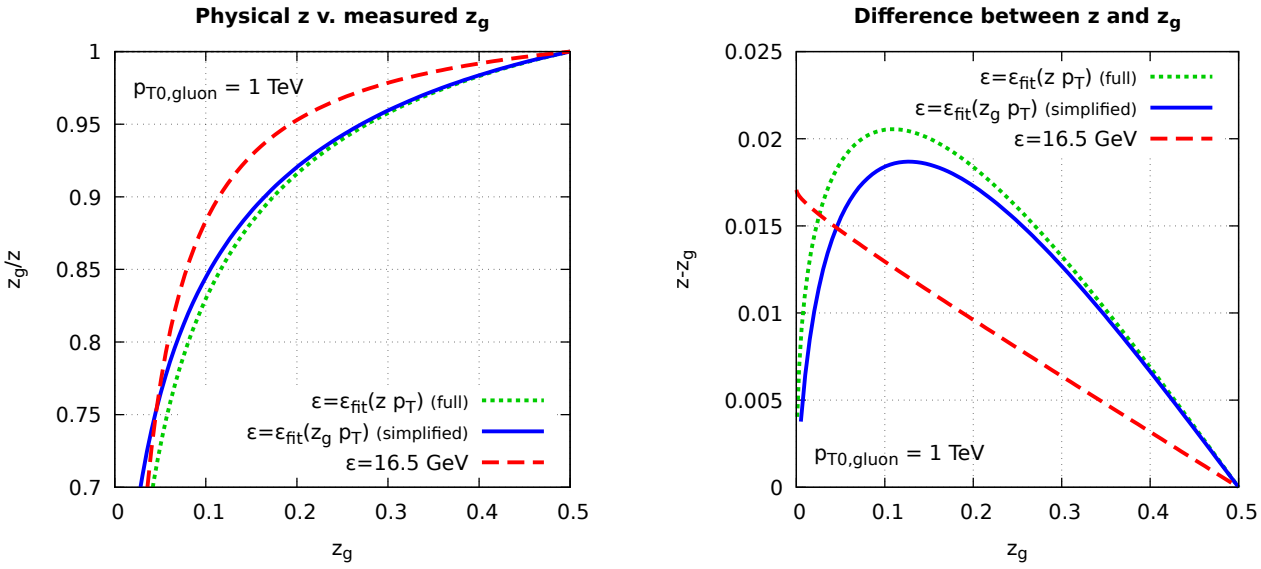

Figure 9.4: The ratio z_g/z (left figure) and the difference $z - z_g$ (right figure) between the splitting fraction z_g measured by SD and the physical splitting fraction z for the hard splitting. This difference is given by Eq. (9.2) that we evaluate with two scenarios for the energy loss by the subjets: a constant energy loss and a p_T-dependent one; for the second scenario, we also show the predictions of the simplified relation (9.5).

the increase in the number of sources for MIEs and increases with the jet p_T, as in Eq. (5.105). Since Eq. (5.105) is not very accurate we will instead use $\mathcal{E}_j = \mathcal{E}_{j,\text{fit}}$ corresponding to the fit of the Monte Carlo result shown in Fig. 8.1. The second scenario corresponds to what would happen in the absence of VLEs, i.e. when only MIEs from the leading parton in each subjet are included. This gives an energy loss which saturates to a constant $\mathcal{E}_j = \varepsilon_j$ at large p_T (see again Fig. 8.1). Clearly, the first scenario is the most physically realistic.

For definiteness, let us first consider the case of a 1-TeV gluon-initiated jet.[4] Fig. 9.4 shows the relation between the physical splitting fraction z and the measured z_g, with the ratio z_g/z plotted on the left panel and the difference $z - z_g$ on the right panel. We see that z is larger than z_g in both energy-loss scenarios. The difference $z - z_g$ decreases when increasing z (at least for $z > z_{\text{cut}}$), while the ratio z_g/z gets close to 1. The effects are roughly twice as large for the full energy-loss scenario than for a constant energy loss. The dotted (green) curve shows the result obtained using the "full" relation (9.2) while the solid (blue) line uses the simplified version, Eq (9.5). As expected, they both lead to very similar results and we therefore make the simplified version our default from now on.

The nuclear modification factor for the z_g distribution obtained from our analytic calculation (9.3), including running-coupling corrections, is shown in Fig. 9.5 for both the self-normalised distribution $p_{\text{med}}(z_g)$ (left) and the N_{jets}-normalised one $f_{\text{med}}(z_g)$ (right). We see that $\mathcal{R}(z_g)$ increases with z_g. This is expected since, at small z_g, $\bar{P}_g(z)/\bar{P}_g(z_g) \simeq z_g/z$ which increases with z_g (see e.g. Fig. 9.4, left). Furthermore, the medium/vacuum ratio of the N_{jets}-normalised distributions (Fig. 9.5, right) is always smaller than one. With reference to the fixed-coupling estimate in Eq. (9.6), this is a combined effect of z being larger than z_g, hence $\bar{P}_g(z) < \bar{P}_g(z_g)$, and of the extra Jacobian in front of Eq. (9.6).

Regarding the comparison between the two scenarios for the energy loss, we see that although they produce similar results for the self-normalised z_g distribution, the (physical) "full

[4]We only included the dominant partonic channel $g \to gg$ in our analytic calculation.

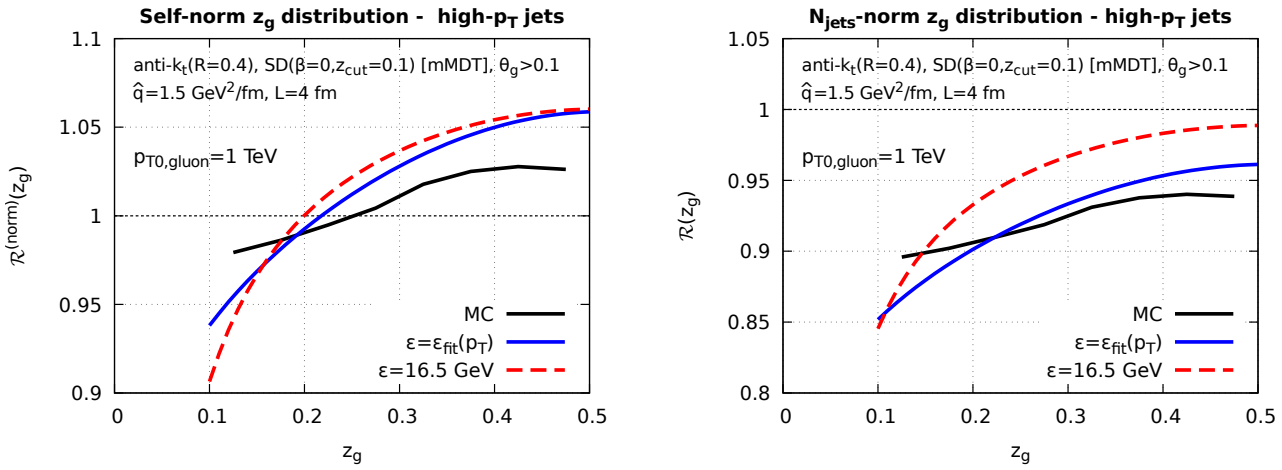

Figure 9.5: Our MC results for the medium/vacuum ratio of the z_g distributions associated with gluon-initiated jets with initial energy $p_{T0} = 1$ GeV are compared to our analytic predictions for the two scenarios of energy loss described in the text. The left plot refers to the self-normalised distributions, cf. Eq. (9.3), and the right plot to the $N_{\rm jets}$-normalised ones.

jet" scenario predicts a larger suppression than the "constant" one for the medium/vacuum ratio of the $N_{\rm jets}$-normalised distributions. In particular, the former predicts a value for $\mathcal{R}(z_g)$ which remains significantly smaller than one even at z_g close to $1/2$. This behaviour is in also in better agreement with our Monte Carlo simulations. Generally speaking, it is worth keeping in mind that the $N_{\rm jets}$-normalised ratio is better suited to disentangle between different energy-loss models than the self-normalised ratio which is bound to cross one by construction.

Since the nuclear modification of the z_g distribution appears to be so sensitive to the energy loss, it is interesting to check whether this observable follows the Casimir scaling of the jet energy loss. We show that this is not the case and that the nuclear modification is even slightly larger for quark than for gluon jets. In practice, the z_g distribution is controlled by the energy loss of the softest among the two subjets created by the hard splitting, which is typically a gluon independently of the flavour of the initial parton. Let us then consider Eq. (9.5) in which we take $\mathcal{E}_1 = \mathcal{E}_{\rm g}$ and $\mathcal{E}_2 = \mathcal{E}_R$, with $R = {\rm q}$ or g depending on the colour representation of the leading parton. Simple algebra yields

$$z^{(\text{g-jet})}(z_g) \;\simeq\; z^{(\text{q-jet})}(z_g) + z_g \,\frac{\mathcal{E}_{\rm g} - \mathcal{E}_{\rm q}}{p_T} \tag{9.7}$$

where $z^{(R\text{-jet})}(z_g)$ is the physical splitting fraction z corresponding to a measured fraction z_g for the case of a leading parton of flavour R, and the energy loss functions $\mathcal{E}_R$ are evaluated at $(1-z_g)p_T$. Since $\mathcal{E}_{\rm g} \simeq 2\mathcal{E}_{\rm q}$ the second term in (9.7) is positive and thus $z^{(\text{g-jet})}(z_g) > z^{(\text{q-jet})}(z_g)$ as expected on physical grounds. Yet, the difference between $z^{(\text{g-jet})}(z_g)$ and $z^{(\text{q-jet})}(z_g)$ is weighted by z_g, hence it suppressed at small z_g, where the energy loss effects should be more important. Furthermore, the effects of the difference $z^{(\text{g-jet})}(z_g) - z^{(\text{q-jet})}(z_g)$ are difficult to distinguish in practice since there are other sources of differences between the z_g distributions of quark and gluon jets like the non-singular terms in the splitting functions and the different Sudakov factors. In practice these effects appear to dominate over difference between $z^{(\text{g-jet})}(z_g)$ and $z^{(\text{q-jet})}(z_g)$

This is confirmed by our analytic calculations in Fig. 9.6. Together with our previous results for a gluon jet, we show two scenarios for quark jets: `(a)` a realistic scenario which takes into account the different quark and gluon energy losses (cf. Fig. 8.1), and `(b)` a fictitious case, which assumes that a quark subjet loses the same energy as a gluon one, i.e. $\mathcal{E}_{\rm q} = \mathcal{E}_{\rm g}$. In both

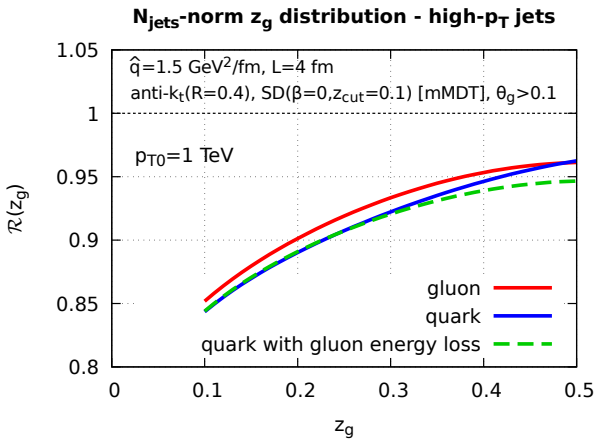

Figure 9.6: The results of the analytic calculations for the medium/vacuum ratio $\mathcal{R}(z_g)$ for both gluon- and quark-initiated jets, together with the fictitious case where a quark-initiated subjet loses the same amount of energy as a gluon-initiated one.

cases, the nuclear suppression of the z_g distribution appears larger for quark-initiated jets than for gluon-initiated jets, in qualitative agreement with our Monte Carlo findings (recall Fig. 9.1). This is clearly driven by effects beyond the energy loss difference between quarks and gluons (cf our case `(b)`), even though this difference has indeed the effect of slightly increasing $\mathcal{R}(z_g)$, especially close to $z_g = 1/2$, as visible by comparing the curves corresponding to the cases `(a)` and `(b)`.

Summary. To sum up, the main lessons one draws from our study of high-energy jets are as follows: `(i)` the incoherent energy loss by the two subjets created by the hard splitting leads to a suppression in the nuclear z_g distribution which is larger at small z_g; `(ii)` the MC results are sensitive to the evolution of the subjets multiplicity via VLEs which leads to an energy loss increasing with the subjet p_T; `(iii)` this last effect may be hidden when studying the self-normalised z_g distribution; in that respect, the $N_{\rm jets}$-normalised distribution is better suited to disentangle between different energy-loss models.

9.1.3 Low-p_T jets: MIEs and energy loss

We now turn to more phenomenologically-relevant case of "low energy" jets, $p_{T0} < \omega_c/z_{\rm cut}$ (with $\omega_c/z_{\rm cut} = 600$ GeV for our default choice of medium parameters), for which the "hard" emission that triggers the SD condition can be either vacuum-like or medium-induced. In both cases, the two ensuing subjets lose energy via MIEs, which, as explained in the previous section, implies that the measured value z_g is different (typically slightly smaller) than the physical value z.

Our main goal in this section is to develop analytic approximations which qualitatively and even semi-quantitatively capture this complex dynamics. For definiteness, we focus on gluon-initiated jets with $p_{T0} = 200$ GeV. This value is at the same time low enough to be representative for the low-energy regime and large enough to justify some convenient approximations, like the single emission approximation for the MIEs captured by SD. For pedagogical reasons it is convenient to first consider two simplified situations — a jet built with MIEs alone and a jet in which the SD condition can only be triggered by a VLE (as in the "high-energy" case) —, before addressing the full picture in Sect. 9.1.3.3.

9.1.3.1 Low-p_T jets: medium-induced emissions only

To study the case where the SD condition is triggered by a MIE, we consider jets generated via MIEs only, disabling VLEs. Since the emission angles of MIEs are controlled by their transverse momentum broadening (cf. Sect. 4.3.3), they are not ordered in angle. Hence, the reclustering of the jet constituents with the C/A algorithm does not necessarily respects the physical ordering of the MIEs in time. In particular, the branching selected by the SD procedure may not be a *primary* emission, i.e. a direct emission by the leading parton. However, as long as $z_{\rm cut}p_{T0}$ is sufficiently large compared to the characteristic scale $\omega_{\rm br} = 3.46$ GeV for multiple branching — which is definitely the case for our 200 GeV jets, — the probability to select a non-primary branching is suppressed by $\alpha_{s,\rm med}$. From now on we can therefore assume that SD selects a *primary* MIE.

Next, we can argue that the MIEs captured by the SD algorithm are soft and located in a small corner near $z = z_{\rm cut}$ and $\theta = \theta_{\rm cut}$. Indeed, the bulk of the MIEs lies below the line $k_\perp = Q_s = 2.4$ GeV and the smallest value of $k_\perp$ that can be selected by SD, namely $z_{\rm cut}p_{T0}\theta_{\rm cut} = 2$ GeV, is only slightly smaller than Q_s. This is visible in the phase-space diagram of Fig. 9.2 (right). Together with the fact that the BDMPS-Z rate (6.21) grows quickly as $z \to 0$, this means that MIEs contribute to the z_g distribution only at small z_g. After SD, one therefore has a soft subjet of transverse momentum p_{T1} corresponding to the MIE and a harder subjet of momentum p_{T2} corresponding to the leading parton.

The differential probability for the emission of a primary MIE with $\omega_1 \equiv \omega \ll p_{T0}$ is given by the BDMPS-Z spectrum (4.48) multiplied by the angular distribution produced via transverse momentum broadening after emission, Eq. (3.64). The latter depends on the distance $\Delta t = L - t$, with t the emission time, travelled by the two subjets through the medium. In principle one should therefore work differentially in t. Since this would be a serious complication, we rather use a picture in which we average over all the emission times t, distributed with uniform probability over the interval $0 < t < L$. This picture is further supported by the angular structure of jets with primary medium-induced emissions after a C/A declustering. In Section 4.3.3.2, we have seen that in the regime $\omega_s(R) = (\hat{q}/(\bar{\alpha}_s^2 R^4))^{1/3} \geq \omega_{\rm br}$, a jet with only primary medium-induced emissions can be seen as an effective angular ordered branching process, with a differential rate for the "hard" splitting taking the form:

$$\mathrm{d}^2\mathcal{P}_{i,\rm med}(\omega,\theta) = \frac{C_i\alpha_{s,\rm med}}{\pi}\Theta\left(\omega_c-\omega\right)\sqrt{\frac{2\omega_c}{\omega^3}}\,\mathcal{P}_{\rm broad}(\omega,\theta)\,\mathrm{d}\omega\mathrm{d}\theta \;\equiv\; \mathcal{P}_{i,\rm med}(\omega,\theta)\mathrm{d}\omega\mathrm{d}\theta, \tag{9.8}$$

where [168]

$$\mathcal{P}_{\rm broad}(\omega,\theta) \equiv \frac{1}{L}\int_0^L \mathrm{d}t\,\frac{2\omega^2\theta}{\hat{q}(L-t)}\exp\left\{-\frac{\omega^2\theta^2}{\hat{q}(L-t)}\right\} = 2\theta\,\frac{\omega^2}{Q_s^2}\,\Gamma\left(0,\frac{\omega^2\theta^2}{Q_s^2}\right), \tag{9.9}$$

This distribution predicts an average value $\bar{k}_\perp = \frac{\sqrt{\pi}}{3}Q_s$ for $k_\perp \equiv \omega\theta$. It shows a peak near $\bar{k}_\perp$, and a rather wide tail at larger values $k_\perp > \bar{k}_\perp$ (see Fig. 9.7, left). Since we have just argued that SD selects emissions in a narrow range in $k_\perp$, close to Q_s, the tail of this distribution plays an important role in our discussion. This is amplified by the fact that $\bar{k}_\perp$ is slightly smaller than Q_s. Note that in terms of the emission angle, this argument means that the emissions selected by SD will need to acquire a θ larger than the peak value $\bar{\theta}(\omega) = \bar{k}_\perp/\omega$ from broadening in order to pass the $\theta_{\rm cut}$ condition. In future work, it will be interesting to study how a description of broadening beyond the Gaussian approximation affects quantitatively our results.

Additionally, we need to account for the fact that both the MIE that triggers the SD condition and the leading parton lose energy. The situation is mostly the same as for our earlier

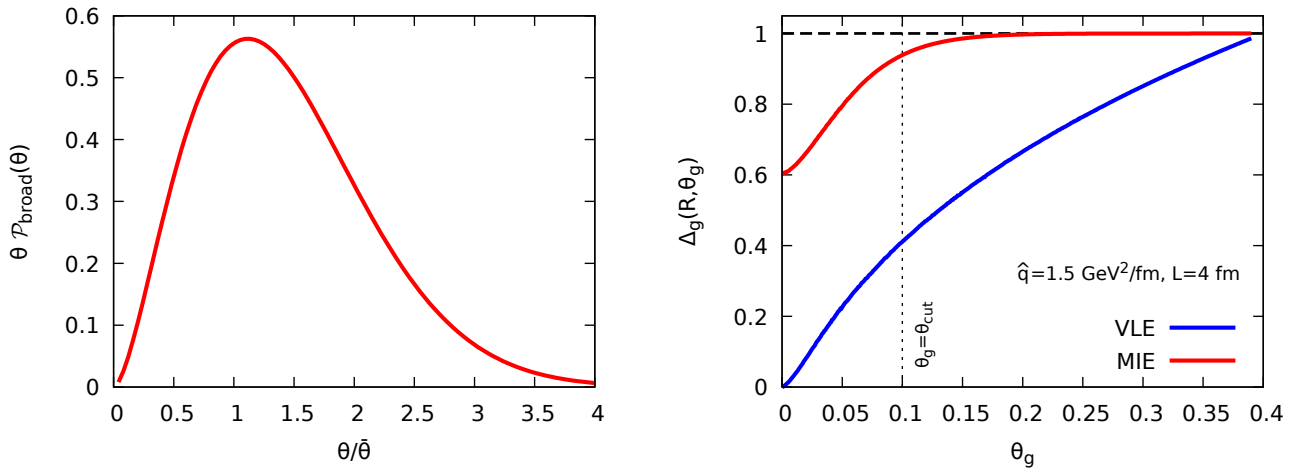

Figure 9.7: Left: after multiplication by θ, the angular distribution $\mathcal{P}_{\rm broad}$ in Eq. (9.9) scales as a function of the ratio $\theta/\bar{\theta}$, with $\bar{\theta} = (\sqrt{\pi}/3)Q_s/\omega$. Right: the Sudakov factors $\Delta_{\rm g}^{\rm MIE}(R,\theta_g)$ for MIEs, cf. Eq. (9.12), and $\Delta_{\rm g}^{\rm VLE}(R,\theta_g)$ for VLEs, cf. Eq. (9.4), for a gluon-initiated jet with $p_{T0} = 200$ GeV and $R = 0.4$.

high-energy case except that now the medium-induced gluon emission can occur anywhere inside the medium, i.e. at any time t with $0 < t < L$. For an emitted gluon of energy ω, one can write $p_{T1} = \omega - \varepsilon_{\rm g}(\omega, \theta_g, \Delta t)$, where the energy loss depends explicitly on the distance $\Delta t = L - t$ travelled by the subjet through the medium. In our kinematic range, this energy loss is relatively small, $\varepsilon_{\rm g} \ll \omega$, and therefore varies slowly with ω (cf. Eq. (5.104) so we can neglect the ω dependence. It depends however quadratically on Δt. For simplicity, we use a time-averaged picture in which $\langle t \rangle \simeq \langle \Delta t \rangle \simeq L/2$ and therefore $\varepsilon_{\rm g}(\Delta t) \approx \varepsilon_{\rm g}(L/2) \simeq \frac{1}{4}\varepsilon_{\rm g}(L) \equiv \bar{\varepsilon}_{\rm g}$, with $\varepsilon_{\rm g}(L) \propto L^2$ the energy loss corresponding to a distance L.

The situation for the harder subjet matching with the leading parton, is more complex, owing to differences between the time ordering of MIEs and the (angular-ordered) C/A clustering used by SD. Indeed, MIEs from the leading parton at times smaller than t and angles smaller than θ_g will be clustered by the C/A algorithm in the harder subjet. These emissions can carry a substantial amount of energy so that, without a full picture of the time evolution of the jet, it is delicate to even define a physical transverse momentum, ω_2, for the harder subjet at the vertex where the MIE triggering the SD condition is emitted. We can however take a different approach and realise that, by definition, the difference $p_{T0} - (p_{T1} + p_{T2})$ corresponds to the energy $\varepsilon_i(p_{T0}, \theta_g)$ lost by the initial parton at angles larger than θ_g. As for the high-energy case, we can neglect the energy lost between θ_g and R and hence write $p_{T1} + p_{T2} \simeq p_{T0} - \varepsilon_i(p_{T0}, R)$.

In fine, the measured value of z_g is related to the initial energy ω of the gluonic MIE subjet via

$$z_g \simeq \frac{\omega - \bar{\varepsilon}_{\rm g}(\omega, \theta_g)}{p_{T0} - \varepsilon_i(p_{T0}, R)} \qquad \text{with } \bar{\varepsilon}_{\rm g}(\omega, \theta_g) = \frac{1}{4}\varepsilon_{\rm g}(\omega, \theta_g) \tag{9.10}$$

Since both energy losses in (9.10) are small, one can ignore their p_T dependence and use the fits to the MC results shown in Figs. 8.2. The z_g distribution created via MIEs can then be computed using a formula similar to that used for VLEs in the previous subsections, cf. Eq. (9.3), namely

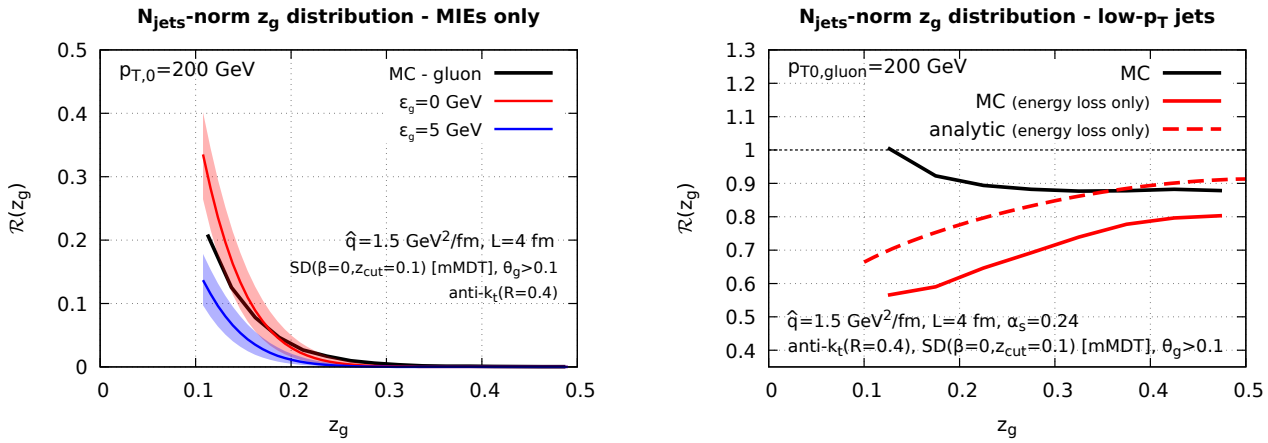

Figure 9.8: Separation of the nuclear effects on the z_g distribution of low-energy jets into a contribution due to the MIEs (left) and a contribution due to the VLEs with energy loss (right). Left: MIEs only (MC vs. analytic calculations). Right: Monte Carlo results for the full parton shower (black) vs. the case where only VLEs with energy loss are included (red). We also show an analytic result for the second case (dashed line).

$$f_{i,\mathrm{med}}(z_g) = \int_{\theta_{\mathrm{cut}}}^{R} \mathrm{d}\theta_g \, \Delta_i^{\mathrm{MIE}}(R,\theta_g) \int \mathrm{d}\omega \, \mathcal{P}_{i,\mathrm{med}}(\omega,\theta_g) \delta\left(z_g - \frac{\omega - \bar{\varepsilon}_{\mathrm{g}}(\theta_g)}{p_{T0} - \varepsilon_i(R)}\right) \Theta(z_g - z_{\mathrm{cut}}) \tag{9.11}$$

with the Sudakov factor $\Delta_i^{\mathrm{MIE}}(R,\theta_g)$ accounting for the probability to have no primary MIEs with $\omega > \omega_{\mathrm{cut}} \equiv \bar{\varepsilon}_{\mathrm{g}} + z_{\mathrm{cut}}(p_{T0} - \varepsilon_i(R))$ and $\theta > \theta_g$ at any point inside the medium:

$$\Delta_i^{\mathrm{MIE}}(R,\theta_g) = \exp\left(-\int_{\theta_g}^{R} \mathrm{d}\theta \int \mathrm{d}\omega \; \mathcal{P}_{i,\mathrm{med}}(\omega,\theta) \, \Theta\left(\omega - \omega_{\mathrm{cut}}\right)\right) \tag{9.12}$$

The self-normalised distribution can be computed as $p_{i,\mathrm{med}}(z_g) = \mathcal{N} f_{i,\mathrm{med}}(z_g)$ with $\mathcal{N} = \frac{1}{1-\Delta_i^{\mathrm{MIE}}(R,\theta_{\mathrm{cut}})}$. The Sudakov factor is plotted for both MIEs, Eq. (9.12), and VLEs, Eq. (9.4), as a function of θ_g in the right plot of Fig. 9.7. In both plots, we use $p_{T0} = 200$ GeV and a gluon-initiated jet. While this factor is clearly important for VLEs at all θ_g, it remains very close to one for MIEs. It is mostly irrelevant for the shape of the z_g distribution and only has a small impact on its overall normalisation.

In Fig. 9.8(left) we compare our analytic approximation for the ratio[5] $f_{\mathrm{med}}(z_g)/f_{\mathrm{vac}}(z_g)$ of the N_{jets}-normalised z_g distributions corresponding the a gluon-initiated jet to the MC results obtained by "switching off" the VLEs from the general numerical code. The energy losses are estimated from the fit to the MC results shown in the left plot of Fig. 8.2, which yields $\varepsilon_{\mathrm{g}} \simeq 16.5$ GeV for the whole jet with $R = 0.4$ and $\bar{\varepsilon}_{\mathrm{g}} \simeq 5$ GeV for the subjet with $\theta_g \simeq \theta_{\mathrm{cut}} = 0.1$. Given the large uncertainty in the calculation of $\bar{\varepsilon}_{\mathrm{g}}$, we present two sets of results, one corresponding to $\varepsilon_{\mathrm{g}} = 0$ GeV and the other one to $\varepsilon_{\mathrm{g}} = 5$ GeV. For each of these 2 choices we indicate by a band the uncertainty associated with $\pm 10\%$ variations in the saturation scale Q_s around its central value $Q_s = \sqrt{\hat{q}L} = 2.4$ GeV. This variation corresponds to the fact that the relation (9.10) between z_g and ω is only approximate and the associated uncertainty in the

[5]Here, the medium/vacuum ratio is not a genuine nuclear modification factor. For example, in the absence of medium effects, it would be equal to zero, not to one.

value of ω has consequences, via Eq. (9.9), on the angular distribution; this uncertainty was mimicked by varying Q_s.

Fig. 9.8(left) shows a qualitative agreement between the MC and the analytic calculations: all the curves have a visible rise at small z_g, reflecting the fact that the BDMPS-Z spectrum behaves like $z^{-3/2}$ which is more singular than the vacuum spectrum $\propto z^{-1}$. This being said, our analytic study is still too poor to quantitatively reproduce the MC results, or to discriminate between various scenarios for the energy loss. In particular, the "zero energy loss" scenario is not in clear disagreement with the MC results. This may be related to the fact that the angular distribution in Eq. (9.9) favours small values $z \sim z_{\rm cut}$ which biases the distribution towards events with a smaller-than-average energy loss.

9.1.3.2 Low-p_T jets: energy loss only

In this section, we consider the situation (opposite to the previous section) where the SD condition is triggered by a VLE. In this case, we turn off the direct contribution of the MIEs to SD, but only keep their (indirect) effect associated with incoherent energy loss of the subjets found by the SD procedure. The physical situation is similar to the high-energy case studied in Sect. 9.1.2 where the "direct" contribution of the MIEs to SD was negligible by definition.

To artificially remove the direct contribution of the MIEs from the MC simulations, we have enforced that all the partons generated via MIEs propagate at angles $\theta \gg R$. This obviously overestimates the jet energy loss, simply because some of the partons which would have remained within the jet are artificially moved outside. This is fine as long as we only focus on illustrating the qualitative effects of the energy loss on the z_g distribution.

In Fig. 9.8(right), we compare Monte Carlo results obtained with this artificial removal of the direct contribution of MIEs ("energy loss only", red, curve) to the full simulation ("full", black, curve), where both VLEs and MIEs contribute directly. Fig. 9.8(right) also shows the prediction of an analytic calculation which ignores the direct contribution of the MIEs to SD. This calculation is the same as the one presented in Sect. 9.1.2 for the case of a high-energy jet, i.e. it is based on Eqs. (9.2), (10.9) and (9.4), now applied to $p_T \simeq p_{T,0} = 200$ GeV. The respective Sudakov factor is plotted in the right plot of Fig. 9.7. By inspection of these curves, we first notice that the effect of energy loss alone is the same for low-energy jets as it was for high-energy jets: it leads to a strong nuclear suppression[6] of the z_g distribution with larger effects at small z_g. Second, adding the direct contribution of the MIEs to SD changes the picture significantly: the medium/vacuum ratio is now increasing at small z_g and can even becomes close to one. The difference between the two curves is, at least qualitatively, consistent with an additional peak at small z_g from MIEs (see e.g. Fig. 9.8, left).

9.1.3.3 Low-p_T jets: full parton showers

Now that we have studied both effects separately, we can provide an analytic calculation for the complete z_g distribution for a low-energy jet, including both VLEs and MIEs.

Due to angular ordering, VLEs selected by the SD procedure are necessarily primary gluon emissions from the leading parton. However, whenever SD selects a MIE with energy fraction z and emission angle θ_g, this emission can be emitted by any of the partonic sources created via VLEs with energy $\omega > zp_{T0}$. Since, by definition, SD selects the largest-angle emission with z_g above $z_{\rm cut}$, these sources of MIE can have any angle in the range $\theta_c < \theta < \theta_g$. Such

[6]This suppression appears to be larger for the respective MC calculation than for the analytical one because, for the former, the energy loss is artificially amplified.

emissions are formally clustered by the C/A algorithm together with the subjet corresponding to the leading parton.

The z_g distribution for a full parton shower generated by a parton of type $i = (\mathrm{q}, \mathrm{g})$ is obtained by incoherently summing up the probabilities for SD to select either a VLE or a MIE:

$$f_i(z_g) = \int_{\theta_{\rm cut}}^{R} \mathrm{d}\theta_g \, \Delta_i^{\rm VLE}(R,\theta_g)\, \Delta_i^{\rm MIE}(R,\theta_g) \tag{9.13}$$
$$\times \int_0^{1/2} \mathrm{d}z \Big[\mathcal{P}_{i,\rm vac}(z,\theta_g)\delta\big(\mathcal{Z}_{g,\rm vac}(z,\theta_g) - z_g\big) + \mathcal{P}_{i,\rm med}(z,\theta_g)\delta\big(\mathcal{Z}_{g,\rm med}(z,\theta_g) - z_g\big)\Big] \Theta(z_g - z_{\rm cut})$$

Here, we have used different functions, $\mathcal{Z}_{g,\rm vac}(z,\theta_g)$ and $\mathcal{Z}_{g,\rm med}(z,\theta_g)$, for the relation between the measured splitting fraction z_g and the physical one z, to take into account the fact that the energy loss is generally different for the subjets produced by a VLE or a MIE. The function $\mathcal{Z}_{g,\rm vac}(z,\theta_g)$ is given by Eq. (9.2), with the p_T of the parent gluon identified with the p_{T0} of the leading parton. As before, we replace θ_g by R in the energy loss and take $\mathcal{E}_1(zp_T, R)$ and $\mathcal{E}_2((1-z)p_T, R)$ from the fits in Fig. 8.1. In the case of a medium-induced splitting, we use a generalisation of Eq. (9.10), that is

$$z_g \simeq \frac{zp_{T0} - \bar{\varepsilon}_{\rm g}(\theta_g)}{p_{T0} - \mathcal{E}_i(p_{T0}, R, z_g)} \equiv \mathcal{Z}_{g,\rm med}(z,\theta_g) \tag{9.14}$$

The main difference w.r.t. Eq. (9.10) refers to the energy loss by the whole jet, i.e. the function $\mathcal{E}_i(p_{T0}, R, z_g)$ in the denominator: not only this has now a strong dependence upon p_{T0}, due to the rise in the number of partonic sources via VLEs, but this must be evaluated for the special jets which include a hard splitting with a given value $z_g > 0.1$ and with any $\theta_g > \theta_{\rm cut} = 0.1$. From our MC calculation illustrated in Fig. 9.3, we know that it is larger than the average energy loss and largely independent of z_g. We use $\mathcal{E}_{\rm g} = 43$ GeV for $p_{T0} = 200$ GeV and $R = 0.4$. As for $\bar{\varepsilon}_{\rm g}(\theta_g)$, we use 5 GeV as in Sect. 9.1.3.1 and study the sensitivity of our results to variations around this value.

The vacuum splitting probability density $\mathcal{P}_{i,\rm vac}$ and the associated Sudakov factor $\Delta_i^{\rm VLE}$ take the same form as in Sect. 9.1.2, Eqs. (10.9) and (9.4). The corresponding medium-induced probability density $\mathcal{P}_{i,\rm med}$ takes a form similar to Eq. (10.10) modified to account for the fact that each VLE produced in the medium can act as a source of MIE. We therefore write

$$\mathcal{P}_{i,\rm med}(z,\theta_g) = \nu(z,\theta_g)\, \frac{\alpha_{s,\rm med} C_i}{\pi} \sqrt{\frac{2\omega_c}{p_{T0}}}\, z^{-3/2}\, \mathcal{P}_{\rm broad}(z,\theta_g) \tag{9.15}$$

The number of MIE sources $\nu(z,\theta_g)$ is obtained from the density $\frac{\mathrm{d}^2 N_{\rm VLE}^{(\rm in)}}{\mathrm{d}\omega \mathrm{d}\theta}$ of VLEs produced inside the medium:

$$\boxed{\nu(z,\theta_g) \equiv 1 + \int_{zp_{T0}}^{p_{T0}} \mathrm{d}\omega \int_{\theta_c}^{\theta_g} \mathrm{d}\theta \frac{\mathrm{d}^2 N_{\rm VLE}^{(\rm in)}}{\mathrm{d}\omega \mathrm{d}\theta}} \tag{9.16}$$

In this last expression, the first term corresponds to the leading parton and the integration boundaries in the second term impose that an MIE which triggers the SD condition has to come from a source of larger energy at an angle between θ_c and θ_g. The associated Sudakov factor $\Delta_i^{\rm MIE}$ is then constructed in terms of $\mathcal{P}_{i,\rm med}$ as in Eq. (9.12). We note however that, although for the case with only MIEs, the exponentiation of the emission probability in the Sudakov factor $\Delta_i^{\rm MIE}$ is relatively straightforward, this does not obviously hold in the presence of multiple sources of MIEs. However, since the Sudakov factor $\Delta_i^{\rm MIE}$ only introduces a small

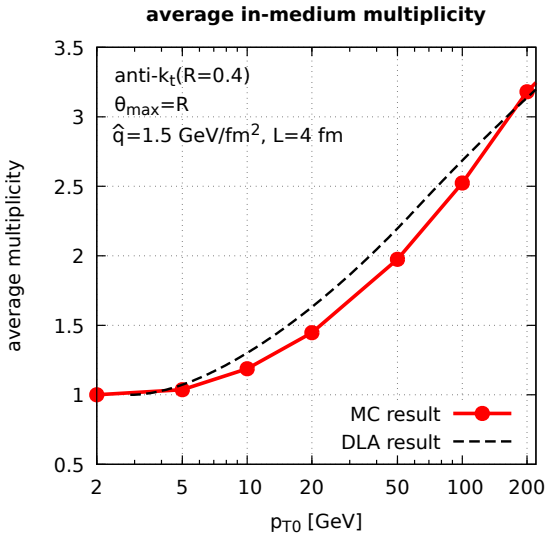

Figure 9.9: The average multiplicity of partons created inside the medium via VLEs by a leading gluon with $p_{T0} = 200$ GeV: the full Monte Carlo results shown by (red) points are compared with a running-coupling extension of the DLA estimate in Eq. (4.24), integrated over the "inside" region of the phase-space of Fig. 5.3.

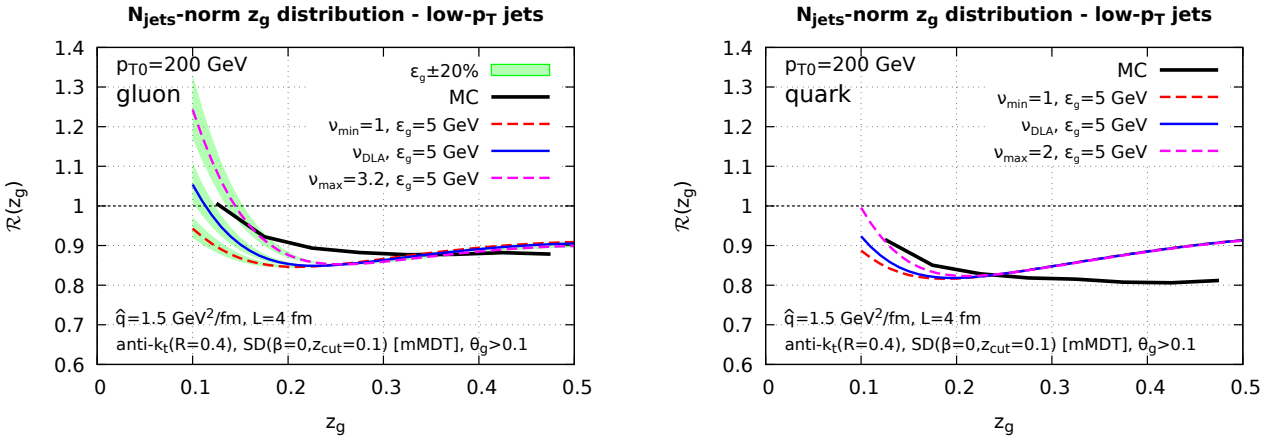

Figure 9.10: $\mathcal{R}(z_g)$ for a leading parton (left: gluon, right: quark) with initial transverse momentum $p_{T0} = 200$ GeV. The Monte Carlo results are compared to analytic calculations corresponding to 3 different approximations for the number ν of sources emitting MIEs (see the text for details).

correction (see Fig. 9.7, right), we have kept the exponential form, Eq. (9.12), for simplicity and as an easy way to maintain the conservation of probability for MIEs.

In practice, we test three different approximations[7] for ν: `(i)` $\nu \equiv \nu_{\min} = 1$ includes only the leading parton, `(ii)` $\nu \equiv \nu_{\max} = 3.2$ is our MC estimate for the average multiplicity of partons created inside the medium via VLEs by a leading gluon with $p_{T0} = 200$ GeV, cf. Fig 9.9. This has to be seen as a maximal value since it ignores the kinematic limits in Eq. (9.16)). `(iii)` $\nu \equiv \nu_{\rm DLA}$ obtained by evaluating Eq. (9.16) with a DLA estimate for the gluon multiplicity, corresponding to Eq. (4.24) with $R \to \theta_g$ and taking the coupling $\bar{\alpha}_s$ at the scale $k_\perp = E\theta_g$. We see in Fig. 9.9 that this DLA approximation gives a reasonable description of the VLE multiplicity in a jet (setting $\theta_g = R$). For the case $\nu = \nu_{\rm DLA}$ we show no variation band in Fig. 9.10 to avoid overlapping bands in an already complicated plot, but it is quite clear what should be the effects of varying $\bar{\varepsilon}_{\rm g}$ and Q_s^2.

In Fig. 9.10, we show our MC results for a full shower generated by a leading parton, gluon

[7]Note also that the formal limit $\nu \to 0$, in which one keeps only the "direct" contribution of the VLEs to Eq. (9.15), corresponds to the analytic result shown with dashed line in Fig. 9.8(right).

(left) or quark (right), with $p_{T0} = 200$ GeV, together with our analytic approximation based on Eq. (9.13) using the three different approximations for ν. In each case, the central curve corresponds to the average values $\bar{\varepsilon}_{\rm g} = 5$ GeV for the subjet energy loss in Eq. (9.14) and $Q_s^2 = \hat{q}L = 6$ GeV^2 for the saturation momentum squared in (9.9). The bands around these central curves correspond to variations by 20% of $\varepsilon_{\rm g}$. Note that varying Q_s^2 by 20% has a smaller effect. The unphysical case $\nu_{\rm min} = 1$ is disfavoured by the comparison with the MC results as it underestimates the peak associated with the direct MIE contribution. The other two cases are at least qualitatively consistent with the MC results.

It is also interesting to notice the dependence of the results upon the flavour of the leading parton. The rise of the nuclear distribution at small z_g appears to be stronger for the gluon-initiated jet than for the quark-initiated one and this difference is rather well captured by our analytic approximations, where it is due to a change in the number ν of partonic sources for a "hard" MIE: one has indeed $\nu - 1 \propto C_R$. At large z_g on the other hand, the analytic approximation appears to be less satisfactory for the quark-initiated jet — most likely, because it underestimates the energy loss by the subjets resulting from a hard VLE. As a matter of facts, a similar difficulty occurs in the high-energy case, as can be seen by comparing the quark-jet results for $p_{T0} = 1$ TeV in Figs. 9.1 and 9.6 respectively.

The main conclusions that we can draw from in Fig. 9.10 and from the overall discussion in this section is that z_g distribution for "low energy jets" is a superposition of two main effects: `(i)` incoherent energy loss for the subjets created by a vacuum-like splitting; this controls the z_g distribution at moderate and large values of z_g, where it yields a nuclear modification factor which slowly increase with z_g, and `(ii)` sufficiently hard medium-induced emissions, with $z \gtrsim z_{\rm cut}$, which leads to a significant growth of the z_g distribution at small values $z_g \sim z_{\rm cut}$. This behaviour is qualitatively reproduced by our simple analytic calculations which shows, for example, that including multiple (VLE) sources of MIEs is important. It is however more delicate to draw more quantitative conclusions as several effects entering the calculation would require a more involve treatment.

9.2 z_g distribution with realistic initial jet spectra

Even if studying monochromatic jets is helpful to understand the dominant physical effects at play, any realistic measurement would instead impose cuts on the $p_{T,\rm jet} \equiv p_T$ of the final jet. For this we need the full p_{T0} spectrum of the hard scattering. Here, we follow our prescription from Section 8.3 and use a LO dijet spectrum where both final partons are showered using our Monte Carlo. One can then cluster and analyse the resulting event.

In the case of the z_g distribution, it is interesting to note that we expect a competition between two effects. On one side, due to the steeply-falling underlying p_{T0} spectrum, cutting on the jet p_T tends to select jets which lose less energy than average. On the other side, we have seen from Fig. 9.3 that jets with $z_g > z_{\rm cut}$ and $\theta_g > \theta_{\rm cut}$ lose more energy than average.

Below, we first study the case of the $N_{\rm jets}$-normalised z_g distribution which is best suited to discuss the underlying physical details highlighted in section 9.1. Our distributions are also qualitatively compared to a recent experimental analysis by ALICE [256]. We then consider the self-normalised z_g distribution which is more easily compared to the CMS measurements [255].

9.2.1 Phenomenology with the $N_{\rm jets}$-normalised z_g

Our main results for the $N_{\rm jets}$-normalised z_g distribution are plotted in Figs. 9.11–9.12. They are the analogue of the results for R_{AA} shown in Figs. 8.3–8.4: they highlight the p_T-dependence of

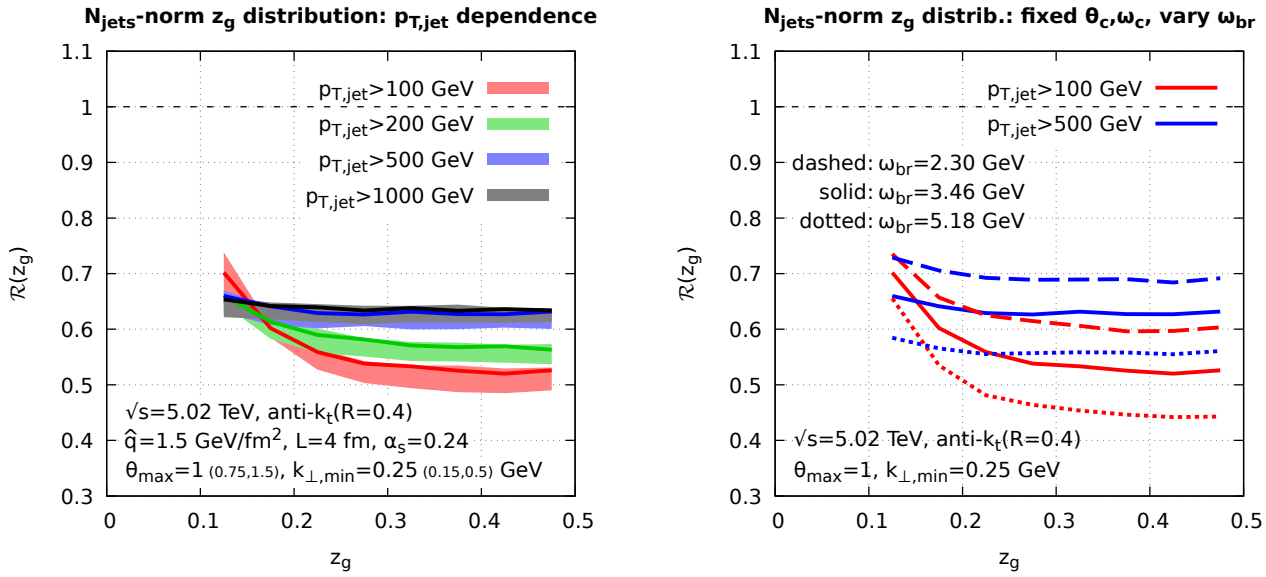

Figure 9.11: Our full MC predictions for the medium/vacuum ratio $\mathcal{R}(z_g)$ of the $N_{\rm jets}$-normalised z_g distributions, including the convolution with the initial jet spectrum. Left: the sensitivity of our results to changes in the kinematic cuts $\theta_{\rm max}$ and $k_{\perp,\rm min}$. Right: the effect of varying $\omega_{\rm br}$ (by $\pm 50\%$) at fixed values for ω_c and θ_c.

our predictions together as well as their sensitivity to changes in the physical ($\hat{q}$, L and $\alpha_{s,\rm med}$) and unphysical ($\theta_{\rm max}$ and $k_{\perp,\rm min}$) parameters. The various curves shown in these figures have been obtained by integrating the z_g distribution over all the values of p_T above a lower cut-off $p_{T,\rm min}$ (explicitly shown for each curve). In practice, our choices for this cut-off are the same as the values taken for p_{T0} in Fig. 9.1. Since the jet p_T spectrum falls rapidly with p_T and the jet energy loss is relatively small compared to the jet p_T, it makes sense to compare the respective results.

First of all, we see from Fig. 9.11, left, that our predictions are robust w.r.t. variations of the unphysical parameters in our Monte Carlo. Then, based on the analyses from Section 9.1, we expect the z_g distribution to be mostly sensitive to changes in the multiple-branching energy scale $\omega_{\rm br}$ which controls both the energy loss and the rate for SD to be triggered by a MIE. When varying $\omega_{\rm br}$ by 50% around its central value, keeping ω_c and θ_c fixed, the z_g distribution is indeed strongly affected, see Fig. 9.11, right. The effects of changing either ω_c or θ_c, at fixed $\omega_{\rm br}$, are much less pronounced as seen in Fig. 9.12. The residual variations observed when varying ω_c or θ_c can be mainly attributed to variations in the phase-space for VLEs, which affect the multiplicity of sources for MIEs and the energy loss (cf. Eq. (9.15)). Besides, for the low-p_T jets, a change in ω_c can have a sizeable effect on the phase-space for MIEs that are accessible to SD (cf. Fig. 9.2). This is indeed seen in Fig. 9.12 which shows a stronger dependence on ω_c than on θ_c, especially for the peak at low p_T and small z_g.

Comparing now to the results for monochromatic jets shown in Fig. 9.1, we observe important differences that can be understood as follows. When studying the $N_{\rm jets}$-normalised ratio, the deviation of $\mathcal{R}(z_g) = f_{\rm med}(z_g)/f_{\rm vac}(z_g)$ from unity is proportional to the ratio, $N_{\rm SDjets}/N_{\rm jets}$, between the number of jets which passed the SD condition and the total number of jets. This ratio is considerably smaller when using a realistic jet spectrum, Fig. 9.11 (left), than for monochromatic jets, Fig. 9.1. This is explained by the fact that jets passing the SD condition lose more energy than average jets and therefore have a more suppressed production rate.

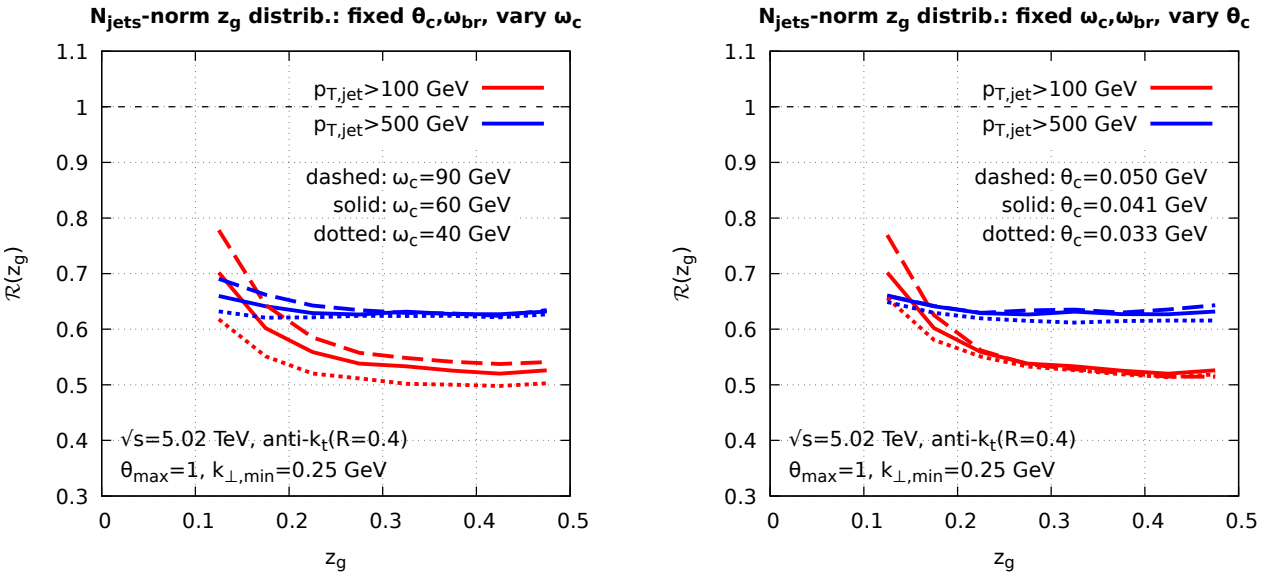

Figure 9.12: The effects of varying $\hat{q}$, L and $\alpha_{s,\mathrm{med}}$ keeping $\omega_{\mathrm{br}} = 3.46$ GeV fixed at its central value (cf. the right plot of Fig. 8.3). Left: we vary ω_c by $\pm 50\%$ at fixed θ_c. Right: we vary θ_c^2 by $\pm 50\%$ at fixed ω_c.

Moreover, among the jets which have passed SD with a given $z_g > z_{\mathrm{cut}}$, the initial cross-section favours those where the subjets have lost less energy, leading to a flattening in the shape of the ratio $\mathcal{R}(z_g)$ at large z_g, in agreement with Fig. 9.11 left. Finally, imposing a lower p_T cut on jets introduces a bias towards quark jets, which lose less energy than gluon jets. Since the former have a smaller $\mathcal{R}(z_g)$ than the latter (cf. Fig. 9.1), this further reduces $\mathcal{R}(z_g)$ for jets.

Another interesting feature of Fig. 9.11 left is the fact that the ratio $\mathcal{R}(z_g)$ is almost identical for $p_T = 500$ GeV and $p_T = 1$ TeV. We believe that this purely fortuitous. First, the normalisation factor $N_{\mathrm{SDjets}}/N_{\mathrm{jets}}$ penalises the jets with $p_T = 1$ TeV more than those with $p_T = 500$ GeV, thus reducing an initially-small difference between the respective results in Fig. 9.1. Second, as p_T increases so does the fraction of quark-initiated jets, thus contributing to a reduction of $\mathcal{R}(z_g)$.

At this point, it is interesting to compare our predictions with the measurements by the ALICE collaboration [256] at the LHC. This is not immediately straightforward as the ALICE

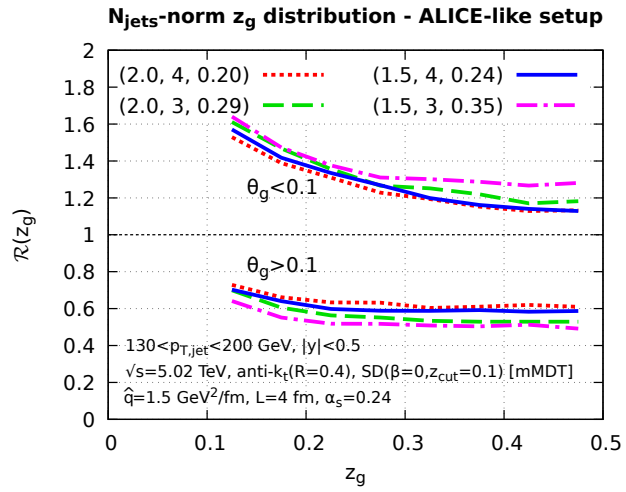

Figure 9.13: Predictions of our Monte Carlo generator for the z_g distribution obtained with a setup similar to the one used in the ALICE measurement of Ref.[256]. We included the distribution obtained with either $\theta_g < 0.1$ (bottom set of curves), or $\theta_g > 0.1$ (top set of curves). In each case we show the result for different sets of medium parameters, $\hat{q}$, L and α_s as indicated in the legend.

measurement is at a different collider energy than what we have considered so far, uses only charged tracks which are not accessible in our parton-level shower, and is not unfolded for the detector effects and residual background fluctuations. For simplicity, we keep the collider energy at 5.02 TeV. Since the charged and full transverse momenta of jets are roughly proportional to one another, we scale the acceptance region for the jet p_T from $[80, 120]$ GeV to $[130, 200]$ GeV and work with all the particles. The discussion below should therefore, at best, be considered as qualitative.

Our findings are presented in Fig. 9.13 where, following Ref. [256] (see the first and third plots in Fig. 3), we have considered both the case $\theta_g > 0.1$ and the case $\theta_g < 0.1$. Our predictions are shown for a range of medium parameters (see also Table 8.1 of Fig. 9.14). In all cases, our results are qualitatively similar to those of the experimental analysis: the ratio $\mathcal{R}(z_g)$ is decreasing with z_g, it shows nuclear suppression ($\mathcal{R}(z_g) < 1$) for the large-angle case $\theta_g > 0.1$ and nuclear enhancement ($\mathcal{R}(z_g) > 1$) for the small-angle case $\theta_g < 0.1$. Within our framework, the enhancement observed for $\theta_g < 0.1$ and the rise at small z_g are both associated with medium-induced emissions[8] being captured by SD. The suppression visible for $\theta_g > 0.1$ is a consequence of incoherent energy loss as seen in Sect. 9.1.

9.2.2 Self-normalised z_g distribution and CMS data

We want to compare the predictions of our Monte Carlo generator to the measurement of the self-normalised z_g distribution by the CMS collaboration in Ref. [255]. This comparison should however be taken with care since the CMS results are not unfolded for detector (and residual Underlying Event) effects and are instead presented under the form of "PbPb/smeared pp" ratios. Without a proper dedicated study, it is delicate to assess the precise effects of this smearing on $\mathcal{R}^{(\mathrm{norm})}(z_g)$.

Our findings are shown in Fig. 9.14(right). In this plot, we show the predictions for the z_g nuclear modification factor for the selection of 4 sets of medium parameters discussed in Section 8.3.1, $\mathcal{R}^{(\mathrm{norm})}(z_g)$, using the same bins and cuts as in the CMS analysis.

Since the interplay between the 3 scales ω_{br}, ω_c and θ_c is different for R_{AA} and $\mathcal{R}^{(\mathrm{norm})}(z_g)$, our 4 sets of parameters predict different behaviours for the latter. However, both observables are predominantly controlled by the energy loss of the jet, so the spread in $\mathcal{R}^{(\mathrm{norm})}(z_g)$ remains limited. Some differences are nonetheless observable, in particular for the two bins with the largest p_T. The predictions obtained with a larger ω_{br} — i.e. larger single-parton energy loss but smaller phase-space for VLEs — show a pattern dominated by energy loss, similar to what was seen in Sect. 9.1 for high-p_T jets. Conversely, the predictions obtained with a smaller ω_{br} — i.e. smaller single-parton energy loss but larger phase-space for VLEs — show an enhancement of the small-z_g peak associated to MIEs.

If we compare these results with the CMS measurements (see e.g. Fig. 4 of Ref. [255]), we see that the two agree within the error bars for both the pattern and the magnitude of the deviation from one. In particular, the CMS data too indicate that $\mathcal{R}^{(\mathrm{norm})}$ decreases quasi-monotonously with z_g at low p_T and become flatter and flatter, approaching unity, when increasing p_T. This supports our main picture where the nuclear effects on the z_g distribution are a combination of incoherent energy loss affecting a vacuum-like splitting and a small-z_g peak associated with the SD condition being triggered by a MIE. With increasing p_T the first mechanism dominates over the over, yielding a flatter distribution, in agreement with the CMS data. That being said, the current experimental uncertainty does not allow one to distinguish between different sets

[8] Since with our parameters the minimal angle for MIEs is $\theta_c \approx 0.04$, MIEs can pass the SD condition even for $\theta_g < 0.1$.

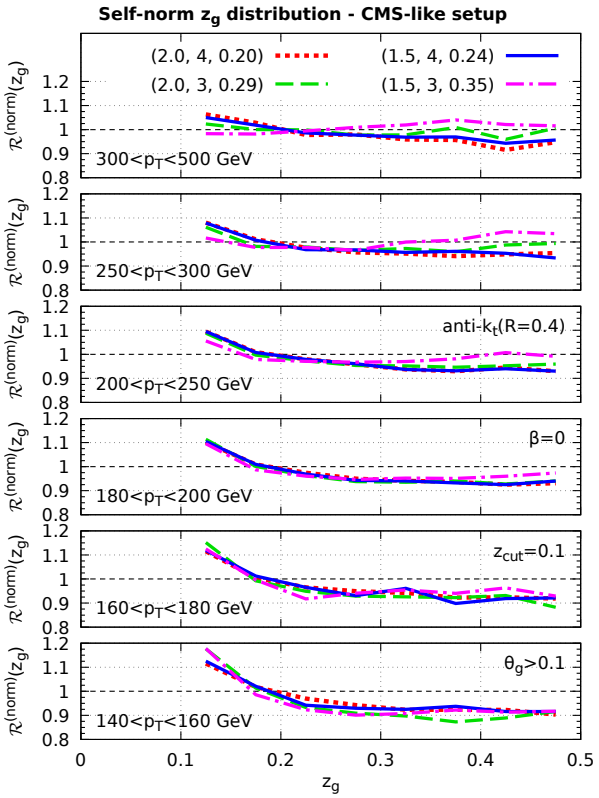

Figure 9.14: Left: our MC results for jet R_{AA} and for 4 sets of medium parameters which give quasi-identical predictions are compared to the ATLAS data [232] (black dots with error bars). Right: the MC predictions for the medium/vacuum ratio $\mathcal{R}^{(\mathrm{norm})}(z_g)$ of the self-normalised z_g distributions are presented in bins of p_T for the same 4 sets of medium parameters as in the left figure.

of medium parameters.

9.3 Other substructure observables

Our final section discusses two substructure observables related to the z_g distribution.

9.3.1 Iterated SD multiplicity.

The first observable we consider is the Iterated SD multiplicity [151], n_{SD}, which has also been measured on track-jets by the ALICE collaboration [256][9]. This observable has been defined in Chapter 4, Section 4.2.3.2.

Our results for the n_{SD} distribution are presented in Fig. 9.15 and show the same trend as the ALICE measurements (Fig. 4 of Ref. [256]). In particular, the n_{SD} distribution is shifted to smaller values for jets created in PbPb collisions compared to pp collisions. This might seem puzzling at first sight since in the low-$p_{T,\mathrm{jet}}$ range probed by the measurement, one could naively expect an enhancement of n_{SD} due to the additional MIEs passing the SD condition. However, we believe that the dominant mechanism at play is the incoherent energy loss which, as discussed in Sect. 9.2 and Sect. 9.1.2, results `(i)` in a statistical bias towards jets with small n_{SD} values as they lose less energy, scenario favored by the steeply-falling initial spectrum, `(ii)`

[9] Our comparison to this measurement is subject to the same caveats that for the z_g distribution in the same paper.

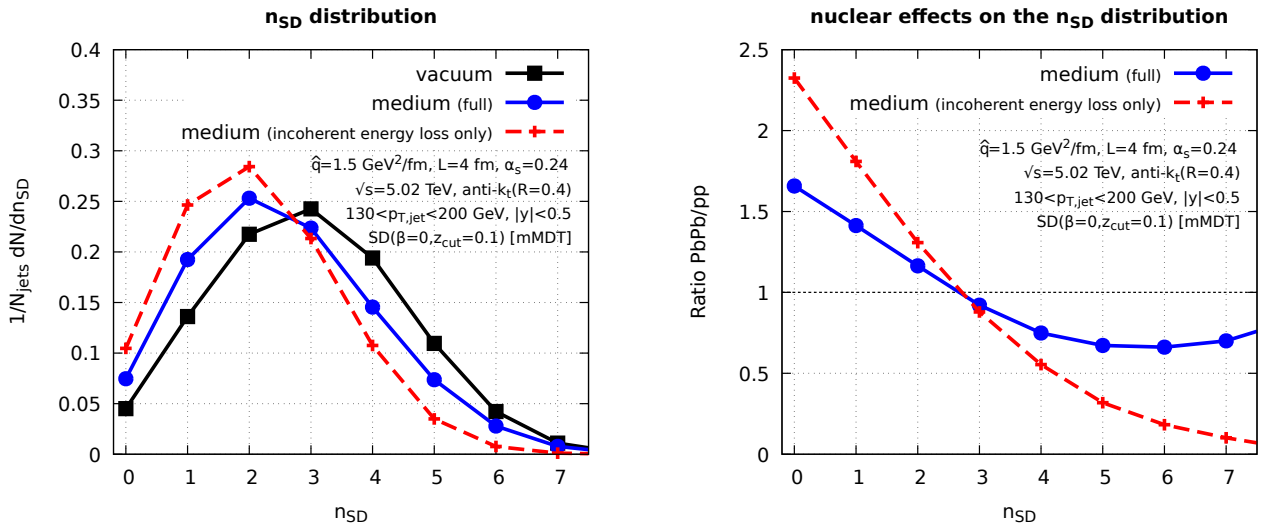

Figure 9.15: $n_{\rm SD}$ distributions emerging from our Monte Carlo simulations. Left: the distributions themselves, for the vacuum shower, for the full in-medium parton shower, and also for the case where the MIEs contribute only to the energy loss (but not directly to SD). Right: the medium/vacuum ratios.

in an effective z_g fraction smaller than the actual momentum fraction z at the splitting. These effects lower the number of measured hard splittings. To support this argument, we have run a variant of our MC simulations where all the partons created via MIEs are moved outside the jet and hence only contribute to the energy loss. The corresponding results, shown as crosses in Fig. 9.15 demonstrate as expected an even stronger reduction in the average value of $n_{\rm SD}$, which is only partially compensated by MIEs captured by the Iterated SD procedure.

Analytic estimate. It is always enlightening to see how these results compare with simple analytic formulas based on the same ideas as those developed in the investigation of the z_g distribution. For the vacuum baseline, the leading-logarithmic estimate is given in Chapter 4, Section 4.2.3.2. When a monochromatic hard spectrum is considered, we identify essentially three physical mechanisms: the veto of vacuum-like emissions, the shift of the splitting fraction caused by large angle energy loss and the existence of relatively hard medium-induced emissions captured by ISD. We believe that any observable relying on the primary Lund plane can be analysed in the same way as the following brief analysis of the $n_{\rm SD}$ distribution[10].

1. **Vetoed region.** The vetoed region included in `JetMed` has an impact on the $n_{\rm SD}$ distribution at DLA e.g. by reducing the area $\rho_{i,\rm LL}$ in the parameter of the Poisson law. However, as shown Fig. 9.2, the phase space area probed by SD does not overlap with this vetoed region for our choice of SD parameters. Consequently, the vetoed region can be neglected at leading logarithmic accuracy.

2. **Incoherent large angle energy loss.** Because of the energy loss shift as given by (9.5), the logarithmic area probed by SD in phase space is reduced, hence the medium/vacuum ratio for the $n_{\rm SD}$ distribution decreases with $n_{\rm SD}$. This is shown in the blue curve, Fig. 9.16.

[10]In the next Chapter, we will disentangle the nuclear modification factors for the large x part of the fragmentation function in this way.

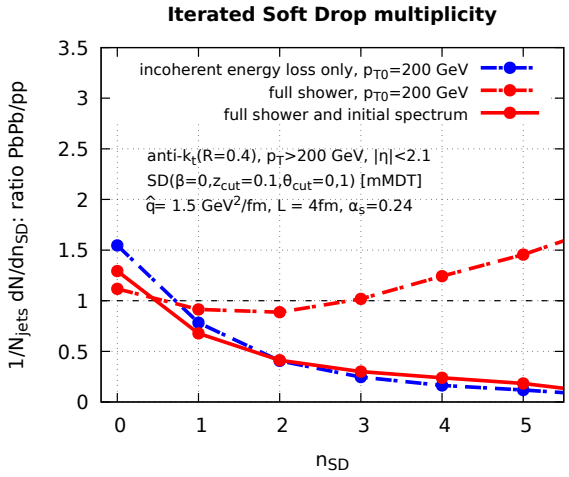

Figure 9.16: Nuclear modification factor $n_{\rm SD}$ distribution calculated with our MC. For the dashed curves, the calculation is done for a gluon with $p_{T0} = 200$ GeV. For the plain curves, we use the Born-level spectrum in p_{T0}. The red curves correspond to the full parton shower. For the blue curves, all the MIEs are artificially sent at very large angles to remove the effect coming from intrajet MIEs.

3. **Intrajet semi-hard MIEs.** The semi-hard MIEs with emission angles $\theta < R$ remain inside the jet and can trigger the ISD condition as for the SD z_g distribution. To estimate the order of magnitude of this effect, we rely again on the C/A declustering of jets from primary medium-induced emissions established in Section 4.3.3.2. For a jet evolving via primary MIEs only, $n_{\rm SD}$ is also Poisson distributed with average value $\rho_{i,\rm med}$ and

$$\rho_{i,\rm med}(\theta_{\rm cut}) = \int_0^{\omega_c/p_{T0}} \frac{\mathrm{d}z}{z^{3/2}} \int_{\theta_{\rm cut}}^{R} \mathrm{d}\theta \frac{\mathrm{d}^2\mathcal{P}_{i,\rm med}}{\mathrm{d}z\mathrm{d}\theta} \Theta(z - z_{\rm cut}(\theta/R)^\beta) \tag{9.17}$$

$$\sim \frac{2\alpha_s C_i}{\pi} \sqrt{\frac{\omega_c}{2p_{T0}}} \int_0^{\omega_c/p_{T0}} \frac{\mathrm{d}z}{z^{3/2}} \int_{\theta_{\rm cut}}^{R} \mathrm{d}\theta \delta\Big(\theta - \frac{Q_s}{zp_{T0}}\Big) \Theta(z - z_{\rm cut}(\theta/R)^\beta) \tag{9.18}$$

where we approximate the angular distribution (9.9) with a delta centered around $k_\perp = Q_s \equiv \sqrt{\hat{q}L}$. If $z_{\rm cut} p_{T0} \theta_{\rm cut} \lesssim Q_s$, one finds $\rho_{i,\rm med} \propto (z_{\rm cut} p_{T0}/\omega_c)^{-1/2}$ which is non-negligible compared to $\rho_{i,\rm LL}$ when $z_{\rm cut} p_{T0} \ll \omega_c$. In this case, $n_{\rm SD}$ follows again a Poisson distribution with average value $\rho_{i,\rm LL} + \rho_{i,\rm med}$. Hence the medium/vacuum ratio increases with $n_{\rm SD}$ as in the red dashed curve in Fig. 9.16-right.

As expected, there is a strong effect of the initial cross-section, as shown with the red plain curve of Fig. 9.16. Jets with large $n_{\rm SD}$ are highly suppressed and the enhancement seen at large $n_{\rm SD}$ in the monochromatic case, due to additional MIEs, is no longer visible. Such a compensation implies that one must be cautious when interpreting a measurement of $n_{\rm SD}$ with $\beta = 0$ [256].

9.3.2 Correlation between R_{AA} and z_g

Given that both R_{AA} and the z_g distribution are primarily controlled by the jet energy loss, it is interesting to study the correlation between these 2 variables [261] (similarly to Fig. 9.3 for the energy loss of monochromatic jets). To that aim, we show in Fig. 9.17 the ratio R_{AA} as a function of $p_T \equiv p_{T,\rm jet}$ for different bins in z_g (imposing $\theta_g > 0.1$) (left plot) and for different bins in θ_g (right plot). For reference, the inclusive R_{AA} ratio is shown by the "all jets" curve. The curve labelled as "no z_g" in the left plot includes both the events which did not pass the

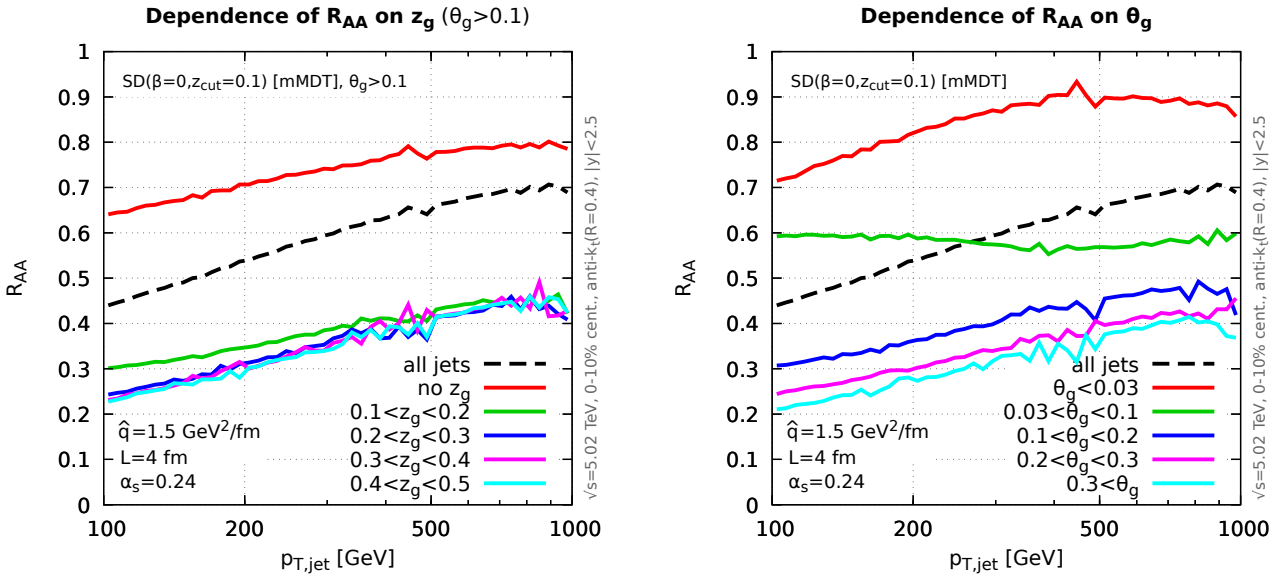

Figure 9.17: Our MC results for the jet R_{AA} as a function of $p_{T,\text{jet}}$ are shown in bins of z_g (left figure) and in bins of θ_g (right figure). The inclusive (all-z_g, respectively all-θ_g) results are shown with dashed lines.

SD criteria and the events which failed the $\theta_g > 0.1$ constraint. Correspondingly, the curve labelled "$\theta_g < 0.03$" in the right plot includes both the events with a genuine splitting passing the SD condition with $\theta_g < 0.03$ and the events which did not pass the SD condition.

The remarkable feature in both plots is the striking difference between the events which passed SD and those which did not. As explained when we discussed Fig. 9.3, this difference reflects the fact that, on average, two-prong jets lose more energy than single-prong ones. These results also reveal the role played by colour (de)coherence and the emergence of a critical angle θ_c. With our choice of parameters, $\theta_c \simeq 0.04$ corresponds to the region in θ_g where R_{AA} changes significantly. For example, the curve corresponding to $\theta_g < 0.03 < \theta_c$ receives almost exclusively contributions from single-prong jets — even more so than the "no z_g curve in the left plot — and thus shows a nuclear factor R_{AA} close to unity. This suggests that measuring R_{AA} in bins of θ_g can be interesting to better characterise the propagation of jets in the quark-gluon plasma.

Chapter 10

Jet fragmentation functions in nucleus-nucleus collisions

The last chapter of this thesis deals with the jet fragmentation function in nucleus-nucleus collision. At first sight, the fragmentation function looks like an ideal observable to study the jet structure in terms of parton showers and its modifications by the interactions with the medium. One should however be cautious as the jet fragmentation function is not a well-defined IRC safe quantity in pQCD as explained at length in Chapter 4. This means that its theoretical predictions are strongly sensitive to non-perturbative (confinement) physics like the modelling of the hadronisation mechanism. Another potential drawback of the fragmentation function, already recognised in the literature [263, 264], is that the nuclear enhancement seen in the LHC data at $x \gtrsim 0.5$ is not necessarily an evidence for new physics in the jet fragmentation at large x, but merely a consequence of the overall energy loss by the jet together with the bias introduced by the initial spectrum for jet production via hard (nucleon-nucleon) scatterings.

After a brief presentation of the `JetMed` results for the IRC unsafe fragmentation in Section 10.1, we disentangle the several medium effects in the large x domain of the fragmentation function in Section 10.2 and in the small x region in Section 10.3. The last Section 10.4 is dedicated to the study of the nuclear modification of the fragmentation function into subjets, which is IRC safe and defined in a similar way as in Section 4.2.3.3. We show that it is sensitive to medium effects while under better perturbative control.

10.1 Monte Carlo results

We start by presenting our Monte Carlo results for the fragmentation function and the associated nuclear modification factor. We want to pay a special attention to their dependence on the two "unphysical" parameters of the Monte Carlo, $\theta_{\max}$ and $k_{\perp,\min}$, and to the 3 "physical" parameters, $\hat{q}$, L and $\alpha_{s,\mathrm{med}}$. We recall that the dependence on the former can be viewed as an uncertainty in our underlying parton-level theoretical description and a large uncertainty would signal a strong dependence of the observable on non-perturbative effects such as hadronisation. Conversely, the dependence on the "physical" medium parameters sheds light on the role and importance of the medium effects at play.

10.1.1 General set-up

In order to describe *pp* and PbPb collisions at the LHC, we consider jets with an initial spectrum given by a *pp* collision with center-of-mass energy $\sqrt{s} = 5.02$ TeV computed at leading-order,

i.e. with Born-level $2 \to 2$ partonic hard scatterings. This is similar to our study of the R_{AA} ratio in Chapter 8, Section 8.3. A key property of this initial parton (or dijet) spectrum is that it is steeply falling with the partons' transverse momentum p_{T0}: $\mathrm{d}N^{\mathrm{hard}}/\mathrm{d}p_{T0} \propto 1/p_{T0}^n$ with $n \gtrsim 5$. For each event, both final partons are showered using our Monte Carlo. Jets are reconstructed using the anti-$k_\perp$ algorithm [134] as implemented in `FastJet` v3.3.2 [184]. The final jets are characterised by their transverse momentum $p_{T,\mathrm{jet}}$, which is generally different from the initial momentum p_{T0}, in particular for jets in PbPb collisions which suffer energy loss. The *pp* baseline is obtained by using the vacuum limit of our Monte Carlo.

We denote the final jet spectrum by $\mathrm{d}N_{\mathrm{jets}}/\mathrm{d}p_{T,\mathrm{jet}}$ and use the upper scripts "med" and "vac" to distinguish between jets in the medium (PbPb collisions) and jets in the vacuum (*pp* collisions), respectively. The jets can be initiated by either a quark or a gluon. In practice, one often considers the jet yield integrated over an interval in $p_{T,\mathrm{jet}}$, that is,

$$N_{\mathrm{jets}}(p_{T,\mathrm{min}}, p_{T,\mathrm{max}}) = \int_{p_{T,\mathrm{min}}}^{p_{T,\mathrm{max}}} \mathrm{d}p_{T,\mathrm{jet}} \, \frac{\mathrm{d}N_{\mathrm{jets}}}{\mathrm{d}p_{T,\mathrm{jet}}} \,. \tag{10.1}$$

For a given jet with transverse momentum $p_{T,\mathrm{jet}}$, we characterise its fragmentation in terms of the longitudinal momentum fraction

$$x \equiv \frac{p_T \cos(\Delta R)}{p_{T,\mathrm{jet}}}, \tag{10.2}$$

where p_T is the transverse momentum of a constituent of the jet and $\Delta R = \sqrt{(\Delta y)^2 + (\Delta\phi)^2}$, with Δy and $\Delta\phi$ the differences between the jet axis and the particle direction in rapidity and azimuth. Note that since our Monte Carlo does not include hadronisation, the jet constituents are partons.

The jet fragmentation function $\mathcal{D}(x)$ and its nuclear modification factor $\mathcal{R}(x)$ are defined as in Chapter 4:

$$\mathcal{D}(x) = \frac{1}{N_{\mathrm{jets}}} \frac{\mathrm{d}N}{\mathrm{d}x} \,, \qquad \mathcal{R}(x) = \frac{\mathcal{D}^{\mathrm{med}}(x)}{\mathcal{D}^{\mathrm{vac}}(x)} \,, \tag{10.3}$$

with N_{jets} the number of jets (in the considered $p_{T,\mathrm{jet}}$ range) and $\mathrm{d}N/\mathrm{d}x$ the number of jet constituents with a given momentum fraction x.

For later conceptual studies, we shall also consider "monochromatic jets" produced by a well identified parton, quark or gluon, with a fixed initial transverse momentum p_{T0}. In such a case, we denote the fragmentation function by $D_i(x|p_{T0})$, where $i \in \{q, g\}$ refers to the flavour of the leading parton. The corresponding medium/vacuum ratio is defined as $\mathcal{R}_i(x|p_{T0}) \equiv D_i^{\mathrm{med}}(x|p_{T0})/D_i^{\mathrm{vac}}(x|p_{T0})$.

10.1.2 Variability with respect to the unphysical cut-offs

Fig. 10.1a displays the sensitivity of our MC results for $\mathcal{R}(x)$ to variations of the "unphysical" parameters around their central values $\theta_{\mathrm{max}} = 1$ and $k_{\perp,\mathrm{min}} = 0.25$ GeV, for fixed values of $\hat{q}$, L and $\alpha_{s,\mathrm{med}}$.

The first observation from Fig. 10.1a is reassuring: the distribution shows a strong enhancement both at small x and at large x, with a nuclear suppression at intermediate values of x. This is in qualitative agreement with experimental measurements (see e.g. [244]).

However, the variations w.r.t. the unphysical parameters appear to be very large. We have checked that they were strongly dominated by variations in $k_{\perp,\mathrm{min}}$. This should not come as a surprise since the fragmentation function, measured directly on individual constituents, is not

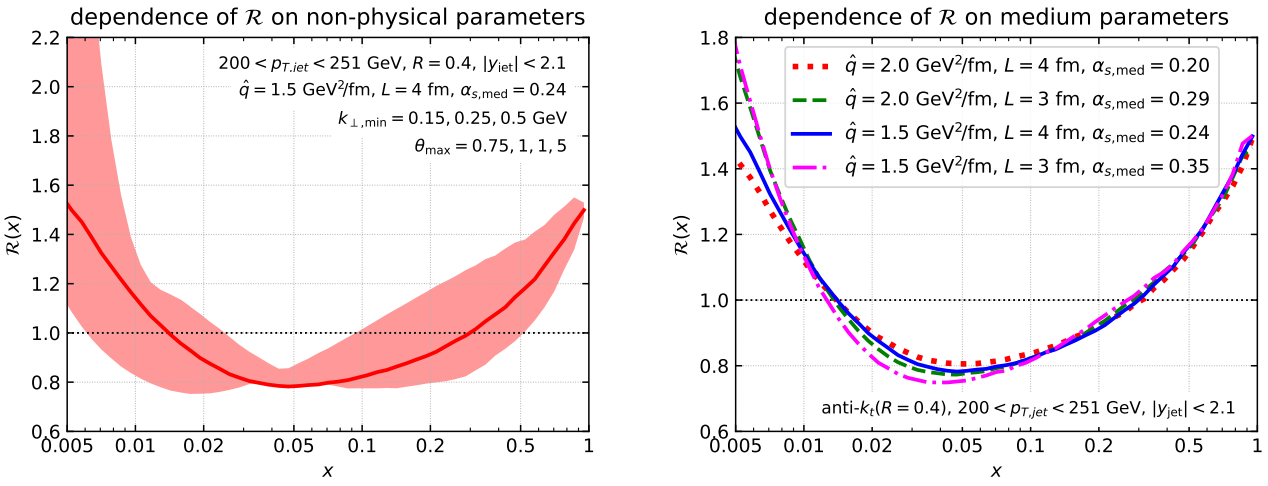

(a) Variations in $\theta_{\max}$ and $k_{\perp,\min}$.

(b) Variations in $\hat{q}$, L and $\alpha_{s,\text{med}}$.

Figure 10.1: The variability of our MC results for the ratio $\mathcal{R}(x)$ w.r.t. changes in the "unphysical" (left) and "physical" (right) parameters. The 4 sets of values for the "physical" parameters are correlated in that they provide similarly good descriptions of the LHC data [232] for the "standard" nuclear modification factor for jets R_{AA} (see the discussion in Chapter 8).

an infrared-and-collinear (IRC) safe observable. The sizeable variations in the small-x region directly come from the variations of the available phase-space for radiating soft gluons when varying $k_{\perp,\min}$. The large variations in the radiation of soft particles directly affect the spectrum of hard particles in the jet, hence the large uncertainty in the large-x region. Only a proper description of hadronisation (including varying hadronisation parameters) would (hopefully) reduce this uncertainty. This should be kept in mind when studying the dependence of our results on the medium parameters and when comparing our MC results in this work with actual experimental data.

10.1.3 Variability with respect to the medium parameters

We now fix the unphysical parameters to their central value and study how $\mathcal{R}(x)$ depends on the medium parameters $\hat{q}$, L, and $\alpha_{s,\text{med}}$. We first consider 4 different sets of values, given in Table 8.1 together with the angular and energy scales θ_c, ω_c and ω_{br} characterising the medium-induced radiation.

The plot in Fig. 10.1b shows our new results for $\mathcal{R}(x)$ for the 4 sets of values for the physical parameters. For large values of x, $x \gtrsim 0.1$, the small variations in ω_{br} (see Table 8.1) are compensated by relatively large variations of ω_c and θ_c. This is similar to what happens for R_{AA}, as discussed at length in Chapter 8. This suggests that for largish $x \gtrsim 0.1$, the nuclear effects on jet fragmentation and on the inclusive jet production are strongly correlated and in particular that they are both controlled by the jet energy loss. Such a correlation has been already pointed out in the literature [263, 264] and used to provide a simple and largely model-independent argument for explaining the enhancement in the ratio $\mathcal{R}(x)$ at $x \gtrsim 0.5$, as observed both in the LHC data [244] and in our MC results in Fig. 10.1b. This argument will be completed in Sect. 10.2.3.

Turning to smaller x values, $x \leq 0.01$, the situation becomes different. There is a clear lift of degeneracy between the 4 sets of values, with two of them — corresponding to the smallest medium size $L = 3$ fm, but larger values for $\alpha_{s,\text{med}}$ — yielding results that are significantly

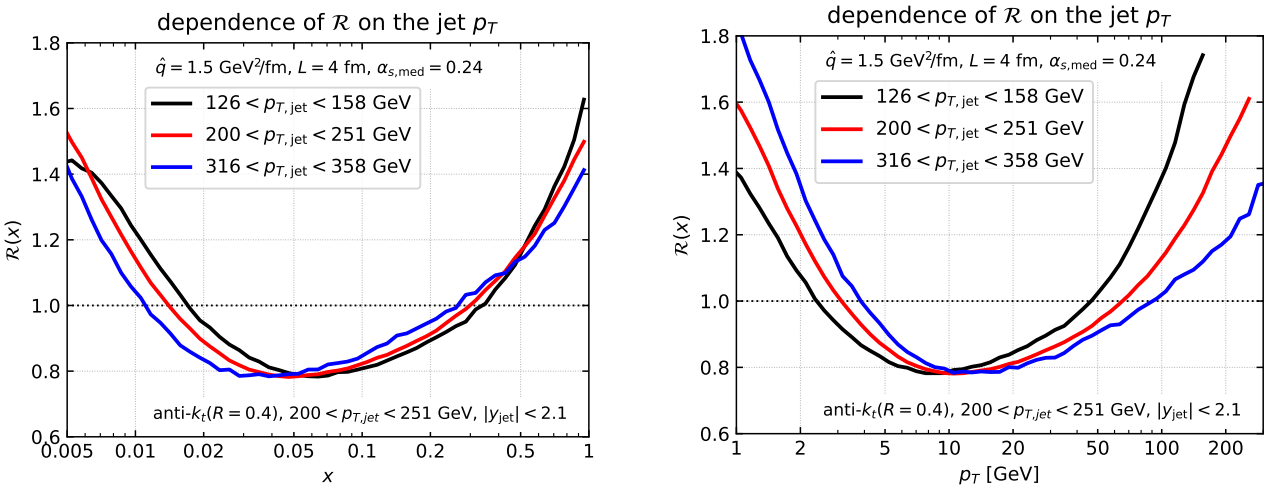

Figure 10.2: Our MC results for the nuclear modification factor $\mathcal{R}(x)$ shown as a function of the energy fraction x of a jet constituent (left) and of its transverse momentum p_T (right), for 3 bins of the jet $p_{T,\mathrm{jet}}$.

larger than those predicted by the two other sets (with $L = 4$). In Section 10.3, we provide physical explanations for these trends.

10.1.4 Dependence on the jet p_T

Our Monte Carlo predictions for the nuclear modification $\mathcal{R}(x)$ are shown in Fig. 10.2 for three bins of $p_{T,\mathrm{jet}}$ and for the default set of (medium and unphysical) parameters, cf. the first line in Table 8.1. Following the experimental analysis by ATLAS [244], we have separately plotted our results as a function of x (left plot) and of the parton p_T (right plot). The left-hand plot shows only a mild dependence of $\mathcal{R}(x)$ on $p_{T,\mathrm{jet}}$ for $x \gtrsim 0.1$ when increasing. This suggests a weak $p_{T,\mathrm{jet}}$-dependence which is likely correlated to the similarly weak dependence observed for R_{AA}. At small x, the x scale below which the ratio is larger than 1 decreases with $p_{T,\mathrm{jet}}$, but the corresponding p_T scale increases with $p_{T,\mathrm{jet}}$. These trends are in qualitative agreement with the respective ATLAS results [244].

10.2 Nuclear effects on the fragmentation function near $x = 1$

With this section, we start our analytic investigations of the nuclear effects on the jet fragmentation function when $1 - x \ll 1$. Since the main goal of the two following subsections 10.2.1 and 10.2.2 is to discuss the nuclear effects neglecting the steeply falling initial jet spectrum, we mostly work with monochromatic jets with a given initial transverse momentum p_{T0}. In the last subsection 10.2.3, the effect of the hard scattering cross-section combined with jet energy loss is taken into account. To guide the reader, we emphasize that the latter effect turns out to be the dominant one in the hard fragmentation region.

We therefore first focus on the jet fragmentation function $D_i(x|p_{T0})$ with $i \in \{q, g\}$, which can be conveniently computed as a derivative of the *cumulative* fragmentation distribution

$$\Sigma_i(x|p_{T0}) \equiv \int_x^1 \mathrm{d}x' D_i(x'|p_{T0})\,. \tag{10.4}$$

For the vacuum calculation of this distribution, we refer the reader to Section 4.2.2.1.

To discuss medium-induced effects, it is sufficient to work in the LL approximation where jet fragmentation function near $x = 1$ is dominated by a single, relatively soft, gluon emitted by the leading parton. From this two-parton system we then have to take three effects into account: (1) emissions in the vetoed region of Fig. 5.3 are forbidden, (2) the leading parton and the emitted gluon can both lose energy via MIEs at large angles, (3) the gluon emission can be a MIE remaining inside the jet. We consider the effect of the vetoed region before the other two.

10.2.1 Effect of the vetoed region

The effect of the vetoed region in Fig. 5.3 can be implemented as a Θ-function excluding this particular region from the phase-space for VLEs. At LL accuracy, this amounts to having an extra factor

$$\Theta_{\rm veto} = 1 - \Theta(\sqrt{2\hat{q}zp_{T0}} - k_\perp^2)\Theta(k_\perp - 2zp_{T0}L^{-1}), \tag{10.5}$$

in the integrand of (4.20). The first (second) Θ-function in the r.h.s. of (10.5) corresponds to the upper (lower) boundary of the vetoed region. For a fixed-coupling approximation, we find assuming for simplicity $1 - x \leq 2/(Lp_{T0}R^2)$ (see Appendix H for the result including running coupling)

$$Lg_{1,i}^{\rm veto}(\alpha_s L, \alpha_s L_0) = Lg_{1,i}^{\rm vac}(\alpha_s L, \alpha_s L_0) + \frac{2\alpha_s C_i}{3\pi} \ln^2 \frac{R}{\theta_c}\,. \tag{10.6}$$

NLL corrections, $g_{2,i}^{\rm veto}$, can be obtained using (4.18). In particular, the hard-collinear term proportional to B_i is not modified by the veto region and therefore cancels in the medium/vacuum ratio.

Our analytic estimate for the ratio $R_i(x|p_{T0})$ is shown in Fig. 10.3a left in green for $p_{T0} = 200$ GeV. For comparison, we also show the corresponding MC result, which only includes VLEs (the green curve in Fig. 10.3b). These results agree well with each other and they both predict a nuclear enhancement near $x = 1$. This enhancement can be easily understood on the basis of (10.6), which implies

$$\ln \frac{\Sigma_i^{\rm veto,LL}(x)}{\Sigma_i^{\rm vac,LL}(x)} = \frac{2\alpha_0 C_i}{3\pi} \ln^2 \frac{R}{\theta_c} > 0\,, \tag{10.7}$$

meaning $\Sigma_i^{\rm med}(x) \simeq \Sigma_i^{\rm veto}(x) > \Sigma_i^{\rm vac}(x)$ and hence $R_i(x) > 1$ when $x \to 1$. Indeed, the presence of the vetoed region reduces the phase-space allowed for the decay of the leading parton.

10.2.2 Effect of medium-induced emissions

The medium-induced emissions (MIEs), as triggered by the interactions with the plasma constituents, affect differently the total jet momentum $p_{T,\rm jet}$ and the energy $\omega_{\rm LP}$ carried by its leading parton. This implies a nuclear modification $\mathcal{R}(x)$ at large $x \equiv \omega_{\rm LP}/p_{T,\rm jet}$.

For convenience, we focus on the case where x is not *too* close to one, such that $\omega_{\rm br}/p_{T0} \ll 1 - x \ll 1$, with $\omega_{\rm br} \sim \alpha_s^2 \hat{q} L^2$ the characteristic scale for multiple branchings. For jets with $p_T \geq 200$ GeV, a phenomenological region $0.80 \lesssim x \lesssim 0.95$ translates into $(1-x)p_{T0} \gtrsim 10$ GeV which is indeed larger than $\omega_{\rm br} \sim 4$ GeV (cf. Table 8.1).

Within this regime, the medium-induced emissions which control the energy loss by the leading parton are relatively hard, with energies $\omega \gg \omega_{\rm br}$. Thus, they remain inside the jet and

can be accurately computed in the single emission approximation. This situation is similar to the one discussed for jets in the vacuum at double-logarithmic accuracy: the parton distribution near $x = 1$ is controlled by a single intra-jet emission, with an energy of the order of $(1-x)p_{T0}$. This emission can be either vacuum-like, or medium-induced. This "semi-hard" emission is accompanied by an arbitrary number of soft MIEs, with energies $\omega \lesssim \omega_{\rm br}$, which propagate outside the jet and take energy away from the jet constituents. The in-medium fragmentation function near $x = 1$ can therefore be evaluated as:

$$D_i^{\rm med}(x|p_{T0}) \,\simeq\, \int {\rm d}\omega\, \Delta_i^{\rm VLE}(\omega)\, \Delta_i^{\rm MIE}(\omega)\, \left[\frac{\partial \mathcal{P}_{i,\rm vac}}{\partial \omega} + \frac{\partial \mathcal{P}_{i,\rm med}}{\partial \omega}\right] \delta\left(x - \frac{p_{T0} - \omega - \varepsilon_i}{p_{T0} - \mathcal{E}_i}\right) \tag{10.8}$$

In this expression, $\partial \mathcal{P}_{i,\rm vac}/\partial\omega$ is the differential probability for emitting a soft gluon with energy ω at any emission angle θ (with $k_{\perp,\rm min}/\omega < \theta < R$) and $\Delta_i^{\rm VLE}(\omega)$ is the Sudakov factor forbidding VLEs with energies larger than ω (including the condition (10.5) for the phase space gap), i.e.

$$\Delta_i^{\rm VLE}(\omega) = \Sigma^{\rm veto}\left(1 - \frac{\omega}{p_{T0}}\right) \qquad \text{and} \qquad \frac{\partial \mathcal{P}_{i,\rm vac}}{\partial \omega} = \frac{{\rm d}\ln \Delta_i^{\rm VLE}}{{\rm d}\omega} \simeq \frac{2\alpha_s C_i}{\pi}\frac{1}{\omega}\,\ln\left(\frac{\omega R}{k_{\perp,\rm min}}\right), \tag{10.9}$$

where the second expression for $\partial \mathcal{P}_{i,\rm vac}/\partial\omega$, shown only for illustration, holds for the case of a fixed coupling α_s and ignores the constraints introduced by the vetoed region.

Furthermore, $\partial \mathcal{P}_{i,\rm med}/\partial\omega$ and $\Delta_i^{\rm MIE}(\omega)$ are the corresponding quantities for the semi-hard MIE inside the jet ($\theta_c < \theta < R$). Its energy is restricted to $\bar\omega < \omega < \omega_c$, where $\omega_c = \hat q L^2/2$ and $\bar\omega$ is a cutoff of order $\omega_{\rm br}$, separating between "semi-hard" and "soft" MIEs.[1] In this regime, one can safely use the single emission approximation, i.e. (compare to Eq. (4.48))

$$\frac{\partial \mathcal{P}_{i,\rm med}}{\partial \omega_m} \simeq \frac{\alpha_{s,\rm med} C_i}{\pi}\sqrt{\frac{2\omega_c}{\omega_m^3}}, \qquad \Delta_i^{\rm MIE}(\omega_m) = \exp\left(-\int_{\omega_m}^{\omega_c} {\rm d}\omega\, \frac{\partial \mathcal{P}_{i,\rm med}}{\partial \omega}\right). \tag{10.10}$$

Next, ε_i and $\mathcal{E}_i$ refer to the energy loss via soft MIEs outside the jet ($\theta > R$), for the leading parton and for the jet as a whole, respectively. Finally, the δ-function in Eq. (10.8) encodes the fact that, in our present approximation, the energy of the leading parton is the energy p_{T0} of the parton initiating the jet minus the energy of the semi-hard emission and the partonic energy loss ε_i, while the energy of the jet is $p_{T,\rm jet} = p_{T0} - \mathcal{E}_i$.

For more clarity, we study separately the two types of medium effects included in Eq. (10.8), namely energy loss at large angles and energy redistribution via intra-jet MIEs.

10.2.2.1 Energy loss at large angles

To study the energy loss effects alone, we temporarily neglect the contribution of the intra-jet MIEs to Eq. (10.8), which then simplifies to (with ω_s the energy of the soft VLE)

$$D_i^{\rm med}(x|p_{T0})\Big|_{\rm e\text{-}loss} = \int {\rm d}\omega_s \frac{\partial \mathcal{P}_{i,\rm vac}}{\partial \omega_s}\, \Delta_i^{\rm VLE}(\omega_s)\, \delta\left(x - \frac{p_{T0} - \omega_s - \varepsilon_i}{p_{T0} - \mathcal{E}_i}\right). \tag{10.11}$$

In the absence of VLEs, a single parton with initial energy ω_0 loses energy by radiating MIEs at large angles ($\theta \gtrsim \theta_c/\bar\alpha_s^2$). This is associated with the "turbulent" component of the

[1] The precise value of this cut-off is not important: as we will show below the energy integration is controlled by the δ-function, and since the energy losses are relatively small one roughly has $\omega \simeq (1-x)p_{T0} \gg \bar\omega \sim \omega_{\rm br}$.

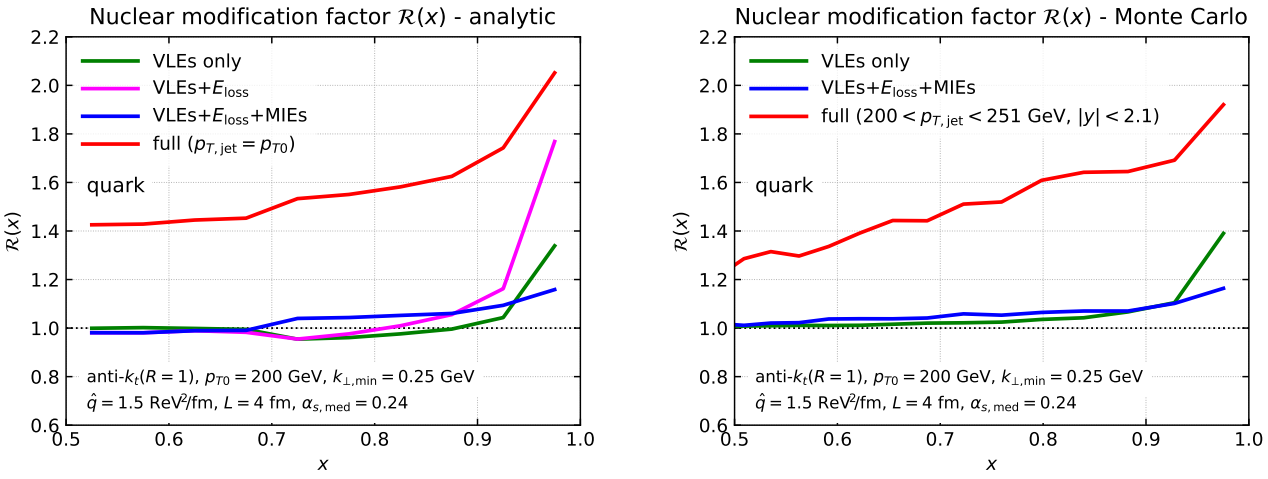

(a) Semi-analytic estimates.

(b) Monte Carlo simulations.

Figure 10.3: Nuclear effects on the fragmentation function at large x for monochromatic jets. Three increasingly more physical scenarios are considered: `(i)` VLEs only (only the nuclear effects from the vetoed region are included), `(ii)` adding energy loss via soft MIEs at large angles (not shown on the right plot), and `(iii)` further adding semi-hard MIEs inside the jet. Additionally, we show the "full" curve in red which includes the bias introduced by the initial hard spectrum and is manifestly the dominant effect.

medium-induced cascades, associated with very soft partons of energies $\omega \lesssim \omega_{\rm br}$, which are deflected at large angles via collisions with the plasma. The average energy loss is estimated by (4.63)

$$\varepsilon_i(\omega_0) = \omega_0\big[1 - \mathrm{e}^{-v_0\omega_{\rm br}/\omega_0}\big], \qquad \text{with} \quad \omega_{\rm br} = \left(\frac{\alpha_{s,\rm med}}{\pi}\right)^2 C_A C_i \,\frac{\hat{q}L^2}{2}\,. \tag{10.12}$$

For a full jet, the energy loss receives contributions of the form of Eq. (10.12) from both the leading parton (LP) and each of the (vacuum-like or medium-induced) *intra-jet* emissions ($\theta < R$) which are radiated within the medium. An estimate is given in (5.105).

For a hard-fragmenting jet made of only two partons (the LP and a relatively soft VLE, as in Eq. (10.11)), we have to consider two options:

- If the VLE is emitted outside the medium, i.e. either with $\theta < \theta_c$ or with $t_{\rm f} = 2/(\omega\theta^2) > L$, only the LP loses energy and we have $\mathcal{E}_i = \varepsilon_i$. For $\theta < \theta_c$, the two partons lose energy coherently, so one can see the energy loss as coming only from the LP.

- If the VLE occurs inside the medium, both partons lose energy and we have $\mathcal{E}_i = \varepsilon_i + \varepsilon_g$, with ϵ_g the energy lost by the VLE. In this case, $t_{\rm f} \ll L$ so the VLE travels a length or order L through the medium.

For a VLE inside the medium, the δ-function in Eq. (10.11) can be equivalently rewritten as

$$\delta\left(1 - x - \frac{\omega_s - (\mathcal{E}_i - \varepsilon_i)}{p_{T0} - \mathcal{E}_i}\right) \simeq \delta\left(1 - x - z + \frac{(1-z)\mathcal{E}_i - \varepsilon_i}{p_{T0}}\right)\,, \tag{10.13}$$

with $z \equiv \omega_s/p_{T0}$ the splitting fraction of the VLE. We have used the fact that the energy loss is relatively small, $\mathcal{E}_i \ll p_{T0}$. The effect of the in-medium energy loss is a small increase of the

splitting fraction, from its initial value in the vacuum, $z_{\rm vac} = 1 - x$, to

$$z = 1 - x + \frac{(1-z)\mathcal{E}_i - \varepsilon_i}{p_{T0}} \simeq 1 - x + \frac{x\varepsilon_g - (1-x)\varepsilon_i}{p_{T0}} \simeq 1 - x + \frac{\varepsilon_g}{p_{T0}} > z_{\rm vac}. \tag{10.14}$$

In the second equality we have used $\mathcal{E}_i = \varepsilon_i + \varepsilon_g$ and $z \simeq 1 - x$. For the third equality we have used $x \simeq 1$ and $\varepsilon_g \geq \varepsilon_i$, making clear that the dominant effect is the energy loss by the soft gluon. [2]

The fact that $z > z_{\rm vac} \equiv 1 - x$ means that the probability $P(z) \propto 1/z$ of its emission is smaller, so there is an *enhancement* in the probability for the leading parton to survive at large x. This effect is reinforced by the associated Sudakov factor: when $\omega_s = zp_{T0} > (1-x)p_{T0}$, there is a reduction in the phase-space for emissions by the leading parton and therefore $\Delta_i^{\rm VLE}(\omega_s) > \Delta_i^{\rm VLE}((1-x)p_{T0})$.

The purple curve in Fig. 10.3-left shows a calculation of $\mathcal{R}_q(x|p_{T0})$ based on Eq. (10.11) together with $\mathcal{E}_q = \varepsilon_q + \varepsilon_g$ and with Eq. (10.12) for the partonic energy loss. Compared to the green curve in the same figure, which includes solely the effect of the vetoed region, the purple curves indeed shows a larger enhancement near $x = 1$.

10.2.2.2 Energy redistribution via a hard MIE

A semi-hard MIE with energy $\omega \gg \omega_{\rm br}$ and which remains inside the jet can modify the fragmentation function $D_i^{\rm med}(x|p_{T0})$ near $x = 1$ in two ways. On one hand, it brings a positive contribution via the term proportional to $\partial\mathcal{P}_{i,\rm med}/\partial\omega$ in Eq. (10.8). On the other hand, the additional Sudakov factor $\Delta_i^{\rm MIE}(\omega)$ induces an extra suppression. These two effects are competing with each other. It turns out that the second effect is stronger, resulting in a *decrease* of $D_i^{\rm med}(x|p_{T0})$ near $x = 1$ as compared to the vacuum, and hence a decrease of the medium/vacuum ratio $\mathcal{R}_i(x|p_{T0})$.

We can actually estimate these two contributions to Eq. (10.8). To that aim, we can neglect the effects of the energy loss at large angles.[3] Using the δ-function to perform the integral over ω we find

$$D_i^{\rm med}(x|p_{T0})\Big|_{\rm MIE} = p_{T0}\left[\frac{\partial\mathcal{P}_{i,\rm vac}}{\partial\omega} + \frac{\partial\mathcal{P}_{i,\rm med}}{\partial\omega}\right]\Delta_i^{\rm VLE}(\omega)\,\Delta_i^{\rm MIE}(\omega)\Big|_{\omega=(1-x)p_{T0}}. \tag{10.15}$$

We need to show that the "medium" Sudakov effect on the VLE (first term in the square bracket) is larger in absolute value than the direct contribution from MIEs (second term in the square bracket):

$$\frac{\partial\mathcal{P}_{i,\rm vac}}{\partial\omega}\left[1 - \Delta_i^{\rm MIE}(\omega)\right] > \frac{\partial\mathcal{P}_{i,\rm med}}{\partial\omega}\,\Delta_i^{\rm MIE}(\omega)\,. \tag{10.16}$$

At leading-order accuracy for the MIE, one can set $\Delta_i^{\rm MIE} \simeq 1$ in the r.h.s. of the above inequality, whereas in the l.h.s. one must also keep the linear term in its Taylor expansion:

$$1 - \Delta_i^{\rm MIE}(\omega) \;\simeq\; \frac{2\alpha_s C_i}{\pi}\sqrt{\frac{2\omega_c}{\omega}}\,. \tag{10.17}$$

[2] Interestingly, for a VLE outside the medium, we can set $\varepsilon_g \to 0$ to get $z = 1 - x - (1-x)\varepsilon_i/p_{T0}$ with $1 - x \ll 1$. The energy loss effect is therefore much smaller than for an in-medium VLE and with an opposite sign.

[3] Indeed, in this case, the intra-jet MIE is the dominant medium effect, whereas the energy loss at large angles is a subdominant effect since $\mathcal{E}_i \sim \varepsilon_i \sim \omega_{\rm br}$ are much smaller than $\omega \simeq (1-x)p_{T0}$.

Using a fixed-order approximation for the vacuum emission probability (cf. Eq. (10.9)), together with Eq. (10.10) for the medium-induced, one finds after simple algebra that Eq. (10.16) is equivalent to

$$\frac{4\alpha_s C_i}{\pi} \ln\left(\frac{(1-x)p_{T0}R}{k_{\perp,\min}}\right) > 1\,. \tag{10.18}$$

This is satisfied both parametrically and numerically under our working assumptions that collinear logarithms are large. For the parameters used in Fig. 10.3, namely $p_{T0} = 200$ GeV, $R = 1$, and $k_{\perp,\min} = 0.25$ GeV, and with $x = 0.9$ and $\alpha_s = 0.3$, one finds that the l.h.s. of Eq. (10.18) is about 5.3.

These considerations are confirmed by the explicit numerical integration of Eq. (10.8). The blue curve in Fig. 10.3a includes all the medium effects discussed in this section (the vetoed region, the energy loss at large angles and the effects of semi-hard MIEs). Comparing it to the purple curve which does not include the effects of semi-hard MIEs, we see that the latter reduce the ratio $\mathcal{R}_i(x|p_{T0})$ near $x = 1$, as expected. This plot also shows that the three medium effects appear to be of similar magnitude and to almost compensate each other, leaving only a modest enhancement at $x \gtrsim 0.9$. This pattern is in very good agreement with what we see from our MC simulations, Fig. 10.3b. Whereas the details of this compensation depend on the specific parameters used in our calculation, we have checked using our MC that such a competition between comparable but opposite effects is a relatively robust prediction from our pQCD scenario.

One can view this conclusion as a little bit deceptive since it shows that the fragmentation function has a reduced sensitivity to nuclear effects associated with the internal dynamics of the jets.

10.2.3 Bias introduced by the steeply falling jet spectrum

The behaviour at large x is in fact largely controlled by the physics of energy loss and its interplay with the initial production spectrum, as we now explain.

A jet which, after crossing the medium, is measured with a transverse momentum $p_{T,\text{jet}}$ has originally been produced from a hard quark or gluon emerging from a hard process with a larger momentum $p_{T0} = p_{T,\text{jet}} + \mathcal{E}(p_{T0})$, where $\mathcal{E}(p_{T0})$ is the energy lost by the jet via MIEs at large angles (see Ref. [39] for an extensive discussion of this quantity). While the energy lost by a *parton* with momentum $p_T \gg \omega_{\text{br}}$ saturates at a value $\epsilon \sim \omega_{\text{br}}$, which is independent of p_T [163], the average energy lost by a jet keeps increasing with p_{T0}, because of the rise in the phase space for VLEs and hence in the number of partonic sources for medium-induced radiation.

Due to the steeply-falling underlying p_{T0} spectrum, cutting on the jet p_T tends to select jets which lose less energy than average. In particular, this bias favours the "hard-fragmenting" jets which contain a parton with large x (say, $x > 0.5$). Such jets correspond to rare configurations, in which the radiation from leading parton is strongly limited in order to have a final x fraction close to one. Since they contain only few partons, the hard-fragmenting jets suffer very little energy loss, of the order of the partonic energy loss $\epsilon \sim \omega_{\text{br}}$. They are therefore less suppressed than the average jets by the steeply-falling initial spectrum. In other terms, the medium acts as a filter which enhances the proportion of hard-fragmenting jets compared to the vacuum.

This bias has already consequences for the *inclusive* jet production, as measured by R_{AA}: the fraction of hard-fragmenting jets among the total number of jets (say, in a given bin in $p_{T,\text{jet}}$) is larger in AA collisions than in pp collisions. The effects of this bias are however expected to become even stronger for the jet distribution $\mathrm{d}N/\mathrm{d}x$ at large x, which by definition selects *only* hard-fragmenting jets. This stronger bias towards hard-fragmenting jets has been proposed

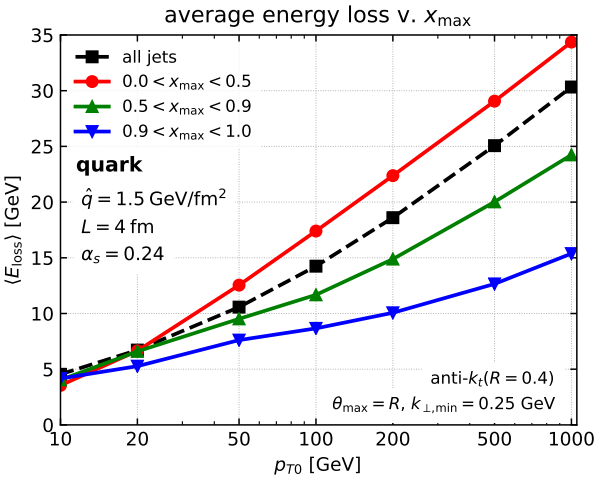

(a) Energy loss as a function of the initial parton transverse momentum p_{T0}.

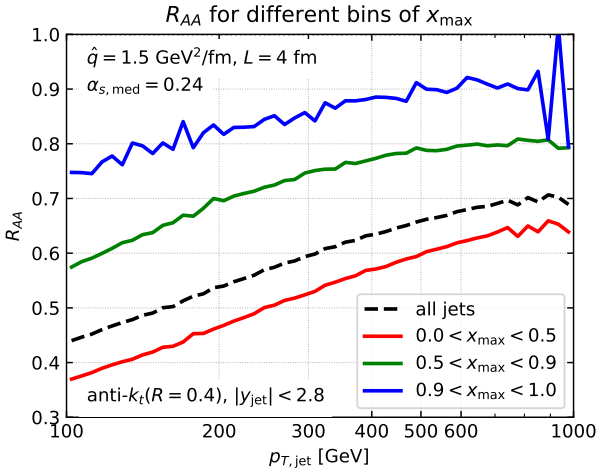

(b) Jet nuclear modification factor R_{AA} as a function of the jet p_T.

Figure 10.4: Energy loss and R_{AA} for different bins of $x_{\rm max}$, the momentum fraction of the jet harder constituent.

as an explanation for the nuclear enhancement in the fragmentation function observed in the LHC data [244] at large $x \gtrsim 0.5$. This argument is very general: it applies to a large variety of microscopic pictures for the jet-medium interactions, assuming either weak coupling [242, 265], or strong coupling [266, 267], or a hybrid scenario [264, 268, 269]. All these scenarios naturally predict that hard-fragmenting jets lose less energy towards the medium than average jets, for the physical reason that we already mentioned: hard-fragmenting jets contain less partonic sources for in-medium energy loss. This physical argument is manifest in both the pQCD [242, 265] and the hybrid approaches [264, 268, 269], which explicitly include a vacuum-like parton shower. It is also implicit in the strong coupling scenario in [266, 267] which is tuned such as to reproduce the angular distribution of jets in p+p collisions at the LHC (itself well described by PYTHIA).

In this section, we argue that this is also the main explanation for the rise seen in our results in Fig. 10.1b at $x \gtrsim 0.5$. Within our pQCD approach this is not entirely obvious since our scenario also allows for nuclear modifications of the fragmentation process itself, via medium-induced emissions and energy loss effects. Similar ingredients are *a priori* present in other scenarios, like JEWEL, but their relative importance has not been explicitly studied to our knowledge. In the previous subsections, we have performed an extensive study of these effects, via both analytical and numerical (MC) methods.

Before we discuss the fragmentation function *per se*, let us first demonstrate that, in our picture too, a hard-branching jet loses less energy than the average one. We have numerically verified this, by selecting (in our MC events) jets for which the harder parton carries a momentum fraction $x_{\rm max}$ in a restricted window. These results are presented in Fig. 10.4a for the energy loss of monochromatic jets and in Fig. 10.4b for the jet R_{AA}, for the 3 bins in $x_{\rm max}$ and (for comparison) also for the inclusive jets. Focusing first on the left figure, we find indeed that the energy lost by jets with $x_{\rm max} > 0.9$, i.e. hard-fragmenting jets, is both considerably smaller and also less rapidly growing with p_{T0} then for the average jets. As $x_{\rm max}$ decreases, both the energy loss and its p_{T0} growth increase. This tendency is confirmed by the study of R_{AA}, Fig. 10.4b, where jets with a large $x_{\rm max}$ show a smaller-than-average nuclear suppression. It would be interesting to experimentally measure the correlation between the jet R_{AA} and the momentum fraction $x_{\rm max}$ and compare to our above predictions (see also [264] for a related

observable, which compares the nuclear suppression for high-p_T hadrons and inclusive jets).

To have a more quantitative argument, let us focus on a single bin in $p_T \equiv p_{T,\mathrm{jet}}$ with a (vacuum) Born-level p_T spectrum. The vacuum fragmentation function can then be easily estimated as

$$\mathcal{D}^{\mathrm{vac}}(x|p_T) \simeq \frac{N_q(p_T) D_q^{\mathrm{vac}}(x|p_T) + N_g(p_T) D_g^{\mathrm{vac}}(x|p_T)}{N_q(p_T) + N_g(p_T)}\,, \tag{10.19}$$

where $N_i(p_T) \equiv \mathrm{d}N_i^{\mathrm{hard}}/\mathrm{d}p_T \propto 1/p_T^n$ are the initial spectra for quarks ($i = q$) and gluons ($i = g$) and the fragmentation functions for monochromatic jets have been introduced at the end of Sect. 10.1.1. To write down the corresponding formula for jets in the medium, let us assume that the only medium effect on the jet production is the energy loss. One can thus write

$$\mathcal{D}^{\mathrm{med}}(x|p_T) \simeq \frac{\sum\limits_{i\in\{q,g\}} N_i(p_T + \varepsilon_i(x)) D_i^{\mathrm{med}}(x|p_T + \varepsilon_i(x))}{\sum\limits_{i\in\{q,g\}} N_i(p_T + \mathcal{E}_i(p_T))} \qquad \text{for } x \simeq 1. \tag{10.20}$$

The quantity $\varepsilon_i(x)$ in the numerator is the energy loss of a hard-fragmenting jet. It depends on x because the focus on large values $x > 0.5$ selects special configurations in which jets are made with only few partons. Its precise x–dependence is not important for what follows. Rather, it suffices to know that $\varepsilon_i(x)$ is a partonic energy loss, of order ω_{br}, and to a good approximation is independent of the jet p_T. The corresponding quantity in the denominator, $\mathcal{E}_i(p_T)$, is the average energy loss by a jet with transverse momentum p_T. It is much larger than $\varepsilon_i(x)$ and increases with p_T. This difference between the *partonic* energy loss $\varepsilon_i(x)$ in the numerator of Eq. (10.20) and the *average* energy loss $\mathcal{E}_i(p_T)$ in its denominator, together with the rapid decrease of $N_i(p_T)$ when increasing p_T, are the origin of the nuclear bias towards hard-fragmenting jets at large x, discussed at the beginning of this section.[4]

On top of their bias towards less energy loss, hard-fragmenting jets also favour quark-initiated jets. There are two reasons for this [39, 263]: `(i)` a quark radiates less than a gluon due to its reduced colour charge ($C_F < C_A$), resulting in a larger probability to contribute at large x, and `(ii)` quark-initiated jets typically contain less partons than gluon-initiated jets and hence lose less energy ($\varepsilon_q < \varepsilon_g$); this feature together with the steeply-falling p_T spectrum favours their production in AA collisions. We can therefore only keep the quark contribution to the numerators of Eqs. (10.19) and (10.20) and write

$$\mathcal{R}(x|p_T) \;\simeq\; \frac{f_q^{\mathrm{med}}(x|p_T)}{f_q^{\mathrm{vac}}(p_T)}\, \mathcal{R}_q(x|p_T)\,, \tag{10.21}$$

with the following definitions:

$$f_q^{\mathrm{vac}}(p_T) \equiv \frac{N_q(p_T)}{N_q(p_T) + N_g(p_T)}\,, \qquad f_q^{\mathrm{med}}(x|p_T) \equiv \frac{N_q(p_T + \varepsilon_q(x))}{\sum\limits_{i\in\{q,g\}} N_i(p_T + \mathcal{E}_i(p_T))}\,. \tag{10.22}$$

For jets in the vacuum, $f_q^{\mathrm{vac}}(p_T)$ is simply the fraction of quark-initiated jets. However, the corresponding quantity for jets in the medium is generally *not* a fraction, because of the different energy losses appearing in the numerator and in the denominator of $f_q^{\mathrm{med}}(x|p_T)$.

The condition of hard fragmentation ($x \sim 1$) only plays a role in the case of the medium, where it distinguishes between the "partonic" energy loss $\varepsilon_q(x)$ in the numerator and the jet

[4] Strictly speaking, the "average" energy loss $\mathcal{E}_i(p_T)$ in the denominator is influenced too by this bias, since it should be computed as an average over an inclusive sample of jets produced in AA collisions. However, this bias is less important for the inclusive sample than for the large-x distribution in the numerator of Eq. (10.20).

energy loss $\mathcal{E}_q(p_T)$ in the denominator. As already discussed, the physical observation that $\varepsilon_q(x) \ll \mathcal{E}_i(p_T)$ implies that the fraction of hard-fragmenting jets in the medium is larger than that in the vacuum, i.e., $f_q^{\rm med}(x|p_T)/f_q^{\rm vac}(p_T) > 1$, which in turn causes $\mathcal{R}(x|p_T)$ to go above one for $x \lesssim 1$. As x decreases, the energy loss of jets contributing at this value of x increases, becoming closer to $\mathcal{E}(p_T)$ and the nuclear enhancement is less pronounced.

It is enlightening to go one step further: let us present a more detailed (numerical) argument, based on simple 2-parton jets, which supports Eq. (10.21). Eq. (10.21) relies on the "fraction" $f_i(x|p_T)$ of hard-fragmenting jets with one constituent having an energy of at least xp_T. In practice, we define (cf. Eq. (10.22))

$$f_q^{\rm vac}(p_T) = \frac{\frac{{\rm d}\sigma_q}{{\rm d}p_T}}{\sum\limits_{i\in\{q,g\}} \frac{{\rm d}\sigma_i}{{\rm d}p_T}}\,, \qquad f_q^{\rm med}(x|p_T) = \frac{\frac{{\rm d}\sigma_q}{{\rm d}p_{T0}}\Big|_{p_T+\mathcal{E}_q^{\rm n=2}}}{\sum\limits_{i\in\{q,g\}} \frac{{\rm d}\sigma_i}{{\rm d}p_{T0}}\Big|_{p_T+\mathcal{E}_i(p_{T0})}}\,, \tag{10.23}$$

where ${\rm d}\sigma_i/{\rm d}p_{T0} \propto p_{T0}^{-n_i}$ is the initial jet spectrum. $n_q = 5$ and $n_g = 5.6$ give a decent description over the kinematic range covered in this paper. $\mathcal{E}_i(p_{T0})$ is the average energy loss by a jet with initial transverse momentum p_{T0} and is numerically extracted from MC simulations in Chapter 8, Section 8.2. $\mathcal{E}_q^{\rm n=2}$ is the energy lost by a simple two-parton jet (a leading quark of energy fraction $x \sim 1$ and a relatively soft gluon of energy fraction $1-x$). The dominant contribution (cf. Sect. 10.2.2.1) comes from events where the quark and gluon lose energy independently of each other[5]: $\mathcal{E}_q^{\rm n=2} = \varepsilon_q(xp_{T0}) + \varepsilon_g((1-x)p_{T0})$, with ε_g and ε_q given by Eq. (10.12).

By combining Eq. (10.23) for the fractions of hard-fragmenting jets with our previous calculations of the ratio $\mathcal{R}_q(x|p_T)$ for monochromatic jets, we can provide a semi-analytic estimate for the physical observable $\mathcal{R}(x|p_T)$ using Eq. (10.21). This is shown by the red curve in Fig. 10.3a, that should be compared to the corresponding MC result in Fig. 10.3b. The two red curves are both in good agreement with each other and with the general trend seen in the LHC data [244]. For x very close to 1 (mainly the last bin in our plots), the pattern observed in our MC calculations is a combination of the bias induced by the jet spectrum and of the medium effects on the internal jet dynamics $\mathcal{R}_q(x|p_T)$, with a strong domination of the former. The current experimental uncertainties in this region of x are too large to draw a stronger conclusion, notably concerning the relative importance of the nuclear effects associated with $\mathcal{R}_q(x|p_T)$, i.e. with the medium modifications of jet fragmentation itself.

10.3 Small-x enhancement: colour decoherence and medium-induced radiations

10.3.1 Qualitative discussion

Let us now consider the situation at small $x \lesssim 0.01$, where our numerical results in Fig. 10.1b show a pronounced medium enhancement of the fragmentation function, in qualitative agreement with the experimental observations [244]. These results also exhibit a (partial) lift of the degeneracy between the various sets of values for the medium parameters, suggesting a weaker correlation between $\mathcal{R}(x)$ and the jet nuclear modification factor R_{AA}. This section provides explanations for these observations within our framework.

[5]Strictly speaking, the energy argument of ε_g and ε_q should be zp_{T0} and $(1-z)p_{T0}$, respectively, with z the gluon splitting fraction, cf. Eq. (10.14), but to the accuracy of interest one can replace $z \simeq 1-x$ and $p_{T0} \simeq p_T$.

We first note that, for the considered range in $p_{T,\mathrm{jet}}$, $x \lesssim 0.01$ corresponds to momenta $p_T \lesssim 2$ GeV for the emitted partons, which are smaller than the characteristic medium scale ω_{br} for multiple branching. In our framework, such soft emissions are dominated by VLEs outside the medium since MIEs with energies $\omega \lesssim \omega_{\mathrm{br}}$ would fragment into very soft gluons propagating at angles larger than the jet radius (i.e. outside the jet). The medium enhancement of VLEs outside the medium has two main origins: `(i)` the violation of angular ordering by the first emission outside the medium, which opens the angular phase-space beyond what is allowed in the vacuum [37, 93], and `(ii)` the presence of MIEs with $\omega > \omega_{\mathrm{br}}$ which remain inside the jet and can radiate VLEs outside the medium [39]. Our analytic study in Section 5.3.1.1 and our numerical investigations in the following section show that both effects contribute to explaining the enhancement visible in the MC results.

The above interpretation of the nuclear enhancement at small x as additional VLEs outside the medium does explain the differences between the various choices of medium parameters seen in Fig. 10.1b. A smaller value for L increases the energy phase-space for the parton cascades developing outside the medium because the energy of the first emission outside the medium, $\omega \sim 2/(L\theta^2)$, with an emission angle $\theta \leq R$, increases with $1/L$. Furthermore, a larger value of $\alpha_{s,\mathrm{med}}$ enhances the rate for MIEs and hence the number of sources for VLEs outside the medium.

Even though our MC results at small x show the same qualitative trend as the relevant LHC data [244], one must remain cautious when interpreting this agreement. Indeed, our current formalism lacks some important physical ingredients, which are known to influence the soft region of the fragmentation function: the hadronisation and the medium response to the energy and momentum deposited by the jet. Whereas one may expect the effects of hadronisation to at least partially compensate when forming the medium-to-vacuum ratio $\mathcal{R}(x)$, the medium-response effect — i.e. the fact that the experimentally reconstructed jets also include soft particles originating from the wake of moving plasma trailing behind the jet (and not only from the jet itself) — is clearly missing in our approach and its inclusion should further enhance the ratio $\mathcal{R}(x)$ at small x. Indeed, we know from other approaches [265, 268, 270, 271], where the medium response is the only (or at least the main) mechanism for producing such an enhancement, that this effect by itself is comparable with the enhancement seen in the data (see also [272] for a different picture).

Of course, it is of utmost importance to complete our formalism with a more realistic description of the medium, including its feedback on the jet. (We shall return to this point in the concluding section.) Before such a more complete calculation is actually performed, it is difficult to anticipate what should be the combined effect of both mechanisms on the behaviour of $\mathcal{R}(x)$ at small x.

10.3.2 Monte Carlo tests

We would like to extend the DLA arguments exposed in Chapter 5, Section 5.3.1.1 to include all the ingredients in our physical picture of jet quenching. Our ultimate goal is to provide a deeper understanding of the MC results presented in Section. 10.1 and discussed qualitatively in the previous section.

For this purpose, it is convenient to think in terms of the factorised picture emerging from our DLA calculation which allows us to write (for $\omega \leq \omega_{cr}$, cf. Eq. (5.81))

$$\omega D^{\mathrm{med}}(\omega) \simeq \mathcal{N}_{\mathrm{in}} \times \left(\omega \frac{\mathrm{d}N^{\mathrm{out}}}{\mathrm{d}\omega}\right) \tag{10.24}$$

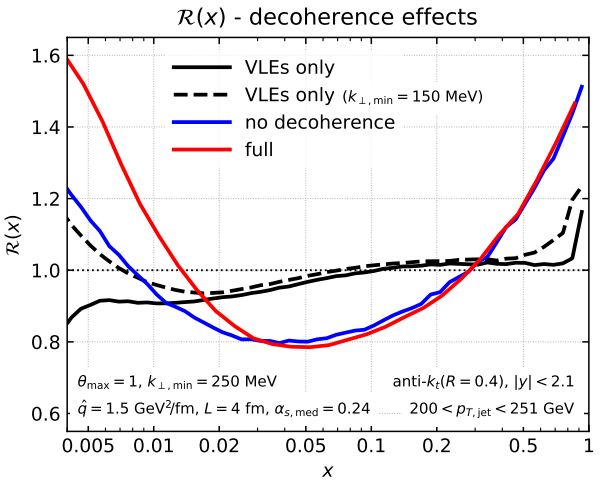

(a) Different physical scenarios: with and without MIEs, and with and without violation of angular ordering.

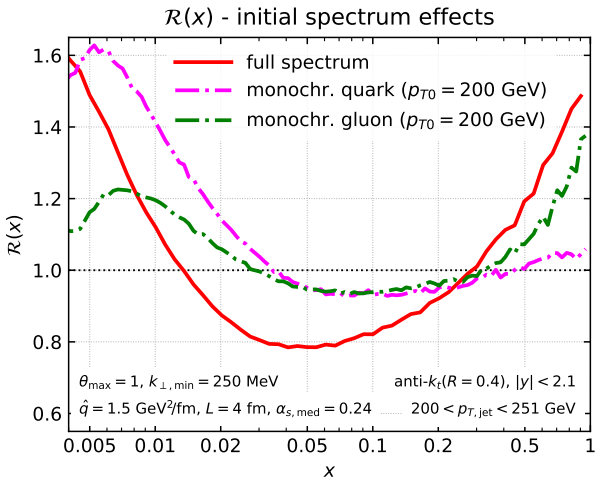

(b) Comparison between quark- and gluon-initiated monochromatic jets and "full" jets including a convolution with the initial, hard spectrum.

Figure 10.5: Nuclear effects on the fragmentation function at small x. Left figure: 3 different physical scenarios,

where $\mathcal{N}_{\mathrm{in}}$ is the multiplicity of partonic sources produced by the jet evolution inside the medium and $\omega \mathrm{d}N^{\mathrm{out}}/\mathrm{d}\omega$ is the fragmentation function generated outside the medium by any of these sources. This picture is a consequence of colour decoherence which allows the first out-of-medium emission to be emitted at any angle. This factorisation is not expected to hold beyond DLA, but can still be used for qualitative considerations.

Beyond DLA, several competing expects should be considered. `(i)` VLEs are emitted with the full (DGLAP) splitting functions (including energy conservation) and with a running coupling. These effects are expected to reduce both factors in Eq. (10.24). `(ii)` Adding the intra-jet MIEs enhances the multiplicity $\mathcal{N}_{\mathrm{in}}$ of the partonic sources. `(iii)` Direct contributions of the MIEs to the fragmentation function $D^{\mathrm{med}}(\omega)$ are also possible, but are expected to be a small effect for the jet kinematics ($p_{T0} \sim 200$ GeV, $x \leq 0.02$) and medium parameters (see Table. 8.1) considered in this paper. Indeed, the relevant energies $\omega \lesssim 2$ GeV are softer than the medium scale $\omega_{\mathrm{br}} \sim 4$ GeV for multiple branching meaning that these MIEs would be deviated outside the jet.

To test these expectations under realistic conditions, we perform MC simulations for inclusive jets (using the full Born-level hard spectrum) with $200 \leq p_T \leq 251$ GeV and $|y| \leq 2.1$, and with three different scenarios: `(a)` the partons from the hard scattering are showered via VLEs only; `(b)` the partons from the hard scattering are showered via both VLEs and MIEs, but angular ordering is enforced all along the shower, including for the first emission outside the medium (labelled "no decoherence"); `(c)` the physical case where the partons from the hard scattering are showered via both VLEs and MIEs and the angle of the first emission outside the medium is unconstrained.

The MC results for $\mathcal{R}(x)$ are shown in Fig. 10.5a for each of these three setups. The black curves correspond to setup `(a)` for two 2 different IR cutoffs (solid: $k_{\perp,\min} = 200$ MeV, dashed: $k_{\perp,\min} = 150$ MeV). compared to the DLA results in Fig. 5.6b the medium enhancement is strongly reduced and can even be replaced by a suppression for larger values of $k_{\perp,\min}$.

Switching on MIEs leads to a robust nuclear enhancement as visible from the blue curve

which corresponds to setup (b) with $k_{\perp,\min} = 200$ MeV. This enhancement is even more pronounced for setup (c) corresponding to the red curves in Fig. 10.5a. This new enhancement is easily associated with the fact that the first "outside" emission can be sourced by any "inside" emissions while in setup (b) it can only be sourced by "inside" emissions at larger angles.[6] Incidentally, the comparison between the blue and the red curves also shows that the decoherence has no sizeable effects at $x \sim 1$.

For a more detailed understanding, we compare in Fig. 10.5b the results for $\mathcal{R}(x)$ with the ratio $\mathcal{R}_i(x|p_{T0})$ corresponding to monochromatic jets with $p_{T0} = 200$ GeV, for both quark-initiated ($i = q$, magenta, dashed-dotted curve) and gluon-initiated ($i = g$, green, dashed, curve) jets. The small-x enhancement appears to be stronger in the case where the LP is a quark, rather than a gluon. Although this might look surprising at first sight, one should recall that the dominant C_i-dependence for monochromatic jets cancels out in the medium/vacuum ratio $\mathcal{R}_i(x|p_{T0})$. The differences between the quark and gluon curves visible in Fig. 10.5b is attributed to more subtle sub-leading effects. For example, a gluon jet loses more energy than a quark jet via MIEs at large angles and hence has a (slightly) smaller energy phase-space for radiating outside the medium (and inside the jet).

10.4 Jet fragmentation into subjets

The fragmentation function defined by Eq. (10.3) is not an infrared-and-collinear (IRC) safe observable. It is sensitive to the details of hadronisation which is not included in our present approach. This translates in the strong dependence, observed in Fig. 10.1a, on the cut-off scale $k_{\perp,\min}$ which regulates the infrared behaviour of our partonic cascade. This strong dependence on $k_{\perp,\min}$ is also present in the analytic calculations of sections 10.2 and 5.3.1.1.

To circumvent this theoretical problem, we propose in this section a different observable which uses subjets instead of individual hadrons to characterise the jet fragmentation, as explained in Section 4.2.3.3. This observable is IRC-safe by construction and is therefore expected to be less sensitive to non-perturbative effects in general and to our $k_{\perp,\min}$ cut-off in particular. There are several ways to define a jet fragmentation function in terms of subjets, e.g. using different jet algorithms or keeping different branches of the clustering tree. The definition we propose below, as in Section 4.2.3.3, relies on the Cambridge/Aachen algorithm [131, 132]. While other approaches, like those based on the k_t algorithm [133], show a similar behaviour, using the Cambridge/Aachen algorithm appears to be slightly more sensitive to medium effects and easier to study analytically.

10.4.1 Definition and leading-order estimate in the vacuum

The fragmentation function $\mathcal{D}_{\text{sub}}(z)$ for jet fragmentation into subjets discussed in this section is defined as follows. For a given jet with transverse momentum $p_{T,\text{jet}}$, we iteratively decluster the jet using the Cambridge/Aachen algorithm following the hardest branch (in p_T). At each step, this produces two subjets p_1 and p_2, with $p_{T1} > p_{T2}$. When the relative transverse momentum of the splitting, $k_\perp = p_{T2}\sqrt{\Delta y_{12}^2 + \Delta\phi_{12}^2}$, is larger than a (semi-hard) cut-off $k_{\perp,\text{cut}}$, we compute and record the splitting fraction $z = \frac{p_{T2}}{p_{T1}+p_{T2}}$ of the splitting ($0 < z < 1/2$). The procedure is iterated with the harder branch p_1 until it can no longer be de-clustered. The fragmentation function into subjets is then defined as the density of subjets passing the $k_\perp > k_{\perp,\text{cut}}$ criterion

[6] For setup (b) the factorisation (10.24) is obviously violated as "inside sources" and "outside emissions" are correlated by angular ordering.

normalised by the total number of jets:[7]

$$\mathcal{D}_{\text{sub}}(z) \equiv \frac{1}{N_{\text{jets}}} \frac{\mathrm{d}N_{\text{sub}}}{\mathrm{d}z} \tag{10.25}$$

The cut-off scale $k_{\perp,\text{cut}}$ regulates the infrared behaviour, guaranteeing that $\mathcal{D}_{\text{sub}}(z)$ be an IRC-safe observable. As long as $k_{\perp,\text{cut}} \gg k_{\perp,\text{min}} \sim \Lambda_{\text{QCD}}$ we therefore expect small non-perturbative effects and a small dependence on the (non-physical) $k_{\perp,\text{min}}$ parameter.

This definition is very close to the ISD fragmentation function discussed in Chapter 4, Section 4.2.3.3: the only difference is the stopping condition that involves the $k_\perp$ of the splitting. This difference produces negligible effects at leading logarithmic accuracy, so that in the soft-and-collinear approximation, we can use the result obtained in Section 4.2.3.3 for $\mathcal{D}_{\text{sub}}(z)$:

$$\begin{aligned}\mathcal{D}^{\text{vac}}_{\text{sub}}(z) &\simeq \left[\int_0^R \frac{\mathrm{d}\theta}{\theta} \frac{2\alpha_s(z\theta p_{T,\text{jet}})}{\pi z} \Theta(z\theta p_{T,\text{jet}} - k_{\perp,\text{cut}})\right] \times \sum_{i=q,g} C_i\, f_i^{\text{vac}}(p_{T,\text{jet}}), \\ &\overset{\text{f.c.}}{\simeq} \frac{2\alpha_s}{\pi z} \log\left(\frac{zRp_{T,\text{jet}}}{k_{\perp,\text{cut}}}\right) \times \sum_{i=q,g} C_i\, f_i^{\text{vac}}(p_{T,\text{jet}}),\end{aligned} \tag{10.26}$$

where $f^{\text{vac}}_{q(g)}(p_{T,\text{jet}})$ is the Born-level cross-section for quark (gluon) production with transverse momentum $p_{T,\text{jet}}$ normalised to the total number of jets, as defined in Eq. (10.23). The second line in the above equation gives the result for a fixed-coupling approximation.

10.4.2 Nuclear modification for $\mathcal{D}_{\text{sub}}(z)$: Monte Carlo results

In this section, we provide Monte Carlo results for the nuclear modification factor for the fragmentation function into subjets, defined as $\mathcal{R}_{\text{sub}}(z) \equiv \mathcal{D}^{\text{med}}_{\text{sub}}/\mathcal{D}^{\text{vac}}_{\text{sub}}$.

As for the study of the jet fragmentation function $\mathcal{D}(x)$, we first study the dependence of the the fragmentation function into subjets, $\mathcal{D}_{\text{sub}}(z)$, on the non-physical parameters θ_{max} and $k_{\perp,\text{min}}$ of our Monte Carlo. This is shown in Fig. 10.6 for two different jet p_T cuts (200 and 500 GeV) and two different lower cut-offs $k_{\perp,\text{cut}}$ (2 and 5 GeV). The medium parameters are taken as their default values (cf. Table 8.1) and the non-physical parameters are varied as for Fig. 10.1a. As expected, the uncertainty bands in Fig. 10.6 are much smaller than what was observed in Fig. 10.1a, confirming that the (IRC-safe) fragmentation function into subjets $\mathcal{D}_{\text{sub}}(z)$ is under much better perturbative control than (the IRC-unsafe) $\mathcal{D}(x)$.

That said, we must keep in mind that taking $k_{\perp,\text{cut}}$ large-enough to guarantee $k_{\perp,\text{cut}} \gg k_{\perp,\text{min}} \sim \Lambda_{\text{QCD}}$ also cuts some of the medium effects occurring below this cut. E.g., it removes the direct contributions to $\mathcal{D}_{\text{sub}}(z)$ coming from MIEs with transverse momenta $k_\perp \lesssim k_{\perp,\text{cut}}$. One should therefore choose the free parameter $k_{\perp,\text{cut}}$ such as to simultaneously minimise the effects of hadronisation and highlight the interesting medium effects.

In Fig. 10.7, we show the subjet fragmentation function for the values of the medium parameters that reproduce the ATLAS R_{AA} ratio (cf. Fig. 10.1b), for the same two values of $p_{T,\text{jet}}$ as in Fig. 10.6 and for $k_{\perp,\text{cut}} = 2$ GeV. Compared to Fig. 10.1b, we notice that the curves are less degenerate at small and intermediate values of z. Most importantly, the dependence on the medium parameters is larger than the uncertainty bands related to non-physical parameters shown in Fig. 10.6.

[7] We use the notation z for the splitting fraction to emphasise that it is defined with respect to the parent subjet, in contrast with the longitudinal momentum fraction x used in the previous sections which is defined as a fraction of the total jet momentum $p_{T,\text{jet}}$.

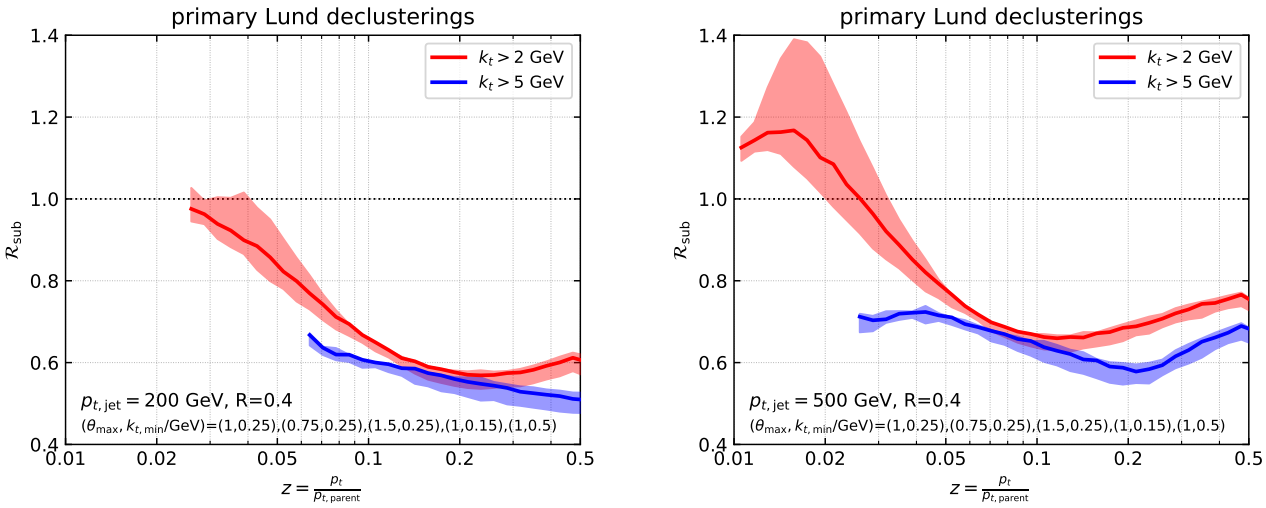

Figure 10.6: Monte Carlo results for the nuclear modification factor $\mathcal{R}_{\rm sub}(z)$ for the fragmentation function into subjets, for jets with $p_{T,\rm jet} > 200$ GeV (left) and $p_{T,\rm jet} > 500$ GeV (right) and for 2 values of the lower momentum cut-off $k_{\perp,\rm cut}$ (2 and 5 GeV). The bands show the variability of our results w.r.t. changes in the "unphysical" parameters around their central values $\theta_{\rm max} = 1$ and $k_{\perp,\rm min} = 250$ MeV.

10.4.3 Analytic studies of the nuclear effects

In this section, we would like to disentangle, based on physics considerations and simple analytic calculations, the various nuclear effects contributing to the behaviour observed in the MC results in Fig. 10.7. To understand how Eq. (10.26) is affected by the medium, it is sufficient to consider jets made of a single splitting (i.e. two subjets) with $k_\perp \geq k_{\perp,\rm cut}$. For definiteness, all the numerical results shown in this subsection correspond to $k_{\perp,\rm cut} = 2$ GeV.

Vetoed region. When only VLEs are taken into account, the leading medium effect is the vetoed region. Its effect is straightforwardly included in Eq. (10.26) by inserting the step-function $\Theta_{\notin \rm veto}$ defined in Eq. (10.5) within the integrand. The largest $k_\perp$ in the vetoed region is $Q_s \equiv (2\hat{q}\omega_c)^{1/4} = (\hat{q}L)^{1/2}$ which is about 2.4 GeV for our default choice of medium parameters. The vetoed region has thus no effect for $k_{\perp,\rm cut} = 5$ GeV and only a small effect for $k_{\perp,\rm cut} = 2$ GeV (see Fig. 10.8 for an illustration).

This is confirmed both by our analytic calculations, based on Eq. (10.26) with the additional constraint $\Theta_{\notin \rm veto}$, and by MC simulations with only VLEs shown as the black curves in Fig. 10.9. Of course, one could enhance the effect of the vetoed region by decreasing the value of $k_{\perp,\rm cut}$, but this would also amplify the sensitivity of $\mathcal{D}_{\rm sub}(z)$ to the non-perturbative, soft, emissions.

Incidentally, the previous discussion also shows that, for the ranges of $k_{\perp,\rm cut}$ considered here, the VLEs which control $\mathcal{D}_{\rm sub}(z)$ do either occur in the "inside" region of the phase-space in Fig. 10.8, or at very small angles $\theta \lesssim \theta_c$ in the "outside" region. They are therefore not significantly affected by colour decoherence. To check that, we have performed MC calculations with and without the effects of decoherence (i.e. by enforcing or not angular ordering for the first outside emission). The results, shown by the red and blue curves in Fig. 10.9b, respectively, are indeed very close to each other.

Energy loss at large angles. From the discussion in Sect. 10.2, we already know that the energy loss by a (sub)jet via MIEs at large angles $\theta \gtrsim R$ may have two main effects on a substructure observable such as $\mathcal{D}_{\rm sub}(z)$: (i) a shift between the measured value z of the

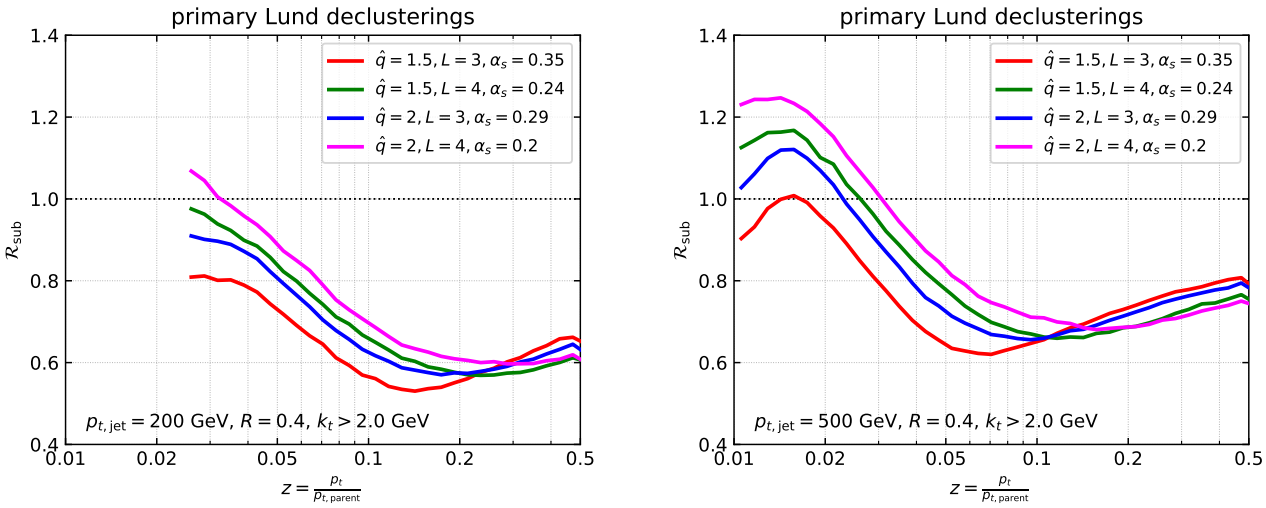

Figure 10.7: Monte Carlo results for the nuclear modification factor $\mathcal{R}_{\rm sub}(z)$ for the values of the medium parameters that reproduce the ATLAS R_{AA} ratio (cf. Fig. 10.1b), for the same two ranges in $p_{T,\rm jet}$ as in Fig. 10.6 and for $k_{\perp,\rm cut} = 2$ GeV. The unphysical parameters are fixed to $\theta_{\rm max} = 1$ and $k_{\perp,\rm min} = 250$ MeV.

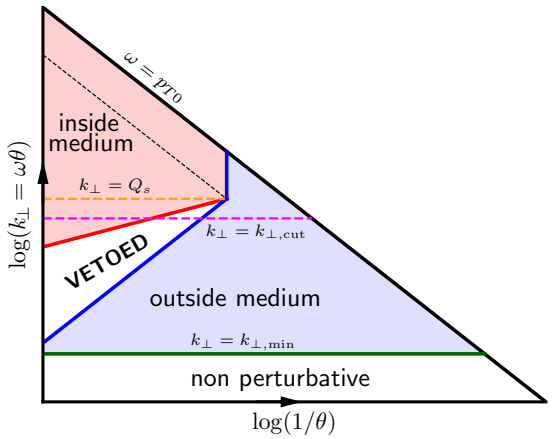

Figure 10.8: The phase-space for vacuum-like gluon emissions by a jet propagating through a dense QCD medium, in logarithmic units. In this plot, the variables are the relative transverse momentum $k_\perp \simeq \omega\theta$ and the inverse of the angle $1/\theta$.

splitting fraction and the respective value at the time of splitting, and `(ii)` a bias introduced by the steeply falling initial spectrum which favours jets losing less energy than average jets, with the second effect being larger than the first one. The same two effects are still at play for $\mathcal{D}_{\rm sub}(z)$. As in the case of the standard fragmentation function discussed in Sect. 10.2, we expect the effects of the energy loss to be more important for relatively large values $z \gtrsim 0.1$ of the splitting fraction. However, their effects on $\mathcal{R}_{\rm sub}(z)$ is opposite to those on $\mathcal{R}(x)$: unlike the hard-fragmenting jets, which lose *less* energy than the average jets (leading to an enhancement in $\mathcal{R}(x)$ at $x \gtrsim 0.5$), the jets selected by $\mathcal{D}_{\rm sub}(z)$ lose *more* energy than the average jets, so we expect a *nuclear suppression*, $\mathcal{R}_{\rm sub}(z) < 1$, at sufficiently large z. The main reason for this larger energy loss is the following: the jets included in $\mathcal{D}_{\rm sub}(z)$ involve at least two (relatively hard) subjets with $z \gtrsim 0.1$ and $k_\perp > k_{\perp,\rm cut}$. For the typical values of z and $k_\perp$, the angle $\theta \simeq k_\perp/p_{T2}$ between these two subjets is larger than the critical angle θ_c characterising the

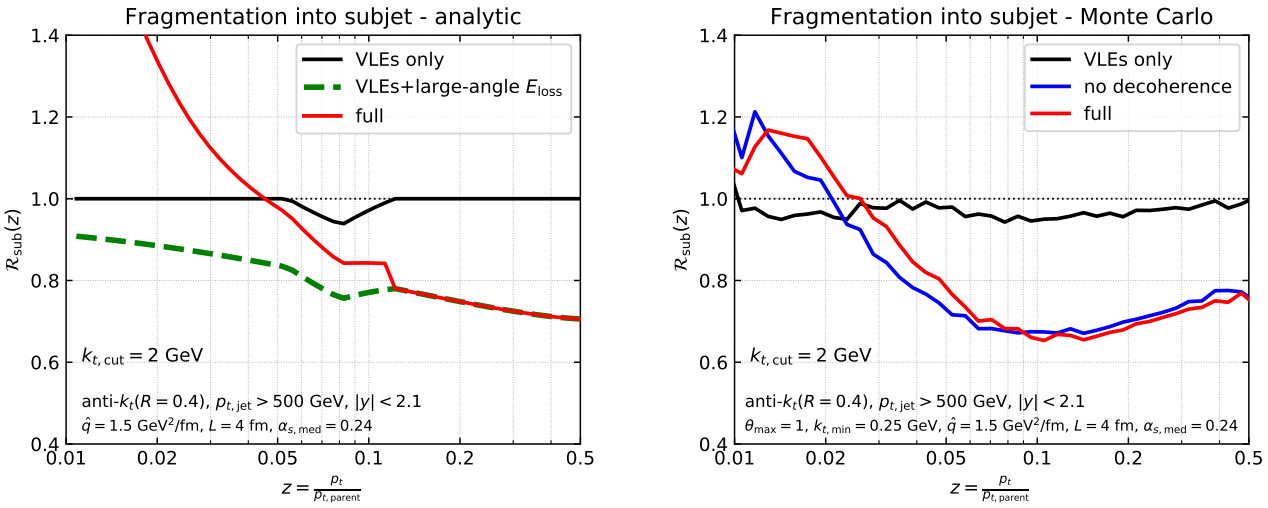

(a) Anaytic results (b) Results from Monte Carlo simulations

Figure 10.9: Disentangling nuclear effects on the subjet fragmentation function. Left: analytic approximations illustrating the effects of the vetoed region, the energy loss at large angles, and the intra-jet MIEs. Right: MC calculations which illustrate the importance of MIEs and the lack of sensitivity to violations of angular ordering.

angular resolution of the plasma ($\theta_c \lesssim 0.06$, see Table 8.1). Accordingly the two subjets lose energy independently from each other and the whole jet loses more energy than a typical jet from the inclusive sample $N_{\rm jets}$ [39, 125] which also includes single-prong jets, as well as two-prong configurations with $\theta < \theta_c$.

This discussion is in qualitative agreement with the MC results in Fig. 10.9b, except at very small z where new effects discussed below contribute. For a more quantitative argument, we notice that, if one neglects the shift in the value of z, then the energy loss at large angles affects only the quark- and gluon-jet "fractions" $f_i^{\rm med}$ in Eq. (10.26). These should be computed following Eq. (10.23), with different energy losses in the numerator and respectively the denominator. In the numerator, $\mathcal{E}_i^{n=2}$ is the energy loss of jets having two subjets with transverse momentum balance z and angle θ ($p_T \equiv p_{T,\rm jet}$)

$$\mathcal{E}_i^{n=2}(z,\theta) = \mathcal{E}_i((1-z)p_T, R) + \mathcal{E}_g(zp_T, R) \qquad \text{if } (z,\theta) \in \text{ inside region}, \tag{10.27}$$

whereas in the denominator, $\mathcal{E}_i = \mathcal{E}_i(p_T, R)$. Using the energy loss as a function of p_T and R extracted from the MC simulations in Ref. [39] in Eqs. (10.23) and Eq. (10.26), one obtains the dashed, green, curve in Fig. 10.9a. This indeed shows a nuclear suppression, $\mathcal{R}_{\rm sub}(z) < 1$. The suppression is more pronounced at large z, as anticipated, since the discrepancy (in terms of energy loss) between the special jets selected by $\mathcal{D}_{\rm sub}^{\rm med}(z)$ and the average jets increases with z.

Intrajet MIEs. A relatively hard subjet with $k_\perp > k_{\perp,\rm cut}$ may also be created by a semi-hard MIE, with energy $\omega \gtrsim \omega_{\rm br}$, which remains inside the jet. To leading order, the respective contributions from VLEs and MIEs can be simply added together, as in Eq. (10.8). Compared to the latter, the calculation of $\mathcal{D}_{\rm sub}^{\rm med}(z)$ must also keep the information about the emission angle, in order to ensure the condition $k_\perp > k_{\perp,\rm cut}$. We therefore write

$$\mathcal{D}_{\rm sub}^{\rm med}(z) = \left[\int_0^R {\rm d}\theta \left(\frac{2\alpha_s(k_\perp)}{\pi z\theta}\Theta_{\notin \rm veto} + \sqrt{\frac{2\omega_c}{p_{T,\rm jet}}}\frac{\alpha_{s,\rm med}}{\pi z^{3/2}}\mathcal{P}_{\rm broad}(z,\theta)\right)\Theta(k_\perp - k_{\perp,\rm cut})\right]\sum_{i=q,g} C_i f_i^{\rm med} \tag{10.28}$$

where $k_\perp = z\theta p_{T,\text{jet}}$ and $\mathcal{P}_{\text{broad}}(z,\theta)$ is the angular distribution due to transverse momentum broadening after emission calculated in 4.3.3.2 and given explicitly by (9.9). In writing Eq. (10.28), we have assumed for simplicity that the energy loss at large angles is given by Eq. (10.27) for both the vacuum-like and medium-induced emissions that generates the subjets. This rough approximation could be relaxed in practice, but is sufficient for our illustrative purposes. The distribution $\mathcal{P}_{\text{broad}}(z,\theta)$ for MIEs is rather strongly peaked near $k_\perp \sim Q_s$ (recall the discussion for the z_g distribution in 9.1.3.1) so its corresponding contribution to Eq. (10.28) is expected to be important only when $k_{\perp,\text{cut}} \lesssim Q_s$, in which case it should be rapidly increasing at small z. This is in agreement with the MC results in Figs. 10.6 and 10.7, which show an enhancement at small z for $k_{\perp,\text{cut}} = 2$ GeV and no visible enhancement for $k_{\perp,\text{cut}} = 5$ GeV.

Eq. (10.28) includes all the medium effects discussed in this section. The red curve in Fig. 10.9a shows the result of numerically evaluating the integral in Eq. (10.28). The new enhancement at small z compared to the dashed, green, curve is due to the intrajet MIEs. The overall behaviour agrees well with the full MC results shown in Fig. 10.9b as well as with Figs. 10.6 and 10.7.

Chapter 11

Conclusion

In this thesis, we have presented a new picture, emerging from perturbative QCD, for the parton showers created by an energetic parton propagating through a dense quark-gluon plasma. This picture is factorised in time with vacuum-like emissions occurring first and creating sources for subsequent medium-induced radiations. Both types of emission are Markovian processes, yielding a modular Monte Carlo implementation of our picture in the parton shower `JetMed`. This allows us to study separately various aspects of the dynamics of jet quenching and assert their relative importance in jet observable measured at the LHC in heavy-ion collisions.

We have focused on three observables for which we believe our approximations to be robust: the jet nuclear modification factor for R_{AA}, the nuclear effects on the z_g distribution given by the Soft Drop procedure and the jet fragmentation function (and notably its new version infrared and collinear safe). For all these observables, we obtained good qualitative and semi-quantitative descriptions of the respective LHC data and we discussed the physical interpretation of the various trends seen in the data. To make our physical discussions more convincing, we supplemented the Monte Carlo calculations with suitable analytic calculations, which were helpful to pinpoint the different mechanisms at play and compare their effects.

In the remaining part of this conclusion, we outline some of our projects for the future. As acknowledged in Section 5.2.5, the current leading-logarithmic picture for the *vacuum-like* evolution has several limitations. Accordingly, the parton shower `JetMed` is currently rather simplistic and we have provided a detailed list of possible improvements in Section 6.5. We point out however that our step-by-step approach is motivated by the following guideline: in the vacuum, the accuracy of a parton shower means logarithmic accuracy. We believe that an in-medium parton shower should also start with a correct resummation of the large logarithms. Thus our first step has consisted in resumming all leading-logarithmic contributions associated with vacuum-like emissions in the presence of a dense QCD medium. Then, we have included the dominant (higher-twist) medium-induced emissions through an effective branching process that encompasses the multiple soft branching regime.

At this stage, the list of physical ingredients that will refine our calculations of jet quenching observables is large and we refer the reader to Table 6.2 for a ranked list of such ingredients. Including the medium expansion is the next step of our project, as well as the emissions à la GLV due to single hard scatterings.

Instead of going through the complex task of completing our Monte Carlo with a detailed description of the medium and of its interactions with the jet, one can alternatively think about using our parton showers as an input for the recently developed JETSCAPE [273, 274] framework, which offers various approaches for treating the interactions between the parton shower and the medium.

Appendix A

Propagators and averaged propagators in the background field $\mathcal{A}_m$

A.1 Gluon propagators beyond the eikonal approximation

In this section, we give all the components of the gluon propagator $G^{\mu\nu}ab(z,x|\mathcal{A}_m)$ in the background field $\mathcal{A}_m$ defined in (3.75) in terms of the scalar propagator $\mathcal{G}$ defined by (3.79).

$$G^{ij}_{ab}(z,x|\mathcal{A}_m) = \int \frac{\mathrm{d}k^+}{2\pi} \frac{e^{-ik^+(z^- - x^-)}}{2k^+} \delta^{ij} \mathcal{G}_{ab}(z^+, z_\perp; x^+, x_\perp|k^+) \tag{A.1}$$

$$G^{-i}_{ab}(z,x|\mathcal{A}_m) = \int \frac{\mathrm{d}k^+}{2\pi} \frac{e^{-ik^+(z^- - x^-)}}{2k^+} \frac{-i}{k^+} \partial^i_{z_\perp} \mathcal{G}_{ab}(z^+, z_\perp; x^+, x_\perp|k^+) \tag{A.2}$$

$$G^{i-}_{ab}(z,x|\mathcal{A}_m) = \int \frac{\mathrm{d}k^+}{2\pi} \frac{e^{-ik^+(z^- - x^-)}}{2k^+} \frac{i}{k^+} \partial^i_{x_\perp} \mathcal{G}_{ab}(z^+, z_\perp; x^+, x_\perp|k^+) \tag{A.3}$$

$$\begin{aligned} G^{--}_{ab}(z,x|\mathcal{A}_m) = \int \frac{\mathrm{d}k^+}{2\pi} \frac{e^{-ik^+(z^- - x^-)}}{2k^+} \Bigg(& \frac{1}{k^{+2}} \partial^i_{z_\perp} \partial^i_{x_\perp} \mathcal{G}_{ab}(z^+, z_\perp; x^+, x_\perp|k^+) \\ & + \frac{2i}{k^+} \delta_{ab} \delta(z^+ - x^+) \delta^{(2)}(z_\perp - x_\perp) \Bigg) \end{aligned} \tag{A.4}$$

with $k^+ \to k^+ + i\epsilon$ for retarted propagators. We refer to [103] or [118] for a derivation of these formulas.

A.2 The broadening factor S_{gg} for Gaussian correlators

We calculate now the following average over the background field configurations, often called the "2-point" function $S^{(2)}_{z^+,y^+}(\bar{z}_\perp, a_\perp; z_\perp, b_\perp)$

$$S^{(2)}_{z^+,y^+}(\bar{z}_\perp, a_\perp; z_\perp, b_\perp) \equiv \frac{1}{N_c^2 - 1} \Big\langle \mathrm{Tr}\, \mathcal{G}^\dagger(z^+, \bar{z}_\perp; y^+, a_\perp|k^+) \mathcal{G}(z^+, z_\perp; y^+, b_\perp|k^+) \Big\rangle \tag{A.5}$$

We follow the derivation presented in the Appendix of [75]. This 2-point function appears in the calculation of the average $\tilde{S}_{gg}$ defined in (3.98):

$$\tilde{S}_{gg}(k_\perp, a_\perp, b_\perp) = \lim_{z^+ \to \infty} \int \mathrm{d}z_\perp \mathrm{d}\bar{z}_\perp \, e^{-ik_\perp(a_\perp - b_\perp)} e^{-ik_\perp(z_\perp - \bar{z}_\perp)} S^{(2)}_{z^+,y^+}(\bar{z}_\perp, a_\perp; z_\perp, b_\perp) \tag{A.6}$$

Using the path integral representation (3.79) and the general result for the average of two Wilson lines (3.175) for Gaussian correlators, one finds the following path integral representation of $S^{(2)}$:

$$S^{(2)}_{z^+,y^+}(\bar{z}_\perp,a_\perp;z_\perp,b_\perp)=\int\mathcal{D}r_\perp(\xi)\mathcal{D}s_\perp(\xi)\exp\left(\int_{y^+}^{z^+}\mathrm{d}\xi\,\frac{ik^+}{2}(\dot{s}_\perp^2-\dot{r}_\perp^2)\right.$$
$$\left.-\frac{g^2}{2}C_A\int_{y^+}^{z^+}\mathrm{d}\xi\,n(\xi)\sigma_d\big(s_\perp-r_\perp\big)\right)\qquad(A.7)$$

It is quite remarkable that this path integral can be calculated exactly for any dipole cross-section $\sigma_d(r_\perp)$. The calculation starts with a change of variable of determinant one $u_\perp=s_\perp-r_\perp$, $v_\perp=(r_\perp+s_\perp)/2$ to take advantage of the translational invariance of the average of two Wilson lines:

$$S^{(2)}_{z^+,y^+}(\bar{z}_\perp,a_\perp;z_\perp,b_\perp)=\int\mathcal{D}u_\perp(\xi)\mathcal{D}v_\perp(\xi)\exp\left(\int_{y^+}^{z^+}\mathrm{d}\xi\,ik^+\dot{u}_\perp\dot{v}_\perp-\frac{g^2}{2}C_An(\xi)\sigma_d\big(u_\perp\big)\right)\qquad(A.8)$$

In terms of these variables, the boundaries of the path integral are $u(y^+)=b_\perp-a_\perp$, $u(z^+)=z_\perp-\bar{z}_\perp$, $v(y^+)=(a_\perp+b_\perp)/2$, $v(z^+)=(z_\perp+\bar{z}_\perp)/2$. Integrating by part the $v_\perp$ dependent integral enables to remove the derivative of $v_\perp$:

$$\int_{y^+}^{z^+}\mathrm{d}\xi\,\dot{u}_\perp\dot{v}_\perp=\frac{z_\perp+\bar{z}_\perp}{2}\dot{u}_\perp(z^+)-\frac{a_\perp+b_\perp}{2}\dot{u}_\perp(y^+)-\int_{y^+}^{z^+}\mathrm{d}\xi\,\ddot{u}_\perp v_\perp\qquad(A.9)$$

so that, by discretising the path integral over $v_\perp(\xi)$, one shows:

$$\int\mathcal{D}v_\perp(\xi)\exp\left(-ik^+\int_{y^+}^{z^+}\mathrm{d}\xi\,\ddot{u}_\perp v_\perp\right)=\mathcal{N}\delta(\ddot{u}_\perp(\xi))\qquad(A.10)$$

up to a normalisation factor $\mathcal{N}$ to be determined afterwards. The $\delta(\ddot{u}_\perp)$ factor means that $u_\perp$ is fixed to the classical path $u_\perp^{\mathrm{cl}}(\xi)$, solution of $\ddot{u}_\perp(\xi)=0$ given the boundaries conditions:

$$u_\perp^{\mathrm{cl}}(\xi)=\frac{1}{z^+-y^+}\Big((z_\perp-\bar{z}_\perp)(\xi-y^+)+(b_\perp-a_\perp)(z^+-\xi)\Big)\qquad(A.11)$$

As the $u_\perp$ path is fixed in the remaining $u_\perp$ integral (A.8) by a delta function of the form $\delta(u_\perp-u_\perp^{\mathrm{cl}})$, the integration is trivial:

$$S^{(2)}_{z^+,y^+}(\bar{z}_\perp,a_\perp;z_\perp,b_\perp)=\mathcal{N}\exp\left(\frac{ik^+}{2(z^+-y^+)}\big((\bar{z}_\perp-a_\perp)^2-(z_\perp-b_\perp)^2\big)\right.$$
$$\left.-\frac{g^2}{2}C_A\int_{y^+}^{z^+}\mathrm{d}\xi\,n(\xi)\sigma_d(u_\perp^{\mathrm{cl}})\right)\qquad(A.12)$$

with again, a normalisation factor absorbed in $\mathcal{N}$. This factor is finally inferred from the $g\to0$ limit where the two-point function should reduce to the product of two free propagators. Using the expression of the free transverse propagator $\mathcal{G}_0$ given in (3.114) plugged in (A.5), one finds:

$$\mathcal{N}=\left(\frac{k^+}{2\pi(z^+-y^+)}\right)^2\qquad(A.13)$$

In order to find the function $\tilde{S}_{gg}$, one must take the Fourier transform as defined in (A.7). The following change of variable considerably simplifies the calculation:

$$p_\perp = \bar{z}_\perp - a_\perp - z_\perp + b_\perp \qquad q_\perp = \bar{z}_\perp - a_\perp + z_\perp - b_\perp \tag{A.14}$$

since the function $\tilde{S}_{gg}$ now reads:

$$\begin{aligned}\tilde{S}_{gg}(k_\perp, a_\perp, b_\perp) &= \mathcal{N}\int \mathrm{d}^2 p_\perp \int \mathrm{d}^2 q_\perp e^{-ik_\perp p_\perp} \\ &\quad \times \exp\left(\frac{ik^+}{2(z^+-y^+)} p_\perp q_\perp - \frac{g^2}{2} C_A \int_{y^+}^{z^+} \mathrm{d}\xi\, n(\xi)\sigma_d\Big(\frac{\xi - y^+}{z^+ - y^+} p_\perp + a_\perp - b_\perp\Big)\right) \qquad (A.15)\\ &= \exp\left(-\frac{g^2}{2} C_A \int_{y^+}^{z^+} \mathrm{d}\xi\, n(\xi)\sigma_d(a_\perp - b_\perp)\right) \qquad (A.16)\end{aligned}$$

which is precisely (3.100) when $z^+ \to \infty$.

A.3 The effective propagator $\mathcal{K}$ in the harmonic approximation

We give first the derivation of formula (3.102), valid for Gaussian correlators for the background field. Our starting point is the function $\mathcal{K}_{qg}$ defined by

$$\mathcal{K}_{qg}(y^+, a_\perp; \bar{y}^+, b_\perp | c_\perp) \equiv \frac{1}{N_c^2 - 1}\Big\langle \mathrm{Tr}\, \mathcal{G}^\dagger(y^+, a_\perp; \bar{y}^+, b_\perp | k^+) \mathcal{W}_{\bar{y}^+}^{y^+}(c_\perp)\Big\rangle \tag{A.17}$$

Using the path integral representation of the gluon propagator (3.79) and the formula for the average of two Wilson lines (3.175), one finds the following path integral representation of the effective propagator $\mathcal{K}_{qg}$:

$$\mathcal{K}_{qg}(y^+, a_\perp; \bar{y}^+, b_\perp | c_\perp) = \int_{r_\perp(\bar{y}^+)=b_\perp}^{r_\perp(y^+)=a_\perp} \mathcal{D}r_\perp(\xi) \exp\left(-\int_{\bar{y}^+}^{y^+} \mathrm{d}\xi \frac{ik^+}{2}\dot{r}_\perp^2(\xi) + \frac{g^2 C_A}{2} n(\xi)\sigma(r_\perp - c_\perp)\right) \tag{A.18}$$

After the shift in the path integral $r_\perp \to r_\perp + c_\perp$, one gets (3.101) and (3.102). In the harmonic approximation, the latter expression reduces to the following Gaussian path integral:

$$\mathcal{K}(y^+, a_\perp; \bar{y}^+, b_\perp) = \int_{r_\perp(\bar{y}^+)=b_\perp}^{r_\perp(y^+)=a_\perp} \mathcal{D}r_\perp(\xi) \exp\left(-\int_{\bar{y}^+}^{y^+} \mathrm{d}\xi \frac{ik^+}{2}\dot{r}_\perp^2(\xi) + \frac{1}{4}\hat{q}_A(\xi) r_\perp^2\right) \tag{A.19}$$

An explicit formula for $\mathcal{K}$ can be found using the Gel'fand and Yaglom formula [275] for Gaussian path integrals. Given a quadratic action:

$$S[x(t)] = \frac{1}{2}\int_{t_0}^{t_1} \mathrm{d}t' \big(m\dot{x}^2 - c(t')x^2\big), \tag{A.20}$$

the Gaussian path integral built from it reads:

$$\int_{x(t_0)=x_0}^{x(t_1)=x_1} \mathcal{D}x(t) \exp(iS[x(t)]) = \left(\frac{m}{2\pi i f(t_1, t_0)}\right)^{1/2} \exp\Big(iS[x_{\mathrm{cl}}(t)]\Big) \tag{A.21}$$

where the function $f(t, t_0)$ satisfies the following linear differential equation:

$$\frac{\partial^2 f}{\partial t^2} + \frac{c(t)}{m} f = 0\,, \qquad f(t_0, t_0) = 0\,, \qquad \partial_{t=t_0} f(t, t_0) = 1 \tag{A.22}$$

and $x_{\rm cl}$ is the classical path, extremum of the action S, with the boundaries conditions $x_{\rm cl}(t_0) = x_0$, $x_{\rm cl}(t_1) = x_1$.

From (A.21), one can find an analytic form for the effective propagator. The dictionary that translates the variable used in (A.21) and those used in (A.19) is:

$$m \leftrightarrow -k^+\,, \qquad c(t) \leftrightarrow -i\frac{\hat{q}_A(\xi)}{2} \tag{A.23}$$

The classical path $r_\perp^{\rm cl}$ satisfies the differential equation:

$$\frac{{\rm d}^2 r_\perp^{\rm cl}}{{\rm d}\xi^2} + \frac{i\hat{q}_A(\xi)}{2k^+} r_\perp^{\rm cl} = 0\,, \qquad r_\perp^{\rm cl}(\bar{y}^+) = b_\perp\,, \qquad r_\perp^{\rm cl}(y^+) = a_\perp \tag{A.24}$$

so that the $S[x_\perp^{\rm cl}(t)]$ reads:

$$S[x_\perp^{\rm cl}(t)] = \frac{-k^+}{2}\left[r_\perp^{\rm cl}(\xi) \frac{{\rm d}r_\perp^{\rm cl}}{{\rm d}\xi} \right]_{\xi=\bar{y}^+}^{\xi=y^+} \tag{A.25}$$

Combining everything together, without forgetting that the path integral (A.19) runs over a 2-dimensional path, one finds precisely the formula (3.106):

$$\mathcal{K}(y^+, a_\perp; \bar{y}^+, b_\perp) = \frac{-k^+}{2\pi i S(y^+, \bar{y}^+)} \exp\left(\frac{-ik^+}{2S(y^+, \bar{y}^+)} \Big(C(\bar{y}^+, y^+) a_\perp^2 + C(y^+, \bar{y}^+) b_\perp^2 - 2 a_\perp b_\perp \Big) \right) \tag{A.26}$$

where the functions S and C have been introduced in the main text as independent scalar solutions of the differential equation (A.24).

Appendix B

Medium-induced spectra for finite jet path length

We provide here the on-shell and off-shell medium induced spectra in the case where the incoming parton has a finite path length L through the medium. Such a finite path length can be implemented with a discontinuous $\hat{q}(t)$ such that $\hat{q}(t) = 0$ for $t \geq x_0^+ + L$. However, in this case, one has to deal with the junction at $t = L$ of the solutions $S(t, t_0)$ and $C(t, t_0)$ of the differential equation (3.107) in such a way that S and C are continuous and derivable in their first argument. A way to circumvent this calculation is to divide the amplitude into three parts, with either $y^+ \leq x_0^+$, or $x_0^+ \leq y^+ \leq L + x_0^+$, or $y^+ \geq x_0^+ + L$. Then, the full on-shell cross-section becomes a sum of six terms (the off-shell one is a sum of three terms). For each term, one inserts the Chapman-Kolmogorov relation in order to use the effective propagator $\mathcal{K}$ on open sets where the form (3.106) is valid, with S and C the solutions of the differential equation (3.107).

The on-shell and off-shell spectra are given by the following sums:

$$k^+ \frac{\mathrm{d}^3 N^{\text{on-shell}}}{\mathrm{d}k^+ \mathrm{d}^2 k_\perp} = \frac{\alpha_s C_R}{\pi^2} \sum_{\substack{m=b,i \\ n=b,i,o}} I^{m/n}\,, \qquad k^+ \frac{\mathrm{d}^3 N^{\text{off-shell}}}{\mathrm{d}k^+ \mathrm{d}^2 k_\perp} = \frac{\alpha_s C_R}{\pi^2} \sum_{\substack{m=i \\ n=i,o}} I^{m/n} \tag{B.1}$$

where the indices b, i and o stands respectively for "before", "in" and "out" according to the integration domain.

B.1 Analytical results for $I^{m/n}$

The analytical results of the six terms $I^{m/n}$, in the multiple soft scattering approximation are:

$$I^{b/b} = \frac{4\pi}{Q_s^2} \int \frac{d^2 q_\perp}{(2\pi)^2} \frac{1}{q_\perp^2} \exp\left(\frac{-(k_\perp - q_\perp)^2}{Q_s^2}\right) \tag{B.2}$$

$$I^{b/i} = 2\mathfrak{Re} \int_{x_0^+}^{x_0^+ + L} \mathrm{d}y^+ \frac{\bar{G}(y^+)}{Q_s^2(y^+) + 2ik^+ \bar{G}(y^+)} \exp\left(\frac{-k_\perp^2}{Q_s^2(y^+) + 2ik^+ \bar{G}(y^+)}\right) \tag{B.3}$$

$$- 2\mathfrak{Re} \int_{x_0^+}^{x_0^+ + L} \mathrm{d}y^+ \frac{G(y^+)}{Q_s^2(y^+) + 2ik^+ G(y^+)} \exp\left(\frac{-k_\perp^2}{Q_s^2(y^+) + 2ik^+ G(y^+)}\right) \tag{B.4}$$

$$I^{b/o} = \frac{2}{k_\perp^2} \mathfrak{Re}\left[\exp\left(\frac{-k_\perp^2}{2ik^+ \bar{G}(x_0^+ + L)}\right) - \exp\left(\frac{-k_\perp^2}{2ik^+ G(x_0^+ + L)}\right)\right] \tag{B.5}$$

$$I^{i/i} = 2\mathfrak{Re}\int_{x_0^+}^{x_0^++L} \mathrm{d}y^+ \frac{G(y^+)}{Q_s^2(y^+)+2ik^+G(y^+)} \exp\left(\frac{-k_\perp^2}{Q_s^2(y^+)+2ik^+G(y^+)}\right) \tag{B.6}$$

$$I^{i/o} = \frac{2}{k_\perp^2}\mathfrak{Re}\left[\exp\left(\frac{-k_\perp^2}{2ik^+G(x_0^++L)}\right)-1\right] \tag{B.7}$$

$$I^{o/o} = \frac{1}{k_\perp^2} \tag{B.8}$$

where $Q_s = Q_s(x_0^+)$.

Note than one cannot recover the formula (3.140) by taking the limit $L \to \infty$ in these formulas. This is because of the adiabatic switching prescription which is not included in the integrals over compact domains.

B.2 Integrated medium-induced spectrum

In this thesis, we have presented two ways of defining the medium-induced spectrum. The first way, which is standard in the literature is to define:

$$k^+\frac{\mathrm{d}N^{\text{mie}}}{\mathrm{d}k^+} \equiv \int \mathrm{d}^2k_\perp \left(k^+\frac{\mathrm{d}^3N^{\text{off-shell}}}{\mathrm{d}k^+\mathrm{d}^2k_\perp} - \frac{\alpha_s C_R}{\pi^2}\frac{1}{k_\perp^2}\right) \tag{B.9}$$

$$= \frac{\alpha_s C_R}{\pi^2}\int \mathrm{d}^2k_\perp \left(I^{i/i}+I^{i/o}\right) \tag{B.10}$$

Each term in this sum leads to a diverging integral, but the divergence cancels exactly in the sum. To see this, it is convenient to write $I^{i/o}$ as a time integral:

$$I^{i/o} = \frac{i}{k^+}\int_{x_0^+}^{x_0^++L} \mathrm{d}\bar{y}^+ \frac{1}{C^2(\bar{y}^+, x_0^++L)} \exp\left(\frac{ik_\perp^2 S(x_0^++L,\bar{y}^+)}{2k^+C(\bar{y}^+,x_0^++L)}\right) \tag{B.11}$$

Integrating over $k_\perp$ both $I^{i/i}$ and $I^{i/o}$, one finds after a bit of algebra:

$$k^+\frac{\mathrm{d}N^{\text{mie}}}{\mathrm{d}k^+} = \frac{2\alpha_s C_R}{\pi}\log\Big(|C(x_0^+, x_0^++L)|\Big) \tag{B.12}$$

Another possibility is to isolate in the on-shell spectrum the contributions without explicit $1/k_\perp^2$ dependence. The full on-shell spectrum for finite path length reads:

$$k^+\frac{\mathrm{d}^3N^{\text{on-shell}}}{\mathrm{d}k^+\mathrm{d}^2k_\perp} = \frac{\alpha_s C_R}{\pi^2}\left(\int\frac{d^2q_\perp}{(2\pi)^2}\frac{1}{q_\perp^2}\exp\left(\frac{-(k_\perp-q_\perp)^2}{Q_s^2}\right)+\frac{1}{k_\perp^2}\left[2\mathfrak{Re}\exp\left(\frac{-k_\perp^2}{2ik^+\bar{G}(x_0^++L)}\right)-1\right]\right.$$
$$\left.+2\mathfrak{Re}\int_{x_0^+}^{x_0^++L}\mathrm{d}y^+\frac{\bar{G}(y^+)}{Q_s^2(y^+)+2ik^+\bar{G}(y^+)}\exp\left(\frac{-k_\perp^2}{Q_s^2(y^+)+2ik^+\bar{G}(y^+)}\right)\right) \tag{B.13}$$

Thus, defining the medium induced spectrum as the $k_\perp$ integral of the last term, one gets:

$$k^+\frac{\mathrm{d}\tilde{N}^{\text{mie}}}{\mathrm{d}k^+} \equiv \frac{2\alpha_s C_R}{\pi^2}\mathfrak{Re}\int\mathrm{d}^2k_\perp\int_{x_0^+}^{x_0^++L}\mathrm{d}y^+\frac{\bar{G}(y^+)}{Q_s^2(y^+)+2ik^+\bar{G}(y^+)}\exp\left(\frac{-k_\perp^2}{Q_s^2(y^+)+2ik^+\bar{G}(y^+)}\right)$$
$$= \frac{2\alpha_s C_R}{\pi}\log\Big(|C(x_0^++L,x_0^+)|\Big) \tag{B.14}$$

For the brick model, where the size of the medium is taken as large as the jet path length, the function C satisfies $C(x,y) = C(y,x)$ so both definitions agree exactly, as emphasized in Chapter 5. In the general case, there is no such symmetry for the function C so $N_{\rm mie}$ and $\tilde{N}_{\rm mie}$ give different results. To see why, let us call λ the typical time scale for the medium dilution. The difference between these two definitions comes from the fact that in $\tilde{N}^{\rm mie}$ there are still implicit vacuum-like components included (due to Bremsstrahlung *after* scattering with the medium since the incoming parton was on its mass shell) when $\bar{G}$ starts behaving like $1/t$ for $t \gtrsim \lambda$, as discussed in Section 4.3.4. If $x_0^+ + L \gg \lambda$, this scenario occurs and leads to the difference observed between the two spectra. If $x_0^+ + L \ll \lambda$, the two spectra tend to an agreement.

B.3 The junction method

To conclude this Appendix, we demonstrate that one recovers formulas (B.2) and (B.6) using the junction method, that is by finding solutions of the differential equation (3.107) continuous and derivable in their first argument.

Example: the brick model. First of all, let us give these solutions in the sinple case of the brick model. The brick model has only two parameters: the constant value $\hat{q}_0$ of the quenching parameter through the path length L of the jet,

$$\hat{q}(t) = \hat{q}_0 \Theta(L-t) \qquad \text{for } t \geq 0 \tag{B.15}$$

The functions $S(t,t_0)$ and $C(t,t_0)$ are defined as the two independent solutions of the differential equation

$$f'' + \frac{i\hat{q}(t)}{2k^+} f = 0 \tag{B.16}$$

with initial conditions $S(t_0,t_0) = 0$, $\partial_{t=t_0} S(t,t_0) = 1$ and $C(t_0,t_0) = 1$, $\partial_{t=t_0} C(t,t_0) = 0$. In particular, S and C must be continuous and derivable as functions of t. The method to solve (B.16) for all $t \in [0,\infty[$ is to solve it on $t \in [0,L[$ and $t \in]L,\infty[$ before adjusting the constants such that S and C have the right initial conditions *and* are continuous and derivable in $t = L$.

One finds, with $\Omega^2 \equiv i\hat{q}_0/(2k^+)$:

$$\begin{aligned} S(t,t_0) = \Theta(L-t_0)\Big[&\Theta(L-t)\Omega^{-1}\sin\big(\Omega(t-t_0)\big) \\ &+ \Theta(t-L)\Big((t-L)\cos\big(\Omega(L-t_0)\big) + \Omega^{-1}\sin\big(\Omega(L-t_0)\big)\Big)\Big] \\ &+ \Theta(t_0-L)\Big[\Theta(t-L)(t-t_0) \\ &+ \Theta(L-t)\Big((L-t_0)\cos\big(\Omega(L-t)\big) - \Omega^{-1}\sin\big(\Omega(L-t)\big)\Big)\Big] \end{aligned} \tag{B.17}$$

and

$$\begin{aligned} C(t,t_0) = \Theta(L-t_0)\Big[&\Theta(L-t)\cos\big(\Omega(t-t_0)\big) \\ &+ \Theta(t-L)\Big(\cos\big(\Omega(L-t_0)\big) + \Omega(L-t)\sin\big(\Omega(L-t_0)\big)\Big)\Big] \\ &+ \Theta(t_0-L)\Big[\Theta(t-L) + \Theta(L-t)\cos\big(\Omega(L-t)\big)\Big] \end{aligned} \tag{B.18}$$

One notices that $S(t,t_0)$ is also continuous and derivable as a function of t_0, whereas $C(t,t_0)$ is only continuous as a function of t_0. Moreover, one has the relation $C(t,t_0) = C(t_0,t)$ for all $t \leq L$, but *not* for all t values.

Junction in the general case. To deal with the general case, one notices that if one has the continuous and derivable solutions $\tilde{S}(t,t_0)$ and $\tilde{C}(t,t_0)$, then the functions $\tilde{G}(t)$ and $\tilde{\bar{G}}(t)$ defined in (3.128)-(3.132) are continuous and their derivative are piece-wise continuous. One can then find $\tilde{G}^{-1}(t)$ and $\tilde{\bar{G}}(t)$ as continuous solutions of the differential equations (3.130) and (3.135). This means that the function $\tilde{G}^{-1}(t)$ satisfies:

$$\tilde{G}^{-1}(t_0) = 0 \tag{B.19}$$

$$\frac{\mathrm{d}\tilde{G}^{-1}}{\mathrm{d}t} = 1 + \frac{i\hat{q}(t)}{2k^+}\tilde{G}^{-2} \qquad \text{if } t_0 \leq t < t_0 + L \tag{B.20}$$

$$\lim_{\epsilon\to 0} \tilde{G}^{-1}(t_0 + L - \epsilon) = \tilde{G}^{-1}(t_0 + L + \epsilon) \tag{B.21}$$

$$\frac{\mathrm{d}\tilde{G}^{-1}}{\mathrm{d}t} = 1 \qquad \text{if } t > t_0 + L \tag{B.22}$$

The solution of this problem is

$$\tilde{G}^{-1}(t) = \Theta(L + t_0 - t)G^{-1}(t) + \Theta(t - L - t_0)\Big(t - t_0 - L + G^{-1}(t_0 + L)\Big) \tag{B.23}$$

with G^{-1} the solution of (B.19) and (B.20). This relation is also true for $\tilde{\bar{G}}$ if one replace G by $\bar{G}$, solution of $\bar{G}' + \bar{G}^2 + i\hat{q}(t)/(2k^+) = 0$ and $\bar{G}(t_0) = 0$. Using these expressions in the on-shell or off-shell cross-section (3.140)-(3.129) calculated in Chapter 3, one finds the expressions (B.2) and (B.6).

Appendix C

Splitting functions

In this Appendix, we give our conventions for the splitting functions used in this thesis.

C.1 Vacuum (DGLAP) splitting functions

We use the leading order unregularised DGLAP splitting functions. In the notation $\Phi_a^{bc}(z)$, a refers to the parent parton, b to the daughter parton carrying the splitting fraction z and c the daughter parton carrying the splitting fraction $1-z$.

$$\Phi_q^{gq}(z) = C_F \frac{1+(1-z)^2}{z} \tag{C.1}$$

$$\Phi_q^{qg}(z) = C_F \frac{1+z^2}{1-z} \tag{C.2}$$

$$\Phi_g^{gg}(z) = 2C_A \left(\frac{1-z}{z} + \frac{z}{1-z} + z(1-z) \right) \tag{C.3}$$

$$\Phi_g^{q\bar{q}}(z) = n_f T_R \Big(z^2 + (1-z)^2 \Big) \tag{C.4}$$

with obviously $\Phi_g^{q\bar{q}}(z) = \Phi_g^{\bar{q}q}(z)$. These are the building rates for the generating functional 4.10 in Chapter 4.

For $i \in \{q, g\}$, we note $P_i(z)$ the i-splitting function summed over all distinct decay channels:

$$P_i(z) \equiv \frac{1}{2!} \sum_{(a,b)} \Phi_i^{ab}(z) \tag{C.5}$$

These splitting functions are convenient when one wants to implement the master equation (4.10) in a Monte Carlo parton shower. When these splitting functions are integrated between 0 and 1, one can exploit the $z \leftrightarrow 1-z$ symmetry to write them in such a way that the soft singularity is only at $z = 0$:

$$P_q(z) = C_F \frac{1+(1-z)^2}{z} \tag{C.6}$$

$$P_g(z) = C_A \left(2\frac{1-z}{z} + z(1-z) + \frac{n_f T_R}{C_A} \big(z^2 + (1-z)^2 \big) \right) \tag{C.7}$$

C.2 Medium splitting functions

When there is no explicit mention of the contrary, $\hat{q}$ always refers to the adjoint $\hat{q}_A$. Hence, in (4.57), there is a $\sqrt{C_A}$ factored out so that the medium-modified splitting kernels $\mathcal{K}_i^{ab}(z)$ read:

$$\mathcal{K}_q^{qg}(z) = C_F \frac{1+(1-z)^2}{z} \sqrt{\frac{C_F}{C_A} z^2 + (1-z)} \tag{C.8}$$

$$\mathcal{K}_q^{qg}(z) = C_F \frac{1+z^2}{1-z} \sqrt{\frac{C_F}{C_A} (1-z)^2 + z} \tag{C.9}$$

$$\mathcal{K}_g^{gg}(z) = 2C_A \frac{(1-z(1-z))^2}{z(1-z)} \sqrt{(1-z)+z^2} \tag{C.10}$$

$$\mathcal{K}_g^{q\bar{q}}(z) = n_f T_R \Big(z^2 + (1-z)^2\Big) \sqrt{\frac{C_F}{C_A} + z(1-z)} \tag{C.11}$$

As for the vacuum splitting functions, we define $\mathcal{K}_i(z)$ as the splitting function of a parton $i \in \{q, g\}$ summed over all distinct decay channels:

$$\mathcal{K}_i(z) \equiv \frac{1}{2!} \sum_{(a,b)} \mathcal{K}_i^{ab}(z) \tag{C.12}$$

or more explicitly,

$$\mathcal{K}_q(z) = \frac{1}{2}\Big(\mathcal{K}_q^{qg}(z) + \mathcal{K}_q^{gq}(z)\Big) \tag{C.13}$$

$$\mathcal{K}_g(z) = \frac{1}{2}\Big(\mathcal{K}_g^{gg}(z) + 2\mathcal{K}_g^{q\bar{q}}(z)\Big) \tag{C.14}$$

Appendix D

Large x jet fragmentation to NLL accuracy

Eq. (4.18) can be deduced from the coherent branching algorithm which resums to all orders leading and next-to-leading logarithms of the form $-\alpha_s \log(1-x)$. Since the fragmentation function is not IRC safe, we introduce a lower transverse momentum cut-off $k_{\perp,\min}$ for any resolvable splitting. The final result strongly depends on $k_{\perp,\min}$ so we need to keep track of any $k_{\perp,\min}$ dependence in the calculation.

D.1 Strict NLL result

We focus on quark-initiated jets and the generalization to gluon-jets is straightforward. To NLL accuracy, one can neglect the quark/gluon mixing terms. We discuss this approximation at the end of this appendix. The MLLA equation for the quark cumulative fragmentation function (10.4) is (integrating (4.17) over x):

$$Q\frac{\partial \Sigma_q(x,Q)}{\partial Q} = \int_0^1 \mathrm{d}z\, K_q^q(z,k_\perp)\left[\Sigma_q\Big(\frac{x}{z},zQ\Big)-\Sigma_q(x,Q)\right] \tag{D.1}$$

where the evolution variable is $Q = p_{T0}\theta$ to account for the ordering in the angle θ of successive emissions and the kernel is

$$K_q^q(z,k_\perp) = \frac{\alpha_s(k_\perp)}{\pi}\Phi_q^{qg}(z)\Theta(k_\perp - k_{\perp,\min}) \tag{D.2}$$

The initial condition for (D.1) is $\Sigma_q(x, k_\perp = k_{\perp,\min}) = \Theta(1-x)$. At NLL accuracy, $k_\perp = z(1-z)Q \simeq (1-z)Q$ and $\Sigma_q(\frac{x}{z}, zQ) \simeq \Sigma_q(\frac{x}{z}, Q)$ since the dominant contribution for $x \simeq 1$ comes from $z \simeq 1$. In Mellin space, one can solve this equation with our approximations. Anticipating our resummed result, we note $\lambda_j = \alpha_s \log(j)$ and $\lambda_0 = \alpha_s \log(p_{T0}R/k_{\perp,\min}) = \alpha_s L_0$, so that the Mellin transform of Σ reads:

$$\log(j\tilde{\Sigma}_q(j,p_{T0}R)) = \int_{Q_0}^{p_{T0}R}\frac{\mathrm{d}Q'}{Q'}\int_0^1 \mathrm{d}z\,(z^j-1)K_q^q(z,Q') \tag{D.3}$$

$$= \frac{C_F}{\pi\beta_0}\left[\log(j)\left(1-\log\Big(\frac{1-2\beta_0\lambda_j}{1-2\beta_0\lambda_0}\Big)+\frac{\log(1-2\beta_0\lambda_j)}{2\beta_0\lambda_j}\right)\right.$$
$$\left.-\gamma_E\log\Big(\frac{1-2\beta_0\lambda_j}{1-2\beta_0\lambda_0}\Big)+B_q\log(1-2\beta_0\lambda_0)\right]+\mathcal{O}(\alpha_s\lambda_j^n,\alpha_s\lambda_0^n), \tag{D.4}$$

where we used the standard trick $z^j - 1 \simeq -\Theta(e^{-\gamma_E}/j - z)$ valid at NLL accuracy and we kept only the singular and finite part $B_q = -3/4$ of the quark splitting function when $z \simeq 1$. Eq. (D.4) resums to all orders leading and next-to-leading logarithms of the form λ_j, λ_0. More explicitly,

$$\log(j\tilde{\Sigma}_q^{\rm NLL}(j, p_{T0}R)) = \log(j) g_1(\lambda_j, \lambda_0) + f_2(\lambda_j, \lambda_0) \tag{D.5}$$

$$g_1(u, v) = \frac{C_F}{\pi\beta_0}\left[1 - \log\left(\frac{1-2\beta_0 u}{1-2\beta_0 v}\right) + \frac{\log(1-2\beta_0 u)}{2\beta_0 u}\right] \tag{D.6}$$

$$f_{2,q}(u, v) = \frac{C_F}{\pi\beta_0}\left[-\gamma_E \log\left(\frac{1-2\beta_0 u}{1-2\beta_0 v}\right) + B_q \log(1-2\beta_0 v)\right] \tag{D.7}$$

The final step is to calculate the inverse Mellin transform of (D.4).

$$\Sigma_q(x) = \frac{1}{2\pi i}\int_{\mathcal{C}} \frac{{\rm d}j}{j}\, e^{-j\log(x)}\left(j\tilde{\Sigma}_q(j)\right) = \frac{1}{2\pi i}\int_{\mathcal{C}} {\rm d}u\, e^{u - \log(u) + G_q[\log(u) - \log(-\log(x))]} \tag{D.8}$$

where $\mathcal{C}$ is a contour parallel to the imaginary axis and $G_q[\log(j)] \equiv \log(j\tilde{\Sigma}_q(j))$. For this, we Taylor-expand the function G_q around $L = -\log(-\log(x)) \simeq -\log(1-x)$.

$$G_q[L + \log(u)] = G_q[L] + \log(u) G_q'[L] + \sum_{k=2}^{\infty} \log(u)^k \frac{G_q^{(k)}[L]}{k!} \tag{D.9}$$

For $k \geq 2$, $G_q^{(k)}[L]$ is certainly beyond NLL accuracy because the derivatives of $\alpha_s\beta_0 L$ with respect to L bring always at least one extra α_s factor. Thus, we truncate the expansion up to the first derivative. Moreover, the derivative of $f_{2,q}(\alpha_s L, \alpha_s L_0)$ with respect to L is also sub-leading. Finally, using

$$\frac{1}{2\pi i}\int_{\mathcal{C}} {\rm d}u\, e^{u + x\log(u)} = \frac{1}{\Gamma(-x)} \tag{D.10}$$

one gets the following result for the cumulative distribution:

$$\Sigma_q^{\rm NLL}(x, p_{T0}R) = \frac{e^{G_q[L]}}{\Gamma(1 - G_q'[L])} = \frac{\exp\left(L g_1(\alpha_s L, \alpha_s L_0) + f_{2,q}(\alpha_s L, \alpha_s L_0)\right)}{\Gamma\left(1 - \frac{\partial u g_1(u, \alpha_s L_0)}{\partial u}_{|u=\alpha_s L}\right)} \tag{D.11}$$

which is exactly (4.16), (4.18).

D.2 Sub-leading j contributions and quark/gluon mixing terms.

Besides N^{2}LL contributions, we have neglected terms of order $\mathcal{O}(\alpha_s^n \log^n(j)/j)$ in formulas (D.1) and (D.4). Among such terms, those associated with quark/gluon mixing give sizeable numerical corrections to the NLL results, especially in the gluon-jet case. The main reason for this is that, even though the (power-suppressed) probability for a gluon to split in a $q\bar{q}$ pair where the quark carries most of the momentum ($x \sim 1$) is much smaller than the probability to find a hard gluon, once such a splitting occurs, the Sudakov appearing in (D.11) becomes that of a quark, i.e. has a much smaller suppression because of the colour factor $C_F < C_A$ appearing in the exponential. In the inclusive fragmentation function, this becomes an increasingly likely situation [276].

Including all terms of order $\mathcal{O}(\alpha_s^n \log^n(j)/j)$ is beyond the scope of this simple analysis of the large x behaviour of the fragmentation function. Instead, one can correct Eq. (D.11) for gluon jets with an additional piece $\Sigma_{g,\mathrm{mix}}(x, p_{T0}R)$ describing the splitting of the gluon in a $q\bar{q}$ pair, with either the quark or the antiquark carrying a large fraction x of the initial energy:

$$\begin{aligned}\Sigma_{g,\mathrm{mix}}(x, p_{T0}R) = &\int_0^{1-x} \mathrm{d}\xi\, P_g^q(\xi) \int_0^R \frac{\mathrm{d}\theta}{\theta} \frac{\alpha_s(\xi p_{T0}\theta)}{\pi} \Theta(\xi p_{T0}\theta - k_{\perp,\min}) \\ &\times \exp\left(-\frac{2C_A}{\pi} \int_\xi^1 \frac{\mathrm{d}z}{z} \int_\theta^R \frac{\mathrm{d}\theta'}{\theta'} \alpha_s(z p_{T0}\theta') \Theta(z p_{T0}\theta' - k_{\perp,\min})\right) \\ &\times \exp\left(-\frac{2C_F}{\pi} \int_\xi^1 \frac{\mathrm{d}z}{z} \int_0^\theta \frac{\mathrm{d}\theta'}{\theta'} \alpha_s(z p_{T0}\theta') \Theta(z p_{T0}\theta' - k_{\perp,\min})\right) \end{aligned} \tag{D.12}$$

with $P_g^q(\xi) = 2n_f T_R(\xi^2 + (1-\xi)^2) \simeq 2n_f T_R$ since $\xi \leq 1 - x \ll 1$. In Mellin space, this is equivalent to solve the linear differential equation with an inhomogeneous term associated with the non-diagonal elements of the kernel matrix. In Fig. 4.1, the analytical "NLL" curve for gluon jets is actually $\Sigma_g^{\mathrm{NLL}}(x) + \Sigma_{g,\mathrm{mix}}(x)$.

Appendix E

The ISD fragmentation function to NLL accuracy

This Appendix deals with the fragmentation function from subjets built from the Iterative Soft Drop procedure as explained in Chapter 4, Section 4.2.3.3. We aim at calculating this observable to next-to-leading accuracy in the soft sector. The large logarithms in this case are $L = \log(1/z)$ and $L_{\rm cut} = \log(1/z_{\rm cut})$.

We start with the evolution equation for the fragmentation function $\vec{D}_{\rm ISD}(z,Q)$ obtained from the master equation (4.38). The logarithmic counting is actually easier when considering the cumulative fragmentation function $\vec{\Sigma}_{\rm ISD}(z,Q)$ and its logarithmic expansion (4.40). The validity of our successive approximations can be checked at the level of the evolution equation satisfied by $\vec{\Sigma}_{\rm ISD}$ which is directly deduced from the following equation:

$$\frac{\partial \vec{D}_{\rm ISD}(z,Q)}{\partial \log(Q)} = \frac{\alpha_s(k_\perp)}{\pi}\Theta_{\rm cut}(z,Q)\vec{P}_{\rm sym}(z) + \int_0^{1/2} {\rm d}z' \Big([{\rm LL}](z',Q)\vec{D}_{\rm ISD}(z',Q) + [{\rm NLL}](z',Q)\big(\vec{D}_{\rm ISD}(z',(1-z')Q) - \vec{D}_{\rm ISD}(z',Q)\big)\Big) \tag{E.1}$$

with $\vec{P}_{\rm sym}(z)$ is the symmetrized splitting function defined as

$$\vec{P}_{\rm sym}(z) = \begin{pmatrix} \Phi_q^{gq}(z) + \Phi_q^{qg}(z) \\ \Phi_g^{gg}(z) + 2\Phi_g^{q\bar{q}}(z) \end{pmatrix} \tag{E.2}$$

The transverse momentum is equal to $k_\perp = z(1-z)Q$ and the matrices [LL] and [NLL] are:

$$[{\rm LL}](z,Q) = \frac{\alpha_s(k_\perp)}{\pi}\Theta_{\rm cut}(z,Q) \begin{pmatrix} -\Phi_q^{qg}(z) & \Phi_q^{qg}(z) \\ 2\Phi_g^{q\bar{q}}(z) & -2\Phi_g^{q\bar{q}}(z) \end{pmatrix} \tag{E.3}$$

$$[{\rm NLL}](z,Q) = \frac{\alpha_s(k_\perp)}{\pi}\Theta_{\rm cut}(z,Q) \begin{pmatrix} \Phi_q^{gq}(z) & \Phi_q^{qg}(z) \\ 2\Phi_g^{q\bar{q}}(z) & \Phi_g^{gg}(z) \end{pmatrix} \tag{E.4}$$

The step function constrains emissions to satisfy the Soft Drop condition, noting $\bar{Q} = p_T R$:

$$\Theta_{\rm cut}(z,Q) = \Theta\big(z - z_{\rm cut}(Q/\bar{Q})^\beta\big) \tag{E.5}$$

E.1 LL analytic result

As explained in the Section 4.2.3.3, one can neglect the NLL matrix to LL accuracy, since the difference $\vec{D}_{\rm ISD}(z',(1-z')Q) - \vec{D}_{\rm ISD}(z',Q)$ regulates the soft divergence of the splitting

functions. In the LL matrix, using $\alpha_s(z(1-z)Q) = \alpha_s(Q)(1 - 2\alpha_s(Q)\beta_0 \log(z(1-z)))$, one sees that one can approximate $\alpha_s(k_\perp)$ by $\alpha_s(Q)$ since the next term generates one extra-power of α_s which is not compensated by a soft logarithmic singularity in the z integration. Finally, in the term proportional to $\vec{P}_{\rm sym}(z)$, one cannot neglect the z dependence inside α_s since the extra α_s power is compensated by the soft singularity of the splitting function. Therefore, one gets the equation (4.41):

$$\frac{\partial \vec{D}_{\rm ISD}(z,Q)}{\partial \log(Q)} = \frac{2\vec{C}_R}{\pi}\frac{\alpha_s(zQ)}{z}\Theta_{\rm cut} + \frac{\alpha_s(Q)}{\pi}[F]\vec{D}_{\rm ISD}(z,Q) \tag{E.6}$$

with the matrix $[F]$ defined as:

$$\begin{pmatrix} -f_F & f_F \\ f_A & -f_A \end{pmatrix} \equiv \int_0^{1/2} \mathrm{d}z \begin{pmatrix} -\Phi_q^{qg}(z) & \Phi_q^{gg}(z) \\ \Phi_g^{q\bar{q}}(z) & -\Phi_g^{q\bar{q}}(z) \end{pmatrix} = \begin{pmatrix} -C_F\left(2\log(2) - \frac{5}{8}\right) & C_F\left(2\log(2) - \frac{5}{8}\right) \\ \frac{2n_f T_R}{3} & -\frac{2n_f T_R}{3} \end{pmatrix} \tag{E.7}$$

This equation can be solved using the variation of parameters method. The general solution of the homogeneous equation vanishes because of the initial condition $\vec{D}^{\rm LL}_{\rm ISD}(z, Q=0) = \vec{0}$, so that only the particular solution remains:

$$\vec{D}^{\rm LL}_{\rm ISD}(z) = \int_0^{p_T R} \frac{\mathrm{d}Q'}{Q'}\frac{2}{\pi}\frac{\alpha_s(zQ')}{z}\Theta_{\rm cut}(z,Q')\exp\left(\int_{Q'}^{p_T R}\frac{\mathrm{d}Q''}{Q''}\frac{\alpha_s(Q'')}{\pi}[F]\right)\vec{C}_R \tag{E.8}$$

The matrix exponential can be calculated exactly:

$$\exp\left(\lambda(Q')\begin{pmatrix} -f_F & f_F \\ f_A & -f_A \end{pmatrix}\right) = \frac{1}{f_A + f_F}\begin{pmatrix} f_A + f_F e^{-\lambda(Q')(f_A+f_F)} & f_F - f_F e^{-\lambda(Q')(f_A+f_F)} \\ f_A - f_A e^{-\lambda(Q')(f_A+f_F)} & f_F + f_A e^{-\lambda(Q')(f_A+f_F)} \end{pmatrix} \tag{E.9}$$

with (noting $\alpha_0 = \alpha_s(p_T R)$,)

$$\lambda(Q') \equiv \int_{Q'}^{p_T R}\frac{\mathrm{d}Q''}{Q''}\alpha_s(Q'') = -\frac{1}{2\pi\beta_0}\log\left(1 + 2\alpha_0\beta_0\log(Q'/(p_T R))\right) \tag{E.10}$$

After some algebra, the remaining integral over Q' gives the result (4.43). In particular, the terms without exponential factors give the term proportional to the function f_0 in (4.43), whereas the others can be integrated explicitly using the incomplete Gamma function.

E.2 NLL equivalent equation

One can find an equation equivalent to (E.1) at NLL accuracy, with a more suitable form for both analytical and numerical analysis. It is convenient to introduce the following set of matrices:

$$[F_2] \equiv \int_0^{1/2}\mathrm{d}z\begin{pmatrix} -\Phi_q^{qg}(z)\log(z) & \Phi_q^{gg}(z)\log(z) \\ \Phi_g^{q\bar{q}}(z)\log(z) & -\Phi_g^{q\bar{q}}(z)\log(z) \end{pmatrix} \tag{E.11}$$

$$= \begin{pmatrix} \frac{C_F}{48}\left(8\pi^2 + 3(1+2\log(2))(-9+8\log(2))\right) & \frac{-C_F}{48}\left(8\pi^2 + 3(1+2\log(2))(-9+8\log(2))\right) \\ \frac{-n_f T_R}{72}\left(29 + 24\log(2)\right) & \frac{n_f T_R}{72}\left(29 + 24\log(2)\right) \end{pmatrix}$$

$$[E] \equiv \int_0^{1/2}\mathrm{d}z\begin{pmatrix} \Phi_q^{gq}(z)\log(1-z) & \Phi_q^{gg}(z)\log(1-z) \\ 2\Phi_g^{q\bar{q}}(z)\log(1-z) & \Phi_g^{gg}(z)\log(1-z) \end{pmatrix} \tag{E.12}$$

$$= \begin{pmatrix} \frac{C_F}{48}\left(33 - 8\pi^2 + 6\log(2)(8\log(2)-5)\right) & \frac{-C_F}{16}\left(-13 + 2\log(2)(7+8\log(2))\right) \\ \frac{n_f T_R}{72}\left(24\log(2) - 23\right) & \frac{-C_A}{72}\left(12\pi^2 + 132\log(2) - 131\right) \end{pmatrix}$$

and to write the differential equation (E.1) in terms of $t \equiv \log(Q/\bar{Q})$, $\bar{Q} = p_T R$. Using the trick

$$\vec{D}_{\rm ISD}(z', t + \log(1-z')) - \vec{D}_{\rm ISD}(z', t) = \log(1-z')\frac{\partial \vec{D}_{\rm ISD}(z', t)}{\partial t} + \mathcal{O}\big(\alpha_0^{n+2}\log^n\big) \tag{E.13}$$

one can rewrite (E.1) as:

$$\frac{\partial \vec{D}^{\rm NLL}_{\rm ISD}(z,t)}{\partial t} = \frac{\alpha_s(k_\perp)}{\pi}\Theta_{\rm cut}(z, \bar{Q}e^t)\vec{P}_{\rm sym}(z) + \left(\frac{\alpha_s(\bar{Q}e^t)}{\pi}[F] - \frac{2\alpha_0^2\beta_0}{\pi}[F_2]\right)\vec{D}^{\rm NLL}_{\rm ISD}(z,t) + \frac{\alpha_s(\bar{Q}e^t)}{\pi}[E]\frac{\partial \vec{D}^{\rm NLL}_{\rm ISD}(z,t)}{\partial t} \tag{E.14}$$

The last term is a consequence of the fact that at NLL accuracy, one must take into account the energy recoil of the hard branch. The term proportional to $\alpha_0^2[F_2]$ comes from the z dependence of the transverse momentum $k_\perp$ in the matrix [LL]. It must be included as it is of the same logarithmic order as the term proportional to $[E]$.

Equation (E.14) can be further simplified by putting the last term of (E.14) on the left hand side of the equation, and multiplying by the inverse matrix:

$$\left(\mathbb{1} - \frac{\alpha_s(\bar{Q}e^t)}{\pi}[E]\right)^{-1} \simeq \mathbb{1} + \frac{\alpha_s(\bar{Q}e^t)}{\pi}[E] + \mathcal{O}\big(\alpha_s^2(Q)\big) \tag{E.15}$$

one gets, using $\alpha_s^2(\bar{Q}e^t)D^{\rm NLL}_{\rm ISD} = \alpha_0^2 D^{\rm NLL}_{\rm ISD}$ at our accuracy,

$$\frac{\partial \vec{D}^{\rm NLL}_{\rm ISD}(z,t)}{\partial t} = \frac{\alpha_s(z\bar{Q}e^t)}{\pi}\Theta_{\rm cut}(z,\bar{Q}e^t)\vec{P}_{\rm sym}(z) + \frac{\alpha_s(\bar{Q}e^t)\alpha_s(z\bar{Q}e^t)}{\pi^2}\Theta_{\rm cut}(z,\bar{Q}e^t)[E]\vec{P}_{\rm sym}(z) + \left(\frac{\alpha_s(\bar{Q}e^t)}{\pi}[F] - \frac{2\alpha_0^2\beta_0}{\pi}[F_2] + \frac{\alpha_0^2}{\pi^2}[E][F]\right)\vec{D}^{\rm NLL}_{\rm ISD}(z,t) \tag{E.16}$$

Finally, one notices that $\alpha_0^2 D^{\rm NLL}_{\rm ISD} = \alpha_0^2 D^{\rm LL}_{\rm ISD} + \mathcal{O}(\alpha_0^{n+2}\log^n)$ at NLL precision. This enables to put the terms proportional to α_0^2 in the inhomogeneous term of the differential equation, since $D^{\rm LL}_{\rm ISD}$ is known exactly. Using $\vec{P}_{\rm sym}(z) \simeq 2\vec{C}_R/z + \vec{B}_R$, where B_i is the finite part of the splitting function, one can put the NLL differential equation into the form (4.47) with the inhomogeneous term $\vec{C}_{\rm NLL}(z,Q)$ reading:

$$\vec{C}_{\rm NLL}(z,Q) = \frac{\alpha_s(zQ)}{\pi}\frac{2}{z}\Theta_{\rm cut}(z,Q)\left(\mathbb{1} + \frac{\alpha_s(Q)}{\pi}[E]\right)\vec{C}_R + \frac{\alpha_s(Q)}{\pi}\Theta\big(Q - p_T R(2z_{\rm cut})^{-1/\beta}\big)\vec{B}_R + \left(\frac{\alpha_0^2}{\pi^2}[E][F] - \frac{2\alpha_0^2\beta_0}{\pi}[F_2]\right)\vec{D}^{\rm LL}_{\rm ISD}(z,Q) \tag{E.17}$$

This allows for a straightforward evaluation of the solution of (4.47) given the initial conditions:

$$\vec{D}^{\rm NLL}_{\rm ISD}(z) = \int_0^{p_T R}\frac{{\rm d}Q'}{Q'}\exp\left(\lambda(Q')\begin{pmatrix}-f_F & f_F\\ f_A & -f_A\end{pmatrix}\right)\vec{C}_{\rm NLL}(z,Q') \tag{E.18}$$

Since the homogeneous term involves only the matrix $[F]$, its exponential has the simple form (E.9).

Other NLL corrections. To claim a full NLL answer for $\vec{D}^{\rm NLL}_{\rm ISD}(z)$, one should also include the two-loop running coupling and splitting functions corrections. These corrections can be incorporated in the function $\vec{C}_{\rm NLL}(z,Q)$ by adding the standard correction $\delta\vec{C}^{\rm 2-loops}(z,Q)$:

$$\delta\vec{C}^{\rm 2-loops}(z,Q) = -\frac{\alpha_0^2\beta_1}{\pi\beta_0}\frac{1}{z}\frac{\log(1+\alpha_0\beta_0\log(zQ)}{(1+\alpha_0\beta_0\log(zQ))^2}\vec{C}_R + \frac{K}{2\pi^2}\frac{\alpha_s^2(zQ)}{z}\vec{C}_R \tag{E.19}$$

where K is the universal two-loop cusp anomalous dimension.

Appendix F

Vacuum-like patterns in the off-shell and on-shell gluon spectra in a dense medium

The purpose of this Appendix is twofold:

1. we want to show that decomposing the off-shell spectrum according to time integration domains is ambiguous and can lead to unphysical results, such as (F.10). In the presence of a dense medium in a finite volume, the quantum formation process is intricate and vacuum formation time arguments can be misleading.

2. for this reason, we prefer the more physical decomposition given by (5.22) which is presented in Chapter 5. We thus demonstrate formula (5.24) and (5.25) as promised.

F.1 Decomposition of the off-shell spectrum from time domains

This section aims at explaining where the Bremsstrahlung contributions in the off-shell spectrum (3.141) comes from in the time integral. The results obtained in this section correspond to those obtained in [124]. As we use analytic expressions valid in the expanding medium case, this analysis can be straightforwardly extended for expanding media using for instance the Taylor expansion method as in Chapter 5, Section 6.1.

Let us begin with a rewriting of the result obtained in (3.141) in a physically more transparent way:

$$\omega\frac{\mathrm{d}^3N^{\text{off-shell}}}{\mathrm{d}\omega\mathrm{d}^2k_\perp}=\frac{\alpha_sC_F}{\pi^2}\left[2\mathfrak{Re}\frac{1}{2i\omega}\int_0^\infty\mathrm{d}y^+\int\mathrm{d}^2q_\perp\,\mathcal{P}(k_\perp-q_\perp,y^+,\infty)\exp\left(\frac{-q_\perp^2G^{-1}(y^+)}{2i\omega}\right)-\frac{1}{k_\perp^2}\right] \tag{F.1}$$

where the ε prescription is implicit. In this form, the final state broadening of the gluon between y^+ and ∞ is convoluted with the emission spectrum *at formation*. Setting by hand $\mathcal{P}(k_\perp-q_\perp)=\delta(k_\perp-q_\perp)$ to remove the effect of broadening, all the physics of the medium is encoded in the function $G(y^+)$ defined in (3.128) (with $x_0^+=0$ in this case.) In the special case of a static medium with constant $\hat{q}$, the function $G^{-1}(y^+)$ is particularly simple (see the derivation in Appendix B):

$$G^{-1}(y^+)=\begin{cases} j\sqrt{\frac{2\omega}{\hat{q}}}\tanh\left(\bar{j}\sqrt{\frac{\hat{q}}{2\omega}}y^+\right) & \text{if } y^+\leq L\\ y^+-L\Big[1-j\sqrt{\frac{\omega}{\omega_c}}\tanh\left(\bar{j}\sqrt{\frac{\omega_c}{\omega}}\right)\Big]\underset{\omega\ll\omega_c}{\approx}y^+-L & \text{if } y^+\geq L\end{cases} \tag{F.2}$$

with $j \equiv (1+i)/\sqrt{2}$ and L is the path length in the medium.

Vacuum formation time. Emission is a quantum process which is not localized in time. The so-called "vacuum formation time" $t_f = 2\omega/k_\perp^2$ which has been derived before from the Heisenberg inequality comes mathematically from the analysis of the integral giving the Bremsstrahlung spectrum in the vacuum:

$$\omega\frac{\mathrm{d}^3N^{\mathrm{brem}}}{\mathrm{d}\omega\mathrm{d}^2k_\perp} = \frac{\alpha_s C_F}{\pi^2}\frac{k_\perp^2}{4\omega^2}2\mathfrak{Re}\int_0^\infty \mathrm{d}y^+\int_0^\infty \mathrm{d}\bar{y}^+ e^{-\varepsilon(y^+ + \bar{y}^+)}e^{ik^-(y^+-\bar{y}^+)} \tag{F.3}$$

Hence, the phase in the exponential is controlled by the scale $k^- = k_\perp^2/(2k^+) = k_\perp^2/(2\omega)$ so that:

$$t_f \equiv |y^+ - \bar{y}^+| \sim \frac{2\omega}{k_\perp^2} \tag{F.4}$$

for Bremsstrahlung emissions in the vacuum. At the level of the amplitude of the process, this formation time controls also the phase of the integral. Consequently, in the vacuum, one has also:

$$t_f \sim y^+ \sim \bar{y}^+ \tag{F.5}$$

In our derivation of the BDMPS-Z spectrum, we have used our lemma (3.122) to integrate over the time $\bar{y}^+$ in the complex conjugate amplitude in order to obtain compact expressions well suited for a numerical analysis. The price to pay is that a spurious $-1/k_\perp^2$ term is generated, spoiling the symmetry of the result all over $k_\perp$. This term comes from a region with y^+ and $\bar{y}^+$ much larger than the typical length of the medium. However, it is to be associated with vacuum-like processes with unconstrained formation time t_f since $y^+ - \bar{y}^+$ can be as small or as large as desired.

The off-shell spectrum at formation. Setting by hand $\mathcal{P}(k_\perp - q_\perp) = \delta(k_\perp - q_\perp)$ to remove the effect of broadening, this spectrum at formation becomes simply the emission *rate* integrated over time:

$$\omega\frac{\mathrm{d}^3N^{\text{off-shell,f}}}{\mathrm{d}\omega\mathrm{d}^2k_\perp} = \frac{\alpha_s C_F}{\pi^2}\left[2\mathfrak{Re}\frac{1}{2i\omega}\int_0^\infty \mathrm{d}y^+\,\exp\left(\frac{-k_\perp^2 G^{-1}(y^+)}{2i\omega}\right) - \frac{1}{k_\perp^2}\right] \tag{F.6}$$

From (F.1), one sees that when the function $G^{-1}(y^+)$ is of the form $G^{-1}(y^+) \sim y^+ + cste$, the spectrum at formation (without broadening) develops a collinear singularity proportional to $1/k_\perp^2$. More precisely, if $G^{-1}(y^+) \sim y^+$ for $y^+ \leq y_1^+$ for instance, the integral in (F.6) gives:

$$2\mathfrak{Re}\frac{1}{2i\omega}\int_0^{t_1} \mathrm{d}y^+\,\exp\left(\frac{-k_\perp^2 G^{-1}(y^+)}{2i\omega}\right) \simeq 2\mathfrak{Re}\frac{1}{2i\omega}\int_0^{y_1^+} \mathrm{d}y^+\,\exp\left(\frac{-k_\perp^2 y^+}{2i\omega}\right) \tag{F.7}$$

$$= \frac{2}{k_\perp^2}\mathfrak{Re}\left(1 - e^{\frac{-k_\perp^2 y_1^+}{2i\omega}}\right) \tag{F.8}$$

which has the Bremsstrahlung form and vanishes for $k_\perp^2 \leq 2\omega/y_1^+$. Note the factor 2 with respect to (5.1). This is expected as in this calculation, it is as if the quark is created instantaneously at time $t = 0$ and vanishes instantaneously at time $t = t_1$, giving twice the genuine spectrum for an accelerated charge.

(1) The domain $t_f \leq t_{f,\mathbf{med}}$. Now, we use in Eq (F.1) the following approximation for the hyperbolic tangent function in (F.2), $\tanh(x) \simeq x$ for $x \leq 1$ valid when $y^+ \leq t_{f,\mathrm{med}} \ll L$ (the second inequality is a consequence of $\omega \ll \omega_c$). One gets $G^{-1}(y^+) \simeq y^+$. One can neglect the y^+ dependence inside the broadening probability $\mathcal{P}$ because the broadening between 0 and t_f of order $k_{f,\mathrm{med}}$ is negligible in front of Q_s. Thus, the y^+ integral gives:

$$\frac{2}{q_\perp^2}\mathfrak{Re}\Big(1-e^{\frac{-q_\perp^2\, t_{f,\mathrm{med}}}{2i\omega}}\Big) \tag{F.9}$$

which is suppressed for $q_\perp \leq k_{f,\mathrm{med}} = (2\hat{q}\omega)^{1/4}$. At the level of the full spectrum (F.1), this contributions plus the $-1/k_\perp^2$ term constrained with $t_f \leq t_{f,\mathrm{med}}$ (i.e $k_\perp \geq k_{f,\mathrm{med}}$) reads:

$$\omega\frac{\mathrm{d}^3N^{\text{off-shell, } t_f<t_{f,\mathrm{med}}}}{\mathrm{d}\omega\mathrm{d}^2k_\perp} = \frac{\alpha_s C_F}{\pi^2}\int \mathrm{d}^2q_\perp\, \mathcal{P}(k_\perp-q_\perp,0,\infty)\left[\frac{2}{q_\perp^2}\Theta(q_\perp-k_{f,\mathrm{med}}) - \frac{1}{k_\perp^2}\Theta(k_\perp-k_{f,\mathrm{med}})\right] \tag{F.10}$$

The first piece is the convolution between a Bremsstrahlung spectrum with a factor 2 and a Gaussian of width $\sim Q_s$ whereas the second piece (coming from the ε prescription and lemma (3.122)) is a genuine Bremsstrahlung spectrum cancelling the factor 2 to restore the expected $1/k_\perp^2$ behaviour for $k_\perp \gg Q_s$.

The latter expression deserves further comments because it is desperately non-symmetrical. The minus term is not convoluted with the broadening probability. Is it an artefact of the way we did the calculation? Actually, it is not as we shall now explain. Coming back to the expression (3.127) where the time in the complex conjugate amplitude is not integrated, it is also possible to factor out the broadening probability as follows:

$$\omega\frac{\mathrm{d}^3N^{\text{off-shell}}}{\mathrm{d}\omega\mathrm{d}^2k_\perp} = \frac{\alpha_s C_F}{\pi^2}2\mathfrak{Re}\int_0^\infty \mathrm{d}y^+\, e^{-\varepsilon y^+}\int \mathrm{d}^2q_\perp \mathcal{P}(k_\perp-q_\perp,y^+,\infty) \times \frac{q_\perp^2}{(2i\omega)^2}\int_0^{y^+}\mathrm{d}\bar{y}^+\,\frac{-e^{-\varepsilon\bar{y}^+}}{C^2(\bar{y}^+,y^+)}e^{\frac{-q_\perp^2\,S(y^+,\bar{y}^+)}{2i\omega C(\bar{y}^+,y^+)}} \tag{F.11}$$

When $t_f = |y^+-\bar{y}^+| \leq t_{f,\mathrm{med}}$ one can use $C(\bar{y}^+,y^+)\simeq 1$ and $S(y^+,\bar{y}^+)\simeq y^+-\bar{y}^+$ as explained in Section 5.1.2. The calculation of (5.7) for $y^+-\bar{y}^+ \leq t_{f,\mathrm{med}}$ using these approximations for C and S and keeping only the terms with an apparent $1/k_\perp^2$ singularity gives:

$$\begin{aligned}\omega\frac{\mathrm{d}^3N^{\text{off-shell, } t_f\leq t_{f,\mathrm{med}}}}{\mathrm{d}\omega\mathrm{d}^2k_\perp} \simeq{}& \frac{\alpha_s C_F}{\pi^2}2\mathfrak{Re}\int_0^{t_{f,\mathrm{med}}}\mathrm{d}y^+\int\mathrm{d}^2q_\perp\mathcal{P}(k_\perp-q_\perp,y^+,\infty)\frac{1}{2i\omega}\Big(-1+e^{\frac{-q_\perp^2\,y^+}{2i\omega}}\Big)\\ &+\frac{\alpha_s C_F}{\pi^2}2\mathfrak{Re}\int_0^\infty \mathrm{d}y^+\,e^{-2\varepsilon y^+}\int\mathrm{d}^2q_\perp\mathcal{P}(k_\perp-q_\perp,y^+,\infty)\frac{\varepsilon}{q_\perp^2}\Big(-1+e^{\frac{-q_\perp^2\,t_{f,\mathrm{med}}}{2i\omega}}\Big)\end{aligned} \tag{F.12}$$

Neglecting the broadening during the formation time $t_{f,\mathrm{med}}$, the first term in this expression gives the first term in (F.10) which has this weird factor 2. In the limit $\varepsilon\to 0$, only large values of y^+ contributes to the integral in the second term so the broadening probability becomes $\delta^{(2)}(k_\perp-q_\perp)$. The integral over y^+ then gives a factor $1/2$ when the ε prescription is removed, and one recovers the second term in (F.10).

To summarize this short detour, we showed that the result (F.10) comes not only from the domain $y^+ \leq t_{f,\mathrm{med}}$ but from the full domain $y^+-\bar{y}^+ \leq t_{f,\mathrm{med}}$ with unconstrained y^+ in agreement with the definition of $t_f = y^+-\bar{y}^+$. The subsequent broadening treats the short

formation times VLEs with $y^+ \leq L$ differently as those emitted outside the medium, leading to the asymmetrical result (F.10). In the next section, we will understand the physical origin of this factor 2 and the mismatch of (F.10) in the regime $k_{f,\text{med}} < k_\perp < Q_s$ where one cannot approximate the probability $\mathcal{P}$ by a Dirac delta.

(2) The domain $y^+ \geq L$ and $t_f \geq t_{f,\text{med}}$ Let us now come back to formula (F.1) and investigate the contribution coming from $y^+ \geq L$ and $t_f \geq t_{f,\text{med}}$ (we have already collected the $y^+ \geq L$ and $t_f \leq t_{f,\text{med}}$ piece in the previous paragraph.) The exact calculation of the $y^+ \geq L$ integral in (F.1), where the broadening probability vanishes, reads:

$$\frac{1}{2i\omega}\int_L^\infty \mathrm{d}y^+\, 2\exp\left(\frac{-k_\perp^2 G^{-1}(y^+)}{2i\omega}\right) = \frac{2}{k_\perp^2}\exp\left(\frac{k_\perp^2 L}{2i\omega} j\sqrt{\frac{\omega}{\omega_c}}\tanh\left(\bar{j}\sqrt{\frac{\omega_c}{\omega}}\right)\right) \tag{F.13}$$

$$= \frac{2}{k_\perp^2}\exp\left(-\bar{j}\frac{k_\perp^2}{k_{f,\text{med}}^2}\right) \text{ for } \omega \ll \omega_c \tag{F.14}$$

$$\approx \frac{2}{k_\perp^2}\Theta(k_{f,\text{med}} - k_\perp) \tag{F.15}$$

so that the contribution from L to ∞ gives a Bremsstrahlung with support for $k_\perp \leq k_{f,\text{med}}$ (and not $k_\perp^2 < 2\omega/L$!). Combined with the $-1/k_\perp^2$, where the constraint $t_f \geq t_{f,\text{med}}$ is imposed, the contribution from times larger than L and $t_f \geq t_{f,\text{med}}$ to the full spectrum reads:

$$\omega\frac{\mathrm{d}^3 N^{\text{off-shell, } y^+>L, t_f>t_{f,\text{med}}}}{\mathrm{d}\omega \mathrm{d}^2 k_\perp} = \frac{\alpha_s C_F}{\pi^2}\frac{1}{k_\perp^2}\Theta(k_{f,\text{med}} - k_\perp) \tag{F.16}$$

Note that one would have obtained a wrong result using the approximation $G^{-1}(y^+) \simeq y^+ - L$ for $y^+ \geq L$, valid when $\omega \ll \omega_c$ though.

(3) The domain $t_{f,\text{med}} \leq y^+ \leq L$. In this regime, the emission rate is roughly constant. Indeed, using $\tanh(x) \approx 1$ for $x \geq 1$, one gets $G^{-1}(t) \simeq j\sqrt{2\omega/\hat{q}}$. This leads to a purely medium induced component in the full spectrum without $1/k_\perp^2$ behaviour:

$$\omega\frac{\mathrm{d}^3 N^{\text{off-shell, } t_{f,\text{med}}<y^+<L}}{\mathrm{d}\omega \mathrm{d}^2 k_\perp} = \frac{2\alpha_s C_F}{\pi^2}\mathfrak{Re}\frac{1}{2i\omega}\int_0^L \mathrm{d}y^+ \int \mathrm{d}^2 q_\perp\, \mathcal{P}(k_\perp - q_\perp, y^+, \infty)\exp\left(-\bar{j}\frac{q_\perp^2}{k_{f,\text{med}}^2}\right) \tag{F.17}$$

As the broadening probability averaged over time appearing in this formula is not controlled by small times, one can safely take $y^+ = 0$ instead of $t_{f,\text{med}}$ in the lower boundary of the time integral. Note that the time integral can be performed exactly in the harmonic approximation and gives the result obtained in (4.78) in a different context. With this expression, the medium-induced mechanism is transparent: gluons are created with a constant formation rate and a transverse momentum of order $k_{f,\text{med}}$ (with Gaussian distribution) all along the medium and then undergo transverse momentum broadening so that they end up with a transverse momentum of order Q_s. For medium induced emissions, one sees that $t_{f,\text{med}} \leq y^+ \leq L \Leftrightarrow t_f = t_{f,\text{med}}$.

Summary. Let us summarize the discussion of the one gluon emission spectrum from an off-shell quark. In the presence of the medium, y^+ and $\bar{y}^+$ for Bremsstrahlung emissions are not any more solely controlled by t_f contrary to the vacuum calculation (F.3), so the discussion involves both y^+ and $\bar{y}^+$ .The full spectrum receives three kinds of contribution from three different integration domains:

1. Short formation time vacuum-like emissions from the domain $t_f = |y^+ - \bar{y}^+| < t_{f,\text{med}}$ so that $k_\perp \geq k_{f,\text{med}}$.

2. Medium induced emissions from the domain $t_{f,\text{med}} \leq y^+ \leq L$ with a constant formation rate. This imposes $|y^+ - \bar{y}^+| \simeq t_{f,\text{med}}$. These emissions produce a peak in the spectrum around $k_\perp = Q_s$ but final state broadening aside, these emissions are peaked around $k_\perp = k_{f,\text{med}}$.

3. Vacuum-like emissions from the domain $y^+ \geq L$ and $|y^+ - \bar{y}^+| \geq t_{f,\text{med}}$, so that $k_\perp \leq k_{f,\text{med}}$.

F.2 The on-shell spectrum in a static medium

To calculate the vacuum-like spectrum defined in 5.21, we need to understand the behaviour of the spectrum (5.21), and especially the contributions which have a double-logarithmic structure, and which should therefore be resummed. To do so, we rely again on the brick model where the analytical calculations are simple. We recall that our aim is solely to extract the physical scales in order to demonstrate the results obtained in Section 5.1.1. For the brick model, the on-shell spectrum reads:

$$\begin{aligned}\omega\frac{\mathrm{d}^3N^{\text{on-shell}}}{\mathrm{d}\omega\mathrm{d}^2k_\perp} = \frac{\alpha_s C_F}{\pi^2}\Bigg[\int\frac{\mathrm{d}^2q_\perp}{q_\perp^2}\mathcal{P}(k_\perp - q_\perp, 0, L)\Theta(|q_\perp| - \mu) - \frac{1}{k_\perp^2} \\ + \frac{2}{k_\perp^2}\mathfrak{Re}\exp\left(-\bar{j}\frac{k_\perp^2}{k_{f,\text{med}}^2}\coth\left(j\sqrt{\frac{\omega_c}{\omega}}\right)\right) \\ +2\mathfrak{Re}\int_0^L \mathrm{d}y^+\int\mathrm{d}^2q_\perp\mathcal{P}(k_\perp - q_\perp, y^+, L)\frac{1}{2i\omega}\exp\left(-\bar{j}\frac{q_\perp^2}{k_{f,\text{med}}^2}\coth\left(\bar{j}\sqrt{\frac{\omega_c}{\omega}}y^+\right)\right)\Bigg]\end{aligned} \tag{F.18}$$

where μ is a regularization scale introduced in Chapter 3-Section 3.3.3.3. One easily checks that this expression vanishes in the limit $\hat{q} \to 0$.

We now prove formula (5.25). The last term of (F.18) is not singular as $k_\perp \to 0$. Actually, the integral over $k_\perp$ of this term gives precisely the integrated BDMPS-Z spectrum. It is interesting to notice that even if the definition (5.5) for the medium-induced spectrum and the alternative definition

$$\omega\frac{\mathrm{d}^3\tilde{N}^{\text{mie}}}{\mathrm{d}^2\omega\mathrm{d}k_\perp^2} \equiv 2\mathfrak{Re}\int_0^L \mathrm{d}y^+\int\mathrm{d}^2q_\perp\mathcal{P}(k_\perp - q_\perp, y^+, L)\frac{1}{2i\omega}\exp\left(-\bar{j}\frac{q_\perp^2}{k_{f,\text{med}}^2}\coth\left(\bar{j}\sqrt{\frac{\omega_c}{\omega}}y^+\right)\right) \tag{F.19}$$

give the same result once integrated over $k_\perp$ (we have demonstrated this in Chapter 3-Section 3.3.3.4 for the brick model, see also Appendix B) they are not equal and do not have the same $k_\perp$ dependence. This term is denoted as "BDMPS-Z" in formula (5.25).

When $\omega \ll \omega_c$, the third term in (F.18) can be approximated by:

$$\frac{2}{k_\perp^2}\mathfrak{Re}\exp\left(-\bar{j}\frac{k_\perp^2}{k_{f,\text{med}}^2}\coth\left(j\sqrt{\frac{\omega_c}{\omega}}\right)\right) \simeq \frac{2}{k_\perp^2}\Theta(k_{f,\text{med}} - k_\perp) \tag{F.20}$$

Finally, decomposing the $-1/k_\perp^2$ term in (F.18) using $1 = \Theta(k_{f,\text{med}} - k_\perp) + \Theta(k_\perp - k_{f,\text{med}})$, one

gets:

$$\omega\frac{\mathrm{d}^3N^{\text{on-shell}}}{\mathrm{d}\omega\mathrm{d}^2k_\perp} \simeq \frac{\alpha_s C_F}{\pi^2}\Big(\int\frac{\mathrm{d}^2q_\perp}{q_\perp^2}\Big(\mathcal{P}(k_\perp-q_\perp,0,L)-\delta(k_\perp-q_\perp)\Big)\Theta(|q_\perp|-k_{f,\text{med}}) + \frac{1}{k_\perp^2}\Theta(k_{f,\text{med}}-k_\perp)\Big) + \text{“BDMPS-Z”} \tag{F.21}$$

$$\simeq \frac{\alpha_s C_F}{\pi^2}\frac{1}{k_\perp^2}\Theta(k_{f,\text{med}}-k_\perp) + \text{“BDMPS-Z”} \tag{F.22}$$

for $\mu = k_{f,\text{med}}$. To get the second line which is precisely formula (5.25), we used the fact that $\mathcal{P}$ is normalised to 1, so that the integral over $k_\perp$ of the first term does not generate any collinear logarithm.

F.3 Leading behaviour of the vacuum-like spectrum

Now, let us explain how this on-shell spectrum combines with the off-shell one. For our purposes here, one can perfectly approximate the cotangent function in the exponential in (F.19) by 1 and one sees that this third term exactly cancels the medium induced term (F.17) in the off-shell spectrum.

The second term, using $\coth(j\sqrt{\omega_c/\omega}) \simeq 1$ for $\omega \leq \omega_c$, cancels the vacuum-like contribution of the off-shell spectrum for $y^+ \geq L$ calculated in (F.13). The $-1/k_\perp^2$ cancels with the mysterious $-1/k_\perp^2$ in the off-shell spectrum. Thus, for $\omega \leq \omega_c$, the in-medium vacuum-like spectrum as defined in (5.21) behaves like:

$$\omega\frac{\mathrm{d}^3N^{\text{VL}}}{\mathrm{d}\omega\mathrm{d}^2k_\perp} \simeq \frac{\alpha_s C_F}{\pi^2}\int\frac{\mathrm{d}^2q_\perp}{q_\perp^2}\mathcal{P}(k_\perp-q_\perp,0,L)\Big(2\Theta(|q_\perp|-k_{f,\text{med}})-\Theta(|q_\perp|-\mu)\Big) \tag{F.23}$$

$$\simeq \frac{\alpha_s C_F}{\pi^2}\int\frac{\mathrm{d}^2q_\perp}{q_\perp^2}\mathcal{P}(k_\perp-q_\perp,0,L)\Theta(|q_\perp|-k_{f,\text{med}}) \tag{F.24}$$

where we have used $\mu = k_{f,\text{med}}$ in the last line according to our discussion in Chapter 5, Section 6.1. This demonstrates formula (5.24).

F.4 Shockwave limit of the gluon spectra

When the size of the medium is taken into account, via the jet path length L, the resulting formula are more complicated and the physics behind may be hidden (see Eqs. (F.1)-(F.18)). It is therefore enlightening to consider the “shockwave limit” defined as:

$$L \to 0\,, \quad Q_s = \sqrt{\hat{q}L} \text{ fixed} \tag{F.25}$$

This limit captures the interplay between the virtuality of the initial process and the subsequent multiple soft scatterings via the unique remaining transverse scale Q_s.

Shockwave limit of the on-shell spectrum. In this limit, the medium-induced spectrum (F.19) vanishes, since the integration range scales with L. The third term in (F.18) has a well-defined limit:

$$\frac{2}{k_\perp^2}\mathfrak{Re}\exp\left(-\bar{j}\frac{k_\perp^2}{k_{f,\text{med}}^2}\coth\left(j\sqrt{\frac{\omega_c}{\omega}}\right)\right) \underset{\substack{L\to 0\\ Q_s=\text{cste}}}{\longrightarrow} \frac{2}{k_\perp^2}\exp\left(-\frac{k_\perp^2}{Q_s^2}\right) \tag{F.26}$$

Combining all the terms of (F.18) in this limit, one finds:

$$\omega\frac{\mathrm{d}^3N^{\text{on-shell, SW}}}{\mathrm{d}\omega\mathrm{d}^2k_\perp} = \frac{\alpha_sC_F}{\pi^2}\left[\int_{|q_\perp|>\mu}\frac{\mathrm{d}^2q_\perp}{q_\perp^2}\mathcal{P}(k_\perp-q_\perp,0,L) - \frac{2}{k_\perp^2}\Big(1-e^{-k_\perp^2/Q_s^2}\Big) + \frac{1}{k_\perp^2}\right] \tag{F.27}$$

$$= \frac{\alpha_sC_F}{\pi^2}\left[\frac{4\pi}{Q_s^2}\int_{|q_\perp|>\mu}\frac{\mathrm{d}^2q_\perp}{(2\pi)^2}\frac{1}{q_\perp^2}e^{-(k_\perp-q_\perp)^2/Q_s^2} - \frac{4\pi}{Q_s^2}\int\frac{\mathrm{d}^2q_\perp}{(2\pi)^2}\frac{2k_\perp q_\perp}{q_\perp^2k_\perp^2}e^{-(k_\perp-q_\perp)^2/Q_s^2} + \frac{1}{k_\perp^2}\right] \tag{F.28}$$

$$= \frac{\alpha_sC_F}{\pi^2}\left(\frac{4\pi}{Q_s^2}\int\frac{\mathrm{d}^2q_\perp}{(2\pi)^2}\frac{q_\perp^2}{(k_\perp-q_\perp)^2k_\perp^2}e^{-\frac{q_\perp^2}{Q_s^2}}\right), \qquad \text{for } \mu\to 0 \tag{F.29}$$

The on-shell spectrum has a Gunion-Bertsch form [277]. The exponential corresponds to the Gaussian probability for momentum transfer $q_\perp$. For $k_\perp \ll Q_s$, the spectrum (F.29) has a Bremsstrahlung tail in $\frac{\alpha_sC_F}{\pi^2}\frac{1}{k_\perp^2}$. This is precisely why it is interesting to look at the on-shell spectrum: all the Bremsstrahlung components are related to the scattering off the medium. For $k_\perp \gg Q_s$, the spectrum behaves like $\frac{\alpha_sC_F}{\pi^2}\frac{Q_s^2}{k_\perp^4}$.

Shockwave limit of the off-shell spectrum. The shockwave limit of the off-shell spectrum can be readily deduced from Eq. (3.141). One must distinguish two cases: either $x_0^+ = x_i^+ = 0$, meaning that the creation vertex x_i^+ of the quark is located at the same position as the shockwave or $x_0^+ > 0$. In the latter case, x_0^+ is the location of the shockwave along the eikonal quark trajectory. For the former case, one can directly take the shockwave limit of (F.10), (F.13) and (F.17):

$$\omega\frac{\mathrm{d}^3N^{\text{off-shell, SW}}}{\mathrm{d}\omega\mathrm{d}^2k_\perp} = \frac{\alpha_sC_F}{\pi^2}\frac{1}{k_\perp^2} \tag{F.30}$$

which is exactly the vacuum Bremsstrahlung spectrum. In this scenario, nothing happens. Actually, we have seen in Section 3.4.3 that if we start with a virtual onium instead of a virtual quark, the medium plays a non trivial role even in this simple situation, via the decoherence of the colour dipole.

The case $x_0^+ > 0$ (with $x_i^+ = 0$) is much more interesting. The function G in (3.141) satisfies:

$$G^{-1}(y^+) = y^+ \qquad \text{if } y^+ < x_0^+ \tag{F.31}$$

$$G^{-1}(y^+) = \frac{1}{\Omega}\frac{\tan\big(\Omega(y^+-x_0^+)\big)+\Omega x_0^+}{1-\Omega x_0^+\tan\big(\Omega(y^+-x_0^+)\big)} \qquad \text{if } x_0^+ \le y^+ < x_0^+ + L \tag{F.32}$$

$$G^{-1}(y^+) = y^+ - x_0^+ - L + \frac{1}{\Omega}\frac{\tan\big(\Omega L\big)+\Omega x_0^+}{1-\Omega x_0^+\tan\big(\Omega L\big)} \qquad \text{if } x_0^+ + L \le y^+ \tag{F.33}$$

with $\Omega^2 = i\hat{q}/(2\omega)$. The integral appearing in (3.141) between x_0^+ and $x_0^+ + L$ vanishes in the limit $L \to 0$. The integral between 0 and x_0^+ reads

$$\frac{2\alpha_sC_F}{\pi^2}\int\frac{\mathrm{d}^2q_\perp}{q_\perp^2}\mathcal{P}(k_\perp-q_\perp,x_0^+,x_0^++L)\Big(1-e^{-\frac{q_\perp^2x_0^+}{2i\omega}}\Big) \tag{F.34}$$

This integral is naturally regularised by the finite value of x_0^+. Note the presence of the factor 2 as in (F.10). The integral with $y^+ \ge x_0^+ + L$ gives:

$$\frac{2\alpha_sC_F}{\pi^2}\frac{1}{k_\perp^2}\exp\left(-\frac{k_\perp^2}{2i\omega}\frac{1}{\Omega}\frac{\tan\big(\Omega L\big)+\Omega x_0^+}{1-\Omega x_0^+\tan\big(\Omega L\big)}\right) \underset{\substack{L\to 0\\ Q_s=\text{cste}}}{\longrightarrow} \frac{2\alpha_sC_F}{\pi^2}\frac{1}{k_\perp^2}\exp\left(-\frac{k_\perp^2}{Q_s^2}\Big(1+\frac{2i\omega}{Q_s^2x_0^+}\Big)^{-1}\right) \tag{F.35}$$

where we emphasize the importance of $x_0^+ > 0$ to get the shockwave limit. Combining all terms together, one finds:

$$\omega\frac{\mathrm{d}^3N^{\text{off-shell, SW}}}{\mathrm{d}\omega\mathrm{d}^2k_\perp} = \frac{\alpha_s C_F}{\pi^2}\mathfrak{Re}\left[2\int\frac{\mathrm{d}^2q_\perp}{q_\perp^2}\mathcal{P}(k_\perp-q_\perp,x_0^+,x_0^++L)\Big(1-e^{-\frac{q_\perp^2x_0^+}{2i\omega}}\Big)\right.$$
$$\left.-\frac{2}{k_\perp^2}\left[1-\exp\left(-\frac{k_\perp^2}{Q_s^2}\Big(1+\frac{2i\omega}{Q_s^2x_0^+}\Big)^{-1}\right)\right]+\frac{1}{k_\perp^2}\right] \tag{F.36}$$

$$= \frac{\alpha_s C_F}{\pi^2}\mathfrak{Re}\left[\frac{4\pi}{Q_s^2}\int\frac{\mathrm{d}^2q_\perp}{(2\pi)^2}\frac{2e^{-(k_\perp-q_\perp)^2/Q_s^2}}{q_\perp^2}\Big(1-e^{-\frac{q_\perp^2x_0^+}{2i\omega}}\Big)\right.$$
$$\left.-\frac{2}{k_\perp^2}\left[1-\exp\left(-\frac{k_\perp^2}{Q_s^2}\Big(1+\frac{2i\omega}{Q_s^2x_0^+}\Big)^{-1}\right)\right]+\frac{1}{k_\perp^2}\right] \tag{F.37}$$

which looks very much like (F.29) except for the factor 2 in front of the Gaussian broadening convolution. To conclude, the spectrum (F.37) can be computed fully analytically:

$$\omega\frac{\mathrm{d}^3N^{\text{off-shell, SW}}}{\mathrm{d}\omega\mathrm{d}^2k_\perp} = \frac{\alpha_s C_F}{\pi^2}\mathfrak{Re}\left(\frac{2e^{-k_\perp^2/Q_s^2}}{Q_s^2}\left[\mathrm{Ei}\left(\frac{k_\perp^2}{Q_s^2}\right)-\mathrm{Ei}\left(\frac{k_\perp^2}{Q_s^2}\Big(1+\frac{Q_s^2x_0^+}{2i\omega}\Big)^{-1}\right)\right]\right.$$
$$\left.+\frac{2}{k_\perp^2}\exp\left(-\frac{k_\perp^2}{Q_s^2}\Big(1+\frac{2i\omega}{Q_s^2x_0^+}\Big)^{-1}\right)-\frac{1}{k_\perp^2}\right) \tag{F.38}$$

with $\mathrm{Ei}(x)$ the exponential integral function. This spectrum behaves like $\frac{\alpha_s C_F}{\pi^2}\frac{1}{k_\perp^2}$ at large and small $k_\perp$. The $k_\perp$-integrated "medium-induced" spectrum reads:

$$\omega\frac{\mathrm{d}N^{\text{mie, SW}}}{\mathrm{d}\omega} = \int\mathrm{d}k_\perp^2\left(\omega\frac{\mathrm{d}^3N^{\text{off-shell, SW}}}{\mathrm{d}\omega\mathrm{d}^2k_\perp}-\frac{\alpha_s C_F}{\pi^2}\frac{1}{k_\perp^2}\right) \tag{F.39}$$

$$= \frac{\alpha_s C_F}{\pi}\log\left(1+\frac{x_0^{+2}Q_s^4}{4\omega^2}\right) \tag{F.40}$$

$$\simeq \frac{2\alpha_s C_F}{\pi}\log\left(\frac{x_0^+Q_s^2}{2\omega}\right), \qquad \text{for } Q_s^2\gg\frac{2\omega}{x_0^+} \tag{F.41}$$

This result is particularly interesting, because it sheds light on the interplay between leading and higher twist effects. As the initial quark is off-shell, it can radiate according to the Bremsstrahlung law: this is a leading twist effect. On top of that, the shockwave can trigger Bremsstrahlung emissions, but these emissions must satisfy $k_\perp \leq Q_s$ since Q_s is the transverse momentum transferred by the shockwave. The result (F.41) has the following physical content:

- the leading twist emissions populate all the phase space,
- whereas the higher twist emissions populate the phase space $k_\perp \leq Q_s$.
- These two mechanisms interfere for $k_\perp^2 \leq 2\omega/x_0^+$, so that a single Bremsstrahlung tail remains at small $k_\perp$.

The net result is a combination of two Bremsstrahlung in the phase space $2\omega/x_0^+ \leq k_\perp^2 \leq Q_s^2$, which gives the logarithmic area of this domain in the $k_\perp$ integrated spectrum (F.41).

Appendix G

Saddle-point method for in-medium intrajet multiplicity at DLA

Our starting point is Eq. (5.77), assuming $\omega_L(R) < k_{\perp,\min}/R$. For definiteness, we also assume $\theta^2 \geq \theta_c^2$, although it turns out that our conclusions remain valid for $\theta^2 \leq \theta_c^2$. It is convenient to use logarithmic variables: $x_1 = \log(p_{T0}/\omega_1)$, $y_1 = \log(R^2/\theta_1^2)$, $x_2 = \log(\omega_2/\omega)$, $y_2 = \log(\theta_2^2/\theta^2)$ and $X \equiv \log(p_{T0}/\omega)$, $Y \equiv \log(R^2/\theta^2)$. The energy scales $\omega_0(R)$ and $\omega_L(R)$, related respectively to the inside and outside domains, become $x_0 \equiv \log(p_{T0}/\omega_0(R))$ and $x_L \equiv \log(p_{T0}/\omega_L(R))$, and the logarithmic scale associated with θ_c^2 is $y_c \equiv \log(R^2/\theta_c^2) = 4(x_L - x_0)/3$. To get the leading asymptotic behaviour of $T_{i,\text{out}}(X,Y)$, one can neglect the δ contribution to T^{vac} in (5.74) since it generates terms with at least one exponential factor missing. We thus get

$$T_{i,\text{out}}(X,Y) = \bar{\alpha}_s^3 \int_0^{\min(X,x_0)} dx_1 \int_0^{\min(y_c,\frac{3}{2}(x_0-x_1))} dy_1 \int_0^{\min(X-x_1,X+Y-x_L)} dx_2 \int_0^{X+Y-x_L-x_2} dy_2 \\ \mathrm{I}_0(2\sqrt{\bar{\alpha}_s x_1 y_1})\,\mathrm{I}_0(2\sqrt{\bar{\alpha}_s x_2 y_2}) \quad \text{(G.1)}$$

The integral over y_1 and y_2 can be performed exactly using the the following relation:

$$\int_0^s dy\,\mathrm{I}_0(2\sqrt{\bar{\alpha}_s x y}) = \sqrt{\frac{s}{\bar{\alpha}_s x}}\mathrm{I}_1(2\sqrt{\bar{\alpha}_s x s}) \overset{\bar{\alpha}_s x s \gg 1}{\simeq} \sqrt{\frac{s}{\bar{\alpha}_s x}}\frac{\exp(2\sqrt{\bar{\alpha}_s x s})}{\sqrt{4\pi\sqrt{\bar{\alpha}_s x s}}}. \quad \text{(G.2)}$$

Using (G.2), one gets

$$T_{i,\text{out}}(X,Y) = \bar{\alpha}_s^3 \int_0^{\min(X,x_0)} dx_1 \int_0^{\min(X-x_1,X+Y-x_L)} dx_2\, R_1(x_1)R_2(x_2) \\ e^{2\sqrt{\bar{\alpha}_s x_1 \min(y_c,\frac{3}{2}(x_0-x_1))}} e^{2\sqrt{\bar{\alpha}_s x_2 (X+Y-x_L-x_2)}} \quad \text{(G.3)}$$

with the two non-exponential functions

$$R_1(x_1) = \frac{1}{\sqrt{4\pi}}\frac{(\min(y_c,\frac{3}{2}(x_0-x_1)))^{1/4}}{(\bar{\alpha}_s x_1)^{3/4}}, \qquad R_2(x_2) = \frac{1}{\sqrt{4\pi}}\frac{(X+Y-x_L-x_2)^{1/4}}{(\bar{\alpha}_s x_2)^{3/4}} \quad \text{(G.4)}$$

The x_2 integrations cannot be performed exactly so we use the saddle-point approximation:

$$\int_{x_1}^{x_2} dx\, f(x)e^{Mg(x)} \overset{M\to\infty}{\simeq} \sqrt{\frac{2\pi}{-Mg''(x^\star)}} f(x^\star)e^{Mg(x^\star)}, \quad \text{(G.5)}$$

where the saddle point $x^\star$ is the *maximum* of $g(x)$ between x_1 and x_2. This formula is valid as long as $x_1 < x^\star < x_2$.

Setting $M_2 \equiv (X+Y-x_L) = \log(\omega_L(\theta)/\omega)$ and integrating over x_2/M_2, one get

$$\mathcal{N}_{\rm out} \equiv \bar{\alpha}_s \int_0^{\min(X-x_1, X+Y-x_L)} dx_2\, R_2(x_2) e^{2\sqrt{\bar{\alpha}_s x_2 (X+Y-x_L-x_2)}} \overset{\sqrt{\bar{\alpha}_s}M_2 \to \infty}{\simeq} \frac{1}{2} e^{\sqrt{\bar{\alpha}_s}M_2}. \tag{G.6}$$

The corresponding saddle point is $x_2^\star = M_2/2 = \log(\sqrt{\omega_L(\theta)/\omega})$ so that the saddle-point approximation is valid if $x_2^\star < X - x_1$. This gives the condition $x_1 \leq X - x_2^\star$ in the first integral, in order to ensure energy conservation along the cascade.

Calling $\mathcal{N}_{\rm med}$ the remaining integral over x_1, which is truly a gluon multiplicity *inside* the medium, we are left with:

$$\mathcal{N}_{\rm med} \equiv \bar{\alpha}_s \int_0^{\min(x_0, X-x_2^\star)} dx_1\, R_1(x_1) e^{2\sqrt{\bar{\alpha}_s x_1 \min(y_c, \frac{3}{2}(x_0-x_1))}}. \tag{G.7}$$

Since $\min(X-x_2^\star, x_0) > x_c \equiv \log(p_{T0}/\omega_c)$, the integral can be split into two pieces: $x_1 < x_c$ where $\min(y_c, 3(x_0-x_1)/2) = y_c$ and $x_1 > x_c$ where $\min(y_c, 3(x_0-x_1)/2) = 3(x_0-x_1)/2$. The first piece is calculated exactly, and we use again the saddle point method to evaluate the second piece, assuming $x_0 = \log(p_{T0}/\omega_0(R)) \to \infty$. We get (using $x_1' = x_1/x_0$)

$$\begin{aligned}
\mathcal{N}_{med} &= \int_0^{x_c} dx_1 \bar{\alpha}_s \sqrt{\frac{y_c}{\bar{\alpha}_s x_1}} \mathrm{I}_1(2\sqrt{\bar{\alpha}_s x_1 y_c}) + \bar{\alpha}_s \int_{x_c}^{\min(X-x_2^\star, x_0)} dx_1\, R(x_1) e^{2\sqrt{\bar{\alpha}_s x_1 \frac{3}{2}(x_0-x_1)}} \\
&= -1 + \mathrm{I}_0(2\sqrt{\bar{\alpha}_s x_c y_c}) + \bar{\alpha}_s^{1/4} \sqrt{\frac{x_0}{4\pi}} \int_{x_c/x_0}^{\min(1,(X-x_2^\star)/x_0)} \frac{dx_1'}{x_1'^{1/2}} \Big(\frac{3(1-x_1')}{2x_1}\Big)^{1/4} e^{2x_0\sqrt{\frac{3}{2}\bar{\alpha}_s x_1'(1-x_1')}} \\
&\overset{\sqrt{\bar{\alpha}_s}x_0 \to \infty}{\sim} \frac{e^{2\sqrt{\bar{\alpha}_s x_c y_c}}}{\sqrt{4\pi\sqrt{\bar{\alpha}_s x_c y_c}}} + \frac{1}{2} e^{\sqrt{\frac{3\bar{\alpha}_s}{2}}x_0}
\end{aligned} \tag{G.8}$$

The first term in equation (G.8) is sub-leading due to the square root in the argument and in the denominator. Thus, the leading term for $\mathcal{N}_{med}$ comes from the "inside-medium" region with $\omega_1 \leq \omega_c$.[1]

The saddle point of the integral over x_1 is $x_1^\star = x_0/2 = \log(\sqrt{p_{T0}/\omega_0(R)})$ so our estimation for $\mathcal{N}_{med}$ is valid only if $x_c < x_1^\star < X - x_2^\star$. The condition $x_c < x_1^\star$ leads to the condition (5.80). The condition $x_1^\star < X - x_2^\star$ leads to the condition (5.81), when $x_2^\star = \log(\sqrt{\omega_L(\theta)/\omega})$ is evaluated at its largest value, that is when $\theta = \theta_{\min} \equiv k_{\perp,\min}/\omega$.

We have thus demonstrated that when both $\sqrt{\bar{\alpha}_s}x_0 \equiv \sqrt{\bar{\alpha}_s}\log(p_{T0}/\omega_0(R))$ and $\sqrt{\bar{\alpha}_s}(X + Y - x_L) \equiv \sqrt{\bar{\alpha}_s}\log(\omega_L(\theta)/\omega)$ are large and $X > x_1^\star + x_2^\star$, i.e. $\omega < \omega_{cr}$, we have

$$T_{i,\rm out}(X,Y) \sim \frac{\bar{\alpha}_s}{4} \exp\left[\sqrt{\bar{\alpha}_s}\left(X + Y - x_L + \sqrt{\frac{3}{2}}x_0\right)\right], \tag{G.9}$$

which is precisely formula (5.82).

From (G.9) and (5.76), one deduces the asymptotic DLA behaviour of the small-x fragmentation function by integrating $T_i(\omega, \theta^2 | p_{T0}, R^2)$ over θ^2 between $k_{\perp,\min}^2/\omega^2$ and R^2. The leading contribution comes from the lower limit of this integral or, in logarithmic units, from the upper bound $2(x_{\max} - X)$ on the integral on Y, with $x_{\max} = \log(p_{T0}R/k_{\perp,\min})$. This reproduces (5.83) in logarithmic units:

$$D_i^{\rm med}(X) = \int_0^{2(x_{\max}-X)} \mathrm{d}Y\, T_i(X,Y) \simeq \frac{\sqrt{\bar{\alpha}_s}C_i}{4C_A} \exp\left[\sqrt{\bar{\alpha}_s}\Big(-X + 2x_{\max} - x_L + \sqrt{\frac{3}{2}}x_0\Big)\right] \tag{G.10}$$

[1] That is why we can trust our final result for $T(\omega, \theta^2)$ even for $\theta^2 \leq \theta_c^2$.

Finally, the asymptotic form of the ratio $\mathcal{R}_i(X) \equiv D_i^{\rm med}(X)/D_i^{\rm vac}(X)$ is obtained from (G.10) and (4.25), using again the asymptotic form of $\mathrm{I}_1(x)$ at large x:

$$D_i^{\rm vac}(X) \simeq \frac{C_i}{\sqrt{4\pi}C_A}\left[\frac{2\bar{\alpha}_s(x_{\rm max}-X)}{X^3}\right]^{1/4}\exp\left(2\sqrt{2\bar{\alpha}_s X(x_{\rm max}-X)}\right) \tag{G.11}$$

$$\mathcal{R}_i(X) \sim \frac{\sqrt{\bar{\alpha}_s\pi}}{2}e^{\sqrt{\frac{3}{2}}x_0-x_L}\left[\frac{X^3}{2\bar{\alpha}_s(x_{\rm max}-X)}\right]^{1/4}\exp\left[\sqrt{\bar{\alpha}_s}\left(\sqrt{X}-\sqrt{2(x_{\rm max}-X)}\right)^2\right]. \tag{G.12}$$

From (G.11), one can estimate the position of the maximum $x_{\rm hump}$ of $D_i^{\rm vac}(X)$. Neglecting the non-exponential prefactor, one finds $\mathrm{d}D_i^{\rm vac}/\mathrm{d}X \propto x_{\rm max}-2X$, so that the $x_{\rm hump} \simeq x_{\rm max}/2$ and $\omega_{\rm hump} \simeq \sqrt{p_{T0}k_{\perp,\rm min}/R}$. For $X \geq x_{\rm hump}$ i.e. $\omega \leq \omega_{\rm hump}$, the derivative is negative, hence $D_i^{\rm vac}(\omega)$ decreases when ω decreases. Similarly, one can study the variation of $\mathcal{R}_i(X)$ from the exponential factor alone:

$$\frac{\mathrm{d}\mathcal{R}_i}{\mathrm{d}X} \simeq \frac{\bar{\alpha}_s\sqrt{\pi}}{2}e^{\sqrt{\frac{3}{2}}x_0-x_L}\frac{\left(\sqrt{2X}+\sqrt{x_{\rm max}-X}\right)\left(\sqrt{X}-\sqrt{2(x_{\rm max}-X)}\right)}{\sqrt{X(x_{\rm max}-X)}}e^{\sqrt{\bar{\alpha}_s}\left(\sqrt{X}-\sqrt{2(x_{\rm max}-X)}\right)^2} \tag{G.13}$$

The derivative is positive when $\sqrt{X}-\sqrt{2(x_{\rm max}-X)} \geq 0$ i.e. when $X \geq 2x_{\rm max}/3$. Hence, for $\omega \lesssim (p_{T0}k_{\perp,\rm min}^2/R^2)^{1/3}$, the ratio $R_i(\omega)$ increases when ω decreases.

Appendix H

Medium-modified Sudakov form factors with running coupling

For the effects of the veto region, the expression corresponding to Eq. (10.6) and including running-coupling effects is found to be

$$Lg_{1,i}^{\text{veto}}(u,v) = Lg_{1,i}(u,v) + \frac{2C_i}{\pi}\mathcal{A}_{\text{veto}}(L) \tag{H.1}$$

where the logarithmic area of the veto region $\mathcal{A}_{\text{veto}}(L)$ is defined as:

$$\mathcal{A}_{\text{veto}}(L) = \int_{e^{-L}}^{1}\frac{\mathrm{d}z}{z}\int_{0}^{R}\frac{\mathrm{d}\theta}{\theta}\alpha_s(zp_{T0}\theta)(1-\Theta_{\text{veto}}) \tag{H.2}$$

and Θ_{veto} is given by (10.5). Introducing the following function:

$$\mathcal{T}(x,y,z) \equiv \frac{y+zx}{z}\ln(1+\alpha_s\beta_0(y+zx))\,, \tag{H.3}$$

the logarithmic area $\mathcal{A}_{\text{veto}}(L)$ reads:

$$\begin{aligned}
\mathcal{A}_{\text{veto}}(L) \overset{1-x<z_L}{=} \frac{1}{2\beta_0}\Big[&\mathcal{T}\big(\ln z_0,0,2\big) - \mathcal{T}\big(\ln z_L,0,2\big) + \mathcal{T}\big(\ln z_c,\tfrac{3}{2}\ln z_0,\tfrac{1}{2}\big) - \mathcal{T}\big(\ln z_0,\tfrac{3}{2}\ln z_0,\tfrac{1}{2}\big)\\
&- \mathcal{T}\big(\ln z_0,\ln z_L,1\big) + \mathcal{T}\big(\ln z_L,\ln z_L,1\big) - \mathcal{T}\big(\ln z_c,\ln z_L,1\big) + \mathcal{T}\big(\ln z_0,\ln z_L,1\big)\Big]\\
\overset{z_L<1-x<z_0}{=} \frac{1}{2\beta_0}\big[&\mathcal{T}\big(\ln z_0,0,2\big) - \mathcal{T}\big(-L,0,2\big) + \mathcal{T}\big(\ln z_c,\tfrac{3}{2}\ln z_0,\tfrac{1}{2}\big) - \mathcal{T}\big(\ln z_0,\tfrac{3}{2}\ln z_0,\tfrac{1}{2}\big)\\
&- \mathcal{T}\big(\ln z_0,\ln z_L,1\big) + \mathcal{T}\big(-L,\ln z_L,1\big) - \mathcal{T}\big(\ln z_c,\ln z_L,1\big) + \mathcal{T}\big(\ln z_0,\ln z_L,1\big)\big]\\
\overset{z_0<1-x<z_c}{=} \frac{1}{2\beta_0}\big[&\mathcal{T}\big(\ln z_c,\tfrac{3}{2}\ln z_0,\tfrac{1}{2}\big) - \mathcal{T}\big(-L,\tfrac{3}{2}\ln z_0,\tfrac{1}{2}\big) - \mathcal{T}\big(\ln z_c,\ln z_L,1\big) + \mathcal{T}\big(-L,\ln z_L,1\big)\Big)\big]
\end{aligned}$$

with $z_0 \equiv \omega_0(R)/p_{T0} = (2\hat{q}/(p_{T0}^3R^4))^{1/3}$, $z_L \equiv \omega_L(R)/p_{T0} = 2/(Lp_{T0}R^2)$ and $z_c \equiv \omega_c/p_{T0}$.

Appendix I

Résumé détaillé en français

Introduction

Le plasma quarks-gluons. La chromodynamique quantique (QCD) est une théorie quantique de l'intéraction forte, la force fondamentale régissant les processus physiques à l'échelle nucléaire et sub-nucléaire, tels que la stabilité des noyaux atomiques ou la formation de nombreux états liés appelés hadrons. Le cadre conceptuel au sein duquel cette théorie est formulée est celui de la théorie quantique des champs. Les degrés de libertés élémentaires de la théorie, c'est à dire les champs quantiques apparaissant dans la description lagrangienne de l'intéraction forte, sont appelés *quarks* et *gluons*. Quarks et gluons, ou génériquement les "partons", sont donc considérés comme les constituants élémentaires de la matière hadronique.

Cette matière existe sous différentes phases en fonction de la température et de la densité (ou plus précisément du potentiel chimique baryonique). Le diagramme des phases probable de la QCD est représenté sur la Fig. 1.1. La nature de ces phases est déterminée par deux propriétés extrêmement importantes de la QCD: le confinement des quarks et des gluons, et la liberté asymptotique de leurs intéractions. À basse température $T \ll T_c$, où $T_c \sim 150$ MeV/k_B est la température critique du système, les quarks et les gluons sont confinés au sein des hadrons. Quand la température du système augmente, $T \gg T_c$, la constante de couplage de la QCD, $\alpha_s(k_B T)$ — évaluée à la valeur typique de l'énergie thermique du système, qui est la seule échelle physique du problème — devient de plus en plus petite de part la liberté asymptotique de l'intéraction forte: $\alpha_s(k_B T) \ll 1$ quant $T \to \infty$. Cela signifie qu'à haute température, un système composé de quarks et de gluons se comporte presque comme un gaz de particules libres sans intéractions: le plasma quarks-gluons.

Les collisions d'ions lourds. Afin d'étudier ses propriétés, ce plasma est créé en laboratoire dans des accélérateurs de particules après la collision à très haute énergie de deux ions lourds, par exemple du plomb $^{208}_{82}$Pb au Grand Collisionneur de Hadrons (LHC). Le déroulement temporel de telles collisions est schématisé sur la Fig. 1.3. La durée de la phase déconfinée est très courte, de l'ordre de 10 fm ; par conséquent, les propriétés de cette phase éphémère sont déterminées grâce à la mesure de la myriade de hadrons produits par la collision et détectés dans l'état final. Ces hadrons peuvent être divisés en deux catégories: les hadrons mous, avec une impulsion transverse p_T plus petite que quelques GeV, considérés comme les relicats d'un milieu déconfiné et thermalisé, et les hadrons très énergétiques ou durs, avec un $p_T \gg 10$ GeV. Le mécanisme de production de ces hadrons durs est essentiellement le même que dans les collisions à haute énergie de petits systèmes, comme les collisions proton-proton (pp) ou électron-positron (e^+e^-): ils proviennent d'un parton source très énergétique produit durant la collision entre les deux noyaux.

La réduction des jets. Ce parton très énergétique est également hautement virtuel, c'est à dire qu'il est loin d'être sur sa couche de masse. Du fait de sa virtualité, il peut radier à nouveau par émission Bremsstrahlung des partons plus mous, et presque colinéaires à l'impulsion initiale du parton source. Dans l'état final, ce processus conduit à la formation de jets, qui sont des gerbes collimatées de hadrons de haute énergie. Le temps caractéristique de formation du parton source, d'impulsion transverse p_{T0}, est $1/p_{T0}$ par le principe d'incertitude d'Heisenberg. Au contraire, le temps caractéristique de développement de la cascade radiative partonique est $1/\Lambda_{\rm QCD}$, où $\Lambda_{\rm QCD}$ est l'échelle de confinement de la QCD. Pour un plasma avec une durée de vie L, on a typiquement $1/p_{T0} \ll L \lesssim 1/\Lambda_{\rm QCD}$. Cela signifie que le parton source est produit très rapidement, avant même la formation du plasma, et que la gerbe partonique qu'il génère se propage en partie à l'intérieur du plasma. Durant sa propagation, les intéractions entre le milieu dense et le jet vont modifier l'évolution du jet et ses propriétés finales par rapport à celle mesurées en collisions pp ou e^+e^-. Ce phénomène physique est connu sous le nom de *réduction des jets*.

Dans cette thèse, nous proposons une nouvelle théorie pour décrire l'évolution des jets dans un plasma quarks-gluons dense. Dans une première partie, nous construisons cette nouvelle image à partir des principes premiers de la QCD en théorie des perturbations, puis dans une seconde partie nous confrontons notre modèle aux mesures expérimentales faites au LHC d'observables caractérisant la réduction des jets.

I.1 Une nouvelle image pour l'évolution des jets dans un plasma quarks-gluons

Outre le processus radiatif de type Bremsstrahlung dû à la grande virtualité du parton à l'origine du jet, cette thèse propose d'inclure de façon cohérente les modifications principales induites par la présence du milieu sur la propagation d'un parton très énergétique. Le milieu est un gaz idéal de quarks et de gluons, à l'équilibre thermodynamique à la température $T_{\rm p}$. Ces charges de couleurs génèrent un champ de jauge fluctuant dans lequel se propage le parton relativiste.

I.1.1 Propagation d'un parton très énergétique dans un milieu dense

Dans un premier temps, nous considérons que ce parton énergétique, le projectile, est sur couche de masse, ce qui revient à négliger les effets de virtualité et nous travaillons dans l'approximation eikonale pour la propagation du parton. Le projectile est de masse nulle et sa direction de propagation permet de définir le système de coordonnées sur le cône de lumière associé à cette direction (cf. Section 3.2.1). Dans ce système de coordonnées, la quadri-impulsion du projectile est $p^\mu = (p^+, p^-, p_\perp)$ avec $p^+ \gg |p_\perp| \gg p^-$ et $p^2 = 2p^+p^- - p_\perp^2 = 0$.

Diffusion transverse. Du fait des collisions multiples avec les centres diffuseurs du milieu, le parton acquiert durant sa propagation entre le temps t_1 et le temps t_2 une impulsion transverse $k_\perp$ selon la loi de probabilité gaussienne $\mathcal{P}(k_\perp, t_1, t_2)$:

$$\mathcal{P}(k_\perp, t_1, t_2) = \frac{4\pi}{Q_s^2(t_1,t_2)} \exp\left(-\frac{k_\perp^2}{Q_s^2(t_1,t_2)}\right), \qquad Q_s^2(t_1,t_2) = \int_{t_1}^{t_2} \mathrm{d}t\, \hat{q}(t) \tag{I.1}$$

Le plasma est caractérisé par le paramètre de réduction $\hat{q}$, défini comme la moyenne de l'impulsion transverse carrée acquise par unité de temps: $\langle k_\perp^2 \rangle \sim \hat{q}\Delta t$. Dans la formule (I.1), $\hat{q}$ dépend du temps du fait de l'expansion longitudinale du plasma conduisant à une dilution de sa densité

au cours de la propagation du parton énergétique dans le plan transverse à la collision. Cette loi est valide dans un régime dominé par les diffusions multiples avec les constituants du milieu: même si chaque diffusion ne transfère qu'une petite impulsion, la somme de tous ces transferts contribue à donner une impulsion totale $k_\perp$. Cette approximation est correcte pour $k_\perp \lesssim Q_s$. Au delà de cette approximation, $\mathcal{P}(k_\perp, t_1, t_2)$ est donnée par Eq. (3.64).

Emissions induites. Outre la diffusion transverse, le milieu peut déclencher des émissions car les collisions avec le milieu mettent le projectile hors de sa couche de masse. Un diagramme de Feynman typique pour ce processus est représenté Fig. 2.1 (droite), dans le cas de deux collisions. Dans le régime des collisions multiples, ces diagrammes doivent être resommés à tous les ordres pour prendre en compte un nombre arbitraire de collisions. Cette resommation permet d'obtenir le spectre d'émission d'un gluon de quadri-impulsion $k^\mu = (k^+, k^-, k_\perp)$ dans l'approximation des diffusions multiples molles. Pour un projectile dans la représentation de couleur $R = A, F$ et sur couche de masse, le résultat est donné par la formule suivante:

$$k^+ \frac{\mathrm{d}^3 N^{\text{on-shell}}}{\mathrm{d}k^+ \mathrm{d}^2 k_\perp} = \frac{\alpha_s C_R}{\pi^2} \left[\frac{4\pi}{Q_s^2(x_0^+)} \int \frac{d^2 q_\perp}{(2\pi)^2} \frac{1}{q_\perp^2} \exp\left(\frac{-(k_\perp - q_\perp)^2}{Q_s^2(x_0^+)} \right) \right.$$
$$\left. + 2\mathfrak{Re} \int_{x_0^+}^{\infty} \mathrm{d}y^+ \frac{\bar{G}(y^+)}{Q_s^2(y^+) + 2ik^+ \bar{G}(y^+)} \exp\left(\frac{-k_\perp^2}{Q_s^2(y^+) + 2ik^+ \bar{G}(y^+)} \right) - \frac{1}{k_\perp^2} \right] \tag{I.2}$$

avec x_0^+ le temps auquel le projectile entre dans le plasma et $Q_s(t) \equiv Q_s(t, \infty)$. La fonction $\bar{G}$ est la solution du problème différentiel non-linéaire de type Riccati:

$$\frac{\mathrm{d}\bar{G}}{\mathrm{d}t} + \bar{G}^2 + \frac{i\hat{q}(t)}{2k^+} = 0\,, \qquad \bar{G}(x_0^+) = 0 \tag{I.3}$$

Dans le cas d'un projectile hors couche de masse, nous obtenons une formule similaire, donnée par Eq. (3.141). Ce dernier spectre est connu sous le nom de spectre BDMPS-Z, et est évalué numériquement Fig. (3.2).

Pour un parton se propageant sur une distance L dans le milieu, le spectre intégré sur $k_\perp$ a le comportement suivant à petite énergie:

$$k^+ \frac{\mathrm{d}N^{\text{on-shell}}}{\mathrm{d}k^+} \approx \frac{2\alpha_s C_R}{\pi} \sqrt{\frac{\omega_c}{2k^+}}\,, \qquad k^+ \ll \omega_c = \frac{1}{2}\hat{q}L^2 \tag{I.4}$$

Contrairement au spectre Bethe-Heitler, qui se comporte en $\alpha_s N_{\text{scatt}}/k^+$ dans la limite molle, avec N_{scatt} le nombre de centre diffuseur, le spectre induit est réduit puisqu'il se comporte en $1/k^{+3/2}$. Cette suppression, appelée effet Landau-Pomerantchuk-Migdal, est une conséquence du fait que le projectile diffuse de façon cohérente avec plusieurs constituants du milieu durant le temps de formation du gluon, qui est fini et d'ordre $t_f \sim 2k^+/k_\perp^2$. Durant ce temps, l'émission acquiert par diffusion une impulsion transverse $k_\perp \sim \hat{q}t_f$. Ces deux égalités fixent à la fois le temps de formation $t_{f,\text{med}} = \sqrt{k^+/\hat{q}}$ et l'impulsion transverse $k_{f,\text{med}} = (\hat{q}k^+)^{1/4}$ pour une émission induite.

Enfin, l'échelle ω_c qui apparaît dans la formule (I.4) est typiquement l'énergie maximale d'une émission induite dans le régime des diffusions multiples molles. Le parton projectile est donc considéré comme hautement énergétique si $p^+ \geq \omega_c$, inégalité qui garantie aussi la validité de l'approximation eikonale pour sa propagation.

Décohérence d'un dipôle neutre. Le dernier effet qu'il sera important de prendre en compte dans la description complète d'un jet évoluant dans un plasma dense est la décohérence de couleur. Pour comprendre cet effet, il est commode de prendre pour projectile un dipôle neutre, c'est à dire une paire quark-antiquark dans un état de couleur singulet. Ce dipôle est créé à $t = x_0^+$ à partir, par exemple, d'un photon ou d'un boson W/Z virtuel. Nous noterons $\theta_{q\bar{q}}$ son ouverture angulaire.

Dans le vide, le spectre d'émission d'un gluon par un tel dipôle est bien connu: les émissions à grands angles, avec $\theta > \theta_{q\bar{q}}$ sont supprimées du fait des interférences quantiques induites par la cohérence de couleur du dipôle. Qualitativement, une émission de longueur d'onde transverse $\lambda_\perp \sim 1/k_\perp \sim 1/(k^+\theta)$ plus grande que la taille du dipôle au moment de l'émission, de l'ordre de $\theta_{q\bar{q}} t_f \sim \theta_{q\bar{q}}/(k^+\theta^2)$ ne sera sensible qu'à la charge de couleur totale du dipôle. Comme le dipôle est neutre, cette charge est nulle et l'émission est supprimée quand $\theta > \theta_{q\bar{q}}$. Par conséquent les émissions Bremsstrahlung dans le vide sont ordonnées en angle: $\theta < \theta_{q\bar{q}}$.

Dans le milieu, les intéractions avec le dipôle modifient sa cohérence de couleur: chaque branche du dipôle subit indépendamment une rotation de couleur du fait des collisions multiples. Après un certain temps Δt passé dans le milieu, le dipôle n'est donc plus dans un état singulet de couleur. Pour quantifier plus précisément cet effet, on introduit le facteur de décohérence du dipôle, noté $S_{q\bar{q}}$ qui est égal au produit des deux rotations de couleur indépendantes du quark et de l'antiquark (plus précisément, des lignes de Wilson le long de leur trajectoire eikonale, cf. Section 3.4.2), moyenné sur les fluctuations statistiques du champ de jauge généré par le plasma:

$$S_{q\bar{q}}(\Delta t) \equiv \frac{1}{N_c^2 - 1} \left\langle \operatorname{Tr} \mathcal{W}_{x_0^+}^{q, x_0^+ + \Delta t} \mathcal{W}_{x_0^+}^{\bar{q}\dagger, x_0^+ + \Delta t} \right\rangle \tag{I.5}$$

$$= \exp\left(-\frac{1}{8} \theta_{q\bar{q}}^2 \int_0^{\Delta t} \mathrm{d}\xi \, \hat{q}(x_0^+ + \xi) \xi^2 \right) \tag{I.6}$$

Pour un milieu statique, avec $\hat{q}$ constant, un temps caractéristique de décohérence $t_{\mathrm{coh}} = (\hat{q}\theta_{q\bar{q}}^2/4)^{-1/3}$ émerge de cette formule.

Les effets de la décohérence sur le spectre d'émission d'un gluon par un dipôle neutre doivent être discutées séparément en fonction du type d'émission. Le cas des émissions induites par le milieu est discuté en détail dans la Section 3.4.2. En résumé, il existe un angle du dipôle critique $\theta_c = 2/\sqrt{\hat{q}L^3}$, vérifiant $t_{\mathrm{coh}}(\theta_c) = L$, tel que si $\theta_{q\bar{q}} < \theta_c$, le spectre d'émissions induites par le dipôle est supprimé par rapport aux résultats (I.2)-(I.4). Physiquement, l'ouverture du dipôle est trop petite pour qu'il soit résolu par une émission induite, qui ne sera donc sensible qu'à sa charge de couleur totale. Au contraire, si $\theta_{q\bar{q}} > \theta_c$, le dipôle est non cohérent au moment de l'émission induite du gluon, et donc le spectre totale est la somme incohérente de deux spectres BDMPS-Z.

Le cas des émissions de type vide (Bremsstrahlung), ayant soit un temps de formation très court devant le temps caractéristique de formation d'une émission induite $t_{f,\mathrm{med}}$, soit un temps de formation grand devant L sera discuté dans le prochain paragraphe. En principe, la décohérence pourrait briser la propriété d'ordonnancement angulaire des émissions de type vide, ce qui présente une sérieuse complication pour la description de l'évolution d'un jet dans un milieu comme un processus de branchement ordonné en angles.

I.1.2 Resommation des émissions de type vide dans l'approximation double-logarithmique

Dans la section précédente, nous avons identifié les effets du milieu, dominants en théorie des perturbations, sur la propagation d'un parton énergétique. A présent, nous allons préciser comment ces effets se combinent avec la grande virtualité du parton produit par le processus dur de la collision.

Resommation dans le vide. Dans le vide, cette grande virtualité est à l'origine de la formation de jets. Nous rappelons ici qu'un parton virtuel (hors couche de masse) peut radier un gluon, et que le spectre de radiation est donné par la loi du Bremsstrahlung,

$$\mathrm{d}N^{\mathrm{brem}} = \frac{\alpha_s C_R}{\pi^2}\frac{\mathrm{d}k^+}{k^+}\frac{\mathrm{d}^2k_\perp}{k_\perp^2} = \frac{2\alpha_s C_R}{\pi^2}\frac{\mathrm{d}k^+}{k^+}\frac{\mathrm{d}\theta}{\theta} \tag{I.7}$$

écrite ici dans la limite molle $k^+ \to 0$ et collinéaire $\theta \to 0$. Pour la seconde égalité, nous avons utilisé $k_\perp \sim k^+\theta$. Le temps caractéristique de formation du gluon est donné par le principe d'incertitude, $t_f \sim k^+/k_\perp^2 \sim 1/(k^+\theta^2)$. Ce spectre est singulier dans la limite molle et colinéaire, ce qui signifie qu'un parton virtuel radie préférentiellement des gluons mous ou colinéaires à l'émetteur, et cette singularité est logarithmique. Pour un parton de virtualité $Q \sim p^+\theta_{q\bar{q}}$ radiant à l'intérieur d'un cône d'ouverture angulaire $\theta_{q\bar{q}}$, la probabilité totale d'émission est

$$N^{\mathrm{brem}} \sim \frac{2\alpha_s C_R}{\pi^2}\log^2\left(\frac{p^+\theta_{q\bar{q}}}{\Lambda_{\mathrm{QCD}}}\right) \tag{I.8}$$

Par conséquent, à très haute énergie $p^+ \gg \Lambda_{\mathrm{QCD}}$, le grand logarithme carré compense la faible constante de couplage $\alpha_s \ll 1$, si bien que $N^{\mathrm{brem}} = \mathcal{O}(1)$. Dans ce régime, un calcul à l'ordre le plus bas tel que celui donné par (I.7) n'est pas suffisant pour décrire précisément le profil d'émission de gluons par un parton virtuel. Tous les termes d'ordre $\alpha_s^n \log^{2n}(p^+\theta_{q\bar{q}}/\Lambda_{\mathrm{QCD}})$ doivent être resommés, avec $n \in \mathbb{N}$. Cette resommation est dite double logarithmique, puisque seuls les termes augmentés d'un logarithmique carré sont pris en compte.

Dans le vide, on peut montrer que cette resommation peut se faire en considérant que les émissions se produisent selon un processus de branchement markovien, ordonné en angle pour prendre en compte la cohérence de couleur expliquée ci-dessus. Ce processus de branchement est à l'origine des émissions multiples observées dans les jets. Un exemple typique d'un tel processus est représenté sur la Fig. 4.2-gauche. Il est aussi commode de représenter un tel processus sur un espace de phase (k^+, θ) où chaque point de cet espace représente une émission dans le jet, cf. Fig. 4.2-droite. Les cascades d'émissions s'écoulent du haut en bas pour respecter l'ordonnancement angulaire, et de la droite vers la gauche pour satisfaire la conservation de l'énergie (chaque émission est plus molle que l'émetteur). L'espace de phase est tronqué pour $k_\perp < \Lambda_{\mathrm{QCD}}$ car dans ce domaine, les degrés de libertés ne sont plus partoniques du fait du confinement. Ce dernier régime correspond au processus d'hadronisation des partons produits dans des d'états liés neutres de couleur.

Espace de phase pour les émissions de type vide dans un plasma. En présence du plasma, la première chose à déterminer est l'espace de phase pour les émissions de type vide (Bremsstrahlung) qui doivent être resommées dans l'approximation double logarithmique. Notons qu'au sein de cette approximation, les émissions induites sont négligeables car le spectre intégré (I.4) ne génère pas de double logarithme (pas de singularité colinéaire). Cette espace de

phase est modifié pour la raison suivante: durant le temps de formation t_f d'un gluon, le milieu donne une impulsion transverse $k_\perp \sim \hat{q}t_f$. Cela signifie qu'un gluon émis par Bremsstrahlung a nécessairement $k_\perp > \hat{q}t_f$ (on remarque qu'au contraire, les émissions induites saturent cette condition puisqu'elles vérifient $k_\perp = \hat{q}t_f$). Cette contrainte, $k_\perp > \hat{q}t_f$ sur les émissions de type vide produite à l'intérieur du milieu, n'est pertinente que dans le régime $k^+ < \omega_c$. En effet, comme ω_c est l'énergie maximale d'une émission induite se formant sur une durée L, toutes les émissions avec $k^+ \geq \omega_c$ sont nécessairement déclenchées par la virtualité du parton source[1].

Par ailleurs, cette contrainte n'a de sens que pour les émissions ayant un temps de formation plus court que la durée L de propagation du jet dans le plasma. Un gluon peut ainsi être émis directement à l'extérieur du milieu si $t_f > L$. Une conséquence directe de ces deux inégalités:

$$\text{Emissions dans le milieu:} \quad k_\perp > \hat{q}t_f \quad \Longleftrightarrow \quad k^+ \gg \omega_0(\theta) = (2\hat{q}/\theta^4)^{1/3} \tag{I.9}$$

$$\text{Emissions à l'extérieur:} \quad t_f \gg L \quad \Longleftrightarrow \quad k^+ \ll \omega_L(\theta) = 2/(\theta^2 L) \tag{I.10}$$

est l'existence d'une région de l'espace, la région "veto", dans laquelle les émissions de type vide sont interdites. Cet espace de phase est représenté sur la Fig. 5.1.

Effets induits par la décohérence. Outre cette modification de l'espace de phase, la décohérence de couleur a aussi des effets sur le développement du processus de branchement. Nous montrons dans un premier temps qu'en réalité, la décohérence ne modifie pas l'évolution des cascades partoniques qui se produisent *dans* le milieu. Considérons un gluon émis par un dipôle neutre, comme dans la section précédente (l'argumentation se généralise aisément aux dipôles chargés). Il est facile d'observer que

$$\frac{t_f}{t_{\rm coh}} = \frac{(2\hat{q}\theta_{q\bar{q}}^2)^{1/3}}{k^+\theta^2} = \frac{\omega_0(\theta)}{k^+}\left(\frac{\theta_{q\bar{q}}}{\theta}\right)^{2/3}. \tag{I.11}$$

A présent, supposons qu'une émission de type vide dans le milieu, qui par construction satisfait $k^+ \geq \omega_0(\theta)$, viole l'ordonnancement angulaire, c'est à dire $\theta > \theta_{q\bar{q}}$. Alors, d'après l'égalité ci-dessus, on a nécessairement $t_f < t_{\rm coh}$, ce qui signifie que le dipôle est toujours cohérent pendant la formation du gluon. Par conséquent, une telle émission ne peut pas exister. Par récurrence, on montre facilement que cet argument se généralise à un nombre arbitraire d'émissions produites dans le milieu et l'on conclut que la propriété d'ordonnancement angulaire reste vrai dans le milieu.

La décohérence a néanmoins un effet très important pour la première émission à l'extérieur du milieu. En effet, pour une telle émission, le dipôle émetteur a parcouru une distance d'ordre L dans le milieu. Si $t_{\rm coh} < L \Leftrightarrow \theta > \theta_c$, ce dipôle a perdu sa cohérence durant sa propagation, et par conséquent, la première émission à l'extérieur peut être émise à n'importe quel angle. Il y a violation de l'ordonnancement angulaire pour la première émission hors du milieu. Le reste de la cascade partonique à l'extérieur se déroule ensuite comme dans le vide, jusqu'à l'hadronisation des partons produits.

Le processus de branchement en présence d'un milieu qui permet de resommer correctement les double logarithmes dus aux radiations Bremsstrahlung est schématisé sur la Fig. 5.3. Nous avons donné ici des arguments physiques simples pour justifier cette nouvelle image permettant de resommer les émissions Bremsstrahlung à tous les ordres dans un milieu dense statique. Dans le Chapitre 5 de cette thèse, des arguments mathématiques précis sont avancés, et le cas du milieu en expansion longitudinale est aussi traité.

[1] En toute rigueur, cela n'est vrai que dans l'approximation des diffusions multiples molles. Une émission avec $k^+ \geq \omega_c$ peut être induite par le milieu via une seule collision dure avec un centre diffuseur. Cependant, ce genre de processus est rare, et sera négligé par la suite.

I.1.3 Factorisation et implémentation au sein d'un générateur Monte-Carlo

Factorisation des émissions induites. L'évolution des émissions de type vide décrite dans la section précédente présente l'avantage de "factoriser" en temps les émissions induites par le milieu. Par factorisation, nous entendons ici que le parton à l'origine du jet évolue d'abord par Bremsstrahlung dans le milieu, produisant une cascade au sein de l'espace de phase en rouge sur la Fig. 5.3. Ce n'est qu'après que les partons produits par cette première cascade ont évacué leur virtualité jusqu'à l'échelle transverse $(\hat{q}k^+)^{1/4}$ qu'ils radient par émissions induites pendant un temps d'ordre L. En effet, on peut montrer que la condition $k^+ \gg \omega_0(\theta)$ satisfaite par les émissions de type vide émises dans le milieu implique que l'énergie (maximale) perdue par émission induite durant la formation, de l'ordre de $\hat{q}t_f^2$ est négligeable devant k^+. En conséquence, on peut négliger les radiations induites pendant le développement des cascades de type vide à l'intérieur du milieu.

Le régime des branchements multiples pour les émissions induites. Ainsi, une fois l'évolution via Bremsstrahlung à l'intérieur du milieu terminée, les partons produits rayonnent selon le spectre BDMPS-Z. Pour ces gluons induits, il est cependant aussi nécessaire d'itérer le processus (I.4) correspondant à une seule émission. En effet, l'intégrale de (I.4) sur toutes les énergies donnent un spectre total d'émission:

$$N^{\mathrm{on-shell}}(\omega) = \int_{\omega}^{\omega_c} \mathrm{d}k^+ \, \frac{\mathrm{d}N^{\mathrm{on-shell}}}{\mathrm{d}k^+} \sim \sqrt{\frac{\bar{\alpha}_s^2 \omega_c}{\omega}} \tag{I.12}$$

qui est d'ordre 1 pour $\omega \sim \omega_{\mathrm{br}} \equiv \bar{\alpha}_s^2 \hat{q} L^2$, avec $\bar{\alpha}_s = \alpha_s N_c/\pi$. Cela signifie que pour des énergies de l'ordre de l'échelle de branchement ω_{br}, on ne peut plus interpréter $\mathrm{d}N^{\mathrm{on-shell}}$ comme la probabilité d'un évènement rare, mais comme un nombre d'émission, puisque $N^{\mathrm{on-shell}}(\omega)$ devient d'ordre 1 malgré le fait que $\alpha_s \ll 1$. Par conséquent, de telles émissions doivent aussi être "resommés". Le large paramètre sans dimension qui doit être resommé à tous les ordres est donné par (I.12), que l'on écrira plutôt sous la forme $\bar{\alpha}_s L/t_{f,\mathrm{med}} = \mathcal{O}(1)$. Cette dernière écriture est plus transparente physiquement: quand la longueur du chemin à travers le plasma du parton source est très grande devant le temps de formation d'une émission induite, de nombreuses émissions peuvent se produire et donc un calcul à l'ordre le plus bas n'est plus suffisant.

Cette resommation dans le régime des branchements multiples $\omega \lesssim \omega_{\mathrm{br}}$ s'effectue par l'intermédiaire d'un processus de branchement markovien ordonné en temps, le temps physique d'émission du gluon induit le long de la trajectoire du parton source. Une émission peut être considérée comme locale en temps, car le temps de formation $t_{f,\mathrm{med}}$ est réduit par un facteur α_s vis à vis du temps de propagation caractéristique entre deux branchements. Le taux d'émission est donné par le spectre BDMPS-Z différentiel en L (taux d'émission par unité de temps) et l'angle des émissions induites est fixé par la loi de diffusion transverse (I.1) entre deux branchements successifs.

Nous démontrons dans le Chapitre 4, Section 4.3 que ce type de cascade permet de transporter très efficacement de l'énergie à des grands angles, mécanisme physique indispensable pour expliquer la réduction des jets mesurée au LHC. L'échelle physique typique de cette perte d'énergie à grand angle est naturellement ω_{br}.

Implémentation Monte-Carlo dans `JetMed`. Une image simple du développement des cascades de partons dans un milieu émerge donc de la QCD en théorie des perturbations. Comme

cette image est markovienne, il est possible de simuler le processus de branchement numériquement grâce à un générateur d'évènements par la méthode de Monte-Carlo. L'implémentation suit la factorisation du processus en trois étapes:

1. une cascade d'émissions de type vide ordonnée en angles dans la région de l'espace de phase correspondant à l'intérieur du milieu: $\omega \geq \omega_0(\theta)$ et $\theta \geq \theta_c$. Les fonctions de branchement de Dokshitzer-Gribov-Lipatov-Altarelli-Parisi (DGLAP) et la variation de la constante de couplage α_s avec l'impulsion transverse du branchement sont prises en compte par le programme. L'angle maximal de la première émission est fixé à une certaine valeur $\theta_{\max}$.

2. Tous les partons produits par la précédente cascade entrent ensuite dans la cascade d'émissions induites suivant l'image explicitée dans le paragraphe précédent. Les branchements quark-gluon, gluon-gluon et gluon-quark sont autorisés, avec les fonctions de branchement données en Appendice C. Durant cette cascade, la constante de couplage α_s est gelée à une valeur fixe $\alpha_{s,\mathrm{med}}$.

3. Finalement, une dernière cascade de type vide ordonnée en angle est générée au sein de l'espace de phase correspondant à l'extérieur du milieu, $\omega \leq \omega_L(\theta)$ ou $\theta \leq \theta_c$, à partir des partons produits par les deux premières cascades . Pour la première émission, l'angle d'émission maximal est à nouveau $\theta_{\max}$, afin de tenir compte de la violation de l'ordonnancement angulaire pour la première émission à l'extérieur du milieu. Cette dernière cascade s'achève lorsque l'impulsion transverse des partons produits atteint la coupure infrarouge $k_{\perp,\min}$ de l'ordre de Λ_{QCD}.

Les paramètres physiques du Monte-Carlo `JetMed` sont le coefficient de transport $\hat{q}$, la longueur L du chemin à travers le plasma des jets et $\alpha_{s,\mathrm{med}}$. Ce dernier paramètre pourrait être évité en évaluant α_s à l'impulsion transverse typique des émissions induites $k_{f,\mathrm{med}}$. Les paramètres non physiques sont $\theta_{\max}$ et $k_{\perp,\min}$. Pour éviter d'introduire de telles coupures non physiques, il faudrait améliorer l'implémentation actuelle en générant des cascades de dipôles et en incluant les effets d'hadronisation. Pour l'heure, ces paramètres seront variés autour des valeurs centrales $\theta_{\max} = 1$, $k_{\perp,\min} = 250$ MeV afin d'étudier leur influence sur nos résultats.

I.2 Etude phénoménologique des observables de jets en collisions Pb-Pb au LHC

Dans cette section, nous présentons succinctement des calculs Monte-Carlo d'observables de jets obtenus avec `JetMed`. Nous mettrons l'accent sur l'interprétation physique de ces résultats. Le corps principal de cette thèse comprend également des études analytiques qui viennent corroborer ces interprétations. Comme la géométrie des collisions est largement simplifiée dans `JetMed`, nous nous intéresserons essentiellement aux collisions centrales (petit paramètre d'impact entre les deux noyaux) et aux jets produits proche du plan transverse à la collision où l'énergie du jet et son impulsion transverse sont égales.

I.2.1 Le facteur de modification nucléaire pour la section efficace de production des jets

Le phénomène de réduction des jets en collisions d'ions lourds est quantifié par le facteur de modification nucléaire pour la section efficace inclusive de jets, noté R_{AA}. Cette quantité est

défini comme le rapport entre la section efficace de production de jets en collisions noyau-noyau et cette même section efficace en collisions proton-proton:

$$R_{AA}(p_T) \equiv \frac{1}{\langle T_{AA} \rangle} \frac{\left.\frac{\mathrm{d}\sigma_{\mathrm{jet}}}{\mathrm{d}p_T}\right|_{AA}}{\left.\frac{\mathrm{d}\sigma_{\mathrm{jet}}}{\mathrm{d}p_T}\right|_{pp}} \tag{I.13}$$

Le facteur $\langle T_{AA} \rangle$ normalise $R_{AA} = 1$ en l'absence d'effets nucléaires autre que l'accroissement de la section efficace dû au nombre plus important de nucléons impliqués dans une collision AA que dans une collisions pp. R_{AA} est une fonction de l'impulsion transverse p_T des jets produits.

Nos résultats pour R_{AA} obtenus par calcul Monte-Carlo avec `JetMed` sont présentés sur la figure 8.3-gauche, superposés aux données expérimentales obtenues par la collaboration ATLAS. Les bandes rouges correspondent aux incertitudes théoriques de notre calcul, obtenues en variant les paramètres non physiques $\theta_{\max}$ et $k_{\perp,\min}$. Les données expérimentales et nos prédictions théoriques présentent deux caractéristiques notables: R_{AA} est significativement plus petit que 1 et cela, même quand l'énergie des jets produits est très grande, jusqu'à 1 TeV !

Le fait que R_{AA} soit plus petit que 1 est une conséquence simple de l'effet combiné de la perte d'énergie des jets dans le plasma et de la section efficace du processus dur qui décroît rapidement avec p_T. En effet, un jet mesuré en collisions Pb-Pb avec une énergie p_T aurait eu une énergie $p_T + \mathcal{E}$ s'il n'avait pas perdu une énergie $\mathcal{E}$ dans le milieu produit par la collision. Comme la probabilité de produire un jet avec une énergie $p_T+\mathcal{E}$ est plus faible que la probabilité de produire un jet avec une énergie p_T, du fait de la chute rapide de la section efficace des jets avec p_T, on a naturellement $R_{AA} < 1$.

Le fait non trivial est que R_{AA} ne tende pas rapidement vers 1 quand p_T augmente: cela devrait être le cas si les jets perdaient une énergie constante $\mathcal{E} \approx \omega_{\mathrm{br}}$. Au sein de notre image factorisée, nous expliquons ce fait expérimental par le mécanisme physique suivant: plus un jet à une énergie importante, plus son évolution via Bremsstrahlung à l'intérieur du milieu sera grande, dans le sens où le nombre de sources partoniques produites dans le milieu, et donc susceptibles de perdre de l'énergie, augmente avec l'impulsion transverse du jet. En nous fondant sur la factorisation mise en avant dans la section précédente, nous proposons une formule approchée pour estimer cette perte d'énergie $\mathcal{E}(p_T)$:

$$\mathcal{E}_i(p_T) \approx \omega_{\mathrm{br}} \times \frac{C_i}{2C_A} \left(\frac{p_T}{\omega_0(R)}\right)^{\sqrt{\frac{3\bar{\alpha}_s}{2}}} \tag{I.14}$$

où i se réfère à la représentation du parton produit par la collision dure et R est le rayon du jet. Le facteur proportionnel à $(p_T/\omega_0(R))^{\sqrt{\frac{3\bar{\alpha}_s}{2}}}$ compte le nombre de sources de type vide produites dans la région de l'espace de phase à l'intérieur du milieu, dans l'approximation double logarithmique. Le facteur ω_{br} représente quant à lui l'énergie typique perdue à grands angles par chacune de ces sources. Cette formule montre clairement que $\mathcal{E}(p_T)$ augmente avec p_T en loi de puissance. Même si l'exposant est *a priori* petit ($\alpha_s \ll 1$), cette augmentation est suffisante pour expliquer le plateau à grand p_T du facteur de modification nucléaire des jets.

I.2.2 La distribution Soft Drop z_g

L'observable R_{AA} est très importante car elle fut historiquement une des premières preuves de la réduction des jets en collisions d'ions lourds. Décrire correctement cette quantité est donc une première étape indispensable à toute analyse phénoménologique plus approfondie des autres observables de jets. A présent, nous nous intéressons à une observable dite de sous-structure,

puisqu'elle quantifie la structure interne des jets, la distribution Soft Drop z_g. Cette observable est connue pour être relativement robuste vis à vis des effets non perturbatifs. Par ailleurs, les collaborations CMS et ALICE l'ont récemment mesurée en collisions Pb-Pb. Pour ces raisons, nous avons décidé de la calculer avec `JetMed`.

Avant de discuter des modifications nucléaires de cette observable, rappelons brièvement sa définition. L'idée générale de cette observable est d'effeuiller le jet de ses émissions molles afin de trouver un branchement suffisamment "dur". Etant donné un jet défini via l'algorithme anti-$k_\perp$ avec un rayon R, ses constituants sont d'abord reclusterisés en utilisant l'algorithme Cambridge/Aachen ordonné en angles. Ensuite, le jet est déclusterisé, ce qui donne deux sous-jets d'impulsions p_{T1} et p_{T2}, séparés par une distance en rapidité-azimuth $\Delta R_{12}^2 = \Delta y_{12}^2 + \Delta\phi_{12}^2$. La procédure s'arrête lorsque la condition SoftDrop est satisfaite:

$$z_{12} \equiv \frac{\min(p_{T1}, p_{T2})}{p_{T1} + p_{T2}} > z_{\rm cut} \left(\frac{\Delta R_{12}}{R}\right)^{\beta}, \tag{I.15}$$

où $z_{\rm cut}$ et $\beta \leq 0$ sont des paramètres de l'observable. Dans la suite, nous imposons aussi une condition sur l'angle ΔR_{12} du branchement qui doit satisfaire $\Delta R_{12} > \theta_{\rm cut}$. Si la condition Soft Drop n'est pas satisfaite, la procédure est itérée avec le sous-jet le plus dur. Les valeurs de z_g et θ_g de ce jet sont alors définies comme étant respectivement z_{12} and ΔR_{12} pour le branchement qui a vérifié la condition Soft Drop, si un tel branchement existe. Si aucun branchement n'est trouvé, on choisit par convention $z_g = 0$ et $\theta_g = 0$. La distribution z_g, notée $p(z_g)$ est ensuite définie comme la section efficace de production de jets ayant une valeur donnée de z_g:

$$p(z_g) \equiv \frac{1}{N_{\rm jets}} \frac{{\rm d}N}{{\rm d}z_g} \tag{I.16}$$

Intuitivement, cette distribution correspond à la probabilité d'avoir un premier branchement dans un jet avec une fraction d'impulsion telle que $z > z_{\rm cut}$. Le terme "premier" est ici entendu vis à vis du processus de branchement ordonné en angles reconstitué par l'algorithme Cambridge/Aachen. Dans le vide, pour $\beta = 0$ et dans l'approximation double-logarithmique cette probabilité est directement proportionnelle à la partie singulière des fonctions DGLAP, c'est à dire $p(z_g) \propto 1/z_g$.

Notre étude Monte-Carlo révèle l'existence de deux régimes en fonction de l'impulsion transverse des jets sélectionnés pour calculer $p(z_g)$. Ces deux régimes diffèrent par la monotonie du ratio entre la distribution mesurée en collisions d'ions lourds et celle mesurée en pp. Pour la discussion qui suit, nous nous référons à la Fig. 9.1, qui représente ce ratio calculé pour un spectre dur monochromatique, i.e. de la forme $\sigma(p_T) = \delta_{iR}\delta(p_T - p_{T0})$. Sur la figure de gauche, le parton initial est un gluon $R = A$, tandis que sur la figure de droite, le parton initial est un quark $R = F$. Les différentes courbes correspondent à différentes valeurs de p_{T0}. A très grande énergie, le ratio avec la distribution du vide est croissant avec z_g, alors que ce ratio devient décroissant quand p_{T0} diminue. L'échelle de transition est de l'ordre de $p_{T0} \sim z_{\rm cut}\omega_c$.

L'existence de deux régimes différents s'explique aisément quand on considère l'espace de phase sondé par la distribution en fonction de $z_{\rm cut}$ et $\theta_{\rm cut}$ (pour $\beta = 0$). Cet espace de phase dans les deux régimes, $p_{T0} \gg z_{\rm cut}\omega_c$ ou $p_{T0} \ll z_{\rm cut}\omega_c$, est représenté sur la Fig. 9.2 en fonction des variables $k_\perp \simeq z p_{T0}\theta$ et R/θ. L'aire encadrée par les traits en pointillés noirs correspond au régime cinématique des branchements sélectionnable par la procédure SoftDrop. On remarque que pour $p_{T0} \gg z_{\rm cut}\omega_c$, la distribution n'est sensible qu'aux émissions de type vide produites à l'intérieur du milieu. Dans cette situation, le seul effet du plasma sur la distribution est la perte d'énergie des deux sous-jets sélectionnés par Soft Drop. Cette perte d'énergie est *incohérente* car les deux sous-jets sont séparés par un angle $\theta_g > \theta_{\rm cut} > \theta_c$. Elle induit alors une modification

de la fraction de branchement z_g mesurée par rapport à la fraction dite "physique" au moment de l'émission. On peut montrer alors que cet effet se traduit mathématiquement par un facteur de modification nucléaire *croissant* pour la distribution z_g.

Au contraire, pour $p_{T0} \ll z_{\text{cut}}\omega_c$, on remarque que Soft Drop est en mesure de sélectionner des branchements avec un sous-jet ayant une énergie plus petite que ω_c, et un $k_\perp$ de l'ordre de Q_s. En d'autres termes, dans ce régime, la distribution z_g est aussi sensible aux branchements induits par le milieu qui restent à l'intérieur du jet. Cette sensibilité aux émissions induites transparaît dans la partie à petit z_g de la distribution. Le pic visible sur la Fig. 9.1 pour $p_{T0} = 100, 200$ GeV est causé par ces émissions, qui dominent la distribution car la partie singulière du spectre induit $\propto 1/z^{3/2}$ est plus divergente que celle du spectre Bremsstrahlung $\propto 1/z$.

Jusqu'à présent, nous avons considéré un spectre dur monochromatique idéalisé dans cette discussion des modifications nucléaires de la distribution z_g. En réalité, le spectre du processus dur est fortement décroissant, et cette forte décroissance favorise les jets qui perdent peu d'énergie dans le plasma. Nos résultats Monte-Carlo pour un spectre initial réaliste sont montré sur la Fig. 9.11. Sur cette figure, les bandes correspondent une nouvelle fois à l'incertitude de nos prédictions obtenue en variant $\theta_{\max}$ et $k_{\perp,\min}$ dans `JetMed`. En comparant avec la Fig. 9.1, nous observons un effet important causé par la forte décroissance du spectre initial: les courbes pour le ratio milieu/vide sont décalées vers des valeurs plus faibles. Cette réduction globale du facteur de modification nucléaire vient du fait que les jets sélectionnés dans la distribution z_g, dont le nombre est le facteur N_{jets} dans la formule (I.16), ont, par définition une sous-structure dure. Or, de tels jets ont tendance à perdre plus d'énergie que la moyenne, car la présence de deux sous-jets durs, séparés par un angle $\theta_g > \theta_{\text{cut}} > \theta_c$, implique un plus grand nombre de sources partoniques formées à l'intérieur du milieu, et donc une plus grand perte d'énergie. En conséquence, les jets sélectionnés par Soft Drop sont produits en moins grand nombre dans le milieu du fait du spectre dur fortement décroissant. L'effet résultant est une suppression du ratio, visible sur la Fig. 9.11 comparée à la Fig. 9.1.

Les résultats mis en avant dans cette section sont en accord qualitatif avec les données expérimentales obtenues par la collaboration ALICE et reproduites Fig. 7.6. Ces données révèlent un facteur de modification nucléaire plus petit que 1, et croissant quand z_g diminue, laissant à penser que des émissions induites qui restent à l'intérieur du jet sont bien capturées par Soft Drop. Cependant, ces données n'étant pas corrigées des effets des détecteurs, nous restons prudent quant à cette dernière interprétation.

I.2.3 La fonction de fragmentation

La dernière observable à laquelle nous nous intéresserons est la fonction de fragmentation qui caractérise le contenu énergétique des jets en termes de hadrons. Plus précisément, cette observable et son facteur de modification nucléaire associé sont définis par:

$$\mathcal{D}(x) = \frac{1}{N_{\text{jets}}}\frac{\mathrm{d}N}{\mathrm{d}x}\,, \qquad \mathcal{R}(x) = \frac{\mathcal{D}^{\text{med}}(x)}{\mathcal{D}^{\text{vac}}(x)}\,, \tag{I.17}$$

où $\mathrm{d}N$ est le nombre de hadrons avec une fraction d'énergie x par rapport à l'énergie totale du jet, parmi les jets sélectionnés (dans une certaine fenêtre en impulsion transverse et en rapidité). Les mesures expérimentales obtenues par ATLAS pour le ratio $\mathcal{R}(x)$ sont données sur la Fig. 7.3 pour trois fenêtres en p_T distinctes. On observe un nombre plus important de fragments durs ($x \sim 1$) et mous ($x \lesssim 0.01$) dans les jets produits en collisions d'ions lourds, par rapport aux collisions *pp*.

Les résultats d'un calcul `JetMed` pour $\mathcal{R}(x)$ sont montrés sur la Fig. 10.1. La figure de gauche présente la variabilité de ces résultats avec les paramètres non physiques $\theta_{\max}$ et $k_{\perp,\min}$. Contrairement à R_{AA} ou à la distribution z_g, l'enveloppe est large. C'est une conséquence du fait que la fonction de fragmentation définie par Eq. (I.17) est fortement sensible aux effets non perturbatifs, et en particulier aux corrections hadroniques. Cette observable est dite non "protégée" contre les divergences infrarouges et colinéaires. En conséquence, elle dépend de la valeur précise du régulateur $k_{\perp,\min}$ nécessaire pour la calculer en théorie des perturbations. Pour remédier à ce problème, nous avons introduit dans cette thèse une nouvelle observable qui caractérise la fragmentation des jets non pas en termes de hadrons, mais en termes de sous-jets. Cette observable, protégée des divergences infrarouges, est définie dans la Section 4.2.3.3, et son facteur de modification nucléaire associé est représenté sur la Fig. 10.6-gauche. Comme attendu, les enveloppes obtenues en variant $k_{\perp,\min}$ et $\theta_{\max}$ sont considérablement réduites, tandis que les effets du milieu sont toujours significatifs. Pour plus de détails, nous renvoyons le lecteur à la Section 10.4.

Retournons à présent à la fonction de fragmentation standard définie par (I.17). Le comportement qualitatif observé sur la Fig. 10.1-gauche est identique à celui mesuré expérimentalement. Sur la figure de droite, nous varions cette fois les paramètres physiques $\hat{q}$, L et $\alpha_{s,\text{med}}$ au sein d'un ensemble qui reproduit correctement le facteur de modification nucléaire pour la section efficace (cf. Fig. 8.5a).

Avec la Fig. 10.1-droite, nous notons tout d'abord qu'il y a aussi une dégénérescence des paramètres physiques dans la région où x est proche de 1: toutes les courbes de cette figure se superposent presque parfaitement pour $x \sim 1$. Cela suggère que le mécanisme physique à l'origine de l'accroissement visible à x proche de 1 est fortement corrélé avec la perte d'énergie, qui est l'ingrédient essentiel expliquant R_{AA}. En effet, une analyse analytique approfondie, détaillée dans la Section 10.2, révèle que l'effet dominant est le biais vers les jets ayant un hadron avec $x \sim 1$ induit par le spectre dur initial et la perte d'énergie. Un jet ayant un hadron avec $x \sim 1$ a une évolution à l'intérieur du milieu limitée par rapport à une évolution moyenne (car si le parton créant le jet émets beaucoup de gluons via Bremsstrahlung dans l'espace de phase correspondant à l'intérieur du milieu, sa fraction d'énergie finale sera nécessairement plus faible). En conséquence, de tels jets perdent moins d'énergie, et sont donc préférentiellement produits en présence du plasma. Cela explique l'accroissement visible dans la partie dure de la fonction de fragmentation, ainsi que la forte corrélation avec R_{AA}.

Dans le domaine $x \lesssim 0.01$ de cette fonction, les ingrédients physiques expliquant le nombre plus importants de fragments mous sont radicalement différents (la dégénérescence des paramètres physiques est d'ailleurs levée). Le mécanisme clé est la décohérence induite par le milieu et la violation de l'ordonnancement angulaire pour la première émission à l'extérieur du milieu qui en résulte. Cette violation de l'ordonnancement angulaire ré-ouvre l'espace de phase angulaire, conduisant à une évolution via Bremsstrahlung accrue à l'extérieur du milieu, et donc à une augmentation du nombre de hadrons mous à l'intérieur des jets en collisions noyau-noyau. Dans l'approximation double-logarithmique, il est possible de montrer rigoureusement la factorisation entre le nombre de sources (essentiellement gluons) produites via Bremsstrahlung à l'intérieur du milieu $\mathcal{N}_{\text{in}}$, et celles produites à l'extérieur N^{out} :

$$\mathcal{D}^{\text{med}}(x) \simeq \mathcal{N}_{\text{in}} \times \left(\frac{\mathrm{d}N^{\text{out}}}{\mathrm{d}x}\right) \tag{I.18}$$

Cette factorisation est rendu possible par la décohérence qui détruit les corrélations quantiques entre les émissions dans le milieu et celles à l'extérieur (effet de perte de mémoire). Au delà de l'approximation double-logarithmique, l'effet est encore accentué par les émissions induites

relativement dures qui restent à l'intérieur du jet, et qui contribuent à augmenter le facteur $\mathcal{N}_{\text{in}}$ dans Eq. (I.18). L'effet net résultant est un nombre plus important de hadrons mous dans les jets produits en collisions Pb-Pb comparées aux collisions *pp*. Ces propos doivent être néanmoins nuancés car d'autres études rendent compte de cette hausse des hadrons mous par la réponse du plasma à la propagation du jet. En se propageant, le parton énergétique entraîne avec lui, par son interaction avec le plasma, des particules molles du milieu qui peuvent être finalement clusterisées avec le jet. Le Monte-Carlo `JetMed` n'incluant pas un tel effet, nous ne sommes pas encore en mesure de quantifier son importance relative vis à vis de celui induit par la violation de l'ordonnancement angulaire.

Conclusion

Pour conclure ce résumé détaillé, nous donnons les limitations principales de nos travaux, et donc nos projets futurs d'améliorations du Monte-Carlo `JetMed`. A ce titre, le tableau 6.2 résume les ingrédients présents et manquants dans `JetMed`, vis à vis des autres approches théoriques existantes dans la littérature à l'heure actuelle.

La modélisation du milieu est largement simplifiée dans les considérations théoriques et les calculs présentés ci-dessus. Incorporer l'expansion du milieu, la géométrie précise des collisions et les effets de réponse du milieu sont des éléments essentiels pour décrire certaines observables comme le profil radial des jets, l'asymmetrie des paires de jets ou bien la dépendance de R_{AA} avec la centralité.

D'autres observables, telles que la corrélation photon-jet, sont sensibles aux radiations dans l'état initial et aux émissions molles à des angles sensables. Inclure proprement ces effets nécessite de décrire l'évolution des jets par des cascades de dipôles. Une telle approche simplifie aussi l'adjonction des corrections d'hadronisation. Ainsi, reformuler le Monte-Carlo `JetMed` en termes de dipôles serait un travail d'une valeur certaine.

Enfin, le traitement des cascades d'émissions induites souffre aussi de quelques lacunes: la constante de couplage de la QCD est gelée, au lieu d'être fixée par l'impulsion transverse du branchement. Les émissions dures, causées par une collision dure avec un centre diffuseur du milieu, ont également été négligées. De récents travaux théoriques rendent maintenant possible l'ajout de ces contributions au sein de l'image factorisée développée dans `JetMed`.

Bibliography

[1] J. Bjorken, "Asymptotic Sum Rules at Infinite Momentum," *Phys. Rev.* **179** (1969) 1547–1553.

[2] J. Bjorken and E. A. Paschos, "Inelastic Electron Proton and gamma Proton Scattering, and the Structure of the Nucleon," *Phys. Rev.* **185** (1969) 1975–1982.

[3] R. P. Feynman, "Very high-energy collisions of hadrons," *Phys. Rev. Lett.* **23** (1969) 1415–1417.

[4] C.-N. Yang and R. L. Mills, "Conservation of Isotopic Spin and Isotopic Gauge Invariance," *Phys. Rev.* **96** (1954) 191–195.

[5] D. J. Gross and F. Wilczek, "Ultraviolet Behavior of Nonabelian Gauge Theories," *Phys. Rev. Lett.* **30** (1973) 1343–1346.

[6] H. Politzer, "Reliable Perturbative Results for Strong Interactions?," *Phys. Rev. Lett.* **30** (1973) 1346–1349.

[7] G. 't Hooft, "Dimensional regularization and the renormalization group," *Nucl. Phys. B* **61** (1973) 455–468.

[8] G. 't Hooft, "The birth of asymptotic freedom," *Nucl. Phys. B* **254** (1985) 11–18.

[9] C. S. Fischer, "QCD at finite temperature and chemical potential from Dyson–Schwinger equations," *Prog. Part. Nucl. Phys.* **105** (2019) 1–60, `arXiv:1810.12938 [hep-ph]`.

[10] K. Fukushima and C. Sasaki, "The phase diagram of nuclear and quark matter at high baryon density," *Prog. Part. Nucl. Phys.* **72** (2013) 99–154, `arXiv:1301.6377 [hep-ph]`.

[11] R. Hagedorn, "Statistical thermodynamics of strong interactions at high-energies," *Nuovo Cim. Suppl.* **3** (1965) 147–186.

[12] N. Cabibbo and G. Parisi, "Exponential Hadronic Spectrum and Quark Liberation," *Phys. Lett. B* **59** (1975) 67–69.

[13] **HotQCD** Collaboration, A. Bazavov *et al.*, "Equation of state in (2+1)-flavor QCD," *Phys. Rev. D* **90** (2014) 094503, `arXiv:1407.6387 [hep-lat]`.

[14] Y. Aoki, G. Endrodi, Z. Fodor, S. Katz, and K. Szabo, "The Order of the quantum chromodynamics transition predicted by the standard model of particle physics," *Nature* **443** (2006) 675–678, `arXiv:hep-lat/0611014`.

[15] P. de Forcrand, "Simulating QCD at finite density," *PoS* **LAT2009** (2009) 010, arXiv:1005.0539 [hep-lat].

[16] E. Iancu, "QCD in heavy ion collisions," in *2011 European School of High-Energy Physics*, pp. 197–266. 2014. arXiv:1205.0579 [hep-ph].

[17] W. Florkowski, *Phenomenology of Ultra-Relativistic Heavy-Ion Collisions*. 3, 2010.

[18] B. Back *et al.*, "The Significance of the fragmentation region in ultrarelativistic heavy ion collisions," *Phys. Rev. Lett.* **91** (2003) 052303, arXiv:nucl-ex/0210015.

[19] **ATLAS** Collaboration, G. Aad *et al.*, "Measurement of charged-particle spectra in Pb+Pb collisions at $\sqrt{s_{\mathrm{NN}}} = 2.76$ TeV with the ATLAS detector at the LHC," *JHEP* **09** (2015) 050, arXiv:1504.04337 [hep-ex].

[20] J. Bjorken, "Highly Relativistic Nucleus-Nucleus Collisions: The Central Rapidity Region," *Phys. Rev. D* **27** (1983) 140–151.

[21] F. G. Gardim, G. Giacalone, M. Luzum, and J.-Y. Ollitrault, "Revealing QCD thermodynamics in ultrarelativistic nuclear collisions," *Nature Phys.* **16** no. 6, (2020) 615–619, arXiv:1908.09728 [nucl-th].

[22] **ATLAS** Collaboration, G. Aad *et al.*, "Observation of Long-Range Elliptic Azimuthal Anisotropies in $\sqrt{s}$ =13 and 2.76 TeV *pp* Collisions with the ATLAS Detector," *Phys. Rev. Lett.* **116** no. 17, (2016) 172301, arXiv:1509.04776 [hep-ex].

[23] **ATLAS** Collaboration, G. Aad *et al.*, "Measurement of the azimuthal anisotropy for charged particle production in $\sqrt{s_{NN}} = 2.76$ TeV lead-lead collisions with the ATLAS detector," *Phys. Rev. C* **86** (2012) 014907, arXiv:1203.3087 [hep-ex].

[24] M. Luzum, "Flow fluctuations and long-range correlations: elliptic flow and beyond," *J. Phys. G* **38** (2011) 124026, arXiv:1107.0592 [nucl-th].

[25] K. Dusling, M. Mace, and R. Venugopalan, "Parton model description of multiparticle azimuthal correlations in pA collisions," *Phys. Rev. D* **97** no. 1, (2018) 016014, arXiv:1706.06260 [hep-ph].

[26] N. Borghini, P. M. Dinh, and J.-Y. Ollitrault, "Flow analysis from multiparticle azimuthal correlations," *Phys. Rev. C* **64** (2001) 054901, arXiv:nucl-th/0105040.

[27] J.-Y. Ollitrault, "Flow systematics from SIS to SPS energies," *Nucl. Phys. A* **638** (1998) 195–206, arXiv:nucl-ex/9802005.

[28] B. H. Alver, C. Gombeaud, M. Luzum, and J.-Y. Ollitrault, "Triangular flow in hydrodynamics and transport theory," *Phys. Rev. C* **82** (2010) 034913, arXiv:1007.5469 [nucl-th].

[29] F. G. Gardim, F. Grassi, M. Luzum, and J.-Y. Ollitrault, "Mapping the hydrodynamic response to the initial geometry in heavy-ion collisions," *Phys. Rev. C* **85** (2012) 024908, arXiv:1111.6538 [nucl-th].

[30] P. Romatschke and U. Romatschke, "Viscosity Information from Relativistic Nuclear Collisions: How Perfect is the Fluid Observed at RHIC?," *Phys. Rev. Lett.* **99** (2007) 172301, arXiv:0706.1522 [nucl-th].

[31] U. Heinz and R. Snellings, "Collective flow and viscosity in relativistic heavy-ion collisions," *Ann. Rev. Nucl. Part. Sci.* **63** (2013) 123–151, arXiv:1301.2826 [nucl-th].

[32] J. Alam, B. Sinha, and S. Raha, "Electromagnetic probes of quark gluon plasma," *Phys. Rept.* **273** (1996) 243–362.

[33] A. Andronic *et al.*, "Heavy-flavour and quarkonium production in the LHC era: from proton–proton to heavy-ion collisions," *Eur. Phys. J. C* **76** no. 3, (2016) 107, arXiv:1506.03981 [nucl-ex].

[34] T. Matsui and H. Satz, "J/ψ Suppression by Quark-Gluon Plasma Formation," *Phys. Lett. B* **178** (1986) 416–422.

[35] P. Caucal, E. Iancu, A. Mueller, and G. Soyez, "Nuclear modification factors for jet fragmentation," arXiv:2005.05852 [hep-ph].

[36] P. Caucal, E. Iancu, A. Mueller, and G. Soyez, "Jet fragmentation function in heavy-ion collisions," in *10th International Conference on Hard and Electromagnetic Probes of High-Energy Nuclear Collisions: Hard Probes 2020* . 9, 2020. arXiv:2009.01350 [hep-ph].

[37] P. Caucal, E. Iancu, A. Mueller, and G. Soyez, "Vacuum-like jet fragmentation in a dense QCD medium," *Phys. Rev. Lett.* **120** (2018) 232001, arXiv:1801.09703 [hep-ph].

[38] P. Caucal, E. Iancu, A. H. Mueller, and G. Soyez, "A new pQCD based Monte Carlo event generator for jets in the quark-gluon plasma," *PoS* **HardProbes2018** (2019) 028, arXiv:1812.05393 [hep-ph].

[39] P. Caucal, E. Iancu, and G. Soyez, "Deciphering the z_g distribution in ultrarelativistic heavy ion collisions," *JHEP* **10** (2019) 273, arXiv:1907.04866 [hep-ph].

[40] P. Caucal, E. Iancu, and G. Soyez, "Nuclear effects on jet substructure observables at the LHC," in *28th International Conference on Ultrarelativistic Nucleus-Nucleus Collisions*. 1, 2020. arXiv:2001.09071 [hep-ph].

[41] E. Shuryak, "Physics of Strongly coupled Quark-Gluon Plasma," *Prog. Part. Nucl. Phys.* **62** (2009) 48–101, arXiv:0807.3033 [hep-ph].

[42] J.-P. Blaizot, E. Iancu, and A. Rebhan, "Thermodynamics of the high temperature quark gluon plasma," pp. 60–122. 3, 2003. arXiv:hep-ph/0303185.

[43] J. Bjorken, "Energy Loss of Energetic Partons in Quark - Gluon Plasma: Possible Extinction of High p(t) Jets in Hadron - Hadron Collisions,".

[44] E. Braaten and M. H. Thoma, "Energy loss of a heavy quark in the quark - gluon plasma," *Phys. Rev. D* **44** no. 9, (1991) 2625.

[45] M. H. Thoma and M. Gyulassy, "Quark Damping and Energy Loss in the High Temperature QCD," *Nucl. Phys. B* **351** (1991) 491–506.

[46] S. Mrowczynski, "Energy loss of a high-energy parton in the quark - gluon plasma," *Phys. Lett. B* **269** (1991) 383–388.

[47] M. Djordjevic, "Collisional energy loss in a finite size QCD matter," *Phys. Rev. C* **74** (2006) 064907, arXiv:nucl-th/0603066.

[48] A. Peshier, "The QCD collisional energy loss revised," *Phys. Rev. Lett.* **97** (2006) 212301, arXiv:hep-ph/0605294.

[49] S. Peigne and A. Peshier, "Collisional energy loss of a fast heavy quark in a quark-gluon plasma," *Phys. Rev. D* **77** (2008) 114017, arXiv:0802.4364 [hep-ph].

[50] X.-N. Wang and Y. Zhu, "Medium Modification of γ Jets in High-Energy Heavy-Ion Collisions," *Phys. Rev. Lett.* **111** (Aug, 2013) 062301.

[51] B. Zakharov, "Parton energy loss in an expanding quark-gluon plasma: Radiative versus collisional," *JETP Lett.* **86** (2007) 444–450, arXiv:0708.0816 [hep-ph].

[52] R. Baier, D. Schiff, and B. Zakharov, "Energy loss in perturbative QCD," *Ann. Rev. Nucl. Part. Sci.* **50** (2000) 37–69, arXiv:hep-ph/0002198.

[53] N. Armesto, B. Cole, C. Gale, W. A. Horowitz, P. Jacobs, S. Jeon, M. van Leeuwen, A. Majumder, B. Müller, G.-Y. Qin, C. A. Salgado, B. Schenke, M. Verweij, X.-N. Wang, and U. A. Wiedemann, "Comparison of jet quenching formalisms for a quark-gluon plasma "brick"," *Phys. Rev. C* **86** (Dec, 2012) 064904.

[54] R. Baier, Y. L. Dokshitzer, S. Peigne, and D. Schiff, "Induced gluon radiation in a QCD medium," *Phys. Lett. B* **345** (1995) 277–286, arXiv:hep-ph/9411409.

[55] R. Baier, Y. L. Dokshitzer, A. H. Mueller, S. Peigne, and D. Schiff, "The Landau-Pomeranchuk-Migdal effect in QED," *Nucl. Phys. B* **478** (1996) 577–597, arXiv:hep-ph/9604327.

[56] R. Baier, Y. L. Dokshitzer, A. H. Mueller, S. Peigne, and D. Schiff, "Radiative energy loss of high-energy quarks and gluons in a finite volume quark - gluon plasma," *Nucl. Phys. B* **483** (1997) 291–320, arXiv:hep-ph/9607355.

[57] R. Baier, Y. L. Dokshitzer, A. H. Mueller, S. Peigne, and D. Schiff, "Radiative energy loss and p(T) broadening of high-energy partons in nuclei," *Nucl. Phys. B* **484** (1997) 265–282, arXiv:hep-ph/9608322.

[58] B. Zakharov, "Radiative energy loss of high-energy quarks in finite size nuclear matter and quark - gluon plasma," *JETP Lett.* **65** (1997) 615–620, arXiv:hep-ph/9704255.

[59] B. Zakharov, "Light cone path integral approach to the Landau-Pomeranchuk-Migdal effect," *Phys. Atom. Nucl.* **61** (1998) 838–854, arXiv:hep-ph/9807540.

[60] B. Zakharov, "Fully quantum treatment of the Landau-Pomeranchuk-Migdal effect in QED and QCD," *JETP Lett.* **63** (1996) 952–957, arXiv:hep-ph/9607440.

[61] R. Baier, Y. L. Dokshitzer, A. H. Mueller, and D. Schiff, "Medium induced radiative energy loss: Equivalence between the BDMPS and Zakharov formalisms," *Nucl. Phys. B* **531** (1998) 403–425, arXiv:hep-ph/9804212.

[62] C. A. Salgado and U. A. Wiedemann, "Calculating quenching weights," *Phys. Rev. D* **68** (2003) 014008, arXiv:hep-ph/0302184.

[63] U. A. Wiedemann and M. Gyulassy, "Transverse momentum dependence of the Landau-Pomeranchuk-Migdal effect," *Nucl. Phys. B* **560** (1999) 345–382, arXiv:hep-ph/9906257.

[64] N. Armesto, C. A. Salgado, and U. A. Wiedemann, "Medium induced gluon radiation off massive quarks fills the dead cone," *Phys. Rev. D* **69** (2004) 114003, arXiv:hep-ph/0312106.

[65] R. Baier, Y. L. Dokshitzer, A. H. Mueller, and D. Schiff, "Radiative energy loss of high-energy partons traversing an expanding QCD plasma," *Phys. Rev. C* **58** (1998) 1706–1713, arXiv:hep-ph/9803473.

[66] C. A. Salgado and U. A. Wiedemann, "A Dynamical scaling law for jet tomography," *Phys. Rev. Lett.* **89** (2002) 092303, arXiv:hep-ph/0204221.

[67] M. Gyulassy, P. Levai, and I. Vitev, "Reaction operator approach to nonAbelian energy loss," *Nucl. Phys. B* **594** (2001) 371–419, arXiv:nucl-th/0006010.

[68] M. Gyulassy, P. Levai, and I. Vitev, "Jet tomography of Au+Au reactions including multigluon fluctuations," *Phys. Lett. B* **538** (2002) 282–288, arXiv:nucl-th/0112071.

[69] U. A. Wiedemann, "Gluon radiation off hard quarks in a nuclear environment: Opacity expansion," *Nucl. Phys. B* **588** (2000) 303–344, arXiv:hep-ph/0005129.

[70] P. B. Arnold, G. D. Moore, and L. G. Yaffe, "Photon emission from quark gluon plasma: Complete leading order results," *JHEP* **12** (2001) 009, arXiv:hep-ph/0111107.

[71] P. B. Arnold, G. D. Moore, and L. G. Yaffe, "Photon and gluon emission in relativistic plasmas," *JHEP* **06** (2002) 030, arXiv:hep-ph/0204343.

[72] Y. Mehtar-Tani, "Gluon bremsstrahlung in finite media beyond multiple soft scattering approximation," *JHEP* **07** (2019) 057, arXiv:1903.00506 [hep-ph].

[73] Y. Mehtar-Tani and K. Tywoniuk, "Improved opacity expansion for medium-induced parton splitting," arXiv:1910.02032 [hep-ph].

[74] M. Gyulassy and X.-n. Wang, "Multiple collisions and induced gluon Bremsstrahlung in QCD," *Nucl. Phys. B* **420** (1994) 583–614, arXiv:nucl-th/9306003.

[75] Y. Mehtar-Tani, "Relating the description of gluon production in pA collisions and parton energy loss in AA collisions," *Phys. Rev. C* **75** (2007) 034908, arXiv:hep-ph/0606236.

[76] J. Barata and Y. Mehtar-Tani, "Improved opacity expansion at NNLO for medium induced gluon radiation," arXiv:2004.02323 [hep-ph].

[77] J. Barata, Y. Mehtar-Tani, A. Soto-Ontoso, and K. Tywoniuk, "Revisiting transverse momentum broadening in dense QCD media," arXiv:2009.13667 [hep-ph].

[78] C. Andres, L. Apolinário, and F. Dominguez, "Medium-induced gluon radiation with full resummation of multiple scatterings for realistic parton-medium interactions," arXiv:2002.01517 [hep-ph].

[79] P. Arnold and S. Iqbal, "The LPM effect in sequential bremsstrahlung," *JHEP* **04** (2015) 070, arXiv:1501.04964 [hep-ph]. [Erratum: JHEP 09, 072 (2016)].

[80] P. Arnold, H.-C. Chang, and S. Iqbal, "The LPM effect in sequential bremsstrahlung 2: factorization," *JHEP* **09** (2016) 078, arXiv:1605.07624 [hep-ph].

[81] P. Arnold, H.-C. Chang, and S. Iqbal, "The LPM effect in sequential bremsstrahlung: dimensional regularization," *JHEP* **10** (2016) 100, arXiv:1606.08853 [hep-ph].

[82] P. Arnold, H.-C. Chang, and S. Iqbal, "The LPM effect in sequential bremsstrahlung: 4-gluon vertices," *JHEP* **10** (2016) 124, arXiv:1608.05718 [hep-ph].

[83] R. Baier, A. H. Mueller, D. Schiff, and D. Son, "'Bottom up' thermalization in heavy ion collisions," *Phys. Lett. B* **502** (2001) 51–58, arXiv:hep-ph/0009237.

[84] R. Baier, Y. L. Dokshitzer, A. H. Mueller, and D. Schiff, "Quenching of hadron spectra in media," *JHEP* **09** (2001) 033, arXiv:hep-ph/0106347.

[85] X.-N. Wang and X.-f. Guo, "Multiple parton scattering in nuclei: Parton energy loss," *Nucl. Phys. A* **696** (2001) 788–832, arXiv:hep-ph/0102230.

[86] A. Majumder, "The In-medium scale evolution in jet modification," arXiv:0901.4516 [nucl-th].

[87] N. Armesto, L. Cunqueiro, and C. A. Salgado, "Q-PYTHIA: A Medium-modified implementation of final state radiation," *Eur. Phys. J. C* **63** (2009) 679–690, arXiv:0907.1014 [hep-ph].

[88] K. C. Zapp, "JEWEL 2.0.0: directions for use," *Eur. Phys. J. C* **74** no. 2, (2014) 2762, arXiv:1311.0048 [hep-ph].

[89] Y. Mehtar-Tani, C. A. Salgado, and K. Tywoniuk, "Anti-angular ordering of gluon radiation in QCD media," *Phys. Rev. Lett.* **106** (2011) 122002, arXiv:1009.2965 [hep-ph].

[90] Y. Mehtar-Tani, C. Salgado, and K. Tywoniuk, "Jets in QCD Media: From Color Coherence to Decoherence," *Phys. Lett. B* **707** (2012) 156–159, arXiv:1102.4317 [hep-ph].

[91] J. Casalderrey-Solana and E. Iancu, "Interference effects in medium-induced gluon radiation," *JHEP* **08** (2011) 015, arXiv:1105.1760 [hep-ph].

[92] J. Casalderrey-Solana, Y. Mehtar-Tani, C. A. Salgado, and K. Tywoniuk, "New picture of jet quenching dictated by color coherence," *Phys. Lett. B* **725** (2013) 357–360, arXiv:1210.7765 [hep-ph].

[93] Y. Mehtar-Tani and K. Tywoniuk, "Jet (de)coherence in Pb–Pb collisions at the LHC," *Phys. Lett. B* **744** (2015) 284–287, arXiv:1401.8293 [hep-ph].

[94] Y. Mehtar-Tani and K. Tywoniuk, "Sudakov suppression of jets in QCD media," *Phys. Rev. D* **98** no. 5, (2018) 051501, arXiv:1707.07361 [hep-ph].

[95] A. Leonidov and V. Nechitailo, "Decoherence and energy loss in QCD cascades in nuclear collisions," *Eur. Phys. J. C* **71** (2011) 1537, arXiv:1006.0366 [nucl-th].

[96] F. Gelis, E. Iancu, J. Jalilian-Marian, and R. Venugopalan, "The Color Glass Condensate," *Ann. Rev. Nucl. Part. Sci.* **60** (2010) 463–489, arXiv:1002.0333 [hep-ph].

[97] S. Catani, D. de Florian, and G. Rodrigo, "Space-like (versus time-like) collinear limits in QCD: Is factorization violated?," *JHEP* **07** (2012) 026, arXiv:1112.4405 [hep-ph].

[98] Z. Bern and G. Chalmers, "Factorization in one loop gauge theory," *Nucl. Phys. B* **447** (1995) 465–518, arXiv:hep-ph/9503236.

[99] D. A. Kosower, "All order collinear behavior in gauge theories," *Nucl. Phys. B* **552** (1999) 319–336, arXiv:hep-ph/9901201.

[100] S. Catani and M. Grazzini, "Infrared factorization of tree level QCD amplitudes at the next-to-next-to-leading order and beyond," *Nucl. Phys. B* **570** (2000) 287–325, arXiv:hep-ph/9908523.

[101] R. Ellis, W. Stirling, and B. Webber, *QCD and collider physics*, vol. 8. Cambridge University Press, 2, 2011.

[102] Y. L. Dokshitzer, V. A. Khoze, A. H. Mueller, and S. Troian, *Basics of perturbative QCD*. 1991.

[103] E. Iancu, A. Leonidov, and L. D. McLerran, "Nonlinear gluon evolution in the color glass condensate. 1.," *Nucl. Phys. A* **692** (2001) 583–645, arXiv:hep-ph/0011241.

[104] J. P. Blaizot, F. Gelis, and R. Venugopalan, "High-energy pA collisions in the color glass condensate approach. 1. Gluon production and the Cronin effect," *Nucl. Phys. A* **743** (2004) 13–56, arXiv:hep-ph/0402256.

[105] F. Gelis and Y. Mehtar-Tani, "Gluon propagation inside a high-energy nucleus," *Phys. Rev. D* **73** (2006) 034019, arXiv:hep-ph/0512079.

[106] L. D. McLerran and R. Venugopalan, "Computing quark and gluon distribution functions for very large nuclei," *Phys. Rev. D* **49** (1994) 2233–2241, arXiv:hep-ph/9309289.

[107] L. D. McLerran and R. Venugopalan, "Gluon distribution functions for very large nuclei at small transverse momentum," *Phys. Rev. D* **49** (1994) 3352–3355, arXiv:hep-ph/9311205.

[108] L. D. McLerran and R. Venugopalan, "Green's functions in the color field of a large nucleus," *Phys. Rev. D* **50** (1994) 2225–2233, arXiv:hep-ph/9402335.

[109] P. Aurenche, F. Gelis, and H. Zaraket, "A Simple sum rule for the thermal gluon spectral function and applications," *JHEP* **05** (2002) 043, arXiv:hep-ph/0204146.

[110] X.-N. Wang and M. Gyulassy, "Gluon shadowing and jet quenching in A + A collisions at s**(1/2) = 200-GeV," *Phys. Rev. Lett.* **68** (1992) 1480–1483.

[111] E. Iancu, P. Taels, and B. Wu, "Jet quenching parameter in an expanding QCD plasma," *Phys. Lett. B* **786** (2018) 288–295, arXiv:1806.07177 [hep-ph].

[112] J. Bjorken, J. B. Kogut, and D. E. Soper, "Quantum Electrodynamics at Infinite Momentum: Scattering from an External Field," *Phys. Rev. D* **3** (1971) 1382.

[113] G. Feldman and P. Matthews, "Light-cone variables and the high energy limit of elastic scattering," *J. Phys. A* **6** (1973) 236–246.

[114] J. Casalderrey-Solana and C. A. Salgado, "Introductory lectures on jet quenching in heavy ion collisions," *Acta Phys. Polon.* **B38** (2007) 3731–3794, arXiv:0712.3443 [hep-ph].

[115] A. Hebecker, "Diffraction in deep inelastic scattering," *Phys. Rept.* **331** (2000) 1–115, arXiv:hep-ph/9905226.

[116] E. Meggiolaro, "Eikonal propagators and high-energy parton parton scattering in gauge theories," *Nucl. Phys.* **B602** (2001) 261–288, arXiv:hep-ph/0009261 [hep-ph].

[117] E. Iancu and R. Venugopalan, *The Color glass condensate and high-energy scattering in QCD*, pp. 249–3363. 3, 2003. arXiv:hep-ph/0303204.

[118] E. Iancu, "The non-linear evolution of jet quenching," *JHEP* **10** (2014) 095, arXiv:1403.1996 [hep-ph].

[119] P. B. Arnold, "Simple Formula for High-Energy Gluon Bremsstrahlung in a Finite, Expanding Medium," *Phys. Rev. D* **79** (2009) 065025, arXiv:0808.2767 [hep-ph].

[120] L. Landau and I. Pomeranchuk, "Electron cascade process at very high-energies," *Dokl. Akad. Nauk Ser. Fiz.* **92** (1953) 735–738.

[121] A. Migdal, "Bremsstrahlung and pair production in condensed media at high-energies," *Phys. Rev.* **103** (1956) 1811–1820.

[122] J.-P. Blaizot, F. Dominguez, E. Iancu, and Y. Mehtar-Tani, "Medium-induced gluon branching," *JHEP* **01** (2013) 143, arXiv:1209.4585 [hep-ph].

[123] L. Apolinário, N. Armesto, J. G. Milhano, and C. A. Salgado, "Medium-induced gluon radiation and colour decoherence beyond the soft approximation," *JHEP* **02** (2015) 119, arXiv:1407.0599 [hep-ph].

[124] Y. Mehtar-Tani, C. A. Salgado, and K. Tywoniuk, "The Radiation pattern of a QCD antenna in a dense medium," *JHEP* **10** (2012) 197, arXiv:1205.5739 [hep-ph].

[125] Y. Mehtar-Tani and K. Tywoniuk, "Radiative energy loss of neighboring subjets," *Nucl. Phys. A* **979** (2018) 165–203, arXiv:1706.06047 [hep-ph].

[126] T. Kinoshita, "Mass singularities of Feynman amplitudes," *J. Math. Phys.* **3** (1962) 650–677.

[127] T. Lee and M. Nauenberg, "Degenerate Systems and Mass Singularities," *Phys. Rev.* **133** (1964) B1549–B1562.

[128] G. F. Sterman and S. Weinberg, "Jets from Quantum Chromodynamics," *Phys. Rev. Lett.* **39** (1977) 1436.

[129] G. Kramer and B. Lampe, "Two Jet Cross-Section in e+ e- Annihilation," *Z. Phys. C* **34** (1987) 497. [Erratum: Z.Phys.C 42, 504 (1989)].

[130] G. P. Salam, "Towards Jetography," *Eur. Phys. J. C* **67** (2010) 637–686, arXiv:0906.1833 [hep-ph].

[131] Y. L. Dokshitzer, G. D. Leder, S. Moretti, and B. R. Webber, "Better jet clustering algorithms," *JHEP* **08** (1997) 001, arXiv:hep-ph/9707323 [hep-ph].

[132] M. Wobisch and T. Wengler, "Hadronization corrections to jet cross-sections in deep inelastic scattering," in *Workshop on Monte Carlo Generators for HERA Physics (Plenary Starting Meeting)*, pp. 270–279. 4, 1998. arXiv:hep-ph/9907280.

[133] S. Catani, Y. L. Dokshitzer, M. Seymour, and B. Webber, "Longitudinally invariant K_t clustering algorithms for hadron hadron collisions," *Nucl. Phys. B* **406** (1993) 187–224.

[134] M. Cacciari, G. P. Salam, and G. Soyez, "The anti-k_t jet clustering algorithm," *JHEP* **04** (2008) 063, arXiv:0802.1189 [hep-ph].

[135] M. Dasgupta, F. Dreyer, G. P. Salam, and G. Soyez, "Small-radius jets to all orders in QCD," *JHEP* **04** (2015) 039, arXiv:1411.5182 [hep-ph].

[136] A. Banfi, G. P. Salam, and G. Zanderighi, "Generalized resummation of QCD final state observables," *Phys. Lett. B* **584** (2004) 298–305, arXiv:hep-ph/0304148.

[137] A. Banfi, G. P. Salam, and G. Zanderighi, "Principles of general final-state resummation and automated implementation," *JHEP* **03** (2005) 073, arXiv:hep-ph/0407286.

[138] K. Konishi, A. Ukawa, and G. Veneziano, "Jet Calculus: A Simple Algorithm for Resolving QCD Jets," *Nucl. Phys. B* **157** (1979) 45–107.

[139] J. Kalinowski, K. Konishi, and T. Taylor, "Jet calculus beyond leading logarithms," *Nucl. Phys. B* **181** (1981) 221–252.

[140] D. Amati, A. Bassetto, M. Ciafaloni, G. Marchesini, and G. Veneziano, "A Treatment of Hard Processes Sensitive to the Infrared Structure of QCD," *Nucl. Phys. B* **173** (1980) 429–455.

[141] S. Catani, B. Webber, and G. Marchesini, "QCD coherent branching and semiinclusive processes at large x," *Nucl. Phys. B* **349** (1991) 635–654.

[142] S. Catani, L. Trentadue, G. Turnock, and B. R. Webber, "Resummation of large logarithms in e+ e- event shape distributions," *Nucl. Phys.* **B407** (1993) 3–42.

[143] V. A. Khoze and W. Ochs, "Perturbative QCD approach to multiparticle production," *Int. J. Mod. Phys.* **A12** (1997) 2949–3120, arXiv:hep-ph/9701421 [hep-ph].

[144] P. Cvitanović, P. Hoyer, and K. Zalewski, "Parton evolution as a branching process," *Nuclear Physics B* **176** no. 2, (1980) 429 – 448.

[145] Y. L. Dokshitzer and M. Olsson, "Jet cross-sections and multiplicities in the modified leading logarithmic approximation," *Nucl. Phys. B* **396** (1993) 137–160.

[146] S. Lupia and W. Ochs, "Hadron multiplicity as the limit of jet multiplicity at high resolution," *Nucl. Phys. B Proc. Suppl.* **64** (1998) 74–77, arXiv:hep-ph/9709246.

[147] M. Dasgupta, A. Fregoso, S. Marzani, and G. P. Salam, "Towards an understanding of jet substructure," *JHEP* **09** (2013) 029, arXiv:1307.0007 [hep-ph].

[148] S. Marzani, G. Soyez, and M. Spannowsky, *Looking inside jets: an introduction to jet substructure and boosted-object phenomenology*, vol. 958. Springer, 2019. arXiv:1901.10342 [hep-ph].

[149] A. J. Larkoski, S. Marzani, G. Soyez, and J. Thaler, "Soft Drop," *JHEP* **05** (2014) 146, arXiv:1402.2657 [hep-ph].

[150] A. J. Larkoski, S. Marzani, and J. Thaler, "Sudakov Safety in Perturbative QCD," *Phys. Rev.* **D91** no. 11, (2015) 111501, arXiv:1502.01719 [hep-ph].

[151] C. Frye, A. J. Larkoski, J. Thaler, and K. Zhou, "Casimir Meets Poisson: Improved Quark/Gluon Discrimination with Counting Observables," *JHEP* **09** (2017) 083, arXiv:1704.06266 [hep-ph].

[152] F. A. Dreyer, L. Necib, G. Soyez, and J. Thaler, "Recursive Soft Drop," *JHEP* **06** (2018) 093, arXiv:1804.03657 [hep-ph].

[153] F. A. Dreyer, G. P. Salam, and G. Soyez, "The Lund Jet Plane," *JHEP* **12** (2018) 064, arXiv:1807.04758 [hep-ph].

[154] A. Lifson, G. P. Salam, and G. Soyez, "Calculating the primary Lund Jet Plane density," arXiv:2007.06578 [hep-ph].

[155] J.-P. Blaizot and Y. Mehtar-Tani, "Jet Structure in Heavy Ion Collisions," *Int. J. Mod. Phys.* **E24** no. 11, (2015) 1530012, arXiv:1503.05958 [hep-ph].

[156] J.-P. Blaizot, F. Dominguez, E. Iancu, and Y. Mehtar-Tani, "Probabilistic picture for medium-induced jet evolution," *JHEP* **06** (2014) 075, arXiv:1311.5823 [hep-ph].

[157] B. Wu, "On p_T-broadening of high energy partons associated with the LPM effect in a finite-volume QCD medium," *JHEP* **10** (2011) 029, arXiv:1102.0388 [hep-ph].

[158] T. Liou, A. Mueller, and B. Wu, "Radiative $p_\perp$-broadening of high-energy quarks and gluons in QCD matter," *Nucl. Phys. A* **916** (2013) 102–125, arXiv:1304.7677 [hep-ph].

[159] J.-P. Blaizot and F. Dominguez, "Radiative corrections to the jet quenching parameter in dilute and dense media," *Phys. Rev. D* **99** no. 5, (2019) 054005, arXiv:1901.01448 [hep-ph].

[160] J.-P. Blaizot and Y. Mehtar-Tani, "Renormalization of the jet-quenching parameter," *Nucl. Phys. A* **929** (2014) 202–229, arXiv:1403.2323 [hep-ph].

[161] B. Wu, "Radiative energy loss and radiative $p_\perp$-broadening of high-energy partons in QCD matter," *JHEP* **12** (2014) 081, arXiv:1408.5459 [hep-ph].

[162] M. A. Escobedo and E. Iancu, "Multi-particle correlations and KNO scaling in the medium-induced jet evolution," *JHEP* **12** (2016) 104, arXiv:1609.06104 [hep-ph].

[163] J.-P. Blaizot, E. Iancu, and Y. Mehtar-Tani, "Medium-induced QCD cascade: democratic branching and wave turbulence," *Phys. Rev. Lett.* **111** (2013) 052001, arXiv:1301.6102 [hep-ph].

[164] L. Fister and E. Iancu, "Medium-induced jet evolution: wave turbulence and energy loss," *JHEP* **03** (2015) 082, arXiv:1409.2010 [hep-ph].

[165] E. Iancu and B. Wu, "Thermalization of mini-jets in a quark-gluon plasma," *JHEP* **10** (2015) 155, arXiv:1506.07871 [hep-ph].

[166] J.-P. Blaizot, L. Fister, and Y. Mehtar-Tani, "Angular distribution of medium-induced QCD cascades," *Nucl. Phys.* **A940** (2015) 67–88, arXiv:1409.6202 [hep-ph].

[167] Y. Mehtar-Tani and S. Schlichting, "Universal quark to gluon ratio in medium-induced parton cascade," *JHEP* **09** (2018) 144, arXiv:1807.06181 [hep-ph].

[168] Y. Mehtar-Tani and K. Tywoniuk, "Groomed jets in heavy-ion collisions: sensitivity to medium-induced bremsstrahlung," *JHEP* **04** (2017) 125, arXiv:1610.08930 [hep-ph].

[169] S. P. Adhya, C. A. Salgado, M. Spousta, and K. Tywoniuk, "Medium-induced cascade in expanding media," arXiv:1911.12193 [hep-ph].

[170] J. Casalderrey-Solana, E. Shuryak, and D. Teaney, "Conical flow induced by quenched QCD jets," *J. Phys. Conf. Ser.* **27** (2005) 22–31, arXiv:hep-ph/0411315.

[171] J. Ruppert and B. Muller, "Waking the colored plasma," *Phys. Lett. B* **618** (2005) 123–130, arXiv:hep-ph/0503158.

[172] H. Li, F. Liu, G.-l. Ma, X.-N. Wang, and Y. Zhu, "Mach cone induced by γ-triggered jets in high-energy heavy-ion collisions," *Phys. Rev. Lett.* **106** (2011) 012301, arXiv:1006.2893 [nucl-th].

[173] X.-N. Wang and Y. Zhu, "Medium Modification of γ-jets in High-energy Heavy-ion Collisions," *Phys. Rev. Lett.* **111** no. 6, (2013) 062301, arXiv:1302.5874 [hep-ph].

[174] Y. He, T. Luo, X.-N. Wang, and Y. Zhu, "Linear Boltzmann Transport for Jet Propagation in the Quark-Gluon Plasma: Elastic Processes and Medium Recoil," *Phys. Rev. C* **91** (2015) 054908, arXiv:1503.03313 [nucl-th]. [Erratum: Phys.Rev.C 97, 019902 (2018)].

[175] S. Cao and X.-N. Wang, "Jet quenching and medium response in high-energy heavy-ion collisions: a review," arXiv:2002.04028 [hep-ph].

[176] P. Caucal, E. Iancu, A. H. Mueller, and G. Soyez, "Jet fragmentation in a dense QCD medium," *PoS* **Confinement2018** (2019) 138, arXiv:1811.12275 [hep-ph].

[177] S. Lupia and W. Ochs, "Low and high energy limits of particle spectra in QCD jets," *The European Physical Journal C - Particles and Fields* **2** no. 2, (Apr, 1998) 307–324.

[178] E. Gerwick, S. Schumann, B. Gripaios, and B. Webber, "QCD Jet Rates with the Inclusive Generalized kt Algorithms," *JHEP* **04** (2013) 089, arXiv:1212.5235 [hep-ph].

[179] D. Pablos, "Jet Suppression From a Small to Intermediate to Large Radius," *Phys. Rev. Lett.* **124** no. 5, (2020) 052301, arXiv:1907.12301 [hep-ph].

[180] A. Buckley, J. Ferrando, S. Lloyd, K. Nordström, B. Page, M. Rüfenacht, M. Schönherr, and G. Watt, "LHAPDF6: parton density access in the LHC precision era," *Eur. Phys. J. C* **75** (2015) 132, arXiv:1412.7420 [hep-ph].

[181] T. Sjostrand, S. Mrenna, and P. Z. Skands, "PYTHIA 6.4 Physics and Manual," *JHEP* **05** (2006) 026, arXiv:hep-ph/0603175.

[182] K. Kutak, W. Pł aczek, and R. Straka, "Solutions of evolution equations for medium-induced QCD cascades," *Eur. Phys. J. C* **79** no. 4, (2019) 317, arXiv:1811.06390 [hep-ph].

[183] E. Blanco, K. Kutak, W. Płaczek, M. Rohrmoser, and R. Straka, "Medium induced QCD cascades: broadening, entropy and rescattering during branching," arXiv:2009.03876 [hep-ph].

[184] M. Cacciari, G. P. Salam, and G. Soyez, "FastJet User Manual," *Eur. Phys. J.* **C72** (2012) 1896, arXiv:1111.6097 [hep-ph].

[185] M. Cacciari, G. P. Salam, and G. Soyez, *FastJet contrib*, 2014 (accessed, March 7, 2020). https://fastjet.hepforge.org/contrib/.

[186] B. Schenke, C. Gale, and S. Jeon, "MARTINI: Monte Carlo simulation of jet evolution," *Acta Phys. Polon. Supp.* **3** (2010) 765–770, arXiv:0911.4470 [hep-ph].

[187] A. Majumder, "Incorporating Space-Time Within Medium-Modified Jet Event Generators," *Phys. Rev. C* **88** (2013) 014909, arXiv:1301.5323 [nucl-th].

[188] S. Cao and A. Majumder, "Nuclear modification of leading hadrons and jets within a virtuality ordered parton shower," *Phys. Rev. C* **101** no. 2, (2020) 024903, arXiv:1712.10055 [nucl-th].

[189] Y. He, S. Cao, W. Chen, T. Luo, L.-G. Pang, and X.-N. Wang, "Interplaying mechanisms behind single inclusive jet suppression in heavy-ion collisions," *Phys. Rev. C* **99** no. 5, (2019) 054911, arXiv:1809.02525 [nucl-th].

[190] T. Luo, S. Cao, Y. He, and X.-N. Wang, "Multiple jets and γ-jet correlation in high-energy heavy-ion collisions," *Phys. Lett. B* **782** (2018) 707–716, arXiv:1803.06785 [hep-ph].

[191] A. D. Polosa and C. A. Salgado, "Jet Shapes in Opaque Media," *Phys. Rev. C* **75** (2007) 041901, arXiv:hep-ph/0607295.

[192] N. Armesto, L. Cunqueiro, C. A. Salgado, and W.-C. Xiang, "Medium-evolved fragmentation functions," *JHEP* **02** (2008) 048, arXiv:0710.3073 [hep-ph].

[193] N. Armesto, G. Corcella, L. Cunqueiro, and C. A. Salgado, "Angular-ordered parton showers with medium-modified splitting functions," *JHEP* **11** (2009) 122, arXiv:0909.5118 [hep-ph].

[194] A. Dainese, C. Loizides, and G. Paic, "Leading-particle suppression in high energy nucleus-nucleus collisions," *Eur. Phys. J. C* **38** (2005) 461–474, arXiv:hep-ph/0406201.

[195] J. Casalderrey-Solana, D. C. Gulhan, J. G. Milhano, D. Pablos, and K. Rajagopal, "A Hybrid Strong/Weak Coupling Approach to Jet Quenching," *JHEP* **10** (2014) 019, arXiv:1405.3864 [hep-ph]. [Erratum: JHEP 09, 175 (2015)].

[196] Z. Hulcher, D. Pablos, and K. Rajagopal, "Resolution Effects in the Hybrid Strong/Weak Coupling Model," *JHEP* **03** (2018) 010, arXiv:1707.05245 [hep-ph].

[197] W. Ke, Y. Xu, and S. A. Bass, "Modified Boltzmann approach for modeling the splitting vertices induced by the hot QCD medium in the deep Landau-Pomeranchuk-Migdal region," *Phys. Rev. C* **100** no. 6, (2019) 064911, arXiv:1810.08177 [nucl-th].

[198] M. van Leeuwen, "Jet Fragmentation and Jet Shapes in JEWEL and Q-PYTHIA," in *7th International Conference on Hard and Electromagnetic Probes of High-Energy Nuclear Collisions*. 11, 2015. arXiv:1511.06108 [hep-ph].

[199] **PHENIX** Collaboration, K. Adcox *et al.*, "Suppression of hadrons with large transverse momentum in central Au+Au collisions at $\sqrt{s_{NN}}$ = 130-GeV," *Phys. Rev. Lett.* **88** (2002) 022301, arXiv:nucl-ex/0109003.

[200] **PHENIX** Collaboration, S. Adler *et al.*, "Suppressed pi0 production at large transverse momentum in central Au+ Au collisions at S(NN)**1/2 = 200 GeV," *Phys. Rev. Lett.* **91** (2003) 072301, arXiv:nucl-ex/0304022.

[201] **PHENIX** Collaboration, S. Adler *et al.*, "Identified charged particle spectra and yields in Au+Au collisions at S(NN)**1/2 = 200-GeV," *Phys. Rev. C* **69** (2004) 034909, arXiv:nucl-ex/0307022.

[202] **PHENIX** Collaboration, S. Adler *et al.*, "High p_T charged hadron suppression in Au + Au collisions at $\sqrt{s}_{NN}$ = 200 GeV," *Phys. Rev. C* **69** (2004) 034910, arXiv:nucl-ex/0308006.

[203] **PHENIX** Collaboration, S. Adler *et al.*, "Dense-Medium Modifications to Jet-Induced Hadron Pair Distributions in Au+Au Collisions at s(NN)**(1/2) = 200-GeV," *Phys. Rev. Lett.* **97** (2006) 052301, arXiv:nucl-ex/0507004.

[204] **PHENIX** Collaboration, A. Adare *et al.*, "Suppression pattern of neutral pions at high transverse momentum in Au+Au collisions at $\sqrt{s_{NN}}$ = 200 GeV and constraints on medium transport coefficients," *Phys. Rev. Lett.* **101** (2008) 232301, arXiv:0801.4020 [nucl-ex].

[205] **PHENIX** Collaboration, A. Adare *et al.*, "Dihadron azimuthal correlations in Au+Au collisions at $\sqrt{s_{NN}}$ = 200 GeV," *Phys. Rev. C* **78** (2008) 014901, arXiv:0801.4545 [nucl-ex].

[206] **STAR** Collaboration, C. Adler *et al.*, "Centrality dependence of high p_T hadron suppression in Au+Au collisions at $\sqrt{s}_{NN}$ = 130-GeV," *Phys. Rev. Lett.* **89** (2002) 202301, arXiv:nucl-ex/0206011.

[207] **STAR** Collaboration, C. Adler *et al.*, "Disappearance of back-to-back high p_T hadron correlations in central Au+Au collisions at $\sqrt{s_{NN}}$ = 200-GeV," *Phys. Rev. Lett.* **90** (2003) 082302, arXiv:nucl-ex/0210033.

[208] **STAR** Collaboration, J. Adams *et al.*, "Transverse momentum and collision energy dependence of high p(T) hadron suppression in Au+Au collisions at ultrarelativistic energies," *Phys. Rev. Lett.* **91** (2003) 172302, arXiv:nucl-ex/0305015.

[209] **STAR** Collaboration, J. Adams *et al.*, "Particle type dependence of azimuthal anisotropy and nuclear modification of particle production in Au + Au collisions at s(NN)**(1/2) = 200-GeV," *Phys. Rev. Lett.* **92** (2004) 052302, arXiv:nucl-ex/0306007.

[210] **STAR** Collaboration, J. Adams *et al.*, "Evidence from d + Au measurements for final state suppression of high p(T) hadrons in Au+Au collisions at RHIC," *Phys. Rev. Lett.* **91** (2003) 072304, arXiv:nucl-ex/0306024.

[211] **STAR** Collaboration, J. Adams *et al.*, "Distributions of charged hadrons associated with high transverse momentum particles in pp and Au + Au collisions at s(NN)**(1/2) = 200-GeV," *Phys. Rev. Lett.* **95** (2005) 152301, arXiv:nucl-ex/0501016.

[212] **STAR** Collaboration, J. Adams *et al.*, "Direct observation of dijets in central Au+Au collisions at s(NN)**(1/2) = 200-GeV," *Phys. Rev. Lett.* **97** (2006) 162301, arXiv:nucl-ex/0604018.

[213] **STAR** Collaboration, L. Adamczyk *et al.*, "Dijet imbalance measurements in $Au + Au$ and pp collisions at $\sqrt{s_{NN}} = 200$ GeV at STAR," *Phys. Rev. Lett.* **119** no. 6, (2017) 062301, arXiv:1609.03878 [nucl-ex].

[214] **STAR** Collaboration, L. Adamczyk *et al.*, "Measurements of jet quenching with semi-inclusive hadron+jet distributions in Au+Au collisions at $\sqrt{s_{NN}} = 200$ GeV," *Phys. Rev. C* **96** no. 2, (2017) 024905, arXiv:1702.01108 [nucl-ex].

[215] **STAR** Collaboration, J. Adam *et al.*, "Measurement of inclusive charged-particle jet production in Au+Au collisions at $\sqrt{s_{NN}}$=200 GeV," arXiv:2006.00582 [nucl-ex].

[216] **ATLAS** Collaboration, G. Aad *et al.*, "Measurement of inclusive jet charged-particle fragmentation functions in Pb+Pb collisions at $\sqrt{s_{NN}} = 2.76$ TeV with the ATLAS detector," *Phys. Lett. B* **739** (2014) 320–342, arXiv:1406.2979 [hep-ex].

[217] **ATLAS** Collaboration, "Measurement of nuclear modification factor $R_{\rm AA}$ in Pb+Pb collisions at $\sqrt{s_{NN}} = 5.02$TeV with the ATLAS detector at the LHC,".

[218] **CMS** Collaboration, S. Chatrchyan *et al.*, "Observation and studies of jet quenching in PbPb collisions at nucleon-nucleon center-of-mass energy = 2.76 TeV," *Phys. Rev. C* **84** (2011) 024906, arXiv:1102.1957 [nucl-ex].

[219] **CMS** Collaboration, S. Chatrchyan *et al.*, "Dependence on pseudorapidity and centrality of charged hadron production in PbPb collisions at a nucleon-nucleon centre-of-mass energy of 2.76 TeV," *JHEP* **08** (2011) 141, arXiv:1107.4800 [nucl-ex].

[220] **CMS** Collaboration, S. Chatrchyan *et al.*, "Study of high-pT charged particle suppression in PbPb compared to pp collisions at $\sqrt{s_{NN}} = 2.76$ TeV," *Eur. Phys. J. C* **72** (2012) 1945, arXiv:1202.2554 [nucl-ex].

[221] **CMS** Collaboration, S. Chatrchyan *et al.*, "Measurement of jet fragmentation into charged particles in *pp* and PbPb collisions at $\sqrt{s_{NN}} = 2.76$ TeV," *JHEP* **10** (2012) 087, arXiv:1205.5872 [nucl-ex].

[222] **CMS** Collaboration, S. Chatrchyan *et al.*, "Jet momentum dependence of jet quenching in PbPb collisions at $\sqrt{s_{NN}} = 2.76$ TeV," *Phys. Lett. B* **712** (2012) 176–197, arXiv:1202.5022 [nucl-ex].

[223] **CMS** Collaboration, V. Khachatryan *et al.*, "Charged-particle nuclear modification factors in PbPb and pPb collisions at $\sqrt{s_{\mathrm{N\,N}}} = 5.02$ TeV," *JHEP* **04** (2017) 039, arXiv:1611.01664 [nucl-ex].

[224] **ALICE** Collaboration, B. Abelev *et al.*, "Centrality Dependence of Charged Particle Production at Large Transverse Momentum in Pb–Pb Collisions at $\sqrt{s_{\mathrm{NN}}} = 2.76$ TeV," *Phys. Lett. B* **720** (2013) 52–62, arXiv:1208.2711 [hep-ex].

[225] **ALICE** Collaboration, B. Abelev *et al.*, "Measurement of charged jet suppression in Pb-Pb collisions at $\sqrt{s_{NN}} = 2.76$ TeV," *JHEP* **03** (2014) 013, arXiv:1311.0633 [nucl-ex].

[226] **ALICE** Collaboration, B. B. Abelev *et al.*, "Production of charged pions, kaons and protons at large transverse momenta in pp and Pb–Pb collisions at $\sqrt{s_{\mathrm{NN}}}$ =2.76 TeV," *Phys. Lett. B* **736** (2014) 196–207, arXiv:1401.1250 [nucl-ex].

[227] **ALICE** Collaboration, J. Adam *et al.*, "Centrality dependence of the nuclear modification factor of charged pions, kaons, and protons in Pb-Pb collisions at $\sqrt{s_{\mathrm{NN}}} = 2.76$ TeV," *Phys. Rev. C* **93** no. 3, (2016) 034913, arXiv:1506.07287 [nucl-ex].

[228] **ALICE** Collaboration, J. Adam *et al.*, "Measurement of jet suppression in central Pb-Pb collisions at $\sqrt{s_{\mathrm{NN}}} = 2.76$ TeV," *Phys. Lett. B* **746** (2015) 1–14, arXiv:1502.01689 [nucl-ex].

[229] **ALICE** Collaboration, S. Acharya *et al.*, "First measurement of jet mass in Pb–Pb and p–Pb collisions at the LHC," *Phys. Lett. B* **776** (2018) 249–264, arXiv:1702.00804 [nucl-ex].

[230] **ALICE** Collaboration, S. Acharya *et al.*, "Transverse momentum spectra and nuclear modification factors of charged particles in pp, p-Pb and Pb-Pb collisions at the LHC," *JHEP* **11** (2018) 013, arXiv:1802.09145 [nucl-ex].

[231] M. L. Miller, K. Reygers, S. J. Sanders, and P. Steinberg, "Glauber modeling in high energy nuclear collisions," *Ann. Rev. Nucl. Part. Sci.* **57** (2007) 205–243, arXiv:nucl-ex/0701025.

[232] **ATLAS** Collaboration, M. Aaboud *et al.*, "Measurement of the nuclear modification factor for inclusive jets in Pb+Pb collisions at $\sqrt{s_{\mathrm{NN}}} = 5.02$ TeV with the ATLAS detector," *Phys. Lett. B* **790** (2019) 108–128, arXiv:1805.05635 [nucl-ex].

[233] **ALICE** Collaboration, S. Acharya *et al.*, "Measurements of inclusive jet spectra in pp and central Pb-Pb collisions at $\sqrt{s_{\mathrm{NN}}} = 5.02$ TeV," *Phys. Rev. C* **101** no. 3, (2020) 034911, arXiv:1909.09718 [nucl-ex].

[234] **ATLAS** Collaboration, G. Aad *et al.*, "Measurements of the Nuclear Modification Factor for Jets in Pb+Pb Collisions at $\sqrt{s_{\mathrm{NN}}} = 2.76$ TeV with the ATLAS Detector," *Phys. Rev. Lett.* **114** no. 7, (2015) 072302, arXiv:1411.2357 [hep-ex].

[235] **CMS** Collaboration, V. Khachatryan *et al.*, "Measurement of inclusive jet cross sections in *pp* and PbPb collisions at $\sqrt{s_{NN}} = 2.76$ TeV," *Phys. Rev. C* **96** no. 1, (2017) 015202, arXiv:1609.05383 [nucl-ex].

[236] **ATLAS** Collaboration, G. Aad *et al.*, "Observation of a Centrality-Dependent Dijet Asymmetry in Lead-Lead Collisions at $\sqrt{s_{NN}} = 2.77$ TeV with the ATLAS Detector at the LHC," *Phys. Rev. Lett.* **105** (2010) 252303, arXiv:1011.6182 [hep-ex].

[237] **ATLAS** Collaboration, M. Aaboud *et al.*, "Measurement of jet p_{T} correlations in Pb+Pb and *pp* collisions at $\sqrt{s_{\mathrm{NN}}} = 2.76$ TeV with the ATLAS detector," *Phys. Lett. B* **774** (2017) 379–402, arXiv:1706.09363 [hep-ex].

[238] **ATLAS** Collaboration, M. Aaboud *et al.*, "Measurement of photon–jet transverse momentum correlations in 5.02 TeV Pb + Pb and *pp* collisions with ATLAS," *Phys. Lett. B* **789** (2019) 167–190, arXiv:1809.07280 [nucl-ex].

[239] **CMS** Collaboration, S. Chatrchyan *et al.*, "Studies of jet quenching using isolated-photon+jet correlations in PbPb and *pp* collisions at $\sqrt{s_{NN}} = 2.76$ TeV," *Phys. Lett. B* **718** (2013) 773–794, arXiv:1205.0206 [nucl-ex].

[240] **CMS** Collaboration, A. M. Sirunyan *et al.*, "Study of jet quenching with isolated-photon+jet correlations in PbPb and pp collisions at $\sqrt{s_{\mathrm{NN}}} = 5.02$ TeV," *Phys. Lett. B* **785** (2018) 14–39, arXiv:1711.09738 [nucl-ex].

[241] **CMS** Collaboration, V. Khachatryan *et al.*, "Measurement of transverse momentum relative to dijet systems in PbPb and pp collisions at $\sqrt{s_{\mathrm{NN}}} = 2.76$ TeV," *JHEP* **01** (2016) 006, arXiv:1509.09029 [nucl-ex].

[242] J. G. Milhano and K. C. Zapp, "Origins of the di-jet asymmetry in heavy ion collisions," *Eur. Phys. J. C* **76** no. 5, (2016) 288, arXiv:1512.08107 [hep-ph].

[243] J. Brewer, A. Sadofyev, and W. van der Schee, "Jet shape modifications in holographic dijet systems," arXiv:1809.10695 [hep-ph].

[244] **ATLAS** Collaboration, M. Aaboud *et al.*, "Measurement of jet fragmentation in Pb+Pb and *pp* collisions at $\sqrt{s_{NN}} = 5.02$ TeV with the ATLAS detector," *Phys. Rev.* **C98** no. 2, (2018) 024908, arXiv:1805.05424 [nucl-ex].

[245] **CMS** Collaboration, A. M. Sirunyan *et al.*, "Jet properties in PbPb and pp collisions at $\sqrt{s_{\mathrm{N\,N}}} = 5.02$ TeV," *JHEP* **05** (2018) 006, arXiv:1803.00042 [nucl-ex].

[246] **ATLAS** Collaboration, M. Aaboud *et al.*, "Comparison of Fragmentation Functions for Jets Dominated by Light Quarks and Gluons from *pp* and Pb+Pb Collisions in ATLAS," *Phys. Rev. Lett.* **123** no. 4, (2019) 042001, arXiv:1902.10007 [nucl-ex].

[247] **CMS** Collaboration, A. M. Sirunyan *et al.*, "Observation of Medium-Induced Modifications of Jet Fragmentation in Pb-Pb Collisions at $\sqrt{s_{NN}} = 5.02$ TeV Using Isolated Photon-Tagged Jets," *Phys. Rev. Lett.* **121** no. 24, (2018) 242301, arXiv:1801.04895 [hep-ex].

[248] **CMS** Collaboration, S. Chatrchyan *et al.*, "Measurement of Jet Fragmentation in PbPb and pp Collisions at $\sqrt{s_{NN}} = 2.76$ TeV," *Phys. Rev. C* **90** no. 2, (2014) 024908, arXiv:1406.0932 [nucl-ex].

[249] **ATLAS** Collaboration, M. Aaboud *et al.*, "Measurement of jet fragmentation in Pb+Pb and *pp* collisions at $\sqrt{s_{\mathrm{NN}}} = 2.76$ TeV with the ATLAS detector at the LHC," *Eur. Phys. J. C* **77** no. 6, (2017) 379, arXiv:1702.00674 [hep-ex].

[250] **CMS** Collaboration, S. Chatrchyan *et al.*, "Modification of Jet Shapes in PbPb Collisions at $\sqrt{s_{NN}} = 2.76$ TeV," *Phys. Lett. B* **730** (2014) 243–263, arXiv:1310.0878 [nucl-ex].

[251] **CMS** Collaboration, A. M. Sirunyan *et al.*, "Jet Shapes of Isolated Photon-Tagged Jets in Pb-Pb and pp Collisions at $\sqrt{s_{\mathrm{NN}}} = 5.02$ TeV," *Phys. Rev. Lett.* **122** no. 15, (2019) 152001, arXiv:1809.08602 [hep-ex].

[252] **ALICE** Collaboration, S. Acharya *et al.*, "Medium modification of the shape of small-radius jets in central Pb-Pb collisions at $\sqrt{s_{\mathrm{NN}}} = 2.76\,\mathrm{TeV}$," *JHEP* **10** (2018) 139, arXiv:1807.06854 [nucl-ex].

[253] **ALICE** Collaboration, S. Acharya *et al.*, "Measurement of jet radial profiles in Pb˘Pb collisions at $\sqrt{s_{\mathrm{NN}}} = 2.76$ TeV," *Phys. Lett. B* **796** (2019) 204–219, arXiv:1904.13118 [nucl-ex].

[254] P. Cal, F. Ringer, and W. J. Waalewijn, "The jet shape at NLL," *JHEP* **05** (2019) 143, arXiv:1901.06389 [hep-ph].

[255] **CMS** Collaboration, A. M. Sirunyan *et al.*, "Measurement of the Splitting Function in *pp* and Pb-Pb Collisions at $\sqrt{s_{\mathrm{NN}}} = 5.02$ TeV," *Phys. Rev. Lett.* **120** no. 14, (2018) 142302, arXiv:1708.09429 [nucl-ex].

[256] **ALICE** Collaboration, S. Acharya *et al.*, "Exploration of jet substructure using iterative declustering in pp and Pb-Pb collisions at LHC energies," arXiv:1905.02512 [nucl-ex].

[257] **CMS** Collaboration, A. M. Sirunyan *et al.*, "Measurement of the groomed jet mass in PbPb and pp collisions at $\sqrt{s_{\mathrm{NN}}} = 5.02$ TeV," *JHEP* **10** (2018) 161, arXiv:1805.05145 [hep-ex].

[258] **STAR** Collaboration, J. Adam *et al.*, "Measurement of Groomed Jet Substructure Observables in *pp* Collisions at $\sqrt{s} = 200$ GeV with STAR," arXiv:2003.02114 [hep-ex].

[259] **ATLAS** Collaboration, "Measurement of suppression of large-radius jets and its dependence on substructure in Pb+Pb at 5.02 TeV by ATLAS detector,".

[260] **CMS** Collaboration, V. Khachatryan *et al.*, "Decomposing transverse momentum balance contributions for quenched jets in PbPb collisions at $\sqrt{s_{\mathrm{N\,N}}} = 2.76$ TeV," *JHEP* **11** (2016) 055, arXiv:1609.02466 [nucl-ex].

[261] H. A. Andrews *et al.*, "Novel tools and observables for jet physics in heavy-ion collisions," arXiv:1808.03689 [hep-ph].

[262] M. Cacciari, G. P. Salam, and G. Soyez, "The Catchment Area of Jets," *JHEP* **04** (2008) 005, arXiv:0802.1188 [hep-ph].

[263] M. Spousta and B. Cole, "Interpreting single jet measurements in Pb + Pb collisions at the LHC," *Eur. Phys. J. C* **76** no. 2, (2016) 50, arXiv:1504.05169 [hep-ph].

[264] J. Casalderrey-Solana, Z. Hulcher, G. Milhano, D. Pablos, and K. Rajagopal, "Simultaneous description of hadron and jet suppression in heavy-ion collisions," *Phys. Rev.* **C99** no. 5, (2019) 051901, arXiv:1808.07386 [hep-ph].

[265] R. Kunnawalkam Elayavalli and K. C. Zapp, "Medium response in JEWEL and its impact on jet shape observables in heavy ion collisions," *JHEP* **07** (2017) 141, arXiv:1707.01539 [hep-ph].

[266] P. M. Chesler and K. Rajagopal, "On the Evolution of Jet Energy and Opening Angle in Strongly Coupled Plasma," *JHEP* **05** (2016) 098, arXiv:1511.07567 [hep-th].

[267] K. Rajagopal, A. V. Sadofyev, and W. van der Schee, "Evolution of the jet opening angle distribution in holographic plasma," *Phys. Rev. Lett.* **116** no. 21, (2016) 211603, arXiv:1602.04187 [nucl-th].

[268] J. Casalderrey-Solana, D. Gulhan, G. Milhano, D. Pablos, and K. Rajagopal, "Angular Structure of Jet Quenching Within a Hybrid Strong/Weak Coupling Model," *JHEP* **03** (2017) 135, arXiv:1609.05842 [hep-ph].

[269] J. Casalderrey-Solana, G. Milhano, D. Pablos, and K. Rajagopal, "Modification of Jet Substructure in Heavy Ion Collisions as a Probe of the Resolution Length of Quark-Gluon Plasma," *JHEP* **01** (2020) 044, arXiv:1907.11248 [hep-ph].

[270] Y. Tachibana, N.-B. Chang, and G.-Y. Qin, "Full jet in quark-gluon plasma with hydrodynamic medium response," *Phys. Rev. C* **95** no. 4, (2017) 044909, arXiv:1701.07951 [nucl-th].

[271] W. Chen, S. Cao, T. Luo, L.-G. Pang, and X.-N. Wang, "Effects of jet-induced medium excitation in γ-hadron correlation in A+A collisions," *Phys. Lett. B* **777** (2018) 86–90, arXiv:1704.03648 [nucl-th].

[272] Y.-T. Chien and I. Vitev, "Towards the understanding of jet shapes and cross sections in heavy ion collisions using soft-collinear effective theory," *JHEP* **05** (2016) 023, arXiv:1509.07257 [hep-ph].

[273] **JETSCAPE** Collaboration, S. Cao *et al.*, "Multistage Monte-Carlo simulation of jet modification in a static medium," *Phys. Rev.* **C96** no. 2, (2017) 024909, arXiv:1705.00050 [nucl-th].

[274] J. H. Putschke *et al.*, "The JETSCAPE framework," arXiv:1903.07706 [nucl-th].

[275] I. Gelfand and A. Yaglom, "Integration in functional spaces and it applications in quantum physics," *J. Math. Phys.* **1** (1960) 48.

[276] T. A. DeGrand, "Structure Functions of Quarks, Gluons, and Hadrons in Quantum Chromodynamics," *Nucl. Phys. B* **151** (1979) 485–517.

[277] J. Gunion and G. Bertsch, "Hadronization by color Bremsstrahlung," *Phys. Rev. D* **25** (1982) 746.

université PARIS-SACLAY

ÉCOLE DOCTORALE
Physique en
l'Île-de-France (PIF)

Titre: Evolution des jets dans un plasma quarks-gluons dense

Mots clés: Chromodynamique quantique, Plasma quarks-gluons, Jet

Résumé: Afin de sonder les propriétés du plasma quarks-gluons créé dans les collisions d'ions lourds, on mesure des observables associées à la propagation de jets en son sein. Un jet est une gerbe collimatée de hadrons de haute énergie générée par des émissions successives de partons à partir d'un quark ou d'un gluon virtuel produit par la collision. Quand de telles gerbes se propagent dans le milieu dense créé par la collision des noyaux, leurs interactions avec ce milieu entraînent une modification dans leurs propriétés, phénomène appelé "réduction des jets". Dans cette thèse, nous développons une nouvelle théorie permettant de comprendre la réduction des jets. Nous calculons pour la première fois les effets du milieu dense sur les émissions de type vide dans les jets, c'est à dire les émissions déclenchées par la virtualité initiale du parton source. Une nouvelle image physique pour l'évolution des jets est présentée, dans laquelle les émissions de type vide sont factorisées en temps par rapport à celles induites par le milieu. Cette image est markovienne, donc adaptée pour une implémentation Monte-Carlo des cascades de partons que nous développons dans le programme `JetMed`. Nous nous intéressons ensuite aux prédictions de notre théorie sur des observables de jets, et en particulier le facteur de modification nucléaire des jets R_{AA}, la distribution Soft Drop z_g et la fonction de fragmentation. Ces prédictions se révèlent être en bon accord avec les mesures du LHC.

Title: Jet evolution in a dense QCD medium

Keywords: Quantum chromodynamics, Quark-gluon plasma, Jet quenching

Abstract: To probe the properties of the quark-gluon plasma created in heavy-ion collisions, a very useful class of observables refers to the propagation of energetic jets. A jet is a collimated spray of particles generated via successive parton branchings, starting with a virtual quark or gluon produced by the collision. When such a jet is produced in the dense environment of a nucleus-nucleus collision, its interactions with the surrounding medium lead to a modification of its properties, phenomenon known as jet quenching. In this thesis, we develop a new theory to describe jet quenching. We compute for the first time the effects of the medium on multiple vacuum-like emissions, that is emissions triggered by the virtuality of the initial parton. We present a new physical picture for jet evolution, with notably a factorisation in time between vacuum-like emissions and medium-induced emissions. This picture is Markovian, hence well suited for a Monte Carlo implementation that we develop in the parton shower `JetMed`. We then investigate the phenomenological consequences of our new picture on jet observables and especially the jet nuclear modification factor R_{AA}, the Soft Drop z_g distribution and the jet fragmentation function. Our Monte Carlo results prove to be in good agreement with the LHC measurements.

Université Paris-Saclay
Espace Technologique / Immeuble Discovery
Route de l'Orme aux Merisiers RD 128 / 91190 Saint-Aubin, France